Bull-46-Pt-3

Bulletin 46
(Part 3 of 5 Parts)

ADA033421

THE SHOCK AND VIBRATION BULLETIN

Part 3
Acoustic and Vibration Testing, Impact and Blast

AUGUST 1976

302 p.

A Publication of
THE SHOCK AND VIBRATION
INFORMATION CENTER
Naval Research Laboratory, Washington, D.C.



Office of
The Director of Defense
Research and Engineering

DDC
RECEIVED
DEC 17 1976
F

Approved for public release; distribution unlimited.

Copy available to DDC does not permit fully legible reproduction

389004

SYMPOSIUM MANAGEMENT

THE SHOCK AND VIBRATION INFORMATION CENTER

Henry C. Pusey, Director
Rudolph H. Volin
J. Gordan Showalter
Barbara Szymanski
Carol Healey

Bulletin Production

Graphic Arts Branch, Technical Information Division,
Naval Research Laboratory

Bulletin 46

(Part 3 of 5 Parts)

THE SHOCK AND VIBRATION BULLETIN

AUGUST 1976

A Publication of
THE SHOCK AND VIBRATION
INFORMATION CENTER
Naval Research Laboratory, Washington, D.C.

The 46th Symposium on Shock and Vibration was held at the Royal Inn at the Wharf, San Diego, California on October 20-23, 1975. The Naval Electronics Laboratory Center and the Naval Undersea Center, San Diego, California were the hosts.

ACCESSION for
NTIS White Section ☑
DDC Buff Section ☐
UNANNOUNCED ☐
JUSTIFICATION .....
.....
BY .....
DISTRIBUTION/AVAILABILITY CODES
Dist. AVAIL. and/or SPECIAL
A

Office of
The Director of Defense
Research and Engineering

DDC
RECEIVED
DEC 17 1976
F

CONTENTS

PAPERS APPEARING IN PART 3

Partial Contents:

Acoustic and Vibration Testing

SIMULATING TACTICAL MISSILE FLIGHT VIBRATION WITH PNEUMATIC VIBRATORS 1
D. G. VandeGriff, W. D. Ayers and J. G. Maloney, General Dynamics Corporation, Pomona, California

A THREE DIRECTIONAL VIBRATION SYSTEM 15
F. M. Edgington, Army Missile Test and Evaluation Directorate, White Sands Missile Range, New Mexico

DUAL SHAKER VIBRATION FACILITY 27
C. V. Ryden, Pacific Missile Test Center, Point Mugu, California

ANALYSIS OF FATIGUE UNDER RANDOM VIBRATION 55
R. G. Lambert, General Electric Company, Utica, New York

RANDOM VIBRATION FATIGUE TESTS OF WELDBONDED AND BONDED JOINTS 73
F. Sandow, Jr., and U. Mauer, Air Force Flight Dynamics Laboratory, Wright-Patterson AFB, Ohio

FATIGUE PREDICTION FOR STRUCTURES SUBJECTED TO RANDOM VIBRATION 87
W. J. Kacena and P. J. Jones, Martin Marietta Corporation, Denver, Colorado

MEAN LIFE EVALUATION FOR A STOCHASTIC LOADING PROGRAMME WITH A FINITE NUMBER OF STRAIN LEVELS USING MINER'S RULE 97
G. Philippin, T. H. Topper and H. H. E. Leipholz, Department of Civil Engineering, University of Waterloo, Waterloo, Ontario, Canada

THERMO-ACOUSTIC SIMULATION OF CAPTIVE FLIGHT ENVIRONMENT 103
W. D. Everett, Pacific Missile Test Center, Point Mugu, California

THE EFFECT OF SIGNAL CLIPPING IN RANDOM VIBRATION TESTING 113
A. G. Ratz, Vibration Instruments Company, Anaheim, California

Impact and Blast

PREDICTION OF STANDOFF DISTANCES TO PREVENT ~~LOSS OF~~ HEARING FROM MUZZLE BLAST 129
P. S. Westine and J. C. Hokanson, Southwest Research Institute, San Antonio, Texas

A STUDY OF THE SPACE SHUTTLE SOLID ROCKET BOOSTER NOZZLE WATER IMPACT RECOVERY LOADS 149
E. A. Rawls, Chrysler Corporation - Space Division, New Orleans, Louisiana and D. A. Kross, NASA, Marshall Space Flight Center, Alabama

AN EXPERIMENTAL INVESTIGATION OF THE AXIAL FORCES GENERATED BY THE OBLIQUE WATER ENTRY OF CONES 163
J. L. Baldwin, Naval Surface Weapons Center, White Oak, Silver Spring, Maryland

DELAMINATION ~~STUDIES~~ OF IMPACTED COMPOSITE PLATES 173
C. A. Ross, University of Florida Graduate Engineering Center, Eglin Air Force Base, Florida and R. L. Sierakowski, Engineering Sciences Department University of Florida, Gainesville, Florida

SIMULATION OF X-RAY BLOWOFF IMPULSE LOADING ON A REENTRY VEHICLE AFT END USING LIGHT-INITIATED HIGH EXPLOSIVE 183
R. A. Benham, Sandia Laboratories, Albuquerque, New Mexico

AN ARC SOURCE FOR INITIATING LIGHT-SENSITIVE EXPLOSIVES 191
P. B. Higgins, Sandia Laboratories, Albuquerque, New Mexico

(cont on p. IV)

BLAST PRESSURES INSIDE AND OUTSIDE SUPPRESSIVE STRUCTURES 197
E. D. Esparza, W. E. Baker and G. A. Oldham, Southwest Research Institute, San Antonio, Texas

DEVELOPMENT OF STRUCTURES FOR INTENSE GROUND MOTION ENVIRONMENTS 215
T. O. Hunter and G. W. Barr, Sandia Laboratories, Albuquerque, New Mexico

DESIGN STUDY OF AN EXPERIMENTAL BLAST CHAMBER 227
W. E. Baker and P. A. Cox, Southwest Research Institute, San Antonio, Texas

FRAGMENT VELOCITIES FROM BURSTING CYLINDRICAL AND SPHERICAL PRESSURE VESSELS 251
R. L. Bessey and J. J. Kulesz, Southwest Research Institute, San Antonio, Texas

DESIGN OF A BLAST LOAD GENERATOR FOR OVERPRESSURE TESTING 261
P. Lieberman, J. O'Neill, D. Freeman, and A. Gibbs, TRW Defense and Space Systems Group, Redondo Beach, California

DEVELOPMENT OF A SHRAPNEL CONTAINMENT SYSTEM FOR EXPLOSIVE-TO-ELECTRIC TRANSDUCERS 277
P. H. Prasthofer, Exxon Production Research Company, Houston, Texas

ANALYSIS OF CONCRETE ARCH MAGAZINE USING FINITE ELEMENT TECHNIQUES 287
J. M. Ferritto, Civil Engineering Laboratory, Naval Construction Battalion Center, Port Hueneme, California

PAPERS APPEARING IN PART 2

KEYNOTE ADDRESS
Rear Admiral Samuel L. Gravely, Jr., Commandant 11th Naval District, San Diego, California

Invited Papers

S AND V IN T AND E
Captain Louis Colbus, USN, Ship Evaluation Division, COMOPTEVFOR, Norfolk, Virginia

REVIEW OF NUCLEAR BLAST AND SHOCK ENVIRONMENT SIMULATION
Dr. Eugene Sevin, Defense Nuclear Agency, Washington, D. C.

METRICATION IN THE NAVY
Mr. John Haas, Chairman, Navy Metrication Group, Naval Ship Engineering Center, Hyattsville, Maryland

Panel Session

VIBRATION REQUIREMENTS FOR RELIABILITY DEMONSTRATION TESTS

Shock Testing and Analysis

EARTHQUAKE TEST ENVIRONMENT - SIMULATION AND PROCEDURE FOR COMMUNICATIONS EQUIPMENT
N. J. DeCapua, M. G. Hetman, and S. C. Liu, Bell Telephone Laboratories, Whippany, New Jersey

AN ALTERNATE APPROACH TO MODAL DAMPING AS APPLIED TO SEISMIC-SENSITIVE EQUIPMENT
L. A. Bergman and A. J. Hannibal, Lord Kinematics, Erie, Pennsylvania

ACTUATOR DEVELOPMENT FOR SYSTEM-LEVEL SHOCK TESTING
G. Richard Burwell, Boeing Aerospace Company, Seattle, Washington

BOUNDED IMPACT A REPEATABLE METHOD FOR PYROTECHNIC SHOCK SIMULATION
R. T. Fandrich, Jr., Harris Electronic Systems Division, Melbourne, Florida

DYNAMIC RESPONSE OF ELECTRICAL CABLES TO SHOCK MOTION
R. W. Doll, TRW Defense and Space Systems Group, Redondo Beach, California

AUTOMATED WHEEL-ON-THE-GROUND DETECTION BY DERAILMENT IMPACT SENSING ANALYSIS AND FULL SCALE TEST RESULTS
W. W. Wassmann and J. H. Armstrong, Naval Surface Weapons Center, White Oak, Silver Spring, Maryland

THE DEVELOPMENT OF A GENERALIZED IMPACT RESPONSE MODEL FOR A BULK CUSHIONING MATERIAL
D. McDaniel, U. S. Army Missile Command, Redstone Arsenal, Alabama and R. M. Wyskida, The University of Alabama in Huntsville, Huntsville, Alabama

BARREL-TAMPED, EXPLOSIVELY PROPELLED PLATES FOR OBLIQUE IMPACT EXPERIMENTS
F. H. Mathews and B. W. Duggin, Sandia Laboratories, Albuquerque, New Mexico

ESTIMATION OF SHIP SHOCK PARAMETERS FOR CONSISTENT DESIGN AND TEST SPECIFICATION
G. C. Hart and T. K. Hasselman, J. H. Wiggins Company, Redondo Beach, California and W. N. Jones, Naval Weapons Center, China Lake, California

PLANE HARMONIC WAVES IN LIQUID OVERLYING A MONOCLINIC, CRYSTALLINE LAYER
S. De, Old Engineering Office, Birbhum, West Bengal (India)

POWER SERIES EXPANSION OF THE DYNAMIC STIFFNESS MATRIX INCLUDING ROTARY INERTIA AND SHEAR DEFORMATION
M. Paz and L. Dung, University of Louisville, Louisville, Kentucky

EFFECT OF PHASE SHIFT ON SHOCK RESPONSE
C. T. Morrow, Vought Corporation Advanced Technology Center, Dallas, Texas

Fluid-Structure Topics

DETERMINATION OF DYNAMIC LOADS FROM MISSILE MODEL WIND TUNNEL DATA
P. G. Bolds and D. K. Barrett, Air Force Flight Dynamics Laboratory, Wright-Patterson AFB, Ohio

FEASIBILITY STUDY OF AN ACOUSTIC ENCLOSURE FOR SHUTTLE PAYLOADS
M. Ferrante and C. V. Stahle, General Electric Space Division, Philadelphia, Pennsylvania and F. J. On, NASA Goddard Space Flight Center, Greenbelt, Maryland

EXPERIMENTAL DETERMINATION OF ROCKET MOTOR STRUCTURAL RESPONSE TO INTERNAL ACOUSTIC EXCITATION
F. R. Jensen and L. R. West, Hercules Incorporated, Bacchus Works, Magna, Utah

VISCOELASTIC DAMPING SYSTEM USE AS A REMEDY FOR POGO EFFECT ON THE DIAMANT SATELLITE LAUNCH VEHICLE
M. Poizat and P. Vialatoux, Societe METRAVIB, Ecully - France and P. Cochery and M. Vedrenne, Centre National D'Etudes Spatiales, Evry - France

VIBRATION AND STABILITY OF FLUID-CONVEYING PIPES
H. Lin and S. Chen, Argonne National Laboratory, Argonne, Illinois

EXPERIMENTAL LIQUID/POSITIVE EXPULSION BLADDER DYANMICS
M. Wohltmann, Martin Marietta Aerospace, Orlando, Florida

PAPERS APPEARING IN PART 4

Measurements and Criteria Development

BOUNDARY LAYER FLUCTUATING PRESSURE DATA OBTAINED IN A HIGH BACKGROUND NOISE ENVIRONMENT ON A SMALL SCALE WIND TUNNEL MODEL
G. L. Getline, General Dynamics Convair Division, San Diego, California

DYNAMIC MEASUREMENT OF LOW-FREQUENCY COMPONENTS OF TRACK-INDUCED RAILCAR WHEEL ACCELERATIONS
S. A. Macintyre, C. T. Jones and R. E. Scofield, ENSCO, Inc., Springfield, Virginia

DEVELOPMENT AND APPLICATION OF A MINIATURE RECORDER/ANALYZER FOR MEASUREMENT OF THE TRANSPORTATION ENVIRONMENT
M. A. Venetos, Air Force Packaging Evaluation Agency, Wright-Patterson Air Force Base, Ohio and J. J. Lorusso, Bolt, Beranek and Newman, Inc., Cambridge, Massachusetts

ADVANCES IN SHIPPING DAMAGE PREVENTION
H. Caruso and W. Silver II, Westinghouse Electric Corporation, Baltimore, Maryland

COHERENCE METHODS USED TO DEFINE TRANSMISSION PATHS IN AIRBORNE ANTENNA VIBRATION
J. Pearson and R. E. Thaller, Air Force Flight Dynamics Laboratory, Wright-Patterson Air Force Base, Ohio

DEVELOPMENT OF COMPONENT RANDOM VIBRATION REQUIREMENTS CONSIDERING RESPONSE SPECTRA
C. V. Stahle and H. R. Gongloff, General Electric Company, Space Division, Philadelphia, Pennsylvania and W. B. Keegan, NASA-Goddard Space Flight Center, Greenbelt, Maryland

STATISTICAL DETERMINATION OF RANDOM VIBRATION REQUIREMENTS FOR SUBASSEMBLY TESTS
J. M. Medaglia, General Electric Company-Space Division, Philadelphia, Pennsylvania

DEVELOPMENT OF SHIP SHOCK LOADS TEST FOR THE RGM-84A MISSILE (HARPOON)
T. L. Eby, Pacific Missile Test Center, Point Mugu, California

EVALUATION OF THE HARPOON MISSILE AIRCRAFT LAUNCH EJECTION SHOCK ENVIRONMENT
J. A. Zara and J. L. Gubser, McDonnell Douglas Astronautics Corporation, St. Louis, Missouri, A. G. Piersol, Bolt, Beranek and Newman, Canoga Park, California and W. N. Jones, Naval Weapons Center, China Lake, California

Isolation and Damping

THE MEASUREMENT OF DAMPING AND THE DETECTION OF DAMAGES IN STRUCTURES BY THE RANDOM DECREMENT TECHNIQUE
J. C. S. Yang and D. W. Caldwell, Mechanical Engineering Department, University of Maryland, College Park, Maryland

RESPONSE ANALYSIS OF A SYSTEM WITH DISCRETE DAMPERS
G. K. Hobbs, D. J. Kuyper and J. J. Brooks, Santa Barbara Research Center, Goleta, California

THE APPLICATION OF ELASTOMERIC LEAD-LAG DAMPERS TO HELICOPTER ROTORS
D. P. McGuire, Lord Kinematics, Erie, Pennsylvania

EVALUATION OF ISOLATION MOUNTS IN REDUCING STRUCTUREBORNE NOISE
T. F. Derby, Barry Division, Barry Wright Corporation, Watertown, Massachusetts

POLYURETHANE FOAM ISOLATORS FOR SHOCK ISOLATED EQUIPMENT FLOORS
W. C. Gustafson, Boeing Aerospace Company, Seattle, Washington

COMPONENT TESTING OF LIQUID SHOCK ISOLATORS AND ELASTOMERS IN SUPPORT OF RECENT SHOCK ISOLATION SYSTEM DESIGNS
J. P. Ashley, Boeing Aerospace Company, Seattle, Washington

ANALYSIS AND TESTING OF FULL SCALE SHOCK ISOLATED EQUIPMENT FLOORS
W. R. Milne, Boeing Aerospace Company, Seattle, Washington

FOCALIZATION OF SEMI-SYMMETRIC SYSTEMS
A. J. Hannibal, Lord Kinematics, Erie, Pennsylvania

THE USE OF GENERAL PURPOSE COMPUTER PROGRAMS TO DERIVE EQUATIONS OF MOTION FOR OPTIMAL ISOLATION STUDIES
W. D. Pilkey, University of Virginia, Charlottesville, Virginia
Y. H. Chen, RCA/Astro-Electronics Division, Princeton New Jersey,
and A. J. Kalinowski, Naval Underwater Systems Center,
New London, Connecticut

PARTICULATE SILICONE RUBBER: AN EFFECTIVE, REMOVABLE ENCAPSULANT FOR ELECTRONIC PACKAGING
R. R. Palmisano and D. W. Neily, Harry Diamond Laboratories,
Adelphi, Maryland

PAPERS APPEARING IN PART 5

Dynamic Analysis

DYNAMIC EARTHQUAKE ANALYSIS OF A BOTTOM SUPPORTED INDUSTRIAL BOILER
N. J. Monroe and N. Dasa, The Babcock & Wilcox Company, North Canton, Ohio

DYNAMIC RESPONSE OF LAMINATED COMPOSITE SHELLS
C. T. Sun, Department of Engineering Science and Mechanics and
Engineering Research Institute, Iowa State University, Ames, Iowa

SPECTRUM AND RMS LEVELS FOR STRESSES IN CLOSELY SPACED STIFFENED CYLINDRICAL SHELLS, SUBJECTED TO ACOUSTIC EXCITATION
G. Maymon, Armament Development Authority, Haifa, Israel

ANALYSIS OF SPACE FRAMEWORKS CONTAINING CURVED BEAMS
M. A. Cassaro and M. Paz, University of Louisville, Louisville, Kentucky

THE VIBRATIONS IN CONSTRUCTION EQUIPMENT
P. A. Drakatos, Institute of Technology, University of Patras, Patras, Greece

MODEL OF SOIL-VIBRATING MACHINE
P. A. Drakatos, Institute of Technology, University of Patras, Patras, Greece

A GENERAL PURPOSE COMPUTER GRAPHICS DISPLAY SYSTEM FOR FINITE ELEMENT MODES
H. N. Christiansen, Brigham Young University, Provo, Utah, University of Utah, Salt Lake City, Utah, B. E. Brown, University of Utah, Salt Lake City, Utah and L. E. McCleary, Naval Undersea Center, San Diego, California

VIBRATION CHARACTERISTICS OF 1/8-SCALE DYNAMIC MODELS OF THE SPACE SHUTTLE SOLID ROCKET BOOSTERS
S. A. Leadbetter, W. B. Stephens, J. L. Sewall and J. W. Majka, NASA Langley Research Center, Hampton, Virginia and J. R. Barrett, Rockwell International, NASA Langley Research Center, Hampton, Virginia

LONGITUDINAL VIBRATION CHARACTERISTICS OF THE SPACE SHUTTLE SOLID ROCKET BOOSTER TEST SEGMENT
J. C. Bartlett and D. L. Linton, IBM Federal Systems Division,
Huntsville, Alabama

MECHANICAL IMPEDANCE TECHNIQUES IN SMALL BOAT DESIGN
B. E. Douglas and H. S. Kenchington, David W. Taylor Naval Ship R&D Center, Annapolis Laboratory, Annapolis, Maryland

FREQUENCIES AND MODE SHAPES OF GEOMETRICALLY AXISYMMETRIC STRUCTURES: APPLICATION TO A JET ENGINE
P. Trompette and M. Lalanne, Institut National des Sciences Appliquees,
Villeurbanne, France

EIGENSOLUTION SENSITIVITY TO PARAMETRIC MODEL PERTURBATIONS
C. W. White and B. D. Maytum, Martin Marietta Corporation, Denver, Colorado

MATRIX METHODS FOR THE ANALYSIS OF ELASTICALLY SUPPORTED ISOLATION SYSTEMS
G. L. Fox, Barry Division, Barry Wright Corporation, Burbank, California

AXISYMMETRIC STRUCTURAL LOADING FOR A TRAVELING OVERPRESSURE PULSE
J. J. Farrell, D. J. Ness, and G. M. Teraoka, TRW Defense and Space Systems Group, Redondo Beach, California

Modal Test and Analysis

MODALAB A NEW SYSTEM FOR STRUCTURAL DYNAMIC TESTING
R. C. Stroud, Lockheed Missiles and Space Company, Sunnyvale, California, S. Smith and G. A. Hamma, Lockheed Missiles and Space Company, Palo Alto, California

DYNAMIC BEHAVIOR OF COMPLEX STRUCTURES, USING PART EXPERIMENT, PART THEORY
J. C. Cromer and M. Lalanne, Institut National des Sciences Appliquees Villeurbanne, France

THE EXPERIMENTAL DETERMINATION OF VIBRATION PARAMETERS FROM TIME RESPONSES
S. R. Ibrahim, NASA Langley Research Center, Hampton, Virginia and E. C. Mikulcik, Department of Mechanical Engineering, The University of Calgary, Calgary, Alberta, Canada

IDENTIFICATION OF STRUCTURAL MODAL PARAMETERS BY DYNAMIC TESTS AT A SINGLE POINT
N. Miramand, J. F. Billaud, F. Leleux, Centre Technique des Industries Mecaniques, SENLIS (FRANCE) and J. P. Kernevez, Universite de Technologie de Compiegne COMPIEGNE (FRANCE)

EXPERIENCES IN USING MODAL SYNTHESIS WITHIN PROJECT REQUIREMENTS
J. A. Garba, B. K. Wada and J. C. Chen, Jet Propulsion Laboratory, Pasadena, California

VIBRATION ANALYSIS OF THE BSE SPACECRAFT USING MODAL SYNTHESIS AND THE DYI. .. IIC TRANSFORMATION
E. J. Kuhar, General Electric Company, Valley Forge, Pennsylvania

VIBRATION ANALYSIS OF STRUCTURES USING FIXED-INTERFACE COMPONENT MODES
C. Szu, TRW Defense and Space Systems Group, Redondo Beach, California

AN INTRODUCTION TO THE APPLICATION OF MODAL ANALYSIS SURVEYS IN THE TEST LABORATORY
H. Caruso, Westinghouse Electric Corporation, Baltimore, Maryland

ACOUSTIC AND VIBRATION TESTING

SIMULATING TACTICAL MISSILE FLIGHT VIBRATION WITH PNEUMATIC VIBRATORS

Don G. VandeGriff, Weston D. Ayers and John G. Maloney
General Dynamics Corporation
Pomona, California

The use of multiple pneumatic vibrators for the simulation of simultaneous three axis broadband random flight vibration is presented for a tactical missile application. The acceleration spectral densities measured during the pneumatic vibration test compare favorably with those telemetered during flight of the tactical missile.

INTRODUCTION

The electronic complexity of tactical missiles is such that a thorough functional checkout under vibration is required at the full missile assembly level during engineering development. Typically such electrical checkout facilities do not include large dedicated electrodynamic drivers for vibration testing. This situation has brought about the need for a portable, simple to use and low cost vibration system to approximate simultaneous three axis broadband random flight vibration for tactical missiles.

TACTICAL MISSILE FLIGHT VIBRATION

The vibration experienced in flight by most tactical missiles is characterized as having broadband random waveform. Random vibration is typically described in terms of acceleration spectral density (ASD). The ASD is the mean square acceleration per unit bandwidth as a function of frequency.

The ASD of two samples of vibration measured on a version of Standard Missile are presented in Figure 1. The vibration measurements, one of which is in the radial (flight vertical) direction and the other of which is in the longitudinal direction, were made with Endevco 2221 D accelerometers located on the inside diameter of the airframe. The accelerometers were attached, using a small mounting block, to a region in the mid-section of the missile which is on the order of 13 millimeters (0.5 inches) thick. The missile vibration data were transmitted during flight using an FM telemetry system with a data bandwidth of 20 to 5000 Hz for the vibration channels. One of the more interesting observations that can be made from the measured flight vibration data is that there is considerable frequency content above the typical vibration specification upper frequency limit of 2000 Hz.

PNEUMATIC VIBRATORS

The missile checkout facilities at General Dynamics, Pomona Division have used a three dimensional hydraulic shaker system for nearly twenty years. The shaker system, which was mounted inside an empty rocket motor, was capable of 136 kilograms (300 pounds) peak sinusoidal force capability at frequencies up to 600 Hz. The shaker system normally took a full shift to set up and required considerable maintenance. When the vibration test requirements for broadband random waveform and an extended frequency content matured, the possibility of using pneumatic vibrators was explored.

Pneumatic vibrators are used in commercial applications such as grain conveyors and parts sorters. Three different sizes of vibrators are shown in Figure 2. The three sizes, which were purchased from the Cleveland Vibrator Company, have piston diameters of 16, 32 and 38 millimeters (.625, 1.25 and 1.5 inches). The vibrators consist of five parts; a free piston, a bias spring, a housing and two end caps. The largest of the three vibrators is shown disassembled in Figure 3. The porting, which induces and sustains the oscillatory motion of the piston, is located entirely in the housing on the largest vibrator.

When driven by compressed air above a threshold of about 1 atmosphere gage pressure the piston oscillates thru its stroke and produces impacts at a repetition rate of 30 to 120 Hz depending on the pneumatic vibrator size and on the magnitude of the supply pressure.

The vibration characteristics of the smallest of the three vibrators have been explored using the set up illustrated in Figure 4. The vibrator was attached to a 12.5 kilogram (27.6 pound) steel block. An accelerometer was mounted on the block opposite the vibrator. The acceleration time histories resulting from a low pressure and then a high pressure are presented in Figure 5. The repetition rate resulting from the lower pressure is approximately 80 Hz and the repetition rate with the higher pressure is about 110 Hz. The ringing of a 3500 Hz resonance is apparent for both pressure levels. The ASD's of the measured acceleration time histories are shown in Figures 6 and 7 for the low and high pressures, respectively. The ASD's are seen to exhibit strong content at nearly all harmonics of the repetition rate. The variation of repetition rate with pressure can be used to smear the frequency content that is produced by the vibrator. The ASD of the acceleration time history resulting from various pressure levels is presented in Figure 8. It is seen that amplitude modulating the pressure supply results in a characteristically smoother ASD than that resulting from a constant pressure.

TEST DEVELOPMENT

The development of the pneumatic vibrator system for the tactical missile application proceeded in a cut and try fashion. One of the first discoveries was that the repetition rate of the vibrator locked onto the first body bending mode frequency when a constant pressure was applied to the vibrator. This resulted in strong excitation of the first body mode with negligible energy at the higher frequencies. It was discovered that modulating the supply pressure prevented the vibrator from locking onto the first body mode and as mentioned earlier the modulation also produces a beneficial smearing of the vibration frequency content.

To minimize the effect on the electronic checkout of the missiles, inert rocket motors have been modified for direct attachment of the vibrators. At the other locations along the airframe a split clamp attachment is utilized which results in no modification to the flight hardware. A total of nine vibrators driven by four pneumatic control channels are utilized. The test configuration is illustrated in Figure 9. A single longitudinal vibrator, attached to the aft closure of the rocket motor, is driven by one of the pneumatic channels. The other eight vibrators apply radial excitation along the airframe. The four pneumatic control channels permit control of the vibration responses in various regions of the missiles. The pneumatic control console is shown in Figure 10.

TEST RESULTS

The pneumatic vibrators have produced rather respectable broadband vibration levels on the Standard Missile. By using pressure settings in the range of 1.4 to 2.7 atmospheres the following broadband (1-5000 Hz) root mean square (RMS) accelerations were achieved.

Missile Region	Broadband Response - g RMS		
	Vertical	Horizontal	Longitudinal
Forward Section	6.8	6.5	6.5
Mid-Section	8.9	11.2	4.4
Aft Section	10.0	14.4	10.6

These overall RMS levels generated by the pneumatic vibration system, are in general agreement with the maximum levels measured in flight on this version of Standard Missile. Comparisons of the acceleration spectral densities of the ground test and flight vibration data are presented in Figures 11 thru 13. Although the acceleration spectral densities are by no means overlays, the spectra induced by the pneumatic vibrators are of the same general shape as those of the flight measurements.

When pneumatic vibrators excite the missile with its numerous resonances, the acceleration waveform that results bears a resemblance to broadband random. A comparison of the instantaneous acceleration distributions for measured flight data, for that resulting from the pneumatic vibrator system and for a Gaussian distribution is presented in Figure 14. It is seen that the distribution for the measured flight is nearly Gaussian. The distribution resulting from the pneumatic vibrators is bell shaped but with more activity near zero and slightly more activity above 2.5σ than the Gaussian distribution.

CONCLUSIONS

The pneumatic vibrator system has been used as an integral part of missile checkout of about thirty engineering development and limited production missiles over the past two years at General Dynamics, Pomona Division. The pneumatic vibrator concept has proven to be a simple to use, low cost means of approximating three axis broadband random flight vibration for tactical missiles.

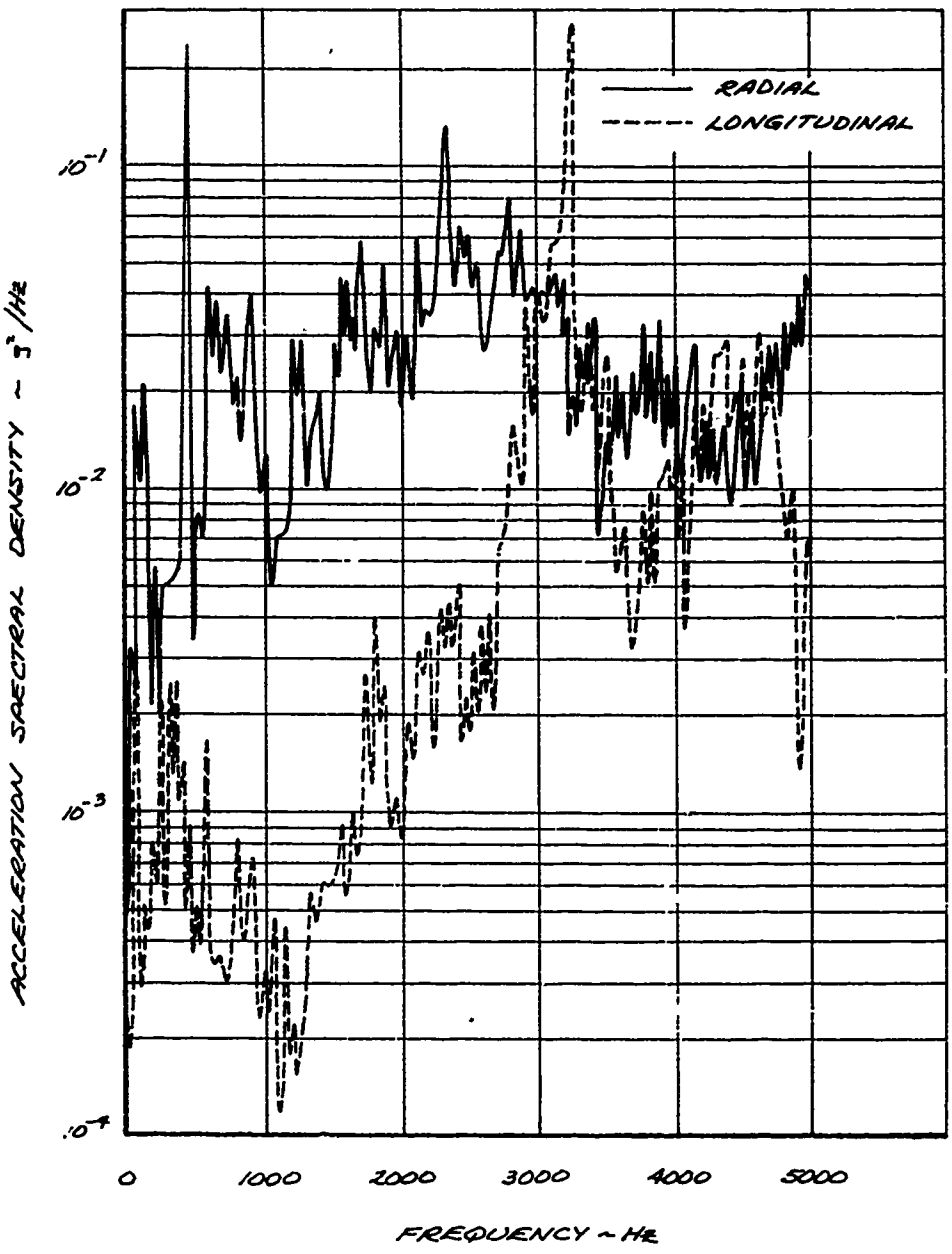


FIGURE 1 - TACTICAL MISSILE FLIGHT VIBRATION MEASURED IN MID-SECTION

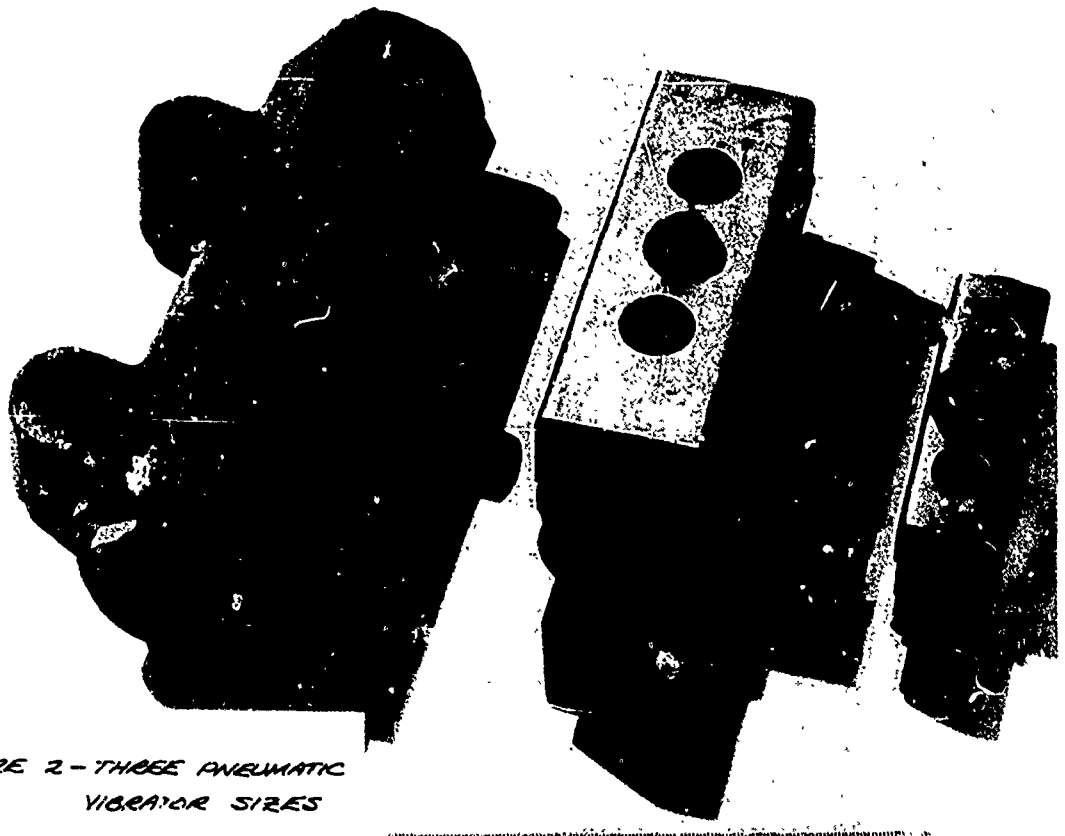
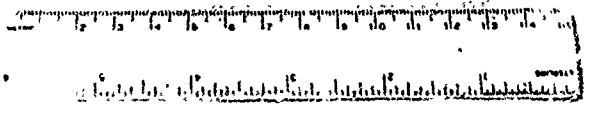


FIGURE 2 – THREE PNEUMATIC VIBRATOR SIZES



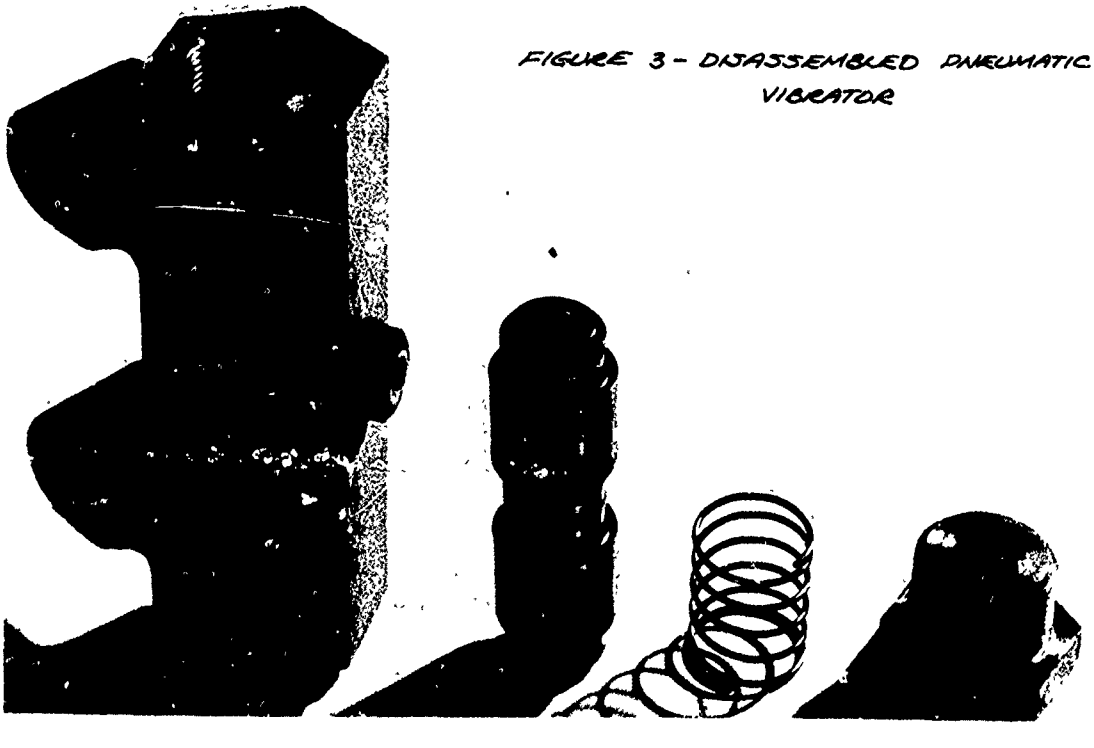


FIGURE 3 – DISASSEMBLED PNEUMATIC VIBRATOR

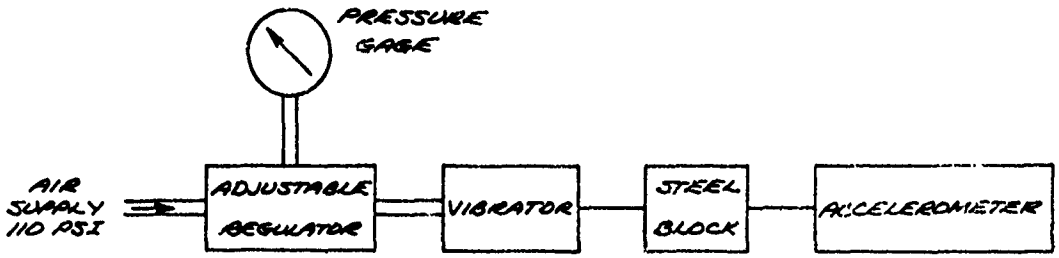


FIGURE 4 PNEUMATIC VIBRATOR RESPONSE CHARACTERISTICS TEST SET UP

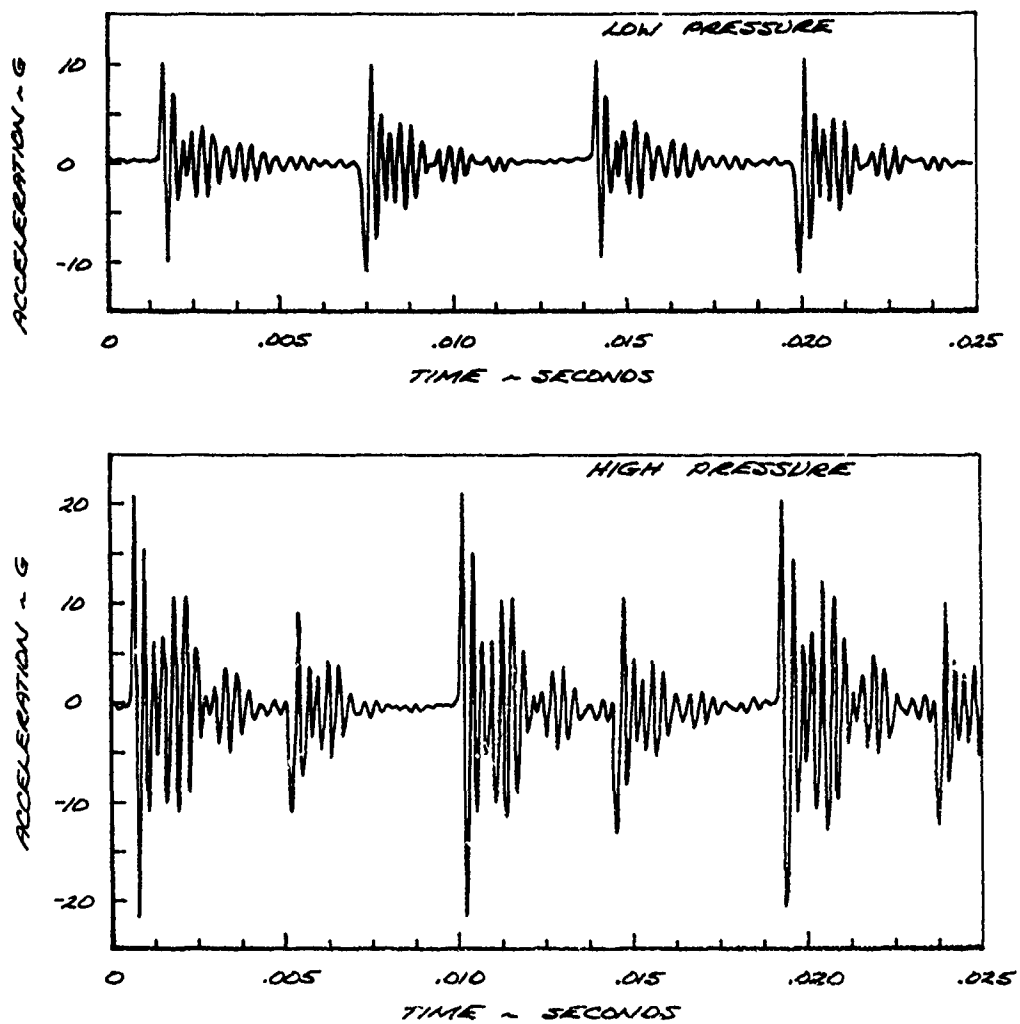


FIGURE 5 - PNEUMATIC VIBRATOR OUTPUT CHARACTERISTICS ACCELERATION TIME HISTORIES

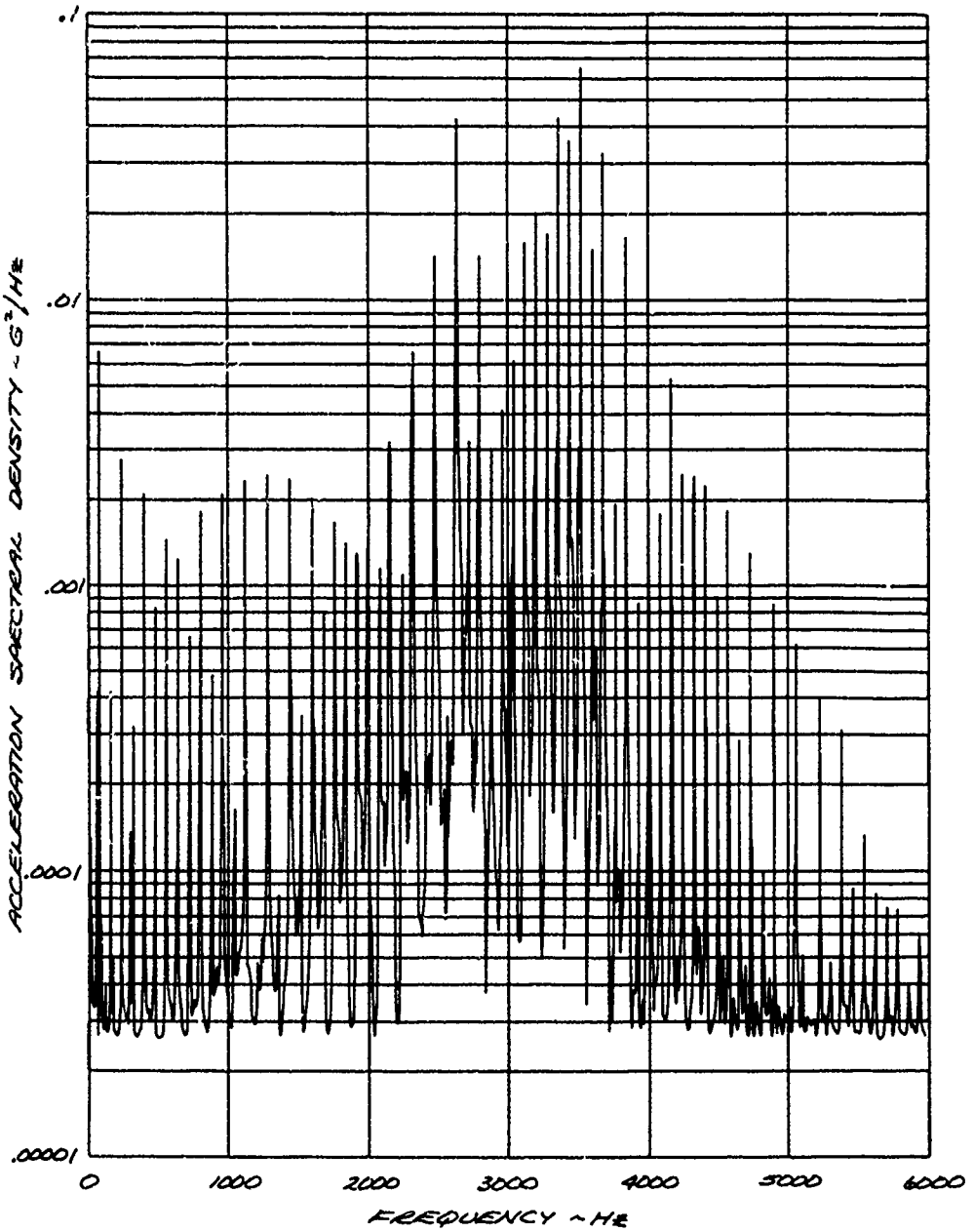


FIGURE 6 - PNEUMATIC VIBRATOR OUTPUT CHARACTERISTICS
ACCELERATION SPECTRAL DENSITY LOW PRESSURE

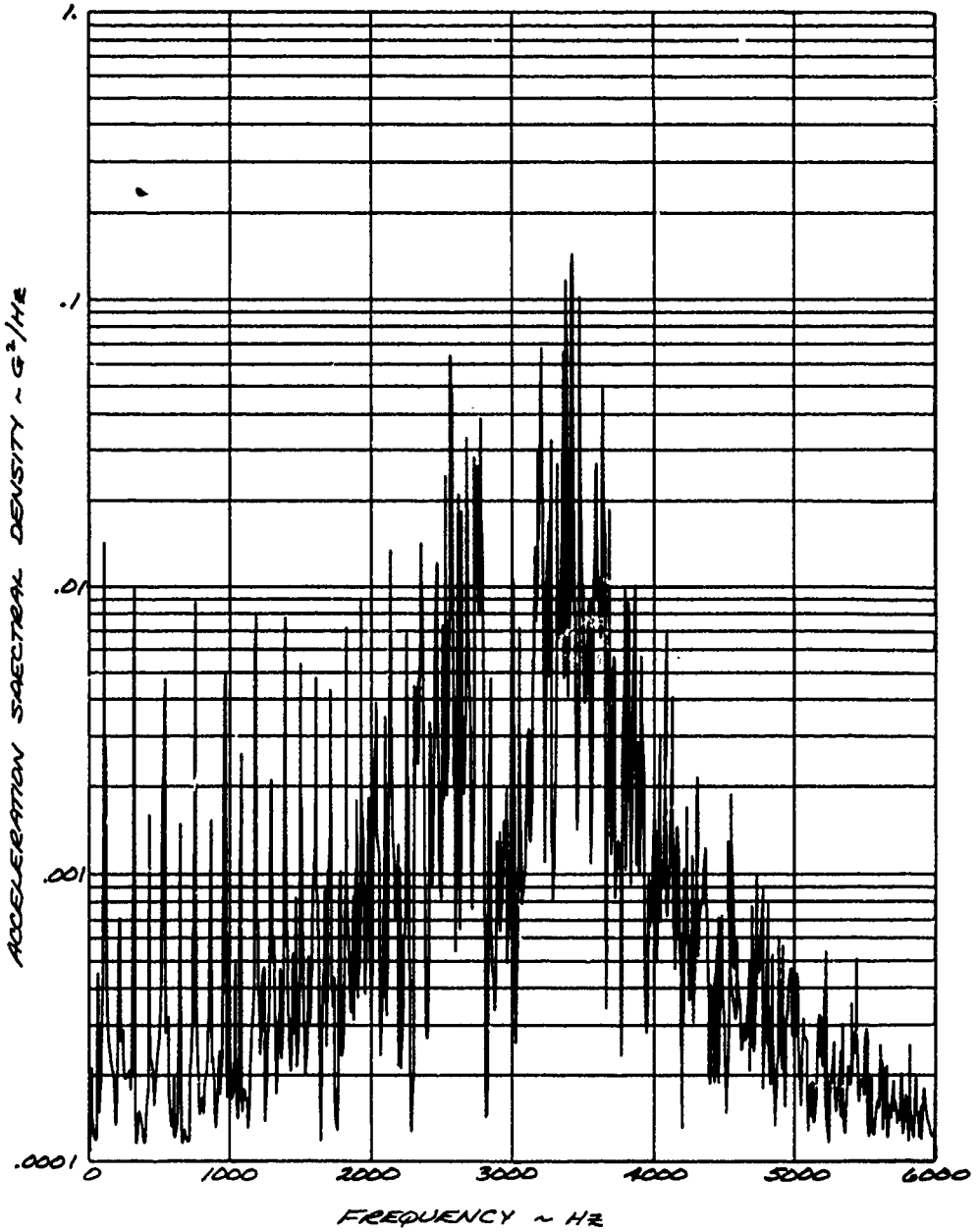


FIGURE 7 - PNEUMATIC VIBRATOR OUTPUT CHARACTERISTICS
ACCELERATION SPECTRAL DENSITY HIGH PRESSURE

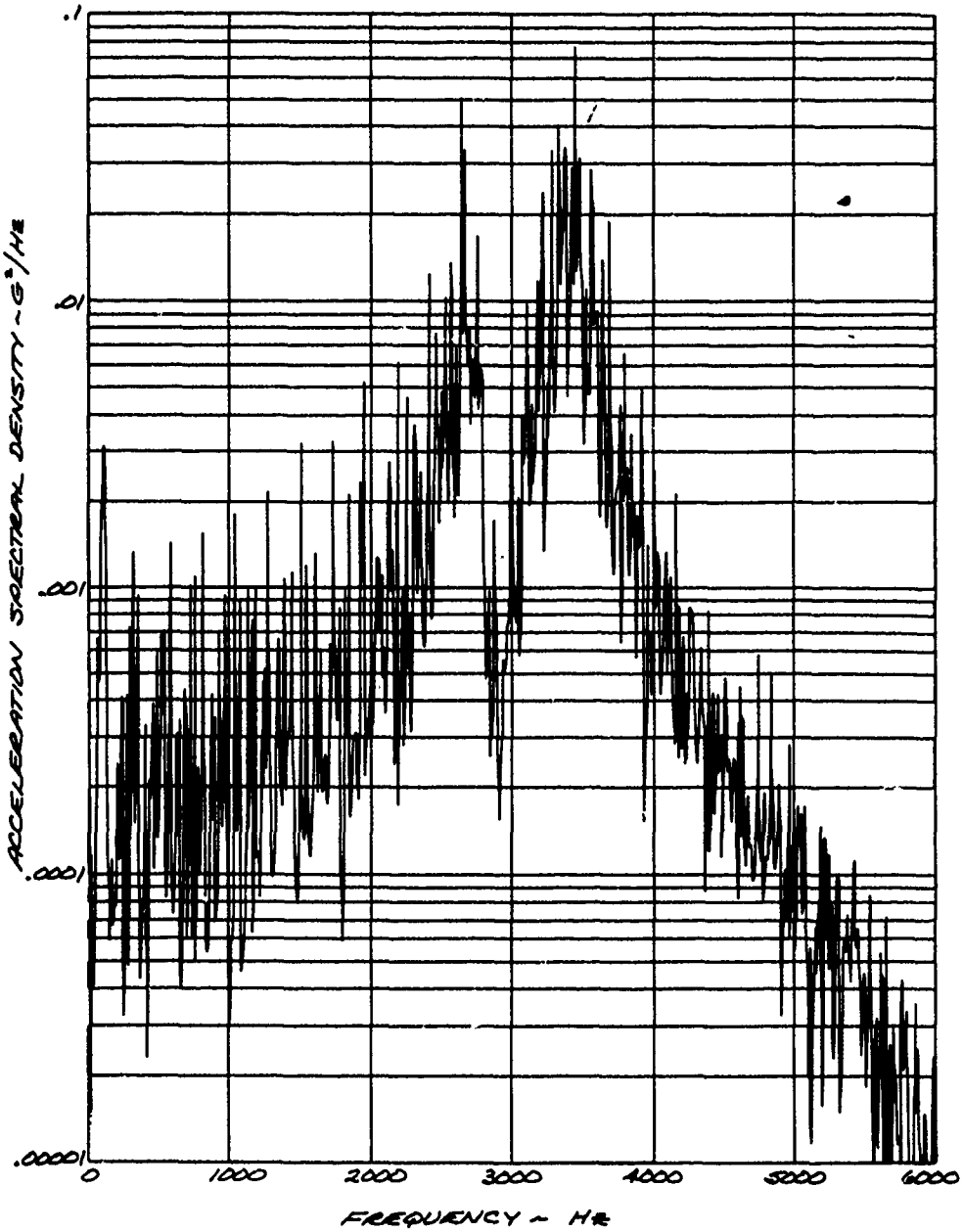


FIGURE 8 - PNEUMATIC VIBRATOR OUTPUT CHARACTERISTICS
ACCELERATION SPECTRAL DENSITY MODULATED PRESSURE

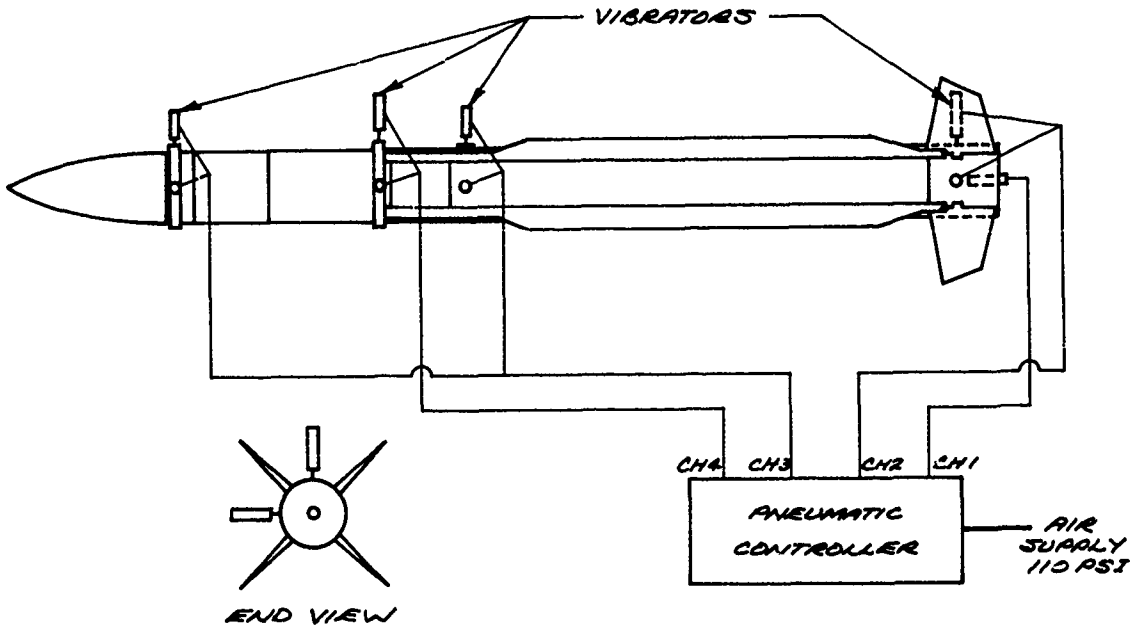


FIGURE 9 - TACTICAL MISSILE WITH PNEUMATIC VIBRATORS

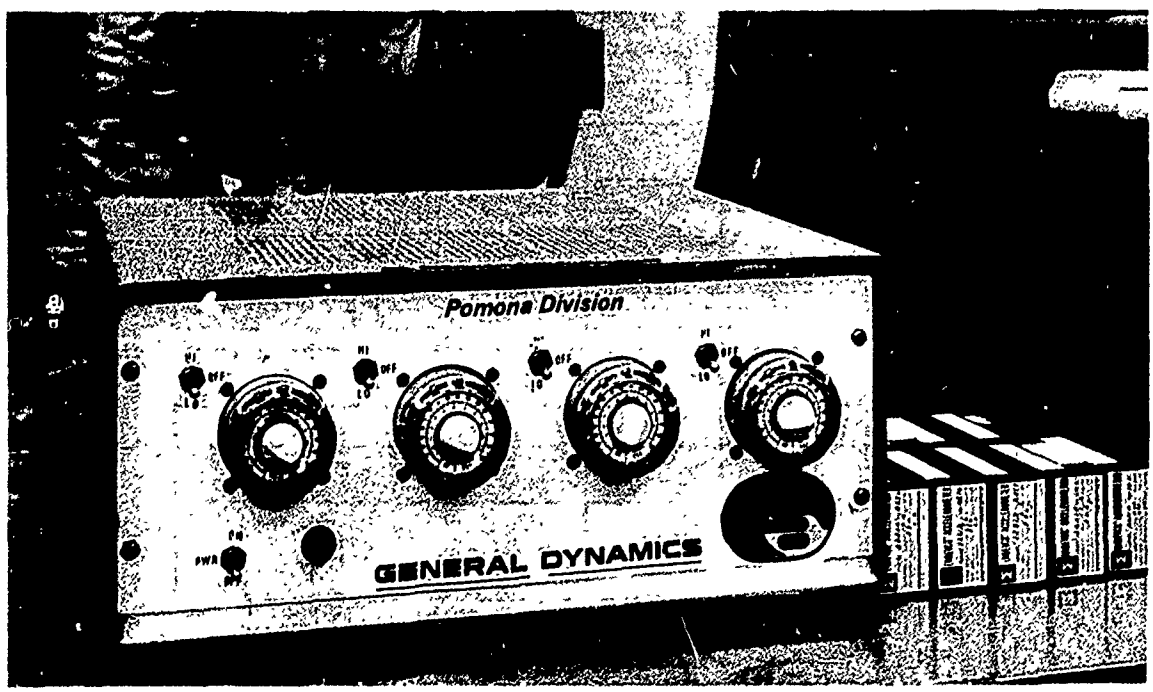


FIGURE 10 - PNEUMATIC CONTROL CONSOLE

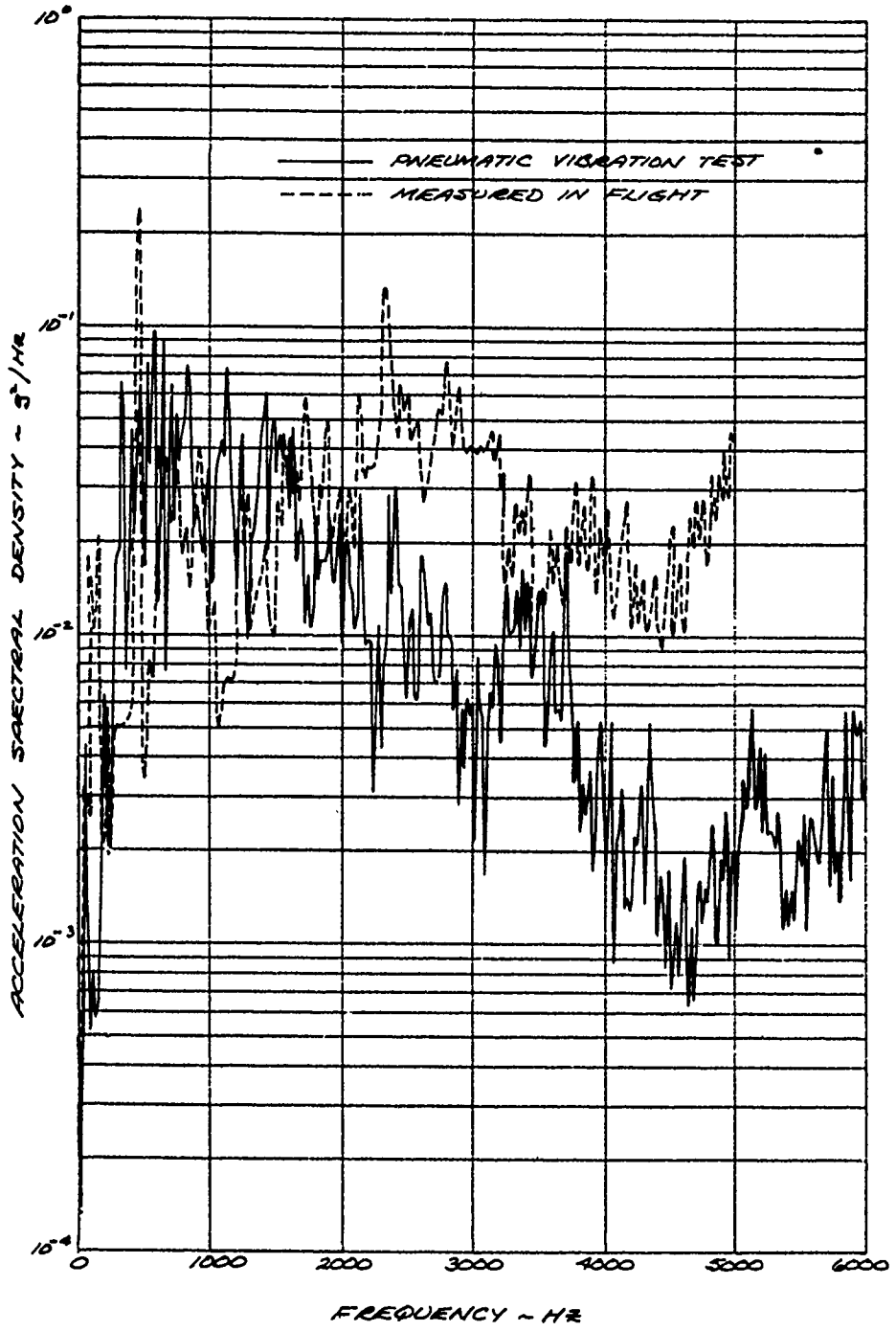


FIGURE 11 - ROUND LEVEL PNEUMATIC VIBRATOR TEST
MID-SECTION VERTICAL - HIGH LEVEL

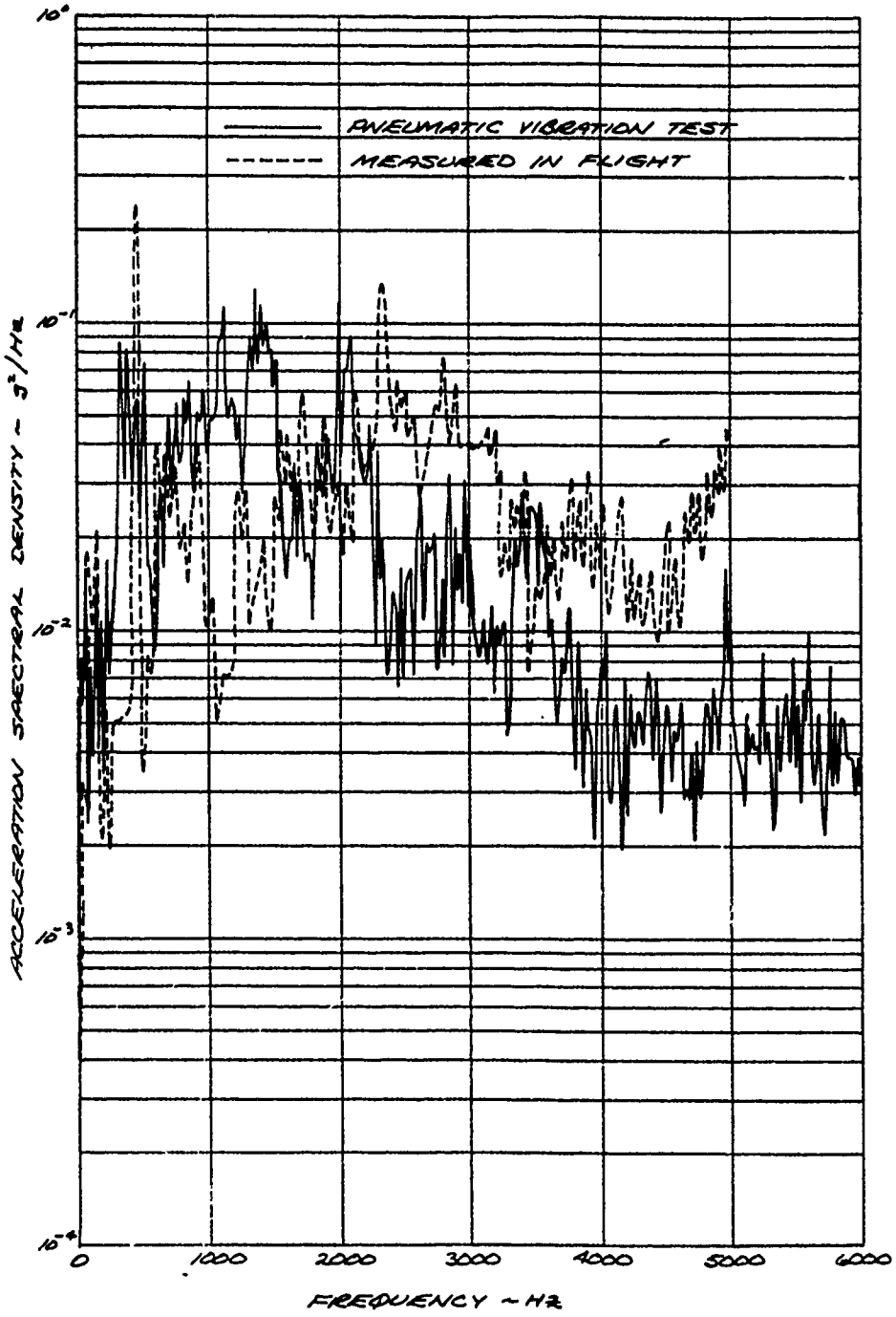


FIGURE 12 - ROUND LEVEL PNEUMATIC VIBRATOR TEST
MID - SECTION HORIZONTAL - HIGH LEVEL

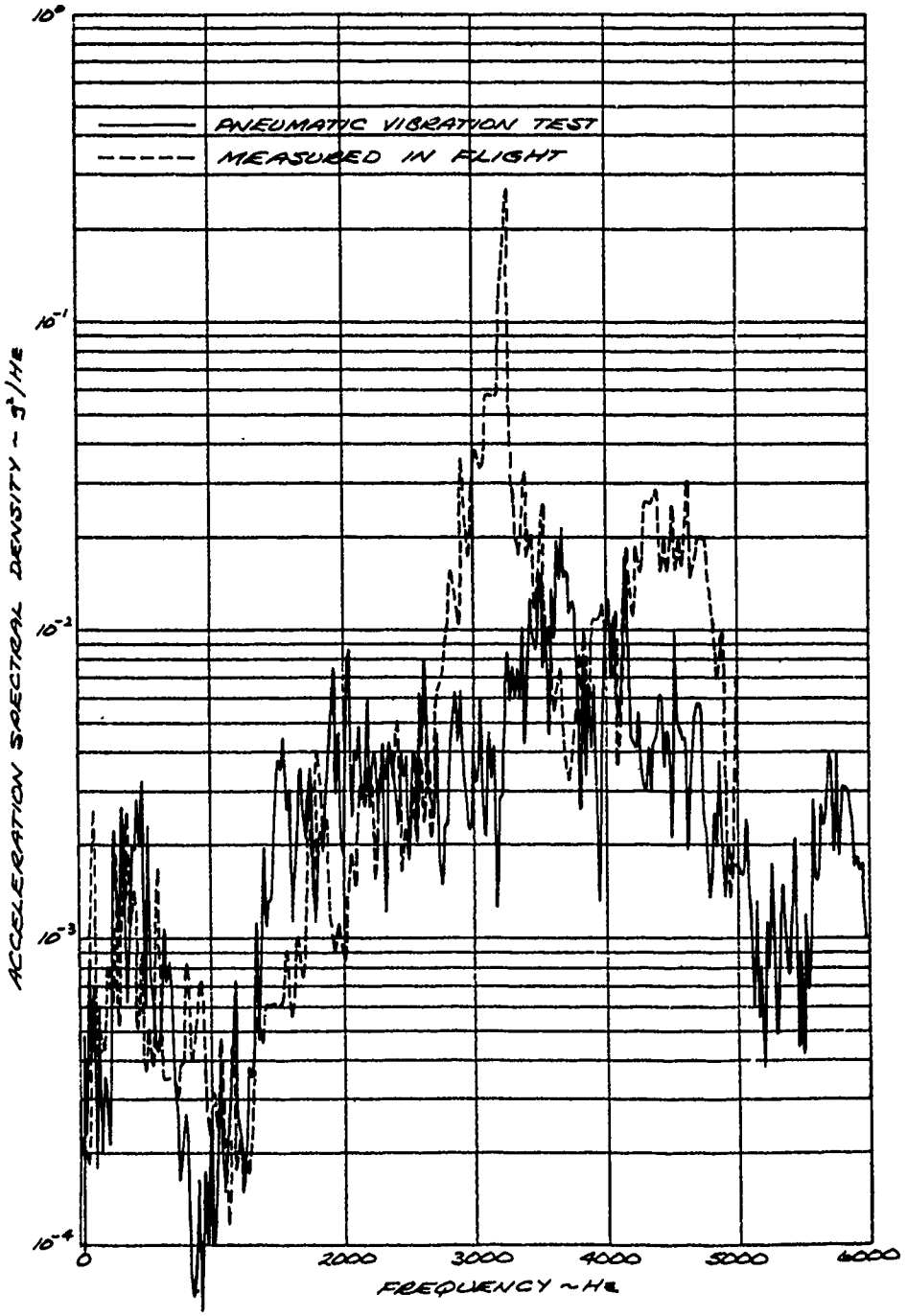


FIGURE 13 - ROUND LEVEL PNEUMATIC VIBRATOR TEST
MID - SECTION LONGITUDINAL - HIGH LEVEL

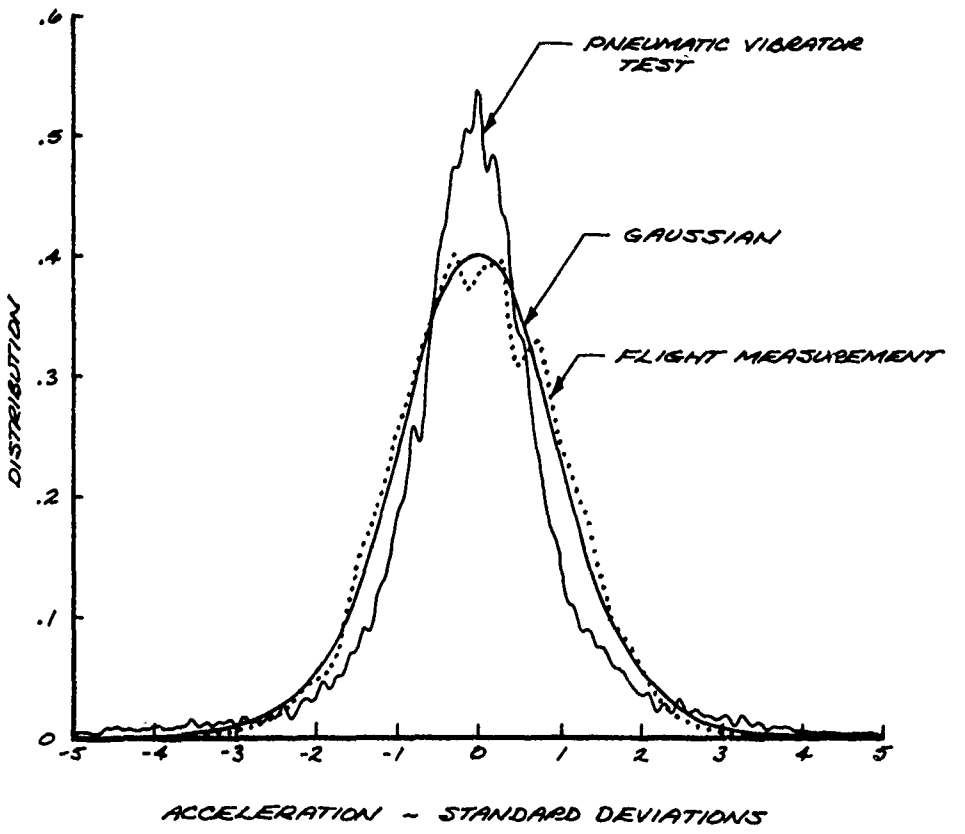


FIGURE 14 - INSTANTANEOUS ACCELERATION DISTRIBUTION COMPARISON
20 - 2000 HZ

Discussion

Voice: Did you run into any problems with the way the missile was supported? When you operated the vibrators were the support locations important as far as generated artificial modes or suppression of significant modes of vibration?

Mr. Maloney: No, I don't feel that they were; we intentionally suspend the missile very softly two or three Hz would probably be the highest suspension frequency. The first elastic mode in a missile configured that way is about 50 Hz so there is tremendous frequency separation between those suspension modes and the lowest vibration modes that we are concerned with.

Mr. Wadleigh: (General Dynamics/Convair): How did you react the actuators?

Mr. Maloney: The vibrators are directly attached to the airframe. In some cases, we have attached them through an elastomer in an attempt to attenuate some of the high frequency. Some of the devices have threads and we can screw studs into them while others have flanges that we can bolt to.

Mr. Wadleigh: I was referring to the opposite end of the actuator away from your test specimen, did you tie into a reaction mass?

Mr. Maloney: No, it is not tied to anything, that end is free.

Mr. Galef, (TRW): Your probability distribution comes out a whole lot closer to gaussian than I would have guessed it did, but it is still pretty far from it. It is sufficiently far that the power spectral density by itself would seem to be a very imcomplete statement of the severity. Did you do any analysis to see what sort of a power spectral density ratio you would have to have between your test and actual flight measurements in order to have approximately the same number of peak values in the course of some finite time, or the same amount of fatigue damage?

Mr. Maloney: I think the answer to that is no we haven't done too much along those lines; but I also think that there is a considerable amount of energy at the high signal levels so you could adjust those overall levels such that you would get a similar distribution of the peaks and some people have done that with broad band random testing. We have not attempted to do that. We are trying to run a fairly severe test.

Mr. White, (Bettis Atomic): You had indicated that the vibrator locked in on the first bending mode of the missile. Did I understand you correctly? How did you overcome that?

Mr. Maloney: By modulating the pressure supply; if you put it on a missile that has a first body lateral resonance of about 50 Hz and if you just apply a steady pressure to it the "rep rate" becomes 50 Hz. We modulated the pressure supply at a rate of about 7 Hzs and it keeps you from locking into that stationary condition. Of course this is obviously not totally stationary for that reason.

Dr. Morrow (Advanced Technology Center): We should remember that distribution is a very delicate thing in a structure and it tends to change as vibration propagates. So if you look at the vibration that is important to an actual failure point that is not necessarily the same distribution as you measure somewhere else, there is ordinarily no simple relationship between the two except that its probably more gaussion that where you made your measurement. It is not very useful to make predictions about fatigue from the distributions where the measurements are made. When you shook this missile did you control a force or a motion at the excitation points?

Mr. Maloney: It was response control.

Dr. Morrow: Response in which terms?

Mr. Maloney: We monitored the overall RMS level in each of three directions at each of the three locations along the missile and we adjusted the pressures so that we got these RMS levels within a certain desired band.

Dr. Morrow: So you are monitoring the response at chosen positions not necessarily the excitation points.

Mr. Maloney: Yes.

Mr. Tustin (Tustin Institute of Technology): Most test specifications say "the vibration shall be gaussian" but very few laboratories ever bother to check this point. Your departures from gaussian wouldn't upset people too much until someday QA starts to check into this matter.

Mr. Maloney: You are saying that they should look at their own distributions first before they throw rocks right? Yest, my experience with the measured data that we have seen in flight is that is is non gaussian and that it has energy beyond 3 sigma. So when you convert it to a test specification you make everything gaussian. You tell them to clip at 3 sigma and you are really destroying some part of the real world when you do that. I do not claim that our flight vibration has the kind of peak RMS ratios that this test produces. It is higher than we have really seen in flight data.

A THREE DIRECTIONAL VIBRATION SYSTEM

Fred M. Edgington
Dynamic Environments Branch
Applied Sciences Division
Army Materiel Test and Evaluation Directorate
White Sands Missile Range, New Mexico

The design and performance of a Three Directional Vibration System to allow the simulation of ground and air transportation vibration environments is presented. The basic system was built at White Sands Missile Range, New Mexico and utilizes a multiaxis drive unit designed and constructed by Team Corporation.

INTRODUCTION

It has been the desire of White Sands Missile Range (WSMR) to have a three directional vibration system for two major reasons. First, the time required to make setups and perform specification type single axis vibration tests would be greatly reduced, especially when the test involved temperature conditioning. Secondly, being able to apply vibration environments in three directions simultaneously would allow more realism to exist when vibration levels measured during equipment operation were to be reproduced in the laboratory. The measurement made on missile components during flight and on radios during helicopter flight indicates very little rotational motion of a vibratory nature exists. Because of this and to allow for single axis vibration testing, the design for the three directional vibration system was to have only orthogonal motion along the three principal axes.

To meet the WSMR needs, three systems have been evaluated experimentally. The first two were discarded for reasons given later. The third system which is described in this paper and in operation has the following additional design criteria.

a. No resonance below 500 Hz

b. Usable to 2 kHz

c. Capable of 0.025 m double amplitude in each of three directions

d. An attachment surface of at least 0.90 x 0.90 m

e. Capable of accelerating a 90 kg package to 10 g's

f. Isolated from its foundation

g. Multiple uses

INITIAL SYSTEM

In the early 60's, the first 3-D System at WSMR was assembled having as the driven unit a 0.13 m aluminum cube. This system is depicted in Figure 1 and used three MB C5-H Exciters to supply the driving force. As is apparent from the sketch, there was no place to mount a test item without causing severe moments about at least two of the driving axes. These moments would cause the drive plates to separate from the cube since they were only attached by a thin film of oil supplied by gravity.

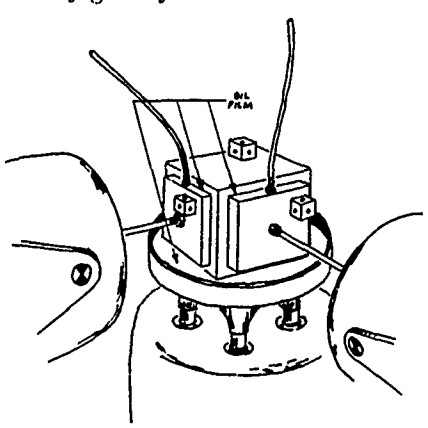


Fig. 1 - Sketch of first 3-direction vibration setup

This system operated extremely well at low frequencies and relatively low accelerations, but as the frequencies were increased, the oil film decoupled causing an attenuation of the acceleration of the cube. This decoupling continued until eventually the cube would separate from the horizontal drive plates. Although the setup did demonstrate the feasibility of a 3-D vibration system, it had no use as a testing tool and was dismantled.

The second 3-D vibration system to be evaluated at WSMR was designed, built and operated by the Wyle Laboratory at Huntsville, Alabama. This system was used to test radios to a three directional vibration environment measured on the radios during helicopter flight. Figure 2 shows the Wyle system as it was set up at WSMR.

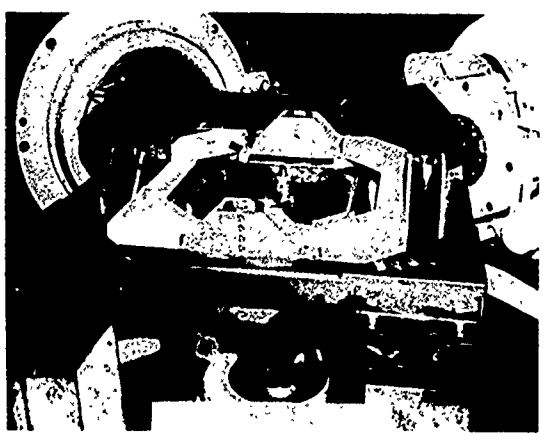


Fig. 2 - The Wyle built 3-Direction vibration table

The vertical input rod was attached to the lower side of the approximately 0.4 m square table while the two transverse input rods were attached to two of the corners of the table. Connected to the exciter were large tubes welded to the armature attachment plate. Four circular steel flexures 90° apart are mounted between the tube and the drive rod. The longitudinal axis of the flexures was the same as the drive rod, thereby, permitting the excitation to be reasonably transmitted while allowing the drive rod and table freedom to move in directions normal to the exciter's direction of motion.

The mechanism used to restrain the rocking motions of the table is two sets of four circular flexures. The first set was attached to each side of the table and to an intermediate frame. The second set of flextures are mounted perpendicular to the first set between this intermediate frame and the main frame that supports the system. The flexures are identified by arrows on the figure. The intermediate frame is free to move, in fact, driven by the flexures in the horizontal direction.

Mechanically, this system was much more complex than the first 3-D Setup and proved to have several advantages. A test item could be mounted on it and it would not fall apart during operations. However, a severe resonance occurred at 150 Hz due to the mass of the input drive rods and at several frequencies, the variation in the acceleration level in the vertical direction was 40 db. Over 100% distortion existed at many frequencies. The distortions were presumably caused by the flexures, intermediate frame, and the input rods. Some distortion was also caused by the shaker support system, main frame, and the wide flange beams that supported the main frame. It was found that a test item having an appropriate mass could be placed on the table such that its mass counteracted the mass of the drive rods. With this mass, some of the bad resonances in the vertical direction were minimized, but resonance problems in the horizontal directions were increased. For these reasons, this system was also disassembled and the exciters put to better use.

CURRENT THREE DIRECTION (3-D) VIBRATION SYSTEM

The previous testing and setups provided enough information on distortion to know that the support system for the exciters and table had to have high stiffness and reasonable damping. As these characteristics would be expensive to obtain, this system had to have something more than salvage value if the three directional concept did not prove to be useful. For this reason, three modes of operation were conceived. These consisted of three axis, vertical, and slip table operations as depicted in Figures 3, 4, and 5. To facilitate uniaxis testing, one exciter could be used for horizontal testing and another used for vertical excitation. The 3-D system was constructed by WSMR and Team Corporation using slightly modified Ling 335-B Exciters. A cut away sketch is shown in Figure 6.

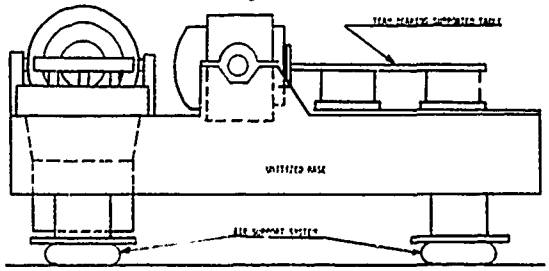


Fig. 3 - Horizontal Uniaxial Testing Mode

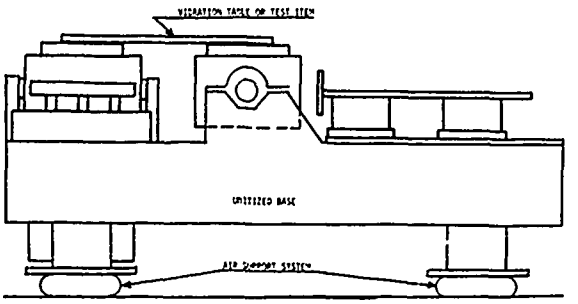


Fig. 4 - Sketch of the vertical uniaxial testing mode

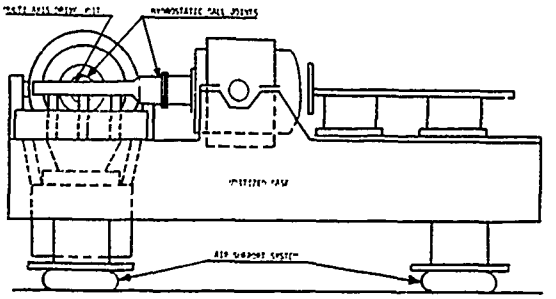


Fig. 5 - Sketch of 3-Directional mode for the current system



Fig. 6 - Cutaway sketch of the new 3-directional vibration system

CONSTRUCTION

The base is approximately 0.915 m thick, built using wide flange beams boxed in by welding .0254 m thick steel plates to each side. The base is L-shaped, having side lengths of 5.10 and 3.30 m. The width of each side is 2.06 m. The wide flange beams are placed around the peripheral of the base and across the sides in front and back of each horizontal exciter. In addition to boxing in the wide flange beams, the plate is used to enclose the area utilized for the Team table support. To dampen the structure, sand has been added to all enclosed volumes and when the sand fill is complete, water will be added to fill all voids. Past tests have shown that the water will double the damping coefficient and increase weight by 20%.

The support for the horizontal exciters are 0.1525 m thick steel plates mounted vertically by welding to the base with the upper end machined to accept a trunnion mounting assembly. This assembly is made so that vertical or horizontal changes (up to .0165 m) in the position of the exciters can be made by the use of shims. After the exciters are positioned, the assemblies are bolted down forcing two wedge shaped portions of the assembly into the side of the 0.1525 m trunnions. The trunnions are pressed into the body of the exciters and then welded. This is the only modification to the standard Ling 335-B Exciter. The vertical exciter is hung from the main structural support plate of the multiaxis drive unit. Bolted to this plate are twenty-four steel rods, .010 m in diameter, .030 m long. These in turn are bolted to an adaption ring bolted to the top body of the exciter. The structural support plate is .020 m thick by 1.37 m square. To provide a flat smooth surface for the support plate to mount on, machine steel strips were placed on stand offs and adjusted until they were in a horizontal plane. The void between these strips and the base was then filled with a high strength epoxy. Using this technique, a minimum amount of machining was required and a solid flat surface was obtained for mounting the multiaxis drive unit.

Vertical excitation is transmitted to nine journal bearing posts .01525 m in diameter through a transition block or head spreader .635 m square by 0.22 m deep attached to the armature. These posts go through journal bearings mounted in the main structural plate. Two bolts going through each post into the transition block hold a lower bearing plate to the posts. The journal bearings restrict the motion of this 0.127 m thick bearing plate to the vertical direction. The top surface of this lower plate has bearing surfaces machined into it, allowing the upper bearing plate or test table to slide in the horizontal directions. The upper bearing plate is held in place by bolts that go through the lower plate, the bearing posts, and into the transition block. Cutouts are made in the lower bearing plate and the posts to allow the upper plate to move .0254 m in any horizontal direction. To reduce high stresses at the ends of these bolts, inserts are mounted in the upper plate and at the lower end of the posts to reduce bending of the thin bolts at these locations.

All bearings in the system operate from a 3.48 MPa hydraulic oil supply and vacuum is used to return the oil to the pump reservoir. Vacuum is also applied between the test table and the lower bearing plate at all non-bearing locations to assist the bolts in counteracting any overturning moments induced by test items. This vacuum can be varied manually from 5 m Hg to 63.5 m Hg and air and dust are prevented from entering the system by teflon seals placed between and along the perimeter of the 0.915 m be 0.915 m bearing plates.

Drive is applied to the table in the horizontal directions through Team 1/2-17 BQ spherical couplings. The mechanical preload on these couplings was increased until they would just be free at 13.7 MPa hydraulic oil pressure and they are operated at a pressure of 19.3 MPa. One pair is used in one direction and two pair are used in the other. All torsional moments created about the vertical axis are transmitted through the two couplings to the exciters flexures and bearing systems. The assembled system ready for an initial evaluation is shown in Figure 7. The moving element weight is 3451 kg in the vertical direction and 1729 kg in the horizontal direction.



Fig. 7 - 3-directional vibration system setup for initial evaluation

When the 3-D system was first operated, no isolation was present between the base and the floor. This operation caused the base to walk across the floor and the cinder block building to vibrate. Although this operation did greatly assist in distributing the sand within the base, it was immediately stopped and an isolation system using five Model 196 Barry stable level air support units was installed. Tests conducted at WSMR demonstrated that each unit will support 10909 kg at 620 KPa (their maximum rated operating pressure). The complete system will weigh 2.07×10^5 kg and weighs 1.88×10^5 kg without the Team slip table. The resonant frequency of the three directional system mounted on this isolation is 2.4 Hz. This means that virtually no vibration forces are transmitted to the floor as a result of the unit operation.

SYSTEM PERFORMANCE

The evaluation of the system performance characteristics was accomplished using sine sweeps in one direction at a time and random noise in three directions simultaneously. During evaluation, accelerometers were mounted in the three directions of excitation at the four locations shown in Figure 8.

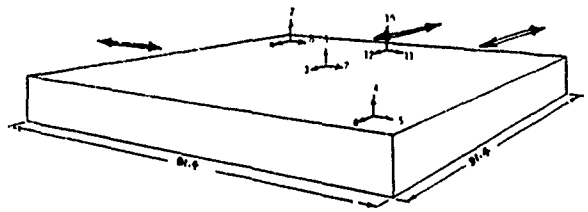


Fig. 8 - 3-Direction sine vibration accelerometer locations

Control was maintained at the center of the table (Accelerometer 1, 2, or 3) for all tests. The cross axis sensitivity of these Endevco Model 2213E Accelerometers ranged from 1.8% to 2.9%. For sine wave operation, all amplifier and field supplies were on, but the inputs to the nonoperating exciters were shorted. Five minute logarithmic sweeps were conducted from 10 Hz to 2 kHz at an input level of one g peak. As the sine wave input level was maintained at one g with less than 0.1 g variation, no plot of the input is presented. Figures 9, 10, and 11 show vertical table responses to a vertical input. Figures 12, 13, and 14 show the responses to inputs from the exciter having one pair of ball joints and Figures 15, 16, and 17 show the response to an input in the final horizontal direction. During sine excitation in the horizontal directions, the cross axis motion in the vertical direction was low, normally less than 50%, however, the other horizontal directions exhibited high cross axis motion. Excitation along the axis of Number 3 accelerator resulted in the cross axis motion shown in Figures 18, 19, and 20, while motion in the direction of accelerometer Number 2 resulted in the cross axis motion shown in Figures 21, 22, and 23. When excitation was in the vertical direction, nearly all

accelerometers exhibited high cross axis motion. These responses are shown in Figures 24 through 29.

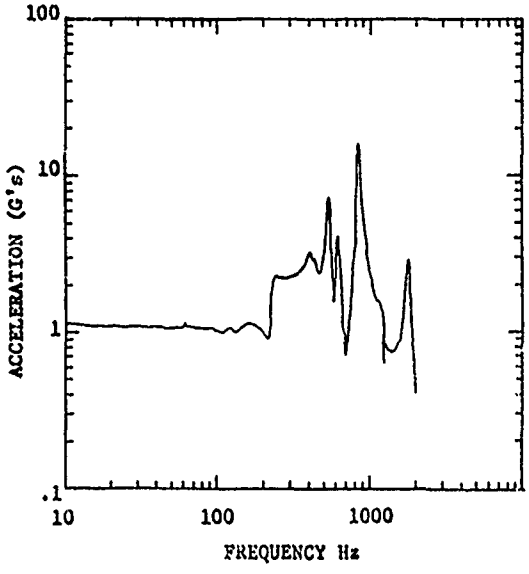


Fig. 9 - Acceleration Measured from No. 4 Accelerometer when No. 1 Accelerometer was maintained at 1 "G" peak

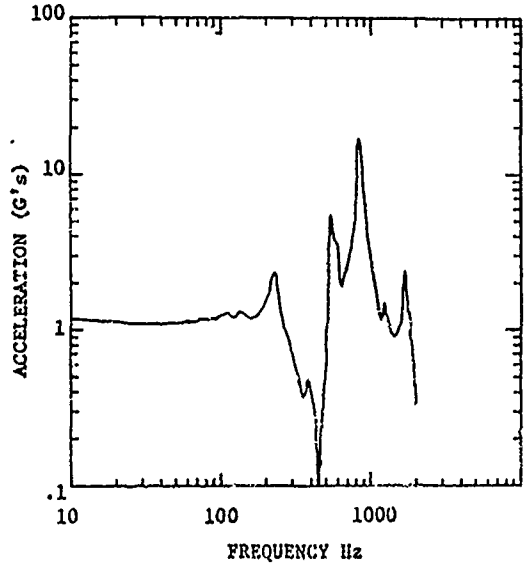


Fig. 10 - Acceleration measured from No. 7 Accelerometer when No. 1 Accelerometer was maintained at 1 "G" peak

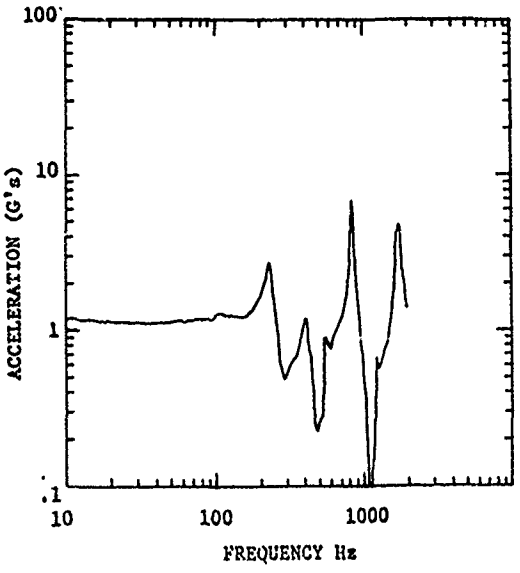


Fig. 11 - Acceleration measured from No. 10 Accelerometer when No. 1 Accelerometer was maintained at 1 "G" peak

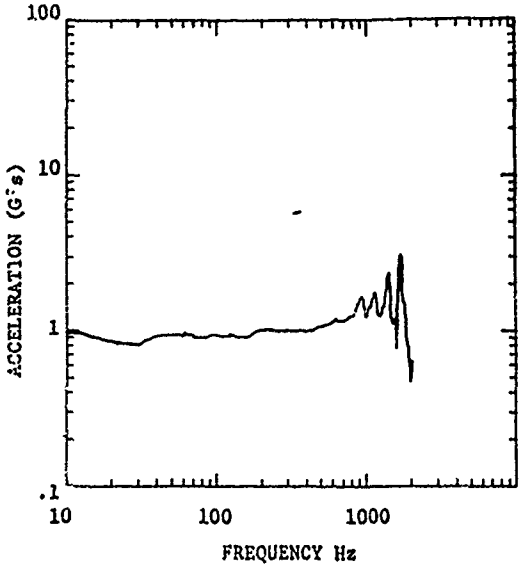


Fig. 12 - Acceleration measured from No. 5 Accelerometer when No. 2 Accelerometer was maintained at 1 "G" peak

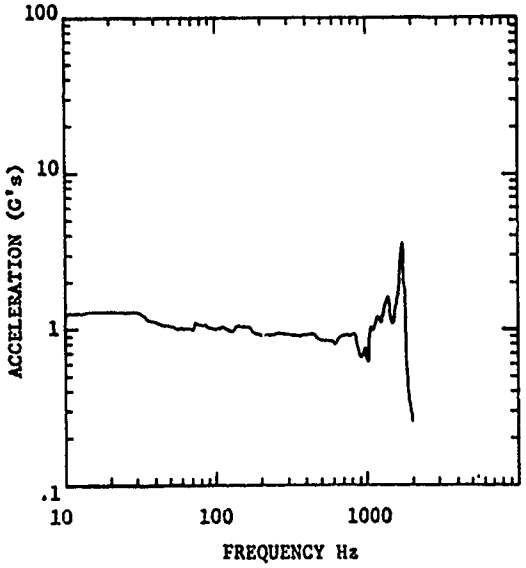


Fig. 13 - Acceleration measured from No. 8 Accelerometer when No. 2 Accelerometer was maintained at 1 "G" peak

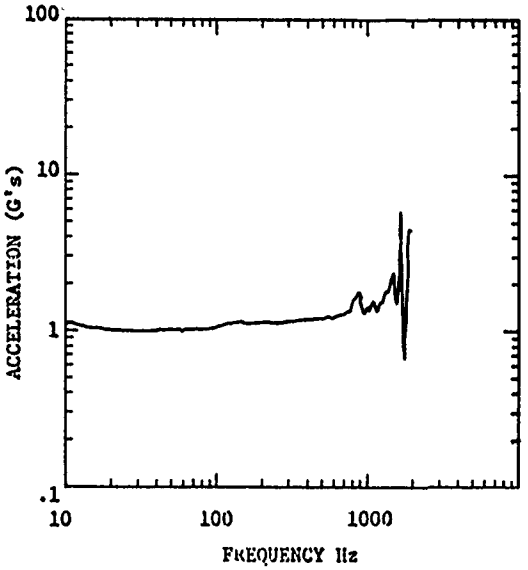


Fig. 15 - Acceleration measured from No. 6 Accelerometer when No. 3 Accelerometer was maintained at 1 "G" peak

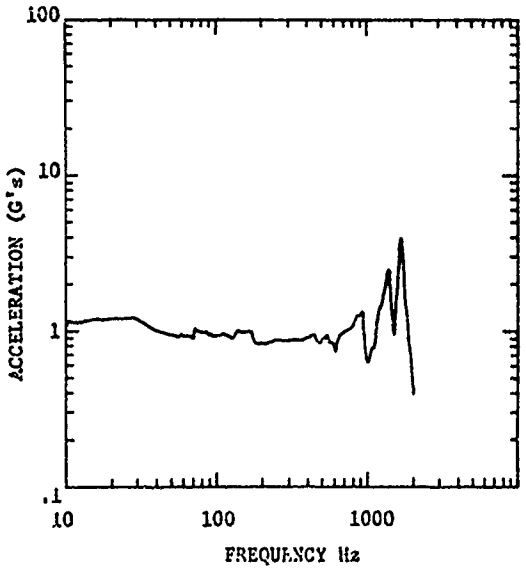


Fig. 14 - Acceleration measured from No. 11 Accelerometer when No. 2 Accelerometer was maintained at 1 "G" peak

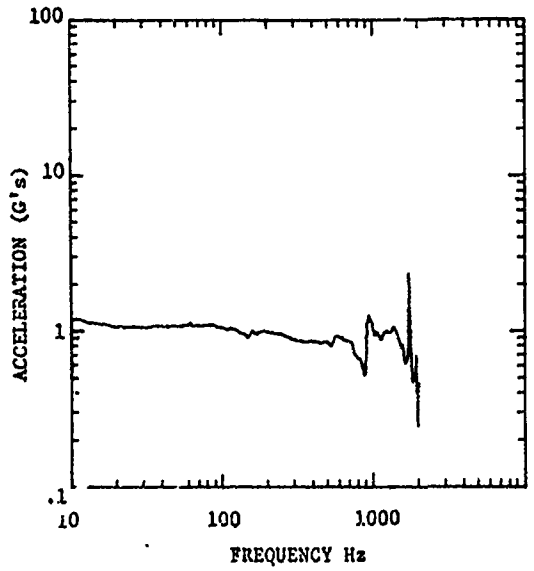


Fig. 16 - Acceleration measured from No. 9 Accelerometer when No. 3 Accelerometer was maintained at 1 "G" peak

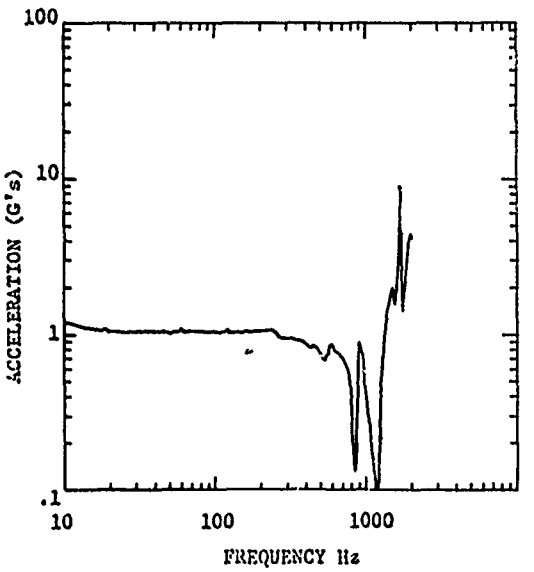


Fig. 17 - Acceleration measured from No. 12 Accelerometer when No. 3 Accelerometer was maintained at 1 "G" peak

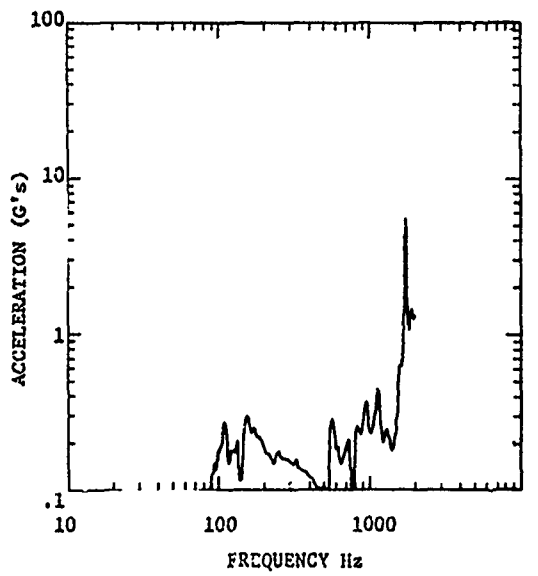


Fig. 18 - Cross Axis Acceleration measured by No. 11 Accelerometer when No. 3 Accelerometer was Excited to 1 "G" peak

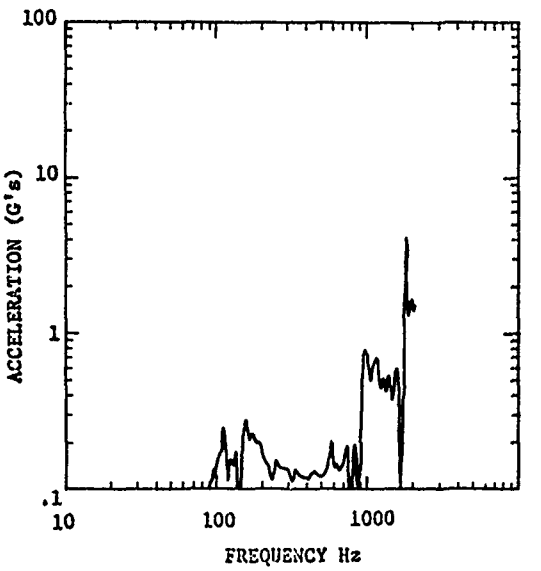


Fig. 19 - Cross Axis Acceleration measured by No. 8 Accelerometer when No. 3 Accelerometer was Excited to 1 "G" peak

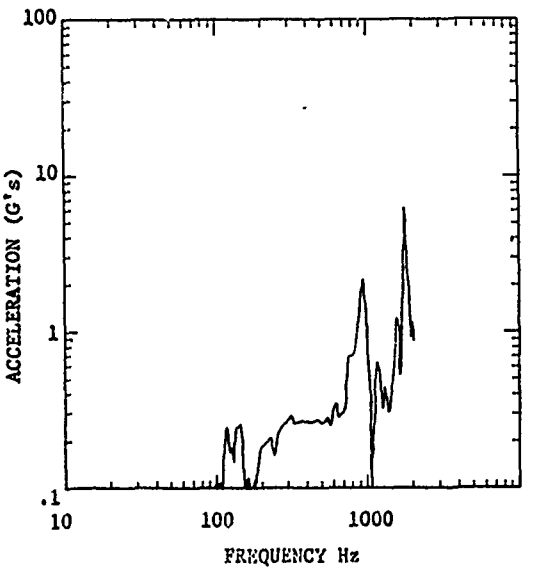


Fig. 20 - Cross Axis Acceleration measured by No. 5 Accelerometer when No. 3 Accelerometer was excited to 1 "G" peak

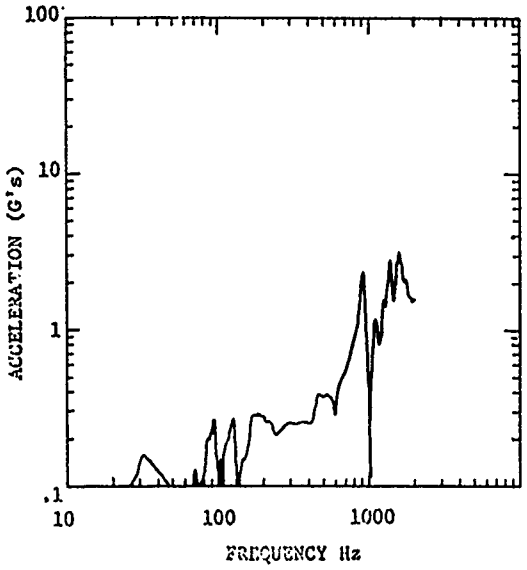


Fig. 21 - Cross Axis Acceleration measured by No. 6 Accelerometer when No. 2 Accelerometer was excited to 1 "G" peak

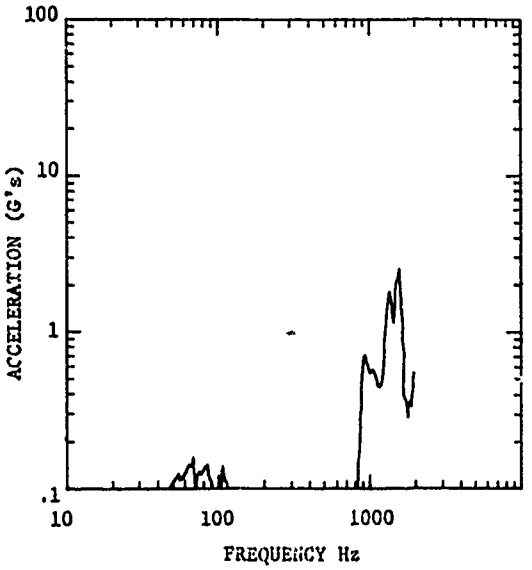


Fig. 23 - Cross Axis Acceleration measured by No. 12 Accelerometer when No. 2 Accelerometer was excited to 1 "G" peak

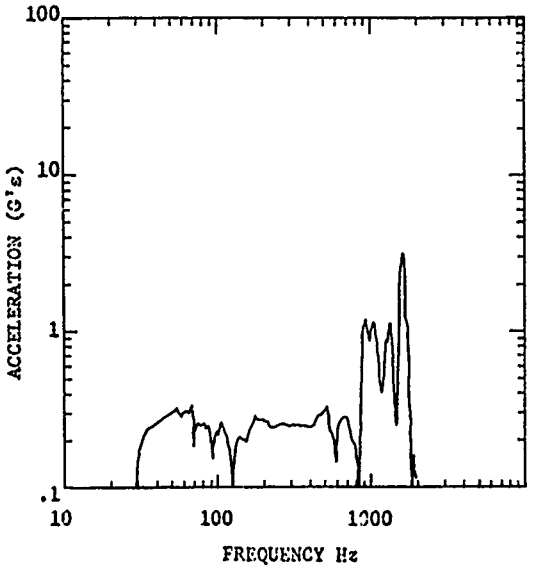


Fig. 22 - Cross Axis Acceleration measured by No. 9 Accelerometer when No. 2 Accelerometer was excited to 1 "G" peak

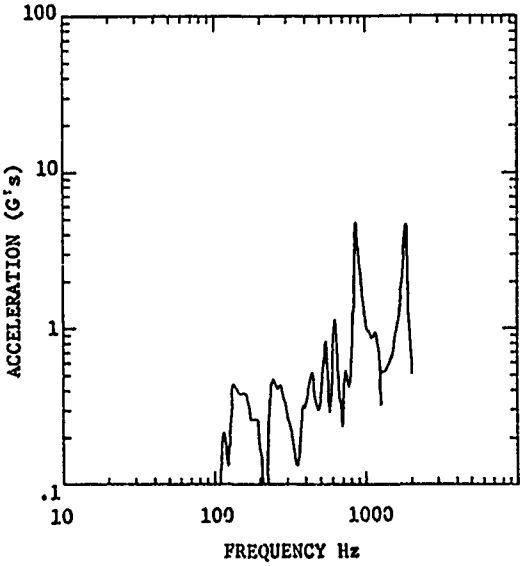


Fig. 24 - Cross Axis Acceleration measured by No. 5 Accelerometer when No. 1 Accelerometer was excited to 1 "G" peak

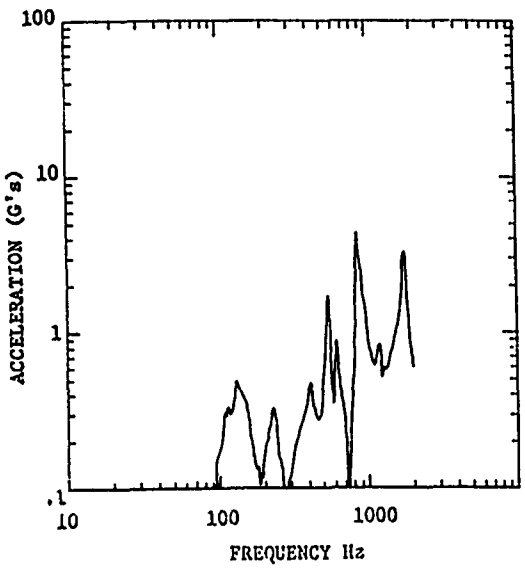


Fig. 25 - Cross Axis Acceleration measured by No. 6 Accelerometer when No. 1 Accelerometer was excited to 1 "G" peak

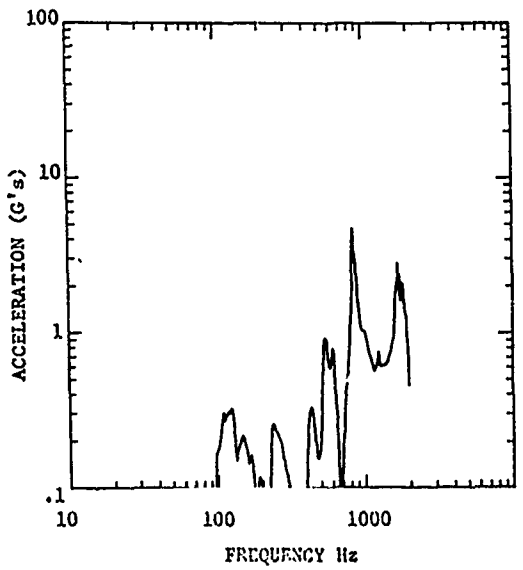


Fig. 27 - Cross Axis Acceleration measured by No. 9 Accelerometer when No. 1 Accelerometer was excited to 1 "G" peak

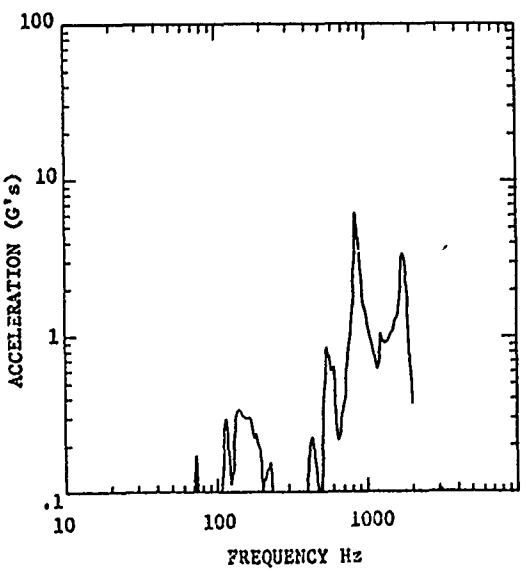


Fig. 26 - Cross Axis Acceleration measured by No. 8 Accelerometer when No. 1 Accelerometer was excited to 1 "G" peak

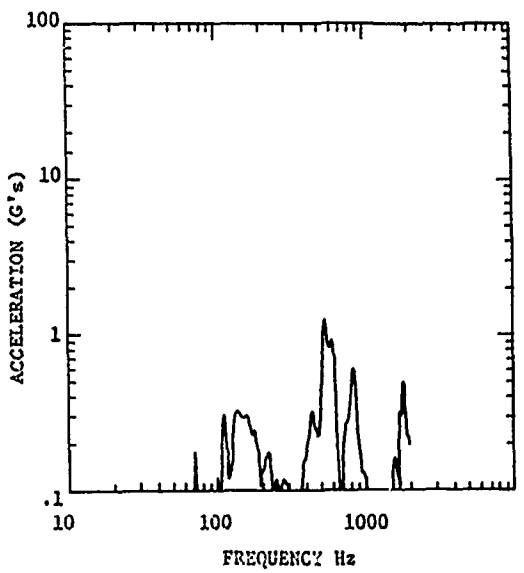


Fig. 28 - Cross Axis Acceleration measured by No. 11 Accelerometer when No. 1 Accelerometer was excited to 1 "G" peak

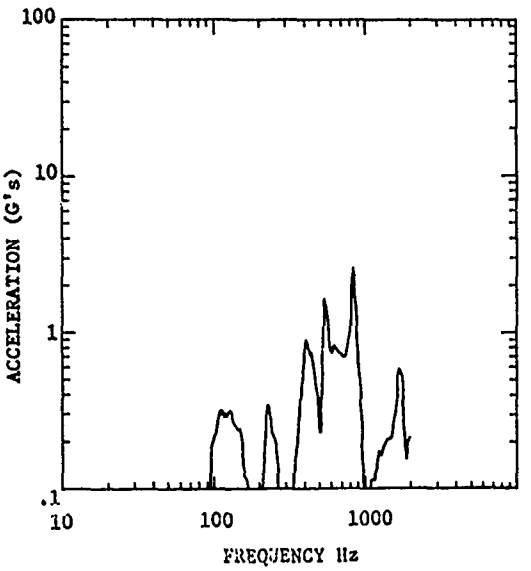


Fig. 29 - Cross Axis Acceleration measured by No. 12 Accelerometer when No. 1 Accelerometer was excited to 1 "G" peak

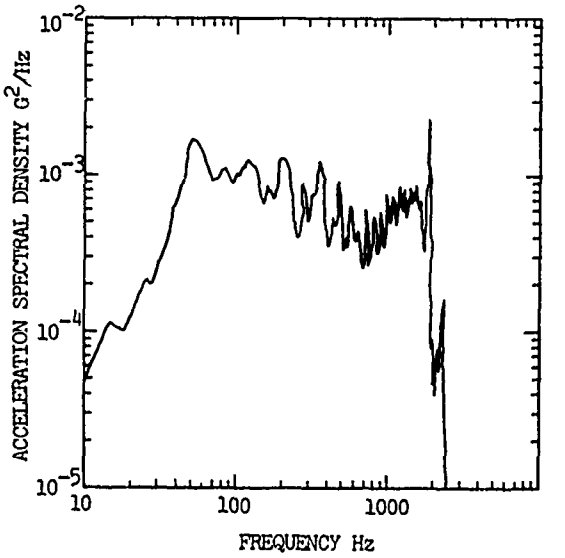


Fig. 30 - Equalization obtained in the Vertical direction during three directional vibration

Measurements have indicated that the variation in the vertical direction and much of the cross axis motion is caused by a lack of stiffness in armature supports of the Ling 335-B Exciters. This lack of stiffness is emphasized when the excitation is applied by the shaker driving through one pair of ball joints. The armature of the other horizontal shaker is rocking such that its outside edge is moving a total of .0048 m. A much stiffer flexure system is available from the manufacturer, however, with the present flexure, the system is usable but may have a reliability problem. This is particularly true if the system is to be operated at low frequencies.

Random vibration was used with the system in two configurations. The first was with no load and three non-correlated inputs were applied in three directions simultaneously. It was attempted to equalize to a flat spectrum using the Accelerometers 1, 2, and 3 for feedbacks. The equipment used for equalization was two MB equalizers, Models 389 and 589, with peak notch and graphic equalizers. The results of this equalization using 12.8 Hz effective bandwidth for analysis are shown in Figures 30, 31, and 32. For the second configuration, one of the horizontal exciters was removed so that the test item (two structural dummy Chaparral missiles) could be attached to the table, see Figure 33.

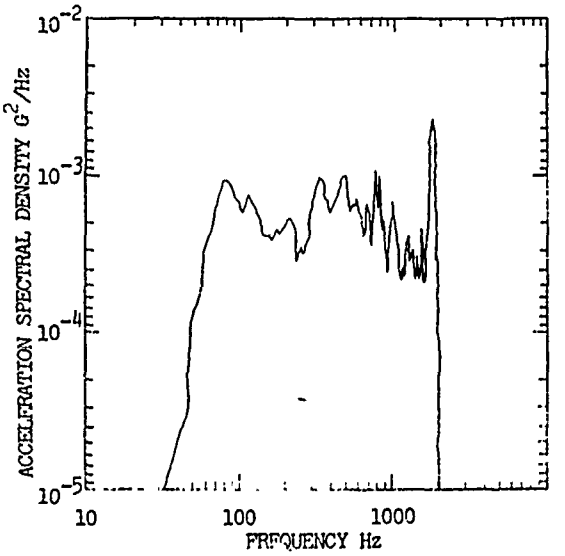


Fig. 31 - Equalization obtained in the No. 2 Horizontal direction during three directional operation

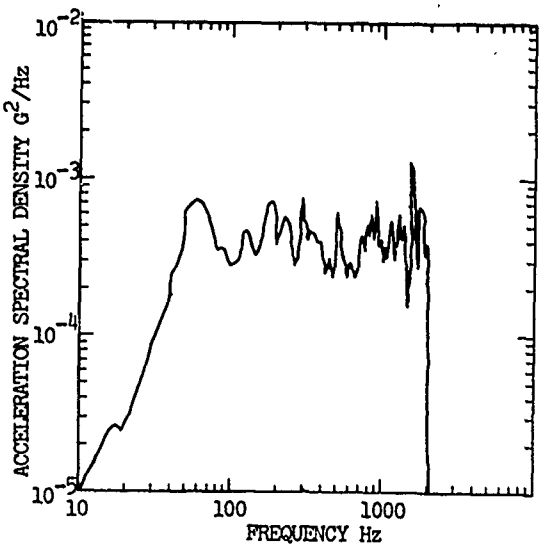


Fig. 32 - Equalization obtained in the No. 3 Horizontal direction during three directional operation

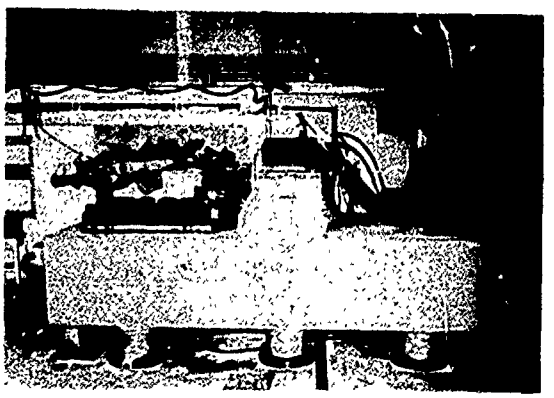


Fig. 33 - Overall view of the setup used to excite two Chaparral missiles in the Vertical and Horizontal directions

The weight of this setup was 225 kg. The input spectrum curves are those actually used for ground transportation testing. The missiles are orientated 13° off of the horizontal axis as they are normally during single axis testing, this is to account for the longitudinal input. The required spectrum and that obtained using an 8 Hz analysis bandwidth are presented in Figures 34 and 35 for the vertical and transverse input directions respectively.

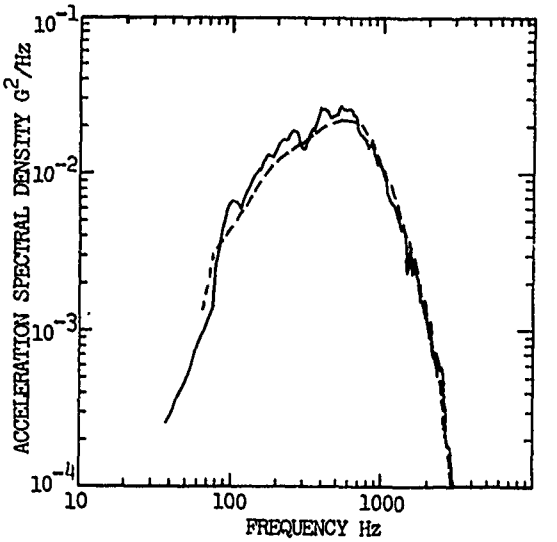


Fig. 34 - Required and desired spectrum from horizontal excitation of the Chaparral missiles

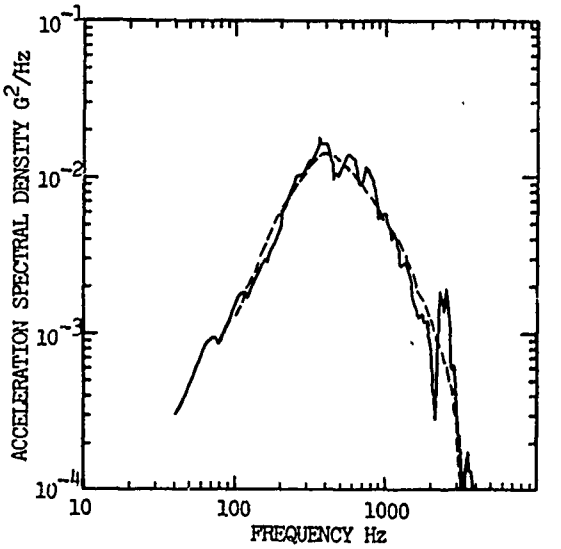


Fig. 35 - Required and desired spectrum from vertical excitation of the Chaparral missiles

It is felt that had beeter equalization equipment been available, the bare table could have been equalized to within 2 db at all but a few points. These points are at 1900 Hz in the vertical direction at 1700

through 1800 Hz in the direction of the one ball joint and at 1550 in the other direction when a flat input spectrum is desirable. As the intent of the system is to test missile and helicopter components to flight environments, both high and low frequency performance will be required. Each type of excitation will have to be checked before the systems capability will be known. If flight levels can be reproduced on all test items as well as the setup used on the Chaparral missiles, the system will well be worth its investment both as a three directional test system and for testing items sequentially using only one setup. This is particularly true if temperature conditioning is required.

PROPOSED CHANGES

To increase the reliability and performance of this system, several changes are anticipated. The first is to install stiffer flexures in the horizontal exciters. This will reduce cross axis motion, flatten the frequency response in the vertical direction and immensely improve the reliability of the system. The second is to transfer the torsional moments about the vertical axis to both horizontal exciters. This will be accomplished by installing a second pair of hydrostatic ball joints between the table and the exciter which only has one set now. A third change is to add an automatic centering system to the vertical exciter. The standard leveling system on the 335B Exciter is extremely difficult to set such that the table will not drift off center after a half hour or longer period. As expected, this drift causes the system to be shut down by the over travel switch. The last is to install a modified armature in the vertical exciter to increase the force output for short tests (reproducing missile flight vibration environments). It is believed that as much as 1.3610^4 kg force can be generated from the exciter by adding an additional cooling system and changing the armature.

CONCLUTIONS

The Three Directional Vibration System represents a vast improvement over what was previously available. This system can be used for the testing of small items to vibration environments measured during missile and aircraft flight or ground transporation. These measured vibration environments or other test specifications can be applied to the test item either simultaneously or sequentially as desired. Modifications are required to improve the three directional vibration system's performance and reliability.

DUAL SHAKER VIBRATION FACILITY

Carl V. Ryden

Pacific Missile Test Center
Point Mugu, California

The requirement for a dual shaker vibration facility was generated by the requirement for vibration testing of the PHOENIX and HARPOON missiles in the All-Up-Round configuration. This configuration is required for a more realistic simulation of vibration throughout the missile and to allow functional operation of the missile during the tests. Also in the case of the PHOENIX, the missiles cannot be disassembled for sectionalized vibration testing because of contractual requirements. Two shakers (one at the forward end of the missile and one at the aft end of the missile) instead of the customary single shaker were needed because of the vibration transmissibility characteristics through the warhead and motor sections, and because of the different levels and spectrums required at the forward and aft missile sections. The transmissibility ratio varies considerably with frequency. There are low frequencies where the transmissibility ratio exceeds one. This is true for both forward and aft directions (from the aft control section to the forward guidance section, and vice versa); however, the frequencies are different. At the higher frequencies the transmissibility decreases towards zero in both directions.

Two complete and independent vibration systems were utilized including random noise generators, equalizers, amplifiers and shakers. Since the signals from the two systems are random and independent there is no constant phase relation (continuously and randomly changing) between the two vibration inputs and their respective transmissibility through the missile. The shakers are therefore independently controlled assuming the system is essentially linear at the critical frequencies and amplitudes. The two shakers were identical in order to reduce setup complication and control problems.

INTRODUCTION

In order to provide a realistic vibration simulation, during laboratory environmental tests, of captive and free vibration for the HARPOON missile and captive flight vibration for the PHOENIX missile, it is necessary to vibrate the missiles with two shakers simultaneously. One shaker is attached near the forward end of the missile and one is attached near the aft end of the missile. A single shaker will not provide a realistic vibration test because of the low vibration transmissibility through the center sections (armament and propulsion) of the missiles, and also because different levels and spectrums are required at the forward and aft missile sections requiring separate inputs. For example, for the HARPOON free flight simulation; the vibration levels for the forward portion of the missile (station 9.64 through 84.50)is 5.8 grms

and for the aft portion of the missile (station 84.51 through 160.50) is 6.5 grms. The test levels for the HARPOON are based on design criteria and for PHOENIX are based on captive flight vibration data.

Since the missiles are functionally operated during the vibration tests, it is necessary to test the missiles in the full length round configuration. Also, in the case of the PHOENIX, the missile cannot be disassembled, because of contractual reasons, for vibration testing of the sections separately.

METHOD

Comparison Of Other Vibration Methods

Other methods of vibration testing which have been used include:

1. Individual missile section vibration
2. Mini round configuration.
3. Short round configuration.
4. Single shaker attached at different locations.

Many tests have been conducted in the past during which each section of the missile was vibrated individually. With this method each section could be tested at its particular level and spectrum. However, since the complete missile was not tested, interactions between the sections were not simulated and time and cost were greater than if the complete missile were vibrated.

The mini round configuration was used for PHOENIX vibration tests. This method used only the guidance and control sections of the missile excluding the armament and propulsion sections. An adaptor was used to connect the guidance and control sections together and provide an attachment to the shaker.

The short round configuration was also used (and still is) for the PHOENIX tests. This method used the guidance, control and inert propulsion sections of the missile excluding the armament section. Adaptors were used to connect the sections together and provide an attachment to a vibration fixture.

In both the mini and short rounds, the levels and spectrums are not realistically simulated at all the missile sections. Some points in the missile are severely undertested when the maximum responding points are held to a "not to exceed" level and spectrum limit. If these points are not held to this limit then they are overtested while other points are undertested, but not as severely.

The method of using a single shaker and attaching it at different locations on the missile was used by Hughes Aircraft (HAC) for PHOENIX vibration testing. In this test, a shaker was attached and vibration applied first, at the joint between the guidance and armament sections at the forward end of the missile, and then, at the joint between the propulsion and control sections at the aft end of the missile. Since the complete missile was not tested at one time, interactions (electrical as well as mechanical) between the sections were not simulated, and the time and costs were greater than if the complete missile was vibrated.

Literature and Test Data Review and Evaluation

A literature review was made of analyses and tests conducted employing multishaker configuration in order to determine potential problem areas, how to avoid these problems, what the best approach in development might be, and if the problems were encountered, how to approach a solution. A list of the articles reviewed are given in the bibliography.

Problems, as pointed out in these articles, were encountered when using sine wave vibration and attempting to control the amplitude and phase relationship between two or more vibration inputs. The problems consisted of high transmissibility from one end of the missile to the other, time delay and phase shifting between the input points to the missile and responses throughout the missile. There was very little information on random vibration inputs, particularly using completely independent vibration systems including independent noise sources.

Prior to testing, preliminary bending frequencies of the HARPOON and

PHOENIX missiles were calculated; however, no detailed analyses were performed since there were many unknown parameters. The values of these would have to be determined experimentally.

Tests were performed to determine the lateral clearance and spring rate of the shakers to be used for these tests and calculations were made to make sure that if maximum excursions of both shaker armatures in opposite directions should inadvertently occur that it would not damage the missile, shakers or fixtures. Also, calculations were made to be sure that the maximum opposite armature excursion occurring during maximum level vibration would not damage the shaker on a continuing basis.

A review was made of data obtained during vibration tests conducted by the HARPOON and PHOENIX missile contractors.

The method employed by McDonnell Douglas Corporation was to excite the HARPOON missile with a small shaker at different points. Results of these tests are shown in Figures 1 through 6.

Figures 1 and 2 show the transmissibility between missile station 24.0 and 142.0. Figures 3 through 6 show the vibration response with respect to the input force at stations 24.0 and 142.0 (using force control input). The transmissibility curves depict the ratio of amplitude of vibration at the two points while the response curves show the response in amplitude of vibration with respect to the input force giving the natural frequencies of the body bending modes.

The method employed by HAC was to vibrate the missile at two locations using a single shaker as described earlier. The results of these tests are shown in Figures 7 though 10.

Figures 1 through 10 show low frequencies where natural frequencies and high transmissibilities occurred. As can be seen from these figures, the natural frequencies and the high transmissibility frequencies are different at the forward and aft ends of the missiles.

Changes occur in the dynamic characteristics of the structure when the mass of the vibration fixture is attached at different locations on the missile. When these changes take place, the frequencies at which high transmissibility occur and the spectrum shape can be expected to change. However, the natural frequencies (as determined from the response in vibration amplitude at a point on the missile with respect to the input force) should remain the same no matter where the fixtures are attached (the force input is applied). This is true since the response is normalized to the force input. This is borne out by comparing the data from the different configurations.

Also, as can be seen from the data, the transmissibility is low at the higher frequencies (e.g. less than 0.01 above 500 Hz) as the results of the low rigidity, high mass, and high damping characteristics of the armament and propulsion section.

Because of the potential problems, as pointed out in the literature review, in attempting to control the amplitude and phase relationship between two inputs, it was decided to use two completely independent systems with independent inputs. Since the natural frequencies, as well as the high transmissibility frequencies, are different at the forward and aft ends of the missile, it was felt that problems of instability due to high transmissibility from one end of the missile to the other (the input at one shaker affecting the vibration level at the other shaker and vice versa) at a common frequency would not likely occur. The additional change in dynamic characteristics by attaching two vibration fixtures was not expected to have a great affect on changing the frequencies. Also, it was felt that since the output inpedance of the shaker is very low (because of the high internal dynamic damping factor of the power amplifier) the response from the opposite shaker would be greatly attenuated, eliminating any transmissibility type of instability in the control of the shakers. In addition it was felt that if this instability (high transmissibility from one end of the missile to the other) could not be completely eliminated, then the control systems could be cross controlled and/or the spectrum level at these frequencies could be attenuated manually.

Systems Design

Two complete and independent random vibration systems were utilized including random generators,

equalizers, amplifiers and shakers. The two shakers used were identical in order to prevent setup complication and control problems.

A block diagram of the major equipment used in these tests is shown in Figure 11. A complete list of equipment is given later. As shown in the diagram either of two equalizers, any of three power amplifiers and associated control equipment including a random noise generator, and either of the two similar shakers can be used for each of the two independent systems.

Test Setup

Figure 12 shows an overall view of the HARPOON setup in the Hieatt Chamber for combined temperature-altitude-vibration tests. Figure 13 is a close-up view of the vibration fixtures. Figure 14 shows an overall view of the test setup for HARPOON missile in the climatic chamber for temperature-vibration tests. Figure 15 is a close up view of the setup, showing the dual shakers, vibration fixtures, carts, rails under the carts, and a brace between the carts to maintain the relative position and distance between them. Figure 16 shows the PHOENIX missile and location for the vibration fixtures on the missile.

Fixture Design

The design and construction of the vibration fixtures for both HARPOON and PHOENIX were performed by Kimball Industries. The design consists of split collars or rings which in the case of the HARPOON missile clamps directly around the missile, while in the case of the PHOENIX missile clamps around ring segments attached to the missile. The split collars are bolted together and attached to a shaker head expander with four expanding pin connectors. The HARPOON fixture including the split collars, head expander, and expanding pin connectors is shown in Figure 13. Figures 17 through 19 show details and exploded views of the PHOENIX vibration fixtures.

Ring segments shown in Figure 17, are attached to the PHOENIX missile at the joints between the guidance and armament section, and between the propulsion and control section at the vibration fixture locations as shown in Figure 16. The ring segments are attached using spaces and flat head screws which replace the regular missile section attaching screws. The spacers fit into the clearance holes in the insulation layer and bear directly against the missile skin the same as the head of the missile screws. The flat head screws connect through the ring segments, which are countersunk to receive the flat head screws and counterbored to receive the spacers, through the spacers, and into the missile sections. The screws are torqued to the same value as the missile screws. This provides an attaching arrangement with similar loading, stresses and dynamic characteristics as the original attaching arrangement between the sections. Figure 18 shows the split collar and launcher hook clamping block for the forward vibration fixture. The split collar clamps around the ring segments, and the clamping block attaches to the launcher hook and the split collar. Figure 19 shows the ring segments, launcher hook clamping block and the split collar for the aft vibration fixture.

Facilities Development

Several laboratory facilities were developed or modified during the implementation of the dual shaker capability as follows:

1. Modification to the floor of the Hieatt temperature and altitude chamber to accommodate two 310 S shakers suspended in low slung carts supported on rails in the Hieatt Chamber. (See Figure 12).

2. Construction of four shaker carts. Two low slung carts for use in the Hieatt Chamber and two high shaker carts for regular laboratory vibration work such as is shown in Figure 14.

3. Installation and refurbishing of a Ling PP 140/150 Power Amplifier and associated equipment including impedance transformers, heat exchanger, field supplies, electrical power supply, cooling water, and cabling interconnect panel.

Equipment

The following is a list of the equipment utilized in the dual shaker facility.

Existing equipment consists of the

following:

1. Ling PP 40/60 and PP 175/240 Power Amplifiers and the associated control equipment.

2. Ling ASDE 40 Spectrum Equalizer

3. MB 80 Channel Random Equalizer

5. The associated instrumentation equipment including; Ampex FR 600 and Bell-Howell VR 3400 magnetic tape recorders, Endevco 2735 and Unholtz-Dickie 8PMCVA charge amplifiers, and Endevco piezoelectric accelerometers.

Modified equipment consists of the following:

1. Two Ling 310 S Shakers - 10,000 lb. force output

2. Hieatt Chamber

3. Ling PP 140/150 Power Amplifier and associated control equipment.

New equipment consists of the following:

1. Two Ling impedance matching transformers for the 310 S shaker.

2. Two Ling field supplies for the 310 S shaker.

3. Two heat exchangers for the 310 S shakers.

4. Four shaker carts designed and built for the 310 S shakers.

5. Vibration fixtures for HARPOON missile.

6. Vibration fixtures for PHOENIX missile.

Test Procedures

Preliminary vibration tests using a "dummy" HARPOON missile were conducted first to establish if stability could be achieved and to work out problem areas, if any. These tests were conducted in the Hieatt Chamber. The setup was the same as shown in Figure 12 (which shows the prototype missile). The "dummy" missile was essentially a pipe with the same outside diameter and with weight added to provide the proper weight, c.g. and moment of inertia as the prototype missile. However, the vibration characteristics were not the same, (e.g. body bending modes and the damping characteristics of the armament and propulsion sections) and actually was a worse condition. An accelerometer was attached on the top of each fixture. Figure 12 shows the accelerometer on the top of the forward fixture.

These preliminary tests consisted of the following:

1. low level vibration (1 grms measured on fixture) input at forward shaker, and no field or armature current applied to aft shaker.

2. Low level vibration input at forward shaker, and field current but no armature current applied to aft shaker.

3. Low level vibration input at aft shaker, and no field or armature current applied to forward shaker.

4. Low level vibration input at aft shaker, and field current but no armature current applied to forward shaker.

During these tests, problems were encountered with two of the power amplifiers because of the system modification to incorporate the PP 140/150 Power Amplifier. Data was not obtained with both shakers operating simultaneously since the second amplifier would cut off before data could be obtained. However, it did indicate stability with both shakers operating. When the amplifiers were repaired and operating, it was decided to resume testing with the prototype HARPOON missile since no problems were encountered with the "dummy" missile, stability was indicated, and the dynamic characteristics are different (the "dummy" missile being the worst case).

The following preliminary tests were performed on the prototype HARPOON missile:

1. Low level vitration (1 grms on fixture) input at forward shaker and no armature or field current applied to aft shaker.

2. Low level vibration input at aft shaker, and no armature or field current applied to forward shaker.

3. Low level vibration input applied to both shakers.

4. Intermediate level vibration input applied to both shakers.

Originally it had been planned to first vibrate each shaker separately, then apply field current to second shaker (for both combinations), then apply field current and armature current but with zero signal (having only the damping affect of the power amplifier and the resulting low mechanical impedance) to the second shaker to determine the damping affect, and then apply vibration to both shakers.

Because of problems with the power amplifier stated before, short time schedule, and since it was not desirable to spend time vibrating the prototype HARPOON missile except when absolutely necessary, and stability was indicated, all the intermediate steps could not be performed as planned.

No dynamic testing has been performed on the PHOENIX missile to date because of limited funds and time schedule. No problems are anticipated since the transmissibility obtained during single shaker vibration tests (shown in Figures 7 through 10) is less than for the HARPOON missile.

TEST RESULTS

Figures 20 through 23 are power spectral density (PSD) plots of vibration at the input shaker and the resulting vibration at the second shaker obtained during the "dummy" HARPOON vibration tests.

By comparing Figure 20 with 21 and Figure 22 with 23, it can be seen that there is very little difference in the vibration response at the second shaker between having the field current on or off.

Figure 20 shows four significant resonances at 400, 560, 1400 and 1570 Hz.

Figure 22 shows only one significant resonance at 420 Hz.

Figures 24 through 31 are power spectral density plots of vibration at both shakers obtained during preliminary tests using the prototype HARPOON missile.

In comparing Figures 24 and 25 three resonances are indicated at 60 Hz, 130 Hz and 210 Hz, and in comparing Figures 26 and 27 a resonance is indicated at 150 Hz. Above 400 Hz there is a minimum attenuation of 10:1 for both directions.

In comparing Figure 24, 27 and 28 (PSD plots for the forward shaker) the affect on the vibration at the forward shaker when adding vibration at the aft shaker can be seen. The shape of the spectrum, particularly at the low frequencies, is changed slightly, as can be seen by comparing Figures 24 and 28. One noticeable change is at 150 Hz where the resonance at 150 Hz, shown in Figure 27, from the aft shaker is evident.

In comparing Figures 25, and 26, and 29 (PSD plots for the aft shaker) the same affect can be seen. Two noticeable changes can be seen at 120 and 210 Hz due to the resonances shown in Figure 25 from the forward shaker.

In both cases the addition of the second shaker tends to smooth out the PSD plots and there is no indication of instability as evident in Figures 28 and 29.

Figures 30 and 31 show the results at approximately 3 grms level at both shakers.

Following the preliminary tests using the prototype missile, combined temperature-altitude-vibration environmental tests were conducted in the Hieatt Chamber. These tests simulated captive flight conditions and consisted of four 30 minute tests at two temperatures and in two missile axes at a vibration level of 5.8 grms for both shakers. Following the temperature-altitude-vibration tests, temperature-vibration tests were conducted in the climatic chamber simulating free flight conditions. The required vibration levels for these tests were 5.8 grms at the forward shaker and 6.5 grms at the aft shaker. Figure 32 shows the required input levels and spectrums. The forward shaker is included in zone I and the aft shaker is included in zone II. A comparison of Figure 32 with Figures 33 and 34 show a close agreement between the results of the tests and the required levels and spectrums. Figures 33 and 34 show the two input control spectrums at the two

vibration fixtures. Ten accelerometers were located within the missile and these were monitored for "not to exceed overall levels and spectrums". Figures 35 through 38 show four representative samples of the spectrum at points within the missile.

Final adjustments were made using the spectrum equalizer to the control spectrums at frequency points where maximum limits were exceeded. Also, as can be seen in Figures 33 and 34, the frequencies below 200 Hz for the forward shaker and below 250 Hz for the aft shaker were attenuated using the manual spectral equalizer control.

At the start of the simulated captive flight tests (in the Hieatt Chamber), it was attempted to control with a flat spectrum using two accelerometers within the missile, one for the forward shaker at missile station 26.6 and one for the aft shaker at missile station 37.8. However, since there was attenuation at these locations with respect to the shaker inputs similar to that shown in Figures 35 and 36, the power input required was considerably higher than when controlling at the shakers, and as a result there was considerable potential over testing (over the maximum level) at several locations within the missile (actual over testing did not occur since the input vibration levels were low). The system, however, was stable even though the control points were within the missile and the levels were relatively high.

The required test levels and spectrums were more realistically simulated and easier to control using the dual shakers than would have been possible using a single shaker because of the added control flexibility of an additional shaker.

CONCLUSION

The results of these tests show that:

1. It is feasible to vibrate with random vibration using two shakers that are independently controlled.

2. Even where resonances exist in the test package structure (in this case a missile) control can be achieved because of the dynamic damping in the power amplifier resulting in a very low mechanical impedance at the point of vibration fixture attachment.

3. The control points can be within the test package and still maintain stability and control.

4. The control to establish the required levels and spectrum at the various points within the test package was easier to achieve with the dual shakers than would be possible with a single shaker.

5. The test levels and spectrum were more realistically simulated using the dual shakers than would have been possible using a single shaker.

BIBLIOGRAPHY

"Derivation of the Mathematical Transfer Function of an Electrodynamic Vibration Exciter," C.P. Chapman, NASA Technical Report No.32-934, May 1966

"Averaging Fundamental Vibration Control Signals: A Theoretical Study," W.W. Shurtleff, Shock and Vibration Bulletin 36, Jan. 1967, Part 3, page 139

"Control Techniques for Multi-shaker Vibration Systems," R.A. Arone and P.A. Brock, Shock and Vibration Bulletin 36, Part 3, Jan. 1967, page 147

"Mutiple Shaker Ground Vibration Test System Designed for XB-70A," R.C. North and J.R. Stevenson, Shock and Vibration Bulletin 36, Jan. 1967, Part 3, page 55

"Control of Multiple Shakers," J.G. Helmuth, Institute of Environmental Sciences, Proc. 1965, pages 493-496

"Control Stabilization for Multiple Shaker Tests," N.F. Hunter nd J.G. Helmuth, Shock and Vibration Bulletin 37, Jan. 1968, Part 3, page 155

"Practical Considerations in the Application of Multiple Shakers," A.C. Grimaldi, 1966 Proceedings of Environmental Sciences, Page 171-176

"Shock and Vibration Testing Using Four-shaker System," D.F. Redford, Shock and Vibrtion Bulletin 36, Jan. 1967, Part 3, page 91

"Design Techniques for Horizontal Drivers," F.G. Tolleth, Shock and Vibration Bulletin 36, Jan. 1967, Part 3, page 101

"Methods of Control of Multiple Shaker Testing System," by J.P. Newton, Shock and Vibration Bulletin 35, Jan. 1966, Part 2, pages 85-96

"Random-force Vibration Testing," J.V. Otts and N.F. Hunter, Shock and Vibration Bulletin 37, Jan. 1968, Part 3. page 61

"Reproduction of Complex and Random Waveforms at Various Points on a Test Item," J.V. Otts and N.F. Hunter, Shock and Vibration Bulletin No. 36, Jan. 1967, Part 3, page 47

"Use of Analog Computer for the Equalization of Electromagnetic Shakers in Transient Testing," Marc R. Trubert, Jet Propulsion Laboratory, Symposium on Transient Loads and Response of Space Vehicles, NASA, Nov. 1967

"Vibration Methods for Multiple Random Excitation," W.E. Noonan, Shock and Vibration Bulletin 37, Jan. 1968, Part 3, page 8

"Random Vibration Test Level Control Using Input and Test Item Response Spectra," A.J. Curtis and J.B. Herra, Shock and Vibration Bulletin 37, Jan. 1968, Part 3, page 47

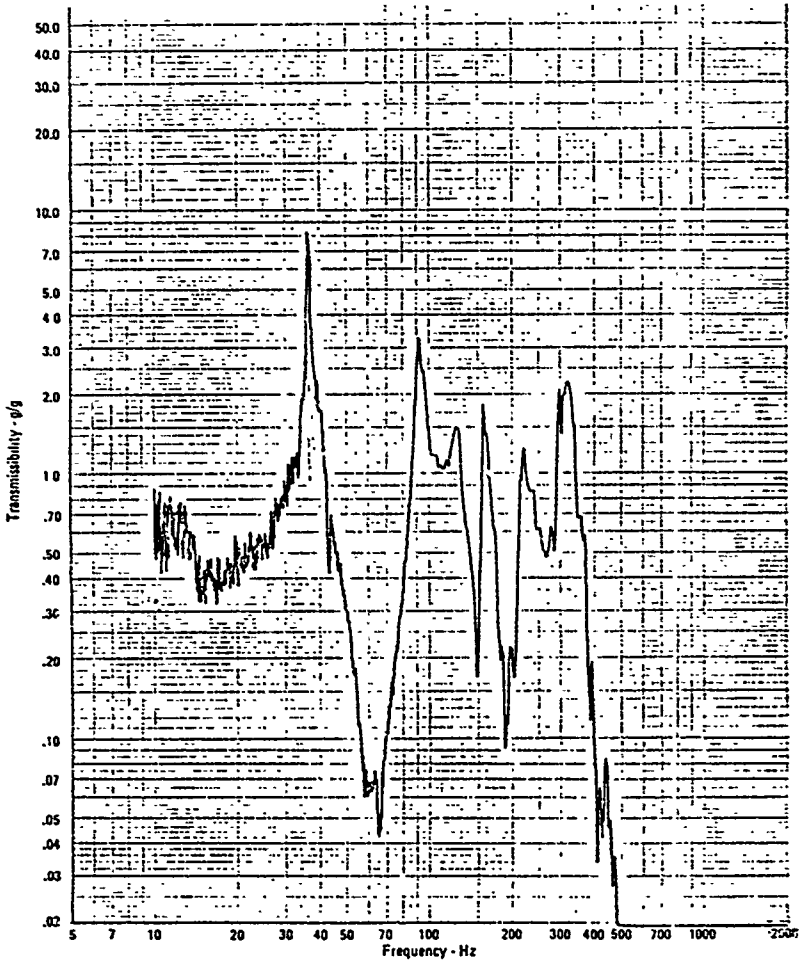


Figure 1. Transmissibility Ratio (g/g) Between Stations 24.0 and 142.0 With The Input Vibration Applied At Station 24.0.

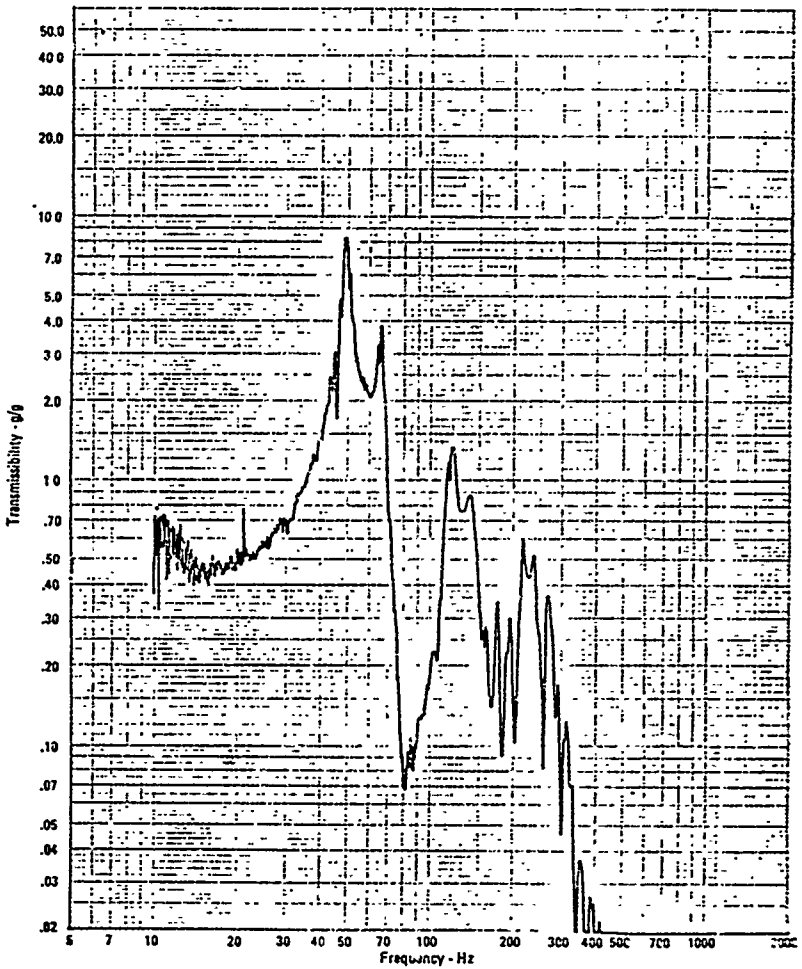


Figure 2. Transmissibility Ratio Between Stations 24.0 and 142.0 With The Input Vibration Applied At Station 142.0.

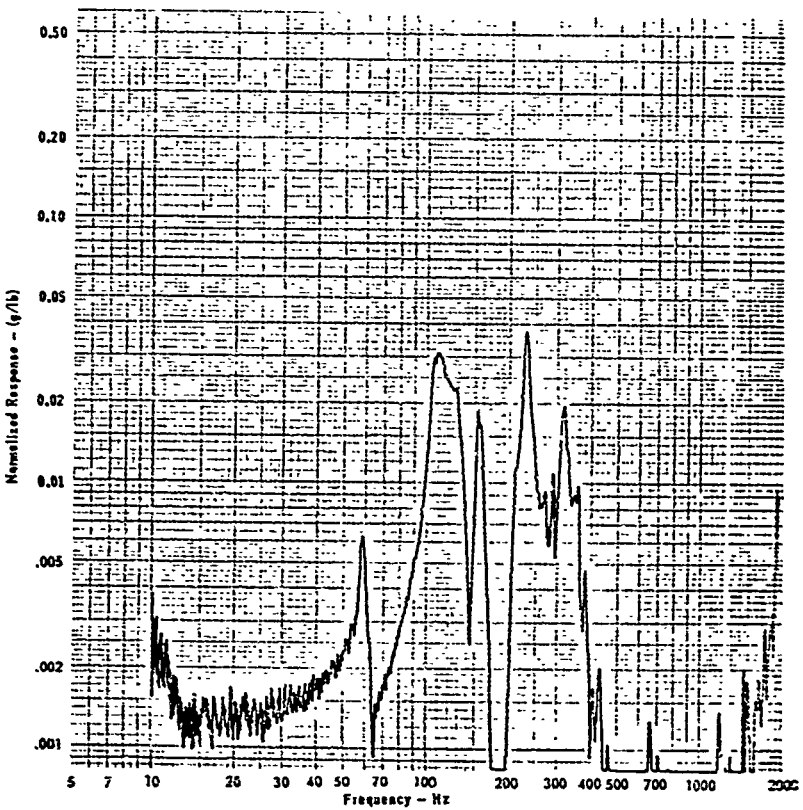


Figure 3. Normalized Response of Vibration At Station 142.0 And Force Input At Station 24.0.

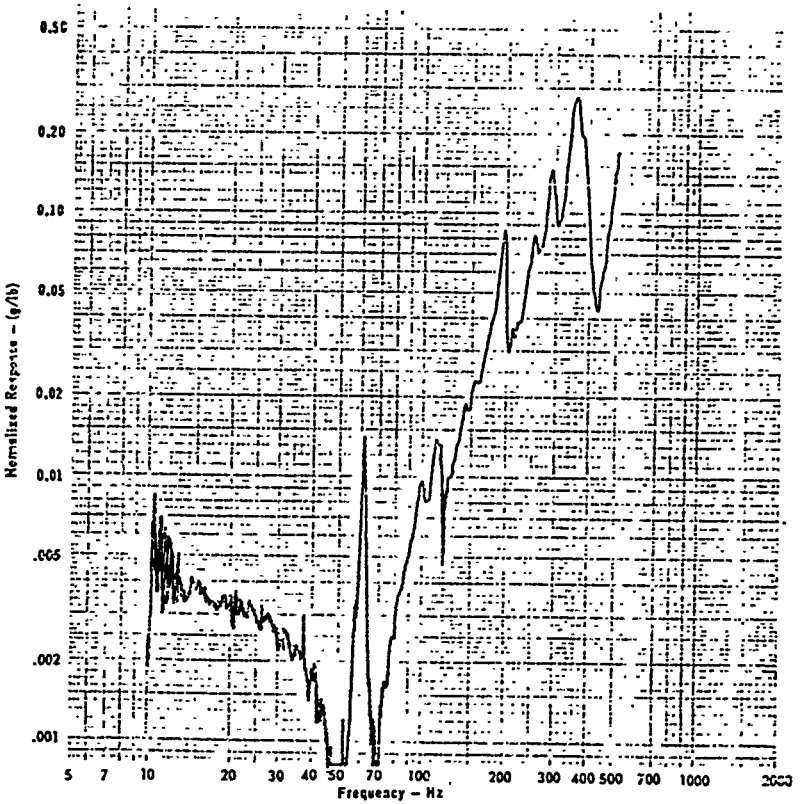


Figure 4. Normalized Response Of Vibration At Station 24.0 And Force Input At Station 24.0.

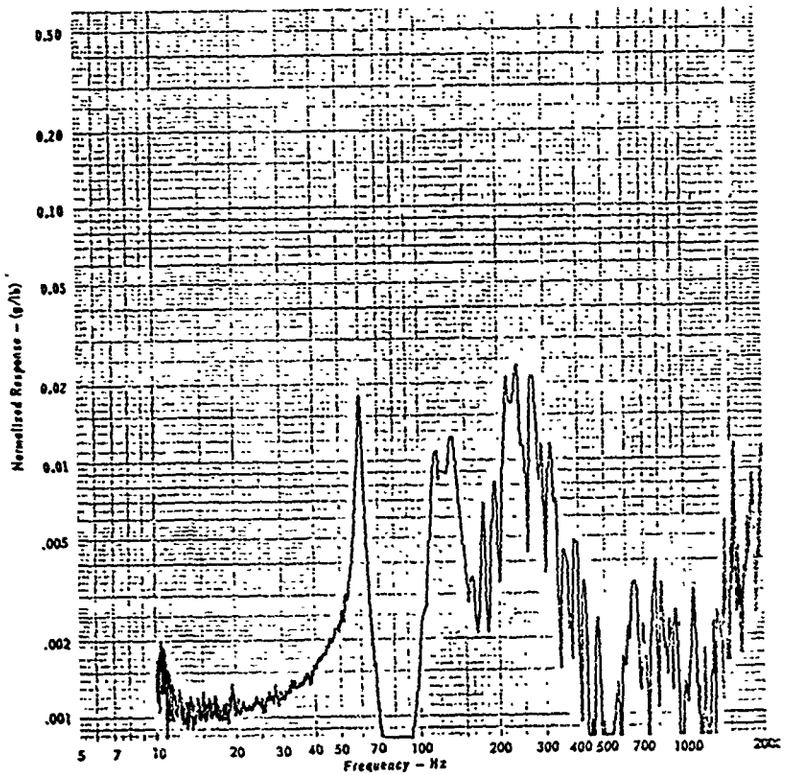


Figure 5. Normalized Response Of Vibration At Station 24.0 And Force Input At Station 142.0.

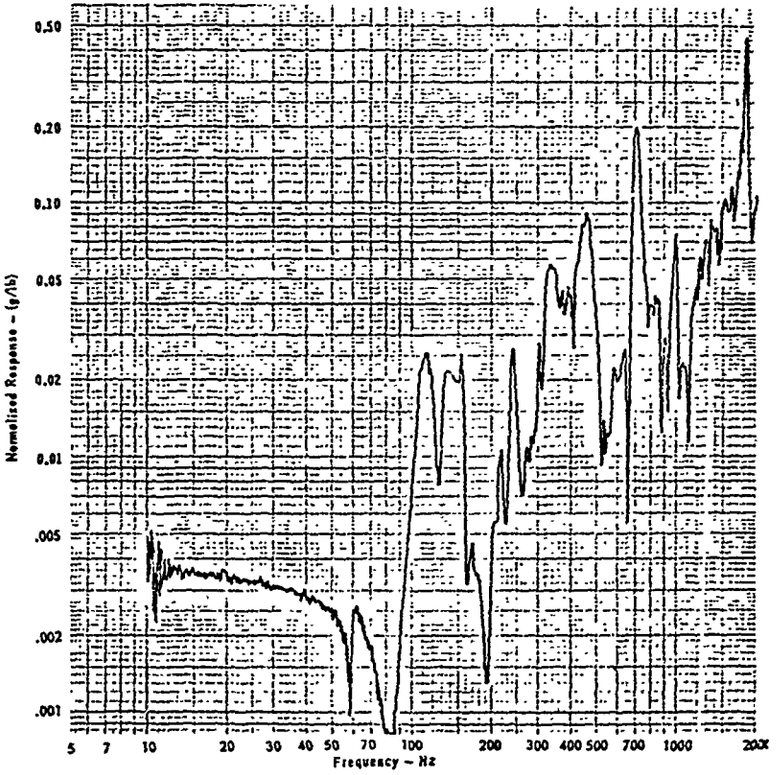


Figure 6. Normalized Response Of Vibration At Station 142.0 And Force Input At Station 142 0.

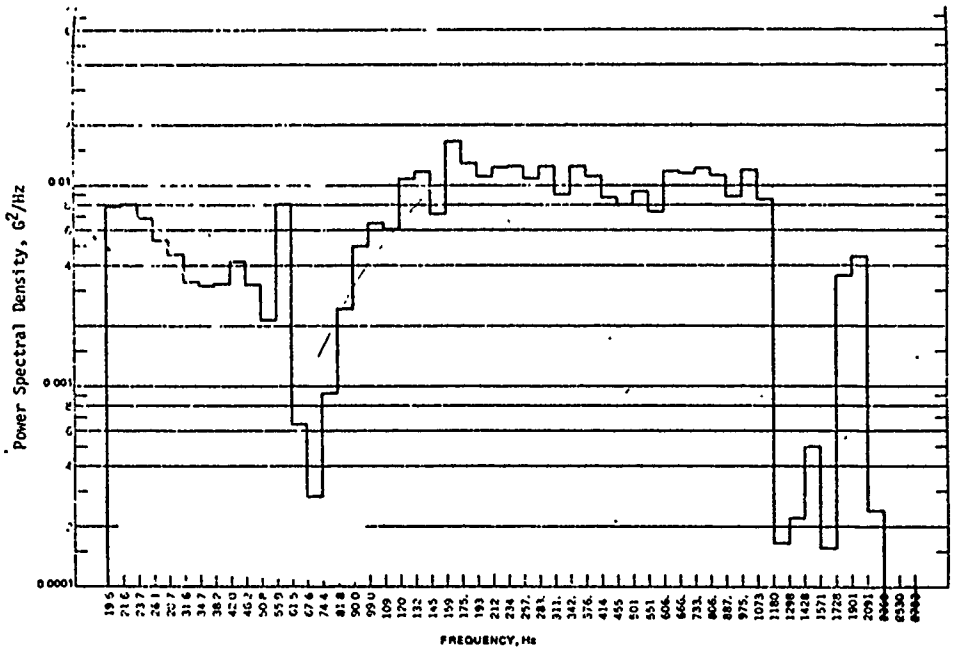


Figure 7. Power Spectral Density of Vibration At The Forward Ejection Ring With Input Vibration At The Forward Ejection Ring.

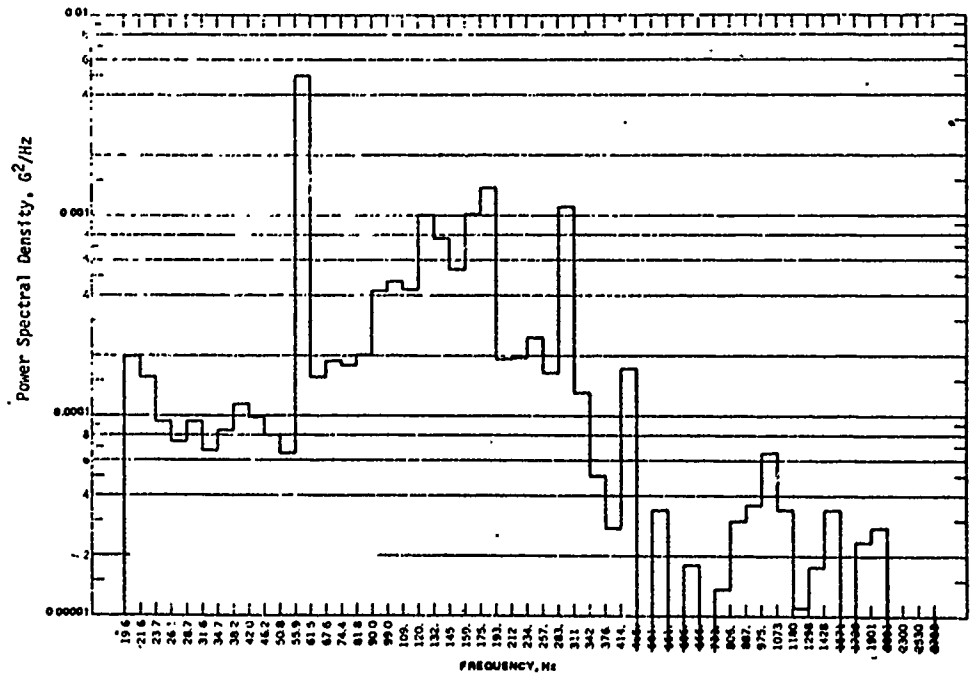


Figure 8. Power Spectral Density of Vibration At The Aft Ejection Ring With Input Vibration At The Forward Ejection Ring.

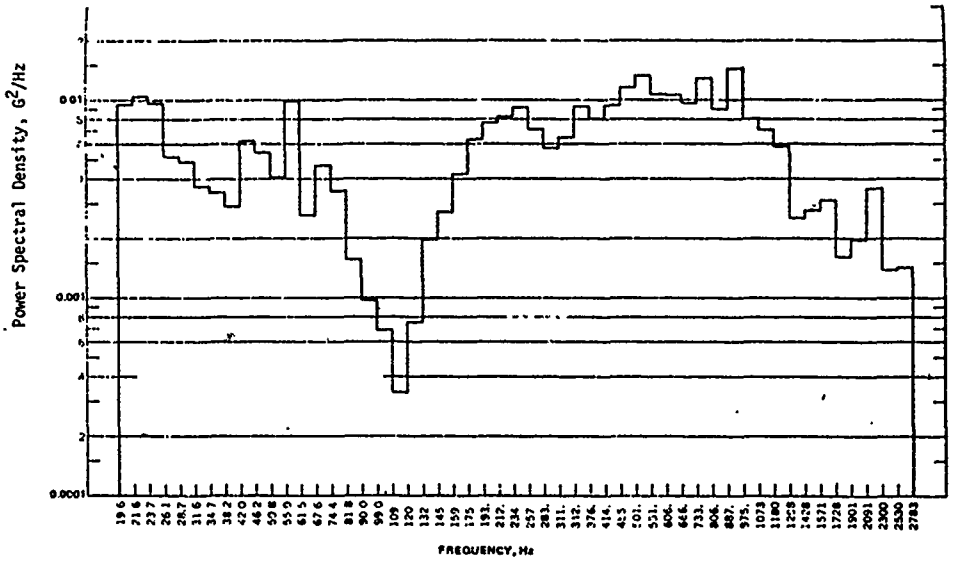


Figure 9. Power Spectral Density of Vibration At The Aft Ejection Ring With Input Vibration At The Aft Ejection Ring.

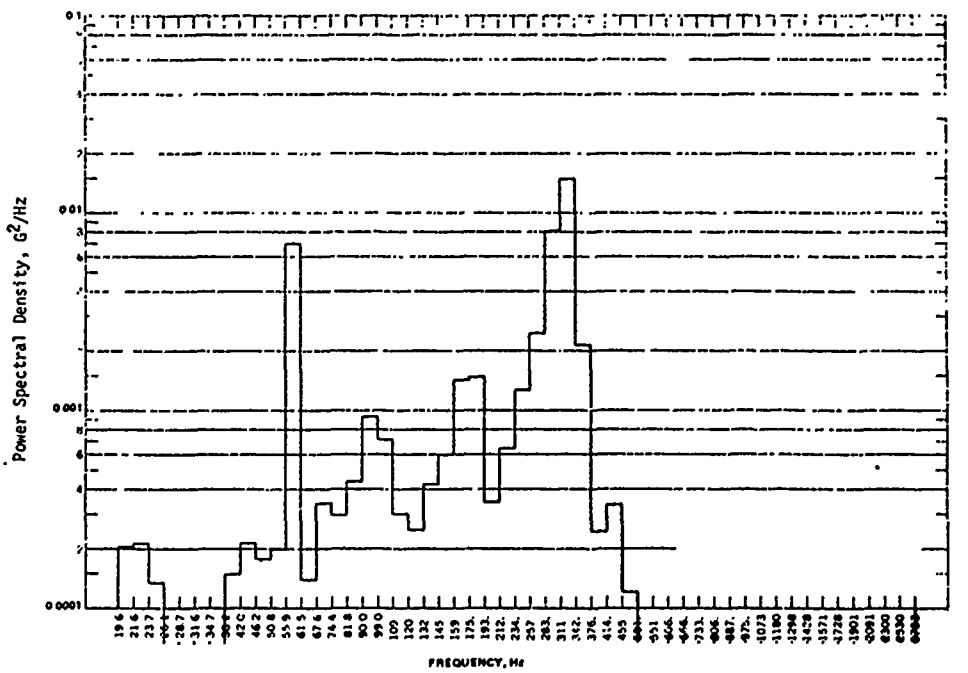


Figure 10. Power Spectral Density of Vibration At The Forward Ejection Ring With Input Vibration At The Aft Ejection Ring.

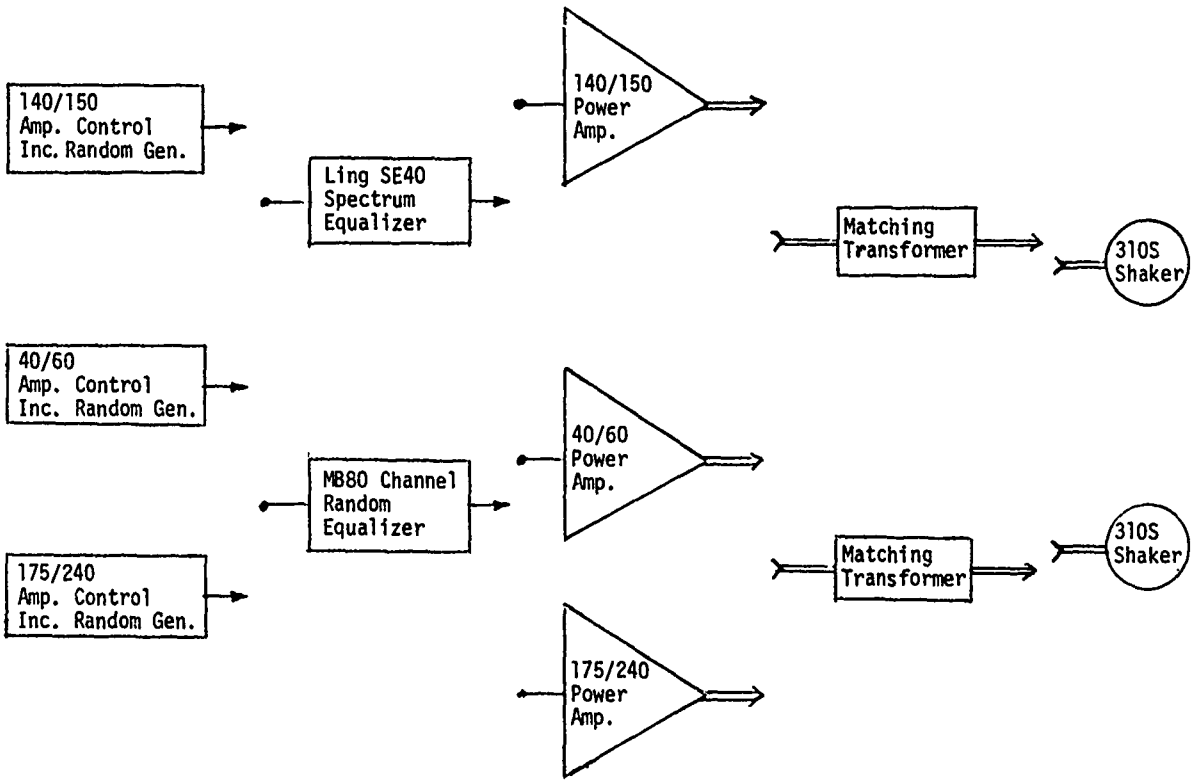


Figure 11. Block Diagram Of The Dual Shaker Vibration System.

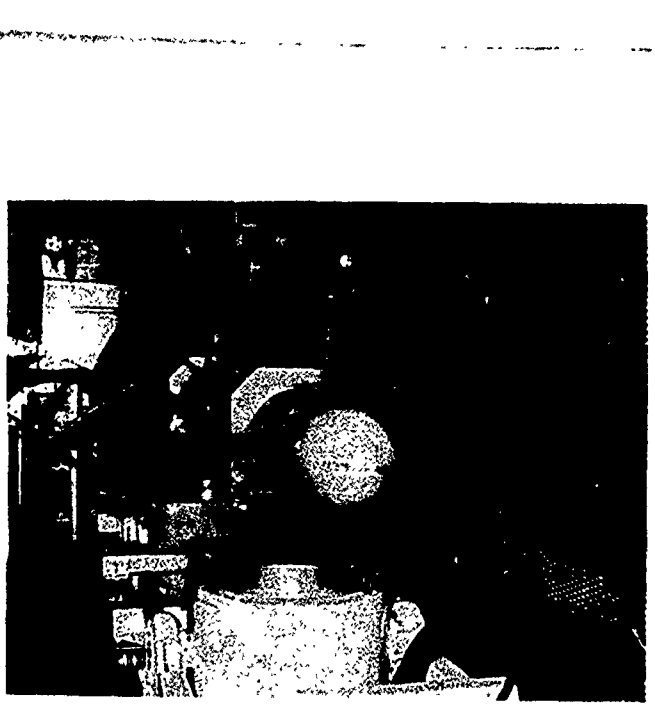


Figure 12 - An Overall View of the HARPOON Missile Combined Temperature-Altitude-Vibration Test Set Up in the Hieatt Chamber

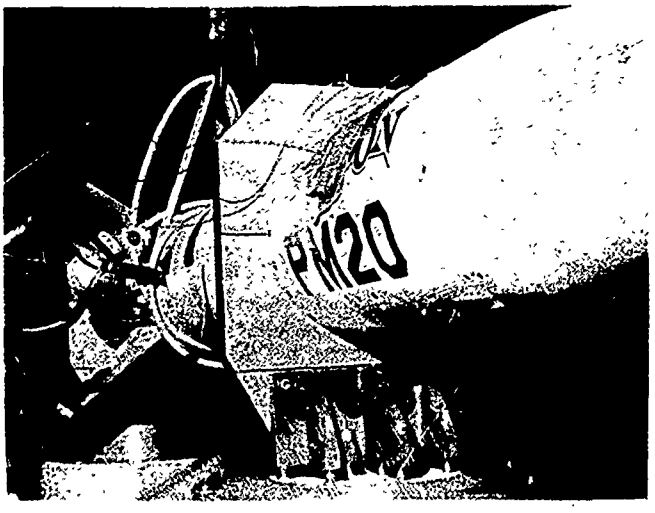


Figure 13 — A Close-Up View of the HARPOON Test Set Up Showing the Vibration Fixture

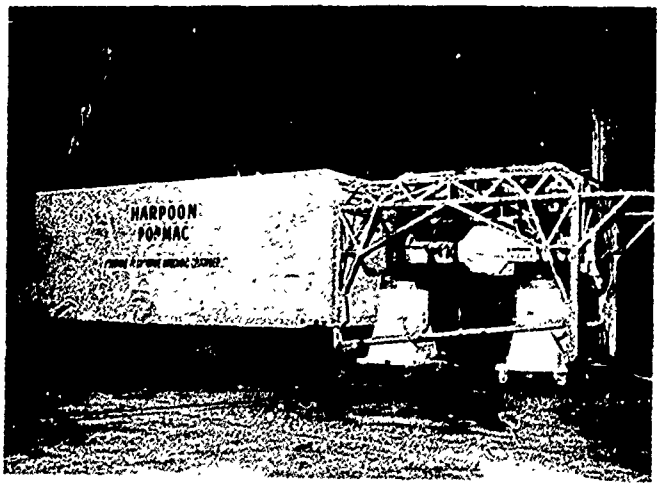


Figure 14 — An Overall View of the HARPOON Missile Combined Temperature-Vibration Test Set Up in the Climatic Chamber

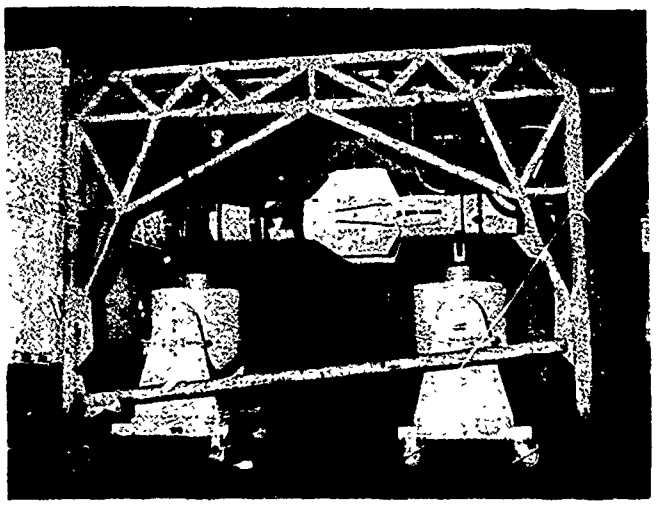


Figure 15 — A Close-Up View of the HARPOON Test Set Up Showing the Dual Shaker and the Vibration Fixture

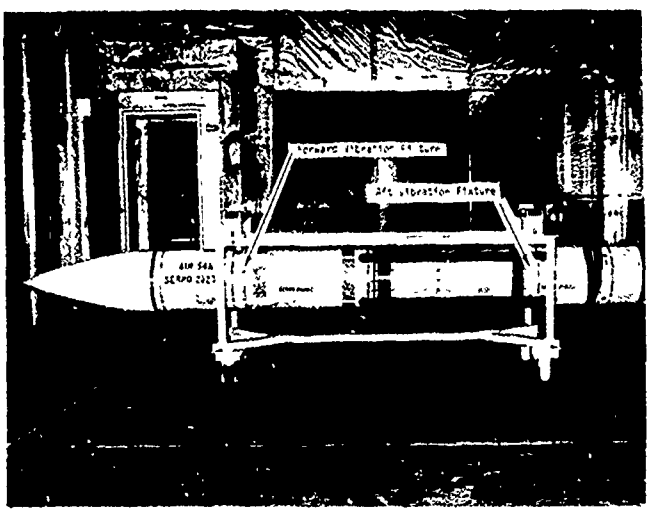


Figure 16 — A View of the PHOENIX Missile Showing Locations of the Vibration Fixtures



Figure 17 — An Exploded View Showing the Ring Segments, Spaces, Flat Head Screws, and Launcher Hook Clamping Block

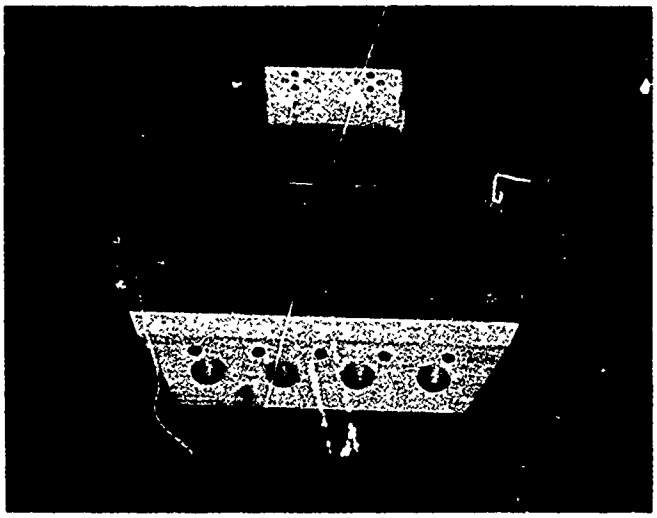


Figure 18 — A View Showing the Split Collar and Launcher Hook Clamping Block for the Forward Vibration Fixture

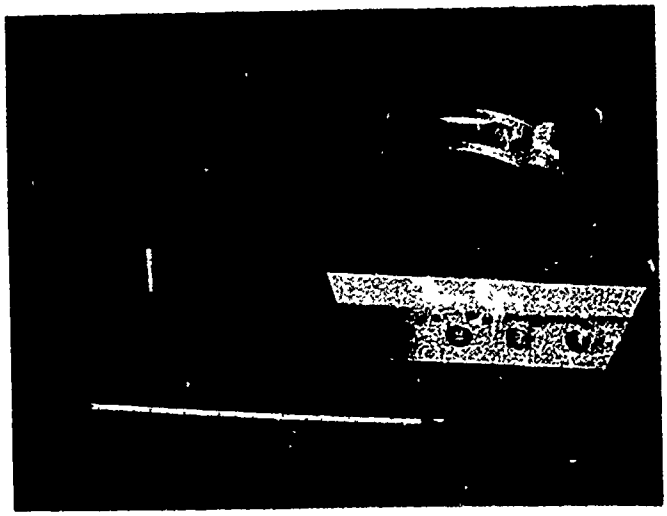


Figure 19 — A View Showing the Ring Segments, Launcher Hook Clamping Block, and Split Collar for the Aft Vibration Fixture

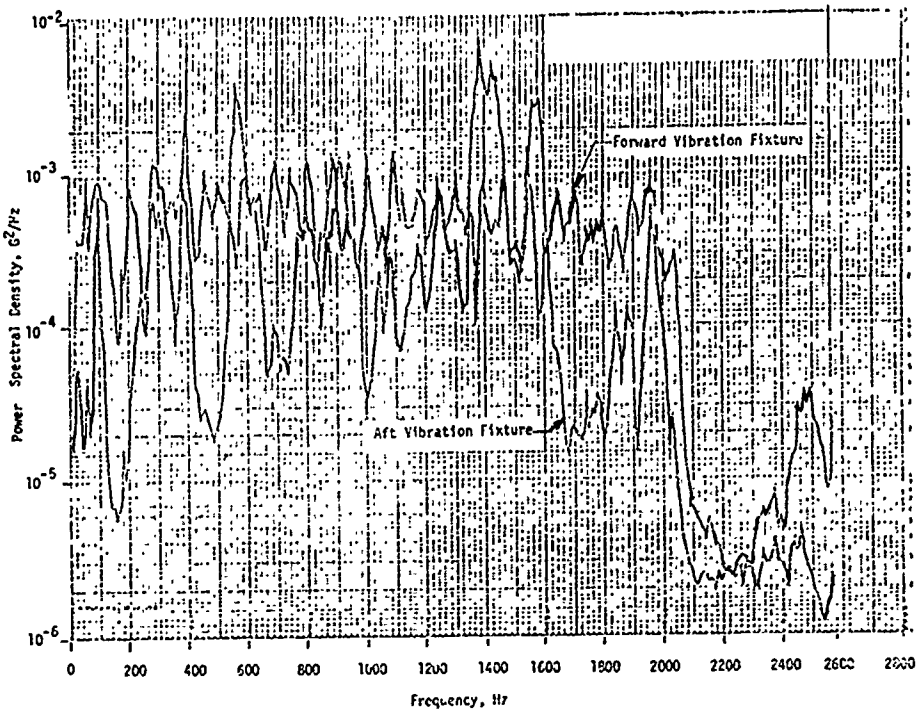


Figure 20. Power Spectral Density of Vibration At The Forward and Aft Vibration Fixtures With Vibration Input At Forward Shaker And No Field or Armature Current At Aft Shaker, Using the "Dummy" HARPOON Missile.

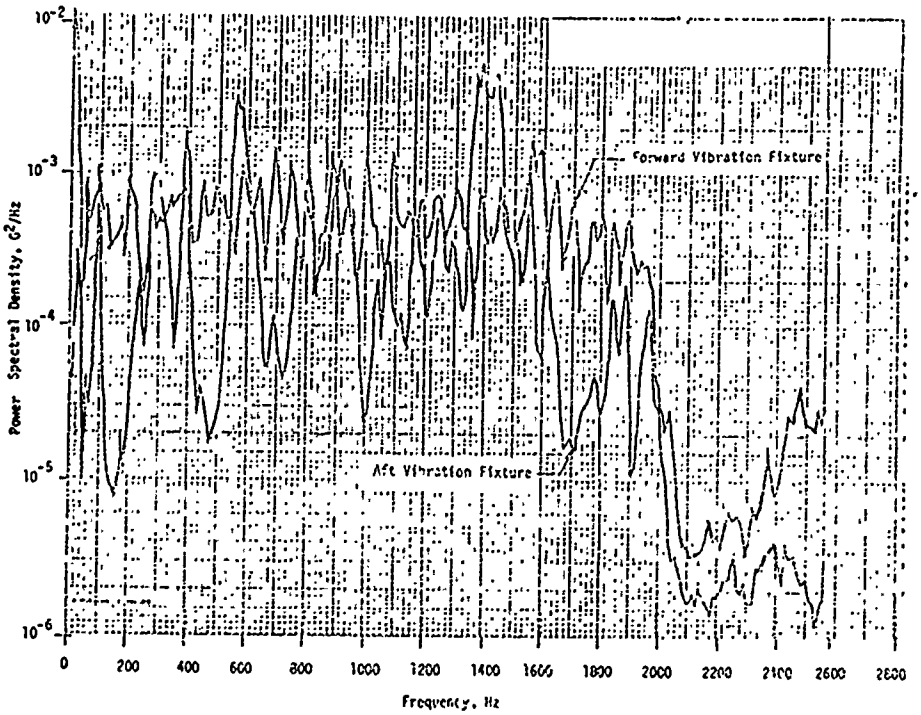


Figure 21. Power spectral Density of Vibration At The Forward And Aft Vibration Fixture With Vibration Input At Forward Shaker And Field Current Only At Aft Shaker Using The "Dummy" HARPOON Missile.

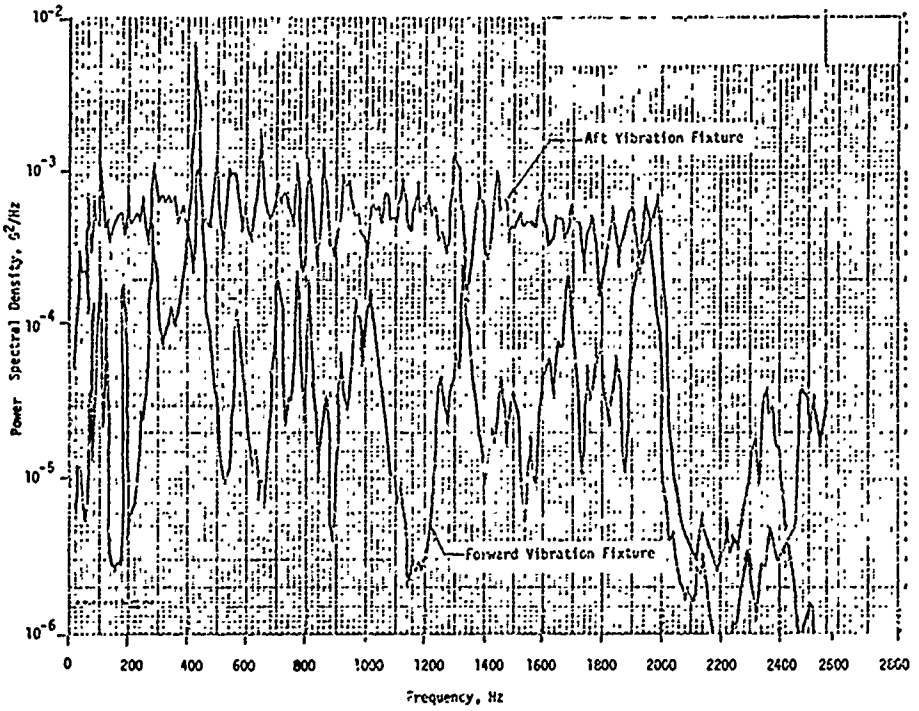


Figure 22. Power Spectral Density of Vibration At The Forward And Aft Vibration Fixtures With Vibration Input At The Aft Shaker And No Field or Armature Current At Forward Shaker, Using The "Dummy" HARPOON Missile.

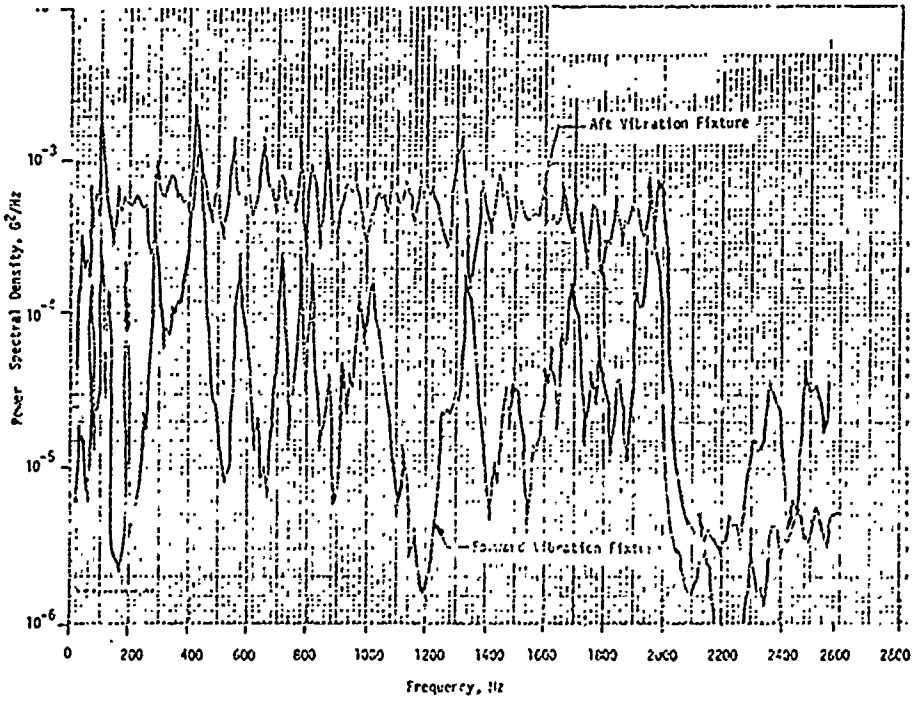


Figure 23. Power Spectral Density of Vibration At The Forward And Aft Vibration Fixture With Vibration Input At The Aft Shaker And Field Current Only At The Forward Shaker, Using The "Dummy" HARPOON Missile.

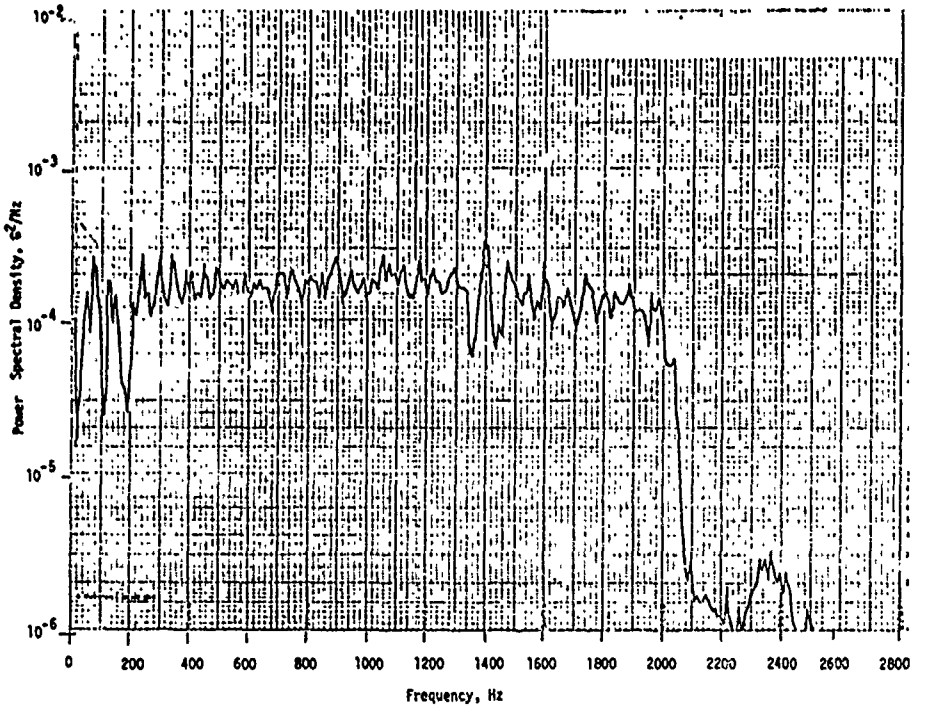


Figure 24. Power Spectral Density of Vibration At The Forward Fixture With Vibration Input At The Forward Shaker And No Field or Armature Current At The Aft Shaker, Using The Prototype HARPOON Missile.

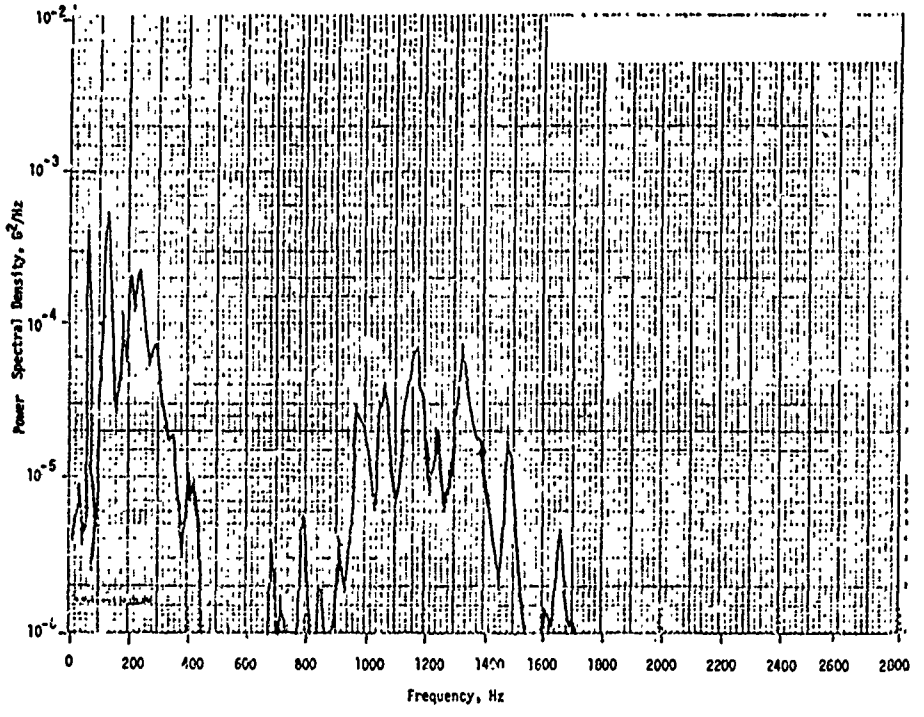


Figure 25. Power Spectral Density of Vibration At The Aft Fixture With Vibration Input At The Forward Shaker And No Field Or Armature Current At The Aft Shaker, Using The Prototype HARPOON Missile.

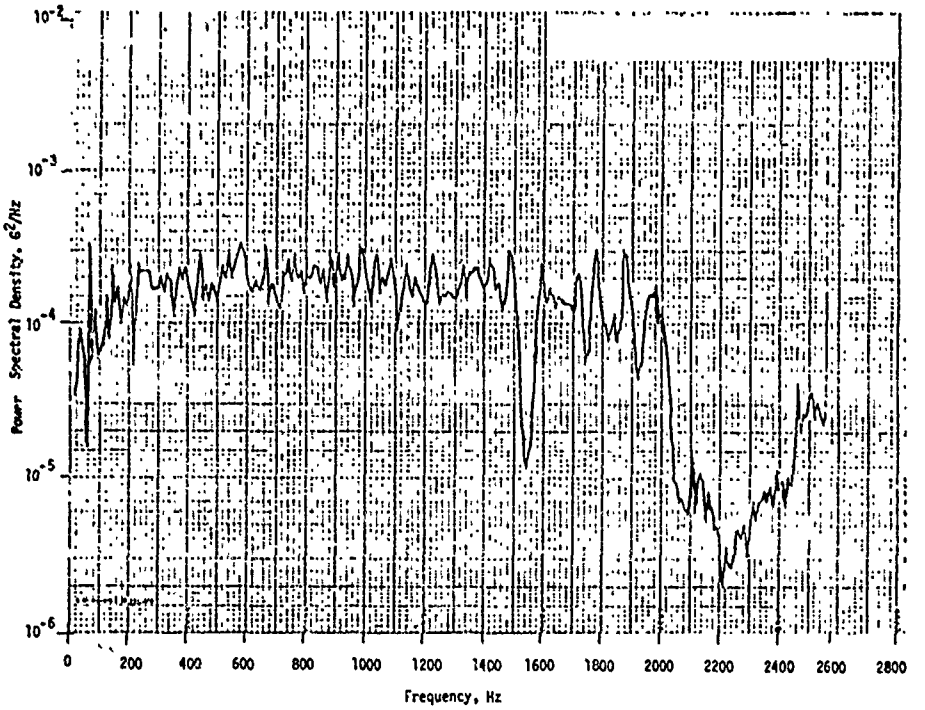


Figure 26. Power Spectral Density of Vibration At The Aft Fixture With Vibration Input At The Aft Shaker And No Field Or Armature Current At The Forward Shaker, Using The Prototype HARPOON Missile.

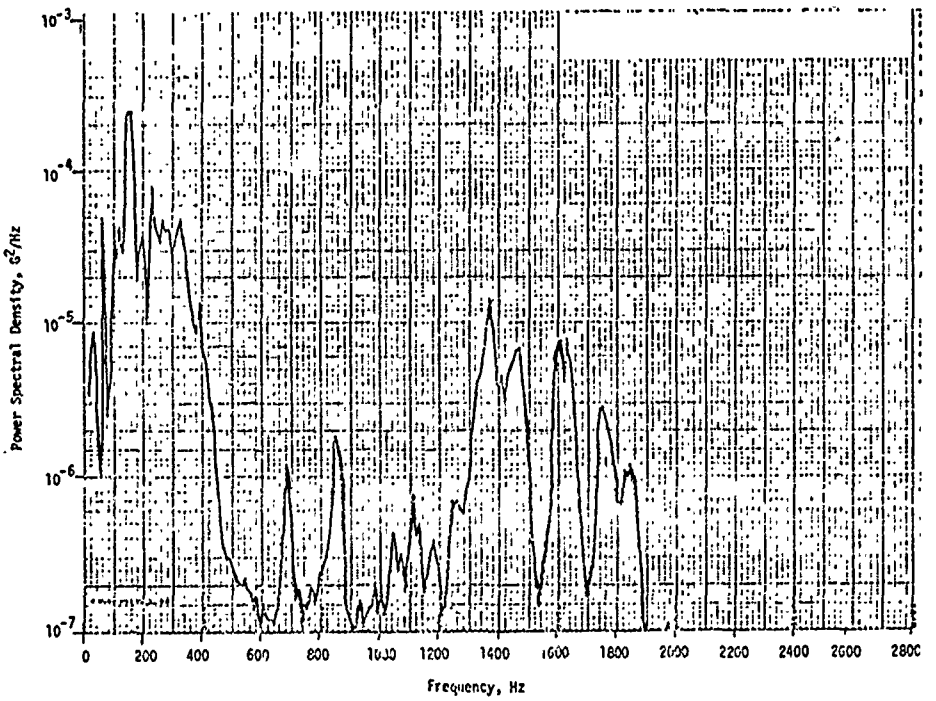


Figure 27. Power Spectral Density of Vibration At The Forward Fixture With Vibration Input At The Aft Shaker And No Field Or Armature Current At The Forward Shaker, Using the Prototype HARPOON Missile.

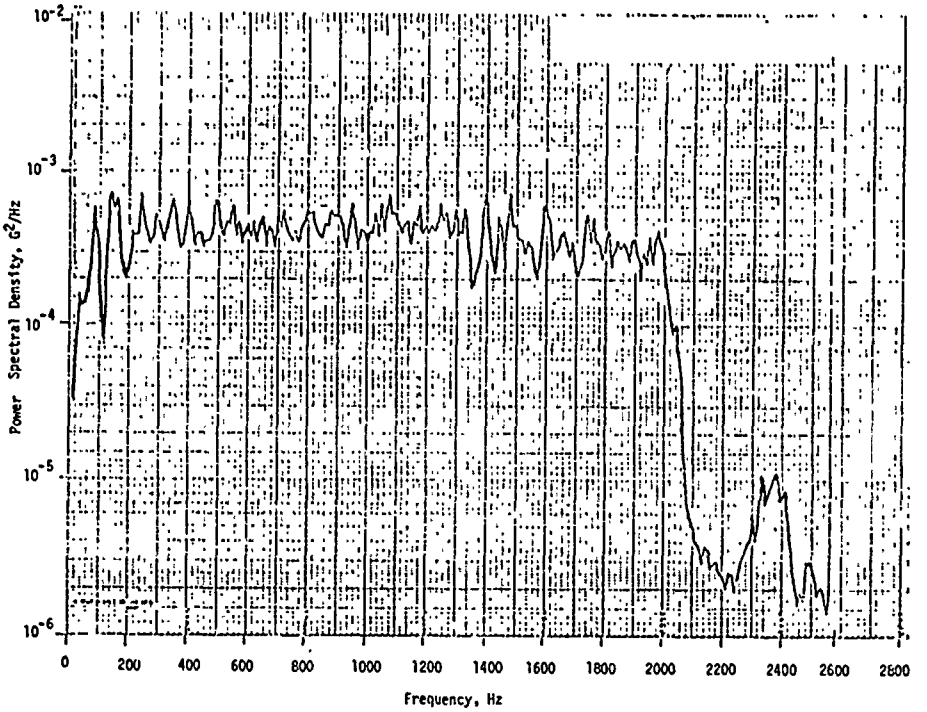


Figure 28. Power Spectral Density of Vibration At The Forward Fixture With Low Level Vibration Input At Both Shakers, Using The Prototype HARPOON Missile.

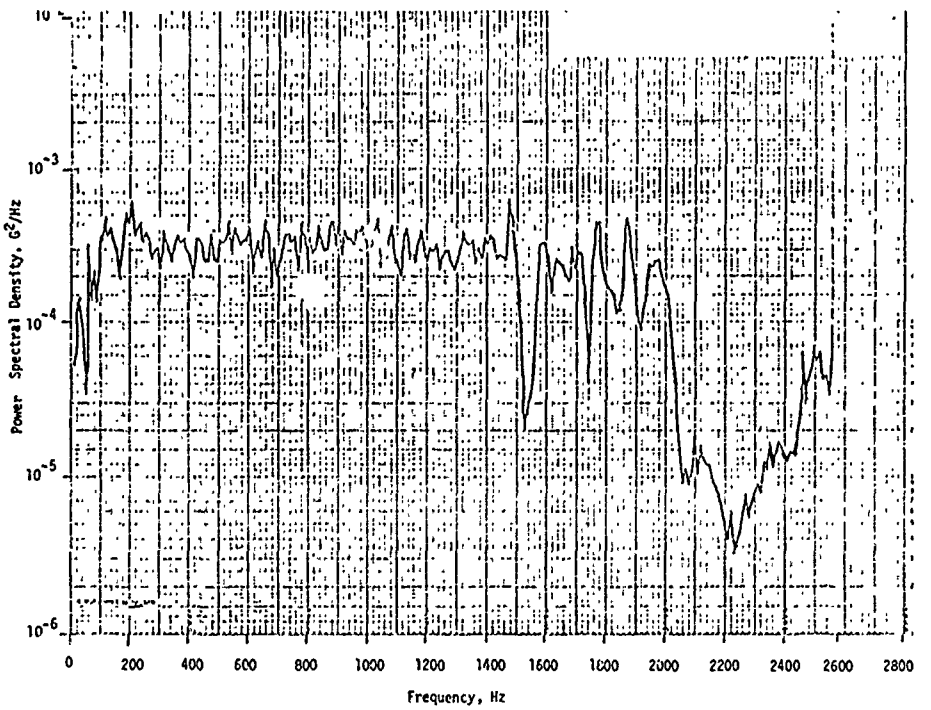


Figure 29. Power Spectral Density of Vibration At The Aft Fixture With Low Level Vibration Input At Both Shakers, Using The Prototype HARPOON Missile.

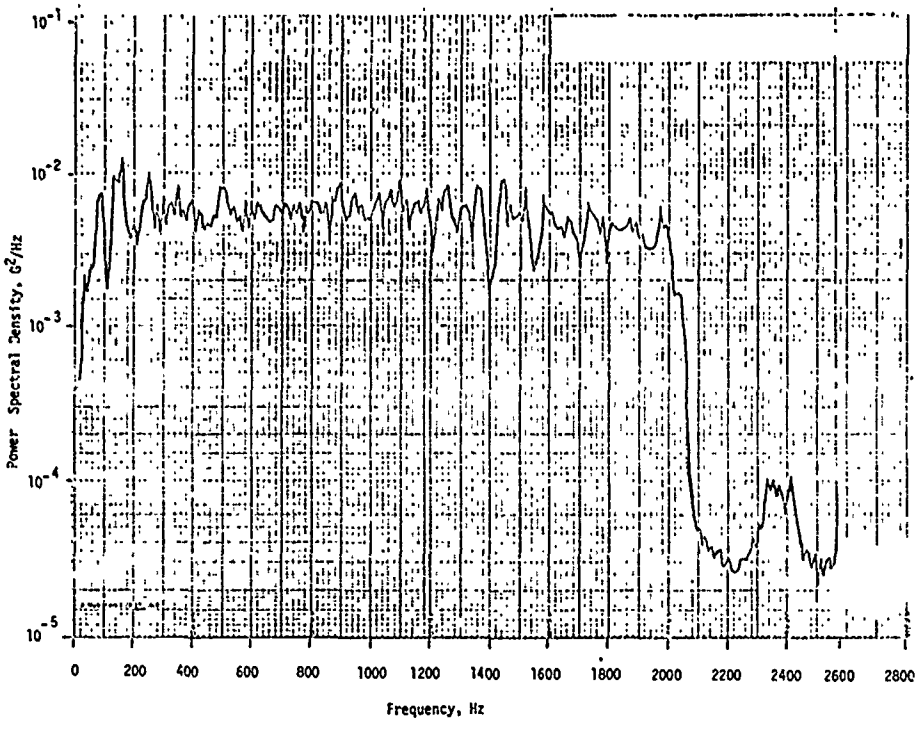


Figure 30. Power Spectral Density of Vibration At The Forward Fixture With Intermediate Level Vibration Input At Both Shakers, Using The Prototype HARPOON Missile.

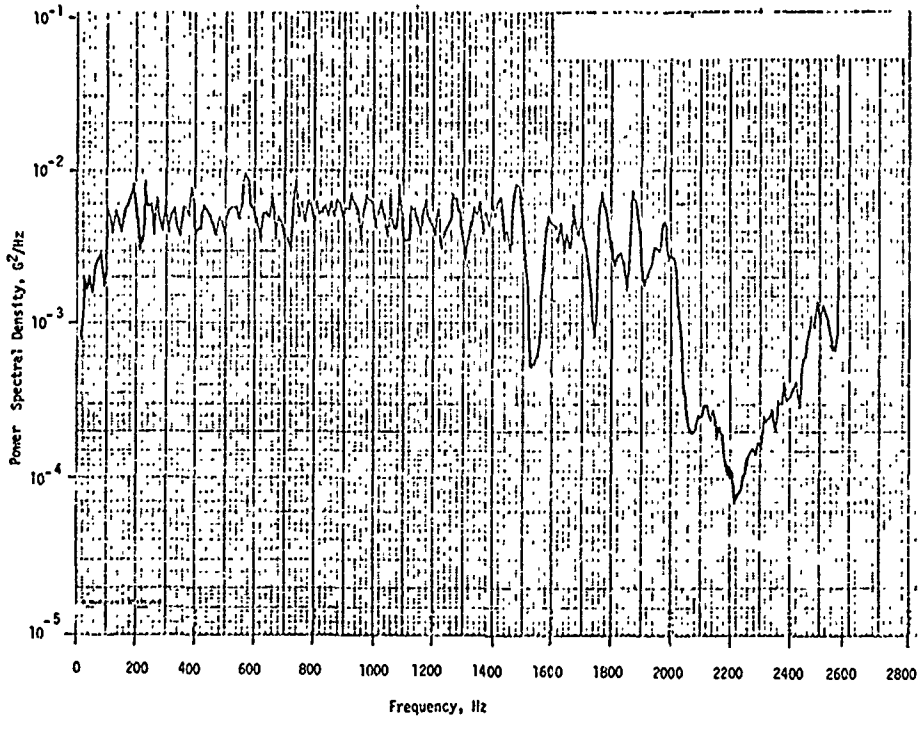


Figure 31. Power Spectral Density of Vibration At The Aft Fixture With Intermediate Level Vibration Input At Both Shakers, Using The Prototype HARPOON Missile.

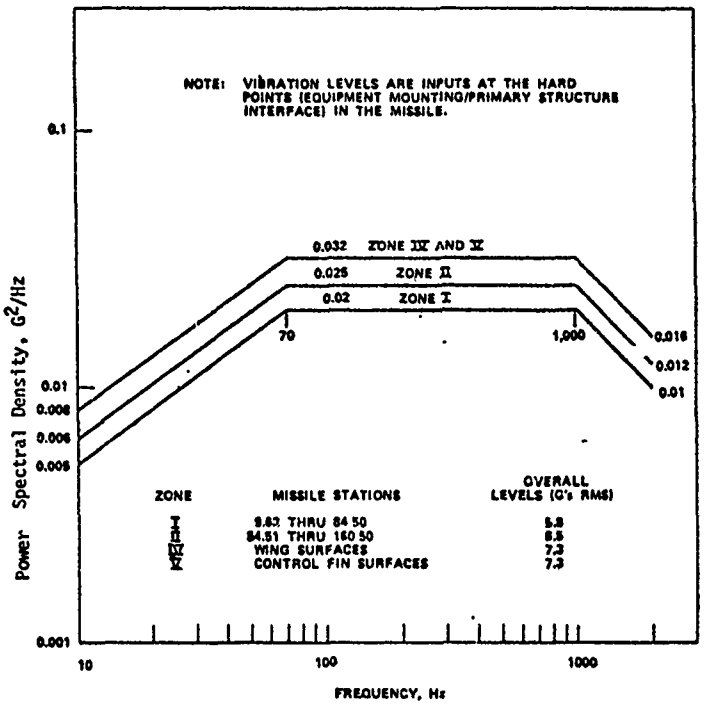


Figure 32. HARPOON Missile Vibration Environment Free Flight.

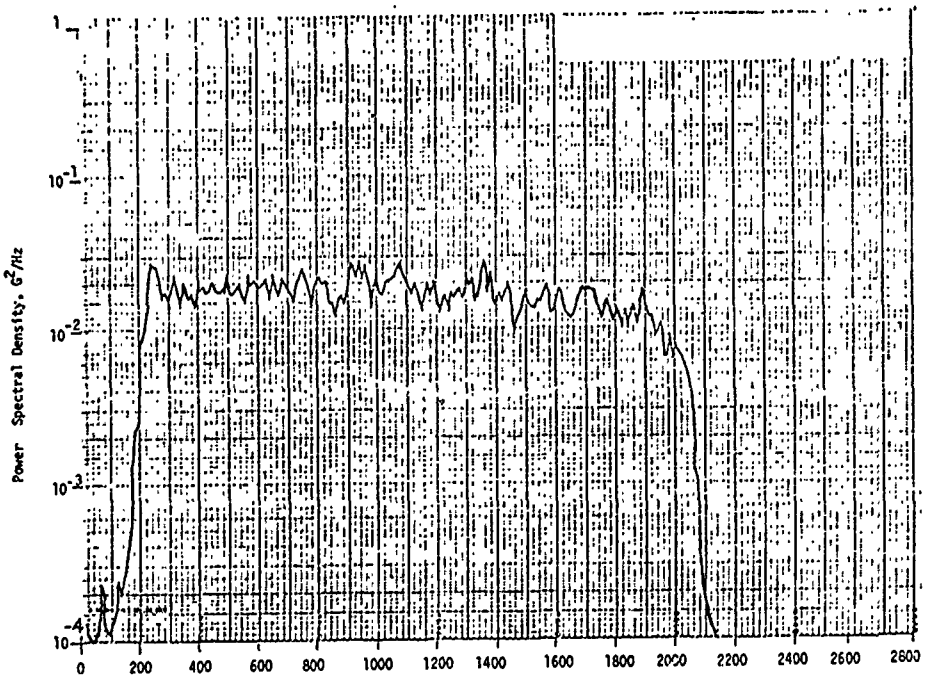


Figure 33. Power Spectral Density of Vibration At The Forward Fixture With Free-Flight Level Vibration Input At Both Shakers, Using The Prototype HARPOON Missile.

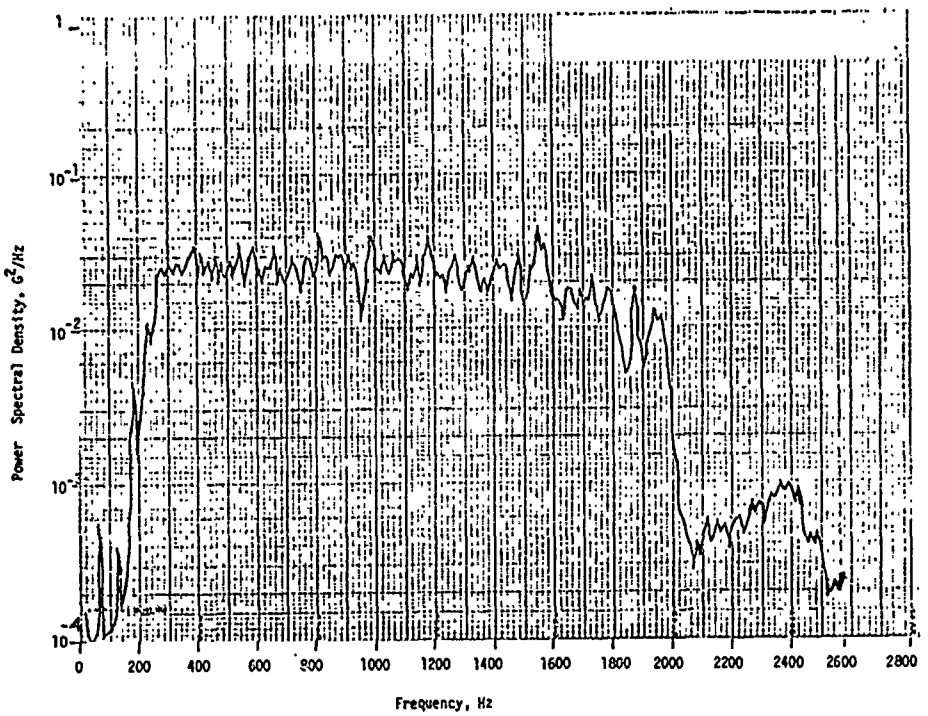


Figure 34. Power Spectral Density of Vibration At The Aft Fixture With Free-Flight Level Vibration Input At Both Shakers, Using The Prototype HARPOON Missile.

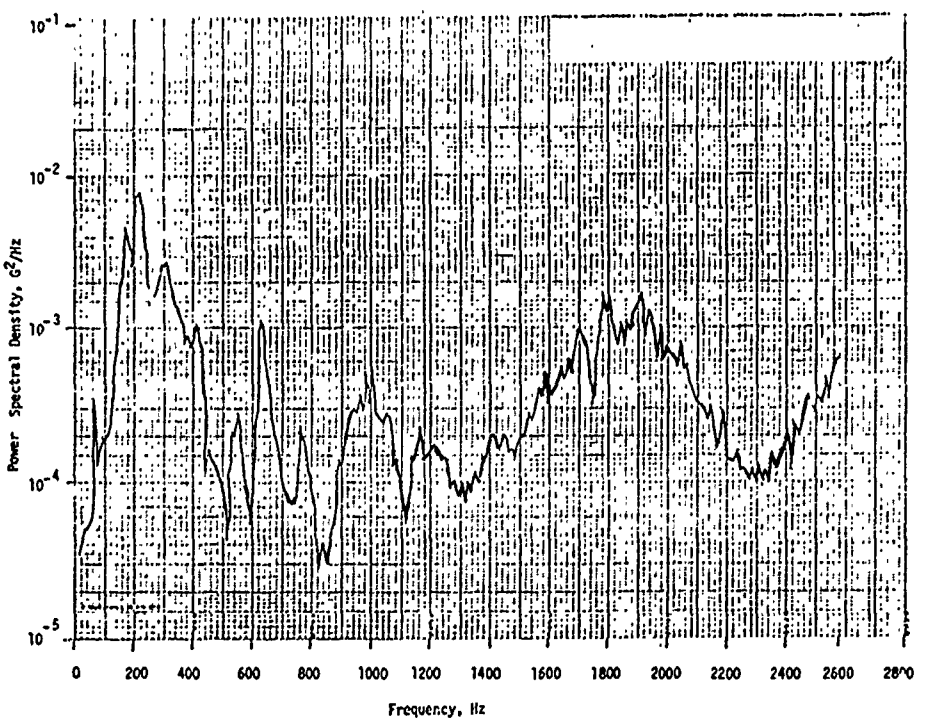


Figure 35. Power Spectral Density of Vibration At Missile Station 37.8, 180° (Z Axis) With Free-Flight Level Vibration Input At Both Shakers, Using The Prototype HARPOON Missile.

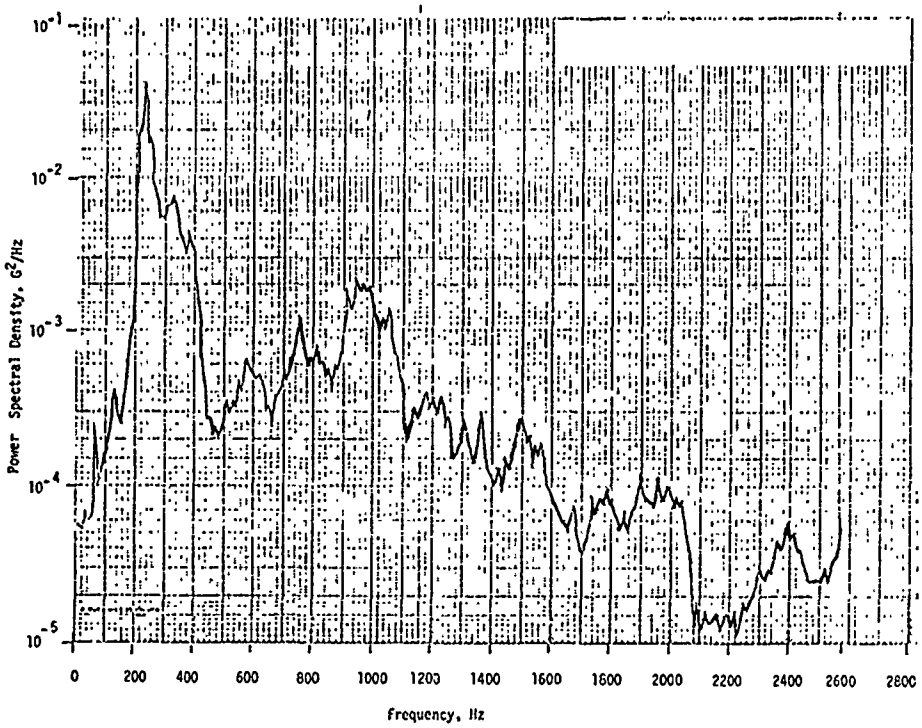


Figure 36. Power Spectral Density Of Vibration At Missile Station 26.6, 330° (Z Axis) With Free-Flight Level Vibration Input At Both Shakers, Using The Prototype HARPOON Missile.

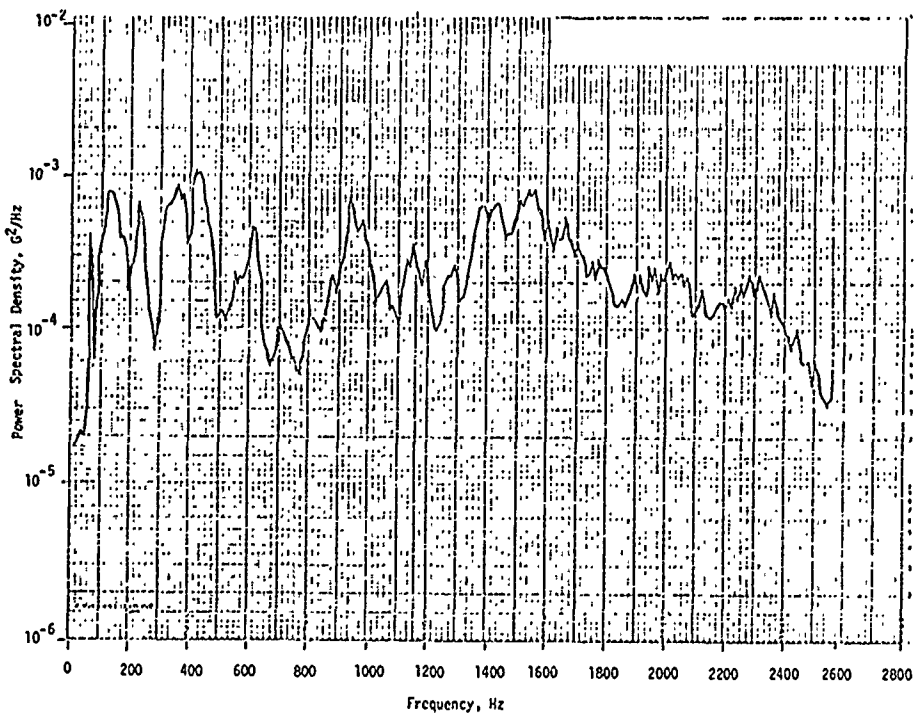


Figure 37. Power Spectral Density of Vibration At Missile Station 37.8, 100° (Y Axis) With Free-Flight Level Vibration Input At Both Shakers, Using the Prototype HARPOON Missile.

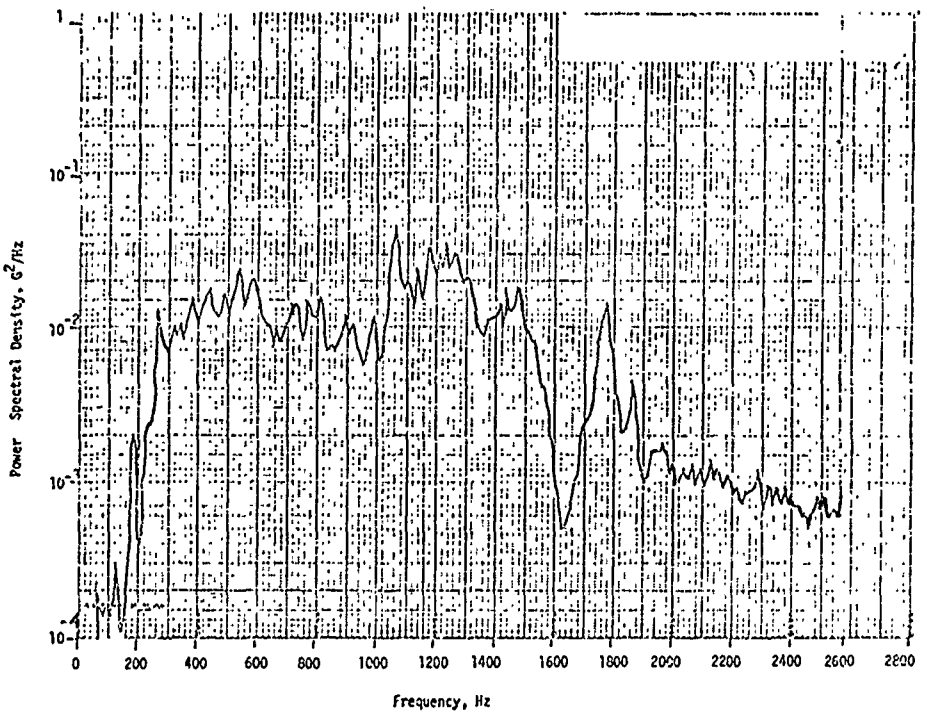


Figure 38. Power Spectral Density Of Vibration At Engine (Z Axis) With Free-Flight Level Vibration Input , Both Shakers, Using The Prototype HARPOON Missile.

Discussion

Mr. Caruso (Westinghouse Electric): Did you have to notch either of the inputs to compensate for inputs from the opposite end of the missile or for fixture resonances?

Mr. Ryden: No. We only notched at the lower frequency to obtain the desired spectrum given in the specification. We felt that we might have to do this but the way it turned out there was enough damping in the power amplifier so that this wasn't necessary.

Mr. Caruso: Did you encounter any problems from feed through from one end of the test item to the other?

Mr. Ryden: No, even with the indicated cross transmissibility on the Harpoon missile of eight to one this was attenuated.

ANALYSIS OF FATIGUE UNDER RANDOM VIBRATION

Ronald G. Lambert
General Electric Company
Aircraft Equipment Division
Utica, New York 13503

Closed form analytical solutions have been derived to quantitatively describe many areas of interest regarding fatigue under random vibration. These areas include relating root-mean-square Gaussian stress to cycles and time to failure, the probability density function of cycles to failure, and the probability of failure to cycles to failure. Also included are the effects of stress limiting and of an endurance limit. Comparisons between analytical predictions and empirical results have been shown to be good whenever such comparisons were made.

INTRODUCTION

This paper deals primarily with the type of random loading that occurs most often in a random vibration test of high reliability electronic equipment for military or space application. The vibration exciter applies random accelerations over a bandwidth of approximately 20 to 2000 Hz. The structures of interest within the components or the unit under test respond at or near their resonant frequencies. The resulting response stresses are narrowband random functions with a root-mean-square (rms) value of σ and a static stress of approximately zero. The envelope of the stress peaks can be expressed as a Rayleigh probability density function (PDF). Stress limiting (i.e., clipping) sometimes occurs if the motion of the stressed structure is limited by snubbers or other clearance-limiting devices or if the vibratory forces are clipped.

All results utilize Miner's cumulative damage hypothesis. The relationships are based on commonly available sinusoidal fatigue "S-N" curves. The sinusoidal fatigue data used in the examples was obtained from Reference 1. Scatterband effects in the sinusoidal S-N fatigue curves are treated. The analysis covers the plastic Coffin-Manson [2] low-cycle life fatigue region as well as the elastic Basquin [2] high-cycle life fatigue region by assuming the stress to be the "true" stress instead of the more usual "engineering" stress. Which of the two stresses is the stress that should be the basis of the analysis for random vibration is an area requiring further investigation. The two stresses become the same in the elastic region above approximately 10^3 cycles, which is the region of interest for the design of high reliability equipment.

SINUSOIDAL S-N CURVE DEFINITION

Fatigue data in the form of the harmonic sinusoidal fatigue S-N curve as shown in Figure 1 is usually available in the literature. This type of fatigue curve can be represented by a power law expression which is a straight line on a log-log plot with slope B and y-intercept A for N = 1 cycle. The instantaneous sinusoidal stress has the familiar saddle shape PDF and the positive peak stress envelope (the dotted line) has an impulse PDF at a stress value of S. Projecting this value of the envelope onto the S-N curve gives a value of N_S as the number of cycles to failure.

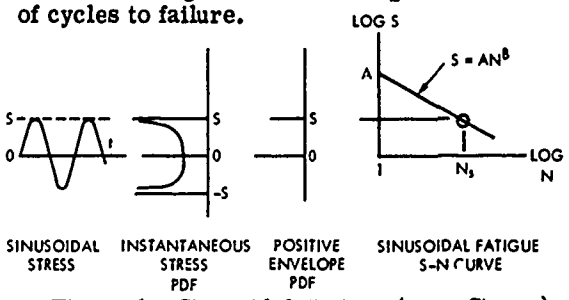


Figure 1. Sinusoidal Fatigue (True Stress)

PRECEDING PAGE BLANK-NOT FILMED

There are two common definitions of stress, engineering and true stress. Engineering stress is defined as the applied load divided by the original area. True stress is defined [3] as the applied load divided by the actual necked-down area. The true stress is larger in value than the engineering stress.

The stress in Figure 1 is taken to be the true stress in which case the material constant A is equal to the true ultimate stress and the slope B is equal to the Basquin coefficient for the material. The S-N curve is a single line [3, 4, 5] even though the corresponding strain-cycles to failure fatigue curve [2] is a double straight line on a log-log plot.

If the stress is taken to be the engineering stress, the sinusoidal S-N fatigue curve in the Coffin-Manson low-cycle life region (i.e., below about 10^3 cycles for common structural materials) becomes truncated [1] as shown in Figure 2. The horizontal truncation implies a lack of cumulative damage in the low-cycle life region which is not consistent with the Coffin-Manson strain-cycles to failure fatigue curves in that same region. Therefore, the stress will be taken to be the true stress for this analysis.

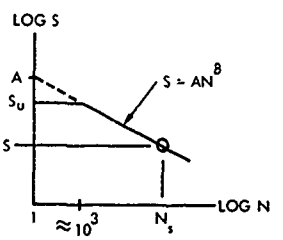


Figure 2. Sinusoidal Fatigue (Engineering Stress)

The single line represented by the power law expression $S = AN^B$ represents the mean value of a scatterband of empirical data points and is usually arrived at by a regression analysis such as a least-squares curve fit. The data points are Gaussianly distributed about the mean value of stress and have a standard deviation from the mean of approximately 5 percent in the vicinity of the ultimate stress and approximately 8 percent in the vicinity of 10^7 cycles (near the endurance limit for some materials) [6].

CUMULATIVE DAMAGE CONCEPT

Fatigue microcrack nucleation (i.e., initiation) occurs at only one percent of the total fatigue life [7]. Many small microcracks undergo two stages of crack growth, then combine into a macrocrack which eventually propagates until the specimen fractures. Fatigue damage is cumulating during the entire fatigue life. Fatigue failure is the catastrophic fracture at the end of fatigue life.

Miner's hypothesis [8] quantitatively expresses damage cumulation and relates it to failure as follows:

$$D_s = \frac{n_s}{N_s} \quad ; \quad \sum D_s = 1 \text{ at failure} \quad \text{(Miner's results)}$$

where

n_s = number of stress peaks at level s

N_s = number of stress peaks at level s to cause failure

D_s = proportion of damage related to stress peaks at level s

Define:

P(s) = fraction of cycles occurring at stress level s

N_T = total number of stress cycles to failure

$$P(s) = \frac{n_s}{N_T} \quad ; \quad n_s = N_T P(s)$$

Thus:

$$D_s = N_T P(s) / N_s$$

Note: N_T is a constant for a given value of rms stress level.

From Miner's hypothesis,

$$1 = \int_0^\infty D_s dS = N_T \int_0^\infty \left[P(s)/N_s\right] dS \qquad (1)$$

Therefore:

$$N_T = \frac{1}{\int_0^\infty \left[P(s)/N_s\right] dS} \qquad (2)$$

Equation (2) is the key equation for the subsequent analysis.

RANDOM FATIGUE CURVE DERIVATION

The purpose of this derivation is to obtain a closed form relationship between the random rms stress and cycles to failure. A typical profile of a narrowband random stress process is shown in Figure 3. The instantaneous

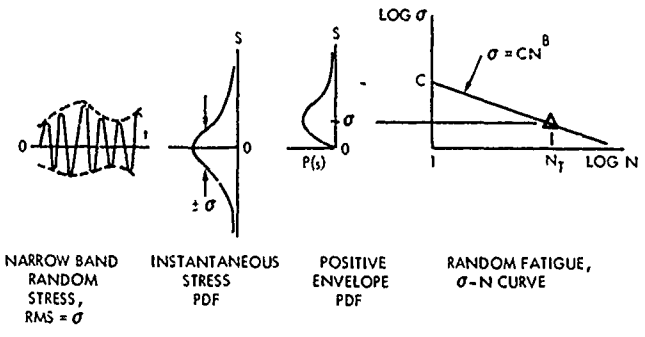


Figure 3. Random Fatigue

stress has a Gaussian PDF. The positive envelope of the stress peaks (upper dotted line) has a Rayleigh PDF. The mode (i.e., the value of stress at which the PDF is a maximum) is equal to the rms level σ of the instantaneous stress. A stress level σ has a corresponding life of N_T cycles to failure. Figure 3 shows the desired power law expression similar to that of the sinusoidal S-N fatigue curve of Figure 1.

The stress peak envelope has a Rayleigh PDF as follows:

$$P(s) = \frac{S}{\sigma^2} \exp\left[-\frac{S^2}{2\sigma^2}\right] \qquad \text{for } S \geq 0 \tag{3}$$

$$P(s) = 0 \qquad \text{for } S < 0$$

From the sinusoidal S-N fatigue curve of slope B on a log-log plot and with y-intercept (i.e., N = 1) of A, the value for N_S may be obtained as follows:

$$N_S = \left[\frac{S}{A}\right]^{1/B} = \left[\frac{S}{A}\right]^{-\beta} \tag{4}$$

where

$$\beta = -1/B \tag{5}$$

B is always a negative value.

β and A are always positive.

Note that A, B, and β are material constants.

In equation (1), D_S represents the damage PDF. If D_S is scaled by the constant factor N_T, the new function, defined as G(s), can be thought of as a scaled damage PDF. As such, it indicates how the fatigue damage is distributed as a function of stress.

$$G(s) = \frac{D_S}{N_T} = \frac{P(s)}{N_S} = \left|\frac{1}{\sigma^2 A^\beta}\right| S^{1+\beta} e^{-S^2/2\sigma^2} \tag{6}$$

Then, from equation (2),

$$N_T = \frac{1}{\int_0^\infty G(s)\,dS} \tag{7}$$

With the substitution $z = S^2/2\sigma^2$ and $x = (2+\beta)/2$ into equations (6) and (2),

$$N_T = \frac{1}{\left|\frac{\sqrt{2}\sigma}{A}\right|^\beta \int_0^\infty z^{x-1} e^{-z} dz} = \frac{1}{\left|\frac{\sqrt{2}\sigma}{A}\right|^\beta \Gamma\left(\frac{2+\beta}{2}\right)} \tag{8}$$

$$N_T = \left\{\left|\frac{A}{\sqrt{2}}\right|^\beta \left[\frac{1}{\Gamma\left(\frac{2+\beta}{2}\right)}\right]\right\} \sigma^{-\beta} \tag{9}$$

or

$$\sigma = \left\{\left|\frac{A}{\sqrt{2}}\right| \left[\frac{1}{\Gamma\left(\frac{2+\beta}{2}\right)}\right]^{1/\beta}\right\} N_T^{-1/\beta} \tag{10}$$

Equations (9) and (10) above represent the expression for the random fatigue "σ-N" curve. The σ-N curve is of the same form as the corresponding S-N curve and has the same slope on a log-log plot.

Equation (10) can also be expressed as follows:

$$\sigma = C N_T^{-1/\beta} \tag{11}$$

where

$$C = \left|\frac{A}{\sqrt{2}}\right| \left[\frac{1}{\Gamma\left(\frac{2+\beta}{2}\right)}\right]^{1/\beta} \quad \text{stress units} \tag{12}$$

The constant C is a function only of the true ultimate stress A and β the negative reciprocal of the slope of the sinusoidal S-N fatigue curve. Both are material constants. C can be thought of as the true ultimate rms random stress, since it represents the y-intercept for $N_T = 1$ in equation (11) on a log-log plot. Figure 4 illustrates equation (11) and compares this curve with the S-N curve of equation (4) for copper wire.

Typical fatigue curve constants are given in Table 1. This data was obtained from Reference 1 by estimating the parameter values using the graphs in Chapter 10.

TABLE 1. TYPICAL FATIGUE CURVE CONSTANTS

Material	True Ultimate Stress, A		Basquin Slope Coefficient, B	$\beta = -1/B$	C	
	(ksi)	(Pa)			(ksi)	(Pa)
Copper Wire	81.9	5.65×10^8	-0.108	9.28	36.9	2.54×10^8
Aluminum Alloy (6061-T6)	109.7	7.56×10^8	-0.112	8.92	49.7	3.43×10^8
(7075-T6)	179.5	12.38×10^8	-0.104	9.65	79.9	5.51×10^8
Magnesium Alloy (AZ31B)	43.3	2.99×10^8	-0.045	22.37	13.6	9.38×10^7
301 Stainless (3/4 Hard)	120.33	8.30×10^8	-0.046	21.85	38.53	2.66×10^8
Wrought Steel (SAE 4130 BHN 267)	175.90	12.13×10^8	-0.057	17.54	61.91	4.27×10^8
Titanium Alloy (Ti-8 Al-1 Mo-IV Sheet) Alternating Axial Load	176.36	12.16×10^8	-0.068	14.62	66.66	4.60×10^8
Soft Solder (37% Lead, 63% Tin)	15.29	1.05×10^8	-0.102	9.85	6.740	4.65×10^7
G-10 Epoxy Fiberglass	80.94	5.58×10^8	-0.083	12.08	33.00	2.28×10^8

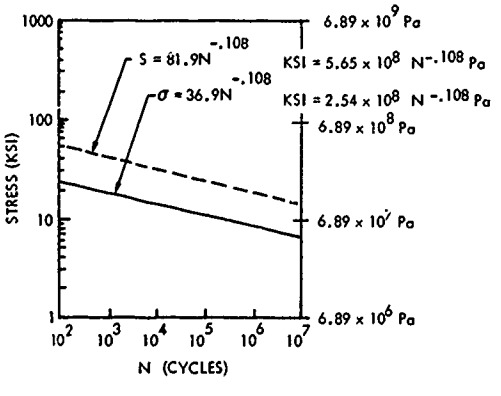


Figure 4. Comparison of Fatigue Curves for Copper Wire

From equation (4),

$$S = AN_s^{-1/\beta} \tag{13}$$

As a check on the analytical accuracy of the constant C in equation (12), the analytically predicted ratio of S/σ can be compared with empirical results. In Reference 9, it is stated that the ratio of S/σ has a value of 3 or more for brittle materials and below 2 for very ductile materials.

$$\frac{S}{\sigma} = \frac{AN^{-1/\beta}}{CN^{-1/\beta}} = \frac{A}{C}$$

For $N_S = N_T = N$, Table 2 shows several S/σ comparisons.

TABLE 2. S/σ COMPARISONS

Material	Ultimate Strain (%)	$S/\sigma = A/C$
Copper Wire	15	2.22
6061-T6	15	2.20
AZ31B	7	3.18

It can be seen that the values of S/σ are approximately 2 for the ductile materials (ϵ_u = 15%) and approximately 3 for the comparatively brittle material (ϵ_u = 7%). This data does not prove that this relationship applies to all mate-

rials, but it does show good agreement with empirical results for the materials checked. On this basis, the expression for C in equation (12) is considered to be reasonably accurate.

The statistical properties of the damage function G(s) in equation (6) can be shown to be as follows:

G(s) is a maximum at the mode S_o

where

$$\text{Mode } S_o = \sigma \sqrt{1+\beta} \tag{14}$$

$$E\{G(s)\} = \overline{G(s)} = \sqrt{2}\,\sigma \left[\frac{\Gamma\left(\frac{3+\beta}{2}\right)}{\Gamma\left(\frac{2+\beta}{2}\right)}\right] \tag{15}$$

$\sigma_{G(s)}$ = standard deviation of G(s)

$$\sigma^2_{G(s)} \quad 2\sigma^2 \left\{ \frac{\Gamma\left(\frac{4+\beta}{2}\right)}{\Gamma\left(\frac{2+\beta}{2}\right)} - \left[\frac{\Gamma\left(\frac{3+\beta}{2}\right)}{\Gamma\left(\frac{2+\beta}{2}\right)}\right]^2 \right\} \tag{16}$$

The above statistical properties of G(s) are linearly proportional to σ and are functions only of the slope parameter β.

Table 3 lists typical parameter values. S_o and $\overline{G(s)}$ are very nearly equal. S_o occurs at about 3σ for most of the materials shown. Refer to equation (14). The AZ31B mode occurs at 4.8σ due to its large value of β. The larger the value of β, the more brittle the material [5]. The last data column $(\overline{G(s)} + 2\sigma_{G(s)})$ indicates the value of stress beyond which very little damage occurs. For most of the materials shown, this stress is approximately 5σ.

The standard deviation of G(s) has a constant value of 0.7σ. The reason for this is not known. Refer to equation (16). It can easily be shown that:

$$\frac{\Gamma\left(\frac{4+\beta}{2}\right)}{\Gamma\left(\frac{2+\beta}{2}\right)} = \frac{2+\beta}{2}$$

TABLE 3. TYPICAL DAMAGE PDF CURVE PARAMETERS*

Material	Mode S_o	$\overline{G(s)}$	$\sigma_{G(s)}$	$G(s)+2\sigma_{G(s)}$
Copper Wire	3.21	3.28	0.7	4.7
Aluminum Alloys (6061-T6)	3.15	3.23	0.7	4.6
(7075-T6)	3.26	3.37	0.7	4.8
Magnesium Alloy (AZ31B)	4.83	4.88	0.7	6.3
301 Stainless (3/4 Hard)	4.78	4.83	0.7	6.2
Wrought Steel (SAE 4130 BHN 267)	4.30	4.36	0.7	5.8
Titanium Alloy (Ti-8 Al-1 Mo-IV Sheet) Alternating Axial Load	3.95	4.02	0.7	5.4
Soft Solder (37% Lead, 63% Tin)	3.29	3.37	0.7	4.8
G-10 Epoxy Fiberglass	3.62	3.69	0.7	5.1

*All the values should be multiplied by σ.

For $\sigma_{G(s)} = 0.7\sigma$, the following must be true:

$$\Gamma(\alpha+\tfrac{1}{2}) \cong \sqrt{\alpha - \tfrac{1}{4}}\ \Gamma(\alpha) \qquad (17)$$

where α does not have to be an integer.

Oddly enough, the above approximation is valid. The approximation improves for large α. See Appendix C.

EXAMPLE:

Material: Copper Wire

σ = 7 ksi = 4.83×10^7 Pa

A = 81.9 ksi = 5.65×10^8 Pa

β = 9.28

N_T = 5×10^6 cycles (from equation (9))

S_o = 3.21σ = 22.4 ksi = 1.54×10^8 Pa

$\overline{G(s)}$ = 3.28σ = 23 ksi = 1.59×10^8 Pa

$\sigma_{G(s)}$ = 0.7σ = 4.9 ksi = 3.38×10^7 Pa

This example is illustrated in Figure 5 using equations (3) and (6). G(s) is similar in shape to a Weibull PDF. Most of the stress peaks occur below 2σ where little damage is done in that region of the S-N fatigue curve. The stress peaks that occur above 5σ are in the damaging portion of the S-N curve, but they occur so seldomly that the net effect is one of little cumulative damage. Most of the damage is done by stress peaks between 2σ and 5σ for this material.

FATIGUE SENSITIVITY

Using equation (9), the fatigue life N_T is sensitive to the rms stress as follows:

$$\frac{N_1}{N_2} = \left(\frac{\sigma_2}{\sigma_1}\right)^{\beta} \qquad (18)$$

EXAMPLE:

$\frac{\sigma_2}{\sigma_1} = 2$; $\beta = 9.28$ for copper wire

$$\frac{N_1}{N_2} = \left(\frac{2}{1}\right)^{9.28} = 622$$

Thus, a reduction in rms stress of 2:1 results in an increase in fatigue life by a factor of 622:1.

PROBABILITY OF FAILURE

F(N) = probability of a fatigue failure in N cycles

= probability that $N > N_T$

R(N) = 1 - F(N) = probability of survival to N cycles = reliability

Since N_T is a constant for a given value of σ and not a random variable, its PDF is an impulse function of unity value at $N = N_T$. Note that all failures will occur at $N = N_T$.

The results shown in Figures 6 and 7 are due to the representation of the σ-N fatigue curve by a line of essentially zero width. That is, the fatigue curves thus far in the analysis

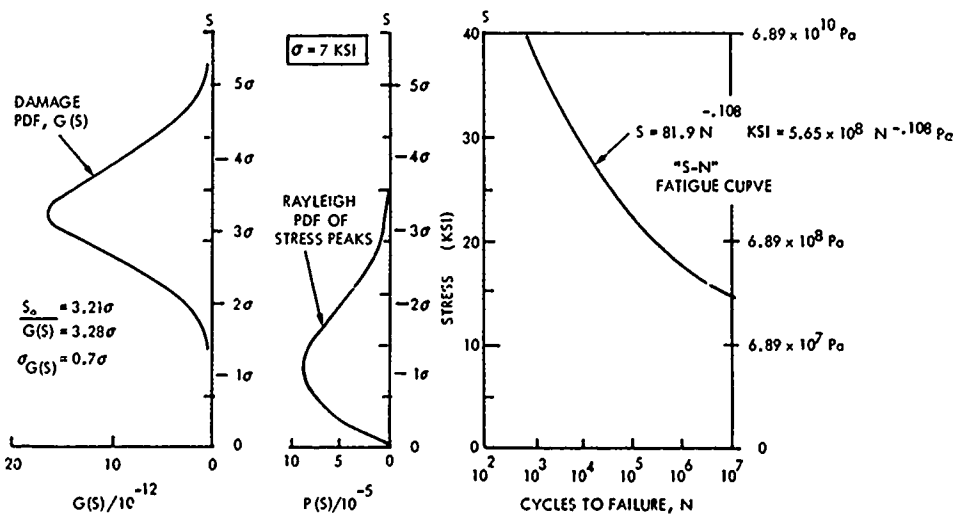


Figure 5. Copper Wire Example

have not represented either a scatterband in the rms stress σ or in the sinusoidal S-N fatigue curves. These cases will be treated in subsequent sections.

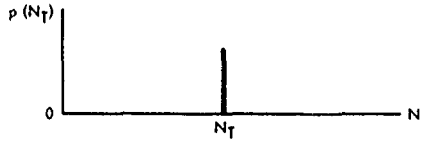


Figure 6. PDF of N_T

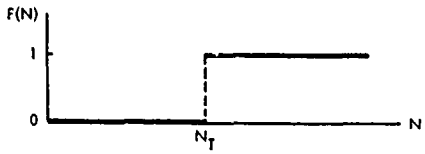


Figure 7. Probability of Failure Curve

TIME TO FAILURE RELATED TO AVERAGE NUMBER OF STRESS REVERSALS

The average number of zero crossings per unit time for a bandpass process is [10]:

$$\lambda = 2f_c \sqrt{1 + \frac{f_B^2}{12 f_o^2}}$$

There will be one stress cycle for every two zero crossings. Therefore,

$$N_T = (\lambda/2)t \tag{19}$$

$$N_T = f_o t \sqrt{1 + \frac{f_B^2}{12 f_o^2}}$$

where

f_o = bandpass center frequency (Hz), usually resonant frequency

t = time to failure (seconds)

f_B = bandwidth (Hz)

The second term under the radical is approximately zero, even for low Q systems ($Q \cong f_o/f_B$).

$$N_T \cong f_o t \quad \text{cycles} \tag{20}$$

VARIABLE RMS STRESS

In the previous case, A, β, and σ were treated as being fixed variables. σ will now be treated as a random variable, which is the usual case. The rms stress usually varies from part to part and subassembly to subassembly even though the applied vibration acceleration level may not vary. Stresses vary due to dimensional and geometrical differences between parts, fabrication and assembly, process variability, and structural damping and stiffness variations of adjacent structures.

From equation (9),

$$N_T = K\sigma^{-\beta} \tag{21}$$

where

$$K = \left| \frac{1}{\Gamma\left(\frac{2+\beta}{2}\right)} \right| \left| \frac{A}{\sqrt{2}} \right|^{\beta} \quad \text{stress units}^{\beta}$$

N_T and σ are random variables.

The PDF of N_T can be expressed in terms of the PDF of σ as follows [10]:

$$p(N_T) = \frac{p(\sigma)}{\left| \frac{df(\sigma)}{d\sigma} \right|} \tag{22}$$

where

$$f(\sigma) = N_T = K\sigma^{-\beta} \tag{23}$$

Let

$$p(\sigma) = \frac{1}{1 - a_t} \cdot \frac{1}{\delta\sqrt{2\pi}} \exp\left[- \frac{(\sigma - \bar{\sigma})^2}{2\delta^2} \right] \tag{24}$$

$$\text{for } \sigma \geq 0$$

$$p(\sigma) = 0 \quad \text{otherwise}$$

where

δ = standard deviation of rms stress

$\bar{\sigma}$ = average value of rms stress

which is a truncated Gaussian PDF. The truncated area is removed because it is impossible to have a negative rms stress. The factor $(1 - a_t)$ in equation (24) is a scaling factor to compensate for the removal of a_t (see Figure 8) so that

$$\int_0^{\infty} p(\sigma)\, d\sigma = 1 \tag{25}$$

$$a_t = \int_{-\infty}^{0} p(\sigma) d\sigma = \text{erf}_p\,(-\bar{\sigma}/\delta) - \text{erf}_p\,(-\infty)$$

$$a_t = 0.5 - \text{erf}_p(\bar{\sigma}/\delta)$$

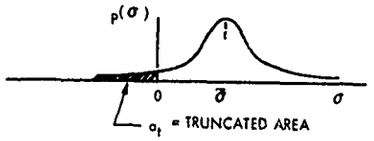


Figure 8. PDF of rms Stress

where

$$\mathrm{erf}_p(\alpha) = \frac{1}{\sqrt{2\pi}} \int_0^{\alpha} e^{-y^2/2}\, dy \qquad (26)$$

$$\mathrm{erf}_p(-\alpha) = -\mathrm{erf}_p(\alpha)$$

$$\mathrm{erf}_p(\infty) = 0.5; \quad \mathrm{erf}_p(0) = 0$$

Therefore, equation (22) becomes:

$$p(N_T) = \frac{1}{\beta\delta\sqrt{2\pi}\,(1 - a_t)N_T} \left(\frac{K}{N_T}\right)^{1/\beta} \exp\left[-\frac{\left\{\left(\frac{K}{N_T}\right)^{1/\beta} - \bar{\sigma}\right\}^2}{2\delta^2}\right] \quad \text{for } N_T \geq 0 \qquad (27)$$

$$p(N_T) = 0 \qquad \text{otherwise}$$

The above expression is plotted in Figure 9 for the copper wire example.

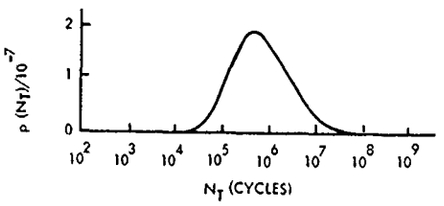


Figure 9. PDF of N_T

F(N) = probability of failure in N cycles (28)

$$F(N) = \int_0^N p(N_T)\, dN_T$$

$$F(N) = \frac{0.5 - \mathrm{erf}_p\left[\dfrac{(K/N)^{1/\beta} - \bar{\sigma}}{\delta}\right]}{0.5 + \mathrm{erf}_p\left[\bar{\sigma}/\delta\right]} \qquad (29)$$

$$F(0) = 0 \quad ; \qquad F(\infty) = 1$$

$F(N) = 0.5$ for $N = K(\bar{\sigma})^{-\beta}$ = median of N

EXAMPLE:

Material: Copper Wire

$K = 2.41 \times 10^{42}$ psi$^{\beta} = 1.01 \times 10^{78}$ Pa$^{\beta}$

$\beta = 9.28$; $1/\beta = 0.108$

$\bar{\sigma} = 7000$ psi $= 4.83 \times 10^7$ Pa

$\delta = 1400$ psi ($\pm 20\%$) $= 9.65 \times 10^6$ Pa

$N_{median} = 5 \times 10^6$ cycles

The value of $\delta = 20\%$ of $\bar{\sigma}$ was arbitrarily chosen for illustration purposes. The resulting curve of Figure 9 appears to be approximately Gaussian (i.e., normal) when plotted as $p(N_T)$ versus log N_T. A log-normal curve could most likely be fitted through the curve of Figure 9. However, equation (27) is not truly log-normal.

The median value of N_T (i.e., the value for which $F(N) = 0.5$) is 5×10^6 cycles. It would be expected by looking at Figure 9 that the average value of N_T would have a value close to but somewhat higher than the mode at 8×10^5 cycles.

$$\overline{N_T} = \int_0^{\infty} N_T\, p(N_T)\, dN_T \qquad (30)$$

This integral becomes infinite; $\overline{N_T}$ does not exist. Intuitively this may not seem correct. However, it is shown to be true in Appendix B; primarily because the moment arm N_T in equation (30) increases at a rate approximately three times more than the area $p(N_T)dN_T$ decreases as N_T is increased. Plotting $p(N_T)$ using a log scale for N_T is somewhat misleading. The linear plot of Figure 10 shows the curve to fall off very slowly due to the low stress side of the PDF of the random variable σ.

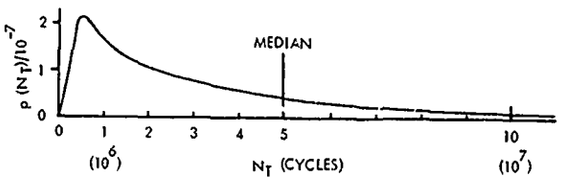


Figure 10. PDF of N_T

$\overline{N_T}$ of a sample is finite as follows:

$$\overline{N_T}_{sample} = \frac{\int_0^{10^{10}} N_T\, p(N_T)\, dN_T}{\int_0^{10^{10}} p(N_T)\, dN_T} = 6 \times 10^7 \text{ cycles}$$

The sample chosen includes 99.7 percent of all failures. Data for Figures 9, 10, and 11 is given in Table 4.

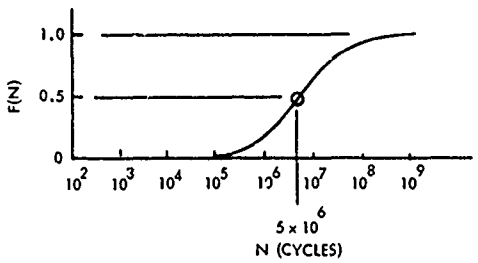


Figure 11. Failure Probability (Variable σ)

The probability of failure F(N) in equation (29) is plotted in Figure 11 for the example. This curve shows that most of the failures occur between 10^5 and 10^8 cycles. The median of cycles to failure is a more useful variable than $\overline{N_T}$ when using equation (29).

All probability distribution functions have the same general shape as that shown in Figure 11 but are quite different from each other in detail. These differences are more apparent when the curves are plotted on probability charts of various types instead of the linear scale as in Figure 11. F(N) curves have substantially different shapes when comparing different load types such as increasing sinusoidal step-stress, decreasing step-stress, up and down step-stress, and random [11, 12]. A good test of the suitability of equation (29) would be to compare its shape with empirical data. The empirical data of Freudenthal and Heller [12] as referenced in [11] is shown as the dotted line in Figure 12. The solid curve is a plot of equation (29). The actual values of $\overline{\sigma}$ and δ were unknown. $\overline{\sigma}$ was chosen so that the curve had a median value of $N = 2 \times 10^5$ cycles. δ was chosen so that the curve passed through $F(N) = 0.15$ for $N = 10^5$ cycles. The remaining points on the curve are constrained to follow equation (29). Equation (29) appears to have the same shape as the empirical data. A choice of $\delta = 6\%$ of $\overline{\sigma}$ is reasonable [6] where the standard deviation of the scatterband varies from 5% to 8% for most structural materials.

SCATTERBAND FATIGUE CURVE (VARIABLE A)

The S-N curve is typically not a single line but a wider scatterband of failure points. The single line usually represents the average. The scatterband of points can be represented by

TABLE 4. DATA FOR VARIABLE σ EXAMPLE

N_T (cycles)	$p(N_T)/10^{-7}$	F(N)
10^3	2.8×10^{-9}	2.7×10^{-11}
10^4	4.8×10^{-3}	9.2×10^{-7}
2×10^4	0.05	2.4×10^{-5}
5×10^4	0.40	6.6×10^{-4}
10^5	1.05	4.3×10^{-3}
2×10^5	1.77	1.9×10^{-2}
5×10^5	2.04	0.08
10^6	1.63	0.17
2×10^6	1.04	0.30
5×10^6	0.43	0.50
10^7	0.19	0.64
2×10^7	0.07	0.76
5×10^7	0.02	0.86
10^8	6.0×10^{-3}	0.916
2×10^8	2×10^{-3}	0.949
5×10^8	4×10^{-4}	0.975
10^9	1×10^{-4}	0.985
10^{10}	2×10^{-6}	0.997

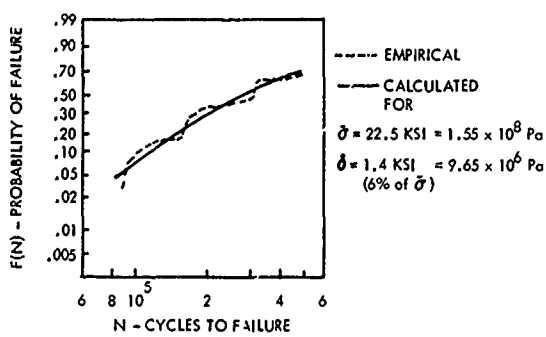


Figure 12. Fatigue Life of 7075-T6 Aluminum Alloy under Random Loading

letting the constant A in equation (9) and Figure 1 become a random variable.

From equation (9)

$$N_T = HA^{\beta}$$

where

$$H = \left[\frac{1}{\Gamma\left(\frac{2+\beta}{2}\right)}\right]\left[\frac{1}{\sqrt{2}\,\sigma}\right]^{\beta} \text{ stress units}^{-\beta} \quad (31)$$

In a fashion similar to that for variable σ in equation (22), let

$$p(A) = \frac{1}{1 - a_T} \cdot \frac{1}{\Delta\sqrt{2\pi}}\, e^{-(A-\overline{A})^2/2\Delta^2} \quad (32)$$

for $A \geq 0$

$p(A) = 0$ otherwise

where

$\overline{A}$ = average value of A
Δ = standard deviation of A (33)

$$1 - a_T = 0.5 + \text{erf}_p(\overline{A}/\Delta)$$

$$p(N_T) = \frac{1}{1 - a_T} \cdot \frac{1}{\beta H \Delta\sqrt{2\pi}} \left(\frac{N_T}{H}\right)^{(1/\beta)-1} \exp\left[-\frac{\left|\left(\frac{N_T}{H}\right)^{1/\beta} - \overline{A}\right|^2}{2\Delta^2}\right]$$

for $N_T \geq 0$

$p(N_T) = 0$ otherwise

$$F(N) = \int_0^N p(N_T)\, dN_T \quad (34)$$

$$F(N) = \frac{\text{erf}_p\left[\frac{1}{\Delta}\left\{\left(\frac{N}{H}\right)^{1/\beta} - \overline{A}\right\}\right] + \text{erf}_p\left[\overline{A}/\Delta\right]}{0.5 + \text{erf}_p\left[\overline{A}/\Delta\right]}$$

EXAMPLE:

Material: Copper Wire

σ = 7 ksi = 4.83×10^7 Pa

$\overline{A}$ = 81 ksi = 5.65×10^8 Pa

Δ = 16.38 ksi (±20%) = 1.13×10^8 Pa

H = 1.27×10^{-39} psi$^{-\beta}$ = 3.01×10^{-75} Pa$^{-\beta}$ (See equation (31))

$\overline{A}/\Delta = 5$; $\text{erf}_p\left[\overline{A}/\Delta\right] = 0.5$

It will be noted that the results for variable σ and A as shown in Figures 11 and 13 respectively are very similar. This is because both σ and A shift the random fatigue curve up or down as they vary rather than change the slope. However, the causes for the shift are entirely different. Variances in σ, as described earlier, are due to dimensional and goometrical variances or assembly variability. Variances in A are due to basic material property variances between lots as would be expected by variances in cold working or quenching and tempering.

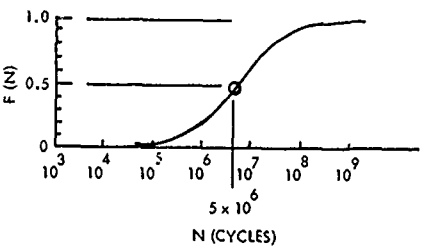


Figure 13. Failure Probability (Variable A)

Quenching and tempering variances will also cause variances in the slope parameter β. The transformation for variable β is considerably more difficult mathematically than for variable σ and A. Refer to equation (22). Variable β will not be treated at this time. While not entirely accurate, the effects of variable β can be included in an analysis by increasing the standard deviation of A.

STRESS LIMITING

Stress limiting (i.e., clipping) can occur if the motion of a structure is limited by snubbers or other means of limited clearance or if the vibratory forces are limited. The stress envelope PDF P(s) of Figure 3 will be modified as shown in Figure 14. The impulse function at S = L is equal in value to a_L.

$$a_L = \int_L^{\infty} P(s)\, dS = e^{-L^2/2\sigma^2} \quad (35)$$

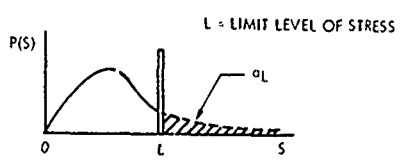


Figure 14. Effect of Limiting on P(s)

Equation (2) is modified as follows:

$$N_T = \frac{1}{\int_0^L \left[P(s)/N_S\right] dS + \frac{a_L}{N_S}\Big|_{S=L}} \tag{36}$$

$$\frac{a_L}{N_S}\Big|_{S=L} = \left[\frac{L}{A}\right]^{\beta} e^{-L^2/2\sigma^2}$$

$$\int_0^L \left[P(s)/N_S\right] dS = \left[\frac{\sqrt{2}\,\sigma}{A}\right]^{\beta} \int_0^T z^{x-1} e^{-z} dz \tag{37}$$

where

$$T = \frac{1}{2}\left(\frac{L}{\sigma}\right)^2 \quad ; \quad x = \frac{2+\beta}{2}$$

$$\int_0^L \left[P(s)/N_S\right] dS = \left|\frac{\sqrt{2}\,\sigma}{A}\right|^{\beta} \gamma(x, T)$$

$\gamma(x, T)$ is the Incomplete Gamma Function

Note: $\gamma(x, \infty) = \Gamma(x)$

Therefore, the random "σ-N" fatigue curve can be obtained from the following expression:

$$N_{T_L} = \frac{1}{\left|\frac{\sqrt{2}\,\sigma}{A}\right|^{\beta} \gamma(x, T) + \left[\frac{L}{A}\right]^{\beta} e^{-T}} \tag{38}$$

The ratio of fatigue life with limiting to that without limiting is as follows:

$$\frac{N_{T_L}}{N_T} = \frac{\Gamma(x)}{\gamma(x, T) + T^{\beta/2} e^{-T}} \tag{39}$$

This ratio is independent of rms stress σ but does depend upon the material slope parameter β.

EXAMPLE:

Material: Copper Wire

σ = 7 ksi = 4.83 x 10^7 Pa

L = 14 ksi = 9.65 x 10^7 Pa

$L/\sigma = 2$; $T = 2$

$$x = \frac{2+\beta}{2} = 5.64$$

$\gamma(5.64, 2) = 1.67874$

$\Gamma(5.64) = 65.71339$

$\frac{\gamma(5.64, 2)}{\Gamma(5.64)} \cong 0.03$ which corresponds to 97% of the PDF G(s) in Figure 5 being limited

$$N_{T_L} = \frac{1}{(0.512 + 1.029) \times 10^{-8}} = 65 \times 10^6 \text{ cycles}$$

Compared to 5 x 10^6 cycles for no limiting, the above value for N_{T_L} represents an increase in fatigue life by a factor of 13. Other limit levels have been analyzed with the results tabulated in Table 5.

Table 6 shows the effect of limiting on fatigue life for AZ31B magnesium alloy. The limit level must be raised to approximately 6σ in order to have no effect of limiting. This corresponds to the location of the PDF G(s) where no damage is being done. Refer to Table 3. Stress limiting in the tails of the stress peaks has a pronounced effect on fatigue life.

TABLE 5. LIMITING EFFECT ON FATIGUE LIFE FOR COPPER WIRE

Limit Level L/σ	Fatigue* Life N_{T_L} (cycles)	N_{T_L}/N_T
∞	5 x 10^6	1
4	5.4 x 10^6	1.08
3	9.3 x 10^6	1.86
2	65 x 10^6	13.0

*For σ = 7 ksi = 4.83 x 10^7 Pa

TABLE 6. LIMITING EFFECT ON FATIGUE LIFE FOR AZ31B

Limit Level L/σ	N_{T_L}/N_T
∞	1
6	1.04
5	1.46
4	5.90
3	178

DOUBLE SLOPE S-N CURVE

Many materials exhibit a double slope as shown in Figure 15. The break point occurs in

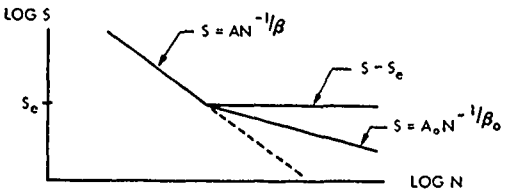


Figure 15. Double Slope S-N Curves

the vicinity of 10^7 cycles. Some materials have an endurance limit ($S = S_e$) below which exists infinite fatigue life. The endurance limit is not always achieved. Some specimens are not sufficiently polished to remove slight surface flaws (i.e., stress raisers). Other specimens may be stressed in a corrosive environment (e.g., high humidity). These effects will tend to reduce fatigue life above the break point. It will be assumed that such a reduction can be represented by a straight line on a log-log plot of slope parameter β_o.

Equation (2) becomes:

$$N_T = \frac{1}{\int_0^{S_e} \frac{P(s)}{N_s}\,dS + \int_{S_e}^{\infty} \frac{P(s)}{N_s}\,dS} \qquad (40)$$

ENDURANCE LIMIT CASE ($S = S_e$)

The first integral in equation (40) has a value of zero because $N_S = \infty$. The second integral is the Incomplete Gamma Function $Q(x, T)$ which is related to both $\Gamma(x)$ and $\gamma(x, T)$ as shown in Appendix A. Equation (40) becomes:

$$N_{TS_e} = \frac{1}{0 + \left|\frac{\sqrt{2}\,\sigma}{A}\right|^{\beta} \int_{\frac{1}{2}\frac{S_e^2}{\sigma^2}}^{\infty} z^{x-1} e^{-z}\,dz} \qquad (41)$$

$$N_{TS_e} = \frac{1}{\left|\frac{\sqrt{2}\,\sigma}{A}\right|^{\beta} \left\{\Gamma\left(\frac{2+\beta}{2}\right) - \gamma\left|\left(\frac{2+\beta}{2}\right), \left(\frac{1}{2}\frac{S_e^2}{\sigma^2}\right)\right|\right\}}$$

The existence of an endurance limit will extend the fatigue life somewhat because $Q(x, T)$ is always smaller in value than $\Gamma(x)$. Refer to equation (8).

$$\frac{N_{TS_e}}{N_T} = \frac{\Gamma\left(\frac{2+\beta}{2}\right)}{\Gamma\left(\frac{2+\beta}{2}\right) - \gamma\left|\left(\frac{2+\beta}{2}\right), \left(\frac{1}{2}\frac{S_e^2}{\sigma^2}\right)\right|} \qquad (42)$$

The random fatigue curve endurance limit is the value of σ that makes equation (42) have an infinite value. In the strict sense, this occurs only for $\sigma = 0$. In the practical sense, this occurs for a larger value of σ.

Table 7 shows the extension in fatigue life for two materials with different values for β. This data indicates the presence of an endurance limit for the random σ-N fatigue curve that is approximately 15 percent of the corresponding endurance limit for the S-N curve. This is also illustrated in Figure 16. The upper edge of the shaded area is for $\beta = 9.28$ and the lower edge is for $\beta = 22.4$. The dotted line is the σ-N curve assuming the material had no endurance limit. However, the random fatigue curve endurance limit is too small to be of great practical value.

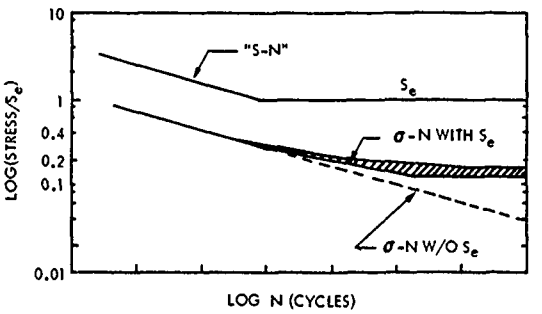


Figure 16. Random Endurance Limit

TABLE 7. RANDOM FATIGUE DATA WITH ENDURANCE LIMIT

	N_{TS_e}/N_T	
σ/S_e	Ductile Material ($\beta = 9.28$)	Less Ductile Material ($\beta = 22.4$)
1.50	1.00	1.00
1.00	1.00	1.00
0.50	1.03	1.00
0.25	6.44	1.00
0.20	93	2.34
0.15	∞	163
0.12	∞	∞
0.10	∞	∞

DOUBLE FINITE SLOPE $(S = A_o N^{-1/\beta_o})$

In equation (40), let

$$I_1 = \int_0^{S_e} = \left[\frac{\sqrt{2}\sigma}{A_o}\right]^{\beta_o} \gamma\left[\left(\frac{2+\beta_o}{\beta_o}\right), \left(\frac{1}{2}\frac{S_e^2}{\sigma^2}\right)\right] \quad (43)$$

$$I_2 = \int_{S_e}^{\infty} = \left[\frac{\sqrt{2}\sigma}{A}\right]^{\beta} \left\{\Gamma\left(\frac{2+\beta}{2}\right) - \gamma\left[\left(\frac{2+\beta}{2}\right), \left(\frac{1}{2}\frac{S_e^2}{\sigma^2}\right)\right]\right\}$$

$$N_T = \frac{1}{I_1 + I_2}$$

Refer to Appendix A for evaluation methods.

Equations (41) and (43) represent the expressions for the random σ-N fatigue curves. The relationship between σ and N is not as simple as the power law expression for the single slope case.

The random fatigue curve should fall between the shaded region and dotted line of Figure 16; namely, between the ones for materials with and without an endurance limit.

STATIC STRESS ADDITION

It has been proposed by Professor Jo Dean Morrow [3] of the University of Illinois that a static (i.e., mean) stress σ_o superimposed on a completely reversed cyclic stress be included in the Coffin-Manson strain fatigue equations by subtracting the static stress from the true ultimate stress. This is equivalent to using a Goodman diagram with the engineering ultimate stress replaced with the true ultimate stress [4].

By inductive reasoning, it is proposed that the static stress be subtracted from the true ultimate stress (defined as A in this paper) for static plus completely reversed random stresses.

CONCLUDING REMARKS

1. The analysis covers both the low-cycle life and high-cycle life fatigue regions by treating the stress as the "true" stress instead of the more usual "engineering" stress. A different random fatigue curve in both the low-cycle life and high-cycle life regions results for each of the two types of defined stress.

2. The resulting closed form analytical expression for random fatigue of a material is of the same mathematical power-law form as the corresponding sinusoidal fatigue expression. The random and sinusoidal curves have the same slope and differ only by a constant term. The sinusoidal fatigue curve constant is the larger of the two by a factor of approximately 2 for ductile materials and approximately 3 for brittle materials. This is in agreement with empirical results.

3. A mathematical expression for the damage probability density function is derived. It is somewhat similar in form to a Weibull function. The derived expression shows that most of the damage is done by stress peaks which have an amplitude between 2 and 5 times the root-mean-square (rms) stress. The statistical properties of the damage function are dependent only on the rms stress and the slope of the sinusoidal fatigue curve.

4. The following mathematical approximation was uncovered:

$$\Gamma(\alpha + \tfrac{1}{2}) \cong \sqrt{\alpha - \tfrac{1}{4}}\ \Gamma(\alpha)$$

where α does not have to be an integer.

5. Expressions are derived for the probability density and distribution functions of the number of cycles to failure for the cases of a variable rms stress and a scatterband fatigue curve. These expressions are useful for predicting mechanical reliability and agree with empirical results.

6. Stress limiting at approximately 3 times the rms stress extends the material fatigue life by a factor of 2 for ductile materials and several orders of magnitude for brittle materials.

7. The random fatigue curve has been found to have an endurance limit if the sinusoidal fatigue curve has one. However, it is too small (approximately 15% of the sinusoidal endurance limit) to be of great practical value.

8. It is proposed that the addition of a static stress to the random stress be treated by subtracting the static stress from the true ultimate stress in the equations in this paper.

9. The "median" number of cycles to failure (i.e., the value for which 50% of the cumulative failures have occurred) is a more useful statistical parameter than the "average" value when analyzing random failures.

SYMBOLS

A	material constant; true ultimate stress
$\overline{A}$	average value of A
A_o	S-N curve-intercept parameter
a_L	area of PDF being limited
a_t	area of PDF being truncated
B	material constant; Basquin coefficient; slope of S-N curve
C	constant of random σ-N fatigue curve
D_s	proportion of damage related to stress S
E{}	expected value of { }
erf_p	error function defined by Papoulis [10]
F(N)	probability of failure in N cycles
f_B	bandwidth
f_o	bandpass center frequency
G(s)	scaled damage PDF
$\overline{G(s)}$	average value of G(s)
H	constant; function of β and σ
I	integral
K	material constant
L	stress limit level
N	number of stress cycles
N_S, N_T, N_{T_L}, N_{T_1}, N_{T_2}	number of stress cycles to failure
$\overline{N_T}$	average number of cycles to failure
N_{TS_e}	number of stress cycles to failure
N_1	number of cycles to failure at stress level σ_1
N_2	number of cycles to failure at stress level σ_2
n_s	number of stress peaks at level S to cause failure
P(s), $p(N_T)$, PDF	probability density functions
$p(\theta)$	probability density function of the general random variable θ
Q(x, T)	Incomplete Gamma Function
R(N)	probability of survival to N cycles
rms	root mean square
S	sinusoidal stress amplitude
S_e	endurance limit
S_o	stress at mode of G(s)
T	parameter of stress limiting
t	time to failure
x	material constant; a function of β
y	a dummy variable
z	a dummy variable
α	general variable
β	negative reciprocal of B
β_o	S-N curve slope parameter
$\Gamma(x)$	gamma function
$\gamma(x, T)$	Incomplete Gamma Function
Δ	standard deviation of A
δ	standard deviation of σ
ϵ_u	ultimate strain
λ	average number of zero crossings per unit time
σ	rms stress level
$\overline{\sigma}$	average value of σ
$\sigma_{G(s)}$	standard deviation of G(s)

REFERENCES

1. Steinberg, D.S., Vibration Analysis for Electronic Equipment, John Wiley and Sons, 1973.
2. Coffin, L.F., "Fatigue at High Temperature--Prediction and Interpretation," General Electric Technical Information Series Report 74CRD066, April 1974.
3. Tucker, L.E., Landgraf, R.W., and Brose, W.R., "Proposed Technical Report on Fatigue Properties for the SAE Handbook," Course Notebook, The Modern View of Fatigue and Its Relation to Engineering Problems, Section 9, Union College Technical Institute Program, Schenectady, New York, July 1975.
4. Dowling, N.E., "Fatigue Life and Inelastic Strain Response under Complex Histories for an Alloy Steel." (Doctoral Thesis, Department of Theoretical and Applied Mechanics, University of Illinois, April 1972), Course Notebook, The Modern View of Fatigue and Its Relation to Engineering Problems, Section 21, Fig. 8, Union College

Technical Institute Program, Schenectady, New York, July 1975.

5. Solomon, H.O., "Materials for Fatigue Resistance," Course Notebook, The Modern View of Fatigue and Its Relation to Engineering Problems, Section 28, Union College Technical Institute Program, Schenectady, New York, July 1975.

6. Haugen, E.B., and Wirsching, P.H., "Probabilistic Design (Part 3)," Machine Design, May 15, 1975.

7. Henry, M.F., "Crack Initiation and Early Growth in Low Cycle Fatigue--A Progress Report," Course Notebook, The Modern View of Fatigue and Its Relation to Engineering Problems, Section 2, Union College Technical Institute Program, Schenectady, New York, July 1975.

8. Miner, M.A., "Cumulative Damage in Fatigue," Trans. ASME, Vol. 67, A159, 1945.

9. Booth, G.B., "Random Motion," Product Engineering, November 1956.

10. Papoulis, A., Probability, Random Variables, and Stochastic Processes, McGraw-Hill Book Co., New York, 1965.

11. McClintock, F.A., Random Vibration (S. Crandall, editor), Chapter 6, "Fatigue of Metals," Technology Press of MIT, 1958.

12. Freudenthal, A.M., and Heller, R.A., Fatigue in Aircraft Structures, pp 146-177, Academic Press, 1956.

13. Abramowitz, M., and Stegun, I., Handbook of Mathematical Functions, National Bureau of Standards, June 1964.

14. Kreyszig, E., Advanced Engineering Mathematics, 2nd ed., John Wiley and Sons, 1967.

APPENDIX A

NUMERICAL METHODS

ERROR FUNCTION $\mathrm{erf}_p(\alpha)$

$$\mathrm{erf}_p(\alpha) = \frac{1}{\sqrt{2\pi}} \int_0^{\alpha} e^{-y^2/2}\, dy$$

$$\mathrm{erf}_p(0) = 0 \quad ; \quad \mathrm{erf}_p(\infty) = 0.5$$

$$\mathrm{erf}_p(-\alpha) = -\mathrm{erf}_p(\alpha)$$

Table 3-1 on page 64 of Papoulis [10] lists values of $\mathrm{erf}_p(\alpha)$ for $0.05 \leq \alpha \leq 3.00$. $\mathrm{erf}_p(\alpha)$ may be approximated accurately for $\alpha \geq 0$ as follows:

Define $t = \dfrac{1}{1 + 0.2316418\alpha}$

$a_1 = 0.2548296$

$a_2 = -0.2844967$

$a_3 = 1.421414$

$a_4 = -1.45315$

$a_5 = 1.06141$

$$\mathrm{erf}_p(\alpha) \cong \frac{1}{2}\left|1 - (a_1 t + a_2 t^2 + a_3 t^3 + a_4 t^4 + a_5 t^5) e^{-\alpha^2/2}\right|$$

EXAMPLE:

$\mathrm{erf}_p(0.8065293)$; $\alpha = 0.8065293$

$t = 0.8425835677$

$$\mathrm{erf}_p = \frac{1}{2}\left|1 - (0.581352028)(0.7223505)\right|$$

$\mathrm{erf}_p(0.8065293) = 0.290300265$

GAMMA FUNCTION $\Gamma(\alpha) = \int_0^{\infty} z^{\alpha-1} e^{-z}\, dz$

Table 6.1, page 267, of Abramowitz [13] lists values of $\Gamma(\alpha)$ for $1 \leq \alpha \leq 2$. For random fatigue $\alpha = (2+\beta)/2$ will be greater than two. The following expression can be used recursively:

EXAMPLE:

$\Gamma(5.64) = 4.64\,\Gamma(4.64) = 4.64 \times 3.64\,\Gamma(3.64) \ldots$

$\Gamma(5.64) = 4.64 \times 3.64 \times 2.64 \times 1.64\,\Gamma(1.64)$ ←

$\Gamma(1.64) = 0.898642$

Therefore

$\Gamma(5.64) = 65.71339$

INCOMPLETE GAMMA FUNCTION $\gamma(x, T)$

$$\gamma(x, T) = \int_0^{T} z^{x-1} e^{-z}\, dz$$

On pages 940, 941 of Reference 13,

$$\gamma(x, T) = \Gamma(x)[1 - P(\chi^2 | \nu)]$$

where

$\chi^2 = 2T$; $\nu = 2x$

EXAMPLE:

$$\gamma(5.64,\ 8) = \Gamma(5.64)[1 - P(16|11.28)]$$

From Table 26.7, pp 978-983 of Reference 13,

$$P(16|11.28) = 0.1551608$$

Therefore,

$$\gamma(5.64,\ 8) = 55.517$$

RELATIONSHIP BETWEEN GAMMA FUNCTIONS

$$\int_0^\infty z^{x-1}e^{-z}dz = \int_0^T z^{x-1}e^{-z}dz + \int_T^\infty z^{x-1}e^{-z}dz$$

or correspondingly

$$\Gamma(x) = \gamma(x,\ T) + Q(x,\ T)$$

where γ and Q are Incompiete Gamma Functions. Thus,

$$Q(x,\ T) = \Gamma(x) - \gamma(x,\ T)$$

APPENDIX B

$\overline{N_T}$ EVALUATION

This Appendix is included to show that the expression for $\overline{N_T}$ is infinite. $\overline{N_T}$ of equation (30) is as follows:

$$\overline{N_T} = \frac{K^{1/\beta}}{\beta\delta\sqrt{2\pi}} \int_0^\infty N^{-1/\beta} \exp\left[-\frac{\left\{\left(\frac{K}{N}\right)^{1/\beta} - \overline{\sigma}\right\}^2}{2\delta^2}\right] dN$$

The above expression was numerically integrated from N = 0 to N = N_O. As N_O was progressively increased from a value of 10^{10}, 10^{11}, 10^{12}, and 10^{13} cycles, it was observed that $\overline{N_T}$ kept increasing and gave no indication of approaching a finite limit.

Let

$$\overline{N_T} = \overline{n}_1 + \overline{n}_\infty$$

where

$$\overline{n}_1 = \frac{K^{1/\beta}}{\beta\delta\sqrt{2\pi}} \int_0^{N_o} N^{-1/\beta} \exp\left[-\frac{\left\{\left(\frac{K}{N}\right)^{1/\beta} - \overline{\sigma}\right\}^2}{2\delta^2}\right] dN$$

and

$$\overline{n}_\infty = \frac{K^{1/\beta}}{\beta\delta\sqrt{2\pi}} \int_{N_o}^\infty N^{-1/\beta} \exp\left[-\frac{\left\{\left(\frac{K}{N}\right)^{1/\beta} - \overline{\sigma}\right\}^2}{2\delta^2}\right] dN$$

The value of N_O may be chosen large such that

$$(K/N_o)^{1/\beta} << \overline{\sigma}.$$

Then

$$\overline{n}_\infty > \frac{K^{1/\beta} \exp\left[-\sigma^2/2\delta^2\right]}{\beta\delta\sqrt{2\pi}} \int_{N_o}^\infty N^{-1/\beta}\ dN$$

If N_O is chosen to be 10^{13} cycles, $\overline{n_1} = 5 \times 10^8$ cycles as determined by numerical integration; $\overline{n_1}$ is finite. $\overline{n_\infty}$ becomes proportional to the following integral:

$$\int_{N_o}^\infty N^{-1/\beta}\ dN = \frac{1}{1 - \frac{1}{\beta}} N^{\left(1 - \frac{1}{\beta}\right)} \Bigg|_{N_o}^\infty$$

For structural materials, $\beta > 5$. β is always positive. Therefore, the term

$$1 - \frac{1}{\beta}$$

is always positive. Thus, N raised to a positive number increases as the value of N increases. The value of the above integral at the upper limit is infinite.

$\overline{N_T}$ does not exist.

APPENDIX C

GAMMA FUNCTION APPROXIMATION

It was observed that the value of $\sigma_{G(s)}$ in equation (16) was independent of the value of β for $8.92 \leq \beta \leq 22.37$. That is,

$$\sigma_{G(s)} \cong (1/\sqrt{2})\sigma.$$

This implies that

$$\Gamma(\alpha + \tfrac{1}{2}) \cong \sqrt{\alpha - \tfrac{1}{4}}\ \Gamma(\alpha)$$

See equation (17).

Equation (16) may be rewritten as follows:

$$\sigma^2_{G(s)} = 2\sigma^2\left\{\alpha - \left[\frac{\Gamma(\alpha+\frac{1}{2})}{\Gamma(\alpha)}\right]^2\right\} \cong \frac{\sigma^2}{2}$$

where

$$\alpha = (2+\beta)/2$$

Therefore

$$\frac{\Gamma(\alpha+\frac{1}{2})}{\Gamma(\alpha)} \cong \sqrt{\alpha - \frac{1}{4}} \qquad (17)$$

for $\alpha \geq 1$

α need not be an integer.

It can be shown from Euler's Beta Function [14] that

$$\frac{\Gamma(\alpha+\frac{1}{2})}{\Gamma(\alpha)} = \frac{\sqrt{\pi}}{2} \cdot \frac{(2\alpha-1)!}{2^{2(\alpha-1)}\left[(\alpha-1)!\right]^2}$$

where n = 1, 2, 3, ...

There is no known exact closed form solution for noninteger values of α. Equation (17) is quite accurate for $\alpha > 2$ as can be seen from Table C-1.

TABLE C-1. APPROXIMATION ACCURACY

α	$\frac{\Gamma(\alpha+\frac{1}{2})}{\Gamma(\alpha)}$	$\sqrt{\alpha - \frac{1}{4}}$	Percent Difference
1	0.886227	0.866025	2.28
2	1.329341	1.322876	0.49
5	2.180949	2.179449	0.07
10	3.123011	3.122499	1.64×10^{-2}
20	4.444275	4.444097	4.00×10^{-3}

ACKNOWLEDGEMENT

The author wishes to thank Professor Jo Dean Morrow of the University of Illinois for suggesting the use of true stress instead of engineering stress in the low cycle region.

Discussion

Mr. Smith (Bell Aerospace): I think you implied that the effective limiting was independent of the spectrum of the stress that you had whether it was narrow band or broad band, or at least I didn't hear you qualify it at all. There surely must be an effect. Second you implied an ability to extend the results to a broadband process, you sort of talked about a narrow band process first and then you talked about the e effect of having two peaks, or two peaks in the spectrum, and then you said you can add them; there must be some limit, ultimately you can't even define what a stress cycle is if it is broadband.

Mr. Lambert: The broadband process that I refer to is what I would call two disjoint narrow band processors, like filters ringing at their resonant frequency. I wouldn't call that a broadband process. To me a broadband process is one where the power spectral density would go from roughly DC to a very high frequency. These are narrow band processes that I have described.

Mr. Smith: If the process is more than a narrowband it becomes difficult to define the meaning of a stress cycle.

Mr. Lambert: This is what I think is an effective number of zero crossings and you can still use this expression. The reason you can use it is because energy is additive and so are the autocorrelation functions and their second derivitives; in his book Poupoulos has a fairly good treatment of this. You said that I implied that the limit level, the extension of fatigue life, was independent of the RMS stress. It is a function of the ratio of the limit level to the RMS stress so indirectly it is related to the RMS stress but not per se. It is a function of the ratio, like are you limiting it to twice the RMS level?

Mr. Kana (Southwest Research Institute): This question is related to the second of the previous two questions. Can you state a maximum bandwidth at the half power point beyond which this analysis would not be valid? Or how narrow does the bandwidth have to be?

Mr. Lambert: In the first case I had a term in in one of the equations, the bandwidth $(F_b)^2$ divided by 12 $(F_0)^2$ which was insignificant compared to one even for low Q systems. This says that you are really independent of the bandwidth. There are some other conditions, which I didn't memorize and I can't cite them exactly as to what constitutes a narrowband process but I do know that if you look on page 495 of Poupoulis' book he defines a narrowband process.

Mr. Kana: In part of your analysis you used a Rayleigh distribution for representing the peak for the process, and that in itself states some kind of limitation on the bandwidth so you would have to relate it through that parameter I suppose.

Mr. Lambert: Yes, you would. I have worked in radar systems where we had a center frequency at 30 megahertz and a bandwidth of 10 megahertz and that is still a narrow band process; when you envelope the detect going from IF frequencies to video frequencies you still get a Rayleigh distribution as long as your amplifiers can handle the dynamic range. You are right there are limitations.

Mr. Stahle (General Electric): How would you consider your results to be applied to accelerated testing if you had to define some sort of a relation between the g level and the time?

Mr. Lambert: I discuss stress sensitivity in the written paper and it turns out that the ratio of the number of cycles to failure at different stress levels on the curve, because of logarythmic relationship is equal to the inverse ratio of the RMS levels raised to the B power. In the case of copper wire it says that if you can reduce your stresses by a factor 2 to 1 we will increase the fatigue life by a factor of 628 I think. This says that it is very sensitive to stress and not so sensitive to the duration of the test. So if you want to accelerate the life test you increase the stress by 2 to 1 and you will cut the life down by a factor of that ratio raised to the B power.

Mr. Stahle: In Harris and Crede's Shock and Vibration Handbook they have something on the order of a cubic relation and it seems as if you have a quite different form.

RANDOM VIBRATION FATIGUE TESTS OF WELDBONDED AND BONDED JOINTS

F. Sandow, Jr., O. Maurer

AIR FORCE FLIGHT DYNAMICS LABORATORY
WRIGHT-PATTERSON AIR FORCE BASE, OHIO

This paper presents the results of a series of random shaker experiments, which were conducted with test articles consisting of thin beams, fastened to a simulated stiffener by the weldbond process, using a so-called spot-weld etch surface preparation treatment, and similar test articles manufactured by the metal bond process, using a metal bond (FPL) etch surface preparation. The test procedure is discussed. To establish base line data, a series of riveted samples of the same basic dimensions were also tested. Fatigue curves in the range of 10^5 to 10^8 cycles were established for skin thicknesses of .032 inch and .040 inch for each of the three joint constructions. Results are also compared to fatigue data obtained elsewhere.

INTRODUCTION

The random vibration testing of simple structural joint samples for the purpose of generating random fatigue design data for aircraft structures has become an accepted practice. The resulting information is applied to supplement data obtained in acoustic fatigue tests conducted with larger and more complicated aircraft structuralcomponents excited by acoustic noise fields. Although there exist significant differences in the two types of tests, where the simple joint specimens are usually excited and responding in a narrow frequency band, while in an acoustic fatigue test a broadband excitation is applied, various investigations have shown that in many cases these differences become neglibible. References 1 and 2 show that when stiffened aircraft panels are excited by acoustic noise one mode frequently predominates the response spectrum and therefore the problem can be treated as a single degree of freedom dynamic system. Most of the available sonic fatigue design methods, for example References 3, 4, and 5 are based on this proposition. From investigations, References 6 and 7, which investigate the fatigue caused from multi-modal and broadband responses versus single mode response, it can be concluded that random fatigue data obtained with a narrow band excitation of a single mode are slightly conservative when applied to structures responding in a multi-modal or broadband fashion. Based on this background a series of random vibration tests with simple weldbonded and bonded joints simulating those of aircraft structures were conducted as a first step of a more comprehensive investigation. The prime purpose of these tests was to obtain basic comparative random fatigue data between the two joining processes and conventionally riveted joints. A second purpose was the generation of random stress-cycle curves which together with simultaneously conducted acoustic fatigue tests will result in acoustic fatigue design data for these structural joining methods.

TEST DESCRIPTION

TEST SAMPLES

The random fatigue tests were conducted with sixty test beams or coupons. These were fabricated with thin clad and bare aluminum aircraft sheet material which was joined in the center to an angle which simulated a typical panel stiffener. The basic construction and dimensions of the test articles together with strain gage locations are shown in Figures 1 and 2.

The joining of the angle stiffeners was accomplished by two processes which have recently received wide interest for possible application to aircraft construction. The weldbond process combines metal bonding and spot welding and in the usage applied here provides for a high quality spot weld by sacrificing some of the bond properties. Details about the process are given in References 8 and 9.

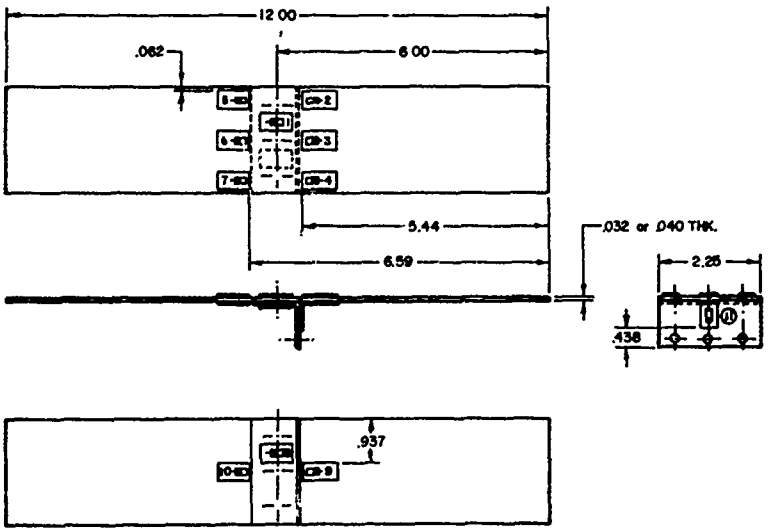


FIGURE 1 - TEST BEAM CONFIGURATION AND STRAIN GAGE LOCATIONS

The metal bond process which was applied in the purely adhesively bonded test articles has already found some application with slight modifications within the aircraft industry. Specifications of this process are given in References 10 and 11. In order to directly compare the random fatigue properties of these joints to conventionally riveted construction riveted specimens of otherwise identical configuration were included in the test.

A detailed listing of the test articles which were used is as follows:

a. Ten .032 inch and ten .040 inch thick samples constructed of clad 2024-T3 aluminum joined by 3 rivets equally spaced along the center line of the stringer.

b. Ten .032 inch and ten .040 inch thick samples constructed of clad 2024-T3 aluminum joined by a weldbond process using a "spot weld etch" surface preparation, three equally spaced weld spots along the center line and the Whittaker X6800 adhesive.

c. Ten .032 inch and ten .040 inch thick samples constructed of bare 7075-T6 aluminum joined by a bonding process using FPL etch surface preparation, Bloomingdale FM137 adhesive, BR127 primer and a .006 inch thick adhesive layer.

Strict quality control was applied during construction of the test specimens and they were also inspected afterwards for possible irregularities in the adhesive. It was found that in a few joints small voids near the adhesive edge existed. These were expected to yield some additional information as to the possible effect of small bond irregularities on the random fatigue of the joint.

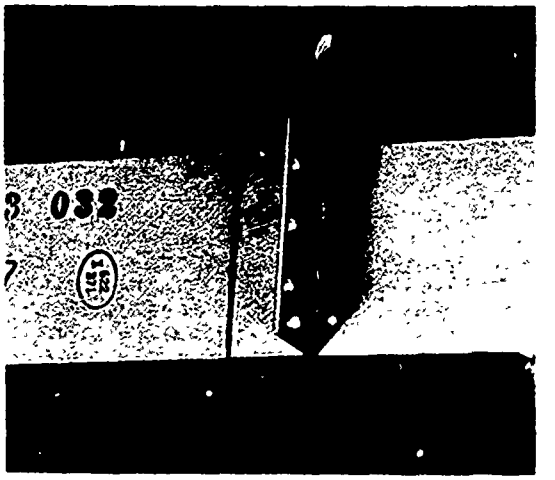


FIGURE 2 - TEST BEAM WITH BONDED STIFFNER

TEST SETUP

For the test the coupon was clamped and bolted on the lower edge of the stiffener into a fixture mounted on an electro-mechanical shaker. With this mounting the beam could be excited to respond closely in symmetrical modes where the highest stresses would apper in the edge of the bond. Each sample was tested in three phases. First, the natural frequencies and modes were determined by a low level constant acceleration sine-sweep. The strain levels were kept extremely low in order to prevent any significant accumulation of

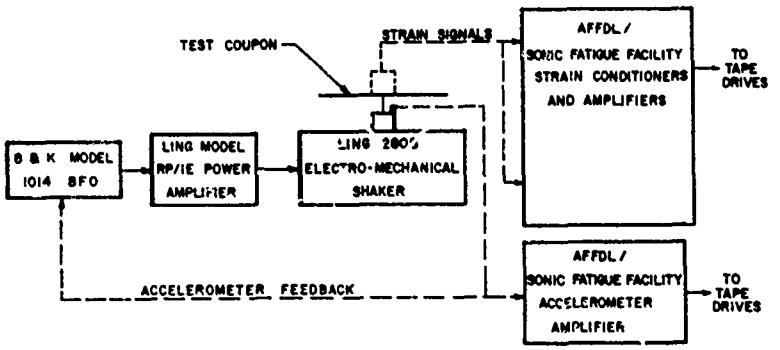


FIGURE 3 - TEST SETUP FOR CONSTANT ACCELERATION SINE SWEEPS

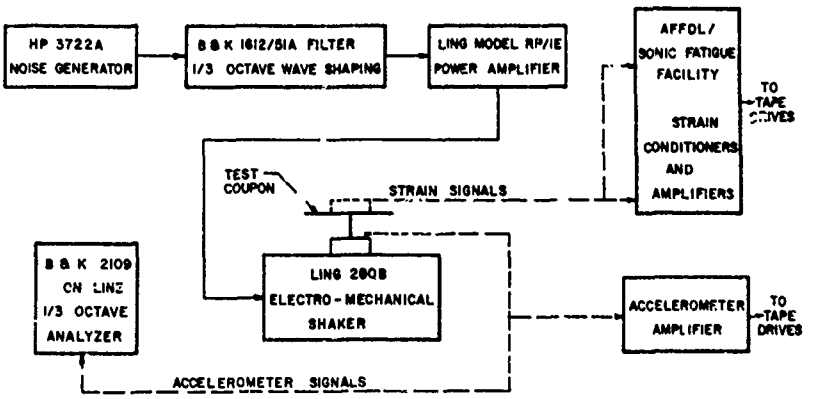


FIGURE 4 - TEST SETUP FOR FATIGUE TESTS

fatigue damage during these preliminary experiments. The outputs of all strain gages were plotted by an oscillograph. This allowed the determination of the presence of beam torsional modes and provided initial information of the strain and deformation distribution in the vicinity of the joint and the stiffener. A block diagram of the basic test setup for this phase is shown in Figure 3.

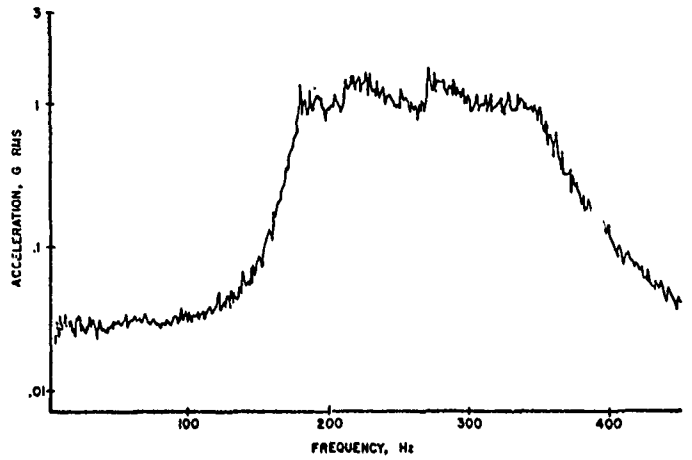
The second step in the testing was the determination of the damping coefficient in order to obtain initial comparative information on the fatigue properties of the three types of joints being investigated. The earlier test setup was used, where the logarithmic decrement or decay method was applied to determine the damping coefficient.

The random fatigue test was conducted with a general setup as shown in Figure 4. The test conditions were established by controlling the flexure rms strain level on top of the beam near the right angle edge of the stiffener (strain gage No 3, Figure 1) and by keeping this strain level constant until complete failure of the sample occurred. In most of the test articles the second symmetrical mode was primarily excited which was coupled to a weak stiffener warping mode. This was done by shaping the excitation spectrum to contain its maximum power within a bandwidth covering the symmetrical response and the lower frequency coupled mode. It was also considered desirable to extend the excitation bandwidth to at least 5 response bandwidths above the symmetrical mode and 3 response bandwidths below the coupled mode. In most cases this minimum requirement was exceeded. Only during the high strain tests the minimum excitation frequency range was approached. A typical excitation spectrum is shown in Figure 5. The corresponding strain response spectrum in Figure 6, as measured near the stiffener edge, shows the major excited mode with the associated coupled mode. Also, a very small contribution of the low frequency first mode is visible.

A few of the beams were tested by exciting the first mode in the same fashion as described. This was done in order to determine whether the stress distributions at the joints were significantly different in the two types of responses to influence the fatigue properties.

The number of cycles to failure required for the establishment of the stress-cycle S-N curves was determined initially by counting the average number of zero crossings to failure and dividing this number by two. It was later

FIGURE 5 - TYPICAL EXCITATION SPECTRUM (1 Hz BANDWIDTH)



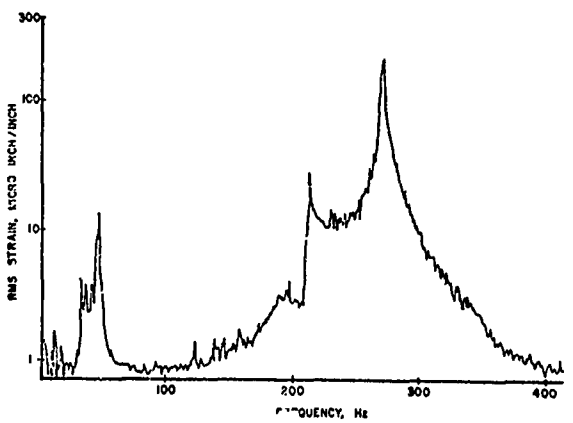


FIGURE 6 - TYPICAL RESPONSE SPECTRUM, .040 INCH WELDBONDED SPECIMEN (1 Hz BANDWIDTH)

found that multiplying the average response frequency by the total time to failure yielded almost identical results. The straight line approximation for the fatigue curves was obtained by a least square fit of the test data. During each test the progress was monitored continuously on a dual trace oscilloscope, a rms digital analyzer and a real time spectrum analyzer using a one Hertz analysis bandwidth. Frequent data samples were recorded for further detailed data reduction and analysis.

RESULTS

SWEEP AND DAMPING SURVEY

During the frequency sweep tests one difference in the general strain response behavior between the six sets of coupons was noticed. At all strain gages in the bonded and weldbonded coupons the same symmetrical behavior in the strain time histories was observed, while in the riveted coupons in the vicinity of the stiffener support the strain response appeared to be unsymmetrical. On top of the beam in the vicinity of the rivet line the compressive strain was predominating, while near the support edge a higher tensile strain was recorded. This effect which was limited in extension over the stiffener supported area was deduced as being caused by a reduced support area during the upswing half cycle and an increasing support area during the downswing. This resulted in the highest compression near the rivet line during the upswing while during downswing the highest tensile strain was experienced near the edge of the support. This effect was also found during later random vibration tests.

All beams appeared to be well balanced and no torsional or twisting strains were discovered.

The strain responses in all coupons as measured in the stiffener were significantly smaller in magnitude than those in the actual beams which were highest near the support edge.

In all eleven strain gage locations a resonant mode was always noted to be characterized by a preceding smaller resonant peak followed by a significantly higher response peak. This modal behavior was interpreted as the coupling between the stiffener warping and beam bending modes. The frequencies at maximum response in these coupled modes were selected as the modal resonant frequencies. Averages of these within the sets of test articles are listed as follows:

	FREQUENCY FIRST MODE	FREQUENCY SECOND MODE
.032 inch riveted	32 Hz	204 Hz
.032 inch weldbonded	34 Hz	206 Hz
.032 inch bonded	33 Hz	206 Hz
.040 inch riveted	39 Hz	239 Hz
.040 inch weldbonded	43 Hz	270 Hz
.040 inch bonded	43 Hz	260 Hz

Small variations from these averages were observed. A comparison between the riveted and bonded or weldbonded coupons indicates a slightly higher stiffness in the bonded or weldbonded beams. No significant difference in magnitude of the average response could be noticed during constant acceleration sweeps between individual beams of equal thickness.

The damping measurements indicated small differences in the average damping properties between the different joining methods. Thus the riveted articles showed the highest damping coefficients followed by the weldbonded and bonded specimens. The average measured damping coefficients c/c_c were:

	c/c_c FIRST MODE	c/c_c SECOND MODE
.032 inch riveted	.0132	.0064
.032 inch weldbonded	.0105	.0039
.032 inch bonded	.0069	.0021
.040 inch riveted	.0135	.0049
.040 inch weldbonded	.0111	.0029
.040 inch bonded	.0062	.0013

FATIGUE TEST

RIVETED SAMPLES

The random vibration tests were conducted with predetermined response strain levels, as measured and controlled at the highest strain point of the beams near the angle edge of the stiffeners. A coarse comparison of oscillograms obtained from the different beams at various strain points show a very similar trend in the time histories except for locations near the centerline of the riveted samples. At the higher strain response levels a pronounced asymmetry was again noticed in the strain amplitudes at this location, while near the support edge a more symmetrical behavior was observed. Figures 7 and 8 show typical oscillograms obtained at the rivetline of a riveted beam and at the spot weld line of a spot welded beam before delamination at the bond edge. Besides the noticeable difference in the distribution of tensile and compressive peaks a significant difference in the magnitude of the strains can be observed. After start of bond delamination the strain near the spot weld line approaches a behavior comparable to that in the riveted sample. This is shown in Figure 9. During the fatigue tests of several of the riveted samples a slight continuous drop in the peak frequency, Figure 10, and an associated increase in strain response, Figure 11, was observed over some length of time. This was attributed to a gradual loosening of the rivets. This effect was noticed to a much lower degree at the control gage. Small continuous adjustments of the control strain partially overcame this problem. Also very careful monitoring and accounting of the stress cycle accumulation was required. Most of the failures in the riveted coupons occurred in the beam near the edge of the stiffener. This is in contrast to other investigations, for example Reference 5, which reports failures occurring in the rivet line. This difference may be explained by a difference in construction of the coupons. It was noted that a large amount of surface pitting near the sharp edge of the stiffener led to damage of the cladding in this location which eventually resulted in

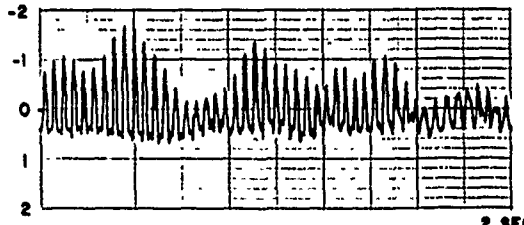


FIGURE 7, RIVETED COUPON

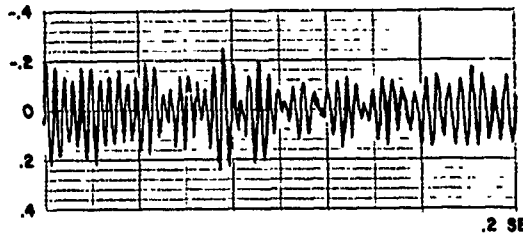


FIGURE 8, WELDBOND COUPON BEFORE FAILURE

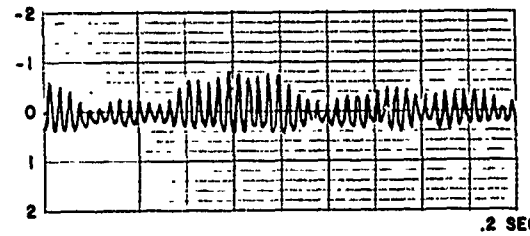


FIGURE 9, WELDBOND COUPON AFTER BOND FAILURE

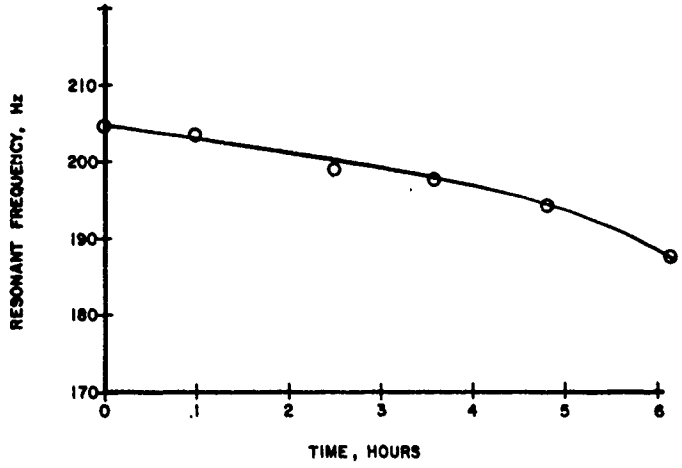


FIGURE 10 - TYPICAL VARIATION IN RESONANT FREQUENCY ON RIVETED COUPONS

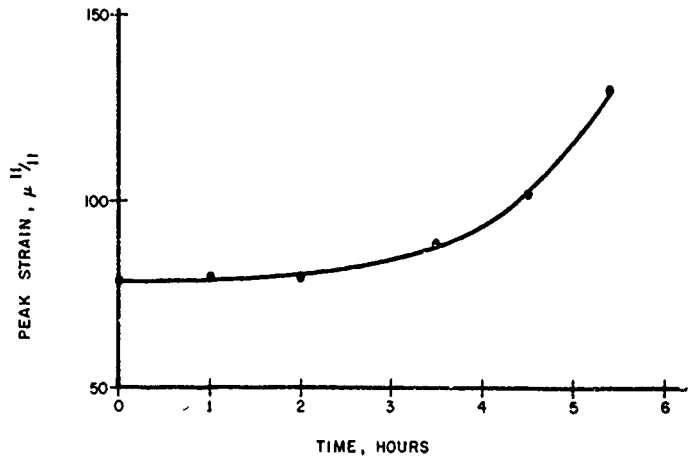


FIGURE 11 - TYPICAL VARIATION OF GAGE 1 ON RIVETED COUPONS

the failure of the beams. Two of the test articles failed in the rivet line. The results of this part of the test are plotted in the S-N curves of Figure 12. The small difference in the two curves obtained with the two thicknesses of beams may be explained by the experimental data scatter. The mean square fit for all test points is also shown in Figure 12.

WELDBONDED SAMPLES

As already indicated and shown in Figures 7, 8 and 9 various differences in the strain response behavior between the riveted and weldbonded samples were noticed. This is further emphasized in Figures 13 and 14. The strain response at the bond or support edge of a weldbonded beam of Figure 14 shows a typical single mode time history while the riveted beam, Figure 13, at the same point exhibits slightly higher tensile amplitudes. After initial bond failure the strain response in the weldbonded beam approaches that of the riveted joint as shown in Figure 15. In Figure 16 the relative frequency of compressive and tensile strain peaks of both oscillations are shown and compared to the Rayleigh probability density. Contrary to the riveted samples the weldbonded joints did not show any changes in peak response frequency with progressive test time until initial bond delamination. This is shown in Figure 17 which is indicative of a typical failure progression in the weldbonded joints. The progression of failure proceeds essentially in three phases. These are: (1) Initiation of a bond failure at the stiffener edge near the control strain gage. This starts as a adhesive delamination, that is the adhesive material in total stays attached to the stiffener while a clear separation of the aluminum beam occurs. The adhesive failure progresses rather rapidly toward the spot weld line, (2) Formation of fatigue cracks at the edge of the spot welds. Since the fatigue properties of aluminum are greatly reduced due to welding, this fatigue crack formation also proceeds rather fast, (3) The final step is the linking of the weld cracks through the skin to form a complete failure of the beam.

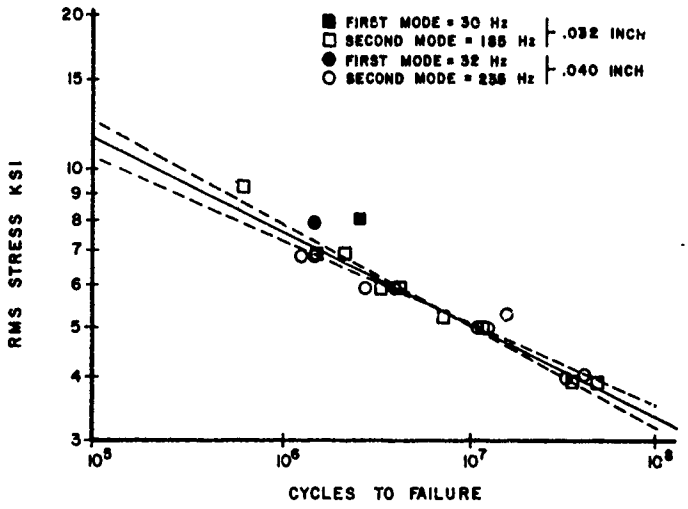


FIGURE 12 - S-N CURVE FOR RIVETED COUPONS

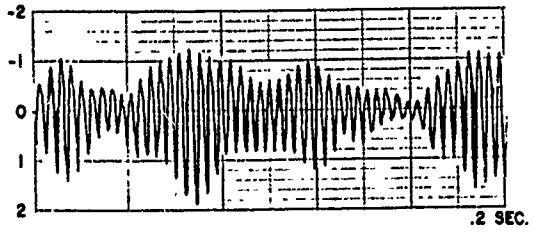


FIGURE 13, RIVETED COUPON

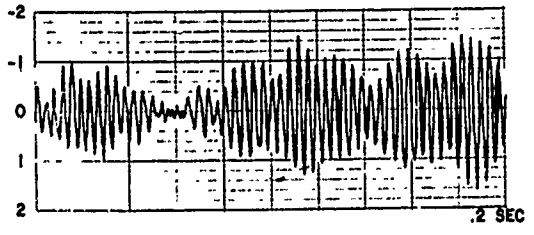


FIGURE 14, WELDBOND COUPON BEFORE FAILURE

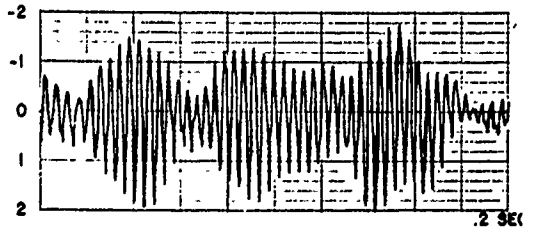


FIGURE 15, WELDBOND COUPON AFTER BOND FAILURE

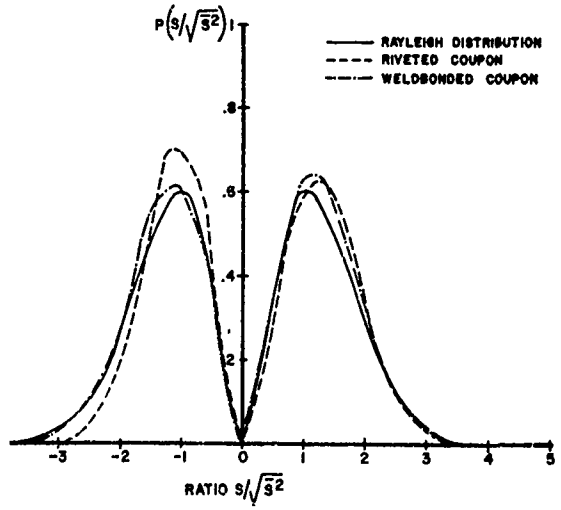


FIGURE 16 - PROBABILITY DENSITY OF COMPRESSIVE AND TENSILE STRAIN PEAKS AT GAGE 3

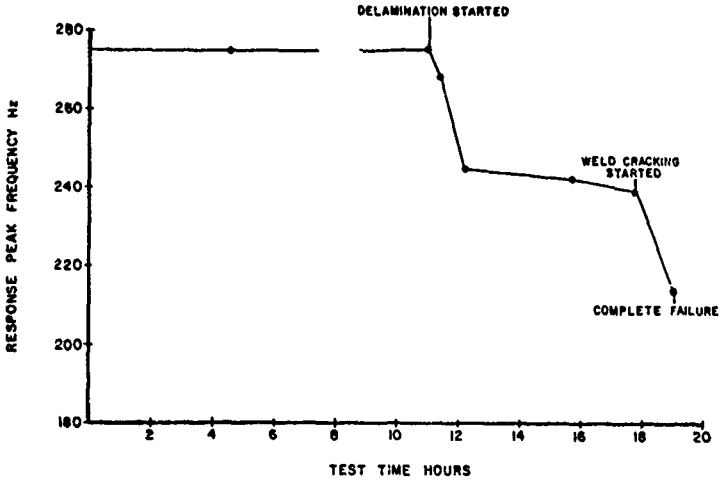


FIGURE 17 - TYPICAL VARIATION IN RESONANT FREQUENCY OF WELDBONDED COUPONS

These three phases are clearly noticeable in Figure 17. Once delamination starts the peak frequency drops as the size of the delaminated area increases. This is associated with a drop in strain response at the original edge of the supported area and an increase of strain toward the spot weld line. Once the delamination has reached the weld line the beam exhibits response characteristics almost identical to that of the riveted joint. A compptely failed weldbonded sample is shown in Figure 18.

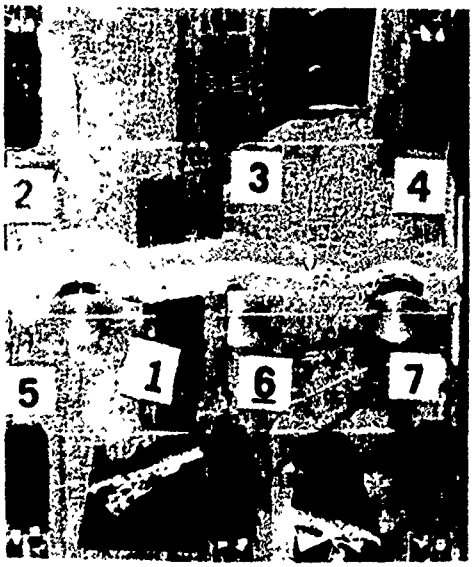


FIGURE 18 - FAILED WELDBONDED TEST BEAM

The one sample which was randomly excited in the first mode exhibited a somewhat different final failure mode in that after delamination final failure occurred in the beam at the edge of the bond or stiffener support. It may be recalled that the control rms strain near the edge of the beam was readjusted to its initial value after delamination. In the second mode this causes high strains in the weld line due to the steep strain gradient, while in the first mode with its very low strain gradient only a very small increase toward the weld line occurs. This more even strain distribution in the first mode together with the surface pitting occurring at the edge are the probable cause of this failure.

The results of the weldbonded coupon random fatigue tests are presented as least square fit S-N curves in Figures 19 and 20. It is clearly noticeable in this form of presentation that the thicker coupons (0.04 inches thick) show a shorter fatigue life relative to the thin (0.032 inches thick) beams. In order to explain this at first glance surprising phenomenon, it must be recalled that the stresses shown were measured at the beam surface over the point of initial failure, however, bond failure is initiated at the bond edge by peel stresses normal to the adhesive area. Presently it is not possible to measure this peel stress which is a function of the bending moment of the beam. The stress on the surface of the bending beam is also a function of the bending moment by the relation

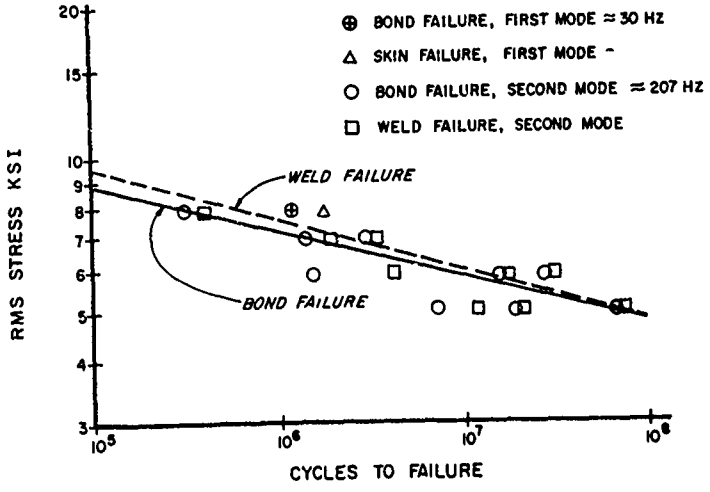


FIGURE 19 - S-N CURVE FOR .032 INCH THICK WELDBOND COUPONS

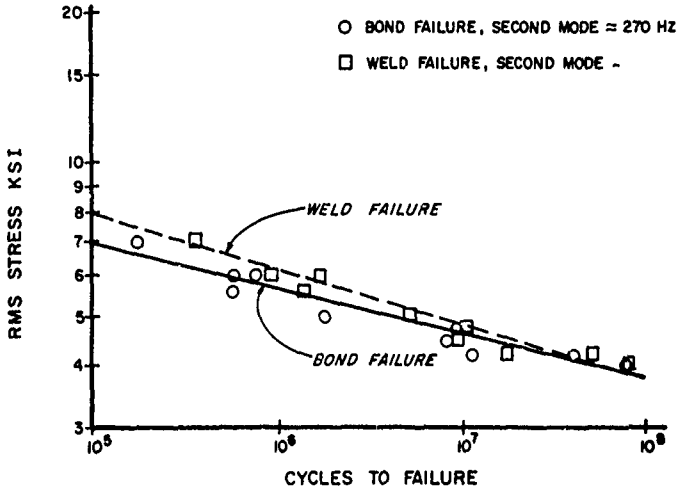


FIGURE 20 - S-N CURVE FOR .040 INCH THICK WELDBOND COUPONS

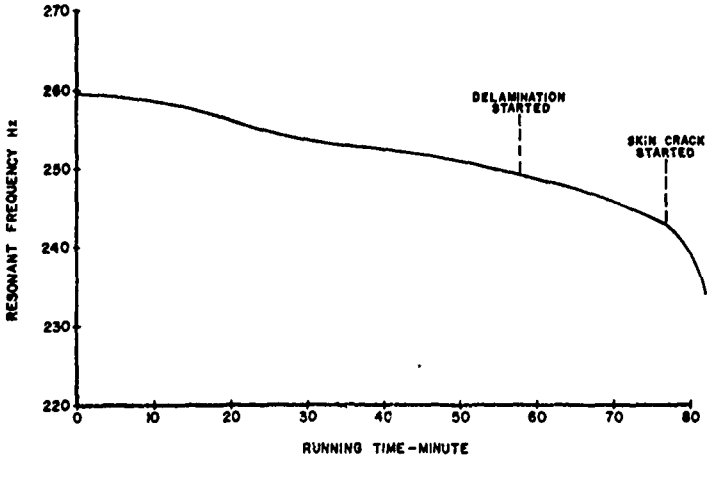


FIGURE 21 - VARIATION OF RESONANT FREQUENCY OF .040 INCH THICK BONDED COUPON DURING TESTING

$$S = \frac{6M}{bh^2}$$

S = Stress

M = Bending Moment

h = Thickness

b = Width.

Therefore, the bending mements of two beams of the same width but with different thicknesses, which are experiencing the same bending stresses, are related by

$$\frac{M_1}{h_1^2} = \frac{M_2}{h_2^2} \quad \text{or} \quad M_2 = \frac{M_1 h_2^2}{h_1^2}$$

This clearly shows that the thicker beam with equal bending stress will experience a higher bending moment. Therefore, if the peel stress in the bond is linearly dependent on the bending moment, a 56% higher peel stress in the 0.04 beam and a resulting earlier fatigue failure would be expected at the same level of bending stress.

A different convention in presenting the data of Figures 19 and 20 for example plotting bending moment as calculated from the measured strains versus cycles to failure would eliminate the ambiguity of showing two sets of data for the same joint configuration.

Comparing the fatigue data of the weldbonded and riveted joints, it was found that the riveted samples show better fatigue properties, at higher stress levels, while at low stress levels the weldbonded samples seemed to be slightly better.

BONDED SAMPLES

Although the bonded joints initially exhibited very similar strain response characteristics as the weldbonded joints, a slight drop in peak response frequency was experienced over the duration of the test which was comparable to that of the riveted joints. A typical plot of this frequency change is shown in Figure 21. It was surmised that the higher ductility of the adhesive material which was used in these joints may be the cause of this change. None of the small irregularities previously experienced with the other joining methods showed up during this phase of the test.

In comparison to the previously discussed joining methods the bonded samples showed a larger variety of failure types. Most of the 0.32 inch beams failed at the bond edge slightly after initiation of bond delamination. In two of the samples the bond separated adhesively and one of the samples failed in the stiffener close to the mounting fixture, however, bond delamination had started before this failure.

In most of the 0.04 inch beams bond delamination occurred as a cohesive separation. In this case the adhesive material separates within itself and a thin layer of adhesive stays attached to the surfaces of both metal components. This is considered a sign of good surface preparation and a good bond, while an adhesive failure indicates that surface corrosion near the bonded metal surface may have started. The final failure mode in these beams occurred by complete delamination of the bond while in several others the beam failed by cracking somewhere over the delamination area and one side of the beam stayed attached to the stiffener while the other separated cohesively. Only one of the 0.04 inch samples showed adhesive failure.

It was attempted to correlate the different types of failures with the bending stress or bending moment levels since it appeared that certain failure types are associated with certain stress level ranges. However, due to the randomness of the failure types and the relatively small number of test samples involved, such a correlation was unsuccessful.

Least square fits of the bonded sample data are shown in the S-N curves of Figures 22 and 23. Comparing the two figures shows that similar to the weldbonded joints the 0.04 inch beams appear to have a lower fatigue life than the 0.032 inch beams at equal bending stress. A possible reason for this has been presented earlier.

CONCLUSIONS

The results of the series of random vibration tests indicate the following conclusions:

1. The dynamic properties of a structure which are influenced by the joint such as stiffness and damping are slightly different in the three types which were investigated. A riveted joint exhibits a somewhat lower stiffness and a higher joint damping than the weldbonded and bonded joining methods applied here. The stiffness in the riveted joint is reduced over long test duration, as was also found in the bonded joints at high strain response levels. In contrast the weldbond joint stiffness generally remained constant up to the time of initial bond failure.

2. From the bonded and weldbonded tests it was found that if delamination occurs the conventional presentation of data, rms stress versus cycles to failure, is not sufficient to present a clear picture for these types of joints due to the multiplicity of curves required for different test article thicknesses.

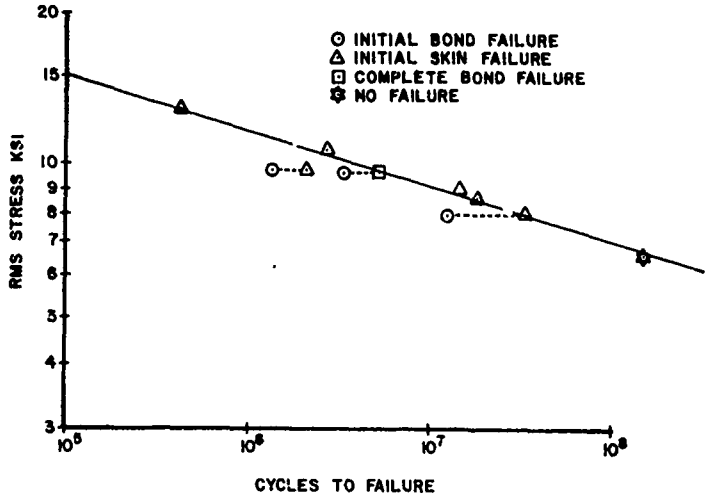
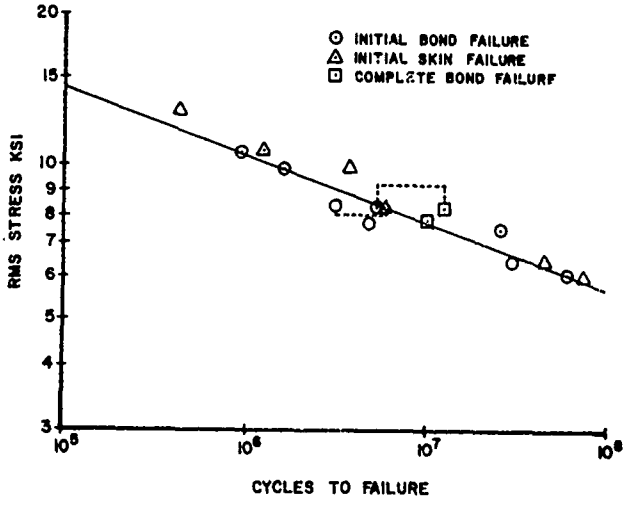


FIGURE 22 - S-N CURVE FOR .032 INCH THICK BONDED COUPONS

FIGURE 23 - S-N CURVE FOR .040 INCH THICK BONDED COUPONS



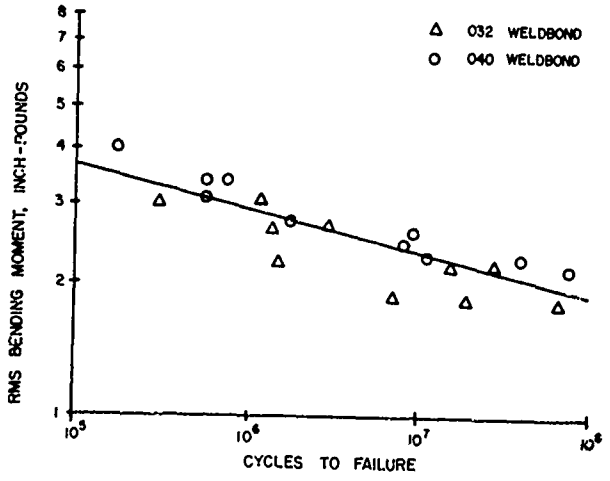


FIGURE 24 - RMS BENDING MOMENT VERSUS CYCLES TO BOND FATIGUE FOR WELD BONDED JOINTS

Since the bond peel stress can not be measured directly, a presentation of rms bending moment on the beam versus cycles to failure results in a closer collapse of the data points as shown in Figure 24.

3. A comparison of the fatigue data obtained from three types of joints which were investigated indicates that the bonding process used in the bonded joints has superior fatigue properties over a wide stress level range.

4. Although the weldbonding process which was investigated indicated good static strength properties, the fatigue results obtained have suggested that this particular process be avoided in structures with high acoustic loading.

REFERENCES

1. Belcher, P.M., Eshleman, A.L., Von Dyke, J.D., "Development of Aircraft Structure to Withstand Acoustic Loads," Aero/Sapce Engineering, Vol 18, No 6, 1959.

2. Clarkson, B.L., "Stresses in Skin Panels Subjected to Random Acoustic Loading," ISV Report, 1967.

3. McGowan, P. R., et. al., "Structural Design for Acoustic Fatigue," ASD-TR-820, 1963.

4. Ballentine, T.R., Rudder, F.F., Mathis, J.T., Plumblee, H.E., "Refinement of Sonic Fatigue Criteria," AFFDL-TR-67-156, 1968.

5. Thomson, A.G.R., "Acoustic Fatigue Design Data, Part I and II," AGARD-AG-162, 1972.

6. Rice, J.R., Beer, F.P., Paris, P.C., "On the Prediction of Some Random Loading Characteristics Relevant to Fatigue," Paper presented at Second International Conference on Acoustic Fatigue, 1964.

7. Bussa, S.L., "Fatigue Life of Low Carbon Steel under Stochastic Conditions," MTS Report 900.21-1, 1967.

8. Fields, D., "Resistance Spotweld Adhesive Bonding Process," AFML-TR-70-227, 1970.

9. Kizer, T.A., "Weldbond Flight Component Design/Manufacturing Program," Program Progress Report IR-834-1, 1973.

10. Military Specification Adhesive Bonding for Aerospace Systems Guidelines MIL-A-8377 (USAF).

11. Lockheed Corporate Process Specification, "Fabrication of Bonded Parts," LCP 79-1053B.

Discussion

Mr. Holehouse (Rohr Industries): The design of the bonded joint overlap, the length of the overlap, is very critical to the fatigue life and I think in your case you got a good joint; but as a general design practice you have to be very careful with the length of overlap if it is too short or too long the tendency to peel increases. Then also the position of your spot welds relative to the high peel area at the edge of the bond would be quite critical. Your other point about the temperature and the moisture, there are data which suggest that you get a decrease due to humidity but it is not very great. I think the temperature properties are fairly well understood so you inferred that you need more data before you can use them. Low adhesives aren't used considerably for stiffness they are used quite extensively in honeycomb structures where they have had very long service life, 50-60,000 hours, without any trouble in highly corrosive and humid environments.

FATIGUE PREDICTION FOR STRUCTURES SUBJECTED TO RANDOM VIBRATION

W. J. Kacena and P. J. Jones
Martin Marietta Corporation
Denver, Colorado

A method is presented for estimating the fatigue damage of complex structures subjected to random vibration. Conventional random vibration analysis techniques that apply specifically to normal mode analyses of lumped parameter systems are used to predict the response stress statistics. For each response stress parameter, the "apparent frequency" of response is determined and used to generate a statistical measure of the number of stress cycles in a given time. A Rayleigh distribution of stress response maxima is assumed, and the fatigue damage prediction is completed using a damage model that depends on the statistics of the random stress maxima and the number of cycles. The governing equations are presented along with an example problem which illustrates the methodology.

INTRODUCTION

Structures subjected to relatively long term or repeated random vibration exposure must be designed for fatigue. Although analytical techniques are readily available to estimate structural response parameters such as rms and "peak" stresses for short term random vibration exposures [1,2,3], fatigue life prediction has been primarily limited to the following approaches:

1) The random response stress is assumed to result from a single predominate mode and the damage is assessed using Miner's Cumulative Damage Rule [4,5,6].

2) A statistical distribution of the random stress magnitude is assumed and used in conjunction with a crack growth model [7] to define the probability of a dangerously large crack.

This paper presents an extension to existing short term random vibration response methodology that estimates both the statistical number of stress cycles in a given time and the statistical stress maxima distribution for structures with multi-modal response. This extended analytical tool generates the stress information required to use either Miner's Rule or a simple crack growth model, and is applicable when the assumption that the response occurs in a single and predominate structural mode is not adequate to describe the response of a complex structure exposed to a wide-band random excitation.

The technique is based on a finite element model of the structural properties in the form of normal modes, natural frequencies, and stress transformations (relating stresses to inertial response). Conventional random vibration analysis methods for an input spectral density are used to predict the rms stress response in each vibration mode. The total rms stress is then determined by root-sum-squaring all the modal rms stresses, as would be done for short term random exposures.

A narrow-band stress response spectral density having the same rms value as the total response stress is used to approximate the damaging effects of the actual response. The frequency of the assumed narrow-band process is selected to preserve not only the variance of the total stress but also the variance of its first derivative. Hence, the "apparent frequency" of response is the radius of gyration of the total stress spectral density about the zero frequency axis [8], and the number of stress cycles in a unit of time is defined. In addition, the probability density function for a stress maximum (assuming a normally distributed narrow-band random response) is a Rayleigh distribution [5,8,9]. The Rayleigh distribution and the number of cycles in a given time are then applied to the desired fatigue damage model, and either the expected life or the accumulated damage is determined.

PRECEDING PAGE BLANK-NOT FILMED

This approach is particularly versatile when applied to Miner's theory, because the damage due to combinations of random levels and durations is easily assessed. Since Miner's theory involves the use of conventional S/N data for the structural material, the effects of combined random and steady stresses can be evaluated by reducing the S/N curve to a level consistent with the manner in which a Goodman Diagram assesses combined steady and sinusoidal stresses.

Crack growth models are considered more representative of the fatigue damage than Miner's theory. However, the use of these models does not allow as much versatility, because the damage accumulation is dependent on the order in which the stress cycles are applied. Due to the extreme differences between these two kinds of fatigue damage models, the subsequent preparation of the governing equations considers the use of both Miner's Cumulative Damage Rule and a simple crack growth model.

NOMENCLATURE

Matricies

$[M]$	mass
$[K]$	stiffness
$[\Phi]$	normal modes
$[Mg]$	generalized mass, $[\Phi]^T [M] [\Phi]$
$[\omega^2 Mg]$	generalized stiffness, $[\Phi]^T [K] [\Phi]$
$[ST]$	stress transformation
$[A]$	$[ST][M][\Phi]$

Vectors

$\{x\}$	discrete absolute coordinates
$\{z\}$	discrete relative coordinates $[\Phi]\{q\}$
$\{T\}$	excitation transformation
$\{q\}$	generalized coordinates
$\{\Gamma\}$	modal participation factor, $[\Phi]^T [M] \{T\}$
$\{S\}$	stress

Symbols

a	crack size
a_o	initial crack size
B_{ir}	$= A_{ir}^2 \frac{\Gamma_r^2}{Mg_r^2 g_r}$
C	material constant
D	accumulated damage
DF	damage factor
f	frequency (Hz)
f_o	frequency of zero crossings
f_p	frequency of peaks
$F_u(f)$	spectral density of u as function of frequency
$F_s(f)$	stress spectral density
g	proportional damping
j	$\sqrt{-1}$
m_o, m_2, m_4	0th, 2nd, and 4th moments of the stress spectral density about the zero frequency axis
n	number of stress cycles
N	number of stress cycles to failure
$p(\ )$	probability density function
S	stress
ΔS	peak-to-peak stress
T	random exposure time
u	base motion
α, ϵ, η	variables in Eq. (13)
	$\eta = S/S_{rms}$
	$\epsilon = \left[1-(f_o/f_p)^2\right]^{\frac{1}{2}}$
δ	fraction of possible cycles
σ	$= \Delta S_{rms} = 2\sqrt{m_o}$
ω	angular frequency (radians per second)

Subscripts

i	discrete degree-of-freedom or stress index
k	identification of stress magnitude
r	index denoting r^{th} mode

RANDOM RESPONSE

The approximate method of random response calculation for a multiple degree-of-freedom system proposed by Thomson and Barton [1,2,3] is used in this development because it minimizes computer time requirements. Consider the equations of motion of a lumped parameter system with proportional damping subjected to a correlated base motion u

$$[M]\{\ddot{x}\} + (1+jg)[K]\{x-u\} = \{0\} \qquad (1)$$

Since the eigenvalue solution is generally performed with respect to the relative motion coordinate $z = x-u$, Eq. (1) is rewritten

$$[M]\{\ddot{z}\} + (1+jg)[K]\{z\} = -[M]\{T\}\ddot{u} \qquad (2)$$

where $\{T\}$ is a vector specifying a correlated direction of excitation. The normal modes and natural frequencies provide a transformation to generalized coordinates, q, that uncouples the equations of motion. (3)

$$[Mg]\{\ddot{q}\} + (1+jg)[\omega_r^2 Mg]\{q\} = -[\Phi]^T [M]\{T\}\ddot{u}$$

If the coefficient of the forcing function in Eq. (3) is relabeled $\{\Gamma\} = -[\Phi]^T [M]\{T\}$ (commonly referred to as the modal participation factor), the generalized equation of motion for the rth mode is

$$\ddot{q}_r + (1+jg)\omega_r^2 q_r = \frac{\Gamma_r}{Mg_r}\ddot{u} \quad . \qquad (4)$$

If it is assumed that the damping is small and that the spectral density of $\ddot{u}$ is relatively constant, the mean-square generalized response in the rth mode is calculated using residue integration of the transfer function squared.

$$\overline{\ddot{q}_r^2} = \frac{\pi}{2} \frac{\Gamma_r^2}{g_r M g_r^2} F_u(f_r) f_r , \qquad (5)$$

where F_u is spectral density of $\ddot{u}$ (assumed to be a Gaussian distribution) in acceleration squared per Hz and f_r is the natural frequency of the rth mode in Hz. The mean-square response of the ith degree-of-freedom is approximated as a summation over the modes.

$$\overline{\ddot{z}_i^2} = \frac{\pi}{2} \sum_r \frac{\Gamma_r^2 \Phi_{ir}^2}{g_r M g_r^2} F_u(f_r) f_r \qquad (6)$$

It is demonstrated by example in [3] that direct substitution of Eq. (6) into an expression for stress is unacceptable because the final response parameter (stress in this case) must be expressed explicitly before mean-square response statistics are performed. Stresses are expressed as a function of the inertial forces in Eq. (7) using the stress transformation [ST].

$$\begin{aligned} \{S\} &= - [ST][M]\{\ddot{x}\} \\ &= - [ST][M] \{\ddot{q}\} - [ST][M]\{T\} \ddot{u} \end{aligned} \qquad (7)$$

Applying Eq. (7) before making the transition to the form of Eq. (6) yields

$$\overline{S_i^2} = \frac{\pi}{2} \sum_r (ST\ M\ \Phi)_{ir}^2 \frac{\Gamma_r^2 F_u(f_r)}{g_r M g_r^2} f_r , \qquad (8)$$

where the appropriate matrix products are formed before the ir^{th} element is squared.

The approximation associated with Eqs. (6) and (8) is that

$$\left[\sum_r \frac{(A_{ir} \Gamma_r / M g_r)}{\left(\frac{\omega}{\omega_r}\right)^2 - 1 + j/g_r}\right] \cdot \left[\sum_r \frac{(A_{ir} \Gamma_r / M g_r)}{\left(\frac{\omega}{\omega_r}\right)^2 - 1 - j/g_r}\right]$$

$$\simeq \sum_r \frac{(A_{ir}^2 \Gamma_r^2 / M g_r^2)}{\left[\left(\frac{\omega}{\omega_r}\right)^2 - 1\right]^2 + (1/g_r)^2}$$

where [A] is either $[\Phi]$ or $-[ST][M][\Phi]$. This approximation is particularly good when the damping is small and there is reasonable frequency separation between modes. Another factor in this approximation is that the cross-terms generated in forming the product of two sums will have a tendency to cancel one another because they can be of opposite sign.

The following discussion will refer to Eq. (8) in the abbreviated form of Eq. (9) below

$$\overline{S_i^2} = \frac{\pi}{2} \sum_r B_{ir} F_u(f_r) f_r , \qquad (9)$$

where $B_{ir} = \frac{A_{ir}^2 \Gamma_r^2}{g_r M g_r^2}$ and $[A] = -[ST][M][\Phi]$.

RESPONSE STRESS STATISTICS

To accumulate the information necessary for a fatigue damage prediction, the random response statistics from Eq. (9) must be used to estimate the statistical number of stress cycles and the statistical distribution of stress maxima. The number of cycles is based on the frequency distribution of the response and estimation of the distribution of stress maxima is simplified when the actual response is represented by an approximately equivalent narrow-band response for which a Rayleigh distribution of maxima exists. The rationale behind this approximation is discussed in the following statistical development.

The response stress associated with the mean-square stress from Eq. (9) is a Gaussian Distribution because it is a linear combination of several narrow-band Gaussian processes. For a normally distributed random response, it is shown [5,8] that the frequency of zero crossings is

$$f_o = \frac{1}{2\pi} \left[\frac{\int_o^\infty F_s(f)\, df}{\int_o^\infty F_s(f)\, df}\right]^{\frac{1}{2}} = \left[\frac{\int_o^\infty f^2 F_s(f)\, df}{\int_o^\infty F_s(f)\, df}\right]^{\frac{1}{2}} \qquad (10)$$

where $F_s(f)$ is the response stress spectral density and $4\pi^2 f^2 F_s(f)$ is the spectral density of $\dot{S}$. Similarly, the frequency of occurrence of a relative maximum is related to the spectral densities of the first and second derivatives of the response stress [9].

$$f_p = \left[\frac{\int_o^\infty f^4 F_s(f)\, df}{\int_o^\infty f^2 F_s(f) df}\right]^{\frac{1}{2}} \qquad (11)$$

The integrals of Eqs. (10) and (11) are the 0th, 2nd, and 4th moments of the stress spectral density about the zero frequency axis and can be evaluated as in Eq. (9).

$$\begin{aligned} m_{o_i} &= \int_o^\infty F_s(f)\, df = \frac{\pi}{2} \sum_r B_{ir} F_u(f_r) f_r \\ m_{2_i} &= \int_o^\infty f^2 F_s(f)\, df = \frac{\pi}{2} \sum_r B_{ir} F_u(f_r) f_r^3 \\ m_{4_i} &= \int_o^\infty f^4 F_s(f)\, df = \frac{\pi}{2} \sum_r B_{ir} F_u(f_r) f_r^5 \end{aligned} \qquad (12)$$

The probability density function for a relative maximum is derived in reference [9].

$$p(\eta) = \frac{1}{\sqrt{2\pi}}\left[\epsilon\, e^{-(\eta^2/2\epsilon^2)} + \sqrt{1-\epsilon^2}\;\eta\, e^{-\eta^2/2}\int_{-\infty}^{\alpha} e^{-S^2/2}\, dS\right] \quad (13)$$

where

$$\epsilon = \left[\frac{m_o m_4 - m_2^2}{m_o m_4}\right]^{\frac{1}{2}} = \left[1 - (f_o/f_p)^2\right]^{\frac{1}{2}}$$

$$\eta = \frac{S}{\sqrt{m_o}} = S/S_{rms}\ , \quad \alpha = \frac{\sqrt{1-\epsilon^2}}{\epsilon}\,\eta$$

Using Eqs. (12) and (13), ϵ is found to range from zero to unity. For a narrow-band process, ϵ is equal to zero, and the density function of Eq. (13) becomes a Rayleigh distribution.

$$p(S) = (S/m_o)\, e^{-(S^2/2m_o)} \quad (14)$$

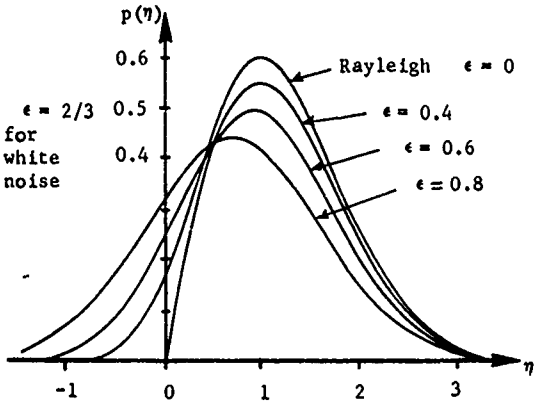
Figure 1a presents a plot of Eq. (13) for several values of ϵ, where the Rayleigh distribution ($\epsilon = 0$) is similar in appearance to the distributions when ϵ is 0.4 or less. When the negative maxima of Fig. 1a are eliminated and the distribution is renormalized to unity probability, Fig. 1b results. Since half of the difference between f_p (the frequency of maxima) and f_o (the frequency of zero crossings) is eliminated by this renormalization, the frequency associated with Fig. 1b is $(f_p + f_o)/2$. The total number of positive stress maxima at a given magnitude is the frequency times the exposure time (T) times the probability from Fig. 1b. This product can be written as

$$n = T\, f_o\left[p(S_{max})\ (f_p + f_o)/2f_o\right]. \quad (15)$$

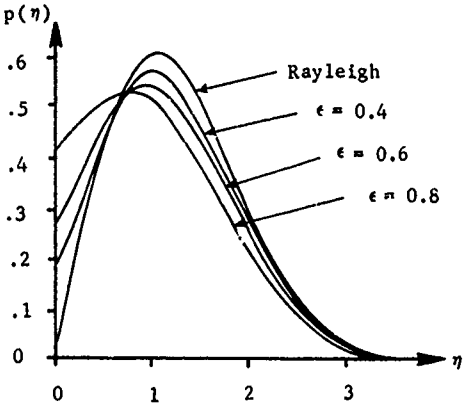
The term in brackets is replotted as a function of ϵ to yield the new density of Fig. 1c, which is normalized to f_o but has a total probability greater than unity.

The significance of Fig. 1c is that the number of positive stress maxima with magnitudes greater than the rms is determined with reasonable accuracy when the frequency f_o and a Rayleigh distribution are assumed. This result holds for practically any Gaussian stress distribution ($\epsilon < 0.8$) whether its spectral density is narrow band or not! Although Fig. 1c shows that there are actually many more stress cycles at levels less than the rms stress than are represented by the Rayleigh distribution, these low-level stresses produce very little damage, as will be illustrated by the results of the subsequent numerical example (Table 2).

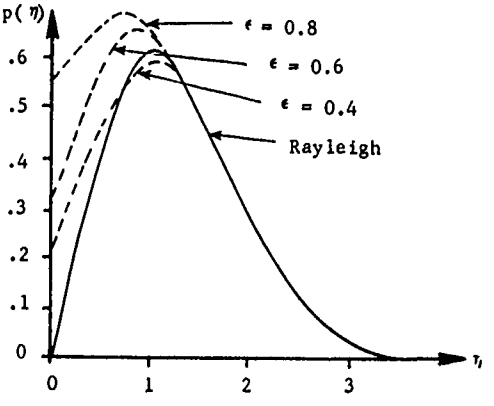
For structures that do not lend themselves to the single mode approach, values of ϵ are found to be in the range 0.3 to 0.8. As an illustration, Table 1 presents the calculated value of ϵ for several simple distributions of modal frequencies using (12) with the assumption that $B_{ir}\, F_u(f_r)$ - constant for all r.



a) P (η) versus η



b) Negative maxima eliminated and curves renormalized



c) Normalized to f_o (factor = $\frac{f_p + f_o}{2f_o}$)

Fig. 1 - Probability of Relative Maxima

Although approximation of the actual distribution by a Rayleigh distribution is slightly unconservative for stresses less than the rms stress, the computational savings by using Eq. (14) rather than Eq. (13) are considerable. In addition, the use of f_o and not f_p eliminates the need to calculate m_4 unless the value of is being checked. Hence, the apparent narrow-band response frequency f_o and a Rayleigh distribution of positive maxima are selected as a reasonable engineering approximation to statistically define the random stress.

TABLE 1

ϵ FOR SEVERAL SIMPLE FREQUENCY DISTRIBUTIONS

Uniform Distributions			Logarithmic Distributions	
$f = A f_1$ for A as tabulated below				
Case 1	Case 2	Case 3	Case 1	Case 2
1.	1.0	1.0	1.0	1.0
2.	1.5	1.1	1.25	1.1
3.	2.0	1.2	1.6	1.25
4.	2.5	1.3	2.0	1.4
5.	3.0	1.4	2.5	1.6
6.	3.5	1.5	3.2	1.8
7.	4.0	1.6	4.0	2.0
8.	4.5	1.7	5.0	2.2
9.	5.0	1.8	6.3	2.5
10.	5.5	1.9	8.0	2.8
ϵ for 1st five frequencies				
0.487	0.454	0.221	0.468	0.308
ϵ for all ten frequencies				
0.497	0.487	0.333	0.613	0.479

APPLICATION TO MINER'S RULE

Miner's cumulative damage theory [6] uses a conventional S/N diagram for the structural material and simply states that the fractional damage caused by n_k stress cycles at a stress level S_k is

$$D_k = n_k / N_k \qquad (16)$$

where N_k is the number of cycles to failure at S_k based on the S/N data. The total damage due to all stress levels then becomes

$$D = \sum_k n_k / N_k \qquad (17)$$

Based on this theory, the expected life of the structure is the random exposure time required for D to become unity.

The expected damage for a given random forcing function in a unit of time T is then determined through the following steps:

1) Numerically integrate Eq. (14) to find the fraction, δ , of maxima that occur within a small range of stress magnitude. An integration step size corresponding to a stress level range of 0.2 S_{rms} has been found to be acceptable for trapezoidal integration.

2) For the kth increment, take the highest stress level in the increment ($S_k = 0.2\ k\ S_{rms}$) and interpolate N_k from the S/N data.

3) Calculate the incremental damage in the kth increment using $n_k = T f_o \delta_k$

$$D_k = T\ f_o\ \delta_k\ /\ N_k$$

4) Sum the incremental damages for all possible values of maximum stress. An integration range of five standard deviations is sufficient for most structural materials.

$$D = T\ f_o \sum_k \delta_k\ /N_k \qquad (18)$$

Because of the linear manner in which damage is predicted using Miner's theory, the damage due to combinations of random forcing functions and exposure times can be assessed using Eq. (18). Also, the effect of steady stresses (due to preloads or steady accelerations) can be incorporated into the damage calculation. This is accomplished using the concept of a Goodman Diagram to generate a downward shift of the S/N curve. The shift factor is calculated using only the ultimate and steady stress values as depicted in the Goodman Diagram of Fig. 2.

S_e = endurance limit

S_r = reduced endurance limit

$$\text{Shift Factor} = \frac{S_r}{S_e} = \frac{S_u - S_s}{S_u}$$

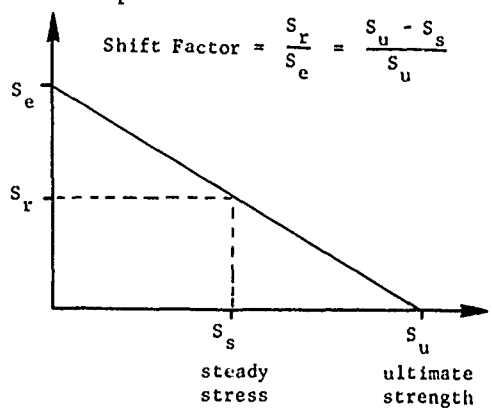


Fig. 2 - S/N shift determined from Goodman Diagram

Strictly speaking, this shift must be applied to the S/N data before using (18). However, to analyze a system with slowly varying steady stress, an approximately equivalent shift of the S/N curve to the left rather than down yields a damage factor (DF) that comes outside the summation of (18). This approximate shift is illustrated by the comparative S/N curves of Fig. 3 . Combined random and varying steady stresses are evaluated by incrementally changing the damage factor, and the exposure time external to the summation of (18).

$$D = f_o \left[\sum_k \delta_k / N_k \right] \left[\sum_j DF_j \, T_j \right] \qquad (19)$$

$$DF = \frac{N(\text{for zero steady stress})}{N(\text{for the actual steady stress})}$$

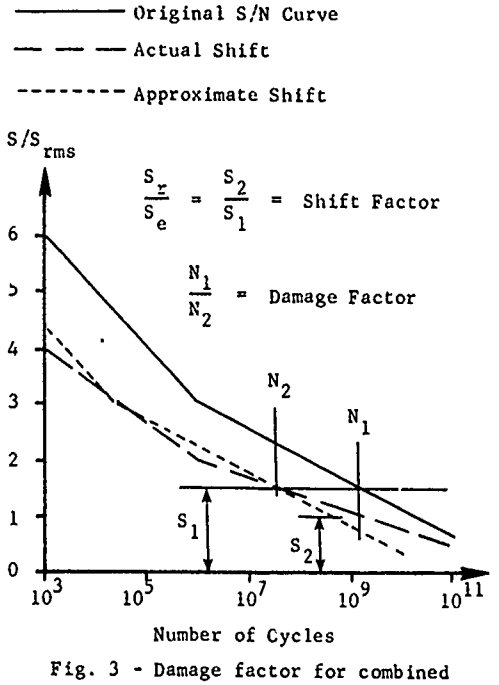


Fig. 3 - Damage factor for combined steady and random stress

The obvious advantage of Eq. (19) is that the summation on k is performed once rather than many times. It is found that when the damage factor is computed such that the approximate and actual shifted S/N curves intersect in the range $S_{rms} < S < 2\,S_{rms}$, there is little difference between using Eq. (18) and the approximation of Eq. (19).

APPLICATION TO A CRACK GROWTH MODEL

Most crack growth models represent the growth rate per stress cycle as a function of the peak-to-peak stress, the steady stress, and the crack size. For ease in usage, these models are usually presented in the form of first order differential equations with separable variables.

$$\frac{da}{dn} = f_1(\Delta S, S_o) \quad f_2(a) \qquad (20)$$

where a is crack size, n is number of cycles, ΔS is peak-to-peak stress, S_o is steady stress, and f_1 and f_2 are functional relationships. As a simple illustration of the application of the response stress statistics to a crack growth model, a typical version of the Paris equation [7] for an aluminum structure is considered.

$$\frac{da}{dn} = C\,(\Delta S)^4 \quad a^2, C \text{ is a constant.} \qquad (21)$$

After separation of variables, Eq. (21) becomes

$$\frac{1}{a_o} - \frac{1}{a} = C \int_0^T f_o \, (\Delta S)^4 \, dn \, . \qquad (22)$$

Since the distribution of peak stress response is represented as an equivalent narrow band process, it is not unreasonable to define the peak-to-peak stress distribution as twice the maximum stress from the Rayleigh distribution of Eq. (14).

$$p(\Delta S) = \frac{\Delta S}{\sigma^2} \, e^{-(\Delta S)^2/2\sigma^2} \qquad (23)$$

where the standard deviation, σ , is twice the value used in dealing with peak stress ($\sigma = 2\ S_{rms}$). Using Eq. (23), the expected value of $(\Delta S)^4$ is

$$\overline{(\Delta S)^4} = \int_o^\infty (\Delta S)^4 \, p(\Delta S) \, d(\Delta S) = 8\sigma^4 \, . \qquad (24)$$

Making the change of variable $dn = T f_o \, p(\Delta S)\, d(\Delta S)$, Eq. (22) becomes

$$\frac{1}{a_o} - \frac{1}{a} = C\,T\,f_o \int_o^\infty (\Delta S)^4 \, p(\Delta S) \, d(\Delta S) \, , \qquad (25)$$

and the expected crack size is

$$a = \frac{a_o}{1 - a_o \, C \, T \, f_o \, (8\sigma^4)} \, . \qquad (26)$$

The result of integrating Eq. (21) depends on the order in which the stress cycles are applied, but the result given by Eq. (26) for the average crack size does not consider the distribution of possible crack sizes. Since the fatigue analyst is more interested in the final crack size that bounds 99% of all possible final cracks rather than the average final crack size, he may pursue one of the following approaches:

1) Not worry about the distribution of crack growth, but rather
   a) Select an initial crack size that is statistically unlikely,
   b) Select a final crack size criteria that is statistically unlikely to be damaging (as is presumably done with the S/N curve when Miner's Rule is used), and
   c) Use the expected crack growth from Eq. (26).
2) Define the limiting crack based on the distribution of final crack sizes using either just the growth statistics or both the statistics of initial crack size and growth.

A Monte Carlo selection of the random order in which the stresses ΔS are applied and integration Eq. (21) written in the form of Eq. (27) yields a distribution of final crack sizes that depends on T as well as the distributions of ΔS and a_o.

$$a_k = a_o + C \sum_{k=1}^{T f_o} (a_{k-1})^2 (\Delta S_k)^4 \qquad (27)$$

Since no general formulation or approximation seems to describe the distribution of cracks except for specific values of T and a_o, use of the expected crack size (as in the first approach discussed above) is the simple and direct approach, but may not be conservative.

NUMERICAL EXAMPLE

Fatigue damage prediction using the apparent frequency f_o, a Rayleigh distribution of peaks, and Miner's Rule is illustrated by the two-degree-of-freedom example shown in Fig. 4. The modal properties for this system are

$$f_1 = 98.4 \text{ Hz}, \quad f_2 = 257.5 \text{ Hz}$$

$$\{Mg\} = \begin{Bmatrix} 1 \\ 1 \end{Bmatrix} \frac{\text{lb-s}^2}{\text{in}} = \begin{Bmatrix} 175 \\ 175 \end{Bmatrix} \text{ Kg}$$

$$[\Phi] = \begin{bmatrix} 0.525 & 0.850 \\ 0.850 & -0.525 \end{bmatrix} \text{ in/in or m/m}$$

$$\{\Gamma\} = \begin{Bmatrix} 1.375 \\ 0.325 \end{Bmatrix} \frac{\text{lb-s}^2}{\text{in}} = \begin{Bmatrix} 241 \\ 57 \end{Bmatrix} \text{ Kg}$$

and the matrix product $[ST][M][\Phi]$ is

$$\begin{bmatrix} 1.375 & 0.325 \\ 0.850 & -0.525 \end{bmatrix} \frac{\text{lb-s}^2}{\text{in}^3} = \begin{bmatrix} 3.73 & 0.88 \\ 2.31 & -1.42 \end{bmatrix} 10^5 \frac{\text{Kg}}{\text{m}^2}$$

When the modal damping g is assumed

$$\{g\} = \begin{Bmatrix} 0.04 \\ 0.02 \end{Bmatrix}$$

and the acceleration spectral density of Fig. 5 is used

$$\{F_u\} = \begin{Bmatrix} 0.0492 \\ 0.1288 \end{Bmatrix} \begin{matrix} \text{X } 386^2 & (\text{in/s}^2)^2/\text{Hz} \\ \text{X } 9.8^2 & (\text{m/s}^2)^2/\text{Hz} \end{matrix}$$

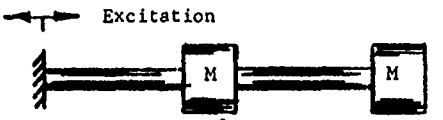
the rms stresses (and their modal contributions) are computed from Eq. (8) as

		Mode 1	Mode 2
$S_{1_{rms}} = \sqrt{m_{o_1}}$	= 10,260 psi (7.07×10^7 Pa)	10,050	2,083
$S_{2_{rms}} = \sqrt{m_{o_2}}$	= 7,076 psi (4.88×10^7 Pa)	6,222	3,369

The corresponding values of f_o, f_p and ϵ from Eqs. (10) through (13) are:

$$f_{o_1} = 110 \text{ Hz}, \; f_{p_1} = 150 \text{ Hz}, \; \epsilon_1 = 0.680$$

$$f_{o_2} = 150 \text{ Hz}, \; f_{p_2} = 218 \text{ Hz}, \; \epsilon_2 = 0.725$$



$$M = 1.0 \frac{\text{lb-s}^2}{\text{in}} = 175 \text{ Kg}$$

Identical Structural Members

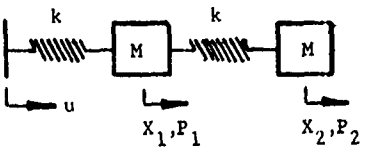
Section area (A) = 1.0 in^2 = $6.4(10^{-4})\text{m}^2$

Young's modulus (E) = 10^7psi = $6.9(10^{10})$Pa

Length (ℓ) = 10.0 in = 0.254 m

Stiffness (k) = 10^6 lb/in = $1.75(10^8)$N/m

Dynamic Model (P = force)



$$M \begin{bmatrix} 1 & 0 \\ 0 & 1 \end{bmatrix} \begin{Bmatrix} \ddot{x}_1 \\ \ddot{x}_2 \end{Bmatrix} + K \begin{bmatrix} 2 & -1 \\ -1 & 1 \end{bmatrix} \begin{Bmatrix} x_1 - u \\ x_2 - u \end{Bmatrix} = \begin{Bmatrix} 0 \\ 0 \end{Bmatrix}$$

Stress Transformation

$$\begin{Bmatrix} S_1 \\ S_2 \end{Bmatrix} = [ST] \begin{Bmatrix} P_1 \\ P_2 \end{Bmatrix} = \frac{1}{A} \begin{bmatrix} 1 & 1 \\ 0 & 1 \end{bmatrix} \begin{Bmatrix} P_1 \\ P_2 \end{Bmatrix}$$

Fig. 4 - Exampie structure

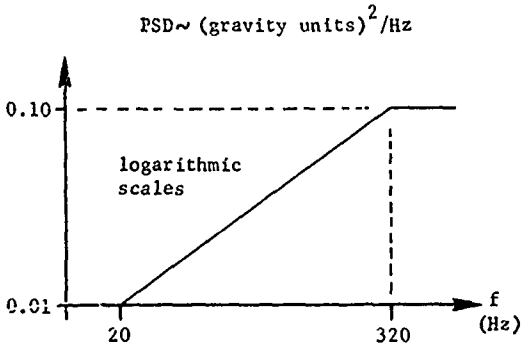


Fig. 5. - Example Problem PSD

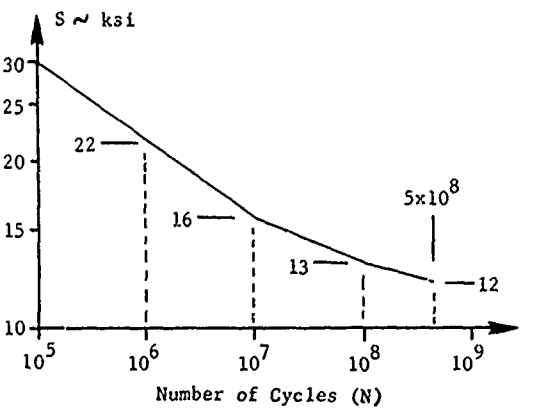


Fig. 6. - Log-Log S/N Data Used in Example Problem

Using Miner's theory in the form of Eq. (18) along with the Rayleigh distribution of peaks from Eq. (14), the damage per second of exposure time is calculated using the S/N curve of Fig. 6,

$$D_{1/T} = 7.8\ (10^{-5})/\text{sec}$$

$$D_{2/T} = 6.4\ (10^{-6})/\text{sec}$$

and the expected safe exposure time is 12,800 seconds. For this system and this S/N data, the equivalent sinuosidal stresses (those which yield the same damage for the same exposure at frequency f_o) are

$$S_{1_{eq}} = 20{,}996 \text{ psi} = 1.448\text{x}10^8 \text{ Pa}$$

$$S_{2_{eq}} = 14{,}822 \text{ psi} = 1.022\text{x}10^8 \text{ Pa}$$

This computer program damage calculation for S_1 is summarized in Table 2. These results reflect straight line extrapolation of the S/N data on a log-log plot for stresses greater than 30,000 or less than 12,000 psi. Although one might expect that for very large stresses extrapolation to either the yield or ultimate stress is more realistic, the straight line extrapolation has been evaluated (reference [10]) and is found to yield reasonable results.

TABLE 2

CALCULATED DAMAGE

S/S_{rms}	Rayleigh p (S)	Cycles to Failure, N(s)	p(s)/N(s)
0.2	0.196	1.31 (10^{24})	1.49 (10^{-25})
0.4	0.369	1.16 (10^{18})	3.18 (10^{-19})
0.6	0.501	3.34 (10^{14})	1.50 (10^{-15})
0.8	0.581	1.03 (10^{12})	5.65 (10^{-13})
1.0	0.606	1.15 (10^{10})	5.24 (10^{-11})
1.2	0.584	2.96 (10^{8})	1.97 (10^{-9})
1.4	0.525	3.29 (10^{7})	1.59 (10^{-8})
1.6	0.445	8.28 (10^{6})	5.37 (10^{-8})
1.8	0.356	3.54 (10^{6})	1.01 (10^{-7})
2.0	0.271	1.65 (10^{6})	1.64 (10^{-7})
2.2	0.196	8.23 (10^{5})	2.37 (10^{-7})
2.4	0.135	4.32 (10^{5})	3.12 (10^{-7})
2.6	8.85 (10^{-2})	2.38 (10^{5})	3.71 (10^{-7})
2.8	5.56 (10^{-2})	1.37 (10^{5})	4.04 (10^{-7})
3.0	3.33 (10^{-2})	8.24 (10^{4})	4.04 (10^{-7})
3.2	1.91 (10^{-2})	5.10 (10^{4})	3.75 (10^{-7})
3.4	1.05 (10^{-2})	3.25 (10^{4})	3.23 (10^{-7})
3.6	5.52 (10^{-3})	2.13 (10^{4})	2.59 (10^{-7})
3.8	2.78 (10^{-3})	1.42 (10^{4})	1.95 (10^{-7})
4.0	1.34 (10^{-3})	9.73 (10^{3})	1.38 (10^{-7})
4.2	6.21 (10^{-4})	6.78 (10^{3})	9.16 (10^{-8})
4.4	2.75 (10^{-4})	4.80 (10^{3})	5.73 (10^{-8})
4.6	1.17 (10^{-4})	3.45 (10^{3})	3.39 (10^{-8})
4.8	4.77 (10^{-5})	2.51 (10^{3})	1.90 (10^{-8})
5.0	1.86 (10^{-5})	1.86 (10^{3})	1.00 (10^{-8})
		$\sum$ =	3.568 (10^{-6})

Damage/sec = $0.2 f_o \sum p(s)/N(s)$ = 7.8 (10^{-5})

Time to Failure = 12,800 sec

rms stress = 10,264 psi = $7.08\text{x}10^7$ Pa

DISCUSSION

In the example problem results of Table 2, the accumulated damage below the rms stress is so low (less than 1%) that it doesn't matter whether the Rayleigh or actual distribution is used. Since the shape of this example S/N data is typical of most structural materials, the approximation that a Rayleigh distribution of maxima represents the actual distribution does not compromise the results when Miner's Rule is used. In addition, the approximation of a Rayleigh distribution has little compromising effect on a typical crack growth model where the low level stresses, which are improperly represented, produce very little growth when the stress is raised to a power. The example also illustrates that when Miner's Rule is used for typical structural materials a stress range of five standard deviations satisfactorily represents the damage. Although this may not be the case when a crack growth model is used, it is definitely reasonable to truncate the distribution at some rarely expected stress level.

Despite the fact that crack growth models are considered more representative of fatigue failure than Miner's Rule, the cumulative damage theory does represent some observed trends in fatigue failure. Furthermore, the linear manner in which Miner's approach considers damage provides the fatigue analyst a simple model with which to assess the following:

1) Determine which structural element is most likely to fatigue under random vibration.
2) Compare and/or combine different random environments. Perhaps even define an equivalent exposure time through which the damaging effects of several random environments are represented by one of them for an extended duration.
3) Combine the damaging effects of random and steady stresses using the Goodman Diagram approach to determine a damage factor.

Certainly, the assessments presented above could be used to eliminate many of the possible calculations for a subsequent crack growth analysis by eliminating many structural members from consideration, by using a single equivalent distribution to represent several random environments, and by pre-determing whether a crack growth model that includes steady stress is necessary. If the inclusion of steady stress appears desirable, an equivalent constant value offers considerable computational savings over the use of a variable. An equivalent steady stress can be calculated in reverse using the time averaged damage factor from Eq. (19), applied to a crack growth model.

An area that deserves further study is the treatment of the distribution of final crack sizes when a growth model is used. The desired result is a relationship that represents the final statistically unlikely crack size as a simple function of S_o, ΔS_{rms}, a_o and T for each credible growth model. This kind of advancement would make the use of a crack growth model almost as convenient as Miner's Rule for determining the random vibration fatigue damage in multiple degree-of-freedom structures.

REFERENCES

1. W. T. Thomson, M. V. Barton, "The Response of Mechanical Systems to Random Excitation," Journal of Applied Mechanics, pp. 248-251. June 1957.
2. W. C. Hurty and M. F. Rubinstein, Dynamics of Structures, Chapter 11, Prentice-Hall Inc., New Jersey, 1965.
3. P. J. Jones and W. J. Kacena, "Comparison of Structural Loads; Static Versus Dynamic" The Shock and Vibration Bulletin, Vol. 41, Part 6, pp. 197-202, December 1970.
4. J. W. Miles, "On Structural Fatigue Under Random Loading," Journal of Aeronautical Science, Vol. 21, pp. 753-762, 1954.
5. S. H. Crandall and W. D. Mark, Random Vibration in Mechanical Systems, Academic Press, Inc., New York, 1963.
6. M. A. Miner, "Cumulative Damage in Fatigue," Journal of Applied Mechanics, Vol. 12, pp. 159-164, 1945.
7. H. Liebowitz, Fracture, Vol. III, Chapter 1, Academic Press, New York, 1971.
8. J. S. Bendat, Principles and Applications of Random Noise Theory, John Wiley, New York, 1958.
9. R. W. Clough and J. Penzien, Dynamics of Structures, Chapters 22 and 23, McGraw-Hill Inc., New York, 1975.
10. D. T. Raske and J. D. Morrow, "Mechanics of Materials in Low Cycle Fatigue Testing," Manual of Low Cycle Fatigue Testing, ASTM STP 465. American Society for Testing and Materials, pp. 1-25, 1969.

Discussion

Mr. Smith (Bell Aerospace): Your whole paper seems to hinge on the fact that when you normalized your non Rayleigh distribution of peaks twice it looked like the Raylcigh distribution. Unfortunately you stopped the comparison at something like 1 to 1½ sigma.

Mr. Kacena: That was just to make the slide simpler. From one sigma on out the actual distribution, if you want to call it that, is lower than the Rayleigh distribution even after both normalizations.

Mr. Smith: Isn't that where they should be equal, if you are then going to assume that you can use the Rayleigh distribution? That is where the damage is going to be done out to 2, 3, or 4 sigma.

Mr. Kacena: The Rayleigh distribution is slightly conservative.

MEAN LIFE EVALUATION FOR A STOCHASTIC LOADING PROGRAMME WITH A FINITE NUMBER OF STRAIN LEVELS USING MINER'S RULE

G. Philippin, T. H. Topper and H. H. E. Leipholz
Department of Civil Engineering, University of Waterloo
Waterloo, Ontario, Canada

This paper is concerned with fatigue life prediction of a material subjected to a stochastic loading programme. Using Miner's rule - recognized to be valid from a probabilistic point of view, - together with a damage parameter associated with each closed hysteresis loop defined in the stress-strain diagram corresponding to the given loading programme, an example of life prediction is presented.

INTRODUCTION

In predicting fatigue life of a material subjected to a stochastic loading programme, it is often believed, that Miner's rule cannot lead to accurate results. In the first part of this paper, it will be shown that, from a probabilistic point of view, Miner's rule is not to be blamed for such a discrepancy between prediction and reality. In contrast, it is an inadequate choice of the damage parameter which is responsible for an unsatisfactory life prediction.

In the second part of this paper, Miner's rule will be applied in the case of a simple random loading programme for which the damage parameter will be chosen as a combination of stress and strain associated with each closed hysteresis loop defined in the corresponding stress-strain diagram.

PROBABILISTIC INTERPRETATION OF MINER'S RULE

An evaluation of the fatigue life of a specimen subjected to a random load programme is often obtained by using a rule first proposed by Miner [1] togetner with experimental stress versus fatigue life data (SN-data). More precisely, if a sequence of loads l_1, l_2, ... is applied and if failure occurs after n_1 applications of l_1, n_2 applications of l_2, etc., the fatigue life N (i.e., the maximum number of reversals that the specimen can support) can be predicted by:

$$N = \sum_{i=1}^{k} n_i$$

where k is such that

$$\sum_{i=1}^{k} \frac{n_i}{N_i} = 1.$$

Here N_i are fatigue lives under constant load amplitudes l_i, they are given as SN-data [1, 2]. As a matter of fact, Miner's rule gives the same life prediction for any sequence of loads of the form $(l_{i1}, l_{i2}, \ldots, l_{iN})$, i.e., for any premutation of $(l_1, \ldots, l_N)$. This is often in disagreement with the reality. A number of improvements has been proposed in order to make Miner's rule sensitive to the order in which the loads are encountered in a fatigue test [3]. This attempt has been only partially successful, and the loss in simplicity of such "improved versions of Miner's rule" makes their application difficult. Recently, however, researchers have obtained good results in predicting fatigue life by using a revised method of counting reversals [4] and inserting more sophisticated forms of fatigue life data in the old original form of Miner's rule [5]: when N_i is expressed in terms of a certain function of stress and strain occurring in the reversal l_i rather than in terms of the stress amplitude corresponding to the reversal l_i, the damage summation

$$\sum_{i=1}^{k} \frac{n_i}{N_i}$$

to failure closely approaches one, and this holds true for a great number of possible realizations of the same random load programme [6]. (Now, n_i is of course the multiplicity of l_i taken with respect to this new parameter). Hence, a correct interpretation of Miner's rule may be possible if suitable damage parameters and reversal counting methods are chosen. Investigations in this sense have already been carried out by Saunders and Birnbaum in two mathematical papers [7, 8]. In this paragraph, a simpler version of such a probabilistic interpretation is presented. Furthermore, it will be shown that the assumption, that the damage occurring as a consequence of a load is a random variable with an IFR - distribution [7], or

even with a NBUE - distribution [8], can be removed.

Given a random loading programme l_1, l_2, ..., we suppose that each reversal l_k is responsible for a corresponding damage X_k, and we assume: X_k is a non-negative random variable for any k = 1, 2, 3, ...

Of course, a connection between X_i and l_i exists and is representative of the physical model for damage, for example $E\{X_i\} = f(|l_i|)$. Let W be the critical amount of damage at which failure occurs, and N the index of the last reversal before rupture of the specimen. W might be considered as a random variable, and the life time N as an integral valued random variable. Between

$$Z_N = \sum_{i=1}^{N} X_i \text{ and } W$$

the following obvious relationship

$$\sum_{i=1}^{N} X_i < W \leq \sum_{i=1}^{N+1} X_i$$

holds (see Figure 1).

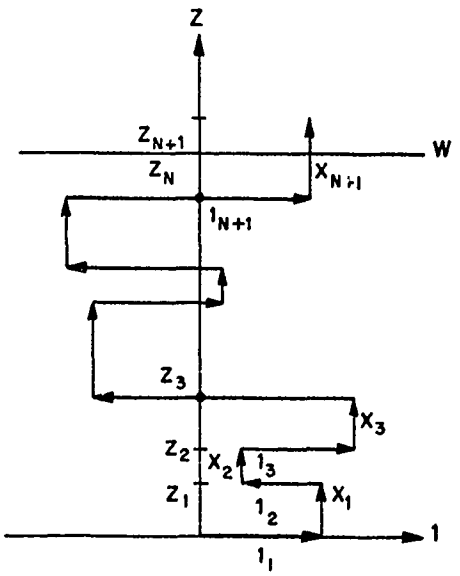


Figure 1 - Relationship Between X_i, N, and W

Taking the expected values of the quantities in the above relationship,

$$\sum_{k=1}^{[\nu^-]} \mu_k < \tau \leq \sum_{k=1}^{[\nu^+]+1} \mu_k, \qquad (1)$$

is obtained, where $\mu_k = E\{X_k\}$ is the mean value of the damage increment corresponding to the load l_k, $\tau = E\{W\}$ is the expected value of the critical damage, $\nu = E\{W\}$ is the expected life time of the specimen. $[\nu^-]$ and $[\nu^+]$ denote two integers such that $[\nu^-] \leq \nu \leq [\nu^+]$, $[\nu^+] = [\nu^-] + 1$. We now consider a fatigue test with constant "load amplitude" l_k. The corresponding sequence of damage increments is X_k, X_k, ..., and therefore we have as a special case of (1):

$$\nu_k \cdot \mu_k < \tau \leq (\nu_k+1)\mu_k, \qquad (2)$$

where $\nu_k = E\{N_k\}$ is the expected value of the life time N_k corresponding to a fatigue test with constant "load amplitude" l_k. From the inequalities on the right hand side in (2), we obtain

$$\frac{\mu_k}{\tau} \geq \frac{1}{\nu_k+1},$$

and by summation over k:

$$\frac{1}{\tau} \sum_{k=1}^{[\nu^-]} \mu_k \geq \sum_{k=1}^{[\nu^-]} \frac{1}{\nu_k+1}. \qquad (3)$$

From the inequalities on the left hand side, we obtain

$$\frac{1}{\tau} \sum_{k=1}^{[\nu^+]+1} \mu_k < \sum_{k=1}^{[\nu^+]+1} \frac{1}{\nu_k}. \qquad (4)$$

Inserting these bounds (3) and (4) in (1) yields:

$$\sum_{k=1}^{[\nu^-]} \frac{1}{\nu_k+1} < 1 < \sum_{k=1}^{[\nu^+]+1} \frac{1}{\nu_k}. \qquad (5)$$

On the other hand, we have:

$$\sum_{k=1}^{[\nu^-]} \frac{1}{\nu_k+1} < \sum_{k=1}^{[\nu^-]} \frac{1}{\nu_k} < \sum_{k=1}^{[\nu^+]} \frac{1}{\nu_k} < \sum_{k=1}^{[\nu^+]+1} \frac{1}{\nu_k}. \qquad (6)$$

From (5) and (6), we conclude that

$$1 \sim \sum_{k=1}^{[\nu]} \frac{1}{\nu_k}, \qquad (7)$$

where $[\nu]$ may be $[\nu^-]$ or $[\nu^+]$. As expected fatigues lives, the ν_k are supposed to be large numbers, therefore the difference

$$\sum_{k=1}^{[\nu^+]+1} \frac{1}{\nu_k} - \sum_{k=1}^{[\nu^-]} \frac{1}{\nu_k+1}$$

is extremely small, and (7) may be considered to be a very good approximation. This result which gives a probabilistic support for Miner's rule, states the exact sense of ν_k and ν (as expected values of the corresponding fatigues lives).

It should be noted that practical application of the foregoing derivation depends on the damage parameter chosen being adequate to collect in classes all equally damaging reversals. Such a damage parameter is a prerequisite to correctly obtain from the experimental data the damage increment μ_k for the kth reversal neces-

sary for the application of equation (1). Once, partitioning of the fatigue process into classes of equally damaging reversals in terms of a parameter which can be associated with the reversal l_k causing the damage μ_k is accomplished, application of Miner's rule is straight forward. While a physical model for the damage process is not yet available, one of the authors has obtained good life predictions by combining a damage parameter $T = \Delta\sigma_M.\Delta\varepsilon$, based on stress and strain at the fatigue crack initiation site, where σ_M is the peak stress and $\Delta\varepsilon$ is the strain range, with a reversal counting method which correctly counts reversals in local stress and strain [9]. On the other hand, however, both failure to choose a suitable damage parameter and to correctly identify events in the stress-strain history can cause serious errors in life prediction [10].

In practice, if the random nature of the load programme is known, we have to determine the corresponding statistics of a damage parameter ρ (correctly chosen), and to find the probability density $f_k(x)$ of the height of rise and fall of the stochastic process $\rho_k(t)$ [11], where t is the time and the index k is used to emphasize the nonstationary character of these quantities. By the height of rise and fall, we mean the increment h of $\rho_k(t)$ as it passes from the k-1th extremum to the kth one.

$$\sum_{k=1}^{E\{N\}} f_k(x)dx$$

is thus the expected number of reversals of magnitude between x and x+dx contributing to the rupture of the specimen. If $\nu(x)$ is the expected live time corresponding to such a reversal, Miner's rule (7) yields

$$\int_0^\infty \frac{\sum_{k=1}^{E\{N\}} f_k(x)}{\nu(x)}\,dx = 1. \qquad (8)$$

In the special case where the probability density $f_k(x) = f(x)$ does not depend on k (i.e., if the stochastic process $\rho_k(x)$ is stationary), the above equation can be solved explicitly:

$$E\{N\} = \left(\int_0^\infty \frac{f(x)}{\nu(x)}\,dx\right)^{-1}. \qquad (9)$$

AN EXAMPLE OF LIFE EVALUATION

The aim of this paragraph is to indicate how mean life evaluation can be obtained for a simplified stochastic loading programme. A combination of stress and strain associated with each closed hysteresis loop defined in the stress-strain diagram corresponding to a given loading programme is chosen as a damage parameter. This idea, which was first proposed by Matsuishi and Endo [12], has been applied successfully by several authors [4, 5, 6]. In each of these investigations, a computer counts closed loops and sums the corresponding damage values. This complicated procedure could be however avoided if statistical information about equally damaging closed hysteresis loops could be obtained from the statistical nature of a given loading programme. The foregoing problem is tractable for a finite number of possible loops in which case it is purely combinatorial. Because the difficulty increases rapidly with the complexity and number of possible closed loops, this investigation is restricted to the simplest case of this kind, in which only two strain levels and a rest state occur.

Let us consider a material subjected to a sequence of k strain peaks randomly chosen from two possible values $\varepsilon_1 < 0 < \varepsilon_2$, with the corresponding probabilities π_1, π_2; $\pi_1 + \pi_2 = 1$. We will further assume that the values $|\varepsilon_i|$ (i = 1,2) are small enough to be in the domain of elasticity of the material. In this case, three different kinds of (degenerated) closed loops h_1, h_2, h_3 are observed as indicated in Figure 2, where h_3 may be generated in two different ways denoted by h_3^+ and h_3^-. It is to be noted, that the state zero is here considered as a certain event occurring after every strain peak. This is not a restriction for an elastic material. Of course, every other prescribed value between ε_1 and ε_2 for the rest state could be chosen without any change in the following calculation, but this values has to be prescribed, otherwise we already have an uncountable set of possible closed loops!

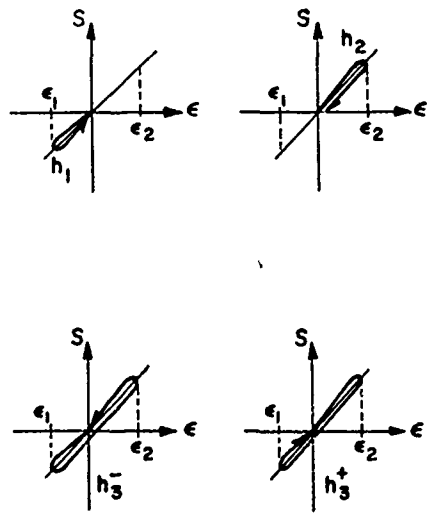


Figure 2 - Illustration of the Three Possible Closed Loops h_1, h_2, h_3.

From the 2^k possible loading programmes with k peaks, we denote by N_k^i (i = 1,2,3) the expected number of programmes finishing with an h_i-loop. For convenience, N_k^3 will be split in N_k^{3+} and N_k^{3-}, the expected number of programmes

finishing with an h_3^+ - resp. with an h_3^- - loop. Between these quantities, the following relationships hold:

$$N_k^3 = N_k^{3+} + N_k^{3-}, \tag{10}$$

$$N_k^2 + N_k^{3-} = 2^{k-1} \cdot 2\pi_2 = 2^k\pi_2, \tag{11}$$

$$N_k^1 + N_k^{3+} = 2^{k-1} \cdot 2\pi_1 = 2^k\pi_1, \tag{12}$$

$$N_k^{3+} = 2\pi_1 N_{k-1}^2, \tag{13}$$

$$N_k^{3-} = 2\pi_2 N_{k-1}^1, \tag{14}$$

$$N_k^2 = (N_{k-1}^2 + N_{k-1}^3) \cdot 2\pi_2, \tag{15}$$

$$N_k^1 = (N_{k-1}^1 + N_{k-1}^3) \cdot 2\pi_1. \tag{16}$$

Inserting (15) into (13) and using (10) and (11) leads to

$$N_k^{3+} = 4\pi_1\pi_2(N_{k-2}^2+N_{k-2}^3) = 2^k\pi_1\pi_2^2+4\pi_1\pi_2N_{k-2}^{3+}. \tag{17}$$

Inserting (16) into (14) and using (10) and (12) leads to

$$N_k^{3-} = 2^k\pi_1^2\pi_2+4\pi_1\pi_2\, N_{k-2}^{3-}. \tag{18}$$

Addition of (17) and (18) gives

$$N_k^3 = 2^k\pi_1\pi_2+4\pi_1\pi_2\, N_{k-2}^3, \quad k = 1,2,3,\ldots \tag{19}$$

Together with

$$N_1^3 = 0, \quad N_2^3 = 8\pi_1\pi_2, \tag{20}$$

the recursion formula (19) has the following solution:

$$N_{2k}^3 = 2^{2k}\pi_1\pi_2\,\frac{1-(\pi_1\pi_2)^k}{1-\pi_1\pi_2} + 2^{2k}(\pi_1\pi_2)^k,$$

$$k = 1,2,3,\ldots, \tag{21'}$$

$$N_{2k+1}^3 = 2^{2k+1}\pi_1\pi_2\,\frac{1-(\pi_1\pi_2)^k}{1-\pi_1\pi_2}, \quad k = 1,2,3,\ldots \tag{21''}$$

Let us denote by $N_k(h_i)$ (i = 1,2,3) the expected number of h_i - loops contained in the total number of 2^k possible loading programmes with k peaks. The expected number $n_k(h_i)$ of h_i - loops in one programme of length k is then

$$n_k(h_i) = \frac{N_k(h_i)}{2^k}, \quad i = 1,2,3;\ k = 1,2,3,\ldots \tag{22}$$

The quantities $N_k(h_i)$ satisfy the following recursion formulas:

$$N_k(h_1) = 2N_{k-1}(h_1)+N_k^1-N_k^{3-}, \tag{23}$$

$$N_k(h_2) = 2N_{k-1}(h_2)+N_k^2-N_k^{3+}, \tag{24}$$

$$N_k(h_3) = 2N_{k-1}(h_3)+N_k^3. \tag{25}$$

By using (10), (11) and (12), the recursion formulas (23) and (24) can be summarised in the following way:

$$N_k(h_i) = 2N_{k-1}(h_i)+2^k\pi_i-N_k^3, \quad i = 1,2;\ k = 1,2,3,\ldots \tag{26}$$

(25) together with $N_1(h_3) = 0$ leads to

$$N_k(h_3) = \sum_{n=2}^{k} 2^{k-n}\, N_n^3,$$

where this last expression can be determined with the aid of (21):

$$N_{2k}(h_3) = \frac{2^{2k+1}\pi_1\pi_2}{1-\pi_1\pi_2}\{k-\pi_1\pi_2\,\frac{1-(\pi_1\pi_2)^{k-1}}{1-\pi_1\pi_2} -$$

$$- (\pi_1\pi_2)^k\}, \quad k = 1,2,3,\ldots \tag{27'}$$

$$N_{2k+1}(h_3) = 2^{2k+1}\,\frac{\pi_1\pi_2}{1-\pi_1\pi_2}\{2k+1 -$$

$$- 2\pi_1\pi_2\,\frac{1-(\pi_1\pi_2)^k}{1-\pi_1\pi_2} - (\pi_1\pi_2)^k, \quad k = 1,2,3,\ldots \tag{27''}$$

(26) together with $N_1(h_i) = 2\pi_i$ (i = 1,2) leads to

$$N_k(h_i) = k2^k\pi_i-N_k(h_3), \quad i = 1,2,;\ k = 1,2,3,\ldots, \tag{28}$$

where $N_k(h_3)$ is given by (27). At this time, we should note, that the $N_k(h_i)$ (i = 1,2,3), given by (27) and (28), are not strictly proportional to the length of the loading programme. Such nonstationary behaviour has already been observed by one of the authors for the distribution of stress-responses of an elastoplastic material subjected to a stationary but discrete distribution of strain [13]. For the asympotic behaviour of $n_k(h_i)$, given by (22), (27) and (28) together with

$$\pi_1\pi_2 \leq \frac{1}{4}$$

lead to

$$n_{2k}(h_3) \xrightarrow{k\to\infty} \frac{\pi_1\pi_2}{1-\pi_1\pi_2}\cdot 2k-2\{\frac{\pi_1\pi_2}{1-\pi_1\pi_2}\}^2, \tag{29'}$$

$$n_{2k+1}(h_3) \xrightarrow{k\to\infty} \frac{\pi_1\pi_2}{1-\pi_1\pi_2}(2k+1)-2\{\frac{\pi_1\pi_2}{1-\pi_1\pi_2}\}^2, \tag{29''}$$

$$n_{2k}(h_i) \xrightarrow{k \to \infty} (\pi_i - \frac{\pi_1\pi_2}{1-\pi_1\pi_2})2k + \\ + 2\{\frac{\pi_1\pi_2}{1-\pi_1\pi_2}\}^2, \quad i = 1, 2, \tag{30'}$$

$$n_{2k+1}(h_i) \xrightarrow{k \to \infty} (\pi_i - \frac{\pi_1\pi_2}{1-\pi_1\pi_2})(2k+1) + \\ + 2\{\frac{\pi_1\pi_2}{1-\pi_1\pi_2}\}^2, \quad i = 1, 2. \tag{30''}$$

By neglecting the constant term

$$2\{\frac{\pi_1\pi_2}{1-\pi_1\pi_2}\}^2 \quad (\leq \frac{2}{9}),$$

the above formulas can be summarised as follows:

$$n_k(h_3) \xrightarrow{k \to \infty} \frac{\pi_1\pi_2}{1-\pi_1\pi_2} k, \tag{29}$$

$$n_k(h_i) \xrightarrow{k \to \infty} (\pi_i - \frac{\pi_1\pi_2}{1-\pi_1\pi_2})k, \quad i = 1, 2. \tag{30}$$

Let us denote by ν_i the mean life corresponding to a loading programme containing only h_i - loops. According to Miner's rule (7), the mean life ν associated with our loading programme is determined by means of the equation

$$\sum_{i=1}^{3} \frac{n_\nu(h_i)}{\nu_i} = 1, \tag{31}$$

from which, together with (29), (30),

$$\nu = \left[\frac{\pi_1 - \frac{\pi_1\pi_2}{1-\pi_1\pi_2}}{\nu_1} + \frac{\pi_2 - \frac{\pi_1\pi_2}{1-\pi_1\pi_2}}{\nu_2} + \frac{\frac{\pi_1\pi_2}{1-\pi_1\pi_2}}{\nu_3}\right]^{-1} \tag{32}$$

is obtained.

ACKNOWLEDGEMENT

This research was carried out under the support of the National Research Council under Grants No. A 7297 and No. A 1694, and under the support of the Air Force Office of Scientific Research under Grant No. AFOSR-71-2120.

REFERENCES

[1] Miner, M. A., "Cumulative Damage in Fatigue", Journal of Applied Mechanics, Vol. 12, pp. A159-A164, (1945).

[2] Palmgren, A., "Die Lebensdauer von Kugellagern", VDI - Zeitschrift, Vol. 68, pp. 339-341, (1924).

[3] Madayag, A. F., "Metal Fatigue: Theory and Design", John Wiley and Sons, Inc., New York, (1969).

[4] Dowling, N. E., "Fatigue Failure Predictions for Complicated Stress-Strain Histories", Journal of Materials, JMLSA, Vol. 7, No. 1, pp. 71-87, March, (1972).

[5] Smith, K. N., Watson, P. and Topper, T. H., "A Stress-Strain Function for the Fatigue of Metals", Journal of Materials, JMLSA, Vol. 5, No. 4, pp. 767-778, December, (1970).

[6] Topper, T. H., Sandor, B. I. and Morrow, JoDean, "Cumulative Fatigue Damage Under Cyclic Strain Control", ASTM, Vol. 4, No. 1, pp. 189-199, March, (1969).

[7] Birnbaum, Z. W. and Saunders, S. C., "A Probabilistic Interpretation of Miner's Rule", SIAM Journal of Applied Mathematics, Vol. 16, pp. 637-652, (1968).

[8] Saunders, S. C., "A Probabilistic Interpretation of Miner's Rule II", SIAM Journal of Applied Mathematics, Vol 19, pp. 251-265, (1970).

[9] Conle, A. and Topper, T. H., "Sensitivity of Fatigue Life Predictions to Approximations in the Representation of Metal Cyclic Deformation Response in a Computer-Based Fatigue Analysis Model", Second International Conference on Structural Mechanics in Reactor Technology, Berlin, Vol. L 8/4, (1973).

[10] Jhansale, H. R., "Evaluation of Deformation Phenomena of Metals for Fatigue Analysis", Journal of Testing and Evaluation.

[11] Rice, J. R. and Beer, P. R., "On the Distribution of Rises and Falls in a Continuous Random Process", Transactions of the ASME, pp. 398-404, (1965).

[12] Matsuishi, M. and Endo, T., "Fatigue of Metals Subjected to Varying Stress", Paper presented at Japan Society of Mechanical Engineers, Fukuoka, Japan, March, (1968).

[13] Philippin, G. A. and Leipholz, H., "On the Distribution of the Stress States of a Material with Ideal Elastoplastic Behaviour, Subjected to a Finite Number of Strain Levels", Mechanics Research Communications, Vol. 2, pp. 215-220, (1975).

THERMO-ACOUSTIC SIMULATION OF CAPTIVE FLIGHT ENVIRONMENT

W. Douglas Everett

Pacific Missile Test Center
Point Mugu, California

A test facility and procedure has been developed wherein the combined thermal and vibration stresses of captive flight are accurately simulated. The facility is essentially a large reverberant acoustic chamber within which is a small temperature chamber or shroud. The flexibility of the thermal shroud is the novel feature of the facility wherein it contains the temperature conditioning air to the immediate vicinity of the test missile, yet it is transparent to the acoustic energy which induces the vibration in the missile. The test procedure is based on an estimate of the lifetime flight-use environment for the tested missile in terms of percentage of life at various flight dynamic pressure (q) conditions.

INTRODUCTION

A test facility and procedure has been developed to provide a realistic simulation of captive flight vibration and thermal stresses. There was a problem of combining an acoustic and a temperture chamber, wherein each normally processes a different kind of air. The solution was the use of a thin flexible shroud around the missile which separated the temperature conditioned air around the missile from air modulator air passing through the acoustic chamber. Another problem concerned operating at the proper vibration stress levels in the missile to simulate the total captive flight life experience of the missile. Because the quantitative relationship between vibration level and failure rate is not known, it is not possible to determine a mean or representative single vibration level to substitute for the actual accumulated lifetime vibration experience of the missile. The solution to this problem was to test with vibration levels repeatedly cycled through the operational range of projected captive flight experiences with an allocation of time at the various levels proportioned to the projected lifetime experience. The resultant facility and procedure has been functioning reliably in the simulation of captive flight stresses.

PRECEDING PAGE BLANK-NOT FILMED

FACILITIES

The thermo-acoustic facility, shown in Figure 1 is essentially the combination of two independent facilities with a supple shroud and of course the test item being the only common elements between the two. A reverberant accustic facility provides the vibration stimulus and a closed loop, high air flow air conditioning facility effects the temperature changes in the AIM-9L test items. The supple thermal shroud, enclosing the guidance and control section (G&C) of the missile, confines the air conditioning air flow close to the

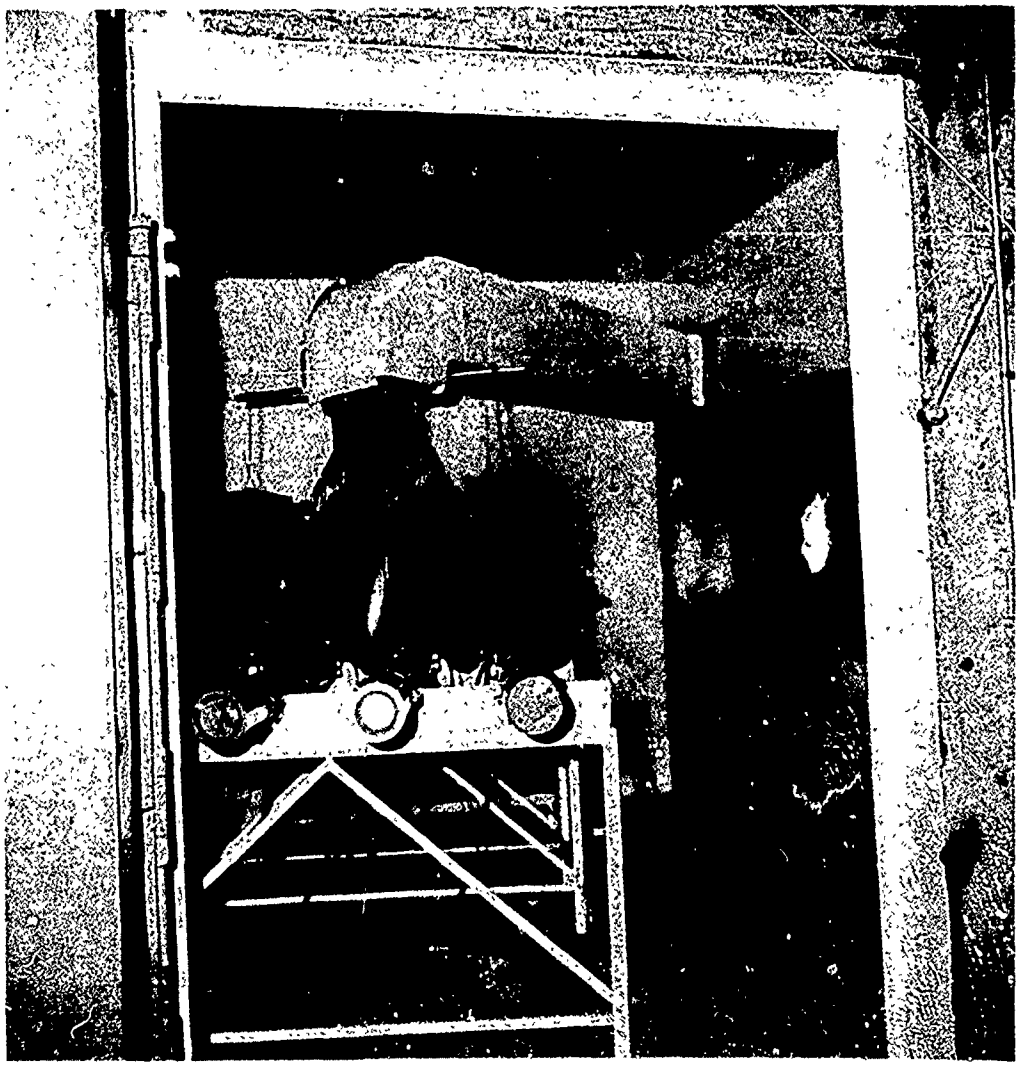


Figure 1. Thermo-Acoustic Facility (Viewed through door of acoustic chamber).

missile surface yet does not interfere with the accustic pressure waves striking the missiles.

Acoustic Facility

The acoustic facility, configured for the AIM-9L captive flight simulation, includes four essential elements. The first element includes the inert ordinance sections of the missile which, coupled to the tested guidance and control sections, yields a complete missile and more realistic vibration responses. The second element is the fifty-seven cubic meter reverberant acoustic chamber which

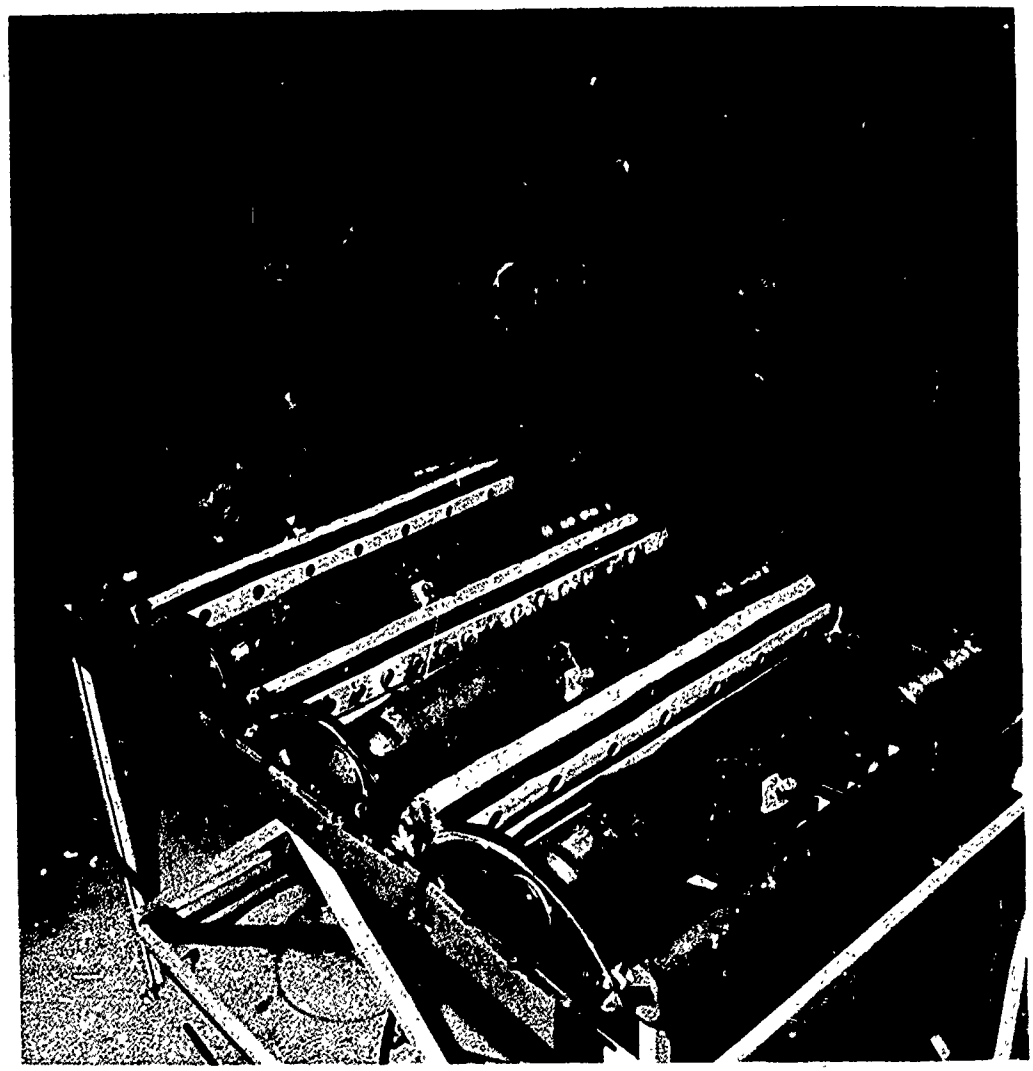


Figure 2. AIM-9L GAC sections within shrouds (top half of shroud raised).

develops a diffuse reverberant acoustic field around the missile. The third element is a ten thousand acoustic watt air modulator which, coupled to the chamber by an exponential horn, provides the acoustic energy for the reverberant field. The fourth element is a tape recorded electrical control signal which determines the air modulator acoustic spectrum and power level.

The AIM-9L test required that four Guidance and Control (G&C) sections be simultaneously evaluated in the simulated captive flight environment. Therefore, the test assembly within the chamber, shown in Figures 1 and 2 includes four complete missiles supported on a rigid frame which simply supports the inert ordinance sections at the motor and warhead sections. A one millimeter thick silicone rubber spacer separates the missile from the semi-circular cradle support of the frame, thus decoupling high frequency vibration between the two.

The Acoustic Chamber is a rectangular room with 200 millimeter thick reinforced concrete walls, ceiling and floor. The room dimensions are 4.8 meters by 3.8 meters by 3.0 meters high which provides a diffuse reverberant acoustic field in the central six cubic meter test volume at frequencies down to one hundred hertz. The room design is somewhat unusual with respect to access ports, which, including the horns and door, occupy approximately 9.3 square meters of wall area. The ports are intended to provide flexibility in the application of the chamber to missile tests in a simulated captive flight environment. The auxiliary port provisions are as follows; 2 each 0.3 meter by 0.6 meter ports for air conditioning ducts into the chamber; 2 each 0.3 meter by 0.6 meter ports for shaker power cables and cooling hoses and for instrumenttion cables; a 200 millimeter diameter port for exhaust air from the chamber; and a 1.5 meter by 1.5 meter port for access to any microwave anechoic chamber and simulated target that might be installed adjacent to the chamber for functional tests of a missile. When the ports are not in use a 19 millimeter thick steel plate covers the hole, flush with the inside surface of the chamber.

The air modulator, supplying the acoustic energy, is a Ling Model EPT 1094 unit rated at 10,000 acoustic watts. The unit operates on compressed air supplied by a large reciprocating compressor through a pressure regulator yielding 0.23 kg/s at 276 kPa pressure. The modulator is coupled to the chamber by a Ling Model EC 100 exponential horn with a computed low cutoff frequency of 100 Hz and a one square meter mouth. The modulator is driven by an amplified electrical control signal at levels up to 200 volt amperes, corresponding to rated output.

The electrical control signal was developed with a random noise source and a manual equalizer to effect realistic vibration responses in the missile. Vibration data from a captive flight of an AIM-9G missile was used as a reference for realistic captive flight environment. Two pairs, of mutually perpendicular accelerometers oriented transverse to the missile longitudinal axis were used. Each pair was located at a different major structural point in the G&C section believed to be in the transmission path of vibration energy between the outside surface (the source of vibration) and the internal components (vibration sensitive receivers). The PSD analyses of data from these four accelerometers were averaged graphically, over 50 Hz bandwidths between zero and two kHz. Signals from the same four accelerometers on the same missile, installed in the acoustic chamber were averaged through a multiplexer and that average signal was analyzed for comparison with the flight data. The random noise electrical control signal to the modulator was limited to an upper frequency of 550 Hz because the modulator efficiency rapidly declines at higher frequencies. The uncontrolled, higher frequency acoustic power in the chamber results from distortion or harmonics of the modulator output in the controlled frequency band. Constant bandwidth analysis of the acoustic power in the higher frequencies shows an approximately 6 dB/octave decline. The equalized control signal was recorded on a continuous loop cartridge type tape recorder to be played back as a control signal during the test. Additionally, signals from a microphone in the acoustic chamber and accelerometers on the missiles were recorded for periodic reference with comparable signals during conduct of the test.

Thermal Facility

The Thermal Facility consists of; an air conditioning unit and ducts into the acoustic chamber, shown with the

air modulator and horn assembly in Figure 3; ducting to and from the enshrouded G&C sections, shown in Figures 1 and 2; and a temperature controller sensing the skin temperature of one of the G&C sections.

The air conditioner is a Thermotron Model ECA 5 LN2 temperature conditioning unit modified to include a total of 9 kW of heating capacity. Cooling is accomplished by circulating LN2 through a refrigeration coil in the air stream. A 2.24 kW fan provides air circulation to and from the test site.

The temperature conditioned air is directed around the G&C sections shown

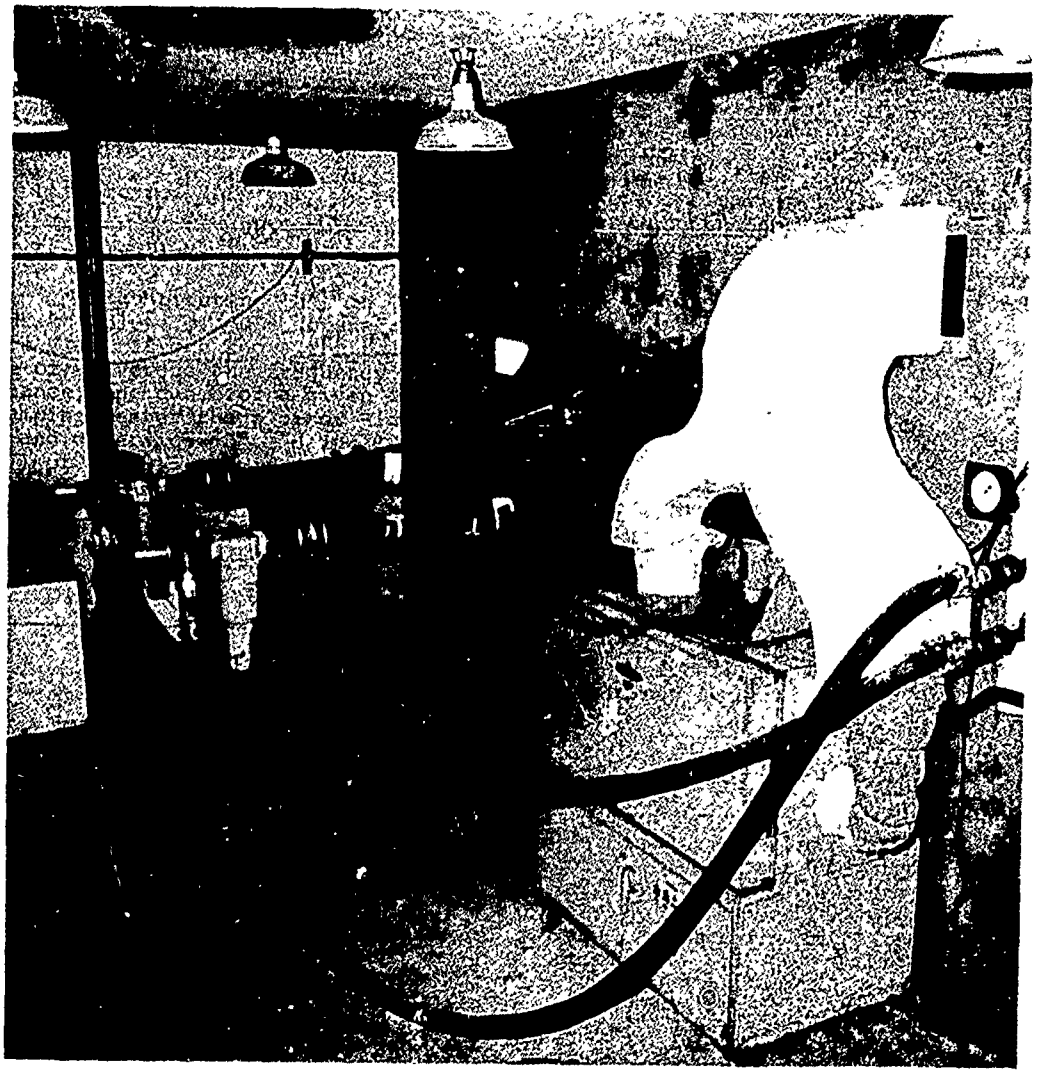


Figure 3. Air Conditioning Unit And Modulator - Horn Assembly.

in Figure 2. The center pipe supplies air to the two center missiles and the two smaller end pipes supply air to the two end missiles. Return air to the air conditioning unit is collected in the remaining two intermediate pipes. The individual turning vanes or scoops in each hole of the supply pipes were adjusted to yield a constant cross flow of air along the length of the G&C sections. The shrouds are made of one millimeter thick silicone rubber supported by a light steel framework. The shape of the frame yields an oval cylindrical shroud with approximately a 12.7 millimeter clearance from the missile at the top and bottom. This relatively small clearance results in high velocity air flow across the missile, thus the high heat transfer coefficient which was required for this test.

The temperature controller is a Honeywell single point temperature controller recorder which is modified to include a second temperature set point. The controller senses the skin temperature of a G&C section and is programmed by a timer actuated switch to control that temperature to either the high or low temperature extreme.

TEST PROCEDURE

The test procedure is an adaptation of the MIL-STD-781B, Reliability Tests procedure, using a temperature cycle combined with acoustic instead of mechanical shaker vibration inputs. It was intended that this adaptation would improve the accuracy in test induced failure rates.

Acoustic Test Procedure

Previous laboratory test experience with Navy air launched missiles has shown that reverberant acoustic energy excites structural vibration responses resembling those resulting from flight.(1) This resemblence can be seen when the comparison is made between: the amplitude of vibration at various points throughout the structure; the amplitude of vibration in two or more directions at the same point in the structure; and the spectral distribution of the vibration energy at any point and direction in the structure. Furthermore, experience as well as intuition indicates that the internal component of a missile is more likely to fail when the vibration level is high: at the location of that component's failure motion; and at the frequency or frequencies of that component's failure motion. It is difficult to determine the quantitative relationship between failure rate and vibration level in a complex mechanical system like a missile, but there is some evidence that failure rates are directly proportional to the vibration level to an exponent of 5 plus or minus 2.(2) If such a relationship is valid and it is important to duplicate the actual flight failure rate in a laboratory test then it is important to accurately simulate the flight vibration at all points, in all directions, and at all frequencies in the missile.

The cumulative captive flight experience of a missile might involve flights through various mission profiles and therefore exposure to various combinations of flight speeds and altitude. It is possible to project what percentage of the missile lifetime might be devoted to different mission profiles and as a result derive the percentage of lifetime allocated to various combinations of flight speed and altitude. It is possible to relate vibration intensity to those combinations of flight speed and altitude, normally through the parameter q, the flight dynamic pressure.

Desireably the relationship is determined through flight vibration measurements, but an alternative for acoustic tests is to use a formula from MIL-STD-810C. Available, at least in the "proposed" version of MIL-STD-810C, Table 515.1-II, is a formula which defines an acoustic test level as a function of flight dynamic pressure in combination with some physical descriptions of the missile. The AIM-9L cumulative captive flight experience in terms of percent of lifetime at various q conditions was based on projected missions aboard and F-14 aircraft. Flight vibration measurements of an AIM-9 missile aboard an F-4 aircraft permitted a determination of the relationship of missile vibration intensity to flight q conditions. It was therefore possible to describe the AIM-9L cumulative captive flight experience in terms of percent of lifetime allocated to various vibration intensities.

The flight instrumented missile was installed in the thermo-acoustic test facility and the acoustic spectrum

was adjusted for the best resemblance of response vibration spectrums to those measured in flight. Figures 4 and 5 show a comparison of the flight and acoustic vibration response spectrums, wherein the flight data corresponds to approximately twice the q simulated by the acoustic test. The acoustic level was then adjusted to yield vibration response levels corresponding to those from several different flight q conditions. With that information it was possible to design an acoustic test that would simulate the cumulative captive flight experience of the missile. Figure 6 tabulates, vs. percent of lifetime, the corresponding flight q condition; the

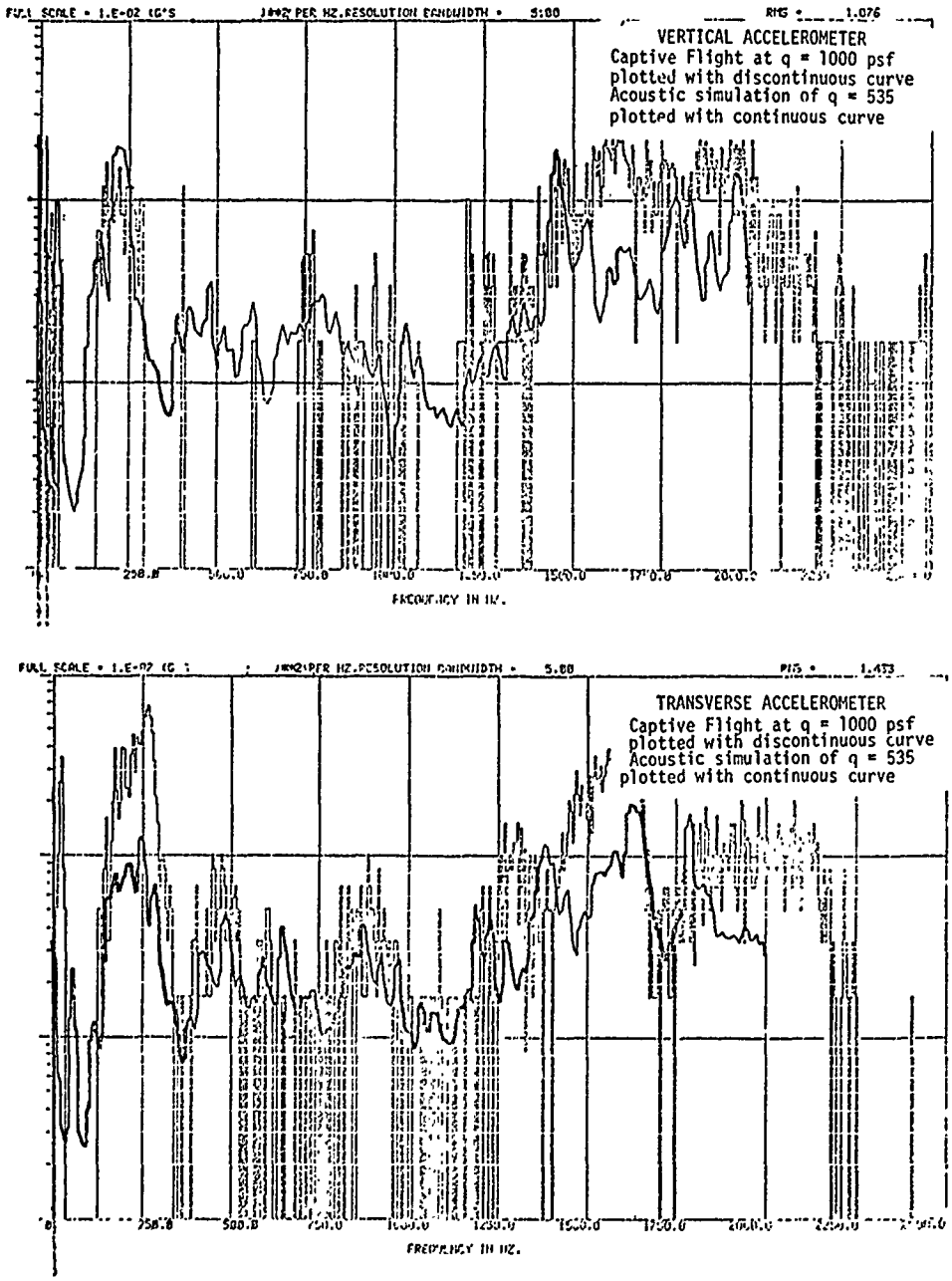


Figure 4. PSD Comparison at G & C Aft End

acoustic sound pressure level, SPL, required to yield corresponding vibration levels in the missile; and for the sake of comparison, the acoustic SPL derived from the MIL-STD-810C formula. A continuous loop tape recorded signal to the acoustic noise generator was then developed wherein the signal strength was changed from one interval of time to the next to effect acoustic levels, at percentages of tape loop time, equal to those tabulated in Figure 6. It is believed that such a cycling of acoustic intensities at representative proportions of time will cause realistic flight fatigue failures and failure rates within the missile.

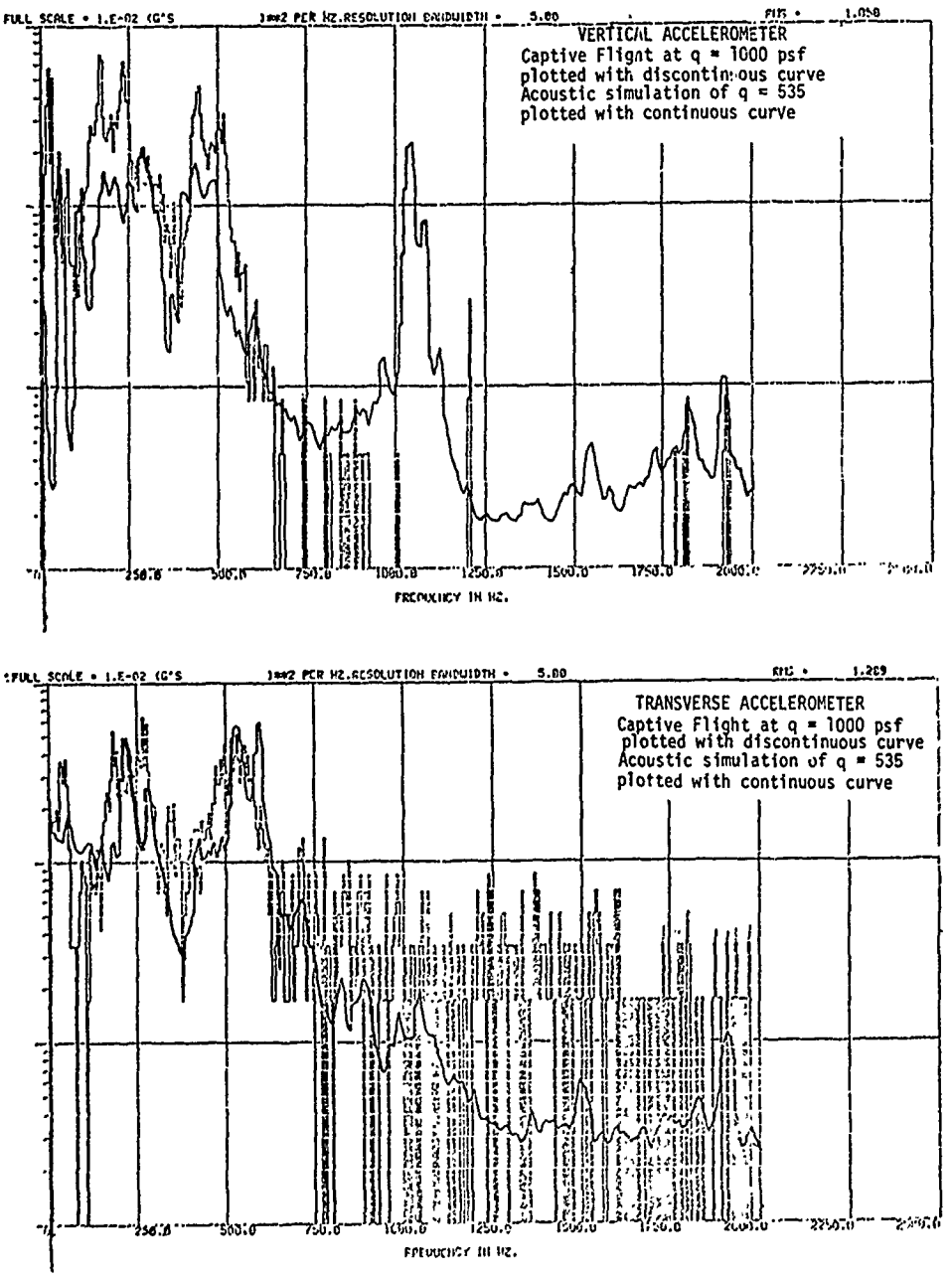


Figure 5. PSD Comparison at G & C Front End

PART OF CAPTIVE FLIGHT LIFETIME	FLIGHT DYNAMIC PRESSURE q	MISSILE AVERAGE VIBRATION RESPONSE	REQUIRED ACOUSTIC LEVEL	MIL-STD-810C ACOUSTIC LEVEL
%	PSF	gRMS	dB	dB
6	126	0.26	138.8	139.0
16	141	0.29	139.7	140.0
30	223	0.46	143.8	144.0
10	302	0.62	146.4	146.6
3	355	0.74	147.7	148.0
23	527	1.09	151.2	151.4

FIGURE 6. AIM-9L CAPTIVE FLIGHT ENVIRONMENT

Thermal Test Procedure

The thermal test procedure is similar to the MIL-STD-781B alternative temperature cycle and was derived from a previous test specification for the missile. The two temperature extremes are 233 degrees K and 333 degrees K which are approximately the same as those measured during extreme captive flight conditions aboard an aircraft. Each temperture extreme, sensed on the outside surface of the missile, is maintained for approximately 14.4 ks, including a 1.8 ks transition time from the other extreme.

Future Captive Flight Thermal Simulations may employ temperature cycles based on the projected cumulative captive flight experience of the missile. If such a technique were to be applied to the AIM-9L missile, using the combination of flight speeds, altitudes, and percentages of lifetime used for determining the vibration intensity cycle. A temperature tabulation comparable to Figure 6; could be made. However, because temperature transients, as well as extremes, may be important, the tabulated information might require supplementary data on transient temperatures. Another method, made possible by the responsive thermal facility used in this test, would be the simulation of the actual flight mission temperature profile or a representative combination of flight missions could be selected to simulate the lifetime thermal experience of the missile with respect to skin temperature extremes, soak times and transients. Were this alternative chosen, it would also be possible to program the acoustic levels to the flight mission q profile.

CONCLUSION

A test facility and procedure has been developed which creates the combined vibration and thermal stresses of a missile's lifetime captive flight experience.

This laboratory test method might be preferred to current peacetime captive flight tests for determining reliability information for the following reasons;

1. It allows for more detailed analysis of missile failures during the test;

2. It provides stresses related more nearly to combat use of the missile;

3. It can "fly" more missiles (10 to 15 missiles) for longer periods of time (continuously) with less resources (2 men and 37 kW of facility power).

REFERENCES

1. Piersol, A. G. and Calkins, J. C., "SPARROW Missile Captive Flight; Simulation of Dynamic Loads." TP-73-35, Naval Missile Center, Point Mugu, California, 1973.

2. Calkins, J. C., Meeker, D. B. and Piersol, A. G., "SPARROW III (AIM-7E-2) Missile Accelerated Reliability Testing," TP-74-12, Naval Missile Center, Point Mugu, California, 1974, (CONFIDENTIAL).

Discussion

Mr. Forkois (NRL): Were you successful in obtaining any failures of the equipment? You never said anything about failures, and nobody ever says anything about failures in these meetings.

Mr. Everett: Yes, we got a few failures and they almost seemed to be workmanship type failures. I think they were having some experience like that in the fleet at the same time so there is some encouragement that maybe we are doing something right.

Mr. Earls (Air Force Flight Dynamics Laboratory) How did you get the temperature environment?

Mr. Everett: I got that the easy way, I just took it out of the MIL-STD-781 reliability test. I really inherited that requirement, it is a cycle between a high temperature and a low temperature and we were able to get between the two temperatures rather quickly which may have an effect on the stresses in a missile. We make the transition between -40 F and 140 F (233K to 333K) and vis versa, as measured on the skin of the missile, in about a half an hour in a continuous cycle.

Mr. Liehr (Lockheed Missiles & Space Co): Do you prefer to test acoustically for captive flight vibration? When do you test mechanically with shakers?

Mr. Everett: I think we are presently in a period of transition; we can do either and there are reasons to perfer a shaker particularly if you want to combine vibration with vacuum or some attempt to simulate altitude which we definitely cannot do with acoustics. I find that the acoustically exciting vibration in a missile yields pretty good responses in the missile in three directions at the various locations throughout the missile; if that is what I am after I would use acoustics.

Mr. Edgington (White Sands Missile Range): How many hours did you run this reliability test and did you run at each of those profiles that you showed?

Mr. Everett: We went through that profile in intensity in a 22½ minute loop time and the loop recorder just kept repeating, so we would essentially spend about 3 minutes at one simulated "q" and then another 2½ minutes at the next and so on.

Mr. Edgington: For how many hours did you conduct the test on these missiles?

Mr. Everett: It was intended to be a 650 hour test, however we had other problems but I guess we accumulated at least 300 hours of running time.

Mr. Kana(Southwest Research Institute): Were you operating in real time or were you time scaling, that is scaling the amplitude up to compress effective time?

Mr. Everett: We have a little bit of data, and we paid a lot of money to get it, that says you cannot go very far with time scaling and so we did not try to do it, we just flew the missile.

THE EFFECT OF SIGNAL CLIPPING IN RANDOM VIBRATION TESTING

Dr. Alfred G. Ratz
Vibration Instruments Co.
Anaheim, California

The effect of clipping the drive voltage is considered, when an electrodynamic exciter is used to carry out wide-band random tests. The theory is worked out, as to how clipping influences the force capacity of the system: the deeper the clipping, the greater the capacity. Clipping the drive signal also affects the motion of the exciter table, generating extraneous spectra and influencing the peak factor of the acceleration wave. The more severe the clipping, the more pronounced the effects. The mechanism is explored, as to how drive-voltage clipping influences the motion, and examples are given. With the formulae given, one can specify the clipping level of the drive voltage to meet the statistical requirements of the motion, without at the same time overdesigning the exciter/drive-amplifier system.

INTRODUCTION

A common form of vibration testing using an electrodynamic exciter involves driving the exciter with a wide-band random signal. The objective is to produce an acceleration wave form at the exciter table, that has specific statistical properties. Usually the two properties of interest are the power spectral density function, and the amplitude probability density function.

Modern techniques of control use spectral feedback to establish the desired power spectral density function of the random acceleration wave, $x(t)$. [1, 2, 3]

The amplitude probability density function is specified to be Gaussian in nature. It is represented by $p(x)$ in Equation A-(1), Appendix A. The function, $p(x)$, has non-zero values for all values of x in the range $-\infty < x < +\infty$. As a matter of practical consideration, brought about by the finite dynamic range of the electronic equipment handling the signal that drives the electrodynamic exciter, the amplitude of the random signal has a Gaussian probability-density function only, inside the range $-k \leq x(t) \leq +k$. For a given value of $|k|$, the waveform of $|x(t)|$ is clipped. All values of $|x(t)|$ that would otherwise exceed $|k|$ are converted to the value $|k|$. Clipping may occur either in the control electronics or in the power amplifier driving the exciter (Figure I). Clipping is especially noticeable when a vibration system is operated at its full force capacity.

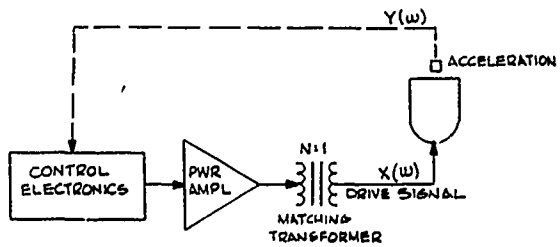


Figure I - Vibration Test System

The clipping level, k, of the drive signal influences the force capacity of a given exciter system. It

is shown in Appendix D that operating with less clipping (i.e., with an increased value for k) usually reduces the output force that can be obtained from the system. The mechanism of how this occurs is worked out in the Appendix. The conclusion is reached that, to get the greatest force possible from a shaker system, one should plan to specify and to use a drive-signal clipping level that is as small as is permissible.

The factors influencing the selection of a particular value of k are therefore of interest. Clipping affects the statistical properties of the motion at the output of the exciter. The properties of interest are the amplitude probability density function and the power spectral density function. The deeper the clipping (i.e., the smaller the value of k), the greater the influence of the clipping on the statistics of the motion. The precise nature of the influence of signal clipping on the statistics is worked out in the Appendices. Knowledge of the relationships between the statistical effects and the clipping level inducing them, is of some importance, since it permits one to set a rational value of k. Once the value of k is determined, the exciter/amplifier system can be sized.

Many system performance specifications specifically define the acceptable value required of the peak factor of the random wave generated during a vibration test. There appears however, to be some inconsistency, as we go from specification to specification, in the definitions. Some specifications establish the peak factor of the acceleration waveform. Others set the peak factor of the voltage driving the shaker armature. (With each definition, the requirement is usually for the signal to maintain a Gaussian amplitude probability density out to a level that is three times its rms value.) The two definitions are not equivalent. The preferred definition would seem to be that related to the acceleration waveform. The peak factor of the output voltage of the driving amplifier need only be good enough, to yield a satisfactory acceleration waveform. As stated above, since the larger peak factor capability at the amplifier, necessitated to meet the definition related to amplifier output, must be paid for with a reduced force capacity from the system or by increased system costs for a given force, it is essential to set the amplifier clipping level, k, to as small a value as possible.

EXCITER-AMPLIFIER SYSTEM CAPABILITY

The amplifier must be matched to the vibration exciter, for the maximum possible force to be generated at the exciter table. Matching is done typically using an audio transformer, of turns ratio, N, as shown in the diagram of Figure I.

The force developed by the exciter is proportional to its armature current, I_d. The theory of matching is developed in Appendix D. It is shown how the value of k selected for clipping the amplifier output, determines the maximum value that can be obtained for I_d, and thus sets the force capacity of the system.

Figure XI illustrates a graphical approach to the matching calculation. An example of what is typical in practice, is illustrated by an 80000-newton exciter, being driven by a 60 KVA amplifier. The test spectrum is flat white, 20 Hz to 2000 Hz. Results are shown in Table I.

TABLE I

k	Force (Newtons)
2.5	53,900
2.7	50,600
2.8	47,800
3.0	45,000

Obviously, to get the most out of such a system one should use as small a value of k as is practicable.

Spectrum Generation. As the clipping becomes more severe several adverse statistical effects develop. The first of these is the generation of a second random signal, which is superimposed on the original. This extraneous signal acts almost like an uncorrelated background noise: for example, its spectrum cannot be shaped or otherwise controlled by the Control Electronics (Figure I).

The theory of the generation of the extraneous signal is developed in Appendix A. The spectrum of the new wave and that of the original wave are related through their correlation functions. Equation A-(7) illustrates the relationship. Usually, for the values of k that are typically used with random testing, only the first

two terms of A-(7) are significant. The constants A_1 and A_3 are functions of k only. The normalized correlation function of the original unclipped signal is given by r(T) in A-(18): as the equations show, the precise form of r(T) depends on the shape of the spectral plot of the original random signal. The correlation function of the superimposed signal is $r^3(T)$. Using A-(19), we can convert $r^3(T)$ into its spectral equivalent.

To sum up, from the original spectrum, W(ω), we determine r(T). Then, from $r^3(T)$, we determine $W_3(\omega)$, the spectrum of the extraneous signal. The two spectra are scaled by the factor, ρ, given in A-(16); this factor depends solely on k. Thus we have a method of computing the spectrum of the extraneous signal generated by clipping the original wave.

The frequency response, H(ω), of the exciter and its specimen, is often quite complex. If the acceleration power density at the exciter table is to conform to $|Y(\omega)|^2$, then the spectrum $|X(\omega)|^2$ of the voltage, x(t), driving the exciter (Figure I) must be servo-controlled to be:

$$|X(\omega)|^2 = \frac{1}{|H(\omega)|^2}\left[|Y(\omega)|^2\right] \qquad (1)$$

If $|Y(\omega)|^2$ is a function that has some complexity, $|X(\omega)|^2$ can be seen from (1) to be even more complex, because of H(ω).

One must resort to computer methods, to derive r(T) from $|X(\omega)|^2$, with any accuracy, and then to go on to generate $r^3(T)$ and $W_3(\omega)$. Our present approach is to employ one or two simple basic forms for H(ω). The results can now be worked out analytically. At the same time, the conclusions are applicable to the exciter operation, to the extent of giving practical guidelines that are useful and reliable. For the first simplification, we give H(ω) the response form of a simple low-pass filter, as represented by $W_L(\omega)$. In Appendix B, the general theory of Appendix A, is applied to $W_L(\omega)$, driven by a flat white random wave. The extraneous signal generated by the clipping has a spectrum, $W_{3L}(\omega)$, plotted in Figure IV: its bandwidth is <u>three times</u> that of the original wave.

The ratio, ρ_L, between the psd of this extraneous signal and that of the original signal is given in B-(6). In most practical cases, the values of k of interest are those between 2.5 and 3.0. For these, ρ_L has the following corresponding values:

TABLE II

k	10 log ρ_L (dB)
2.5	-27.3
2.6	-28.8
2.7	-30.3
2.8	-31.8
3.0	-34.8

To see how the results of Table II can be applied, let us consider an electrodynamic exciter driving a mass load, equalized to a flat white spectrum, 20 Hz to 2 kHz. Figure II illustrates the programmed spectrum, $|Y(\omega)|^2$, as well as $|X(\omega)|^2$, the spectrum typically belonging to the signal driving into the exciter armature. The frequency f_r is the axial resonance of the exciter. For large exciters, it occurs in the upper-frequency portion of the test spectrum, as shown in Figure II. Above the frequency f_b, the drive spectrum is decreased, as the effect of the axial resonance comes into play. As shown, most of the energy in the drive signal occurs over the spectral region from 20 Hz to f_b Hz. If we approximate the drive spectrum by a flat white noise to f_b Hz, we can obtain from Table II the level of the spectrum of the "noise" floor induced by the clipping. This spectrum is shown to be flat out to $3f_b$, and thus it overlaps the exciter axial frequency, f_r. We can now establish the largest value of the Q-factor of the axial resonance that can be tolerated. If we hope to maintain a flat output spectrum, $|Y(\omega)|^2$, at all frequencies between 20 Hz and 2000 Hz, then we must make sure that the effect of the "extraneous noise" does not cause a peak at the axial frequency that cannot be equalized.

The automatic equalizer can, of course, shut off the drive spectrum at the axial frequency, as is shown in Figure II, but it has no control over the "extraneous noise". The axial resonance amplifies the spectrum of the "extraneous noise". For satisfactory operation, therefore, the amplified spectrum must be kept less than $|Y(\omega)|^2$. Satisfactory operating conditions exist when

$$-20 \log Q - 10 \log \rho_L \geq 0$$

or

$$Q \leq \rho_L^{-\frac{1}{2}}$$

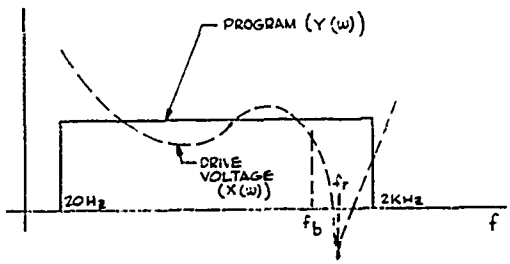


Figure II - Equalizer Spectra

From Table II, we can deduce the limiting values of Q for various values of k. These are tabulated in Table III:

TABLE III

k	Q at Axial (Maximum)
2.5	23
2.6	27.5
2.8	39
3.0	55

Typically, exciter axial resonances have Q-factors of the order of 15. Thus it would seem that clipping is not a consideration, limiting the ability of a system to equalize the axial resonance of an exciter, for a flat white output spectrum.

For smaller exciters, the value of the axial frequency, f_r, may exceed 2000 Hz; now, the extraneous spectrum generated by the clipping, with its bandwidth three times the drive bandwidth, may excite the axial resonance preventing its complete suppression. Figure III illustrates the effect. The axial causes a narrow band of noise to occur, as shown, W dB below the test level:

$$W = 20 \log Q - 10 \log \rho_L.$$

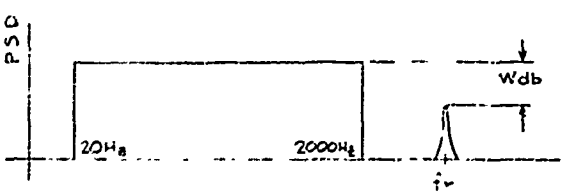


Figure III - Spectral Spur

For a value of Q equal to 15, as is typical, W is given by the values tabulated in Table IV, for various values of k.

TABLE IV

k	W (dB)
2.5	4.0
2.6	5.5
2.8	7.0
3.0	8.5
3.0	11.5

The only sure way of suppressing the anomaly at f_r Hz, as shown in Figure III, is to use a low-pass filter, with its -3dB cut-off frequency set to 2 kHz. Unfortunately, such a filter is not always practical.

The example is also given in Appendix B of a clipped narrow-band random wave. This is of particular interest, if the system is to be equalized to produce a spectrum $|Y(\omega)|$ at the exciter table when the specimen has a prominent notch in its response function. This notch must be equalized. The spectrum of the drive voltage must, of course, peak up at the frequency of the notch. If the notch has a large Q-factor, the effect of any clipping is obviously to produce a narrow-band extraneous signal centered at a frequency that is three times that of the notch. Usually, since the spectral peaks are masked by the rest of the drive spectrum, the effect is not significant. It is mentioned here, however, since it is the only mechanism whereby a harmonically-related extraneous effect can be generated through the action of clipping.

Regeneration of the Peaks of a Random Wave. As has been discussed above, there is an economic advantage to holding the peak factor of the voltage driving the exciter to as low value as is possible. On the other hand, the acceleration signal is usually required to be Gaussian. Any heavy clipping is considered intolerable by most workers in the field. Fortunately, the transfer-function of the exciter, $H(\omega)$, severely reactive as it is, tends to restore the Gaussian character of a signal, and the peak factor of the acceleration wave therefore exceeds that of the drive voltage by a significant amount. The fact has been widely observed qualitatively. The objective here is to establish a means of getting a quantitative measure for the increase in peak factor, so that, for example, if the acceleration wave is required to be Gaussian out to

a value of k equal to three, it is possible to compute exactly the more severe clipping level permitted at the output of the power amplifier.

The general theory is worked out in Appendix C. A quantity, ρ_M, defined by C-(7), is used as a measure of the effectiveness of the transfer-function to restore the peak factor. The improved peak factor, K_y, is given as a function of ρ_M, both in C-(18), and in the plot of Figure VI. We see that a value of $\rho_M \geq 1$ restores the acceleration waveform to a peak factor of three sigma, independent of the amount of clipping of the drive voltage for all but the deepest clipping.

To determine the efficacy of the exciter and specimen transfer-functions to restore the peak factor for the general case requires computer assistance, because of the complex nature of the frequency functions involved.

To get a first estimate of the effect of the complex reactive transfer characteristics, examples are worked out in Appendix C, using simple basic circuits to represent $H(\omega)$. Of considerable interest is the effect of a second-order tuned system, to be equalized flat over the band from zero frequency to Ω_a. (Note: Ω is the frequency in Hz normalized by the resonance frequency). The system is aimed at approximating the effect of the axial resonance of the exciter. In the plot of Figure VII, the frequency of axial resonance is set at unity. Thus, if Ω_a is greater than unity, the axial resonance has its frequency inside the bandwidth of the spectrum. The condition is typical of the larger exciters. A value for Ω_a of 1.3 is representative: examination of the curves shows that, for all values of the damping factor, c, from near critical to highly resonant, ρ_M is very significant, approaching (or indeed often exceeding) unity in value. The value of ρ_M from the plot of Figure VII is now used to enter the plot of Figure VI. The plot of Figure VI shows that the peak factor is again restored to the three-signal level, except for those cases where the amplifier output is most severely clipped.

Based on the above examples, one can conclude that, with shakers of the larger size, a three-sigma peak factor is restored at the accelerometer for any practical level of clipping of the amplifier signal. The conclusion is rendered stronger, when one recalls there are several resonant effects in an exciter, of which the axial resonance is only one.

As the shaker size decreases the axial-resonance frequency increases, (and thus moves outside the operating frequency band). In Figure VII, Ω_a decreases. It is not until Ω_a is less than 0.75, however, that a state of affairs is reached in which the axial resonance affords no assistance. The frequency effects that occur in a shaker, are certainly not limited to the simple tuned system of Appendix C. Each of the several individual resonance effects in the shaker contributes somewhat to peak-factor restoration. It is not even necessary to have resonances to obtain contributions to peak factor restoration. Thus a simple low-pass network generates significant values of ρ_M, provided Ω_a, the upper frequency limit of the spectrum, normalized to the break-point of the network response, is of the order of unity or greater.

With an exciter, however, the axial resonance is the dominant phenomenon, and so the representative resonance system of Appendix C can be used to estimate peak factor restoration. Thus, all but the very smallest exciters will exhibit significant restorations.

Enhancement of the peak factor is also assisted to some extent by the extraneous spectrum generated by the clipping action, discussed previously. The effect, however, is ignored here, since calculations indicate its influence is somewhat minor, compared to that of the reactive transfer-function of the exciter.

CONCLUSION

The clipping permitted of the drive voltage affects the random force rating of a vibration system. It is desirable to clip the voltage as deeply as possible.

The acceleration signal is generally required to be Gaussian out to at least three sigma. With it, heavy clipping is not desirable. Fortunately, the frequency response of the vibration exciter and its specimen restores the peak factor. The amount of restoration to be expected can be conservatively estimated by the formulae developed in Appendix C. A rule-of-thumb approximation is given in the Appendix, that is widely applicable.

Clipping of the drive voltage induces a new spectrum, which acts as a uncontrollable background noise on the acceleration wave. The amount of clipping permitted must be judged with this extraneous noise taken into consideration. Exact formulae are given for the purpose in Appendix A, with rule-of-thumb approximations in Appendix B.

If three-sigma (k=3) acceleration waveforms are desired, the rule-of-thumb approximations for both the peak-factor restoration and the generation of the extraneous wide-band "noise" spectrum, indicate that voltage clipping as deep as 2.7 sigma is quite acceptable for almost every practical case; in most cases, indeed, 2.5 sigma is acceptable.

APPENDIX A : Spectrum Generation by Clipping a Gaussian Signal

Let x(t) be the time history of a random wave with stationary Gaussian properties. If x(t) is clipped at +k and at -k, the effect is to generate extraneous random spectra. It is the purpose of the present Appendix to work out the mechanism by which the additional spectra are generated, and to end up with a general formula that can be applied to any situation.

The amplitude probability density function of x(t) is given by p(x) in A-(1). The rms level of x(t) has been normalized to a value of unity.

$$p(x) = \left(1/\sqrt{2\pi}\right) \exp\ (-x^2/2) \qquad A\text{-}(1)$$

The joint probability density function of x(t) is given by p(x,y) in:

$$p(x,\gamma) = \left(1/2_\pi\right) \cdot \left(1/\sqrt{1-r^2}\right) \exp \left[-(x^2 + \gamma^2 - 2rx\gamma)/2(1-r^2)\right] \qquad A\text{-}(2)$$

Here γ is the value of x, taken T seconds after the corresponding value of x. The parameter r is the normalized autocorrelation function: it is a function of T; i.e.,

$$r = r(T) \qquad A\text{-}(3)$$

Using the work of Stieljes and Sheppard, p(x,y) from A-(2) can be written:

$$p(x,\gamma) = \sum_0^\infty \frac{p^{(n)}(x) \cdot p^{(n)}(\gamma)}{\lfloor n} (r)^n \qquad A\text{-}(4)$$

Here $p^{(n)}(x)$ is the n-th derivative of p(x).

The correlation function of x(t) is given by R(T):

$$R(T) = \int_{-\infty}^{+\infty}\int_{-\infty}^{+\infty} x \cdot \gamma\ p(x,\gamma)\,dx\,d\gamma \qquad A\text{-}(5)$$

Let $x_c(t)$ represent x(t) clipped at $\pm k$. The correlation function, $R_c(T)$, of $x_c(t)$ is still obtained using the integral of A-(5). Now, however, all the probability associated with the values of x(t) outside the range -k to +k is assigned to x = -k and x = +k, appropriately. Substituting the series expansion for p(x,y) from A-(4) reduces the problem to evaluating integrals of the form of:

$$\int_{-k}^{+k} x p^{(n)}(x)\,dx\ ,\quad \int_{+k}^{+\infty} k p^{(n)}(x)\,dx,$$

We can now write $R_c(T)$ as an infinite series (i is an integer):

$$R_c(T) = \sum_{i=1}^{i=\infty} A_i\ r^i(T) \qquad A\text{-}(6)$$

For all even values of i, A_i is zero. Hence,

$$R_c(T) = A_1 r(T) + A_3 r^3(T) + A_5 r^5(T) \ldots \qquad A\text{-}(7)$$

$$A_1 = 4\ [P(k)]^2 \qquad A\text{-}(8)$$

$$A_3 = \frac{2}{3} \cdot [p^{(1)}(k)]^2 \qquad A\text{-}(9)$$

$$A_5 = \frac{1}{30}\ [p^{(3)}(k)]^2 \qquad A\text{-}(10)$$

$$A_i = \frac{4}{\lfloor i}\ [p^{(i-2)}(k)]^2,\ i \text{ odd} \qquad A\text{-}(11)$$

$$P(k) = \int_0^k p(x)\ dx \qquad A\text{-}(12)$$

$$\lfloor i = i(i-1)(i-2)\ldots 1 \qquad A\text{-}(13)$$

For the accuracy requirements of most practical cases, we can cut off the series of A-(7) at the second term. In A-(7), r(T), of course, is the normalized autocorrelation function of the original unclipped waveform. The function, $r^3(T)$, is the normalized autocorrelation function of a new random signal generated by the clipping action. The total power in the original wave is maintained at unity by the normalization of the data (See A-(1), above.)

The effect of clipping is to reduce the power in the original wave

from S_o to the value S_1

$$S_1 = A_1 r(0) = A_1 \qquad \text{A-(14)}$$

The total power associated with the extraneous spectrum is S_3:

$$S_3 = A_3 r^3(0) = A_3 \qquad \text{A-(15)}$$

The ratio, ρ, S_3 to S_1, is given by:

$$\rho = \frac{S_3}{S_1} = \frac{A_3}{A_1} = \frac{1}{6} \cdot \left[\frac{p^{(1)}(k)}{P(k)}\right]^2 \qquad \text{A-(16)}$$

If W(w) is the power spectral density plot of the original unclipped wave, x(t), then, from the Wiener-Khintschine relationships,

$$R(T) = \int_o^\infty W(w) \cos wT \, dw \qquad \text{A-(17)}$$

$$r(T) = \frac{R(T)}{R(O)} \qquad \text{A-(18)}$$

In the present discussion, all signals have been normalized, and R(O) is equal to unity. The extraneous spectrum generated by clipping is given by $W_3(w)$ in:

$$W_3(w) = \frac{2A_3}{\pi} \int_o^\infty r^3(T) \cos wT \, dT \qquad \text{A-(19)}$$

The original spectrum W(w), is attenuated by a constant factor A_1, under the influence of clipping:

$$W_1(w) = A_1 W(w) \qquad \text{A-(20)}$$

The constants A_1 and A_3 are tabulated as functions of k in Table A-I.

TABLE A-I

k	A_1	A_3 $\times 10^{-2}$	10 log dB
2.0	0.91	1.82	-17
2.2	0.94	1.22	-19
2.4	0.98	0.79	-21
2.6	0.99	0.40	-24
2.8	1.00	0.20	-27
3.0	1.00	0.10	-30
4.0	1.00	0.025	-56

APPENDIX B: Examples of Spectrum Generation by Clipping.

Low-Pass Spectrum. Suppose the unclipped signal, x(t) is formed by passing white noise through a low-pass filter, having a cutoff frequency of w_o (rad/sec). If the noise power at the filter output is normalized to unity, the spectral density of the unclipped wave is given by $W_L(w)$:

$$W_L(w) = \frac{2}{\pi w_o} \cdot \frac{1}{(1+\xi^2)} \qquad \text{B-(1)}$$

where

$$\xi = w/w_o \qquad \text{B-(2)}$$

The correlation function corresponding to $W_L(w)$, defined as $r_L(T)$, is obtained by applying A-(17) and A-(18) to $W_L(w)$. Since $W_L(w)$ is in the normalized form, R(O) is equal to unity, and $r_L(T)$ is therefore given by:

$$r_L(T) = \exp(-w_o T) \qquad \text{B-(3)}$$

The extraneous spectrum generated by clipping x(t), is obtained by inserting $r_L(T)$ for r(T) in A-(19). Let us call the resulting spectrum $W_{3L}(w)$.

$$W_{3L}(w) = \frac{2}{3\pi} \cdot \frac{A_3}{w_o} \cdot \frac{1}{[1 + (\xi/3)^2]} \qquad \text{B-(4)}$$

The original spectrum is attenuated by the factor, A_1, as shown in A-(20). Of interest is the ratio ρ_L:

$$\rho_L = \frac{W_{3L}(O)}{A_1 W(O)} = \frac{1}{3}\left(\frac{A_3}{A_1}\right) = \rho/3 \qquad \text{B-(5)}$$

Plots of $W_L(w)$, $W_{1L}(w)$ and $W_{3L}(w)$ are given in Figure IV. The plots illustrate the fact that the new spectrum generated by clipping has a bandwidth three times that of the original signal. The flat portion of the new spectrum is $(-10 \log \rho_L)$ dB below that of the attenuated (by clipping) original spectrum.

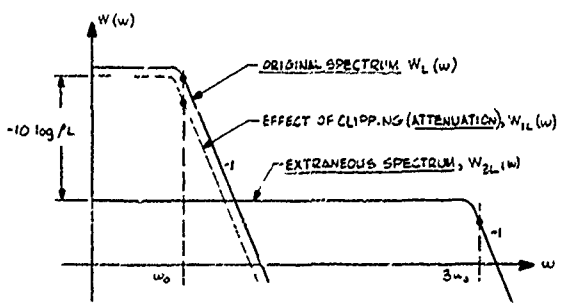


Figure IV - Clipping Spectra (Low Pass)

$$10 \log \rho_L = 4.8 + 10 \log \rho \qquad \text{B-(6)}$$

Thus, for various values of k, 10 log ρ_L can be computed using Table A-I.

Band-Pass Spectrum. Suppose the unclipped random signal, x(t), is formed by passing white noise through a sharply-tuned single-tuned circuit. Suppose w_c (rad/sec) is the resonance frequency, and D (rad/sec) is the -3 dB bandwidth.

If $W_c(w)$ is the normalized spectral density of x(t), the auto-correlation function, $r_b(T)$, is given by substituting $W_c(w)$ for W(w) in A-(17). Recalling that R(0) = 1, we get for $r_b(T)$:

$$r_b(T) = \exp(-\tfrac{1}{2}TD) \cdot \cos(w_c T) \qquad \text{B-(7)}$$

The extraneous spectrum generated by clipping is now given by substituting $r_b(T)$ for r(T) in A-(19): let the value of $W_3(w)$ so obtained be defined as $W_{3c}(w)$. The determination of $W_{3c}(w)$ is helped by the identity:

$$r_b^3(T) = \tfrac{1}{4} \exp(-\tfrac{3}{2}TD) \cdot \left[\cos 3w_c T + 3 \cos w_c T\right] \qquad \text{B-(8)}$$

Inserting $r_b^3(T)$ in A-(19), as proposed above, results in a spectrum with two parts:

(a) A narrowband spectrum with the same shape as the plot of $W_c(w)$, centered at w_c, but with a bandwidth equal to 3D. The magnitude of this spectrum is defined by the ratio ρ_{ca}:

$$\rho_{ca} = \frac{W_{3c}(w_c)}{A_1 W_c(w_c)} = \tfrac{1}{4} \cdot \left(\frac{A_3}{A_1}\right) = \rho/4 \qquad \text{B-(9)}$$

(b) A narrowband spectrum of the same shape as $W_c(w)$, centered at $3w_c$, with a bandwidth equal to 3D. The magnitude of this spectrum is defined by the ratio ρ_{cb}:

$$\rho_{cb} = \frac{W_{3c}(3w_c)}{A_1 W_c(w_c)} = \frac{1}{12}\left(\frac{A_3}{A_1}\right) = \rho/12 \qquad \text{B-(10)}$$

Plots of $W_c(w)$, $W_{3c}(w)$ and $A_1 W_c(w)$ are given in Figure V. The two spectral peaks of $W_{3c}(w)$, at w_c and at $3w_c$, are scaled relative to $A_1 W_c(w)$, respectively, by:

$$10 \log \rho_{ca} = 6 + 10 \log \rho \qquad \text{B-(11)}$$

$$10 \log \rho_{cb} = 11 + 10 \log \rho \qquad \text{B-(12)}$$

Thus, for various values of k, 10 log ρ_{ca} and 10 log ρ_{cb} can be computed from Table A-I.

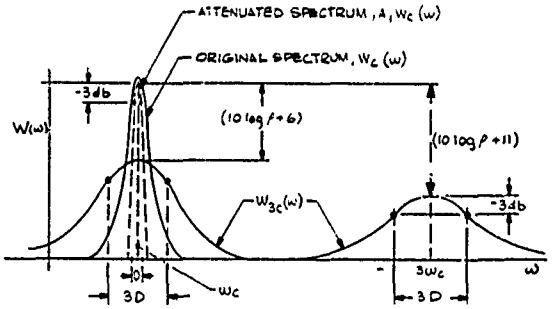


Figure V - Clipping Spectral (BandPass)

APPENDIX C: Effect of System Transfer-Function on the Peak Factor of a Clipped Waveform

It is a well known experimental fact that a random waveform clipped at +k and at -k, and passed through a network with a frequency response having reactive components, tends to have its peak values restored. The transfer-function of the network is the mechanism whereby the peak factor is restored; this Appendix develops several formulae predicting the restoration of the peak factor for a given transfer-function.

Suppose the Gaussian random noise signal, x(t), clipped at ±k, be represented as in Appendix A by $x_c(t)$. Suppose $x_c(t)$ is applied as the input signal to a transfer-function H(w); let y(t) represent the corresponding output signal.

Let Y(w) (= |Y(w)| arg d(w)) be the Fourier transform of y(t). Let X(w) (=|X(w)| arg θ(w)) represent the Fourier transform of $x_c(t)$. The values of |X(w)| and θ(w) are such that, when all the frequency components are combined, the clipped wave, $x_c(t)$ is generated. The waveform of y(t) is identical to that of $x_c(t)$, provided H(w) is resistive only. Thus, with H(w) resistive, y(t) is clipped in the identical fashion to $x_c(t)$. But if, for any reason, H(w) (≡ | H(w)| arg h(w))

is reactive or has reactive components, the frequency components of y(t) no longer have the correct amplitude and phase relationships, to maintain its waveform clipped identically to that of $x_c(t)$. The clipping tends to degenerate and higher peak factors are obtained, the more the functions and d(w) differ from |X(w)| and Θ(w), respectively.

The time history, y(t), can be considered as made up of: (1) a time history $y_c(t)$, with its spectrum $Y_c(w)$, having a waveform identical to the clipped wave $x_c(t)$, plus (2) a waveform z(t), with its spectrum Z(w), which can be considered a masking wave, superimposed on $y_c(t)$:

$$Z(w) = Y(w) - Y_c(w) \qquad C-(1)$$

Obviously (t_o is a constant):

$$y_c(t) = Mx_c(t-t_o) \qquad C-(2)$$

and

$$|Y_c(w)| = M\,|X(w)| \arg \alpha \qquad C-(3)$$

Here the constant M represents a gain, and the angle α a constant phase angle applied to each spectral line. The correct values of M and α are those for which the masking effect of z(t) is a minimum. This is assumed to occur when $\overline{z(t)}^2$ is a minimum.

We can compute the value of |Z(w)| from the vector diagram relating Z(=|Z(w)|), X (=|X(w)|), and Y (=|Y(w)|):

$$Z^2 = Y_c^2 + Y^2 - 2Y_cY\cos(h-\alpha)$$

$$= Y^2\left[1 + |H_o(w)|^{-2} - 2\,|H_o(w)|^{-1}\cos(h-\alpha)\right] \qquad C-(4)$$

In C-(4):

$$H_o = H_o(w) = \frac{H(w)}{M} \qquad C-(5)$$

By applying to the integral of Z^2 the processes to obtain the minimum we obtain the values of the parameter M and α for which $\overline{z(t)}^2$ is a minimum. With the use of C-(4), the minimizing values of M and α are substituted into:

$$\rho_M^2 = \frac{\text{(mean square of the masking signal, z(t))}}{\left(\begin{array}{l}\text{mean square of the portion of}\\ \text{the output wave with the same}\\ \text{time history as } x_c(t)\end{array}\right)}$$

$$= \frac{\int_o^\infty |Z(w)|^2 dw}{\int_o^\infty |Y_c(w)|^2 dw} \qquad C-(6)$$

The ratio ρ_M is a key parameter in estimating the enhancement of the peak factor.

Flat-White Output Spectrum. The condition of interest is that when the output signal is servo controlled. Thus, if the output spectrum is equalized to be band-limited flat white, from zero frequency to a w_a rad/sec, C-(6) can now be written:

$$\rho_M^2 = \frac{\int_o^{w_a}(1+H_o^{-2})\,dw - 2\psi}{\int_o^{w_a} H_o^{-2}\,dw} \qquad C-(7)$$

$$\psi^2 = \left[\int_o^{w_a} H_o^{-1}\cdot\cos hw.dw\right]^2 + \left[\int_o^{w_a} H_o^{-1}\sin hw\,dw\right]^2 \qquad C-(7a)$$

The value of M to be substituted into C-(5) is given by:

$$M = \frac{\psi}{\int_o^\infty H_o^{-2}dw} \qquad C-(8)$$

Peak Factor. The problem of determining the peak factor of a given random wave is closely related to determining the closeness of approximation of its probability density function to the Gaussian. A technique for estimating quantitatively how closely the Gaussian is approached is based on the use of Edgeworth's series.

For an ac waveform, x(t), the amplitude probability density function is given by $G_E(x)$:

$$G_E(x) = G(x) - \frac{1}{\lfloor 3}\cdot\frac{u_3}{u_2^{3/2}}G^{(3)}(x) + \frac{1}{\lfloor 4}\left(\frac{u_4}{u_2^2} - 3\right)G^{(4)}(x) - \frac{1}{\lfloor 5}\left(\frac{u_5}{u^{5/2}} - \frac{10u_3}{u_2^{3/2}}\right)G^{(5)}(x) + \frac{10}{\lfloor 6}\cdot\frac{u_3^2}{u_2^3}G^{(6)}(x) \qquad C-(9)$$

with $G(x) = p\left(\frac{x}{\sigma}\right)$. $\qquad C-(10)$

Here, σ is the rms value of $x(t)$ and $p(x)$ is obtained from A-(1); $G^{(j)}(x)$ is the j-th derivative of $G(x)$. Cramer [5] shows that, for the type of conditions arising with instrumentation signals, $G_E(x)$ is an asymptotic expansion in terms of $G(x)$ and $G^{(j)}(x)$: the remainder term is of the same order of magnitude as the first term neglected.

The quantity u_i is the i-th central moment; with $x(t)$ symmetrical about zero, the odd central moments are zero in value, so that C-(9) reduces to

$$G_E(x) = G(x) + \frac{1}{\lfloor 4} C \cdot G^{(4)}(x) \qquad C-(11)$$

The quantity C is defined as the coefficient of excess. From C-(11), we see that

$$C = \left(\frac{u_4}{u_2^2}\right) - 3 \qquad C-(12)$$

As is well-known, for a truly Gaussian wave, C is zero. Thus, C is zero for the unclipped wave, $x(t)$.

For $x_c(t)$, the coefficient of excess is obtained by first computing u_2 and u_4 for the clipped wave ($\sigma = 1$):

$$u_2 = \int_{-k}^{+k} x^2 G(x)\,dx + 2k^2 \int_{k}^{\infty} G(x)\,dx \qquad C-(13)$$

$$u_4 = \frac{1}{\sqrt{2\pi}} \left[\int_{-k}^{+k} x^4 e^{-x^2/2}\,dz + 2k^4 \int_{k}^{\infty} e^{-x^2/2}\,dx \right] \qquad C-(14)$$

Clipping affects the rms value of the wave, reducing it from σ to s:

$$s = \sqrt{u_2} \qquad C-(15)$$

We can define a clipping ratio, K:

$$K = \frac{k}{s} \qquad C-(16)$$

For the range of clipping that we are interested in, K is within 1½% of k, so that, to the accuracy of the calculations, K and k can be used interchangeably.

Table C-I tabulates the values of the coefficient of excess for the various pertinent levels of clipping.

TABLE C-I

Peak Factor of Clipping (k)	Coefficient of Excess (C)
2.5	-0.25
2.6	-0.20
2.7	-0.15
2.8	-0.13
2.9	-0.10
3.0	-0.08
3.2	-0.05
3.5	-0.02
∞	0.000

Since $z(t)$ is truly Gaussian, superimposing it on $y_c(t)$ reduces the absolute value of the coefficient of excess of the wave, and increases the peak factor. A conservative method of estimating the enhancement of the peak factor is to first enter Table C-I, with the value of k, and obtain the corresponding value of C. Next, from C-(6) (or C-(7) if applicable), deduce ρ_M, and compute the effect of $z(t)$ on C. The coefficient of excess C_c with $z(t)$ superimposed on $y_c(t)$, is given by:

$$C_c = \frac{C}{1+\rho_M^2} \qquad C-(17)$$

Here, C is the coefficient of excess for $x_c(t)$ alone.

Now, enter C_c, the new value of C, into Table C-I, and deduce the enhanced value of k for the "combined" wave, $y(t)$. (Call this value K_y.)

Plots of K_y versus ρ_M^2 (and ρ_M) are given in Figure VI, for various values of k. For $\rho_M < 0.8$, we can write:

$$K_y = k + 0.4\,\rho_M^2 \qquad C-(18)$$

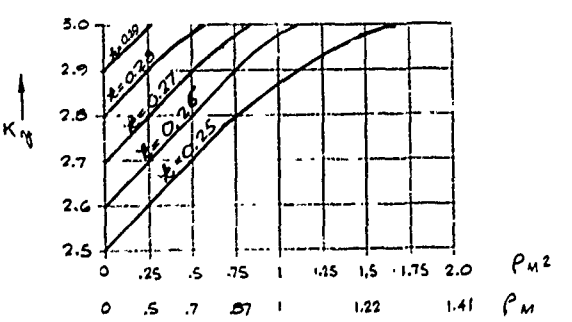


Figure VI - Peak Factor Enhancement

Example: A Second-Order Transfer Function Equalized Flat Over a Band from Zero Frequency to w_a Rad/Sec.

The objective here is to use the above theory to generate some simplified formulae that can be used as practical guides in a given physical situation. (Accurate calculations will still have to be based on the formulae of C-(6) and C-(7) for a real exciter.)

For simplicity, let (w_r = frequency of resonance):

$$\Omega = \frac{w}{w_r} \quad , \quad \Omega_a = \frac{w_a}{w_r} \qquad \text{C-(19)}$$

A representation form for the transfer function of a second-order system is $|H^1|$ (= $|H^1(\Omega)|$):

$$|H^1| = \frac{1}{(1-\Omega^2) + 4_c{}^2\,\Omega^2} \qquad \text{C-(20)}$$

$$h = \arccos\,(AH^1) \qquad \text{C-(21)}$$

$$A = (1-\Omega^2) \qquad \text{C-(22)}$$

Substituting $|H^1|$ in C-(7) yields the plots of $\rho_M{}^2$ versus Ω_a in Figure VII. If one knows the relative value of w_a versus the frequency of resonance, one can, for a given amount of damping, enter the plot of Figure VII, and determine $\rho_M{}^2$. Using $\rho_M{}^2$ in C-(17) or C-(18), and if needed, referring to Table C-I, one can compute the resulting peak factor, K_y.

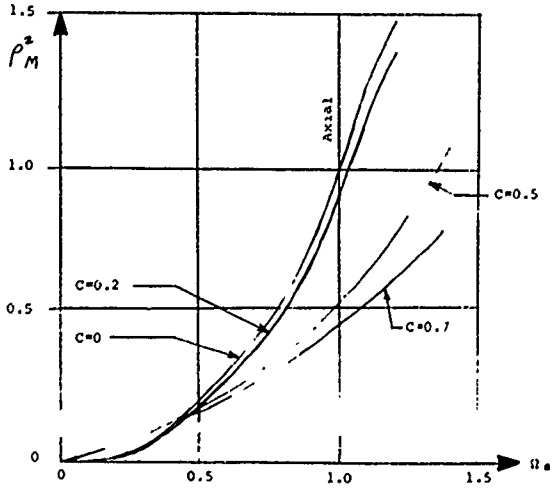


Figure VII - Masking Signal Ratio

Investigation reveals that there is always a significant enhancement of the peak factor, if H(w) has effective reactive components. Computer assisted computations are in order, once the plots of Y(w) and H(w) depart in complexity from those of the simpler systems.

APPENDIX D: Effect of Clipping, Exciter/Amplifier Matching

It is very important to match the exciter to its driving amplifier, to assure optimum transfer of power. Matching is usually done using an audio transformer. The new solid state amplifiers have made possible new direct-coupled techniques. However, for the purpose here, to illustrate the influence of clipping on the matching, the more customary method of using a transformer is employed.

Three factors influence the matching: the output-current capacity of the amplifier power supply, the power dissipation limit of the amplifier, and the amplifier clipping limits. Both the power supply output current and the power dissipation limits of the amplifier are affected by the clipping to some extent: the influence of clipping here is minor compared to the main clipping limit; however, it is not always insignificant, as will be shown.

Power Supply Current Capacity. The amplifier driving an exciter is designed to operate in Class B. The current demanded of the power supply is related to the load current by the turns ratio of the transformer. The load current is assumed to be Gaussian, clipped at $\pm kI_d$. Here I_d is the rms value of the current with clipping removed. If i is the instantaneous value of the load current, the average power supply current is given by $I"_{dc}$ in:

$$I"_{dc} = \frac{2}{N}\int_0^{kI_d} i \cdot \bar{\psi}\left(\frac{i}{I_d}\right) di + \frac{2}{N}\,kI_d \int_{iI_d}^{\infty} \bar{\psi}\left(\frac{i}{I_d}\right) di \qquad \text{D-(1)}$$

Here the function $\psi(\lambda/\sigma)$ is given by:

$$\bar{\psi}\left(\frac{x}{\sigma}\right) = \frac{1}{\sqrt{2\pi\sigma}} \exp\,-\left(\frac{x^2}{2\sigma^2}\right) \qquad \text{D-(2)}$$

The quantity N is the turns ratio of the audio transformer coupling amplifier and exciter. See Figure I.

Of interest is the rms level of the exciter current, I"$_d$, when the clipping is finite:

$$\left(\frac{I_d''}{I_d}\right)^2 = 1 + 2P(kI_d) - \sqrt{\frac{2}{\pi}}k \cdot \exp\left(-\frac{k^2}{2}\right) \qquad \text{D-(3)}$$

$$\text{Here } P(x) = \int_x^\infty \bar{\psi}\left(\frac{y}{\sigma}\right) dy \qquad \text{D-(4)}$$

Combining equations, we obtain:

$$I''_{dc} = K_D \frac{I''_d}{N} \qquad \text{D-(5)}$$

The constant K_D is a function of the clipping level, k. It is plotted in Figure VIII.

Equation D-(5) is most conveniently used in its logarithmic form:

$$\log I''_d = \log N + \log I''_{dc} - \log K_D \qquad \text{D-(6)}$$

Thus we see that for heavier clipping, when the value of k is reduced, the value of K_D drops accordingly, and the permitted value of I''_{dc} increases. Clipping therefore tends to improve the perfomance of the amplifier power supply.

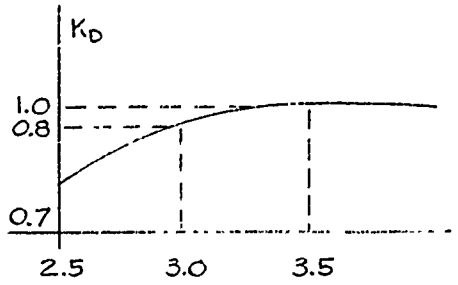


Figure VIII - Current Constant

Amplifier Power Dissipation Limit. The output stage of the amplifier is push-pull in form. The average power dissipated in the push-pull output stage is twice that dissipated in one side of the output stage. In other words, if $\underline{v}(t)$ and $\underline{i}(t)$ are the instantaneous values of voltage and current, for one side of the push-pull output stage of the amplifier, then the dissipated power P_d is given by:

$$P_d = 2\,\overline{\underline{v}\cdot\underline{i}} \qquad \text{D-(7)}$$

Now, the voltage $\underline{v}$ is related to the voltage v_T across the primary of the audio transformer.

$$\underline{v} = E_B - V_T \qquad \text{D-(8)}$$

Here, E_B is the dc voltage of the amplifier power supply. Combining D-(7) and D-(8), we get, for

$$P_d = E_B I_{dc} - P_o \qquad \text{D-(9)}$$

where P_o is the output power. If the clipping level is finite, I_{dc} is replaced by I''_{dc}. The quantity P_o is given by

$$P_o = \int_0^\infty \bar{\omega}(f)\, df \qquad \text{D-(10)}$$

where $\bar{\omega}(f)$ is the power spectral density into the load, given in Watts per Hz, and

$$\bar{\omega}(f) = I_{xx}(f) \cdot R(f) \qquad \text{D-(11)}$$

$I_{xx}(f)$ is the "power" spectral density of the current, in Amperes Sqd per Hz; R(f) is the real component of the impedance of the shaker presented to the amplifier through the transformer. For simplicity, it is useful to set P_o equal to I_d^2R. R is defined as the "average noise resistance" of the load. Each time the test spectrum is changed, $I_{xx}(f)$ is changed. In turn, a change in $I_{xx}(f)$ means a change in $\bar{\omega}(f)$. But, for any given $I_{xx}(f)$, R is independent of I_d, since

$$I_d^2 = \int_0^\infty I_{xx}(f)\, df \qquad \text{D-(12)}$$

Combining the above equations yields, for infinite clipping:

$$20 \log_{10} I_d = 20 \log_{10} N - 20 \log 0.8E_B + 20 \log (P_d + I_d^2 R) \qquad \text{D-(13)}$$

By making P_d the maximum permissible dissipation, this equation sets the second limit on amplifier output, amplifier based on power dissipation.

As stated, D-(13) is for the infinite-clipping case only. A study of the effect of finite clipping indicates there are no practical adjustments needed for the relationship, for $2.2 \leq k \leq \infty$.

Amplifier Clipping Limit. The peak factor has considerable influence on the clipping performance of the amplifier, as one would expect. The analysis of the clipping limitation uses the joint probability between current i and voltage, v. The probability is found of the instantaneous operating point falling into the clipping region of the output stage.

The characteristics of the output tube are shown is Figure IX. We can arrange that the plot of Figure IX applies to ac signals only, if we employ the point P as the origin. Areas A_A and A_B are clipping regions. The plot can be translated to represent conditions on the secondary side of the matching transformer. If v and i now represent the instantaneous voltage and current, respectively, on the secondary side of the transformer, the slope of the clipping line is $\left(\frac{N^2}{r}\right)$. The clipping effects due to the grid drivers is ignored here because of their relative unimportance. Curve E_{cm} (Figure IX) is represented by:

$$v = \frac{E_B}{N} - \frac{r}{N^2}\, i \qquad D\text{-}(14)$$

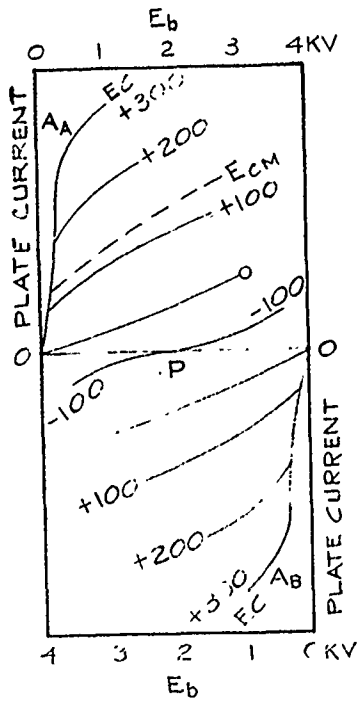


Figure IX - Tube Characteristics

The joint probability density relationship, p(v, i), is given by:

$$p(v,\, i\,) = \frac{1}{\sqrt{2\pi S^2}} \exp - \left[\frac{V^2 i^2 + I^2 v^2 - 2P_o \cdot vi}{2S^2}\right] \qquad D\text{-}(15)$$

where $S^2 = V^2 I_d^{\,2} - P_o^{\,2}$ D-(16)

and V and I are the rms values of v and i, respectively, P_o is the total output power as before. The probability of clipping is given by Π_c:

$$\Pi_c = 2\iint p(v,\, i)\, dv\, di \qquad D\text{-}(17)$$

The integration is taken over the clipping areas, and Π_c becomes:

$$\Pi_c = 2\int_0^\infty di \int_{v_c}^\infty p(v,i)\, dv \qquad D\text{-}(18)$$

where $v_c = \left(\frac{E_B}{N} - \frac{r}{N^2}\, i\right)$ D-(19)

We once again employ R, the average noise resistance. We also define an "average noise impedance," $\bar{Z}$, equal to (V/I_d). Changes in the spectral distributions of $I_{xx}(f)$ and $V_{xx}(f)$, as is shown below, change I_d and V, but for any given relative distribution, $\bar{Z}$ is indeed a constant. Note that

$$V^2 = \int_0^\infty V_{xx}(f)\, df = \int_0^\infty I_{xx}(x)\, |\bar{Z}(f)|^2\, df$$

$$= \bar{Z}^2 \int_0^\infty I_{xx}(f)\, df = \bar{Z}^2 I_d^{\,2} \qquad D\text{-}(20)$$

Hence, we can rewrite P(v,i) as :

$$p(v,i) = \frac{1}{2\pi I^2 \sqrt{X^2}} \exp - \left[\frac{v^2 + \bar{Z}^2 i^2 - Rvi}{2I_d^{\,2}(X^2)}\right] \qquad D\text{-}(21)$$

where $X^2 = \bar{Z}^2 - R^2$ D-(22)

Normalizing i and v further simplifies the result; let us write:

$$\phi = i/I = \frac{v - Ri}{I_d\, X} \qquad D\text{-}(23)$$

Modifying D-(21), and combining it with D-(18) gives:

$$\Pi_c = 2\int_0^\infty \frac{1}{\sqrt{2\pi}} \exp\left(-\frac{\phi^2}{2}\right) dw \qquad D\text{-}(24)$$

$$\int_L^\infty \frac{1}{\sqrt{2\pi}} \exp\left(-\frac{\phi^2}{2}\right)dw \qquad \text{D-(25)}$$

where $L = D - H\phi$

From D-(23), D and H can be shown to be given by

$$D = \frac{E_B}{NI_d X} \qquad \text{D-(26)}$$

and

$$H = \frac{r + RN^2}{XN^2} \qquad \text{D-(27)}$$

Π_c is difficult to evaluate in its general form. However, what we are interested in is the locus of limiting acceptable values for L, for a given specific value of Π_c. If we set Π_c equal to 0.0027, the probability of a simple Gaussianly-distributed voltage, v, exceeding in amplitude three times its rms value, V, we can determine for each arbitrary value of D, the corresponding value of H, to make Π_c equal to 0.0027. The corresponding pairs of D and H are plotted in Figure X. Figure X also shows the plots of (D,H) pairs for Π_c set at the probabilities of the simple Gaussian voltage exceeding 2.5V and 3.5V, respectively.

These plots are computed. However, the limiting conditions for these plots can be dealt with analytically, to help us to give some insight as to the mechanism relating R and X to D and H. Suppose we set tan θ equal to zero; for this

$$-RN^2 = r \qquad \text{D-(28)}$$

must be true. The curves of Figure X meet the X-axis at points set by D-(28). Of course, a negative resistance is impossible to achieve in any practical sense. Usually r is smaller than N^2R: hence, there is a line Y-Y^1 close to and parallel to the D axis, below which no admissible (D,H) pairs are permitted. The (D,H) plots are valid from Y-Y^1 up to infinity.

The values of the intercepts of the plots of Figure X at the D-axis, satisfying D-(28) are established by:

$$\Pi_c = \frac{1}{\sqrt{2\pi}} \cdot \int_D^\infty \exp\left(-\frac{x^2}{2}\right)dx \qquad \text{D-(29)}$$

Thus, we see that as the clipping level of the equivalent single variable, v, increases from "2.5V" to "3.5V", with the value of Π_c decreasing correspondingly, D must increase. Another limiting case is achieved by assuming a truly resistive load (X=0); then v and i are completely correlated. D and H both go to infinity, but

$$D/H = \frac{E_B \cdot N}{I_d(h+RN^2)} \cdot D \to \infty \qquad \text{D-(30)}$$

Thus, the curves of Figure X approach the same "resistive" asymptote at infinity, regardless of the value of Π_c used. It is now possible to derive a "clipping limit" curve. The most straightforward way to do this is to assume several values of N. For each value of N, H is computed from D-(27); from the desired plot of Figure X, D is selected for each value of H computed. For each (D,H) pair, I_d is computed, giving one point on the I_d vs N curve.

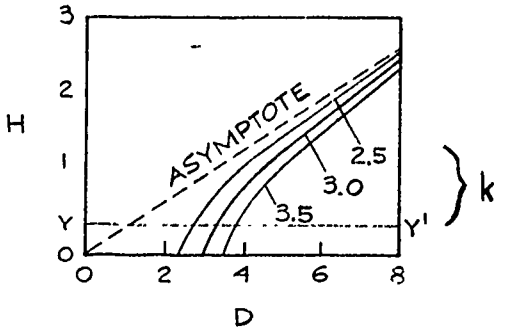


Figure X - Clipping Parameters

Of interest here is the effect on the (I_d, N) curve of changing the peak factor. For each value of N selected, corresponding value of H yields a smaller value of D, if the peak factor is reduced (Figure X). From D-(26) it is seen that a smaller value of D in turn implies a larger value of I_d. Thus, the effect of a reduced peak factor is to increase the allowable value of I_d, for a given value of N.

The effect is illustrated in the plot of Figure XI. The plot shows the limit conditions imposed by amplifier power supply capacity and amplifier dissipation. The area to the right of curves AA' and BB' and to the left of curve CC' is the useable area. Any (N, I_d) pair selected from this area is acceptable. Obviously, the optimum (N, I_d) pair of interest in matching is that pair with the largest value of I_d. The optimum point is point P. The value of N associated with point P sets the transformer turns ratio for the largest permissible value of current into the exciter, and hence gives the largest value of the force.

As shown in Figure XI, reducing the value of k moves the point P upward, permitting the exciter/amplifier system to be operated at higher force levels. On the other hand, if k is required to be increased in value, the point P is pulled down, and the force capacity of the system is reduced. (The point P moves upward with a reduced value of k, because curve CC^1 moves up to the right, and curve AA^1 moves up to the left as k is reduced. As shown, curve AA^1 does not influence P; but it might, since its position relative to curve BB^1 is quite arbitrary).

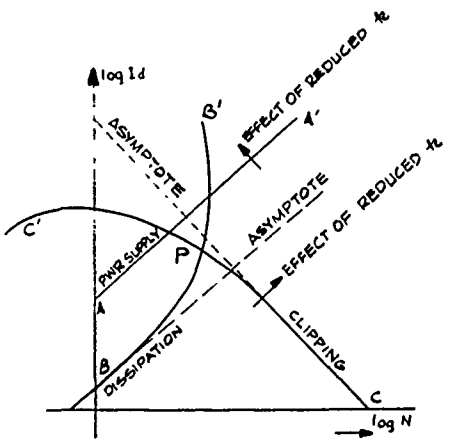


Figure XI - Performance Calculations

REFERENCES

1. C. E. Maki, "Vibration Testing System", U. S. Patent No. 3147045, Nov. 17, 1964.

2. A. G. Ratz, "Statistical Effects in Automatic Random Equalizers", Trans. IEEE, Instrumentation and Measurement,Vol. IM-16, No. 4, Dec. 1967.

3. A. G. Ratz, "The Development of Digital Control Systems for Electrodynamic Vibration Exciters" I.E.S., Proc. 17-th Annual Meeting, Los Angeles, CA, April, 1971.

4. S. O. Rice, "Mathematical Analysis of Random Noise", Selected Papers on Noise and Stochastic Processes, Dover Publications, New York, 1954, p.p. 133-195.

5. H. Cramer, "Mathematic Methods of Statistics, Princeton University Press, Princeton, N.J. 1946.

6. A. H. Church, "Mechanical Vibrations", John Wiley and Sons, New York, 1957.

7. T. Usher, "Performance of Class B Audio Amplifier with Random Noise Signals", Communications and Electronics, AIEE, Jan.,1959.

IMPACT AND BLAST

PREDICTION OF STANDOFF DISTANCES TO PREVENT LOSS OF HEARING FROM MUZZLE BLAST

Peter S. Westine, and James C. Hokanson
Southwest Research Institute
San Antonio, Texas

The recently issued MIL-STD-1474 (MI) specifies what maximum side-on sound pressure levels are tolerable for different durations of incident waves if personnel around hazardous noise sources are to be protected from hearing loss. In the case of gun crew hearing loss from muzzle blast, the code either presumes that blast pressures and durations are known, expects blast pressure and duration to be calculated, and/or demands that blast pressures and durations be measured around all guns. In response to MIL-STD-1474, this paper presents empirically derived equations for estimating pressure, duration, and time of arrival for reflected shocks relative to incident shocks in the blast field around the muzzle of guns.

Experimental test data from different 105-mm howitzer as well as Naval gun firings were used to curve fit pi terms from a model analysis to overpressure, duration and time of arrival tests data. The results can be applied for any of three angles of gun tube elevation to any closed breech weapon without a muzzle brake or flash suppressor.

Because gun crews and weapon designers wish to establish limiting safe standoff positions without the use of complex secondary analysis procedures, design nomographs are also presented which graphically permit predictions of standoff locations whether ears are unprotected, protected with plugs, protected with muffs, or protected with both plugs and muffs. Experimental test data from 105-mm howitzer firings demonstrate that MIL-STD-1474 is met when these graphical procedures for predicting safe standoff are applied.

INTRODUCTION

Whenever a gun is fired, a very intense blast wave is emitted from the muzzle with such severity that hearing loss is common in gun crews. Presently the U. S. government makes annual payments of over several million dollars to citizens with damaged hearing from muzzle blast. In response to this and other hazardous noise problems, the Surgeon General's Office recently issued MIL-STD-1474(MI) [1] based on work performed by Mr. Georges Garinther at the Human Engineering Laboratories. This standard specifies what maximum side-on sound pressure levels are tolerable for different durations of incident waves.

To apply the hearing loss standard to field artillery muzzle blast problems, one must be able to calculate peak pressures and durations at any position around guns. Such a calculation using computer codes is a very complicated procedure. In fact, whenever ground reflections are significant, as in reality, computer calculations are impossible unless one of the three geometric coordinates can be ignored. On the other hand, gun designers and field personnel must be able to establish safe locations to prevent hearing loss in gun crews. They need simple design charts that permit accurate estimates after only a few multiplications or additions. The fundamental question to gun designers and field personnel is where can crew mem-

PRECEDING PAGE BLANK-NOT FILMED

bers safely stand for a particular gun at an arbitrary angle of elevation, propelling charge, length of barrel, etc.? These people do not wish to deal with indirect quantities such as pressure and duration, because the basic quantity of interest to them is distance. For these reasons, the primary purpose of this paper is the development of graphical procedures for estimating safe standoff distances around artillery.

HEARING LOSS MIL STANDARD

Fig. 1 shows the sound pressure limits for hearing loss from gun blast as presented in MIL-STD-1474 for three different levels of ear protection. Peak pressure is denoted in kilo-pascals and in decibels. As applied to the gun blast problem, the W curve is the threshold for no ear protection, the Y curve is the threshold whenever either plugs or muffs are being worn, and the Z curve is the threshold if both plugs and muffs are worn. These curves, based on a noise exposure rate of 100 per day, were obtained at HEL from various investigators' test data on monkeys, themselves, and soldiers until temporary but recoverable loss in hearing was experienced by 25% of the personnel subjected to a grazing or incident blast pressure wave. It is assumed in the standard that repeated exposure to a temporary hearing loss would result in some permanent non-recoverable loss in hearing. The W curve is a continuation of requirements from earlier criteria, TB MED 251.

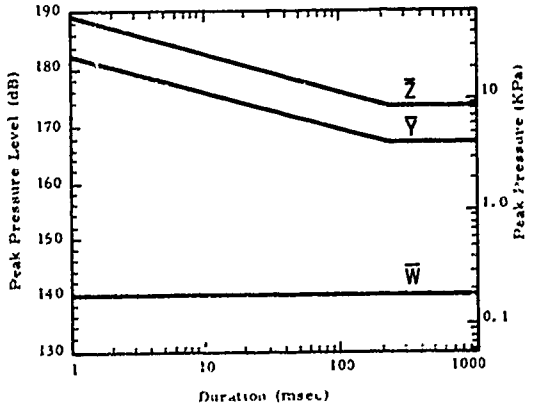


Fig. 1. Peak Pressure Level and Duration Limits

Both HEL and the writers of this report feel that for short duration pressures, the W pressure levels should also increase with decreased durations; however, insufficient data exist to offer a modified W-curve at at this time.

Because the hazardous noise standard was developed for other sources as well as guns, we must discuss the developer's thoughts on how to interpret the time axis for an impulsive muzzle blast noise source. In general, a blast wave emitted from a gun must diffract and reflect from obstacles such as the gun carriage and ground. The obstructions cause reflected blast pressure waves to interact with the incident air blast wave emitted from the muzzle of a gun. For field artillery in particular, the ground becomes a very significant reflecting surface. If other reflecting surfaces are assumed to be insignificant, as they are relative to the ground, idealized transient blast pressure histories can be obtained as seen in Fig. 2. Three different pressure histories are shown in Fig. 2, because the character of the pressure history at a point in space above a reflecting plane

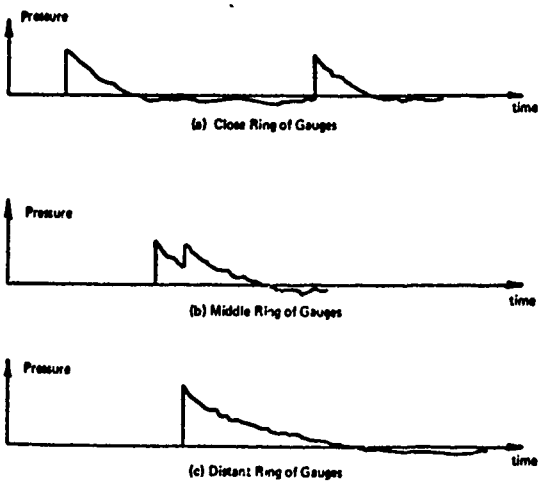


Fig. 2. Incident and Reflected Gun Blast Waves

differs depending upon the duration of the incident air blast wave and the time lag between the incident and reflected air blast fronts. In Fig. 2a, the reflected wave arrives after the incident wave is fully dissipated. Fig. 2b shows an air blast wave in which the reflection has overtaken the incident wave to form a new blast wave in the Mach stem. Because HEL, as developers of the code, wished to avoid confusion as to how durations could be defined when decaying waves asymptotically approach a baseline, they specified that peak pressures should be measured and then envelopes established on both sides of the baseline at 10% of the peak pressure level or 20 dB from the peak as in Fig. 3. Fig. 3 from the code is the illustrative example of

how the durations are to be established for use in Fig. 1. The duration according to the code is the sum of the times from A to D and from E to F. If no reflection existed, the time would be that associated with the incident wave whenever all pressure fluctuations positive and negative are between 10% and 100% of the peak pressure level. Unfortunately, this illustrative example from the code looks nothing like an air blast wave.

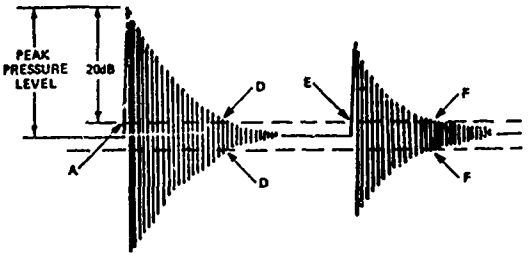


Fig. 3. Idealized HEL Pressure-Time History of an Impulse Noise

Fig. 4 shows four different air blast waves measured at various positions around the muzzle of an XM204, 105 mm howitzer with LC-33 piezoelectric, pencil gauges. Notice that noise exists on all the records; nevertheless, these traces would usually be thought of as recordings of excellent quality. To follow the code quite literally, and this is what is expected, requires the user to carry the duration to point C in Fig. 4a, point D in Fig. 4c, point F in Fig. 4d, and beyond recorded time in Fig. 4b. Quite frankly, these deviations are <u>not</u> associated with the rarefaction wave from a muzzle blast, they are associated with instrumentation noise and the RC time constant of the recording system. Perfect recordings cannot be made; instrumentation noise is always present. Piezoelectric elements are subject to thermal drift from such phenomena as the sun passing behind clouds and radiation from the gun's fireball. Usually thermal drift is slow relative to durations 10 times longer than the positive wave with a low frequency instrumentation discharge asymptotically approaching a limit. Fig. 4b is probably an example of thermal heating from the howitzer's fireball. Other sources of noise include cable whip, shocks through the gauge, flutter in the tape recorder, dampness in connectors, and noise on power lines. Because the frequency response is in the AM radio band, cables even when shielded act as antennae and present radio broadcasts as extraneous noise sources. The durations BC and DE that could be subtracted from the overall duration F in Fig. 4d are probably examples of one of the aforementioned extraneous noise sources. These instrumentation problems are not unique to this program; everyone measuring blast around large weapons has these difficulties. In telephone conversations with HEL, they implied that test records could be repeated, even where measured with different instrumentation systems. Unfortunately, all instrumentation systems used to piezoelectrically record blast pressure signals have low frequency responses in the area of 2 cps. This argument simply means that systematic errors can be repeated. Whenever we applied the code to Rock Island 105 mm muzzle blast records, we obtained negative envelope durations of 20 ± 7 ms except for a wave such as Fig. 4b with thermal energy introduced into the recording system. This result is probably a consequence of the low frequency response for the instrumentation and has nothing to do with negative blast wave durations. Based on our analysis of hundreds of records, we believe that the rarefaction durations cannot be measured around artillery, and that observed results are measures of the instrumentation RC time constant and extraneous instrumentation noise sources which exaggerate the total pulse duration.

To circumvent this instrumentation limitation, procedures were developed for predicting peak pressures, times of arrival for reflected waves, and total duration of all wave fronts using only the positive or compressive wave durations. This procedure is not in strict compliance with the code, but we believe these to be the only times which can be accurately measured, and are representative of blast pressure durations. Then, so that negative times may be included to approximate the observed total duration as defined by the HEL code (an observation that we believe measures instrumentation noise and time constants) a factor N was introduced into the solution for the $\bar{Y}$ and $\bar{Z}$ criteria.

If N equals 1.0, the duration is that associated with a decay intersecting only the positive 20 dB or positive 10% envelope line. No negative durations are considered when N equals 1.0. An N of 5.0 closely approximates the total instrumentation times (positive + negative) for 105 mm howitzer firings whenever incident and reflected waves are separated as in Fig. 2a. An N value of 10 more closely approximates the recorded total durations for the 105 mm howitzer firings whenever waves are in the Mach stem

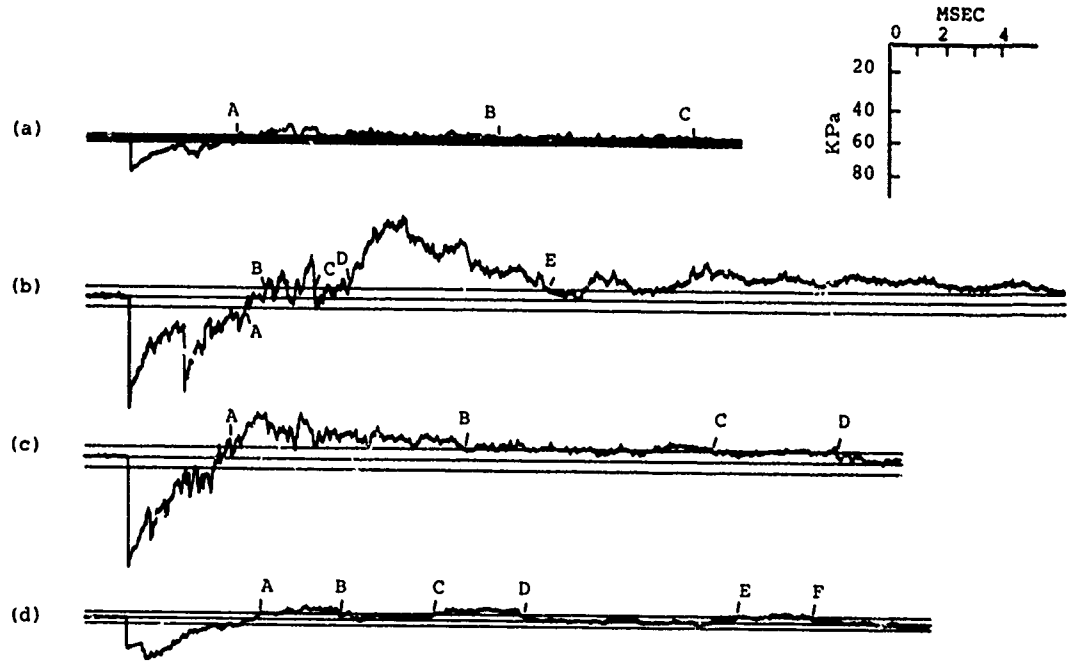


Fig. 4. Examples of Field Traces for XM204 Howitzer Muzzle Blast

as in Fig. 2c. Although these values are given as guidelines, we leave it up to the individual to decide what value of N is most appropriate for his weapon system.

DEVELOPMENT OF EMPIRICAL RELATIONS FOR PRFDICTING PRESSURE AND DURATION AROUND WEAPONS

General

This section presents the development of empirical relations for predicting peak pressure around guns. Interested readers may find a similar development of empirical relations for predicting duration and time of arrival for a reflected wave relative to an incident muzzle blast wave in Reference [2]. All three of these relationships have been developed by first conducting a model analysis and then curve fitting the nondimensionalized parameters or pi terms to experimental test data. Because these relations have been nondimensionalized, they may be used to predict peak pressures, durations or relative times of arrival around a wide variety of weapon systems.

The test data used in all curve fits come from one of two sources. Reference [3] by Mark Walther is a compilation of all Naval Weapons Laboratory muzzle blast test data. Included in this compilation are data obtained by both NWL and its contractors. Unfortunately, most of the information is peak pressure for various locations around the muzzle of many guns including 20 mm, 40 mm, 3"/50, 5"/38, 5"/54, 6"/47, and 8"/55 guns. No angle of gun tube elevation α is reported although the writers know from personal conversations that the angles are near 0°. The height of guns, neights of gauges, durations, and arrival times are unreported; hence, these data are largely limited to peak pressure fits for an α of zero. The second source of data comes from 105-mm howitzer test firings conducted by Mark Salsbury of Rock Island Arsenal. Tests on a M102 howitzer firing zone 7 propelling charges are reported in Reference [4]; however, the vast bulk of the data is as yet unreported XM204 tests firing zone 5, zone 7, and zone 8 charges at gun tube angles of 1.5°, 16.8°, and 68.6°. All parameters are known in these experiments, including height of gun, height of gauges, pressures, durations, and times of arrival for reflected shocks. Gauges were usually placed along radial lines every 15° from 15° to 165°. A diagram showing gauge locations is represented by the dots or gauge locations on Fig. 8. Atlantic Research LC-33 pencil gauges and a magnetic ta-

recorder with a frequency response of from 2 cps to 20,000 cps were used on all tests.

Model Analysis

Various investigators have previously used model analyses to evaluate blast field around the muzzel of guns. The earliest efforts at Princeton [5] under BRL sponsorship and at David Taylor Model Basin [6] for the Navy lead to an accurate, but awkward-to-apply replica modeling law. Provided rigorous geometric similarity was maintained, projectile masses and propellant energy scaled as the cube of the geometric scale factor, and projectile velocities were invariant, the Princeton and DTMB efforts correctly stated that at homologous locations, pressures would be identical and times would scale as the geometric scale factor. These statements are a direct extension of Hopkinson's Law [7] of 1915 for scaling air blast around H. E. charges. The major limitation to this early replica modeling law is that changes in some key parameters such as barrel length, amount of energy in the propellant, mass of projectile, and/or projectile velocity prevented new predictions of the muzzle blast field until new experiments had been conducted.

The next effort to overcome replica modeling limitations and scale pressures only was at Armour Research Institute [8] where an equivalent spherical explosive charge was located on the bore axis at a distance from the muzzle. To create an approximation to the peak pressures, Armour created a "reduced energy" using Eq. (1),

$$W = n\left[E - \frac{1}{2} m V^2\right] \qquad (1)$$

where

W = effective energy entering blast

E = energy in propellant

$\frac{1}{2} m V^2$ = kinetic energy of projectile at ejection

n = nondimensional coefficient dependent upon chemistry and heat of a propellant.

Creation of this equivalent energy release simplified future model analysis by using an equation instead of independently modeling projectile velocity, and total energy in the propellant. Three weaknesses existed in the Armour approach. First, all contours were spherically symmetric instead of being elongated as in nature because a stationary point charge was envisioned as an equivalent muzzle blast source. Second, the same equivalent energy release used to predict pressures would not predict durations, and third, the scaled barrel length $\frac{\ell}{c}$ was not included in the analysis because all weapons tested at that time possessed virtually the same scaled barrel length.

Finally, Westine in 1968 [9] and 1969 [10] modified the Armour approach and developed the procedures in use today. In these reports, Westine recognized that the Armour concept of an equivalent energy release greatly simplified any analysis, and that it could be applied without using the concept of a point charge provided a model analysis is conducted. The most detailed of these model analyses by Westine appears in Reference [11]. We will follow the procedure used in Reference [11] to briefly reconstruct that model analysis for this study.

Any model analysis begins by defining the problem so parameters can be listed. Our problem is to determine the pressure-time history at some arbitrary point in space above a rigid reflecting plane, the ground. The blast pressures are created by a closed-breech gun with no muzzle brake or flash suppressor also located above this same reflecting surface and having an equivalent energy release W. A polar coordinate system will be used with its origin directly below the gun muzzle but in the plane under the weapons. The $\theta = 0$ axis will be the projection of the line of fire upon the reflecting surface, and the standoff distance L will be the distance in the reflecting plane of an arbitrary location of interest from the projection of the gun muzzle onto the plane. The gun itself will be of caliber c, barrel length ℓ, and have an equivalent energy release W based upon Eq. (1). Its muzzle height above the reflecting plane is h, and it has a gun tube angle α to the horizon. A point or location of interest in space is specified by θ and L and the height H over the surface. This location in space will experience peak overpressure P, duration T, and time of arrival τ of a reflected wave relative to an incident wave.

Three ambient atmospheric conditions

are needed to complete this model analysis and permit the blast wave to propagate through space. Although the choice of these parameters is somewhat arbitrary, we will use atmospheric pressure P_o, sonic velocity a_o, and the ratio of specific heats γ_o. Table A lists the significant parameters presented in this model analysis together with their fundamental units of measurement in an engineering system of force p, length x, and time t.

Several different procedures exist for obtaining pi terms from a list of parameters, several of which are demonstrated in various texts or the reader can follow the procedure presented in Reference [11]. Because these procedures involve only tedious algebra and no new assumptions, we will present only the results. If pi terms are obtained by solving in terms of the exponents on c, W, and a_o, the 11 nondimensional ratios presented in Table B will result from the 14 parameters listed in Table A.

The first seven pi terms are statements of geometric similarity, pi terms 7 and 8 place environmental restraints on the system, and the last three pi terms are the responses which are of interest. This analysis shows that scaled response for a muzzle blast wave is a function of geometric similarity and two environmental restraints. In functional analytical format the response for either scaled pressure or scaled duration, or scaled time of arrival may be written as Eq. (2):

TABLE A
List of Significant Muzzle Blast Parameters

Symbol	Quantity	Fundamental Dimensions
Geometry		
θ	reference angle in polar coordinate system	--
L	standoff distance in polar coordinate system	x
h	height of muzzle	x
c	caliber of gun	x
ℓ	length of gun barrel	x
H	height for location of interest	x
α	angle of gun barrel with the horizon	--
Ambient Atmospheric Environment		
P_o	atmospheric pressure	p/x^2
a_o	sonic velocity	x/t
γ_o	ratio of specific heats	--
Energy Release		
W	equivalent energy release $\gamma(E - \frac{1}{2}MV^2)$	px
Response Parameters		
P	maximum overpressure	p/x^2
T	duration	t
τ	time of arrival for reflected waves relative to incident waves	t

TABLE B
Pi Terms for Muzzle Blast

$\pi_1 = \frac{\ell}{c}$	Geometric similarity
$\pi_2 = \frac{L}{c}$	
$\pi_3 = \frac{h}{c}$	
$\pi_4 = \frac{H}{c}$	
$\pi_5 = \theta$	
$\pi_6 = \alpha$	
$\pi_7 = \frac{P_o c^3}{W}$	Environmental restraints
$\pi_8 = \gamma_o$	
$\pi_9 = \frac{Pc^3}{W}$	Response pi terms
$\pi_{10} = \frac{Ta_o}{c}$	
$\pi_{11} = \frac{\tau a_o}{c}$	

$$\begin{bmatrix} \frac{Pc^3}{W} \\ \frac{Ta_o}{c} \\ \frac{\tau a_o}{c} \end{bmatrix} = F\left(\frac{\ell}{c}, \frac{L}{c}, \frac{h}{c}, \frac{H}{c}, \theta, \alpha, \frac{P_o c^3}{W}, \gamma_o\right) \quad (2)$$

Eq. (2) can be simplified further by deleting constants. For all practical purposes, a_o, γ_o, and P_o are constants, provided we restrict ourselves to muzzle blast under sea level ambient conditions and weak shocks without ionization or disassociation of the air. Neither of these conditions creates an invalid analysis when we delete a_o, P_o, and γ_o from Eq. (2) and obtain:

$$\begin{bmatrix} \frac{Pc^3}{W} \\ \frac{T}{c} \\ \frac{\tau}{c} \end{bmatrix} = F\left(\frac{\ell}{c}, \frac{L}{c}, \frac{h}{c}, \frac{H}{c}, \theta, \alpha, \frac{c^3}{W}\right) \quad (3)$$

Eq. (3) is the most general solution. It does present an eight-parameter space for curve fitting to experimental results. Further reductions in this experimental space and the development of curve fits will now be evaluated for pressure. Similiar discussions for duration and relative time of arrival are found in Reference [2].

Predicting Pressure

To predict maximum overpressure, we apply Eq. (3) in the format of:

$$\frac{Pc^2\ell}{W} = F\left(\frac{L}{c}, \theta, \alpha\right) \quad (4)$$

Four empirical observations are needed before this approximate format can be substituted for Eq. (3). The first of these observations is that c^3/W is insignificant, the second is that Pc^3/W and ℓ/c may be combined to form $Pc^2\ell/W$, the third is that h/c is insignificant, and the fourth is that H/c is insignificant.

In 1970, Westine [11] demonstrated that c^3/W was insignificant for predicting pressure by plotting scaled pressure versus scaled position in space for a wide variety of weapons with different values of c^3/W. Because scaled pressure as a function of scaled position plotted as a single unique function, the results showed that c^3/W was unimportant. This observation was made using 12 different weapon systems and included a range in c^3/W of from 3.6×10^{-11} to 5.1×10^{-8} m^2/Nt, a range of over three orders of magnitude. If the term c^3/W is rewritten as $c/W^{1/3}$, it can be interpreted as a statement of geometric similarity, and an analogy can be noted between it and $r/W^{1/3}$ in Hopkinson's scaling law [7] for the blast field around an explosive charge. An alternate method of rewriting Hopkinson's law is to write r/d, where d is a charge diameter. Similarly, $c/W^{1/3}$ can be thought as c/d where d is a linear dimension associated with the energy release. Physically, the insignificance of this parameter implies that positions of interest in space are large relative to weapon caliber or relative to d. No contradictions for this empirical observation are to be found in Rock Island howitzer firings when the only change in XM204 tests is the energy release W because of a zone 5, zone 7, or zone 8 experiment.

Westine [9, 10] also made the second empirical observation that scaled barrel length could be combined with the dependent normalized pressure term to form one term $Pc^2\ell/W$. Experimental tests on very short barrel weapons such as a 0.45 pistol and several 40-mm grenade launchers agreed with more conventional long barrel weapons only when these terms were combined. The difference in barrel length expressed in calibers for a 0.45 pistol and a 22 caliber long rifle is one order of magnitude from approximately 8.8 to 92. Physically this second observation implies that $Pc^2\ell/W$ can be thought of as pressure relative to an effective chamber pressure $W/c^2\ell$, not actual chamber pressure but rather an effective one for an adiabatic process. No contradiction to this empirical observation exists from the Rock Island 105-mm howitzer firing with zone 7 propelling charges in the 26.6 caliber long M102 or the 33.9 caliber long XM204 guns.

The last two empirical observations concerning the insignificance of scaled muzzle height h/c and scaled location H/c on predicted pressure are somewhat harder to substantiate. All observations on the influence of these two parameters come from this study. Rock Island does report the muzzle height on their howitzer firings; however, the variation in this parameter is very limited. For 0° to 1.5° gun tube elevations, howitzer muzzle height h/c only varied from 7.26 calibers to 9.86 calibers above the deck. In these same experiments, gauge locations H/c ranged from 7.26 to 13.07 to 18.87 calibers for the M102 tests, and 10.65 to 14.52 calibers for the XM102 experiments. Within such a limited range, no trend could be noted. In the Navy gun resume, Walther [3] does not report either muzzle locations or gauge heights. For the 3"/30 and 8"/55 Naval gun experiments, we know that these weapons were 17.4 calibers above the ground, as the senior author of this report witnessed these tests. With a wide variation in weapons of from 20 mm up through 8"/55 Naval guns, we can probably presume with some degree of assurance that muzzle heights and gauge positions varied. All comparisons of scaled pressures for different weapon systems

were based upon the assumption that h/c and H/c were not highly significant.

An empirical curve fit for predicting peak pressure was developed based upon the validity of Eq. (4). Many plots of $Pc^2 \ell/W$ versus L/c for constant values of θ and α were made for many different weapon systems. Included in these plots were three different α gun tube elevations of 0°, 16.8°, and 68.6°. Scaled pressures were plotted along radial lines for 15° increments from θ = 15 to 165 degrees. Eight of these plots may be seen in Figs. 5 as examples of this effort.

The first four graphs in Fig. 5 are for $\alpha = 0°$. If more than one gauge were on a pole in a howitzer experiment, the maximum pressures were averaged and plotted in these figures together with guns from Reference [3]. The scatter is very little, especially when one considers the range of weapons which are involved. These results help to imply that h/c and H/c were relatively insignificant for this variation in test conditions.

The last four graphs in Fig. 5 are for α's of 16.8 and 68.6 degrees. Many less data points are on these graphs because only the XM204 with zone 7 and 8 propelling charges were fired at these higher angles. No averaging of pressures for two gauges on a pole was performed in these tests, as we wished to emphasize that sometimes the lowest gauge recorded the highest pressure, whereas on other occasions the highest gauge recorded the highest pressure. In all the 16.8 and 68.6 gun tube experiments, gauge heights were either 10.65 calibers or 14.52 calibers off the ground; hence, the variation in h/c is small. As can be seen in Figs. 5, scaled pressures also correlate for the higher gun tube elevations, but peak pressure is a strong function of α.

The straight lines through the data points in Figs. 5 are the curve fits to these data given by Eq. (5). As can be seen, results are fairly accurate. One standard deviation σ for these data points about the curve fit can be found in Table C. A higher standard deviation exists for $\alpha = 0$ than for α = 16.8 or 68.6 degrees because the curve fit is over a larger variation in L/c for the lowest angle and because some uncertainty exists in some results from Reference [3]. Scatter may appear to be larger in Fig. 5 for larger angles, but this results is deceiving, as $Pc^2 \ell/W$ covers three rather than one order of magnitude for gun tube elevations of 0 degrees.

$$\frac{Pc^2 \ell}{W} = e^{\xi + \epsilon \cos\left(\frac{\theta}{\gamma} - \delta\right)} \left(\frac{c}{L}\right)^{\beta + \gamma \cos\left(\frac{\theta}{\gamma} - \delta\right)} \quad (5)$$

Several quantities in Eq. (5) require further explanation. The coordinate system for the observer's position relative to the muzzle of a closed-breech gun is a radial coordinate system with its origin as the perpendicular projection of the muzzle onto the ground under the gun, and its reference line, the projection of the line of fire onto the ground. In other words, θ equal to zero is the line of fire, θ equal to π radius is directly aft, and L is the standoff distance from the muzzle when measured parallel to the ground. No slant distances are involved from the ear of the observer to the gun muzzle.

Eq. (5) for pressure is not a strong function in the region measured of either the height of the muzzle h off of the ground or the height of the observer H off of the ground. These parameters are therefore not included. The angle of the gun barrel α relative to the ground does make a significant difference; hence, its influence is included in the numerical values for the six Greek letter coefficients (ξ, ϵ, γ, δ, β, and γ). Table C presents these nondimensional coefficients as functions of α for three different gun tube elevations. Because these coefficients come from an empirical curve fit to experimental test data, one standard deviation σ for using these coefficients to predict pressure is also presented in Table C. As can be seen, one standard deviation for predicting pressure is essentially 25% over the range of test results.

The final quantity requiring considerable discussion is the effective energy release W, given by Eq. (1). Essentially, Eq. (1) is an energy balance. It states that the energy in the propellant that does not enter the kinetic energy of the projectile goes into muzzle blast. Actually, other forms of energy dissipation do exist, particularly thermal losses; however, provided these losses are directly proportional to $E - 1/2\ mV^2$, Eq. (1) will be valid. The quantity E is determined by multiplying the weight of propellant times the heat of explosion for the propellant. The proportionality coefficient η is both a correction factor for thermal losses and a coefficient that depends upon the chemistry of propellants. It does appear to be a nonlinear function of heat of

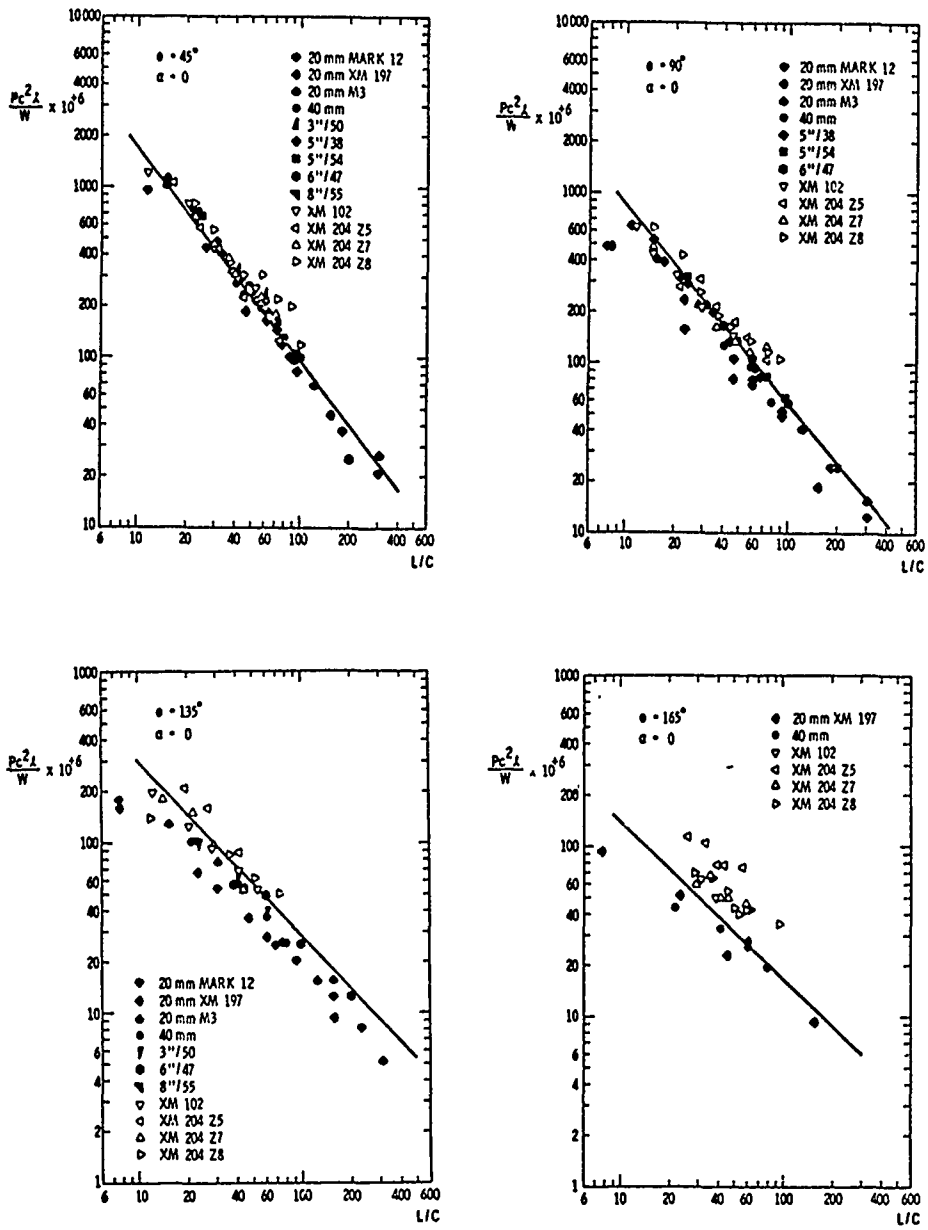


Fig. 5. Scaled Pressure vs Scaled Standoff Distance

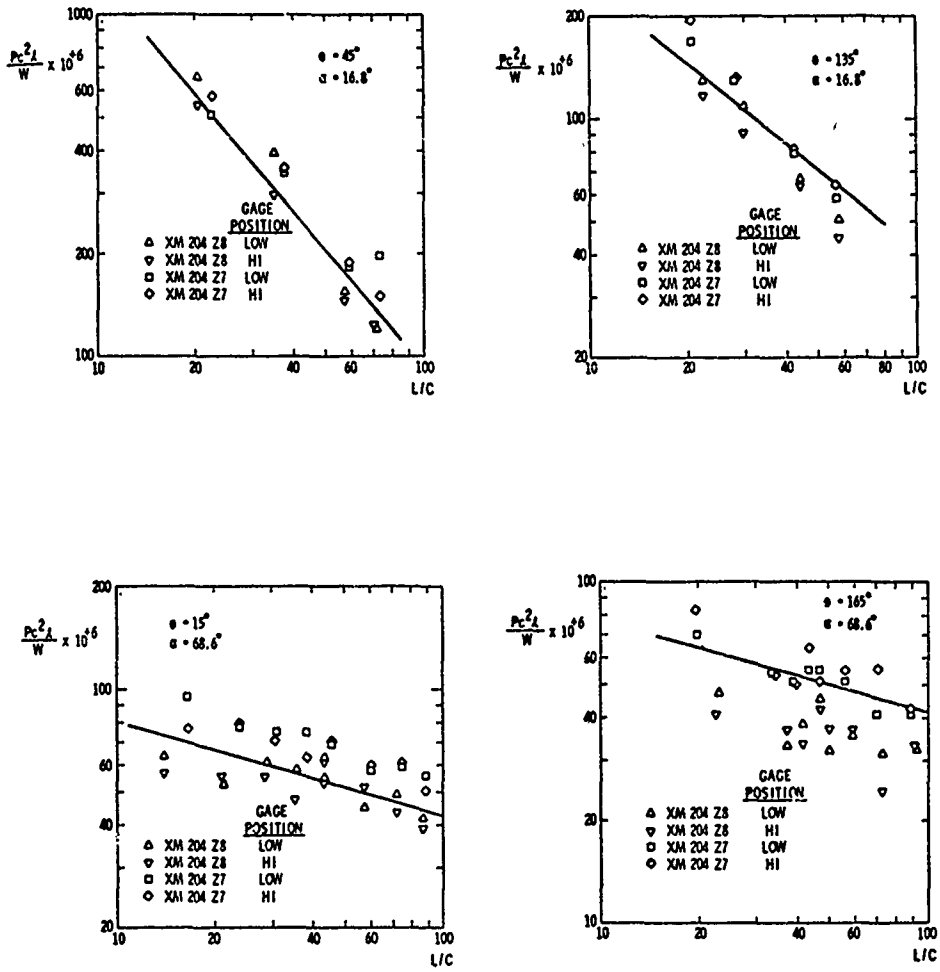


Fig. 5. Scaled Pressure vs Scaled Standoff Distance (concluded)

TABLE C
Coefficients for Pressure Equation

α(radians)	σ	ξ	ε	γ	δ	β	ψ
0	28.2%	-6.652	3.502	1.80	0.0	0.9352	0.3551
0.293	18.3%	-6.484	2.468	1.00	0.7854	0.7843	0.3601
1.197	12.9%	-8.635	0.365	0.457	1.454	0.2737	0.8618

explosion. Table D presents values of n for propellants that we have encountered in experimental tests.

TABLE D
Numerical Values of n For Energy Releases

Type of Propellant	Heat of Explosion (J/Kg)	n
Navy NACO	$2.75 \times 10^{+6}$	1.00
Army M1	$2.93 \times 10^{+6}$	1.00
Navy PYRO	$3.14 \times 10^{+6}$	1.00
Unknown (20 mm)	$3.47 \times 10^{+6}$	1.06
Dupont IMR	$3.62 \times 10^{+6}$	0.693
Army M30A1	$4.07 \times 10^{+6}$	0.716
Hercules Unique	$5.05 \times 10^{+6}$	0.511

The development of equations for predicting muzzle blast durations and time of arrival are presented in Reference [2]. Both results have a format similar to that given by Eq. (5) for pressure; however, they are deleted from this paper in the interest of brevity.

DEVELOPMENT OF SAFE STANDOFF CONTOURS

General

Two procedures are discussed in this section, one for computing the safe standoff position whenever no ear protection is offered, and the other for computing safe standoff position with protection such as plugs and/or muffs. Two separate solutions must be presented because the $\overline{W}$ no-ear-protection threshold is independent of muzzle blast duration, whereas the $\overline{Y}$ and $\overline{Z}$ protected-ear thresholds are functions of duration (see Fig. 1).

Solution for $\overline{W}$ Criterion

The maximum free field overpressure around a gun muzzle over a reflecting plane such as the ground is given by Eq. (5).

Because the $\overline{W}$ threshold of hearing loss criterion is a constant pressure criterion (see Fig. 1), we have only to substitute the amplitude Z for P in Eq. (5). Whenever this substitution is made, the solution for threshold of hearing loss becomes a four-parameter space of nondimentional numbers that can be written in functional format as:

$$F\left[\frac{Z c^2 \ell}{W}, \alpha, \theta, \frac{L}{c}\right] = 0 \qquad (6)$$

The value for Z is 0.197 KPa if $\overline{W}$ from Fig. 1 is considered to be the appropriate threshold. Eq. (6) can also be used for the $\overline{Y}$ and $\overline{Z}$ thresholds if durations are greater than 200 milliseconds. Such a computation is an academic rather than practical considera-

tion because a 1.02 m gun would be requird for a duration around 200 milliseconds. If one believed that durations are a function of the instrumentation system, as has already been discussed, and wanted to use a constant $\underline{Y}$ or $\underline{Z}$ pressure for a constant duration from a given gun, Fig. 1 could be used to obtain Z and Eq. (6) with the appropriate Z would still apply.

A four-parameter solution has the advantage that it can be displayed graphically. Fig. 6 is one graph from a series depicting Eq. (6), only rectangular rather than polar coordinates are beinr used. The parameter $L_{\perp}$ is the standoff ıistance from the muzzle perpendicular to the line of fire, and $L_{\parallel}$ is the distance parallel to the line of fire. Negative values for $L_{\parallel}$ are aft of the gun muzzle. Several figures like Fig. 6 are found in Reference 2 for different gun tube elevation angles α. Any self-consistent set of units can be used when applying Fig. 6, as the parameters are all nondimensional. The isoclines throughout the figure are for constant values of $Z c^2 \ell/W$. For a particular gun and propelling charge, c, ℓ, and W will be constants. Select the appropriate value for Z from Fig. 1 (Z = 0.197 KPa if the W criterion is being applied) and compute the numerical value of the isocline $Z c^2 \ell/W$. Fig. 5 shows in gun tube calibers where the pressure will be greater or less than the constant pressure hearing loss threshold. Inside the limiting isocline of $Z c^2 \ell/W$, we would predict hearing loss, whereas outside this same isocline, we would predict no hearing loss.

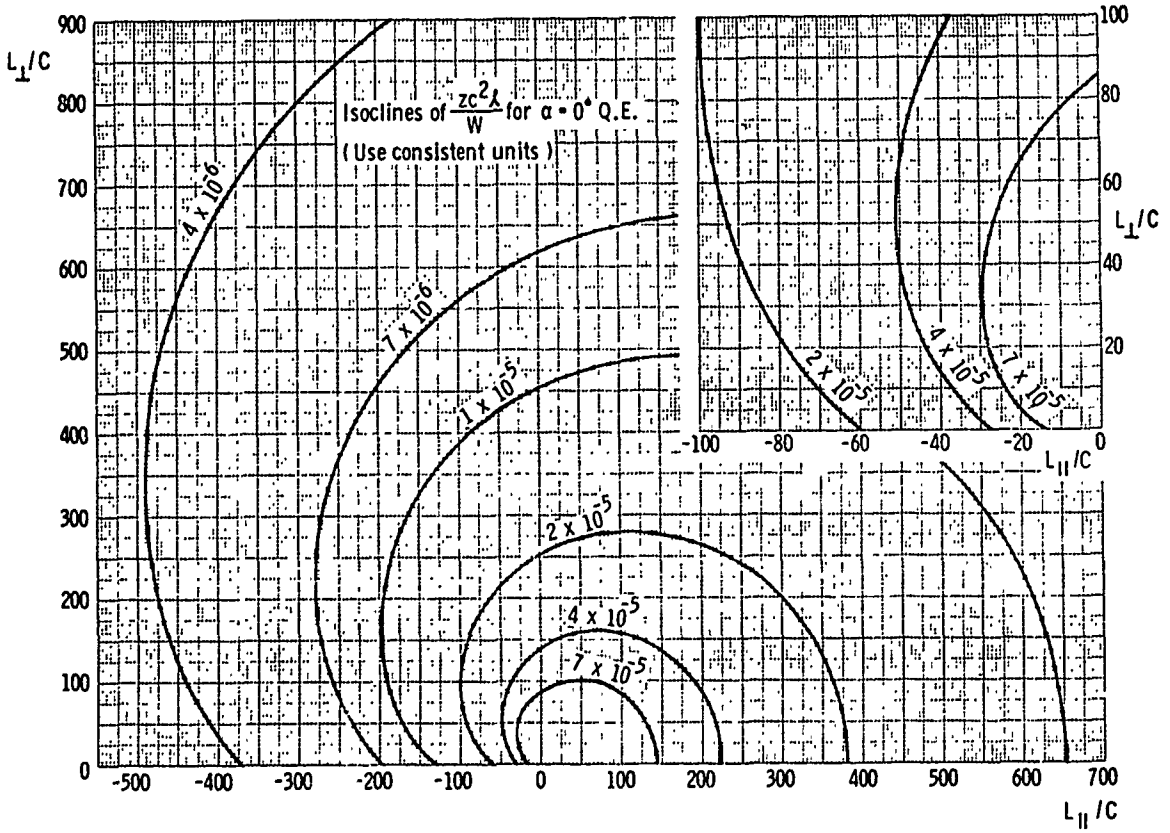


Fig. 6. Safe Standoff Distances for No Ear Protection ($\overline{W}$ Criterion)

The 100-caliber square region aft of the muzzle has been enlarged and inserted in Fig. 6 as this domain covers the area where gun crews stand. The most severe muzzle blast occurs whenever the gun is fu'ly depress ed to 0 degrees. For artillery this condition may be too severe a restriction in the field, as essentially all rounds are fired with a gun tube elevation of at least 300 mils. The only time an artillery piece is fired at 0 degrees is whenever a position is being

overrun, a time for kill or be killed with no concern for hearing loss and the positioning of people. The code [1] incidentally does recognize and accept the existence of such circumstances.

Mr. Mark Salsbury at Rock Island Arsenal supplied muzzle blast test data on zone 5, 7, and 8 firings from 105-mm howitzers. All of his gauges at 0 degrees gun elevation were located at various positions up to maximums of approximately 100 calibers along radial lines spaced 15 degrees apart. Every one of these gauges measured pressures greater than 0.197 KPa; that is, the blast pressure recorded by all gauges was, according to the $\bar{W}$ criterion, sufficient to cause threshold hearing loss at each gauge position when no ear protection is provided.

Solution for $\bar{Y}$ and $\bar{Z}$ Criteria

For muzzle blast durations of less than 200 milliseconds (which is true for all known guns) and ear protection in the form of either plugs and/or muffs, the hearing loss thresholds as seen in Fig. 1 are funtions both pressure and time. Because the $\bar{Y}$ and $\bar{Z}$ criteria from Fig. 1 are parallel straight lines on a log-log plot of maximum pressure P versus duration T, the equation for these lines can be written as:

$$PT^{0.345} = Z(\text{prot}) \qquad (7)$$

The exponent 0.345 is the slope of the $\bar{Y}$ and $\bar{Z}$ lines seen in Fig. 1. The parameter Z(prot) for level of ear protection has units of Nt - $ms^{.345}/m^2$ and is a constant dependent only upon the type of ear protection. For the $\bar{Y}$ level of ear protection Z(prot) equals 26.9 KNt - $ms^{0.345}/m^2$, and for the $\bar{Z}$ level of ear protection it equals 56.5 KNt - $ms^{0.345}/m^2$.

Both pressure and duration equations are needed to substitute into Eq. (7) and develop a functional relationship. Eq. (5) for maximum side-on overpressure is still valid as the blast pressure field is independent of the type or lack of ear protection. The total free field duration for muzzle blast around a gun muzzle over a reflecting plane such as the ground, derived in Reference [2] is given by:

$$\frac{T\ell^{5/12}}{NW^{1/3}c^{5/12}} = 0.904\left[\frac{(a+b\theta)\frac{L}{c}}{\left|d+\frac{L}{c}\right|} + \left|e-f\theta^2\right|\right] \qquad (8)$$

where

T = total duration of all compressive waves

N = nondimensional factor to account for negative durations as well as positive durations

a, b, d, e, f = coefficients given by Table E which are functions of gun tube angle α

W, ℓ, c, L, θ = parameters already defined

Just as Eq. (5) for pressure was not a strong function in the region tested of either the height of the muzzle h off of the ground or the height of the observer H, so, too, duration is treated as being independent of these two parameters. The angle of the gun barrel α relative to the ground does make a significant difference; hence, its influence is included in the numerical value for the five coefficients (a, b, d, e, and f). Table E presents these nondimensional coefficients as functions of α for three different gun tube elevations. Because these duration coefficients come from an empirical curve fit to experimental test data, one standard deviation σ for using these coefficients to predict duration is also presented in Table E. As can be seen, one standard deviation for predicting duration is essentially 25% over the range of test results.

Whenever the coefficients from Table E are substituted into Eq. (8), the scaled duration $\frac{T\ell^{5/12}}{NW^{1/3}c^{5/12}}$ will have units of $\frac{ms}{m^{1/3}Nt^{1/3}}$. After the effective energy release as defined by Eq. (1) has been substituted into the scaled duration, the duration T is obtained in units of milliseconds. The duration T, as has already been discussed, is the sum of all the positive durations associated with compressive blast wave pressure decays intersecting only the positive 20 dB or positive 10% envelope line. No negative or rarefaction durations are considered unless N equals a number greater than 1.0. The parameter N is a nondimensional factor for approximately estimating the sum of all positive and negative durations as defined in the code. We have already discussed that for the muzzle blast field

TABLE F
Coefficients for Duration Equation

α(radians)	σ	a	b	d	e	f
0	23.0%	0.1192	-0.02346	28.0	0.03224	-0.001215
0.293	26.0%	0.1971	-0.04871	42.0	0.04200	0.0
1.197	22.7%	0.05603	-0.000228	42.0	0.05617	+0.004501

around artillery, measured results reflect the low frequency RC time constant and instrumentation noise rather than the reality of an accurately measured duration associated with a rarefaction. The choice of an appropriate value for N is left up to the individual. For blast fields measured around 105-mm howitzers, we have indicated that an N of 5.0 approximates negative instrumentation times whenever incident and reflected waves are separated, and an N of 10.0 approximates negative and positive durations for waves in the Mach stem.

If waves are to be in or out of the Mach stem and have different values of N assigned, one must be able to predict where the triple point passes when guns are fired at different angles over a reflecting plane. For gun tubes at angles of 16.8° and 68.6°, the gauges were not located over a sufficiently extended region to predict passage of the triple point. All of these higher gun tube angles had transducers measuring separate incident and reflected waves. For a gun at 0° QE, we were able to develop from time of arrival curves described in Reference [2] the standoff distance L/c along various radial lines θ for which the triple point passes essentially at ear level. An algebraic expression from these $\alpha = 0°$ curve fits is given by:

$$\left(\frac{L}{c}\right)_{\substack{\text{triple}\\ \text{point}}} = 70.46 + 2.216\theta^2 \qquad (9)$$

Equation (9) indicates that at $\theta = 0.262$ radians (15°), L/c = 70.6 calibers; at $\theta = 2.880$ radians (165°), L/c = 88.8 calibers for the passage of the triple point at ear level. For distances beyond these values, an observer would be in the Mach stem and an N of 10 is more appropriate. Inside these values, N is closer to 5 provided you accept the instrumentation as being adequate.

A graphical solution for the $\bar{Y}$ and $\bar{Z}$ criteria can now be developed similar to that already presented for the $\bar{W}$ criterion. To develop this solution, the pressure equation (Eq. (5)), the duration equation (Eq. (8)), and the equation for the hearing loss threshold (Eq. (7)) must be combined. Unfortunately, the resulting expression is not an explicit one in either L/c or θ In functional format, the result is another four-parameter space given by:

$$F\left[\frac{Z(\text{prot})c^{1.855}\ell^{1.14}}{N^{0.345}W^{1.115}}, c, \theta, \frac{L}{c}\right] = 0 \qquad (10)$$

This four-parameter solution can also be presented graphically on three different plots for the different α values. Fig. 7 is one graphical representation of Eq. (10) with polar coordinates θ and L/c having been transformed into rectangular coordinates $L_\perp/c$ and $L_{||}/c$. Because the isoclines in Fig. 7 are $\frac{Zc^{1.855}\ell^{1.14}}{N^{0.345}W^{1.115}}$, a quantity that has not been made nondimensional by using constants such as the speed of sound in air and ambient atmospheric pressure, units of measure for these charts must be in milliseconds, meters and newtons. The most severe case occurs when the gun tube is fully depressed to 0 degrees. Once again as in the discussion with the $\bar{W}$ criterion, designers would probably be justified in using a 16.8° gun tube curve.

Comparison with Test Results

It is interesting to compare predicted safe standoff distances with experimentally measured results. As has already been indicated, test data on the XM204 firing a zone 8 has been obtained by placing blast pressure transducers at various locations

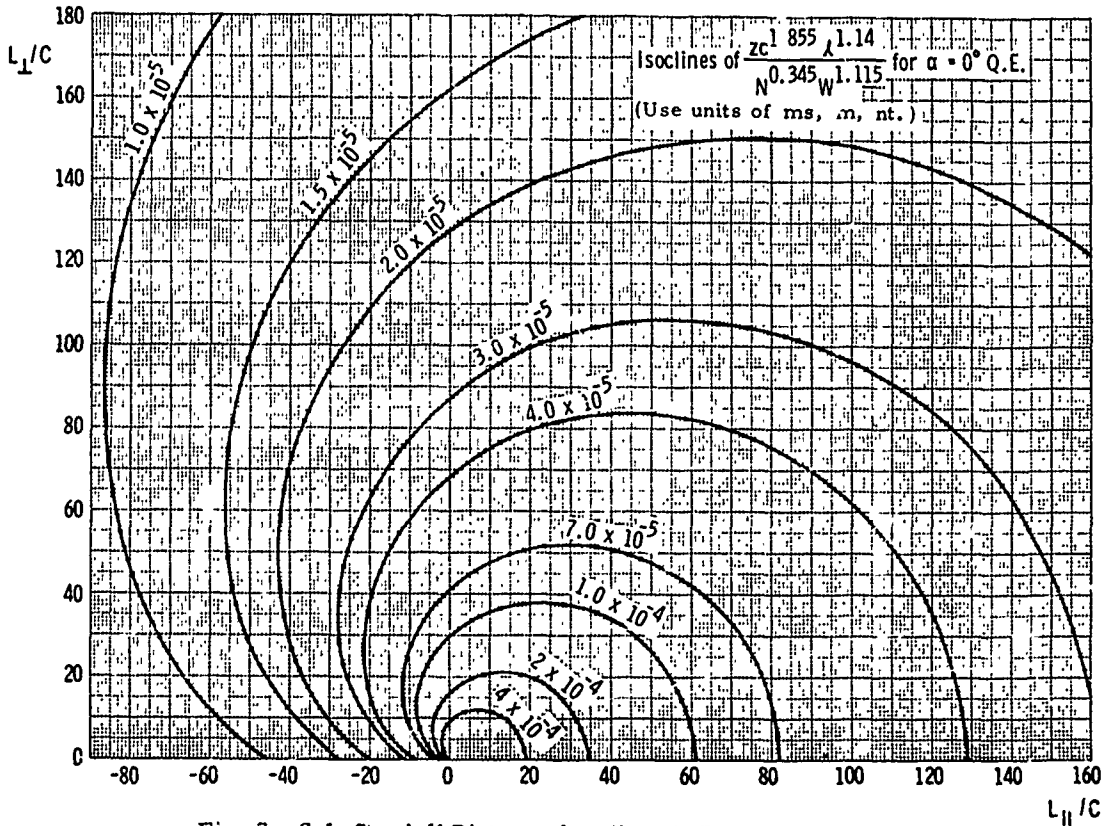


Fig. 7. Safe Standoff Distance for Y and Z ear Protection Levels

around gun muzzles. The different dots in Fig. 8 represent transducer locations. Both the maximum pressure and the sum of all positive durations were recorded outside the 20 dB envelope. These average recorded durations were multiplied by 5 to obtain an average estimated positive and negative duration. Fig. 1 from the noise standard was then entered using average pressure and duration to assess whether or not hearing is damaged. Blackened-in dots indicate that Fig. 1 predicts a definite hearing loss, whereas the white or open dots indicate no hearing loss. All partially shaded points in Fig. 8 indicate that this location was within one standard deviation for pressure (within 25%) of the Y or Z threshold from Fig. 1. Scatter does occur in pressure measurements, and such a procedure is a method of denoting uncertainty caused by this scatter. If the location showed that the threshold was exceeded by less than 25%, the dot has its lower half colored. If the location or the average was close to the threshold but under it, the dot has its right hand side colored. As can be seen in Fig. 8, the predicted threshold appears to separate hearing loss and no loss of hearing domains appropriately.

A large variety of conditions shown in Fig. 8 demonstrate that hearing loss and no loss of hearing domains are predicted accurately for the Z criterion as well as Y criterion, various values of N, other angles of gun tube elevation, and zone 7 as well as zone 8 charges. In all these figures, all blackened and open dots appear in the appropriate region and only occasionally do partially shaded dots appear in the wrong domain. Whenever a partially shaded dot is incorrect, it is close to the predicted threshold, and any errors are random. The fact that none of the partially colored dots are incorrect aft of the muzzle is probably good fortune rather than well conditioned physical behavior. By comparing the various Fig. 8 with each other, readers can obtain a feel for how changes in gun tube elevation, propelling charge, N factor, and level of ear protection influence safe standoff position.

For a 105-mm howitzer gun crew, gunner and assistant gunner positions are essentially 55 calibers aft. Figs. 8 imply that no hearing loss should result provided crew members wear either ear plugs or muffs. Loss of hearing should be expected whenever 105-mm howitzer crews wear no ear protection.

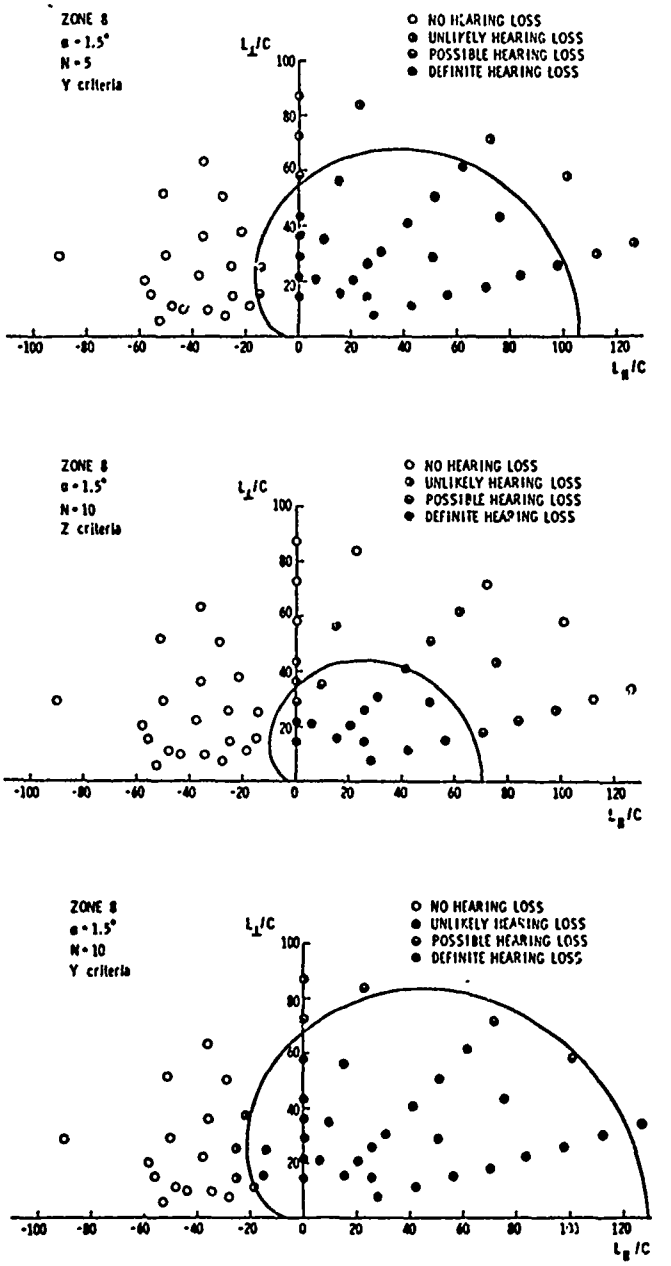


Fig. 8 Comparison Between Predicted and Measured Safe Standoffs for XM204 Howitzer

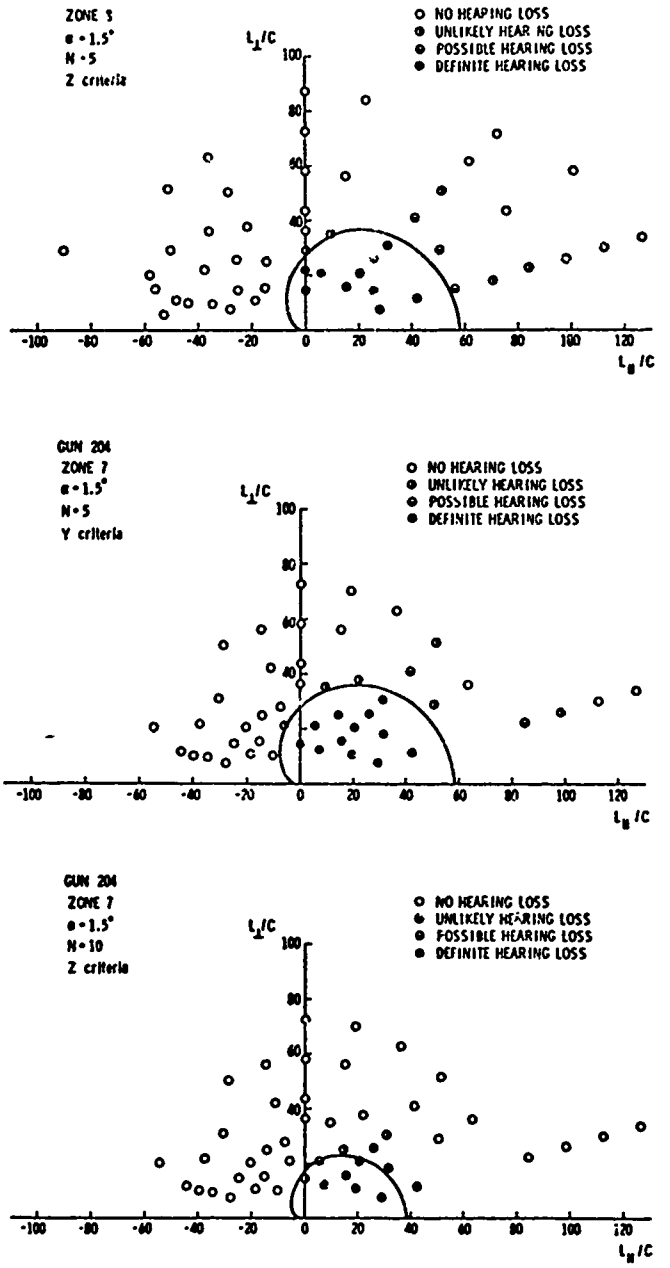


Fig. 8 Comparison Between Predicted and Measured Safe Standoffs for XM204 Howitzer (continued)

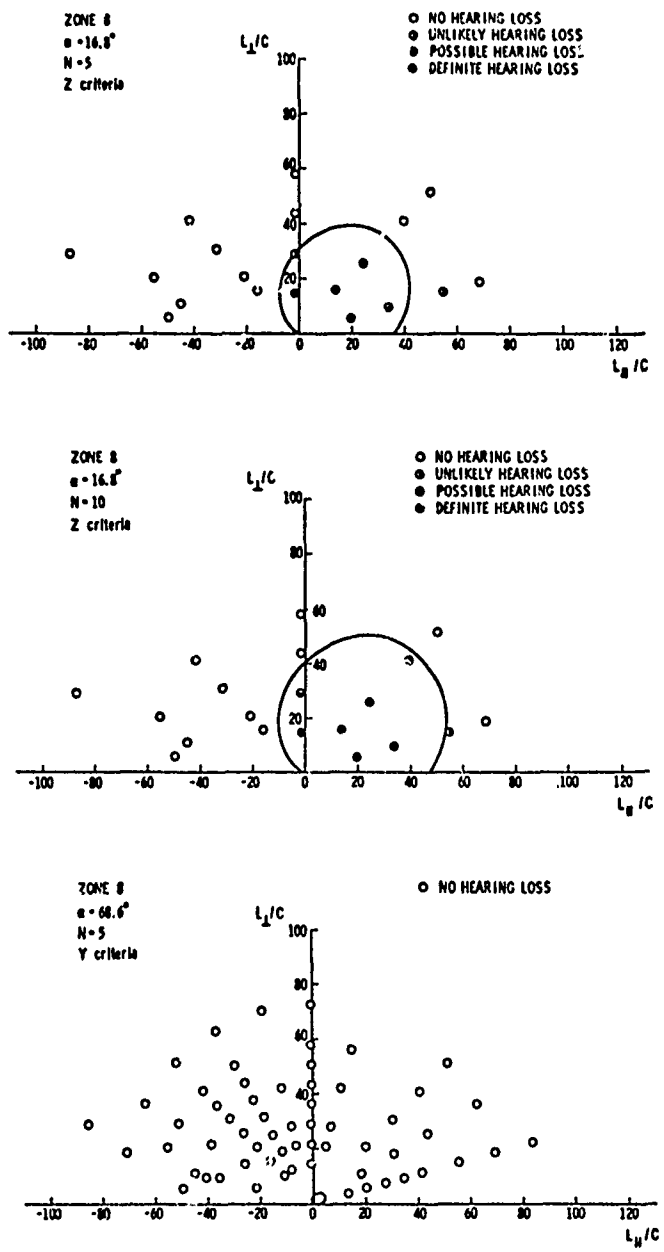


Fig. 8 Comparison Between Predicted and Measured Safe Standoffs for XM284 Howitzer (concluded)

SUMMARY

The primary purpose of this program was to establish a procedure for predicting safe standoff contours to protect gun crews from hearing loss. The contours were developed through a multi-step process by first conducting a model analysis to interrelate the parameters of interest. Then, the experimentally measured muzzle blast parameters, peak pressure and duration, were nondimensionalized and curve fit to empirically derived relationships as predicted from the model analysis. Finally, the empirical relationships were combined in a manner consistant with MIL-STD-1474 to produce the desired safe standoff contours for temporary hearing loss. Design nomographs are presented which graphically permit predictions of safe standoff locations whether ears are unprotected, protected with either plugs or muffs, and finally if ears are protected with both plugs and muffs. Experimental data from different 105 mm howitzer as well as Naval gun firings were used to verify the empirical relations for pressure and duration as well as to demonstrate that MIL-STD-1474 is consistent with these graphical procedures.

ACKNOWLEDGMENTS

The Army Technical Monitor on this program has been Mr. Mark Salsbury of Rock Island Arsenal, Rock Island, Illinois. His many positive suggestions and prompt cooperation contributed greatly to the overall success of this study.

At Southwest Research Institute, the authors are indebted to Miss Carolyn Evans, Mr. Emil Matula, and Mr. David McNew for the tedious job of reducing data from muzzle blast records. Mr. James Kulesz assisted the curve-fitting of empirical equations to test data, Mr. Victor Hernandez drew all figures, and Mrs. Sue Miller typed this paper. The cooperation of these individuals and those who are always inadvertently overlooked is appreciated.

REFERENCES

1. Military Standard Noise Limits for Army Material, MIL-STD-1474 (MI), March 1, 1973.

2. P.S. Westine and J. C. Hokanson, Prediction of Standoff Distances to Prevent Loss of Hearing from Muzzle Blast, SwRI report for Artillery and Armored Weapons Systems Directorate, No. R-CR-75-003, Rock Island Arsenal, Illinois, February 1975.

3. M. F. Walther, Gun Blast From Naval Guns, NWL Technical Report TR-2733, August 1972.

4. Mark J. Salsbury, Blast Field Study for Proposed RIA Firing Tunnel, Rock Island Arsenal TR-74-007, February 1974.

5. George T. Reynolds, Muzzle Blast Measurements, Report No. PMR-21, Princeton University for BRL, April 15, 1944.

6. U. S. Navy Gun Blast Committee, Survey of Research on Blast, First Interim Report, pp. 15-25, 1946, Confidential.

7. B. Hopkinson, British Ordnance Board Minutes 13565, 1915.

8. H. J. Barton, R. J. Heyman, and T. Schiffman, Correlation of Muzzle Blast Pressures Over Flat Surfaces, Armour Research Foundations of Illinois Institute of Technology, (undated, but apparently in mid-1950's).

9. Peter S. Westine, Structural Response of Helicopters to Muzzle and Breech Blast, Volume I, Blast Field About Weapons, SwRI Report for BRL under Contract No. DAAD05-67-C-0201, November 1968.

10. Peter S. Westine, The Blast Field About the Muzzle of Guns, The Shock and Vibration Bulletin, Part 6 of 6, pp. 139-149, March 1969.

11. Peter S. Westine, Modeling the Blast Field Around Naval Guns and Conceptual Design of a Model Gun Blast Facility, Final Report by SwRI for NWL under Contract No. N00178-69-c-0318, September 1970.

Discussion

Mr. Lepor (Naval Undersea Center): Part of our function is to develop noise exposure criteria for the Navy. Part of the problem has been to develop a nomogram but the problem really is that pistol shots have a different rise time and duration than the larger guns. How do you get all this on one line and still consider the rise time, the duration, and the number of firings per unit time? How does all of this fit in with these curves, aren't there other conditions that have to be stipulated?

Mr. Westine: The rise time is often for all practical purposes a question of transducer size relative to the wave length because it takes time for the wave front to traverse the sensing element and that is often what is recorded as a rise time. You can consider any of the rise times to be infinitely steep; an instrumentation phenomena is often observed and and I do not consider that to be reality. Of course you have tough instrumentation problems when you talk about a pistol because a pistol shot has such a short wave length and the transducer size has to be very small relative to the overall wave length. Sometimes you have to build your own transducers in order to measure around pistols or thirty caliber rifles because of the short wave length; and then often much of the data in the literature was using combinations that shouldn't have been used so you have to be judicious. Pistol propellants are very hot and a forty five caliber pistol uses an exceptionally hot propellant. In that the effective energy release at a value of "n" is very high for a pistol relative to what it would be for a three inch naval gun or any of the common naval guns. It is almost one for any of the naval guns and it would be about 50% or 60% higher for some of the Hercules powders that are used in pistols. In regard to the durations they scale and again you have to nondimensionalize them. There is more scatter on duration and one of the problems is that durations become asymptotic to zero pressures, and what is the duration when a wave dissipates and becomes very asymptotic to a line? But then there is a difference between scatter, whether it is random scatter or systematic scatter and I don't really feel that it is necessarily systematic.

Mr. Lepor: Do you use energy concepts as a basis of your calculations, and if so how do you handle the reduction of time by a factor of one half?

Mr. Westine: I am not in total agreement with that criteria, but I know its source. You have more familiarity than most of the audience and you would obviously avoid it because it becomes controversial. Instead of taking an absolute duration as you would observe it in the record they in essence made a ten percent curve which is 20 db below the peak and they put in bars above and below and they used that. I think that is an instrumentation phenomena that we often observe and I have been objecting quite strongly to that as a criteria. Yes, you can put that in this consideration and it is done by another factor N which goes along with those curves.

Mr. Lepor: Would this apply to the Red-eye weapon for example?

Mr. Westine: I am not familiar with that weapon but I think it is a tube launched rocket. For recoiless rifles or guns with open breeches however I would use some other results. You could use this type of procedure but I would use some other results. This as applied here is only for closed breech guns; you can't apply this yet, if you have screwed on a muzzle brake, a flash syppressor, or anything that would divert the flow of gasses coming out the muzzle. I have ideas on how it could be done and presented in the same way.

A STUDY OF THE SPACE SHUTTLE SOLID ROCKET BOOSTER NOZZLE WATER IMPACT RECOVERY LOADS

E. A. Rawls
Chrysler Corporation – Space Division
New Orleans, Louisiana

and

D. A. Kross
NASA, Marshall Space Flight Center
Marshall Space Flight Center, Alabama

Solid Rocket Booster (SRB) nozzle water impact environments are predicted by simplified analytical techniques in combination with scale model testing. The analytical approach, which provides preliminary design data, is based on an equivalent wedge approximation for the significant design events of maximum positive and negative applied loadings. The experimental program is performed to verify the analysis and to obtain more detailed design data.

Scale model water impact tests are conducted at the Naval Surface Weapons Center's Hydroballistics Facility using an 8.56 percent model and atmospheric pressure scaling. The vertical and horizontal initial impact velocities, as well as initial impact angle, are varied to obtain parametric loads information. Overall vehicle accelerations, local pressures, and nozzle/bulkhead interface loads are measured. Test results are compared to the analytically derived values.

INTRODUCTION

The National Aeronautics and Space Administration's Space Shuttle system, illustrated in Fig. 1, will employ an expendable External Fuel Tank (ET) and two reusable Solid Rocket Boosters (SRB). After burnout of the SRB Solid Rocket Motor (SRM), the boosters will separate from the Orbiter and ET, reenter the atmosphere, be decelerated by a parachute recovery system, and terminal impact in the ocean approximately 120 miles down range of the launch site. The complete SRB including major subsystem components are to be designed to survive all environmental loads of the recovery sequence of Fig. 2 to some minimum attrition or damage loss rate.

To minimize reentry stability, parachute packaging, and water impact load design requirements, the boosters will impact tail or nozzle first.

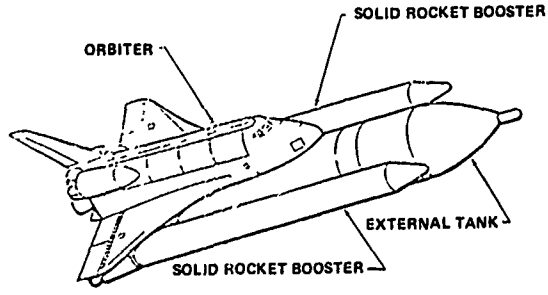


Fig. 1 - Space Shuttle configuration

This mode of water entry will take advantage of the higher drag tail-first configuration, thus preventing excessive penetration hydrostatic pressure loads while utilizing the hydropneumatic piston effect of the motor case and nozzle/skirt annulus to attenuate initial impact acceleration loads as well as retard

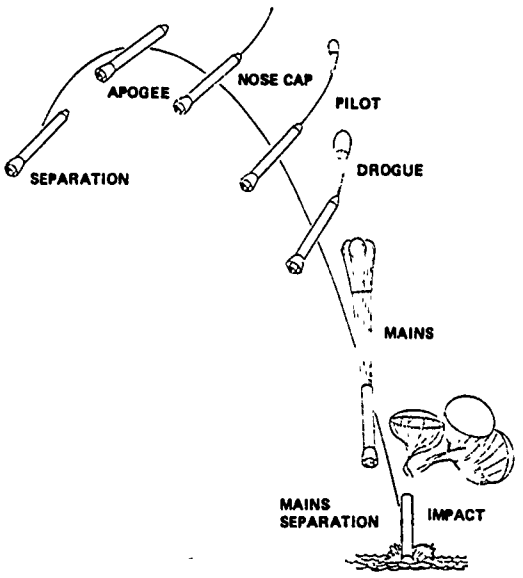


Fig. 2 - SRB recovery sequence

rebound. Water penetration will, however, subject the nozzle, aft skirt, and aft bulkhead to large impact pressure loads. The severe dynamic load applied to the gimbaled nozzle presents a unique design problem since this load must be reacted by the nozzle/bulkhead interface, flexible seal, actuators, and structural supporting systems illustrated in Fig. 3. SRB water entry may include oblique attitudes up to 10 degrees with a significant horizontal drift velocity component.

Definition of SRB structure and component loads during water impact does not lend itself readily to complete theoretical or empirical flow analyses. Also, available literature of water impact analyses is neither abundant nor widespread. That which does exist is primarily divided into four categories: (1) impact of sea plane floats on water or similar applications such as done by T. vonKarman [1]; (2) impact of torpedoes, warheads, or similar high speed projectiles as done by Hoover [2]; (3) impact of data or cargo modules such as data cassettes, camera pods, or manned capsules (Mercury, Gemini, and Apollo); and (4) academic studies of simple geometries such as disks, hemispheres, cones, and blunt-nosed bodies [3]. Reference searches have revealed almost no work to date on inverted cones and especially none on double annular conical surfaces such as the SRB nozzle/skirt presents.

The purpose of this paper is to present a review of the investigation conducted to define

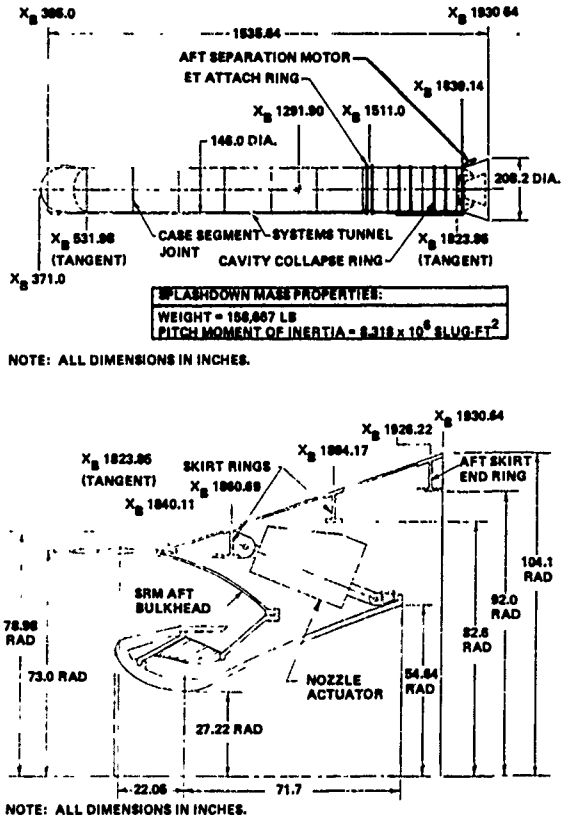


Fig. 3 - November 1, 1974 baseline SRB water impact configuration

transient dynamic loads applied to the Space Shuttle SRB nozzle on water impact. A description of flow phenomena, scale model test results, and comparisons with analytical estimates are presented and discussed for conditions pertinent to design of the SRB nozzle system.

WATER ENTRY DYNAMICS

As the SRB enters the water there are various phases that comprise the total dynamic sequence of motion (Fig. 4). Experimental test photographic studies adequately illustrate the body external flow phenomena for definition of its pertinent phases; however, nozzle and skirt internal flow phenomena can only be defined by interpretation of the various force and pressure measurements made during the scale model tests. Since all major nozzle loads occur during initial impact, nozzle filling, nozzle/skirt annulus filling, and stagnation of the annulus flow, we will only concern ourselves here with the first two vehicle dynamic flow conditions illustrated by Fig. 4. The various dynamic events are defined

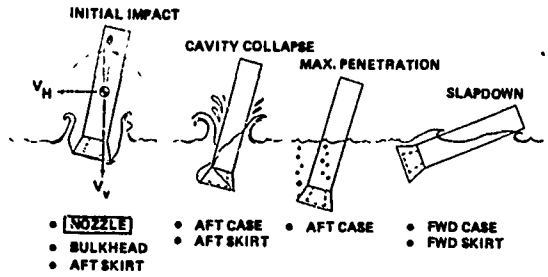


Fig. 4 - Water impact loading events

in order of their occurrence for an initial vertical impact condition with no horizontal velocity component. These events actually overlap and may alter slightly in time for impact conditions of oblique attitude or with increasing horizontal velocity.

Nozzle and Skirt Exit Plane Impact

Propagation of an acoustical pressure wave at initial water contact for this body configuration is insignificant. However, as the skirt aft ring penetrates accelerating an "induced mass" of water, the first deceleration force is sensed by the vehicle and a small downward inertial reaction nozzle force is applied at the nozzle/bulkhead interface. The impact of the skirt aft ring seals the volume of air captured in the complete nozzle/skirt/motor case internal chamber. The impact of the nozzle exit plane ring milliseconds later divides the captured air volume into two distinct compartments: (1) the nozzle internal and motor case chamber; and (2) the annular cavity between the nozzle and skirt, as illustrated in Fig. 5. The compression of these air volumes has a significant role in the vehicle dynamics as it continues to penetrate.

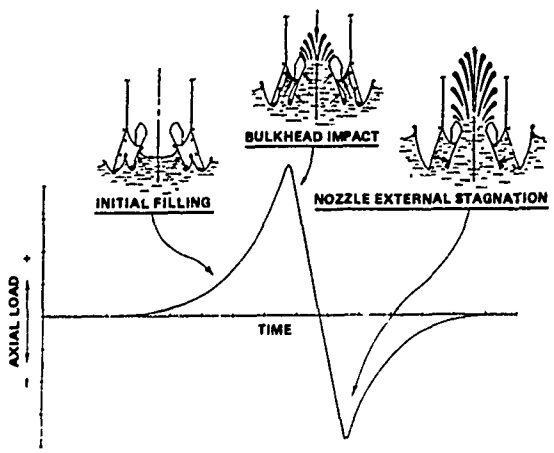


Fig. 5 - Load transient flow field

Nozzle Internal Flow Establishment

As the nozzle internal volume fills, positive axial forces are applied to the nozzle forcing it into the bulkhead. These forces are a function of the "induced or added mass" characteristics of the nozzle internal conical convergent surface (i.e., the rate of change of effective water displacement by the inverted cone geometry). This geometric convergence also results in the water level in the nozzle rising with increasingly greater velocity than the vehicle external free water surface, as depicted in Fig. 5. Impact conditions of oblique attitude and/or with a horizontal velocity component result in asymmetric flow fields producing large resultant forces normal to the nozzle axis in addition to the axial loads.

After penetrating the nozzle throat, water is jettisoned into the motor case chamber and a quasi-steady-state flow is established in the nozzle. During initial filling of the nozzle, compression of the trapped air volume in the nozzle/motor case chamber is insignificant and can be neglected. However, with continued penetration depth after collapse of the vehicle external open cavity, this trapped air volume is the primary buoyancy force defining terminal deceleration and final penetration depth.

Nozzle/Skirt Annulus Flow

Simultaneous with nozzle filling, a water head is also penetrating the annular cavity between the nozzle and skirt. To define flow development in this region, it must be remembered that the skirt has large internal structural rings, as shown previously in Fig. 3. Each of the rings produces local flow cavitation wakes that collapse as the water head stagnates on impact with the SRM aft bulkhead surface. As the annulus initially fills, pressures and forces are defined by impact of the water head on the various local surfaces. Immediately following impact with the bulkhead, the complete annulus volume stagnates collapsing all local cavitation wakes, which results in maximum vehicle axial forces. This stagnation condition produces a negative axial load, pulling the nozzle away from the bulkhead as a result of the difference in the annulus stagnation pressures and the lesser nozzle internal pressures that are approaching steady state values. For initial impact conditions of oblique angles or with a horizontal velocity component, impingement of the water head with the bulkhead is not symmetric, but propagates from the effective keel to lee side producing large resultant lateral load transients as well.

ANALYTICAL PREDICTION OF NOZZLE AXIAL FORCES

Predictions of nozzle axial forces can be made to an acceptable accuracy for initial impact conditions of vertical entry with no horizontal velocity by a two-phase flow analysis. The first axial force phase, thrusting the nozzle into the bulkhead, can be treated solely as a function of the nozzle internal flow assuming that nozzle external pressures are small. This should at least provide an estimate of the maximum positive axial forces, while the nozzle negative axial forces pulling the nozzle away from the bulkhead can be estimated by assuming stagnation pressures in the nozzle/skirt annulus and quasi-steady-state pressures in the nozzle. Only the maximum values of both types of forces have been evaluated by this approach, even though it should be feasible to set up a more exact time-stepping computerized solution to provide a reasonable approximation of the load time transient. Also the multiple phase flow analyses required to analyze oblique entries or entries with a horizontal velocity component would be another order of complexity and have not been attempted except for the initial phase of maximum positive axial forces considering only oblique angles of impact with no horizontal velocity component. Fig. 6 presents the nozzle analytical geometry used in the analytical predictions.

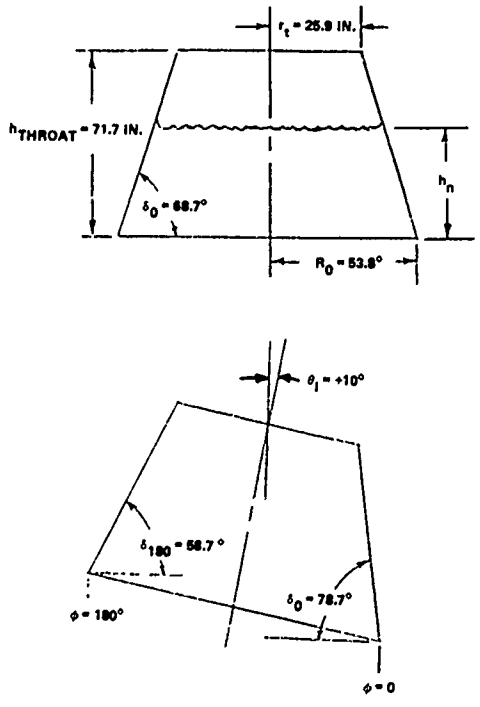


Fig. 6 - Nozzle analytical geometry

Phase I -- Maximum Positive Nozzle Forces

Since no reference data could be found on the hydrodynamic drag or water impact "added mass" characteristics of convergent conical surfaces, an equivalent wedge approximation was used as presented by Kwark [4]. Using the Schwartz-Christoffel mathematical transformation and potential flow theory, the resultant force per unit width on one side of a wedge may be expressed as:

$$f_{wed} = \rho \cdot V^2 \cdot h \cdot \frac{1}{\sin \delta} \left\{ \frac{\pi - 2\delta}{\sin 2\delta} \cdot \frac{\pi}{\left[\Gamma\left(1 - \frac{\delta}{\pi}\right) \cdot \Gamma\left(\frac{1}{2} + \frac{\delta}{\pi}\right)\right]^2} - 1 \right\} \qquad (1)$$

where

ρ = density of water

V = free stream velocity

δ = wedge dead rise angle

Γ = gamma function

h = depth at time, t .

This relationship may be applied to evaluate the impact force per unit circumferential arc in the nozzle, assuming:

1. The effect of radial curvature of the nozzle wall on the axial flow field is small for low convergence angles (δ = 68.7° for the SRB nozzle).

2. The flow field in the nozzle is not affected by flow external to it, except for some reduction in total vehicle velocity.

Generally, initial impact solutions of wedges and other simplified external flow bodies assume no change in penetration velocity over the period of maximum deceleration buildup ($V = V_o$ = cont.), and depth (h) is defined as $V_o \cdot t$. However, due to conical convergence of the nozzle internal surface, both water velocity and height in the nozzle would be significantly accelerated above that of the external free surface; therefore, adjustments should be made to the wedge approximation by:

1. The difference between the hypothetical external free surface h and the real nozzle internal water surface can be adjusted by letting,

$$h_n = \bar{V} \cdot \Delta t = \left(\frac{r_E}{\bar{r}}\right)^2 \cdot V_o \cdot \Delta t = \left(\frac{r_E}{\bar{r}}\right)^2 \cdot h \qquad (2)$$

where

h = external free surface height ($V_o \cdot \Delta t$)

h_n = water surface height in nozzle

r = nozzle radius at level, h_n

r_E = nozzle exit radius

and

2. The change in flow velocity in the nozzle can be estimated by letting V equal some average velocity $\bar{V}$ between the initial exit plane impact value (V_o) and the local value (V) at nozzle internal water level h_n, and applying constant mass flow relationships, giving:

$$\bar{V} = V_o \left(\frac{r_E}{\bar{r}}\right)^2 \qquad (3)$$

where

$\bar{V}$ = average velocity of nozzle internal flow at time, t

$\bar{r}$ = nozzle radius at centroid of nozzle wetted area.

Substituting relationships (2) and (3) into Eq. (1) defines the force per unit arc width normal to the internal nozzle surface as:

$$f_{ARC} = \rho \cdot V_o^2 \cdot \left(\frac{r_E}{\bar{r}}\right)^6 \cdot h \cdot f(\delta) \qquad (4)$$

where

$$f(\delta) = \frac{1}{\sin \delta} \left\{ \frac{\pi(\pi - 2)}{\sin 2\delta \left[\Gamma\left(1 - \frac{\delta}{\pi}\right) \cdot \Gamma\left(\frac{1}{2} + \frac{\delta}{\pi}\right)\right]^2} - 1 \right\} \qquad (4a)$$

At oblique angles of impact less than the nozzle half-cone angle (21.3 degrees), Eq. (1) indicates that water impact forces are single-valued functions of the nozzle equivalent wedge angle, δ. The effective equivalent wedge angle δ_ϕ of each radial element is an explicit function of the radial angle for oblique impact. Consequently, axial and lateral forces acting on the nozzle at the maximum positive axial loading event can be calculated by summing the forces on each radial element of the nozzle wetted internal surface. This produces the relationships:

$$F_{AX} = 2\left(\frac{r_E}{\bar{r}}\right)^6 \cdot h \cdot \cos^3 \theta_i \cdot \rho V_o^2 \cdot \frac{\sin \alpha}{57.3} \int_0^{180} f(\delta_\phi)\, d\phi \qquad (5)$$

$$F_{LAT} = 2\left(\frac{r_E}{\bar{r}}\right)^6 \cdot h \cdot \cos^3 \theta_i \cdot \rho V_o^2 \cdot \frac{\cos \alpha}{57.3} \int_0^{180} f(\delta_\phi) \cos d\phi \qquad (6)$$

where

$$f(\delta_\phi) = \frac{1}{\sin \delta_\phi} \left\{ \frac{\pi(\pi - 2\delta_\phi)}{\sin 2\delta_\phi \left[\Gamma\left(1 - \frac{\delta_\phi}{\pi}\right) \cdot \Gamma\left(\frac{1}{2} + \frac{\delta_\phi}{\pi}\right)\right]^2} - 1 \right\} . \qquad (7)$$

From these expressions maximum positive forces due to nozzle internal flow, disregarding external flow pressures, occur when the nozzle internal waterline reaches the throat, where h_n equals total nozzle length from exit plane, o indicates throat, and $\bar{r}$ is a minimum.

For the Space Shuttle SRB configuration considered here, these values are, approximately:

r_E = 53.8 inches

r_{throat} = 25.9 inches

$\bar{r}$ = 42.6 inches

δ = 68.7 degrees

h_n = 71.7 inches.

Fig. 7 presents the variation of nozzle positive axial and lateral loads with initial vertical

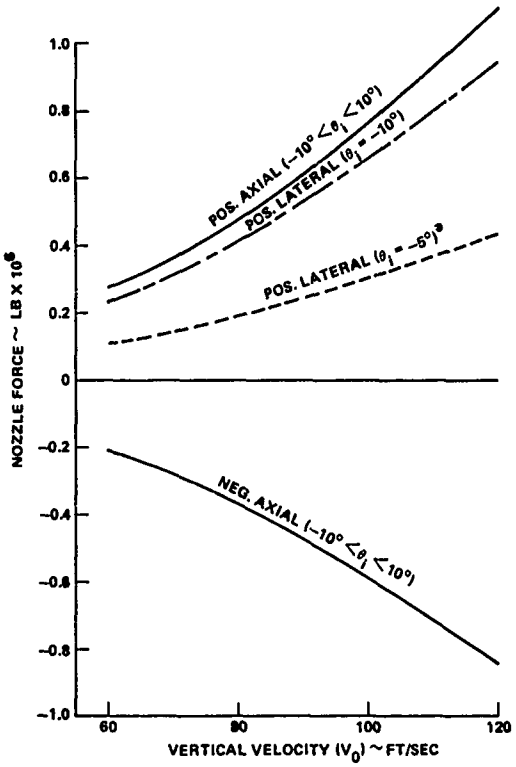


Fig. 7 - Analytical estimates of nozzle maximum forces

impact velocity. As can be seen by inspection of the equations, forces vary by the square of the velocity (V_o) or linearly with the dynamic load (ρV_o^2) for a given nozzle geometry and impact attitude (θ_i).

Phase II — Maximum Negative Axial Forces

Immediately following complete filling of the nozzle, the nozzle/skirt annular flow impacts the bulkhead and stagnates the cavity. By this time, nozzle internal pressures have decayed to quasi-steady-state flow values. The differential between internal static and external stagnation pressures then produces a sharp reversal of the previously defined positive applied loads to large negative loads. Estimates of maximum values can be made by defining the stagnation pressure forces applied to the nozzle external surface and the steady state pressure forces applied to the internal surface.

Assuming peak stagnation pressure, let

$$P_{ANNULUS} = 2 \cdot q_o = 2 \cdot \frac{\rho}{2} \cdot V_o^2 \qquad (8)$$

where

q_o = water dynamic head at initial impact $\left(\frac{1}{2}\rho V_o^2\right)$.

The resultant axial force applied to the nozzle external surface becomes

$$F_{X_{ext}} = P_{ANNULUS} \cdot A_{P_{ext}} = \rho \cdot V_o^2 \cdot A_{P_{ext}} \qquad (9)$$

where

$F_{X_{ext}}$ = nozzle externally applied axial force

$A_{P_{ext}}$ = axial projection of exposed external nozzle surface area.

As before, an equivalent wedge approximation can be used to define the nozzle internal surface axial force component. For steady state cavitating flow, the drag coefficient of a wedge half angle ($\alpha = 21.3°$) is $C_{P_{wed}} \approx 0.154$ as defined by Lamb [5]. Therefore,

$$F_{X_{int}} = C_{P_{wed}} \cdot A_{P_{int}} \cdot \bar{q}_{int} \qquad (10)$$

where

$F_{X_{int}}$ = nozzle internal surface axial force component

$C_{P_{wed}}$ = pressure coefficient on equivalent wedge surface

$A_{P_{int}}$ = axial projection of nozzle internal surface area

$\bar{q}_{int}$ = mean dynamic pressure in nozzle (varies with length due to convergent area acceleration of flow).

The effect of nozzle internal surface convergence on velocity is handled the same as before, i.e.,

$$\bar{q}_{int} = \frac{\rho}{2} \cdot \bar{V}_{int}^2 \qquad (11)$$

where from Eq. (3)

$$V_{int} = V_o \left(\frac{r_E}{\bar{r}}\right)^2$$

This gives

$$F_{X_{int}} = C_{P_{wed}} \cdot \frac{\rho}{2} \cdot V_o^2 \left(\frac{r_E}{\bar{r}}\right)^4 \cdot A_{P_{int}} \quad (12)$$

Now, solving for the net applied axial force using Eqs. (9) and (12)

$$F_{X_{net}} = F_{X_{ext}} - F_{X_{int}}$$

$$F_{X_{net}} = \rho \cdot V_o^2 \left[A_{P_{ext}} - \frac{1}{2} C_{P_{wed}} \left(\frac{r_E}{\bar{r}}\right)^4 A_{P_{int}}\right] \quad (13)$$

By this approximation, maximum impact negative axial loads vary only with impact velocity (V_o) for vertical entry with no horizontal velocity component. Fig. 7 presents the variation of nozzle maximum negative axial force with initial vertical impact velocity.

SCALE MODEL TEST PROGRAM

Performing water impact tests on a full scale vehicle is impractical because of the cost and time of both constructing and testing a full scale structure. The most feasible approach is to investigate the theory of water entry and to perform scale model tests of the SRB using proper scaling relationships. Loads on the full scale vehicle can then be defined by extrapolation of the scale model test data. As part of the experimental research study a 12.5 inch diameter (8.56 percent) scale model was subjected to a series of water impact tests measuring nozzle pressures, accelerations, and forces, as well as other pressures and forces acting on the total vehicle during the various phases of water penetration and rebound. Initial impact conditions were varied over the complete range to develop design load dependency relationships.

Scaling Parameters

At the onset of initial contact with a water surface, the compressibility effects of the water are of importance. Pressures exerted on the vehicle have the magnitude of $\rho V_o c$, where c is the speed of sound in water. Although the acoustic pressure ($\rho V_o c$) is large, it acts over such a short time duration and small area of this configuration that it does not influence the vehicle or local loads to a significant degree. Therefore, scaling of initial contact acoustic pressures was not included in the SRB model testing.

During the remainder of the initial impact phase, the nozzle and skirt fill with water exerting pressure forces that decelerate the vehicle. To simulate full scale vehicle dynamics in scale model tests, the significant vehicle properties pertinent to this phase must be correctly scaled. In the case of nozzle initial impact loads, this requires scaling of the vehicle momentum and buoyancy relationships. Kwark [6] presents a concise derivation of applicable scaling laws for each of these, which requires Froude scaling for momentum conservation and pressure scaling for buoyancy force simulation. For momentum scaling the relationships are:

Dimensional Lengths	$L_m = \lambda L_p$
Velocity	$V_m = \sqrt{\lambda}\, V_p$
Time	$t_m = \sqrt{\lambda}\, t_p$
Pressures	$P_m = \lambda P_p$
Forces	$F_m = \lambda^3 F_p$
Area	$A_m = \lambda^2 A_p$
Accelerations	$a_m = a_p$
Mass	$M_m = \lambda^5 M_p$

where

m = model value

p = full scale prototype value.

Buoyancy force scaling requires that the pressure of the air sealed in the nozzle and skirt at initial impact also be reduced to $P_m = \lambda P_p$. This was achieved by lowering the atmospheric pressure above the water to $P_{AMB} = \lambda \cdot 14.7$ psia.

Test Program Description

The model used for this test program was an 8.56 percent Froude scaled rigid body simulation of the Space Shuttle 146 inch diameter cylindrical body section, 123.2 inches long with a short 18° 45' flared skirt giving an overall model length of 131 inches. The forward end of the model is closed with a flat bulkhead, and the aft end has a hemispherical bulkhead with a 3.9 to 1 area ratio nozzle. The model was fabricated from 2219 aluminum with a skin thickness of 0.08 inches. Fig. 8 illustrates the model geometry and principal dimensions. This configuration represents the SRB with the nozzle extension jettisoned.

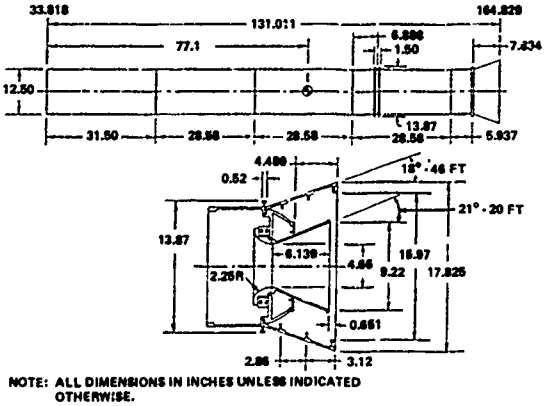


Fig. 8 - Model geometry

The model with instrumentation weighed 107 pounds with the center of gravity 77.1 inches aft of the forward bulkhead and a pitch moment of inertia of 40.9 slug-ft^2. These mass characteristics do not include the model instrument cable, which weighed approximately 0.97 pounds per foot, attached to the model.

Testing was conducted in the Hydroballistics Tank at the Naval Surface Weapons Center, White Oak, Maryland. The tank is 35 feet wide, 100 feet long and 75 feet deep with a water depth variable from 0 to 65 feet. To preserve water clarity, the tank is lined with stainless steel and the water is continuously filtered. A 2 foot thick reinforced concrete honeycomb structure surrounds the tank and is designed to permit reduction of air pressure above the water for model scaling. Steam ejectors located on the building roof are used to evacuate the tank for pressure scaled tests.

The test model was instrumented with 56 strain gage type transducers. These consisted of 5 accelerometers, 47 pressure transducers, and a 4-component strain gage force balance which measured nozzle loads. Model cylinder body transducers included 14 keel pressures, 6 transducers on the lee side to measure cavity collapse pressures, and 2 internal pressures at the aft bulkhead to indicate internal water depth during slapdown. An axial and a pitch accelerometer were mounted on the model forward and aft bulkheads, with a third pitch accelerometer mounted near the center of the model.

Fig. 9 illustrates the tail section pressure transducer locations, consisting of 3 bulkhead, 8 nozzle, and 12 skirt transducers. Those on the nozzle and skirt were arranged to measure both internal and external pressure distributions. Fig. 10 presents a photographic view of the actual model from the base.

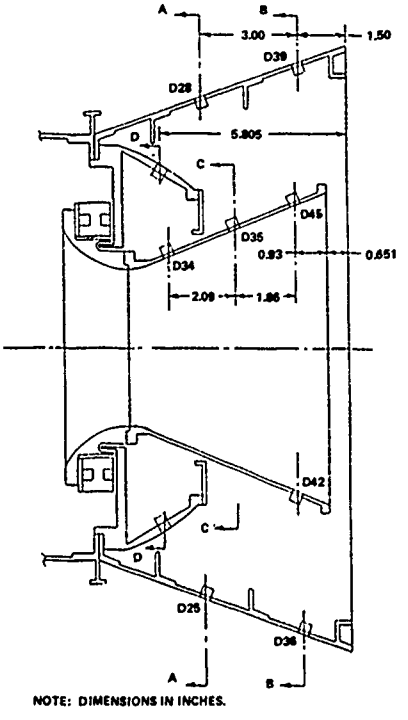


Fig. 9 - Model nozzle/skirt pressure transducer locations

The nozzle and bellmouth were attached to the aft bulkhead through a four-component strain gage force balance. This balance encircled the bellmouth 1 inch forward of the nozzle throat and was of a moment cage design so that forces and moments are measured by individual strain gage bridges (Fig. 11). Components measured were axial force, normal force, pitching moment, and yawing moment.

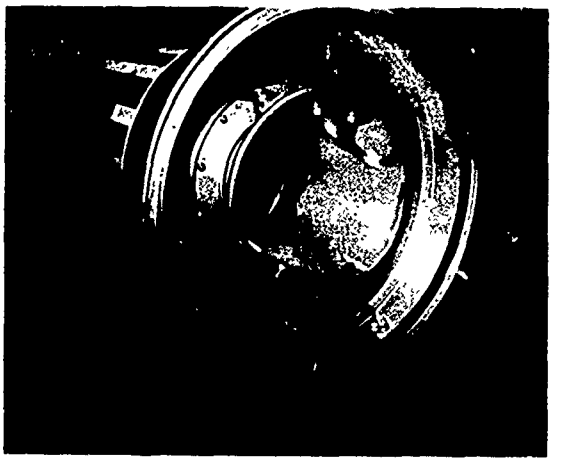


Fig. 10 - Test model nozzle/skirt section

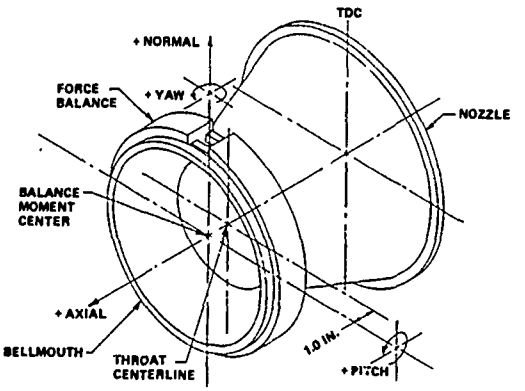


Fig. 11 - Nozzle force balance

Transducer signals were transmitted from the model through an instrument cable that was attached to the model top centerline near the center of gravity. This cable was approximately 1.5 inches in diameter, 50 feet long, and weighed 48.5 pounds. Model instruments were waterproofed with a combination of scotch cast epoxy resin, RTV, and silicone grease. To protect the pressure transducers from thermal shocks, the diaphragms were recessed approximately 1/16 inch below the model skin and covered with RTV.

Photographic coverage for this test was provided by two high speed 16 mm data cameras, one 16 mm documentary camera, and a television camera. The data cameras were set up in portholes perpendicular to the model pitch and yaw planes at the water surface. Data cameras were sighted so that the lens centerline was at the water surface to permit split waterline viewing above and below water with each camera. Both cameras ran at approximately 250 frames/second and had a 60 cps timing signal.

The test program was conducted from October 4, 1974, through November 1, 1974. A total of 69 drops were made during the test program. Forty drops were made at a scaled atmospheric pressure of 1.26 psia, and 29 drops were made without pressure scaling. Impact conditions consisted of model scale vertical velocities of 23.4 and 29.3 ft/sec, at horizontal drift velocities of 0, 4.4, 8.8, and 13.1 ft/sec, and with impact angles of 0, ±5°, and ±10°. Model test velocities were Froude scale values of full scale conditions corresponding to 80 and 100 ft/sec vertical and 0, 15, 30, and 45 ft/sec horizontal. Fig. 12 is a photographic view of the model in the launcher system employed to provide horizontal velocities. Reference 7 presents all measurements made in these tests with complete definitions of test program, instrumentation, data system, and data processing.

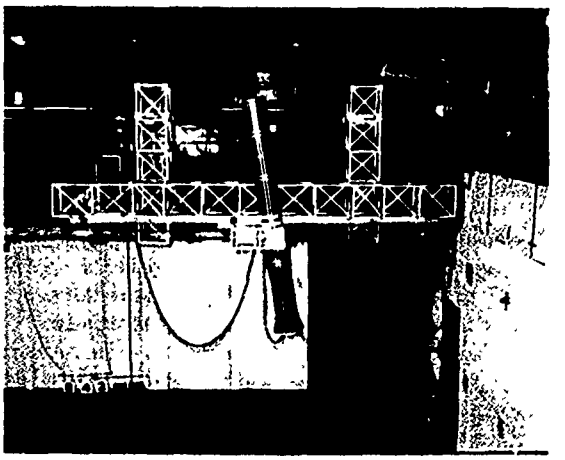


Fig. 12 - Model test setup

TEST DATA ANALYSIS

In the process of demultiplexing each channel of the test analog data tape, all data were filtered to 100 Hz for clarity. This would be equivalent to approximately 30 Hz full scale, which is sufficient definition of the forcing function for the nozzle system which should have a design natural frequency of approximately 7 Hz. Next the data were converted from a real time analog signal to a digital format consistent with the UNIVAC 1108 Fortran IV computer system. All data were adjusted for initial bias, and strain gage force balance measurements were corrected for interactions. Data of all

transducers were then plotted as a function of model scale time for use in analyses.

Nozzle Applied Hydrodynamic Forces

Since the strain gage force balance mounted between the nozzle and bulkhead measured only the interface load at that point, nozzle applied hydrodynamic forces must be defined by adding the nozzle inertial reaction force time history to this measurement time history, or

$$F_{APPLIED_{@t}} = F_{MEASURED_{@t}} + (Mass_{noz} \times a_{@t}) \quad . \quad (14)$$

For all practical purposes the strain gage force balance flexures were rigid compared to the frequency of the applied force; therefore, bulkhead accelerometer measurements could be applied directly as nozzle accelerations.

Time histories of nozzle axial and lateral scale model test loads compared to analytically defined peak values are shown in Fig. 13 for a typical maximum loading initial impact condition. The forces and time scale can be ratioed to prototype values by the Froude relationships presented. These loads actually represent those that would be applied to a rigid system and do not include attenuation or amplification which might occur due to elastic properties of the full scale vehicle system. A complete dynamic response analysis of the system using these loads will be conducted to define actual response design loads; however, a simplified one-dimensional analysis of this forcing function to the design natural frequency of the nozzle/actuator/flexible seal system indicates attenuation and/or amplification will be small and rigid body peak magnitudes of the data may be applied. Fig. 14 presents carpet plots of full scale positive and negative load peaks as functions of initial impact conditions.

As stated previously, compression of the air column between the nozzle and skirt was quite significant to nozzle forces. Fig. 15 shows a comparison of pressure scaled versus non-pressure-scaled test data at identical impact conditions. There is little similarity between the two and it can be rationalized that non-pressure-scaled data differs because:

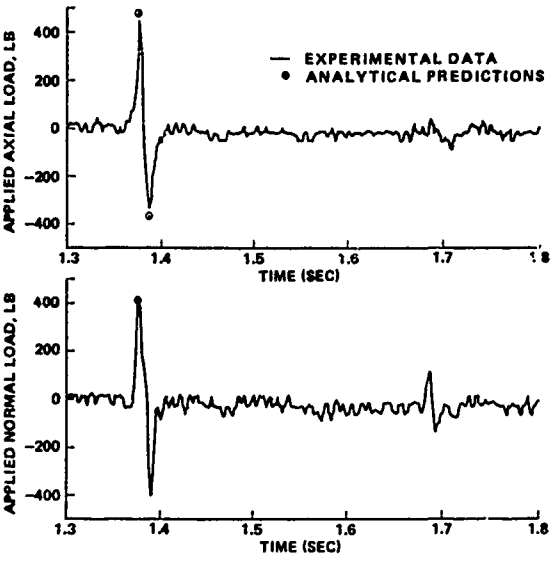


Fig. 13 - Model scale nozzle load time histories (V_V = 100 ft/sec, V_H = 0, θ = -10°)

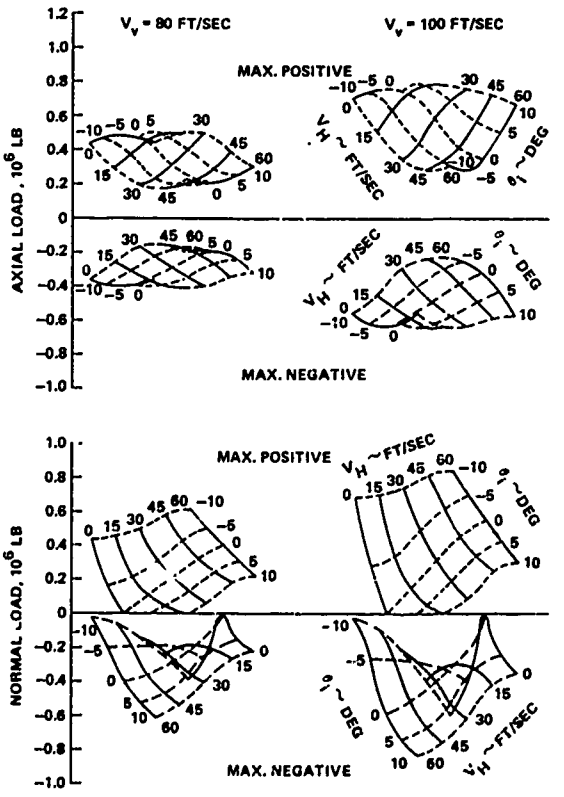


Fig. 14 - Nozzle maximum applied loads

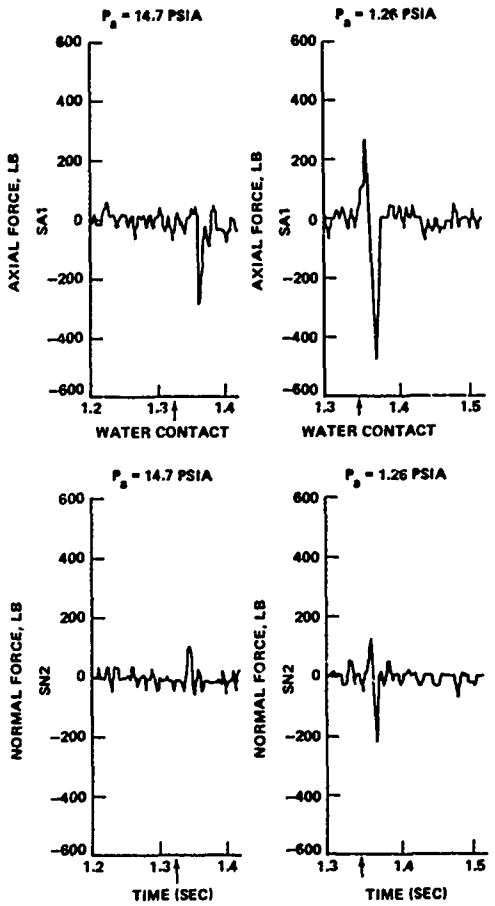


Fig. 15 - Comparison of test model nozzle/bulkhead interface forces for pressure scaled and unscaled test condition ($V_V/V_H/\theta$ = 100/0/-10°)

1. Rapid compression of the air column between the nozzle and skirt produces higher nozzle external pressures prior to bulkhead impact than the pressure scaled simulation.

2. Stagnation impact of the annulus flow with the bulkhead is attenuated and diffused by the compressed air column, resulting in very small negative rebound nozzle loads.

Nozzle Pressures

Pressures measured on the internal and external nozzle surfaces as well as skirt internal and bulkhead pressures substantiate the force measurements. Using typical cosine radial distribution factors, the pressures were integrated, comparing well with measured applied forces. The pattern of pertinent pressures, forces, and accelerations illustrated by the time traces of Fig. 16 give a vivid description of the sequence of events defining nozzle/skirt internal flow.

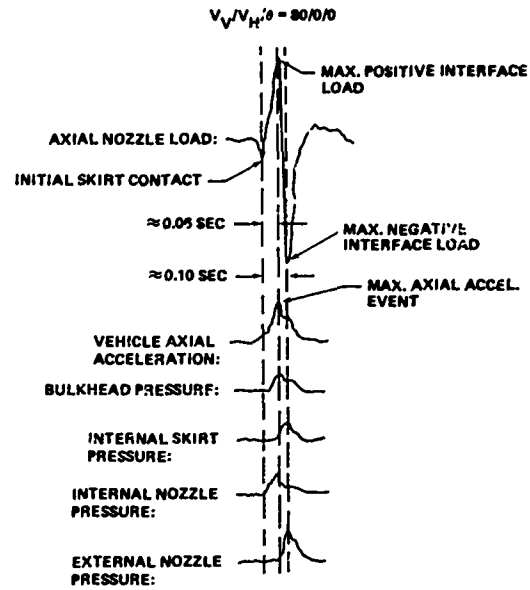


Fig. 16 - Time correlation of data transients

At initial impact of the aft skirt ring, the nozzle is seen to first experience a slight negative (nozzle being pulled away from the bulkhead) axial resultant load, due to the applied deceleration of the vehicle prior to wetting of the nozzle. Vheicle axial deceleration immediately begins to rise and as the nozzle becomes wet, internal surface pressures are applied and maximum positive nozzle loading occurs. Peak vehicle deceleration occurs with impact of the water hydrodynamic head on the bulkhead reflected by its measured pressure, and complete stagnation of the nozzle/skirt annulus is exemplified by peak skirt internal and nozzle external pressures. At this time, nozzle axial load bottoms out at its maximum negative value.

SUMMARY

Water impact recovery of NASA's Space Shuttle Solid Rocket Boosters will be tail first, subjecting the Solid Rocket Motor nozzles to large transient hydrodynamic and inertial loads. Since it was not cost effective to conduct full scale vehicle tests to define these loads, an 8.56 percent scale model experimental study was conducted in the Naval Surface Weapons Center's Hydroballistic Tank by Marshall Space Flight Center in October 1974. These tests measured nozzle pressures, vehicle

accelerations, and nozzle/bulkhead interface forces, as well as other data necessary to define additional vehicle loading conditions.

Analytical estimates of the peak nozzle loads can be made that agree well with the test data for simplified entry conditions of no horizontal velocity and small oblique angles. Results of this study have been used to define SRB prototype design requirements by analyses and correlation of the test data and application of proper scaling laws. This paper presents a review of: (1) the various flow phases defined by water penetration, (2) the analytical approach for preliminary estimates of loads, and (3) the scale model experimental program.

NOMENCLATURE

a	— acceleration
A	— area
A_p	— axial projected area
c	— speed of sound in water
c.g.	— center of gravity
C_d	— coefficient of drag, DRAG/qS
D	— diameter
D1, D2, D3, etc.	— pressure transducers (see Fig. 9)
f	— local force per unit area
$f(\delta)$	— function, Eq. (4a)
$f(\delta_\phi)$	— function, Eq. (7)
F	— total force
Fr	— Froude number
g	— gravitational acceleration, 32.1725 ft/sec^2
h	— water height in nozzle
I	— moment of inertia
L	— length
M	— mass
m	— added or virtual mass
P	— pressure
q	— dynamic pressure, $1/2\,\rho V^2$
$\bar{q}$	— mean dynamic pressure
r	— local nozzle radius
$\bar{r}$	— average nozzle radius
t	— time, sec
Δt	— time increment, sec
V	— velocity, ft/sec
$\bar{V}$	— average velocity [see Eq. (3)]
W	— weight
x	— centerline axis of vehicle
y	— vertical displacement
z	— axis normal to vehicle centerline in pitch plane
α	— nozzle conical half angle, 21.3° (see Fig. 6)
Γ	— gamma function
δ	— complement of flow defection angle
δ_o	— δ for $\theta_i = o$ (see Fig. 6)
δ_ϕ	— δ at radial angle (see Fig. 6)
θ	— angle between vehicle centerline and vertical (pitch plane angle)
θ_i	— pitch plane angle at initial impact
λ	— linear Froude scale factor (0.0856 for model tested)
π	— mathematical constant, 3.141593
ρ	— density of water
ϕ	— nozzle radial angle

Subscripts

a	— ambient air
ANNULUS	— conditions in nozzle/skirt annular cavity
APPLIED	— applied force
ARC	— per unit arc width
AX	— in axial direction
B	— body station (inches)
E	— values at nozzle exit plane
ext	— nozzle external values
F.S.	— full scale values
i	— values at initial impact
int	— nozzle internal values
LAT	— in lateral direction
m	— scale model
MAX	— maximum value
MEASURED	— force balance measured value
n	— nozzle
net	— resulting net nozzle force
noz	— nozzle
o	— value at initial impact
P	— full scale prototype
' or "HROAT	— at nozzle throat
T	— total
v	— vertical component
wed	— wedge
X	— axial direction parallel to vehicle centerline
Z	— lateral direction normal to vehicle centerline
ϕ	— function of radial angle, ϕ

Abbreviations

ET	— External Tank of the Space Shuttle System
MSFC	— Marshall Space Flight Center of NASA
NSWC	— Naval Surface Weapons Center of White Oak, Maryland
PVC	— Polyvinyl Chloride, type of plastic
RTV	— Room Temperature Vulcanizing rubber
SRB	— Solid Rocket Booster of the Space Shutle System
SRM	— Solid Rocket Motor of the Space Shuttle Solid Rocket Booster

REFERENCES

1. T. vonKarman, "The Impact on Seaplane Floats During Landing," NACA TN-321, 1929.

2. W. R. Hoover and P. J. Reardon, "Approximate Impact Drag Coefficient for the Vertical Water-Entry of Families of Cone, Ellipsoidal, and Tangent Ogive Nose Missiles," NOL TR 64-110, October 1964.

3. V. Dawson and A. Siegel, "The State of Art of Water-Entry Technology," NOL TR 70-209, September 1970.

4. K. C. Kwark, "Maximum Water Impact Loads for the Space Shuttle 5/1/75 Baseline Configuration with Severed Nozzle," Chrysler Corporation — Space Division Technical Bulletin TB-AD-75-21, August 1975.

5. H. Lamb, Hydrodynamics, Sixth Edition, Dover Publications, 1932.

6. K. C. Kwark, "Sealing of Tail-First, Vertical Entry Model Tests of the Space Shuttle Solid Rocket Booster," Chrysler Corporation — Space Division Technical Bulletin TB-FT-75-19, July 1975.

7. Aero/Hydrodynamics Group, "Data Book for MSFC Test #TMS-333, Pressure Scaled Water Impact Test of a 12.5 Inch Diameter Model of the Space Shuttle Solid Rocket Booster — 6/6/74 Baseline Configuration," Chrysler Corporation — Space Division Technical Note TN-FT-75-58, April 1975.

AN EXPERIMENTAL INVESTIGATION OF THE AXIAL FORCES GENERATED BY THE OBLIQUE WATER ENTRY OF CONES

John L. Baldwin
Naval Surface Weapons Center
White Oak, Silver Spring, Maryland

An experimental program is described in which the axial acceleration was measured during the oblique water entry of cone-nosed missiles. Tests were conducted on models with total cone angles of 45, 60, and 90 degrees entering the water at angles of 45, 55, and 70 degrees to the horizontal at speeds ranging from 5.2 to 64 meters/second. The results include: the axial force coefficient as a function of distance for each cone angle and entry angle combination, the dependency of the axial force coefficient upon velocity, and the loading rate during the initial increase of the axial force coefficient. An estimate of the cross force coefficient for 90-degree cones is also included.

INTRODUCTION

Missiles which enter water from air experience a rapid change in velocity due to the substantial increase in fluid density. The forces present may damage or destroy the missile structure or internal components. The concept that the surface crossing may be replaced by an impulsive change in velocity has existed for some time and may still be used to advantage for some problems; however, the dynamic analysis of the missile structure and internal components requires at least the knowledge of the external forces as a function of time. An analysis of this type was described in Reference (1). Recent advances in instrumentation and test facilities have made possible the direct experimental determination of the water-entry forcing function for many cases. A systematic investigation of entry forces has been part of the continuing investigation of water-entry phenomena at the White Oak Laboratory of the Naval Surface Weapons Center.

The first configuration for which water-entry forces were determined was that of cones at vertical entry (Ref. (2)). Previously developed theory predicted that a self-similar flow existed during the wetting of a constant velocity cone (Refs. (3), (4)). Circular symmetry also simplified this problem as shown by equation (1).

$$G\left(x,y,\beta,t\right) = t\ \phi\left(\frac{x}{t},\frac{y}{t}\right) \qquad (1)$$

where x, y, β are axial, radial, and azimuthal cylindrical coordinates, respectively, t is time and G and ϕ are functions describing particle positions in the self-similar flow, e.g., elevation of the free surface above the undisturbed surface. A direct consequence of self-similar flows is that the axial force (X) acting on the cone during wetting is given by

$$X = Ks^2 \qquad (2)$$

where "s" is the penetration of the nose relative to the undisturbed water surface and K is a constant. The axial force builds up to a maximum value and after wetting has been completed, the force should decay to a steady-state value as the surface recedes.

A self-similar flow should also exist during the point-first oblique entry of cone-shaped missiles. An experimental program studying the oblique water entry of cones was conducted at the White Oak Laboratory to

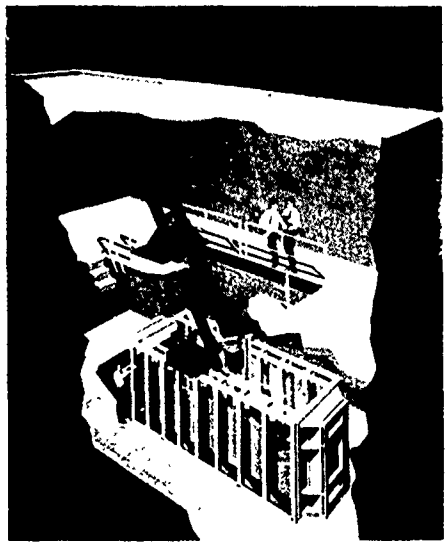
verify the theory and to determine the quantitative values of the axial force.

TEST PROCEDURE

All experiments were conducted in the Hydroballistics Pilot Facility at the Naval Surface Weapons Center, White Oak Laboratory (Figure 1). The test procedure consisted of launching a simple cone-nosed model containing an axially mounted crystal accelerometer from an air gun and recording the gage output during water entry. A schematic of the test arrangement is shown in Figure 2. The accelerometer was connected to the stationary electronics by a trailing wire. A light screen located near the water triggered the recording system and a strobe lamp. An opened plate camera recorded the position of the model at several times just before water contact as it was illuminated by the strobe lamp. Typical photographs of the model are shown in the upper portion of Figure 3. The output from a photo pickup located beside the camera was mixed with the accelerometer voltage signal on one channel of a dual-beam oscilloscope. The other channel displayed only the accelerometer voltage at a different amplification. Typical accelerometer voltage traces are shown at the bottom of Figure 3. Appropriate conversion factors are shown on the figure to convert the accelerometer voltage signal to acceleration in meters/second^2. Optical pickups located near the muzzle triggered the electronic timer to provide a secondary measurement of launch velocity. The models used were the same as used in the study of vertical entry (Ref. (2)). Design details of the models are shown in Figure 4.

RANGE OF VARIABLES

In this program the effects of entry angle, cone angle, and entry speed were studied. The maximum base diameter and the minimum entry angle were limited by the facility as was the selection of entry angles.



ARTIST'S CONCEPT

FIG. 1 HYDROBALLISTICS PILOT TANK

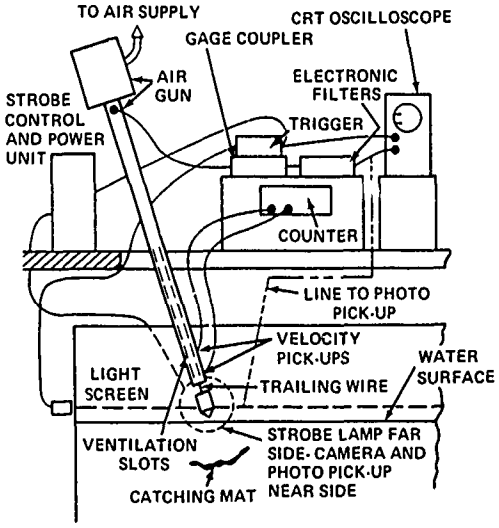
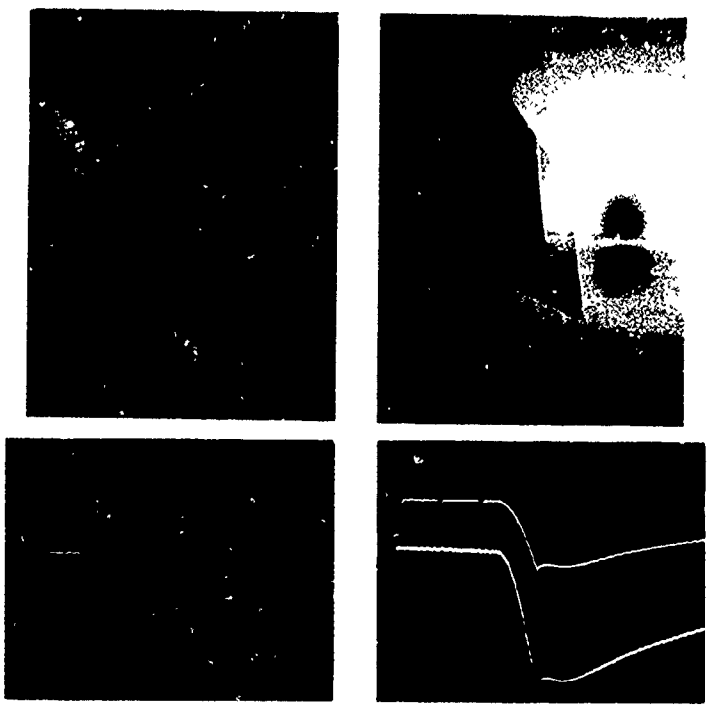


FIG. 2 TEST EQUIPMENT SCHEMATIC



OSCILLOSCOPE GAIN

.2 VOLTS/CM
5 VOLTS/CM

UPPER TRACE
LOWER TRACE

2 VOLTS/CM
1 VOLTS/CM

COMMON CONDITIONS

OSCILLOSCOPE SWEEP 1 MIL SEC/CM
LOW PASS FILTER SET AT 11KH$_z$
GAGE CONSTANT = 677 METER/SEC/VOLT
TIME CONSTANT - 011 SEC

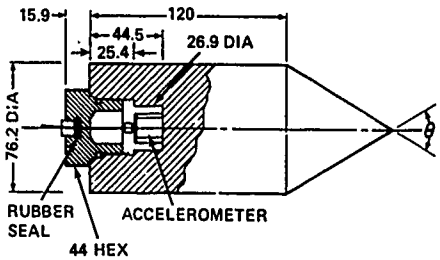
Figure 3 — Samples of test data

Cones of 90, 60, and 45 degrees total angle were selected for study. Blunter cones were limited in the range of trajectory angle available before line contact occurred, while finer cones had demonstrated only small water-entry effects during vertical entry. Overall, the launch speeds varied between 5.2 and 64 meters/second. Table 1 shows the number of tests conducted at each combination of cone angle and entry angle.

Table 1

Test Conditions

Entry Angle Measured from Horizontal	Cone Angle		
	90	60	45
70	7	7	6
55	5	9	4
45	4	9	8



ALL DIMENSIONS ARE IN MILLIMETERS

θ	L	WT(GM)	MATERIAL
90	120.6	1676	ALUMINUM
60	120.6	1829	ALUMINUM
45	120.6	1922	ALUMINUM

FIG. 4 DRAWING OF MODELS.

DATA REDUCTION AND RESULTS

Preliminary data reduction was done manually and involved changing the photographic records to digital form. The plate camera photograph was used to determine the entry speed and to locate the water surface relative to the oscilloscope trace. The accelerometer trace was read relative to the synchronizing pip.

The values obtained from the photographs were entered into a time shared digital computer along with recorded information such as model diameter, mass, scope gain, and entry angle. After calculating read voltage (V_{read}) and time, a correction had to be applied because of the voltage decay caused by the resistance (R) and capacitance (C) of the circuit. The true voltage (V_{true}) was obtained from:

$$V_{(true)} = V_{(read)} + \frac{1}{RC} \int_0^t V_{(read)} dt \qquad (3)$$

The acceleration was then computed and velocity and distance determined for each data point using trapezoidal integration.

An equation relating the momentum just before initial water contact with the momentum in the axial direction at some later time was written as follows:

$$U_o M = U(M+m) + \int_0^t (B-Mg) \sin\Psi dt + \frac{\rho}{2} \int_0^t C_{xs} AU^2 dt \qquad (4)$$

where U_o and U are the initial and instantaneous velocities, respectively, A is the base area of the model, M is the model mass, m is the added mass of water, B is the buoyancy (weight of water of same volume as part of cone beneath the original water surface), Ψ is the entry angle measured from the horizontal, and C_{xs} is the axial steady-state force coefficient. Differentiation of equation (4) yields the following:

$$\frac{dU}{dt}(M+m) + U\frac{dm}{dt} + (B-Mg)\sin\Psi + \frac{\rho}{2} C_{xs} AU^2 = 0 \qquad (5)$$

The summation of forces (F = ma) was also written as:

$$\frac{dU}{dt}(M+m) + (B-Mg)\sin\Psi + \frac{\rho}{2} C_x AU^2 = 0 \qquad (6)$$

Subtracting equation (5) from equation (6) yields an equation for the total axial force coefficient (C_x).

$$C_x = \frac{2}{\rho A}\frac{dm}{ds} + C_{xs} = C_{xt} \qquad (7)$$

$$+ C_{xs} = \frac{2}{\rho A}\left(\frac{dm}{ds} + \frac{dm^*}{ds}\right)$$

where C_{xt} is the transient axial-force coefficient and m* is the steady-state added mass.

The steady-state axial force coefficient normally defined as

$$C_{xs} = \frac{\text{Steady-State Drag Force}}{1/2\ \rho\ AU^2}$$ was interpreted as the rate at which momentum added mass was added to the flow field in regions which would not later directly influence the motion of the missile. In particular, the steady-state axial force coefficient is associated with cavity development and viscous wakes. The quantitative description of the steady-state drag during water entry has been a continuing problem. Neither theory nor experiment has been successful.

Acceleration had been measured only near the surface; hence, wakes and cavities were small and the size of m* small. Therefore, it was assumed that the steady-state axial force coefficient was equal to zero. The total axial force coefficient (C_x) was computed at each data point using equations (8) and (9) in an iterative process in which the initial value of added mass was set equal to zero.

$$C_x = \frac{2}{\rho AU^2}\left(\frac{-dU}{dt}\ (M+m)\ +\ (Mg-B)\sin\Psi\right) \quad (8)$$

$$m = \frac{\rho A}{2}\int_0^s C_x ds \quad (9)$$

The average values of total axial force coefficients (C_x) for each cone angle are shown in Figures 5, 6, and 7.

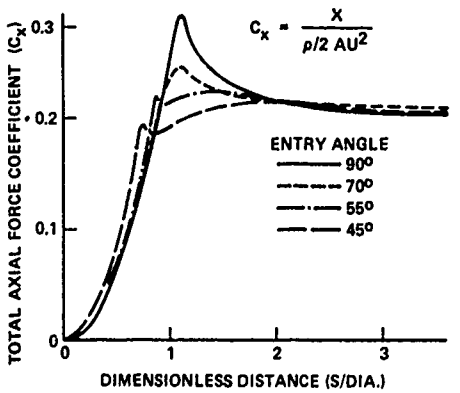


FIG. 5 AXIAL FORCE DURING WATER ENTRY OF 45° TOTAL ANGLE CONES.

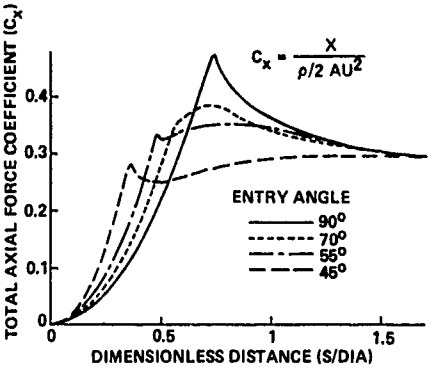


FIG. 6 AXIAL FORCE DURING WATER ENTRY OF 60° TOTAL ANGLE CONES

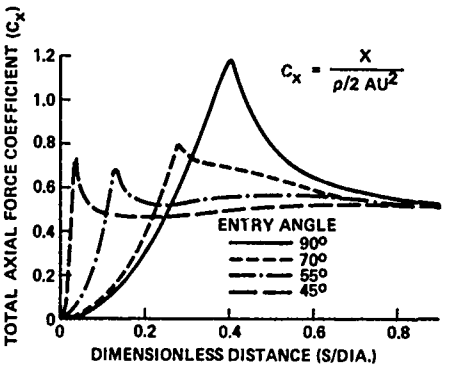


FIG. 7 AXIAL FORCE DURING WATER ENTRY OF 90° TOTAL ANGLE CONES.

Theory has indicated that equation (2) holds during oblique entry up until the time the wetting reaches any portion of the shoulder of the cone.

The test results were correlated with the theory by comparing the distance traveled by the model below the original water surface, as determined from the synchronizing photograph, with the computed distance that gave the best constant instantaneous drag coefficient (C_{xi}) in the least square sense.

$$C_{xi} = \frac{2X}{\pi\rho\left(\tan\frac{\theta}{2}\right)^2 U^2 S^2} = \frac{C_X A}{\pi\left(\tan\frac{\theta}{2}\right)^2 S^2} \quad (10)$$

This analysis used the data points which had values of the axial force coefficient lying between .2 and .9 of the first maximum of C_x. The normalized standard deviation for the seven or eight points used per test was approximately of .03, except for 90-degree cones entering at 55 and 45-degree entry angles, where deviations of about .07 resulted.

The computed distance traveled by the model less the measured distance was normalized by dividing by the cone length. The average difference of 1.0 percent was about twice as large as had been obtained for vertical entry (Ref. (2)).

The average values of instantaneous drag coefficient (C_{xi}) as a function of entry angle are shown in Figure 8.

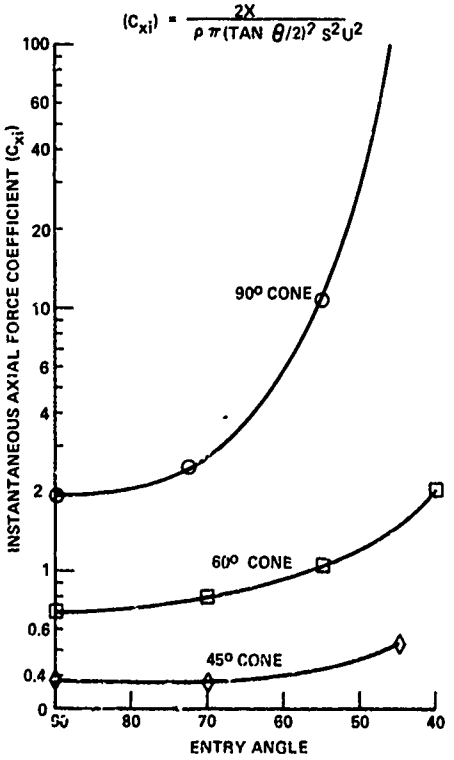


FIG. 8 INSTANTANEOUS AXIAL FORCE COEFFICIENT VS ENTRY ANGLE

DISCUSSION

The influence of entry speed was investigated by normalizing the values of the first maximum of the total axial force coefficient and performing a least square fit to

$$C_x = C_{xo} + KU_o \quad (11)$$

When all of the data was used the result was

$$C_x = 1.015 - .00016U_o \quad (12)$$

which was in agreement with the results for the vertical entry case given in Reference (2) as

$$C_x = 1.008 - .00012U_o \quad (13)$$

When the fit was performed on data for each cone angle, the slope changes from -.00015 for 90-degree cones to -.00019 for 45-degree cones. Hence, the major effect was not a reduction in friction due to an increase in Reynolds number. The major cause of the negative slope remains unknown.

From equation (9), the added mass is proportional to the integral of the total axial force coefficient with respect to distance, i.e., the area under the curves shown in Figures 5 - 7. After entry the added mass for each cone became approximately the same for each entry angle. For those cases where buoyancy, weight and steady-state drag may be neglected, equation (4) reduces to:

$$U_o M = U(M+m) \quad (14)$$

or

$$\frac{U}{U_o} \quad \frac{M}{M+m} \quad (15)$$

and the velocity ratio becomes independent of entry angle.

The loading rate (force/time) was obtained from the instantaneous force coefficient (C_{xi}) via equation (10).

$$\frac{dX}{dt} = \pi\rho C_{xi}\left(\tan\frac{\theta}{2}\right)^2 U^3 s\left[\left(\frac{s}{U^2}\frac{dU}{dt} + 1\right)\right] \quad (16)$$

For dense missiles the first term in the bracket was neglected and $U \approx U_o$, $s \approx U_o t$ so equation (16) becomes

$$\frac{dX}{dt} = \pi\rho C_{xi}\left(\tan\frac{\theta}{2}\right)^2 U_o{}^4 t \qquad (17)$$

The force at the end of this loading period is approximately the first maximum of the axial force which in coefficient form is given in Figure 9, and the distance traveled after water contact until the first maximum is reached is given in Figure 10.

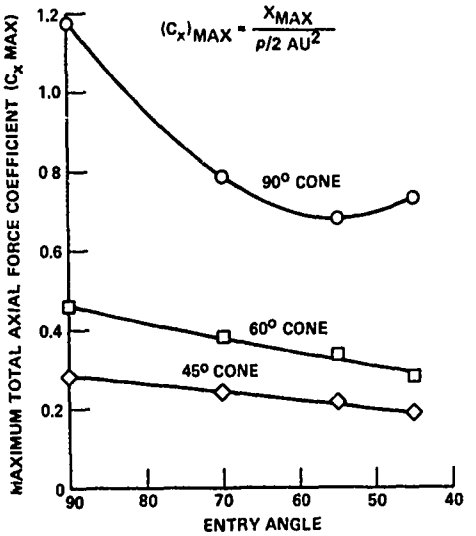


FIG. 9 MAXIMUM AXIAL FORCE COEFFICIENTS VS ENTRY ANGLE.

The work described herein has resulted in the determination of the axial force. It is only a component of the total force. Of particular interest may be the transverse component (Z) which governs bending moments in the missile structure.

A result of self-similar flows is that the angle between the missile axis and the force vector is constant up until the time the shoulder is wetted. Hence, the transverse force coefficient (C_z) can be expressed as a function $f(\Psi)$ of the entry angle and the total axial force coefficient by the following equation:

$$C_z = f(\Psi)C_x \qquad (18)$$

The values of C_z were estimated for the entry of a 90-degree cone. For vertical entry, symmetry indicates that the force vector acts vertically and $C_z = 0$. During 45-degree entry, the first maximum of C_x occurs just after water contact. The surface of the cone in contact with the water is in the horizontal plane; therefore, the force vector is vertical and $C_z = C_x$.

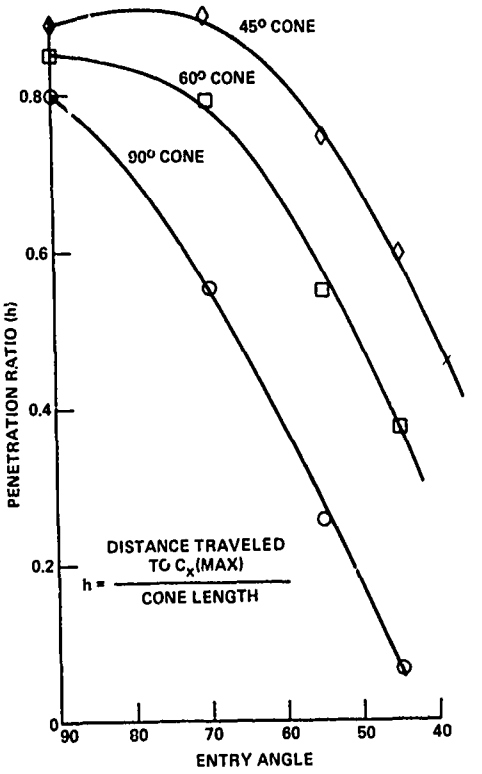


FIG. 10 PENETRATION RATIO VS ENTRY ANGLE

A potential flow model of the oblique water entry of a cone showed that the pressure acting along an incremented area could be divided into three components: (1) the pressure that would result from vertical entry at the same vertical speed of a cone with the same angle between the inward surface normal and the vertical, (2) changes in pressure due to changes in pressure on neighboring elements and changes in neighboring surface shape, and (3) pressure due to translational velocity. A simplified mathematical

model was formulated to predict the cross force that neglected the corrections due to neighboring elements and the horizontal velocity. The average pressure was computed from vertical entry data for each of 36 area elements. The value of C_x/C_z was then calculated and the value of C_z shown in Figure 11 obtained from the oblique C_x data. The results obtained from these calculations for 90-degree and 45-degree entry angles of a 90-degree cone agreed with the expected values from the previous discussion.

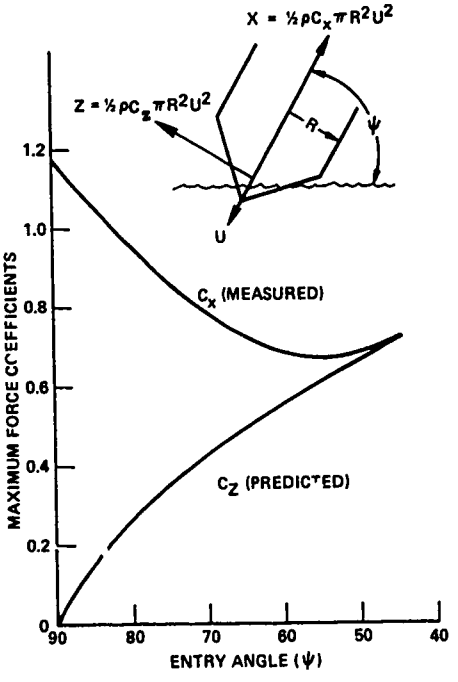


FIG. 11 ESTIMATED MAXIMUM TRANSVERSE FORCE COEFFICIENT FOR WATER ENTRY OF A 90° CONE VS ENTRY ANGLE

At a 60-degree entry angle, the maximum value of C_z would be .69 caused by all pressure being concentrated on the lower element, and the minimum value would be .39 resulting from a vertical force vector. The predicted value of .51 is about 35 percent from the upper bound which gives some indication as to the accuracy of this method.

During these tests the barrel of the air gun was located close to the water surface in order to reduce the angle of attack induced by gravity during air flight. This was particularly necessary for the low-speed launches. The air trapped in the unslotted muzzle of the barrel was driven by the model against the water with at least visible effects (see Figure 3). The problem should be eliminated in future test programs.

CONCLUSIONS

The results of the experimental program showed that:

1. The total axial force coefficient function was almost independent of entry speed between five and 64 meters per second.

2. The axial force coefficient was of the form $X = Ks^2$ during the initial wetting, and the maximum force occurred when the distance penetrated was less than the cone length.

3. After penetration of several cone lengths, the force coefficient approached a steady value approximately equal to the steady-state drag at zero cavitation number.

4. Blunt cones had much larger force coefficients and more rapid loading rates than did fine cones.

5. For a fixed cone angle, the maximum force coefficient occurred at vertical entry and the maximum loading rate at the shallowest entry angle.

6. Examination of Figures 8 and 9 show that both the maximum force coefficient and the loading rate were very dependent on entry angle for blunt cones, and only slightly dependent on entry angle for fine cones.

The maximum transverse force coefficient was estimated to monotonically increase from zero at vertical entry to $C_z = C_x \cot \frac{\theta}{2}$ at an entry angle of $90 - \left(\frac{\theta}{2}\right)$. The detailed description of the transverse force should be the subject of a future investigation.

NOMENCLATURE

A	base area of cone
B	buoyancy force
C	electrical capacitance
C_x	total axial force coefficient

NOMENCLATURE (Con't)

C_{xi}	instantaneous axial force coefficient based on varying area
C_{xo}	total axial force coefficient at zero entry speed
C_{xs}	steady-state axial force coefficient
C_{xt}	transient axial force coefficient
C_z	transverse force coefficient
D	diameter of cone base
f	a function
G	a function describing water particle positions
g	gravitational constant
h	penetration ratio
k,K	a constant
M	mass of missile
m	added mass related to transient force
m*	added mass related to steady-state force
R	radius of missile, electrical resistance
RC	instrumentation leakage time constant
s	distance traveled after water contact
t	time
U	speed of missile
U_o	initial speed
V	electrical voltage
X	axial force
Z	cross force
x,y,β	axial, radial, azimuthal cylindrical coordinates
ρ	mass density of fluid
Ψ	entry angle from horizontal
θ	total cone angle
ϕ	a function describing self-similar motion of the water

REFERENCES

1. Waser, R. H., Matteson, G. L., Honaker, J. W.. "Structural Response Modeling of a Free-Fall Mine at Water Entry", The Shock and Vibration Bulletin Part A, 39-46 (1975)

2. Baldwin, J. L., "Vertical Water Entry of Cones", NOLTR 71-25 (1971)

3. Birkhoff, G., "Hydrodynamics", Princeton University, Princeton, N.J. (1960)

4. Shiffman, M. and Spencer, D. C., "The Force of Impact on a Cone Striking a Water Surface (Vertical Entry)", Comm. Pure and Appl Math 4, 379-417, (1951)

ACKNOWLEDGEMENTS

The author would like to acknowledge Dr. J. E. Goeller and J. J. O'Neill for their advice during the preparation of this paper and D. F. Newell for his assistance with the electronic instrumentation used in the experimental program.

SPONSOR

This program was sponsored by NAVSEA 0351, Dr. T. Peirce.

Discussion

Mr. Baker (Southwest Research Institute): What range of velocities were you firing?

Mr. Baldwin: It was between 20 and 180 ft/s (6.2 to 55.8 m/s). We get very very little change in the coefficients from velocity. There is a slight reduction in the coefficient with increased velocity and it was in both the verticaldata and the oblique data. It may well be a systematic error in the way we ran the experiment. We may be running into some filtering problems, since we filter our data to some extent.

Mr. Baker: How do you use this?

Mr. Baldwin: You can use it for predicting the response of components in an object that enters in the water. Last year Bob Wasser presented a paper that involved free fall mine water entry and he showed that by taking the forcing function that was derived from accelerometer data and running it through the NASTRAN program you could get very good results compared to a test of an instrumented scaled model or a full scale model. There correlation was very good so as a first step at least you can use it this way. In the future we will have actually measured pressure distributions and transverse forces rather than predicted values.

* DELAMINATION STUDIES OF IMPACTED COMPOSITE PLATES

C. A. Ross
University of Florida Graduate Engineering Center
Eglin AFB, Florida 32542

and

R. L. Sierakowski
Engineering Sciences Department, University of Florida
Gainesville, Florida 32611

Both steel-epoxy and fiberglass-epoxy composite crossplied plates were impacted with blunt ended cylindrical impactors at velocities below the critical penetration velocity. Failure mechanisms in the form of lamina delamination were observed for thirteen different types of ply arrangements. Lamina delamination was found to be the dominant failure mode and fiber breakage or pullout occurred only in the area in direct contact with the impactor. It was found for impacted fiberglass-epoxy plates that the number of plies within a given lamina, especially the first several laminae, are very important in the resulting progressive delamination. The extent of the damage appears to be related to kinetic energy imparted to the plate by the impactor.

INTRODUCTION

The impact resistance of single component materials in general depends upon many material properties such as fracture strength, hardness, ductility; with particular properties being more important within certain impact velocity ranges. However, impact resistance of composite materials is not only dependent on the specific constituent material properties but also on the geometrical arrangement of the imbedded fiber arrays.

Some early experimental studies dealing with the impact resistance and penetration characteristics of composite plates have been reported. Gupta and Davids [1] have studies the penetration resistance of fiberglass plates of varying thickness and density. Further investigations on the impact resistance characteristics of fiberglass plates were conducted by Wrzesien [2] who examined the influence of placing steel sheeting in glass fiber composites. A noticeable improvement in the impact resistance of such reinforced type plates was observed. Additional studies on the impact resistance of fiberglass plates examining the influence of filament orientation and volume fraction have been reported by Ross and Sierakowski [3]. It was found that certain ply arrangements have greater impact resistance for the same volume fraction of fibers. Studies on impacted graphite-epoxy plate composites with comparison to dynamic diagnostic tests have been reported by Askins and Schwartz [4].

Most recently Hearle and Sultan [5] have examined the impact resistant properties of woven and non-woven textile materials. They have reported an improvement in penetration resistance for fiber materials having a stiffening effect at high elongations. A recent theoretical model proposed by Roylance, et al., [6], shows promise for examining the impact resistance of some textile type fiber composites. The principle thrusts of the above investigation have been directed toward examining the penetration and/or impact resistance of fiber reinforced composites. In order to understand the impact resistance mechanisms which occur during progressive failure in fiber composites, impact models and diagnostic tests have been proposed and reported on by Cristescu et al. [7,8].

In the present investigation, the above studies are extended to examine the mode of progressive failure in structurally layered fiber composites and the sequential layering effects

*Work Performed Under Grant from U.S. Army Research Office, Triangle Park, North Carolina

dominant in controlling the impact resistant properties of such materials at velocities below the penetration limits of the specimens. The qualitative description of events occurring answers several questions raised in a previous investigation by Cristescu, et al. [7] and forms the basis of a quantitative description to be developed.

SPECIMEN FABRICATION

Some of the terms used to describe the various elements of a composite plate are included at this point to clarify the fabrication process described in this section and the failure mechanisms described in later sections. Attention is also directed to Figure 1 for further clarification. A plate or laminate is defined to be a flat piece of composite material, containing one or more layers and/or lamina, whose thickness is small compared to the other dimensions. A lamina represents a given thickness of a composite plate or laminate, containing one or more layers whose fibers are all aligned in the same direction. A layer or ply is defined as a given thickness of a composite plate or laminate containing only one filament thickness. A fiber or filament represents the reinforcing phase of the material and is held in place by the matrix. All the filaments or fibers used in this study are continuous and are uniaxially aligned in each layer with a 90° orientation difference between lamina. Plates having a 90° orientation difference between laminae are usually referred to as cross plied plates.

Two types of plate test specimens were fabricated to be representative of an extensible and inextensible fiber imbedded in a brittle matrix as shown schematically in Figure 2. The plate materials studied were:

Fibers - Owens-Corning Fiberglass, Type ECG-150 precision-controlled roving, density 2540 kg/m^3 and elastic modulus 72.4 GPa; Stainless-steel type 304, density 7833 kg/m^3 and elastic modulus 206.2 GPa.

Matrix - Shell Epon 828 Epoxy, and Magnolia Plastics Curing Agent D.

Several size plate configurations of different cross ply orientations were prepared of nominal dimensions .15m square and .30m square and containing fifty per cent by volume fraction of fiber. A special 6061-T6 aluminum plate fixture attached to a lathe assembly was used in preparing the specimens, with lathe speed and cross feed adjusted to insure controlled fiber spacing. Layer spacing was controlled

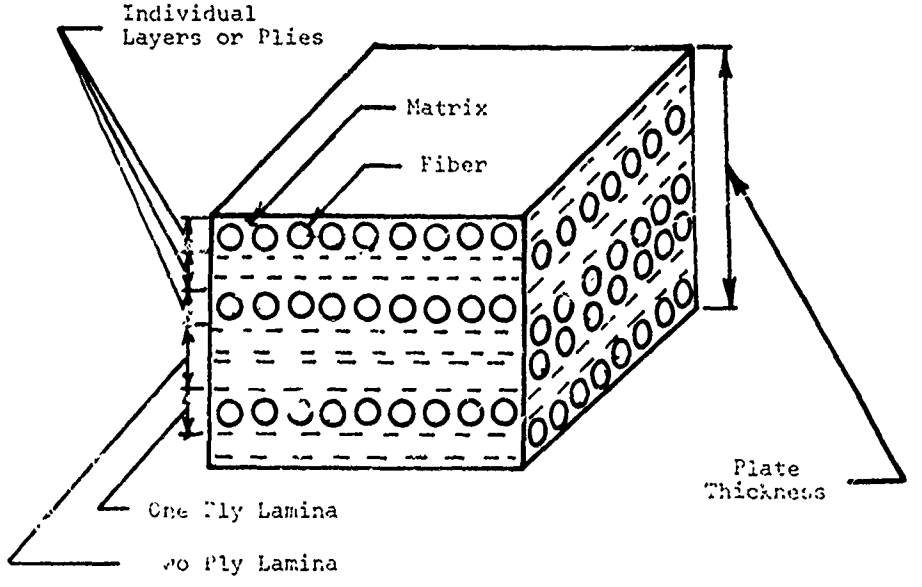


Fig. 1 - Composite plate nomenclature

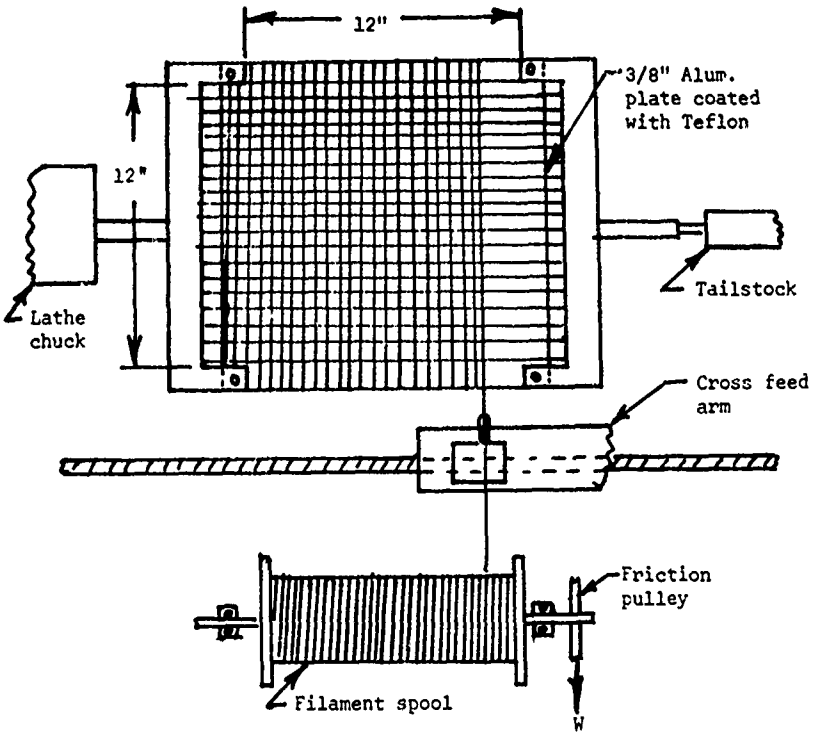


Fig. 2 - Winding assembly

by use of shim stock placed along the edges of the mandrel assembly (nominally 4 x 10^{-3}m). For the steel-epoxy specimens, the epoxy matrix material was poured over the wound steel wire assembly with the edges of the assembly sealed for leakage, while for the fiberglass specimens the epoxy matrix was brushed on after each successive layer had been wound. In order to construct a specific laminate, (0° - 90° ply orientations) the mandrel assembly was rotated as necessary in the holder assembly.

After completing the plate lay up, which consisted of 15 layers total thickness of approximately .67 x 10^{-2}m, cover plates of either aluminum (6061-T6) or wood, of nominal dimensions comparable to the mandrel were clamped to the specimen and adjusted to predetermined thickness stops. Both cover plates and mandrel assembly were sprayed with teflon release agent to insure easy removal of the fabricated specimens from the mandrel assembly. The mold assembly was then placed in a furnace to cure at 150°F for 2 hours and then air cooled. In addition to the .15m square and .30m square plate specimens, some smaller bar specimens of nominal dimensions .15m x .025m x .005m were prepared.

TEST BACKGROUND AND PROCEDURES

It has been recognized that impacted composite plates may fail due to existence of several different failure mechanisms occurring separately or in some combination such as: shear cut-out of a plug; fiber debonding, stretching, and/or breaking and fiber pull out; delamination; and matrix failure. In a previous paper [7] a delamination mechanism was introduced and described as an important feature which may account for the improved impact resistance of a class of multilamina plates having several fiber layers in each lamina. Elements of this mechanism have been also observed for other than fiberglass composite systems in [4]. The essential features of this mechanism shown in Figure 3, for the case of moderate impact velocities (i.e., below plate penetration), consist of an initial shearing action as the penetrator cuts through the first layers of the composite, followed by delamination of

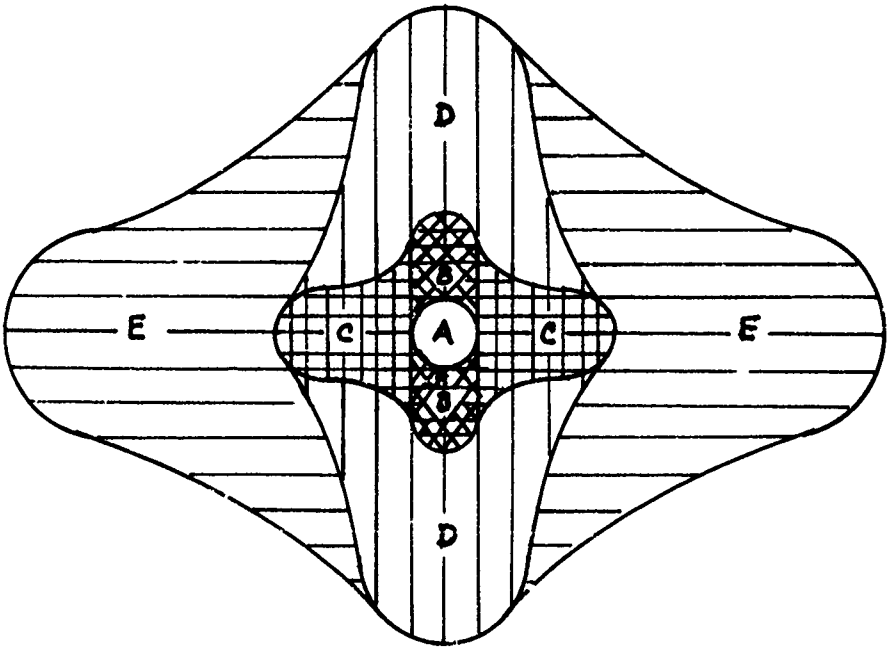
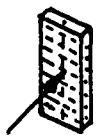
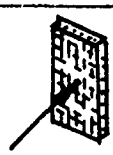
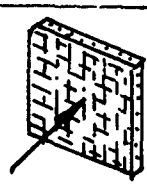


Fig. 3 - Delamination schematic showing initial generator strip. A projectile; B initial generator strip; C first delamination area; D second delamination area; E third delamination area

successive laminae. Upon impact the projectile pushes a strip of the first lamina one projectile diameter wide rearward and the length of this strip is partially dependent on the time for the projectile to cut through the first lamina. This first stage of the delamination process, area B of Figure 3, in turn loads transversely the second lamina along the length of this strip and generates a delamination in the second lamina. The generation of the delamination process in the second lamina by a strip in the first lamina leads to the term first generator strip to define this strip. Subsequent generator strips are formed as delamination occurs rearward from one lamina to another. The successive lengths of these generator strips appear to follow some type of arithmetic or geometric progression, with limiting repeated delamination determined by the total number of lamina and by the plate boundary. An important feature of this failure mechanism is that the sequence of events occur in a front to back manner as opposed to monolithic materials in which spalling occurs due to reflected tensile waves. To examine many of these questions an extensive series of impact tests using 2.54cm x .97cm diameter blunt ended penetrators have been performed on plates of various ply arrangements to examine (a) the successive stages as they develop in the delamination mechanism, (b) the influence of sequential lamina stacking on controlling the generator strip mechanism and (c) the effect of changes in fiber length on the observed delamination mechanisms. Initial testing reported on in [8] described some diagnostic type tests which were conducted in this study in order to better understand the mechanism of sequential lamina delamination. Controlled coupon specimens of nominal size (.25m x .1m x .005m) with three lamina consisting of different fiber numbers and orientation were impact tested at low velocities as shown in Table I. For these tests the top lamina or top and bottom lamina, were machined away to observe the threshold loading for noting the tendency to form a generator strip. For the specimens tested, an impact velocity of 12.7m/sec was found necessary to initiate the tendency for formation of a generator strip. Since for the most part the steel epoxy specimens appeared to show a symmetrical fracture pattern as shown in Figure 4,

TABLE 1
Specimen Types Used for Dynamic Impact Tests

a). Single fiber sandwiched between two multifilament lamina in a matrix; steel and glass fiber	
b). Three fibers sandwiched between two multifilament lamina in a matrix; steel fiber	
c). Multiple fibers sandwiched between two multifilament lamina in a matrix; steel and glass fiber	
d). Impact tests on 0°-90° cross-plied multifilament in a matrix plate; steel-epoxy and glass epoxy	

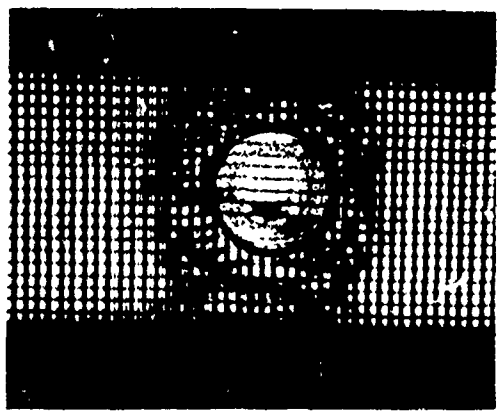


Fig. 4 - Impacted Steel Epoxy Specimen

the remainder of the tests were conducted on fiberglass specimens. For this reason, fiberglass plate specimens of different geometries have been selected for further study, as indicated in Table 2, with the tested

TABLE 2
Plate Geometries Studied

(a) Square Plate
(.15 m x .15 m x .006 m)

(b) Square Plate
(.30 m x .30 m x .006 m)

ply arrangements given in Table 3. All plates were fixed along all edges and were impacted with similar blunt ended penetrators of mass 14.8g, length 2.54cm and diameter of .97cm.

DISCUSSION AND RESULTS

In the delamination mechanism described here, the influence of reflected dilatational and shear waves from the lamina interfaces and interlamina shear waves appears to be minimal. Therefore principal attention has been focused upon the generator strip mechanism and stacking sequence importance in ply delamination.

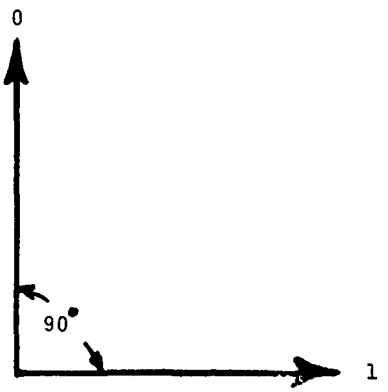
To examine these mechanisms the plate configurations indicated in Table

TABLE 3
Ply Arrangements for Glass Roving Plates

Sequence as shown runs from impacted side to back of plate

Pure Epoxy

1 1 1 1 1 1 1 1 1 1 1 1 1 1 1
1 0 1 0 1 0 1 0 1 0 1 0 1 0 1
1 0 0 1 1 1 0 0 0 0 1 1 1 1 1
1 1 0 1 1 0 1 1 0 1 1 0 1 1 0
1 1 0 0 1 1 0 0 1 1 0 0 1 1 0
1 1 1 0 1 1 1 0 1 1 1 0 1 1 1
1 1 1 0 0 1 1 1 0 0 1 1 1 0 0.
1 1 1 0 0 0 1 1 1 0 0 0 1 1 1
1 1 1 0 0 0 0 1 1 1 0 0 0 0 1
1 1 1 1 0 0 0 0 1 1 1 1 0 0 0
1 1 1 1 1 0 1 1 1 1 1 0 1 1 1
1 1 1 1 1 0 0 0 0 0 1 1 1 1 1
1 1 1 1 1 1 1 1 0 0 0 0 0 0 0



Filament directions

TABLE 4

Plate Type	No. of Lamina	Strip length (m)	Ply Arrangement[a]
a	4	.119	111100001111000
b	5	.038	100111000011111
c	5	.114	111000111000111
d	6	.127	111001110011100
e	7	.114	111011101110111
f	8	.091	110011001100110
g	15	.043	101010101010101

a) Layer or ply sequence runs from impacted side to back of plate.

4, which constitute a part of the listing in Table 3, are discussed. For studies of these plates a fixed impact velocity of 110 m/sec was used. In comparison impact failure of pure epoxy plates occurred at 28 m/sec and for fiberglass epoxy plates with a single lamina (all fifteen fiber layers in the same direction) failure occurred at 60 m/sec. The second column of Table 4 indicates the total number of representative lamina with different numbers of individual layers for plates identified for convenience by the symbols a through g. If we compare plates b and g each of which start with a single initial layer (a 1 type direction lamina containing only one layer), and approximately the same generator strip length, the resultant delamination in case b is found to

be greater than in g due to the additional thickness of the second lamina in b which allowed development of the generator strip through the additional plies contained within each lamina of b as shown in Figure 5. Further if we examine plate e, Figure 6, which has a single ply lamina alternating between



(Plate b)



(Plate g)

Fig. 5 - Ply delamination for plates b and g respectively

multi-ply laminae, we note that the initial generator strip is approximately three times that developed in plates types b and g. However, because of the single ply alternating secondary lamina, the delamination in the direction perpendicular to the initial multi-ply lamina direction is not fully developed as shown in Figure 6. If we compare



Fig. 6 - Ply delamination for plate type e

plate types e and c with the same number of plies in the first lamina (impact side), with one plate containing more plies or layers in the second lamina, that is c versus e, we can observe a greater overall delamination occurring in case c as shown in Figure 7. Comparison of delamination patterns of plates type c, d, and e indicates that the second lamina stacking sequence constrains the resultant delamination growth once the generator strip has developed. Plate types a and f further reinforce this observation with



Fig. 7 - Ply delamination for plate type c

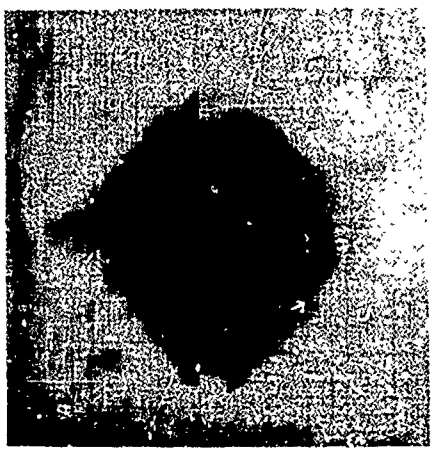




Fig. 8 - Delamination on plate types f and a respectively

results shown in Figure 8. The influence of development of the generator strip through multiple plies of lamina on the extent of damage is apparent in the elongated damaged area of plate c.

Two additional aspects of the generator strip mechanism were investigated as they relate to the specimen size necessary to observe the delamination sequence; edge boundary effects, and the effect of changing fiber length on progressive delamination. The first question was investigated by using large specimens as indicated in Table 2. Impacting such specimens with penetrators used in the smaller plate studies and at comparable impact velocities (110 m/sec) produced the same equivalent damage level. This is evident in Figure 9 which shows a typical impacted large plate of type c from Table 4. As to changing fiber length, several circular holder assemblies of varying diameter (.010, .013, .015m), Figure 10, were used to change the fiber length during impact using penetrators projected at 110 m/sec. Once again the same delamination mechanism was evident.

Finally, to evaluate stages in the progressive delamination sequence of events, plates of type c from Table 4



Fig. 9 - Impacted large plate specimen

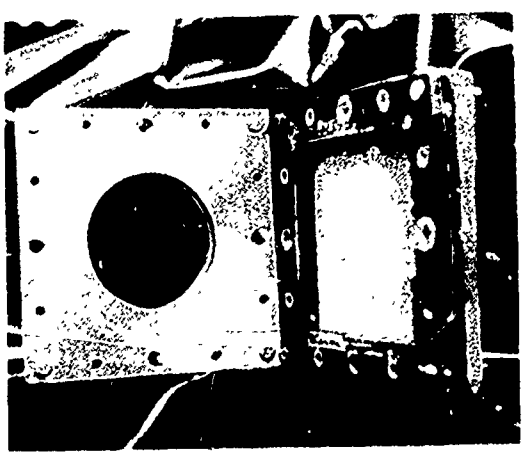


Fig. 10 - Typical specimen holder assemblies

were impacted using blunt penetrators at successive incremental impacts of 50 m/sec starting from 150 m/sec up to 450 m/sec at which point incipient penetration was evident. The generator strip mechanism was found to form with progressive delamination occurring from the impacted face to the rear of the plate in a systematic incremental progression. The progression appears first to be arithmetic until sufficient damage has occurred that boundary effects begin to influence ply delamination near the penetration velocity.

CONCLUDING REMARKS

The deformation and failure of monolithic homogeneous isotropic plate under normal impact is quite regular resulting in very symmetrical crack patterns, damaged areas, and spall patterns. For multi layered composite plates the resulting damaged area may become highly unsymmetrical by simply changing the ply arrangement or by varying some lamina thicknesses.

For static loading, the ply arrangement is very important in determining plate stiffness but in the analysis the loading direction is unimportant; whereas for impact loading plate damage is highly dependent upon the ply arrangement on the side of the plate being loaded. Also, for dynamically impacted systems it appears that the number of plies within a given lamina, particularly the first several laminae, are very important in the formation of the generator strip and the resulting progressive delamination. Specifically, this latter growth phenomenon (total damaged area) appears to be related to the amount of kinetic energy imparted to the plate by the impactor.

In this paper only the 0°-90° lamina orientation difference was investigated, however other orientation differences should produce very similar delamination sequences. The generator strip formation may not be as distinct as in the crossplied case but the load transfer and delamination of adjacent laminae are expected to be very similar to that observed in the crossplied plates.

REFERENCES

1. B. P. Gupta and N. Davids, "Penetration Experiments with Fiberglass-reinforced Plastics," Experimental Mechanics, Vol. 6, 1969, pp. 445-456.
2. A. Wrzesien, "Improving the Impact Resistance of Glass-Fibre Composites," Composites, Vol. 3, July 1972, pp. 172-174.
3. C. A. Ross and R. L. Sierakowski, "Studies on the Impact Resistance of Composite Plates," Composites, Vol. 4, 1973, pp. 157-161.
4. D. R. Askins and H. S. Schwartz, "Mechanical Behavior of Reinforced Plastic Backing Materials for Ceramic Armor," AFML-TR-71-283, Wright-Patterson AFB, Ohio, Feb., 1972.
5. J. W. S. Hearle and M. A. I. Sultan, "A Basic Study of the High-speed Penetration Dynamics of Textile Materials," Dept. of Textile Technology, University of Manchester, Manchester, England, May, 1974.
6. D. Roylance, A. Wilde, and G. Tocci, "Ballistic Impact of Textile Structures," Army Symposium on Solid Mechanic, October, 1972.
7. N. Cristescu, L. E. Malvern, and R. L. Sierakowski, "Failure Mechanisms in Composite Plates Impacted by Blunt-Ended Penetrators," ASTM STP 568, Jan. 1975, pp. 159-172.
8. N. Cristescu, R. Sierakowski, and C. A. Ross, "Fiber Pull Out and Delamination Processes in Composite Materials," 11th Annual Meeting of the Society of Engineering Science, Nov. 11-13, 1974, Durham, North Carolina.

Discussion

Mr. Keith (Kaman Sciences): The results you showed were for point loadings on the plates; in the first part of your talk, you talked about flier plate loadings or impulsive loads, area loadings. Were the results that you obtained from the area loadings of the same tread?

Mr. Ross: I probably mislead you there. I intended to say at that point we were only in that one area and we were talking about central impact with a point load. We have not looked at the so called blast or flier plate loading; there has been some work on either boron or graphite plates under pressure loading and I think it is in the April 1975 Journal of Composite Materials.

SIMULATION OF X-RAY BLOWOFF IMPULSE LOADING ON A REENTRY VEHICLE AFT END USING LIGHT-INITIATED HIGH EXPLOSIVE*

Robert A. Benham
Sandia Laboratories
Albuquerque, NM 87115

This paper describes an experimental method in which X-ray blowoff impulse effects are simulated by the detonation of a spray deposited coating of explosive initiated by an intense flash of light. A specific experiment is described in which the complex aft surface of an advanced development reentry vehicle is simultaneously loaded with a distributed impulse including load step discontinuities.

I. INTRODUCTION AND SUMMARY

The possibility of a Comprehensive Test Ban Treaty emphasizes the importance of nuclear effects simulation. Several experimental techniques have been developed to study the material and structural response caused by X-ray exposure. These techniques include the electron beam[1] and the laser beam,[2] used primarily for material response studies, and propagating sheet and rod[3] explosive as well as magnetically driven flyer plates,[4] used primarily for structural response studies. This paper presents a reliable experimental method in which X-ray induced blowoff effects are simulated for the study of structural response phenomena. The structure is remotely spray coated with an explosive which is initiated by an intense flash of light, thus delivering a simultaneously applied impulse. A specific experiment is described involving the impulse loading of the complex curved aft surface (flat-cone-toroid) of an advanced development program reentry vehicle. The thickness of the silver acetylide-silver nitrate explosive is varied to produce an impulse load which matches values calculated for X-ray blowoff. The explosive is surface initiated to produce a pressure pulse lasting about two microseconds. Measurements of strain, displacement, and acceleration during experiments at increasing impulse levels allow detailed understanding of structural dynamics, with verification of a failure impulse.

Previous investigations at this facility[5] and others[6, 7] have demonstrated that the technique is reliable and can be used for a variety of impulse simulation experiments. This paper describes a closely controlled simulation experiment using light-initiated explosive for structural experiments involving large complex surfaces with load discontinuities. The development of this technique represents an improvement in laboratory X-ray simulation capability.

II. TEST FACILITY

Since the explosive is a primary (i.e., easily detonated), all operations involving any significant quantity of explosive are performed remotely. The test facility was described at the 45th Shock and Vibration Symposium.[8] The spray operation is conducted in a spray booth by an operator using master slave manipulators. After spraying is complete, the test unit is remotely transported to a firing chamber where the light source causes surface initiation of the explosive.

*This work was supported by the U.S. Energy and Research Development Administration.

III. TEST VEHICLE

The test assembly consisted of an aft cover assembly, a frustum aft cover support, and a steel ballast (Figure 1). It weighed 110 kg and simulated the reentry vehicle overall weight as well as the structural characteristics of the aft end support. The portion to be spray painted was the aft cover assembly, which consisted of a flat plate on the unit axis and a conical transition area blending into a toroidal section. Instrumentation consisted of 12 strain gages mounted as biaxial pairs on the inner surface of the cover and an Endevco 2264-4500 accelerometer mounted on the ballast weight. This accelerometer, which was oriented to sense axial acceleration, was bonded with a 0.5 mm thick layer of RTV-108 material to obtain mechanical isolation from the transducer-damaging shock waves. All strain and acceleration data were recorded by an Ampex FR-1400 tape recorder located in a trailer at the test facility. The frequency response of the tape recorder channels was 20 kHz.

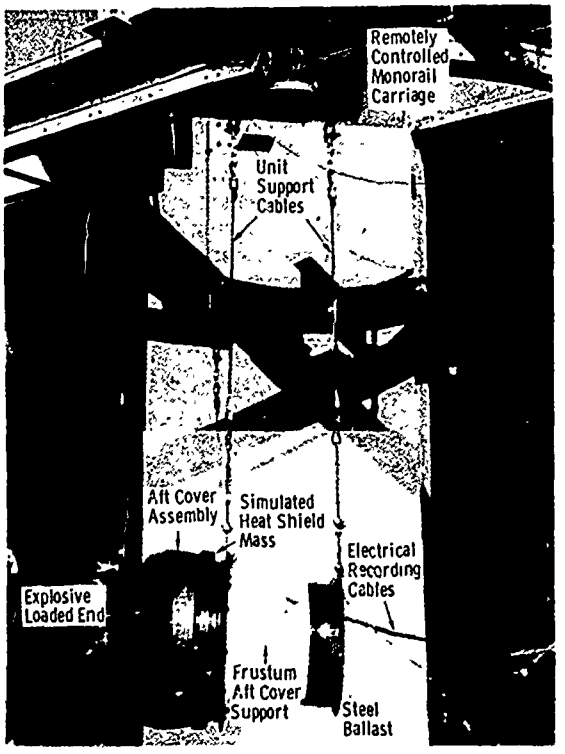


Fig. 1 - Impulse test unit

IV. TEST TECHNIQUE

Several steps, all done by remote control, were involved in performing the tests on this structure. The surface was sprayed with the proper mass distribution of explosive to produce a loading which varied as cos θ* over the surface when the explosive was detonated. The surface was spray-painted with explosive in a sequence of three separate operations: the flat section, the conical section, and then the toroidal section. The sprayed weight distribution was checked periodically throughout the spraying process by remotely removing the weighing coupons placed on the aft cover surface. The coupons were returned to the surface, and the spraying was continued until the proper thickness (areal density) of explosive was obtained. When the spray operation was completed, the instrumentation wires were connected to the recording system.

The sprayed test unit was remotely attached to a carriage on a monorail system. The carriage transported the test unit to the proper location in front of the pulsed light source. The explosive on the test unit aft surface was then initiated, producing the impulsive load. The response data were recorded. High-speed cameras and a displacement gage were used to provide a measurement of the total impulse applied to the test surface.

Spray Method

The spraying technique was developed and qualified by conducting trials on a full size wooden model. Figure 2 shows the spray booth setup with the test unit in place. The unit could be moved up and down as well as rotated at a controlled speed. The spray gun could be rotated to three positions as well as moved horizontally (traverse across the end of the unit at a controlled speed and moved in and out with respect to the unit surface).

A series of separate spray operations using masks machined from 0.96 kg/m^3 polyurethane foam (Figure 3) allowed accurate control of the explosive weight distribution while meeting requirements of small explosive waste

*θ is the angle between the unit axis and the normal to the surface at the point of interest.

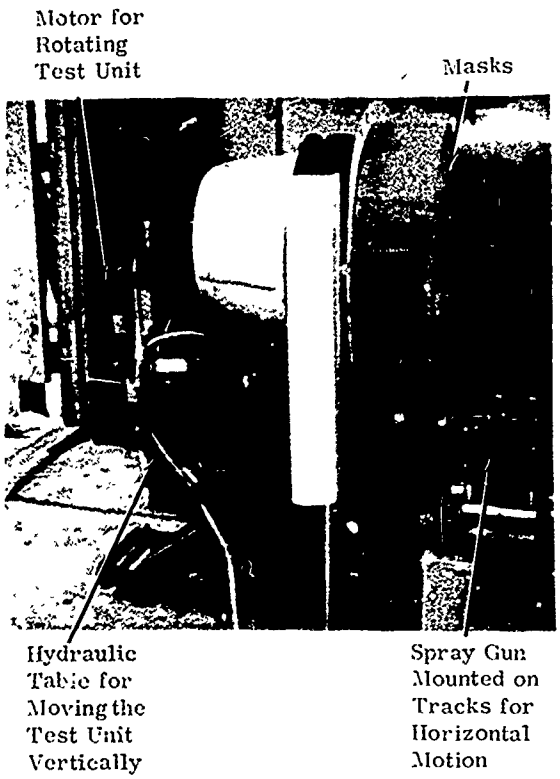


Fig. 2 - Spray booth setup

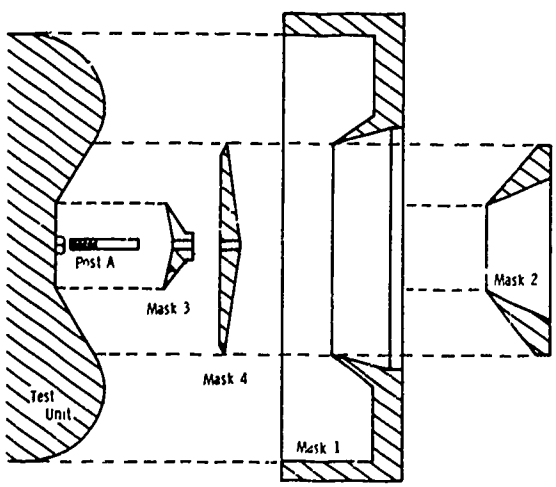


Fig. 3 - Masks used to spray the aft end

and remote control handling of the explosive. A uniform layer of explosive was deposited on the flat aluminum center portion of the aft cover in the first spray operation. This was accomplished by masking off all of the unit except the aluminum section with masks 1 and 2 (Figure 4). The unit was positioned vertically at 51 mm increments, and the spray gun traversed the surface at a constant speed of 0.13 m/s for a given number of passes at each vertical position, with the spray gun axis perpendicular to the sprayed surface and 0.15 m away. The overlapping spray pattern gave a constant thickness of explosive across the flat surface. Phenolic coupons 21 mm in diameter and 0.8 mm thick, attached to the flat cover surface, were sprayed and periodically weighed during the spray operation to insure the proper weight distribution of explosive. The desired weight was determined from empirically determined curves of delivered impulse as a function of explosive areal density.

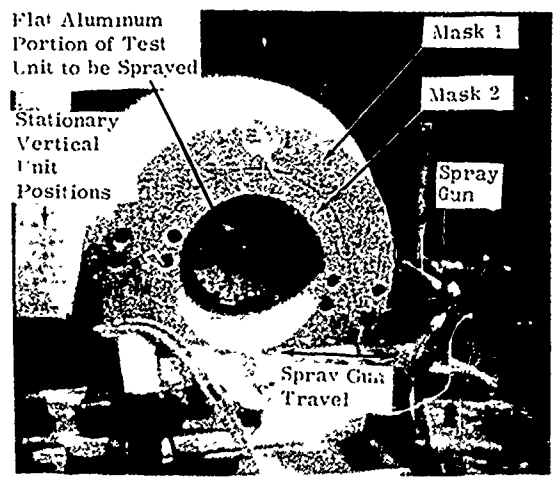


Fig. 4 - Mask arrangement for spraying the flat section

The second spray operation deposited a uniform layer of explosive on the conical section of the aft cover. This was accomplished by remotely removing mask 2, screwing in a centered post, and placing mask 3 over the explosive sprayed on the flat section (Figure 5). The spray gun was positioned to be perpendicular to the conical surface and 0.15 meter distant. The unit was rotated at a rate which produced a surface velocity directly under the stationary gun of 0.13 m per second. The spray gun was actuated for a predetermined number of revolutions and then moved to a second position for another series of spray revolutions. Coupons were weighed and the spray process continued until the desired areal density was obtained.

In the third spray operation, a cosine distributed layer of explosive was deposited on

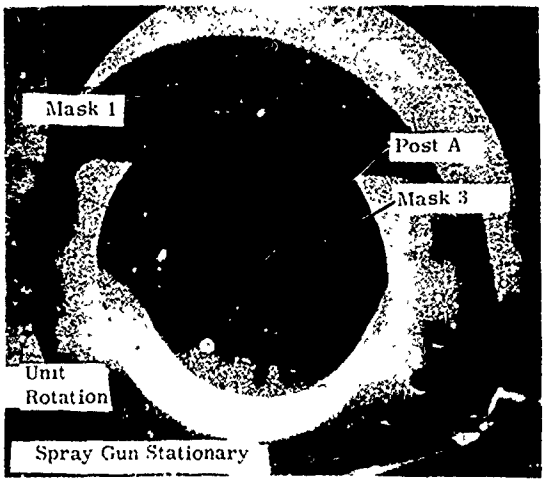


Fig. 5 - Mask arrangement for spraying the conical section

the toroidal section of the cover. This was accomplished by removing mask 1 and placing mask 4 on the post (Figure 6). The cosine distribution was obtained by positioning and spraying with the spray gun in three separate locations, the first at the 0° position of the toroid. Sprays at plus and minus 50° built up the sides to the proper distribution. This procedure was determined by measuring the angular distribution of the spray pattern during trial sprays on cylinders. Coupons at 0°, 30°, and 45° were used to verify the proper distribution for this cosine spray on the aft cover.

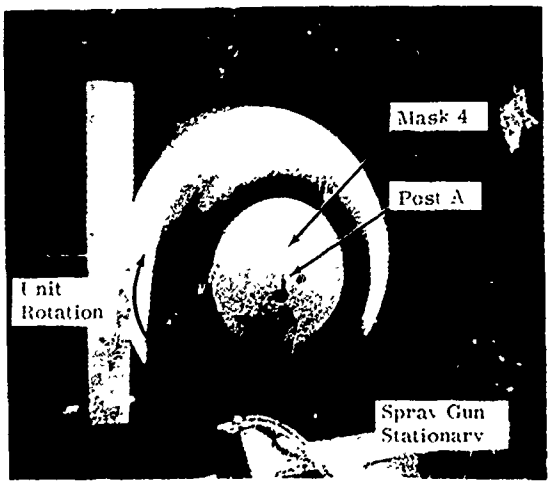


Fig. 6 - Mask arrangement for spraying the toroidal section

Figure 7 shows the aft cover at the completion of the spray operation. The impulse indicated by coupon weight is compared to the desired impulse in Figure 8.

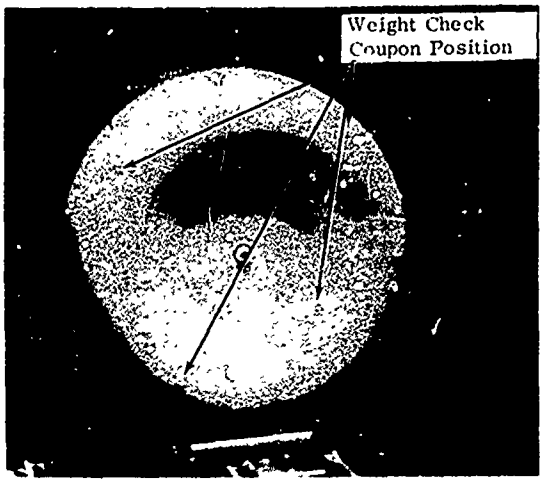


Fig. 7 - Aft cover after spray completion

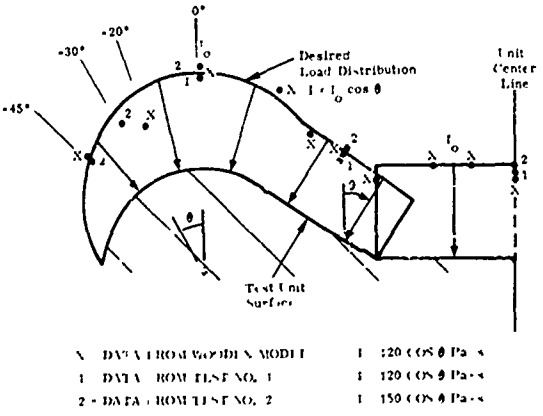


Fig. 8 - Explosive spray results

Light Array

The light source used for this test series consisted of tungsten wire, 0.076 mm. in diameter, stretched between two terminal busses to form a planar array 0.75 m square. The test specimen was placed at the center of this array with the closest point of the sprayed surface 89 mm from the light-producing tungsten wires. A Refrasil cloth reflector was placed behind the wires to increase the light intensity

at the test unit surface. A hole in the array backboard, 0.61 m in diameter, allowed the blast pressure from the explosive to pass through the light array without being reflected back to the test surface.

A capacitor bank was connected across the copper terminal busses. A damping foil was placed in the capacitor circuit to dissipate electrical energy after the explosive detonated,[9] thus reducing a source of electrical noise after explosive detonation. When the capacitor bank was discharged, an arc was formed in the air, producing light of sufficient intensity to detonate the explosive.

The capacitor bank, 36 kJ when charged to 40 kV, had a ringdown frequency of 40 kHz.

A preceding investigation[9] has shown that explosive initiation occurs within 1 μsec over the surface for this light array setup geometry and that the applied pressure pulse is about 2 μsec in duration. Similar results are expected for this experiment.

V. IMPULSE VERIFICATION

The load level was verified by data from a streak camera running film at 1 foot/second. The rigid body velocity was then related to the distributed impulse applied. An electrical displacement gage attached to the test unit near the center of mass was also used to record rigid body motion. Figure 9 shows the test unit after the test. The desired peak impulse level was 150 Pa·s, the test data indicated that 141 Pa·s was actually delivered to the unit. One strain gage record is shown in Figure 10 to demonstrate the quality of data obtained.

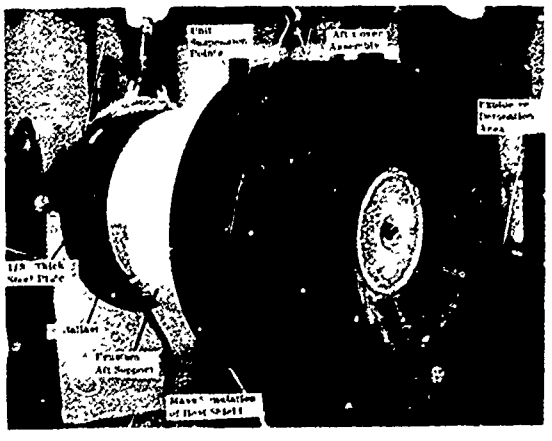


Fig. 9 - Posttest, aft end

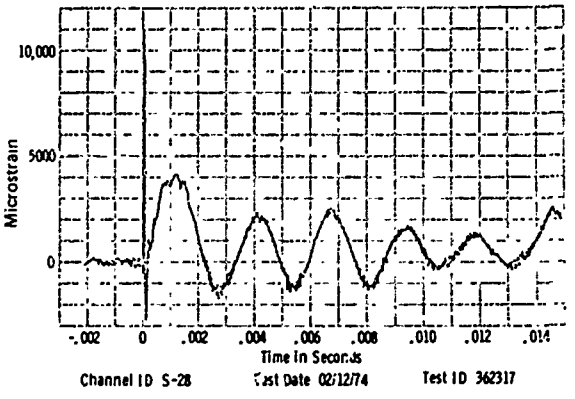


Fig. 10 - Strain record

VI. CONCLUSION

An experimental technique has been developed for producing an impulse test on a complex aft cover of an advanced development reentry vehicle and is presented here. The technique combines the safe handling of the sensitive explosive with the ability to closely control the spray deposition of explosive on a large complex structure that includes load discontinuities. The detonation of this explosive with a light flash delivers a simultaneous impulse loading to the structure. The technique is a good simulation of X-ray generated impulse loading for studying structural response.

This paper describes in detail for the first time in the open literature an experiment on a large complex structure including load discontinuities.

REFERENCES

1. G. Dunbar, "Compendium of Electron Beam Data," Physics International Report, PI FR-422, Feb. 1973.

2. W. F. Hartman, M. J. Forrestal, and J. C. Bushnell, "An Experiment on Laser-Generated Stress Waves In A Circular Elastic Ring," Sandia Laboratories, ASME Paper No. 71-APMW-2.

3. G. R. Abrahamson, "Explosively Induced Impulses," Stanford Research Institute, Poulter Laboratories, PLTR 009-62, July 20, 1962.

4. Forrestal, M. J., Tucker, W. K., and Von Riesemann, W. A., "Impulse Loading of Finite Cylindrical Shells," AIAA, Vol. 13, No. 10, Oct. 1975, pp. 1396-1398.

5. Benham, R. A., "Light-Initiated Explosive for Impulse Experiments on Structural Members," Sandia Laboratories, Report SAND75-0516, Jan. 1976.

6. Wenzel, A. B., and Baker, W. E., "The Use of Light-Initiated Explosives for Impulsive Loading of Structures," Proc. 16th Annual Meeting of the Institute of Environmental Sciences, Boston, Mass., April 1970.

7. Hoese, F. O., Langhner, C. G., and Baker, W. E., "Simultaneous Initiation Over Large Areas of A Spray Deposited Explosive," Experimental Mechanics, Vol. 8, Sept. 1968.

8. Benham, R. A., Mathews, F. H., "X-Ray Simulation with Light-Initiated Explosive," The Shock and Vibration Bulletin, Part 4, June 1975, pp. 87-91.

9. Higgins, P. B., "An Arc Light Source for Initiating Light-Sensitive Explosive," The Shock and Vibration Bulletin, 1976.

ACKNOWLEDGEMENT

The author wishes to acknowledge the very able assistance of Dave Shirey, Ben Duggins, and Phil Higgins who made this work possible.

Discussion

Mr. Kilroy (Naval Ordnance Station, Louisville): Normally you don't have screw threads around explosives, how do you handle that situation?

Mr. Benham: Very carefully. In order to complete any of these tests we have to do some things that we know are not accepted practice and that is one of them. We never had a detonation even though we did that particular operation three times on that system. The only thing that saved us was that the explosive does not get down into that hole during any spray operation because when we sprayed the flat portion it was covered with a coupon and then for any other operations after that the thread was in the hole during the spraying. Yes it was a potential problem.

Mr. Miller (Toole Army Depot, Toole, UT): What types of measurements were you making with the instrumentation?

Mr. Benham: We had strain gages mounted on the aluminum substructure underneath the cover. We had some accelerometers mounted down the line from the explosive on the blast mass and then we had displacement gages inside. We have used non contacting displacement gages in some cases for displacement measurements.

AN ARC SOURCE FOR INITIATING LIGHT-SENSITIVE EXPLOSIVES

Philip B. Higgins
Sandia Laboratories
Albuquerque, New Mexico

A pulsed light source for the initiation of light-sensitive primary explosives to produce impulse is described. Advantages of an array of air arcs initiated by heated tungsten wires are discussed, and methods are presented for controlling the undesired pressure generated by the air arcs. A method is described for reducing the duration of instrumentation blackout caused by coupling of transducer wiring to the heavy current in the light source.

INTRODUCTION

This paper describes a pulsed light source used to initiate a primary (very sensitive) explosive which has been previously sprayed on the surface of a structure. When properly initiated the explosive delivers an impulse to the surface which simulates a radiation-induced impulse [1]. The basic arrangement of the light source and structure is illustrated in Figure 1.

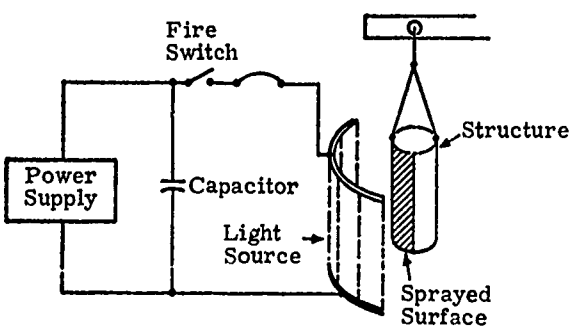


Fig. 1 - Arrangement for irradiating a sprayed structure

LIGHT SOURCE DEVELOPMENT

A rechargeable xenon lamp has been used to initiate a sprayed primary explosive, silver acetylyde-silver nitrate (SASN) [2]. Xenon lamps up to 1.5 m in length have initiated several samples of sprayed lead azide, another primary explosive, within a 1-μs time interval [3]. In each case the lamp(s) was energized by high-voltage capacitor banks.

Xenon lamps can be designed to survive many high-current discharges but will usually be destroyed by the shock wave resulting from the initiation of nearby explosives powerful enough to produce impulse levels of interest. Since each lamp costs in the neighborhood of $200, an experiment requiring several calibration shots and using as many as 15 lamps per shot becomes expensive.

An alternate method of generating light of sufficient intensity to initiate SASN utilizes an air arc [4]. If a slender (0.08-mm-diameter) tungsten wire is connected across a capacitor charged to a suitable voltage, the temperature of the wire will increase as a result of Joule (i^2R) heating, resulting in a corresponding increase in the wire resistance. After a repeatable quantity of energy has been imparted to

PRECEDING PAGE BLANK-NOT FILMED

the wire, an arc will form along the length of the wire in the air immediately surrounding it [5]. The resistance between the terminals holding the wire will drop coincidentally with formation of the arc, resulting in high power dissipation in the expanding arc. By choosing suitable circuit parameters an intense white light will be radiated by the arc which will initiate SASN after a few microseconds exposure.

The chief advantage of a wire-initiated air arc over a xenon lamp for "one-shot" initiation purposes is the cost savings. Even when the wire is inserted in a Pyrex tube to contain pressure effects due to the expanding arc, replacement cost of a tungsten source is less than 5 percent of an equivalent xenon lamp.

Two other considerations recommended wire-initiated arcs as a light source: the energizing circuitry is simple and parallel feed of many wires (normally, the most convenient mode of operation) tends to give simultaneous arc formation because of equal heating of each wire in an array of identical wires. This self-regulating feature results from the positive temperature coefficient of resistance of tungsten, which tends to equalize the energy delivered to each wire until such time as the light-producing arc forms.

CONFIGURATION

Tungsten wires have been grouped in various configurations to form arcs for the proper illumination of sprayed structures having different shapes. Flat, half-cylindrical, and half-conical arrays of up to 15 wires have been used. The distance separating the source wires from the sprayed structure runs between 10 and 14 cm.

Two techniques are frequently used to alter the basic bare-wire array. For low-level tests requiring impulse under 100 pascal-seconds, the tungsten wires are inserted in Pyrex tubes which are left open at either end to divert expanding gases away from the sprayed structure. This precaution essentially eliminates the long-term, low-level force that would otherwise be added to the desired impulse delivered to the test structure by the explosive.

Frequently it is desirable to use an existing fixture to illuminate a new structure which has only approximately the mating configuration. Reflectors can often be used to compensate for a poor fit between array and test structure. A white cloth woven of glass fibers (Trade Name: Refrasil) is used. It is an excellent light reflector but of sufficiently light weight to reflect an insignificant amount of the pressure wave generated by the explosive. (A reflected pressure wave from the explosion would add undesirable late time forces to the structure.)

A technique equivalent to increasing the intensity of the light source involves presensitizing the sprayed explosive immediately before initiation. A few minutes of "sunburning" by exposure to direct sunlight darkens the explosive surface and produces a significantly denser detonation pattern when the exposed sample is later initiated by the arc array. Presently, this procedure is used only as "insurance" to guarantee rapid initiation.

SOURCE VERIFICATION

Streaking-camera photographs were made to establish the light distribution of the air arc which forms around the heated tungsten wire. Figure 2 was taken with the slit of the camera coincident with one wire of an array of 12 wires, each 56 cm long. Time increases from top to bottom in the photograph; the bright area indicates saturation of the film during the first current peak in the arc. Light intensity along the length of the arc is displayed horizontally. Only minor variations of intensity are seen, indicating fairly uniform radiation along the length of the wire. The vertical "waviness" of the photograph results from coupling between the light-source circuit and the electronic imaging circuits in the streaking camera.

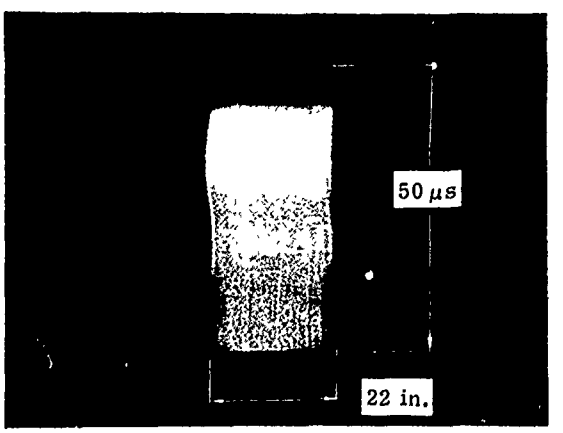


Fig. 2 - Streak photograph of a single air arc

The slit of the streaking camera was rotated 90 degrees so that a small area of each of 12 arcs could be photographed for the aperture period of approximately 100 μs. In Figure 3, time increases from left to right. The original print shows three bright areas of diminishing brightness which correspond to the first three peaks of the damped current trace in Figure 4. The distribution of light intensity from wire to wire is seen to be quite uniform at a given point in time.

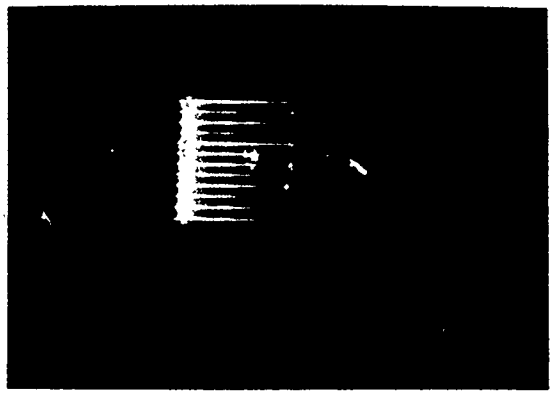


Fig. 3 - Streak photograph of short length of each of 12 air arcs. Horizontal scale: approximately 100 μs.

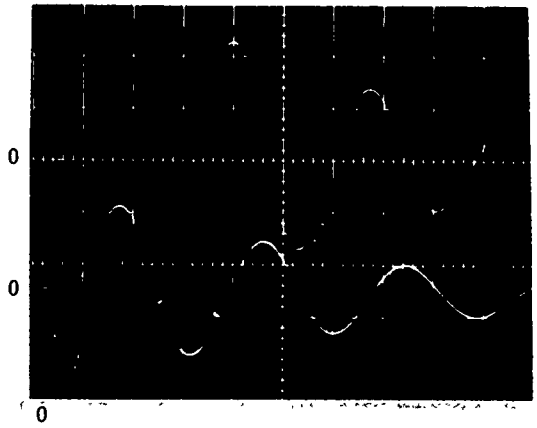


Fig. 4 - Upper trace: time derivative of total arc current. Vertical scale uncalibrated. Lower trace: total current in 12 uncontained arcs, without series exploding foil. Vertical scale: 150 kA/div. Horizontal scale: 10 μs/div. Arcs form approximately 8 μs after t = 0.

ARC CURRENT CONTROL

When arcs form across the uncontained tungsten wires, the capacitor bank discharges in the damped fashion shown in Figure 4. The top trace is the output of a Rogowski sensing coil which generates a voltage proportional to the time derivative of current in the wires

$$V = k\frac{di}{dt} \quad .$$

The bottom trace of Figure 4 shows the decaying arc current derived from the output of the Rogowski coil by electrical integration.

A total peak current of several hundred kiloamps flows through the air arcs and is almost inevitably coupled into the instrumentation wiring located on the sprayed structure less than 30 cm away. If allowed to ring down naturally as in Figure 4, this coupled component of the bank current would swamp the low-level instrumentation data for as much as 100 μs.

An exploding foil connected in series with the wires (arcs) is used to interrupt the arc current a short time after first peak [6]. In Figure 5, it is seen that the total current in the 12 uncontained arcs (upper trace) has been damped to an undetectable level within 20 μs. The lower trace shows di/dt.

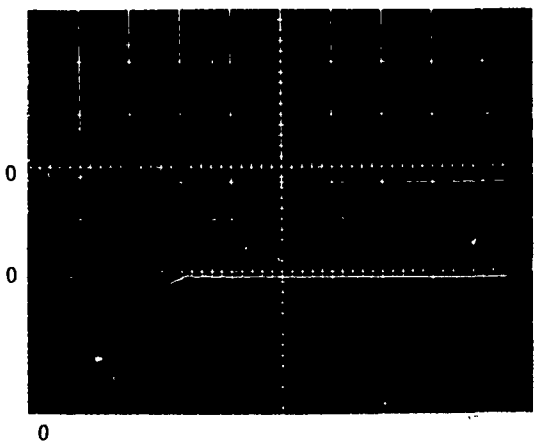


Fig. 5 - Upper trace: total current in 12 uncontained arcs, with series exploding foil, 150 kA/div. Lower trace: time derivative of total current, uncalibrated. Horizontal scale: 10 μs/div.

Reduced current results when the wires are enclosed in 11-mm-ID Pyrex tubes, as indicated in Figure 6. This is attributed to the higher resistance of an arc partially contained by a tube. A foil similar to that used in obtaining Figure 5 was utilized in performing the experiment with the tubes.

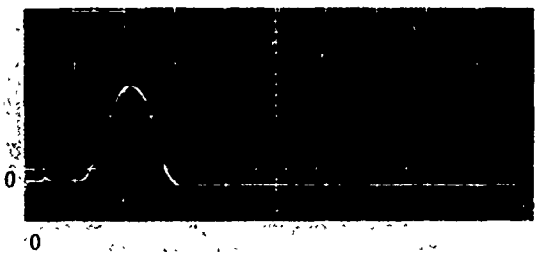


Fig. 6 - Total current in 12 arcs contained by Pyrex tubes in series with exploding foil. Vertical scale: 150 kA/div. Horizontal scale: 10 μs/div.

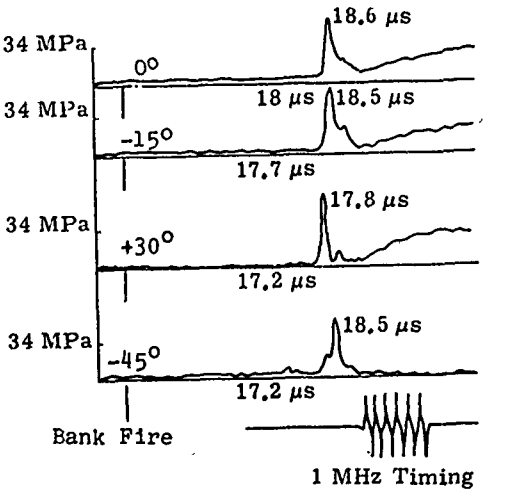


Fig. 7 - Pressure measurements from cylinder sprayed with SASN. Vertical and horizontal scales as indicated.

PRESSURE SIMULTANEITY

Impulse resulting from x-ray deposition occurs essentially simultaneously over an irradiated surface. To measure the asimultaneity of pressure peaks occurring across a surface of light-initiated SASN, four Susquehanna ST-4 gages were mounted flush with the outer surface of an aluminum cylinder of radius 20.5 cm. Surface and gages were sprayed with SASN having an areal density of 12.8 to 16 mg/cm^2. The gages were located in a plane normal to the axis at 0°, -15°, +30°, -45°, where 0° represented the angular midpoint of the sprayed surface.

The instrumented cylinder was then placed concentrically inside a semicylindrical array of 12 tungsten wires 71 cm long. Wire-to-surface spacing was 10.1 cm.

Gage outputs were recorded on a multitrack disc recorder having a bandwidth of 1.5 MHz. The results are shown in Figure 7, where the time jitter between first and last pressure peak is seen to be 1.4 μs. Noted on each gage output is the time from capacitor bank firing to initial pressure and to peak pressure, respectively. The slow rise following the pressure pulse is "noise" induced in the gage lines by the heavy arc currents.

CONCLUSIONS

An inexpensive "one-shot" light source has been developed for initiating silver acetylyde-silver nitrate, a primary explosive used to simulate radiation impulse. A 60-kJ capacitor bank, discharged into an appropriate array of tungsten wires, will create a light source capable of initiating 1100 cm^2 of SASN sprayed on a cylindrical surface. Peak pressures developed over the surface will be simultaneous within ±0.8 μs.

An exploding foil is used to reduce the outage time of sensitive instrumentation by rapidly damping current in the source. With the described system, recovery of a 20-kHz recording system is within 50 μs after initiation of the explosive, normally soon enough to recover structural response data.

ACKNOWLEDGMENT

The author wishes to thank D. L. Shirey for his essential role in obtaining the photographic data.

REFERENCES

1. R. A. Benham and R. H. Mathews, "X-ray Simulation with Light-Initiated Explosive," Shock and Vibration Bulletin, 45, Part 4, p. 87.

2. F. D. Hoese, C. G. Langner, W. E. Baker, "Simultaneous Initiation Over Large Areas of a Spray-Deposited Explosive," Experimental Mechanics, Vol. 8, 1968, pp. 392-397.

3. P. B. Higgins, "Fast-Rise Light Source for Detonating Sensitive Explosives," Applied Optics, Vol. 11, No. 1, Jan. 1972.

4. R. I. Butler, private communication, Sandia Laboratories, Albuquerque, New Mexico.

5. T. J. Tucker and F. W. Nielson, "The Electrical Behavior of Exploding Wires: A Survey of Various Materials," SC-TM-334-59 (51), Sandia Laboratories, Albuquerque, New Mexico.

6. P. B. Higgins, "A Convenient Method of Increasing the Current Damping Produced by an Exploding Foil," Rev. Sci. Instrum., Vol. 45, No. 4, April 1974.

BLAST PRESSURES INSIDE AND OUTSIDE SUPPRESSIVE STRUCTURES*

E. D. Esparza, W. E. Baker, G. A. Oldham
Southwest Research Institute
San Antonio, Texas

Suppressive structures are uniformly vented structures designed to remain intact under blast loads from internal explosions and are intended to attenuate the blast waves which emanate from them. This paper covers past analytical and experimental studies in explosion venting, and summarizes much of the recent blast loading work in the suppressives structures program. Scaling laws are briefly reviewed, as is the concept of an effective vent area ratio. Curve fits to external blast overpressures and impulses are given for a variety of vent panel designs, including nested angles, perforated plates, zees, louvres, and interlocking I-beams. Internal blast loads consist of initial and several subsequent reflected shocks, followed by a much longer blowdown or quasi-static pressure. Curves are given for prediction of the initial reflected wave overpressure and impulse. Theories for the blowdown phase are discussed, followed by presentation of curves for scaled peak blowdown pressure and duration. A computer code for prediction of intrapanel pressures during the blowdown phase is described.

INTRODUCTION

In facilities that contain and process high explosives, there is always the potential for an accidental explosion. To prevent the propagation of this explosion to other facilities containing explosives or to minimize injuries and damage in habitable buildings, such facilities are widely dispersed. Another method to reduce the hazards from an accidental explosion is to use partial confinement walls and cubicles to direct and control the output from the explosion. To further reduce the required spacing between high explosives facilities, the U. S. Army, under its ammunition plant modernization program, is developing uniformly vented suppressive structures which will significantly reduce or suppress the external blast overpressures, the fragment hazard, and the thermal effects. The suppressive structures tested to date have been rectangular enclosures consisting of a main frame with multi-layered vented panels making up the sides and roof. The technology for vented suppressive structures has not yet reached the stage where the design is a straightforward process. Consequently, development programs supported by the Edgewood Arsenal (EA) are being conducted to develop this technology so that suppressive structures can be routinely applied to explosive processing operations to better protect personnel and adjoining facilities while reducing the safety distance required between them.

The loading from an explosive charge detonated within a vented or unvented structure consists of two almost distinct phases. The first phase is that of reflected blast loading. It consists of the initial high pressure, short duration reflected wave, plus perhaps several later reflected pulses arriving at times closely approximated by twice the average time of arrival at the chamber walls. These later pulses are attenuated in amplitude because of irreversible thermodynamic process, and

*Work performed under Contract No. DAAA-15-75-C-0083 with the Edgewood Arsenal, Aberdeen Proving Ground, Maryland.

PRECEDING PAGE BLANK-NOT FILMED

they may be very complex in waveform because of the complexity of the reflection process within the structure, whether vented or unvented. If the structure has solid walls, the blast loading can be estimated by using sources of compiled blast data for normally reflected blast pressures and impulses such as References {1} and {2}, and the well-known Hopkinson's blast scaling law (see Chapter 3 of Reference {3}). The effect of vented areas in the suppressive structures on reduction of the reflected blast loading can be very complex, and will not be addressed in detail in this paper.

As the blast waves reflect and rereflect within the structure and as unburned detonation products combine with the available oxygen, a quasi-static or gas pressure rise occurs, and the second phase of loading takes place. Measurements of this pressure rise and its duration have been made by various investigators prior to the suppressive structures program using chambers having a single opening for venting. Work has also been conducted to develop a theory for predicting time histories of pressures in vented structures. However, from the present program, data are now also available from structures uniformly vented through the sides and roof. From all of the above data, one obtains the answer that for the particular ratios of vent area to chamber volume tested, the venting has no effect on the peak quasi-static pressure. Thus, peak quasi-static pressures for unvented or poorly vented structures are the same. Unfortunately, essentially no data exist for quasi-static pressures within well-vented structures, and the crucial question of the actual maximum gas pressure rise within such chambers remains unanswered. We must at present use the unvented pressure rise for design purposes. An important point that needs to be made is that, although quasi-static pressure measurements have been made in various vented and unvented structures, the determination of the peak value is subject to interpretation because the reflected pressures are also present on the data records. Because suppressive structures consist of multi-layered walls, how the quasi-static pressure loads each layer is also of interest to the designer. At this time, no data are available for these intrapanel pressures. However, as part of this program, a computer program has been developed to predict these pressures. When experimental data become available the program's accuracy can be assessed.

In addition to determining the reflected blast loading and the quasi-static gas pressure rise and decay that are needed in designing these structures, the amount of venting required to reduce the blast pressures outside to a desired level must be estimated. Using limited data, Baker, et al. {4}, generated a method of correlating emitted blast waves from suppressive structures and comparing them to free-field blast data to determine the degree of blast attenuation. Since a suppressive structure is made up of several vented layers, this method introduced an effective vent area ratio, α_{eff}, which can be computed for a variety of combinations of vented elements in a suppressive structure. In References {5} and {6}, more and better blast pressure data are now available, and we have updated the equations for predicting the reduction in overpressure over a considerable range of distances outside the structure. Also, good external side-on impulse measurements were made by Schumacher and Ewing {5} so that the reduction in impulse can also be predicted.

SCALING

Blast Waves

The scaling of properties of blast waves from various explosives sources is a common procedure, and most blast data are reported in scaled parameters from the Hopkinson-Cranz or Sachs' scaling laws. These laws, and others used in blast technology, are derived and discussed in detail in Chapter 3 of Reference {3}. Blast waves from explosions in the open are affected by mass W (or total energy) of the explosive, distance R from the center of the explosive, geometry and energy density of the explosive source, and ambient atmospheric conditions such as pressure p_o and sound velocity a_o. For charges of different total energy but same type and geometry detonated under the same ambient conditions, the Hopkinson-Cranz scaling law applies. It predicts {3} that overpressures (P), scaled impulses $(i/W^{1/3})$, and scaled time $(t/W^{1/3})$ are functions of Hopkinson-scaled distance $(R/W^{1/3})$. (If ambient conditions differ between one experiment or analysis and another, another scaling law must apply. The law usually used in this case is Sachs' Law {3}.)

Suppressive structures are intended to attenuate the blast waves from accidental explosions by reflecting the initial waves striking their inner surfaces, and venting the gas pressures

behind the shock fronts at a relatively slow rate. In attempting to scale the properties of the waves emanating from these structures, one must include parameters which describe the geometry and venting characteristics of the structure as well as the conventional scaled distance. A scaling law for the side-on pressure and scaled impulse, including these additional parameters was postulated by Baker, et al. {4}, and is as follows:

$$P_s = f_1(R/W^{1/3},\ X/R,\ \alpha_e) \qquad (1)$$

$$(i_s/W^{1/3}) = f_2(R/W^{1/3},\ X/R,\ \alpha_e)$$

The new parameters in this law are a characteristic length X of the suppressive structure and an effective vent area ratio α_e. Model and prototype structures are assumed to be geometrically similar for exact scaling, but the characteristic length X can be thought of as the square root of the wall area of interest or the cube root of the structure's internal volume V, for the law to apply in at least an approximate manner. The definition of α_e will be discussed in the next section of the paper. Also inherent in the law are the same assumptions inherent in Hopkinson scaling, i.e., no change in ambient conditions, explosive type, or geometry. Heat transfer to the suppressive structure is also not considered in the development of the scaling law. The scaling law, of course, does not specify the actual functions f_1 and f_2. These will be treated later in the paper.

Quasi-Static Pressures

As the blast waves from explosions within suppressive structures reflect and re-reflect, and as the energy available from the explosive source is added to the air within the structure, long-term pressures can build up within the structure. These pressures are termed "quasi-static pressures" because they can last long enough to apply essentially static internal gas pressure loads to the structure.* Some data existed for pressures within vented chambers prior to the suppressive structures program {7-9}, and some analyses of blowdown pressures had also been made {7,10,11}. To compare such data and also to collate data being generated in suppressive structures testing, Baker, et al. {4}, conducted a model analysis of the explosion venting process. The resulting scaling law has been somewhat modified in Reference {12} and is:

$$\left(\frac{P}{P_o}\right) = f_3\left[\left(\frac{\alpha_e A_s}{V^{2/3}}\right),\ \left(\frac{P_1}{P_o}\right),\ \left(\frac{t a_o}{V^{1/3}}\right),\ \gamma\right] \qquad (2)$$

Based on a theoretical analysis of chamber venting by Owczarek {12,13}, the scaled pressure, $\bar{P} = (P/P_o)$, is a function of γ and a new scaled time

$$\bar{\tau} = \bar{A}\,\bar{t} = \left(\frac{\alpha_e A_s}{V^{2/3}}\right)\left(\frac{t a_o}{V^{1/3}}\right) \qquad (3)$$

Here, P is absolute pressure at any time t, A_s is internal surface area of the structure, P_1 is maximum (initial) absolute quasi-static pressure, and γ is ratio of specific heat for the gases within the structure. An alternate form of Eq. (2) is then

$$\bar{P} = f_4(\bar{P}_1,\ \tau,\ \gamma) \qquad (2a)$$

The initial pressure $\bar{P}_1$ for structures with no venting or small venting can be shown to be related {4,7,8,11} to another scaling term,

$$\bar{P}_1 = f_5(E/p_o V) \qquad (4)$$

where E is a measure of total energy released by the explosion. For tests with explosives of the same type and no change in ambient conditions, a dimensional equivalent of Eq. (4) is:

$$P_1 = f_6(W/V) \qquad (4a)$$

where W is charge mass and V is chamber volume.

VENT AREA RATIO

From the model analysis used to develop the functional expression for the side-on overpressure outside the structure, it is obvious that the only parameter which lacks exact definition for a multi-layer, uniformly vented enclosure

*With large vent areas, these pressures can conceivably vent quickly enough that venting times are comparable to structural response periods. In this case, the term "quasi-static" is inappropriate. Perhaps "blowdown or gas pressure" is a more appropriate term.

is α_e. For a single layer structure, the vent area ratio is the vent area divided by the total area of the wall. For a multi-layer wall, however, we assumed that {4}

$$\frac{1}{\alpha_e} = \sum_{i=1}^{N} \frac{1}{\alpha_i} \qquad (5)$$

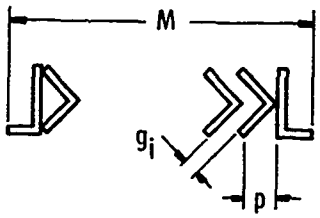
This relationship has at the moment no theoretical proof. However, it does reach the appropriate limits for large and small numbers of plates, and provides a relative measure of venting for a variety of panel configurations. Unfortunately, no external pressure data currently exist for a one-layer structure with equal openings on all sides and roof. Consequently, we have established as our base line the α_e computed for a series of perforated plates using Eq.(5) where the vent area ratio for each layer is simply

$$\alpha_1 = \frac{(\text{Vent Area})_1}{\text{Wall Area}} ,$$

$$\alpha_2 = \frac{A_{v2}}{A_w} , \ \ldots \qquad (6)$$

For other wall elements such as angles, louvres, zees, and I-beams used in suppressive structures, the meaning of Eq. (6) is less obvious. In obtaining a reasonable curve fit to the data, the definition for α_e for these types of elements is as shown in Fig. 1. For nested angles which have approximately one opening per projected length (see Fig. 1), the data indicate that they are about twice as efficient as a perforated plate in breaking up the side-on peak pressure as it vents. For closer nested angles such that there are about two openings per projected length, the angles seem to be four times as efficient as a comparable perforated plate. However, angles which are side by side and zees seem to be as efficient as a perforated plate. Louvres seem to be more efficient than perforated plates by a factor of two. On the other hand, using the open areas as shown in Fig. 1, interlocking I-beams appear to be only half as efficient as perforated plates. Note that for a uniformly vented structure, the α_e of the structure is exactly equal that of a wall since the walls and roof all have the same vented area ratio. Thus, in computing α_e the area of the floor is not used. Furthermore, since we are interested in comparing to free field data in which the charge would still have the floor as reflecting surface, the area of the floor should not be used in computing α_e.

The peak gas pressure is, in general, a function of the charge weight, volume of the container, and the vent area. However, the data in Reference {8} indicate that for low vent area to volume ratios, the peak pressure does not depend on this ratio. The duration does depend on the vent area ratio, and, as in the case of the external pressure, a definition of α_e is required. Prior to the suppressive structures program, all the experimental data on quasi-static pressures and durations were from cubicles with a portion or all of a wall or roof missing. For these cases, the vent area is the area of the opening, and the definition of α_e that satisfies the scaling law is the ratio of the open area to the total interior area of the container (including floor). However, for a multi-layer suppressive structure, α_e has to be defined. Because some data are available for the one-opening cubicles, the results from the suppressive structures can be compared to them to obtain an equivalent α_e. The duration of the quasi-static pressure is a function of the peak-pressure, which is sometimes difficult to interpret, and the α_e will, of course, vary accordingly. However, if the quasi-static pressure from the multi-layer test structure is read in a fashion similar to the data from the one-opening cubicles, a comparison can be made. As will be shown later (see Fig. 5), the peak pressure was defined by drawing a smooth curve through the mean amplitude of the oscillations and extrapolating back to about the end of the second reflection, which is still considered part of the reflected pressure loading. This also accounts to a certain extent for the small increment of time that is required for the quasi-static pressure to build up within the enclosure. With this maximum pressure, the duration time as read from the records, and the volume of the structure, the only other parameter required to plot the uniformly vented data is a value of α_e. For the structures using I-beams, if one uses the α_e as computed for the external pressure data fits to determine the effective vent area, the quasi-static pressure data compare reasonably well with the one-opening cubicle data. For the structure using perforated plates alone and in combination with angles, if the external pressure α_e is multiplied by two, the quasi-static pressure data also compare well with the one-opening cubicle data. Thus, using this method for computing α_e, durations can be estimated for a multi-layer, uniformly vented structure.



$A_{vent} = \lambda \sum_{1}^{n} g_i / N$

λ = length of element

p = projected length of angle

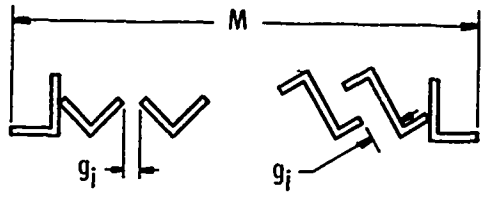
N = 2 or 4 (see text)

A_{wall} = LM

L = length of wall

α = A_{vent} / A_{wall}

(a) Nested angles



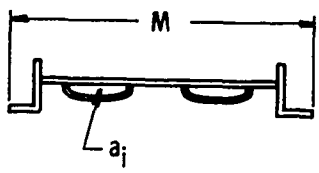
$A_{vent} = \lambda \sum_{1}^{n} g_i$

n = number of openings

A_{wall} = LM

α = A_v / A_w

(b) Side-by-side angles or zees



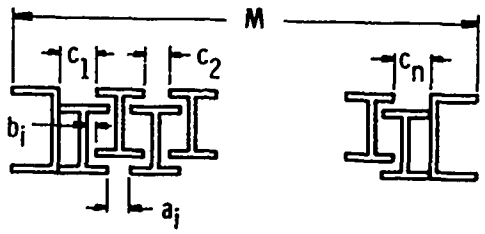
$A_{vent} = \lambda \sum_{1}^{n} a_i / 2$

a_i = open area of louvre

A_{wall} = LM

α = A_v / A_w

(c) Louvres



$A_{v_1} = 2\lambda \sum_{1}^{n} a_i$

$A_{v_2} = A_{v_3} = 2\lambda \sum_{i}^{n} b_i$

$A_{v_4} = 2\lambda \sum_{1}^{n} c_i$

$\alpha_1 = A_{v_1} / A_w$, ...

(d) Interlocked I-beams

Fig. 1 - Definition of effective area ratio for various structural elements

PRESSURES OUTSIDE SUPPRESSIVE STRUCTURES

From the model analysis, the functional expression for the side-on overpressures outside of a suppressive structure is

$$P_s = f_1(R/W^{1/3},\ X/R,\ \alpha_e) \qquad (1)$$

As shown in Reference {4}, this equation is assumed to nave the form

$$P_s = A(Z)^{N1}(X/R)^{N2}(\alpha_e)^{N3} \qquad (7)$$

Taking logarithms of both sides and making the equation linear, a least-squares curve fit can be developed using the experimental data and stating that

$$\begin{bmatrix} 1.0, & \ln Z, & \ln Z/R, & \ln \alpha_e \end{bmatrix} \begin{bmatrix} \ln A \\ N_1 \\ N_2 \\ N_3 \end{bmatrix} = \begin{bmatrix} \ln P_s \end{bmatrix} \qquad (8)$$

or substituting matrix notation,

$$[L]\ [N] = [P] \qquad (8a)$$

A least-squares fit results for the N matrix when

$$[N] = [L^T L]^{-1}\ [L^T]\ [P] \qquad (9)$$

The experimental data used to make this curve fit have been generated by the Edgewood Arsenal {6,14,15} and the Ballistic Research Laboratories (BRL) {5} using a variety of multi-layer vented structures. In Reference {4}, a similar fit was made with the limited data that were available at that time. However, subsequently, many more measurements have been made, and better and more up-to-date curve fits are presented here. Because of the large data base now available, some of the early data have been eliminated when there was a justifiable reason. For example, over half of the early data were from a cubic structure in which one wall was changed to test different numbers of layers as well as different types of elements to obtain a variety of α_e. The other three walls and the roof remained the same throughout the tests. Measurements were then made of the side-on pressure exiting through the interchangeable wall. Thus, the structure was not uniformly vented.

The structures tested by the EA have consisted of panels of perforated plates, angles, zees, and louvres. Those tested by the BRL were of basically two types. One type had similar cross-sections as the EA structures and consisted of a series of perforated plates by themselves or plus angles. The second type of structure consisted of interleaved I-beams which had not been tested before. Table 1 lists the different types of cross-sections used and the equivalent vent area ratio computed as outlined earlier in the paper. The main problem encountered in reducing all the data to a common base was determining the relative vent area ratios, especially for the interlocking beams. Since the structures tested by the EA were of similar cross-section to the O-configurations tested by the BRL, the data from these two sets of experiments were used to make the first curve fit. After some trials to obtain the relative α_e's, the data fit very well, as shown by Eq. (A) in Table 2. The estimate of the standard deviation, S, for the experimental data about the equation is ±12.7%, and the limits of the pi-terms for which the equation is valid are also presented in the table.

The data for the interlocking I-beams were then used to determine their α_e's so that a good curve fit to the entire data base could be made. Using the α_e's listed in Table 1 for these three configurations, the data points from the I-beam structures were fitted, and the results are shown in Table 2. Again, Eq. (B) fit the data very well with S = ±14.2%. For comparison purposes, the BRL data from only the O-configurations were fitted, and the results are shown in Table 2. Equation (C) fit the data very well with an S of ±11.9%. Thus, the two sets of BRL data, as well as the one set obtained by the EA, correlate well within themselves.

Finally, the total experimental data base was curve fitted to obtain a general expression for P_s. The resulting equation is shown in Fig. 2. The resulting value of S was ±19.9%, slightly worse than before, but nevertheless rather good considering the great variety of cross-sections involved. Again, the limits of the pi-terms should not be violated, or considerable error could result in predicting P_s or determining an α_e for a particular structure.

Since one of the primary purposes of a suppressive structure is to reduce

TABLE 1
Effective Vent Area Ratios for Various Structures Tested

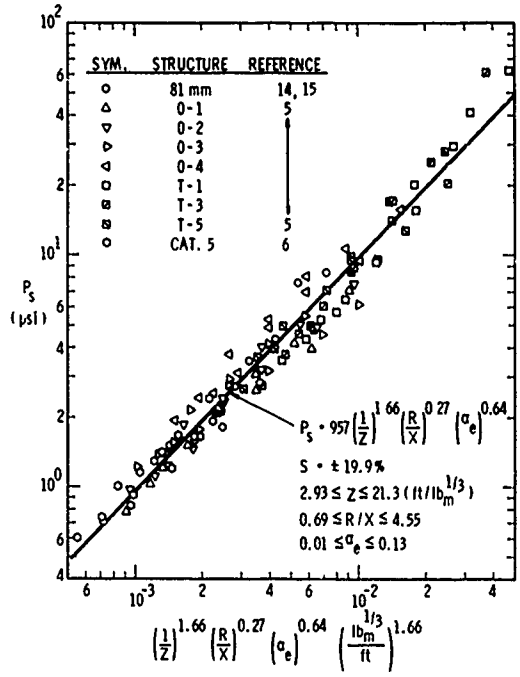
Structure	Cross-Section Elements	α_e
81 mm, Ref. (18)	Zees, Perforated Plates, and Louvres	0.025
T-1, Ref. (5)	Interlocking I-beams	0.130
T-3, Ref. (5)	Interlocking I-beams	0.090
T-5, Ref. (5)	Interlocking I-beams	0.047
O-1, Ref. (5)	Nested angles and Perforated Plates	0.010
O-2, Ref. (5)	Nested Angles and Perforated Plates	0.011
O-3, Ref. (5)	Perforated Plates	0.012
O-4, Ref. (5)	Perforated Plates	0.023
Cat. 5, Ref. (6)	Side-by-side Angles and Perforated Plates	0.017

TABLE 2
Prediction Equations for External Side-on Pressures from Various Suppressive Structures

Eq.	Structure	Side-on Pressure (psi)*
A	81 mm; Refs. (14,15) O-1,2,3,4; Ref. (5) Cat. 5; Ref. (6) Perforated plates with and without angles or zees and louvres	$P_s = 4384 \left(\frac{1}{Z}\right)^{1.64} \left(\frac{R}{X}\right)^{0.45} \left(\alpha_e\right)^{1.03}$ $S = \pm 12.7\%$ $2.93 \leq Z \leq 21.3$ (ft/lb$_m^{1/3}$)** $0.69 \leq R/X \leq 4.55$ $0.01 \leq \alpha_e \leq 0.025$
B	T-1,3,5; Ref. (5) Interlocking I-beams	$P_s = 1901 \left(\frac{1}{Z}\right)^{2.3} \left(\frac{R}{X}\right)^{0.64} \left(\alpha_e\right)^{0.55}$ $S = \pm 14.2\%$ $2.94 \leq Z \leq 15.0$ (ft/lb$_m^{1/3}$)** $1.16 \leq R/X \leq 4.55$ $0.047 \leq \alpha_e \leq 0.13$
C	O-1,2,3,4; Ref. (5) Perforated plates with and without nested angles	$P_s = 3586 \left(\frac{1}{Z}\right)^{1.51} \left(\frac{R}{X}\right)^{0.319} \left(\alpha_e\right)^{1.02}$ $S = \pm 11.9\%$ $2.93 \leq Z \leq 15.0$ (ft/lb$_m^{1/3}$)** $1.16 \leq R/X \leq 4.55$ $0.01 \leq \alpha_e \leq 0.023$

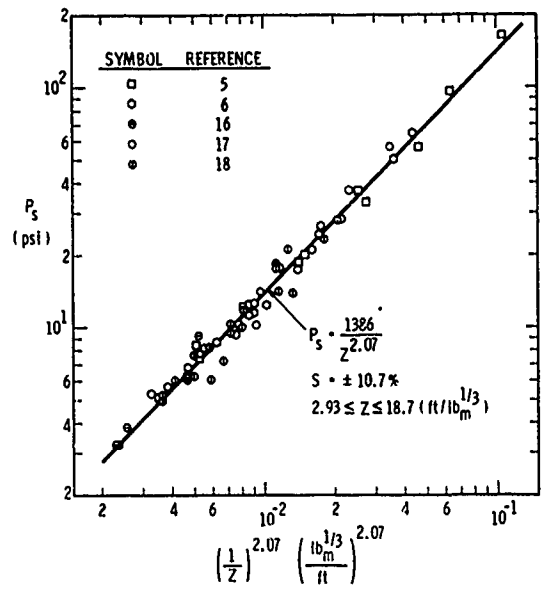
*1 psi = 6.895×10^3 Pa

**1 ft/lb$_m^{1/3}$ = 0.3967 m/kg$^{1/3}$



1 PSI = 6.895 kPA
1 FT/LB$_M^{1/3}$ = 0.3967 M/KG$^{1/3}$

Fig. 2 - Curve fit to side-on pressures outside suppressive structures



1 PSI = 6.895 kPA
1 FT/LB$_M^{1/3}$ = 0.3967 M/KG$^{1/3}$

Fig. 3 - Free-field peak side-on blast pressure

the external side-on overpressures, the degree of reduction by a particular structure is determined by comparing the external pressure at a given distance from a charge to what it would have been without the structure, i.e., the free-field pressure. Consequently, free-field pressure data, also generated by the EA {6,16-18} and the BRL {5}, have been curve-fitted in a similar fashion to the structural external pressure data to provide a free-field comparison curve. From the scaling laws, the free-field overpressure is proportional to the scaled distance, $Z = R/W^{1/3}$. However, because one portion of the data is from experiments where the charge was placed over earth, while the other portion is from experiments over a concrete pad, the difference in the quality of the reflecting surface prevents direct comparison of both sets of data. Because all of the suppressive structures tested to date have a concrete floor (or equally good reflective surface), the earth data were adjusted by multiplying the charge weight used by an empirical factor of 0.62, which made the data fit the best. Within the specific limits of Z shown in Fig. 3, the free-field data fit very well about the equation shown with an S of ±10.7%. This curve then provides the free-field peak pressures at various values of Z for estimating the reduction caused by a suppressive structure.

From the experiments conducted by BRL {5}, side-on impulse was also obtained by integrating the pressure-time histories. The maximum impulses measured, divided by the cube root of the explosive charge weight (scaled impulse), are reported. The scaling law for the external scaled impulse from a suppressive structure stated earlier in the paper is

$$\left(i_s/W^{1/3}\right) = f_2(R/W^{1/3},\ X/R,\ \alpha_e) \qquad (1)$$

Using a similar method as for the peak pressures, the scaled impulse was curve-fitted to obtain a prediction equation. Again, the only parameter which lacks an explicit definition is α_e. Using the vent area ratios derived for the peak pressure data fit as the starting point, a least-squares fit was

attempted. The majority of the data fit well except for the data from the two structures which had nested angles. In these two cases, the angles appeared to have attenuated the impulse more than the peak pressure compared to the perforated plate structures. If the angles were assumed to be twice as effective in reducing the impulse as was computed for the peak pressure case, the impulse data fit very well. Thus, using the newly computed α_e's of 0.008 and 0.010 for the O-1 and O-2 configurations, respectively, the data from the perforated plate cross-section with and without angles provide an excellent fit, as shown in Table 3. The impulse data from the I-beam structures fit even better about Eq. (E), shown in Table 3 with an S of ±6.5%. Both sets of data were then used together to derive the equation shown in Fig. 4. This last equation fits the data slightly worse than the two individual sets did. However, it is as good a fit as was achieved previously with the corresponding peak side-on pressure data.

PRESSURES INSIDE SUPPRESSIVE STRUCTURES

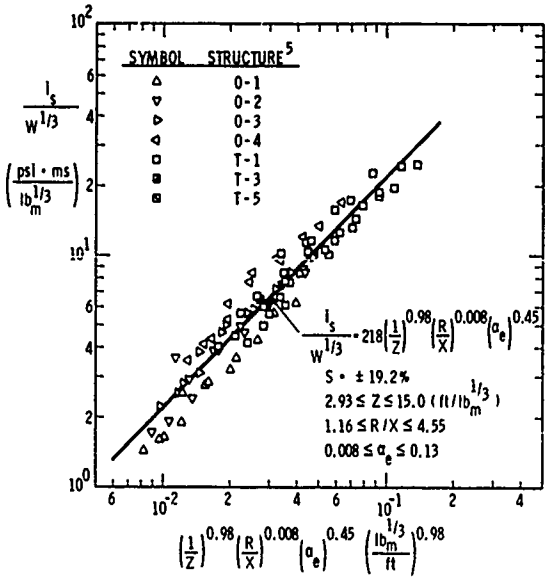
When an explosion occurs within a suppressive structure, the blast wave reflects from the inner surfaces of the structure, implodes toward the center, and re-reflects one or more times. The amplitude of the reflected waves usually decays with each reflection, and eventually the pressure settles to a slowly decaying level, which is a function of the volume and vent area of the structure and the nature and energy release of the explosion. A typical time history of pressure {19} at the wall of a suppressive structure is shown in Fig. 5. The process of reflection and pressure buildup in either unvented or poorly vented structures has been recognized for some time, dating from World War II research on effects of bombs and explosives detonated within enclosures {20}. More recently, study of these pressures has revived because of interest in design of vented explosion chambers, and we will discuss here the recent work.

TABLE 3
Prediction Equations for External Side-on Scaled Impulse from Various Suppressive Structures

Eq.	Structure	Side-on Scaled Impulse $(psi\text{-}ms/lb_m^{1/3})^*$
D	O-1,2,3,4; Ref. {5} Perforated plates with and without nested angles	$\frac{i_s}{W^{1/3}} = 1412 \left(\frac{1}{Z}\right)^{0.88} \left(\frac{X}{R}\right)^{0.074} \left(\alpha_e\right)^{0.90}$ S = ±12.3% $2.93 \leq Z \leq 15.0$ $(ft/lb_m^{1/3})^{**}$ $0.22 \leq X/R \leq 0.86$ $0.008 \leq \alpha_e \leq 0.023$
E	T-1,3,5; Ref. {5} Interlocking I-beams	$\frac{i_s}{W^{1/3}} = 134 \left(\frac{1}{Z}\right)^{1.16} \left(\frac{R}{Z}\right)^{0.15} \left(\alpha_e\right)^{0.18}$ S = ±6.5% $2.94 \leq Z \leq 15.0$ $(ft/lb_m^{1/3})^{**}$ $1.16 \leq R/X \leq 4.55$ $0.047 \leq \alpha_e \leq 0.13$

*1 $psi\cdot ms/lb_m^{1/3}$ = 8.974 $kPa\cdot ms/kg^{1/3}$

**1 $ft/lb_m^{1/3}$ = 0.3967 $m/kg^{1/3}$



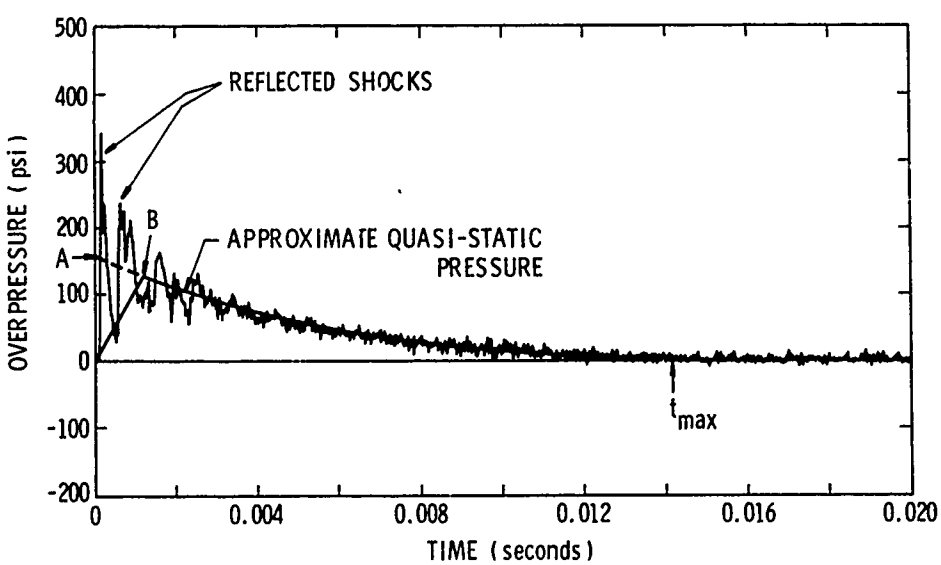
1 FT/LB$_M^{1/3}$ = 0.3967 M/KG$^{1/3}$

1 PSI·MS/LB$_M^{1/3}$ = 8.974 KPA·MS/KG$^{1/3}$

Fig. 4 - Curve fit to scaled side-on impulse outside suppressive structures

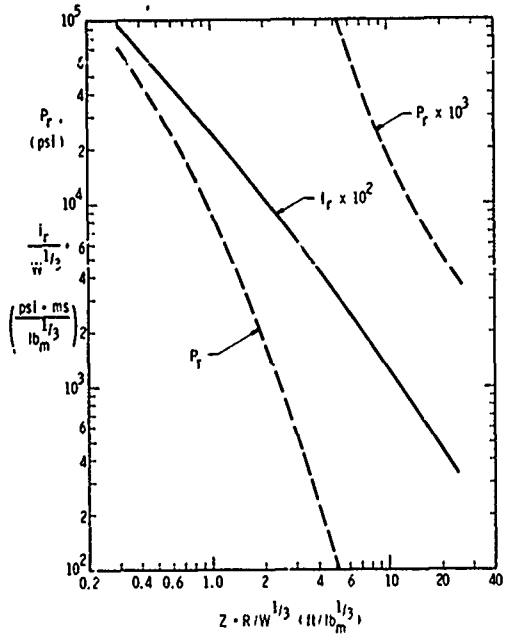
Reflected Pressures

The initial shock impinging on the inner surfaces of suppressive structures applies an intense loading of short duration to these surfaces. This loading is complicated by the geometry of the surface, i.e., the innermost layer of the wall, and by the overall geometry of the structure. If the wall inner surfaces consist of relatively flat surfaces such as perforated plates or flanges of nested I-beams, the initial blast wave will reflect more or less normally from such surfaces. The reflected pressures and impulses can then be estimated with reasonable accuracy from tests of blast waves normally reflected from rigid, plane surfaces {2,21,22}, or from sources of compiled data based on such tests {1-3}. But, if the inner surfaces of the suppressive structure consist of geometries such as closely nested angle irons, the initial reflection process is much more complex, and measurement or prediction of the initial shock loading on such surfaces is quite difficult. An upper limit to the loading on each angle iron can perhaps be estimated by applying normally reflected pressures and impulses to the areas not shielded by adjacent angles. Curves of scaled reflected pressure P_r and impulse i_r are included here as Fig. 6 for prediction



1 PSI = 6.895 KPA

Fig. 5 - Typical time history of internal pressure at inner surface of a suppressive structure



1 PSI = 6.895 kPA
1 PSI·MS/$LB_M^{1/3}$ = 3.974 kPA·MS/$KG^{1/3}$
1 FT/$LB_M^{1/3}$ = 0.3967 M/$KG^{1/3}$

Fig. 6 - Normally reflected peak pressures and impulses for bare, spherical Pentolite

of the initial shock loading. These curves are fitted to data for bare Pentolite spheres from References {1,2,21 22}. To date, there are insufficient data on reflected pressure loads on actual suppressive structures to improve on curves such as these figures, although references such as Koger and McKown {6} do give a few data points.

The initial and later reflected shock loads on the walls of suppressive structures are complicated not only by the character of their surfaces, but also by the overall structural geometry. Only for spherical chambers is the reflection process regular and easily predictable. But, rectangular box or cylindrical geometries are more practical shapes and are more adaptable to the vented panel designs common in suppressive structures. Complex reflections and reinforcements can occur in corners of such structures, and the implosion process after shock reflection is complex and irregular. Fortunately for one's ability to predict these loads, the latter shocks seem from data such as those in Reference {19} to be greatly attenuated compared to the first shock, so that ignoring reflected waves, or "smoothing" through the pressure-time traces, usually provides an acceptable approximate pressure loading.

Quasi-Static Pressures

Prior to the suppressive structures program, several experimental studies were conducted to measure the maximum pressures and venting times for certain vented chambers. Weibull {23} reports maximum pressures for vented chambers of various shapes having single vents with a range of vent areas of $(A/V^{2/3}) \leq 0.0215$. These maximum quasi-static pressures are shown by Weibull to be independent of the vent area ratio, and to be a function of charge mass-to-volume ratio (W/V) up to 0.312 lb/ft^3 (4.998 kg/m^3). He fit a single straight line to his data, but Proctor and Filler {7} later showed that fitting a curve to the data, with asymptotes to lines related to heat of combustion for small (W/V) and to heat of explosion with no afterburning for large (W/V), was more appropriate. Additional data on maximum quasi-static pressures and on venting times have been obtained by Keenan and Tancreto {8}, and by Zilliacus, et al. {9}. Data from Reference {8} were used in Reference {4} to give predictions of maximum quasi-static pressures P_1 versus (W/V), and a scaled duration of this pressure versus scaled vent area ratio for initial design of suppressive structures. Concurrent with experimental work which preceded applications to suppressive structures, Proctor and Filler {7} developed a theory for predicting time histories of quasi-static pressures in vented structures. Kinney and Sewell {11} did likewise, and also obtained an approximate formula for this time history. Converted to the scaled parameters discussed earlier, this equation is:

$$\ln \bar{P} = \ln \bar{P}_1 - 2.130\ \bar{\tau} \qquad (10)$$

This equation gives a value for scaled venting time $\bar{\tau}$ of

$$\bar{\tau}_{max} = 0.4695 \ln \bar{P}_1 \qquad (11)$$

The problem of blowdown from a vented chamber is also solved theoretically by Owczarek {12,13}, given initial conditions in the chamber, but assuming isentropic expansion through the vent area.

A few measurements were made of peak quasi-static pressures early in the suppressive structures program {16},

but only recently have sufficient additional data been recorded for this class of structure to add significantly to the measurements for other types of vented or unvented chambers. Reference {19} contains most of the suppressive structures venting data to date, supplemented by several measurements reported in Reference {6}. In comparing such data with either previous data or theory, there are several questions raised by the general physics of the process and by the differences in venting through layered panels as opposed to venting through single openings in walls. Referring to Fig. 5, one can see that the maximum quasi-static pressure is quite difficult to define because it is obscured by the initial shock and first few reflected shocks. Obviously, several reflections must occur before irreversible processes attenuate the shocks and convert their energy to quasi-static pressure. It therefore seems inappropriate to call point A in Fig. 5 the peak quasi-static pressure, although this is the point used in Reference {19} to compare with code predictions from Proctor {7} and the Kinney and Sewell equation [Eq. (10)]. We have chosen to allow some time for establishing the maximum pressure, such as point B in Fig. 5. For the records in Reference {19}, this time was chosen to be 1 ms, which allowed at least two shock reflections. Koger and McKown {6} employed a somewhat similar method to estimate peak quasi-static pressure.

Figure 5 also illustrates another problem inherent in reduction of vented pressure data, i.e., accurate determination of duration of this pressure. When the pressure traces approach ambient, the shock reflections have largely decayed. But, they approach the baseline nearly asymptotically, so that the duration is quite difficult to determine accurately. A possible duration t_{max} is shown in the figure.

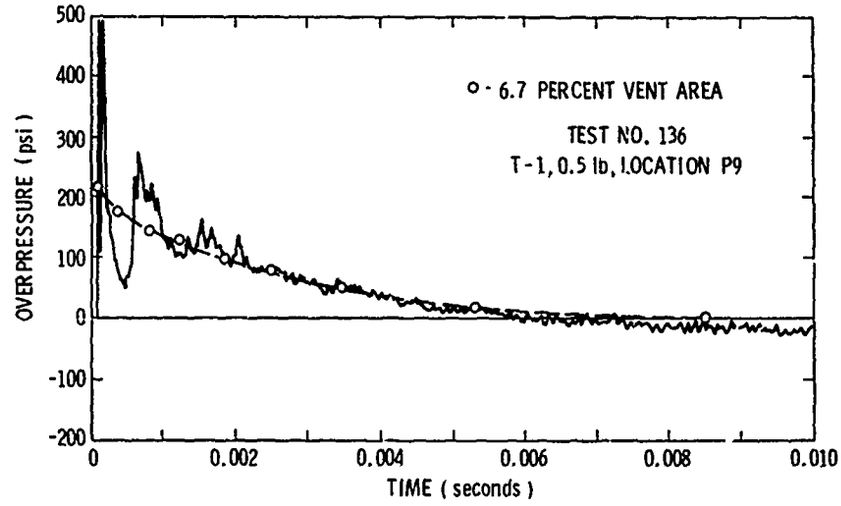
As has been pointed out previously, the definition of α_e for suppressive structures is not well defined. A possible definition of an α_e has been given earlier, but the specific value of this quantity for a given structure is not necessarily the same for venting and for external blast because the physical processes occur on much different time scales. Kingery, et al. {19} estimate α_e for blowdown by curve-fitting to calculations using Proctor's computer program {7}. An example of their estimating is shown in Fig. 7, indicating an α_e of 0.067 for this particular test and configuration. We found, however, that values of α_e that were adjusted to give good correlation with attenuation of blast pressures outoutside the structure also seemed to give reasonable correlations of data from Reference {19} with scaled venting times for curves from Reference {4}.

For use in predicting maximum quasi-static pressures and venting times, we present two graphs. The first, Fig. 8, is identical to the one originally made in Reference {4} of P_{max} versus (W/V). Additional data points from References {6} and {19} have been added, but these are close enough to the original curve that no change seems warranted. The second plot in Fig. 9 shows data from four references for scaled durations of vented pressures $\bar{\tau}_{max}$ versus scaled absolute maximum pressure $\bar{P}_1$. This form of scaled presentation is dimensionless and replaces the earlier dimensional one of Reference {4}. It also allows predictions from theory to be compared with data. Kinney and Sewell's Eq. (11) is plotted in this figure, as is a theoretical curve developed from Owczarek in Reference {12}.* Data scatter is great enough that curve-fitting is difficult. But, Kinney and Sewell's equation seems to fit much better than the more sophisticated theory of Owczarek. We suggest using Eqs. (10) and (11) until more data become available. Note that the scatter in the data results from the fact that two measured quantities, maximum pressure and duration time, are plotted against each other, and thus the measurement errors are amplified.

Intrapanel Pressures

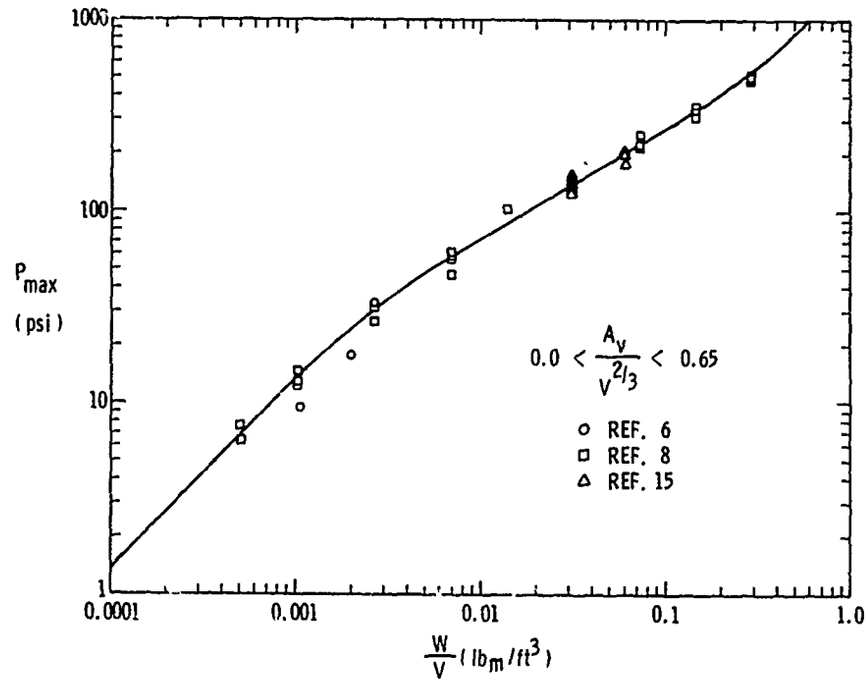
To properly design a suppressive structure to survive the blast loading, it has been necessary to estimate the loads due to gas pressure on the structural components of each layer of the walls. The flow makes a series of turns through varying areas and volumes to reach the lower pressure environment of the atmosphere. The pressure in these various compartments differs from the peak quasi-static pressure that is established in the initial compartment after the blast. Since no data presently exist for these intrapanel pressures, an analysis of the flow through the series of compartments has been conducted to estimate the pressure-time history in each compartment. Venting

*Predictions of time histories of vented pressures are also given in Reference {12}.



1 PSI = 6.895 kPA

Fig. 7 - Comparison of measured data and computer output for Proctor's program



1 PSI = 6.895 kPA

1 LB_M/FT^3 = 16.02 KG/M^3

Fig. 8 - Peak quasi-static pressure in partially vented enclosures

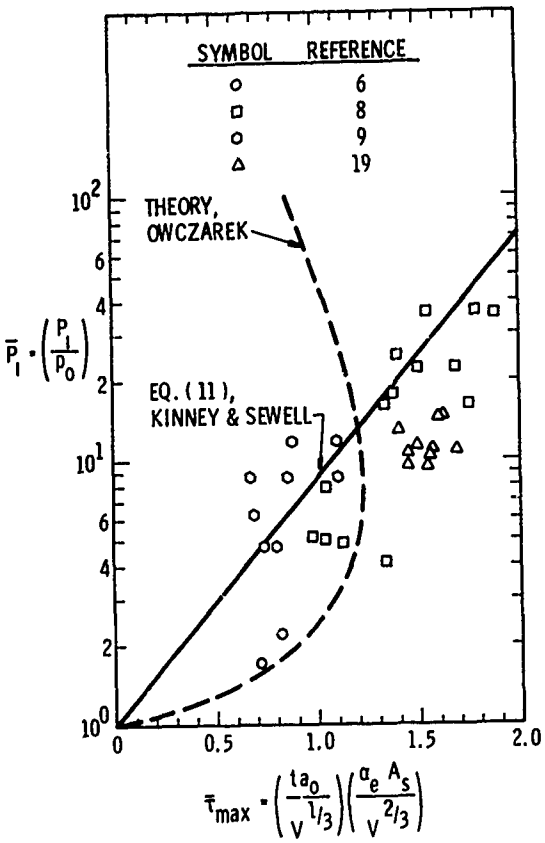


Fig. 9 - Scaled blowdown duration vs scaled maximum pressure

of a gas in a container through an open opening has been investigated by other researchers {10,11}. Kinney and Sewell {11} considered a confined volume of air that has been pressurized due to an internal explosion. The gas obeys the ideal equation of state from which the pressure rate is determined as

$$\dot{P} = (RT/MV)\dot{m} + (P/T)\dot{T} \qquad (12)$$

where P is the absolute pressure, m the mass of gas retained in volume V, R the molar gas constant, M the formula mass, and T the absolute temperature. The mass flow rate is given by:

$$\dot{m} = A\rho u \qquad (13)$$

where ρ is the gas density, A is the cross-sectional vent area, and u is the velocity of the escaping gas.

The maximum attainable flow rate for a given upstream pressure is:

$$\dot{m} = C_D AP/(RT/M)^{1/2}\left[(2\gamma/\gamma+1)^{1/2} \cdot (2/\gamma+1)^{(1/\gamma-1)}\right] \qquad (14)$$

where γ is the ratio of specific heats, and C_D is the discharge coefficient of the vent area.

The temperature rate $\dot{T}$ which is due to the energy carried away by the vented stream and the heat transfer between the gas and the walls is given by:

$$\dot{T} = T(\gamma-1)\dot{m}/m + \left[T(\gamma-1)/PV\right]\dot{q} \qquad (15)$$

where $\dot{q}$ is the heat flow rate. In cases where the venting rate is very great, the heat transfer term can be neglected. These equations can be so solved to give the pressure rate using a numerical procedure which Kinney and Sewell {11} outline in their report. The seemingly limiting assumption of this analysis is that the pressure rate can only be calculated down to the minimum overpressure required to give the maximum or sonic flow. Loads of importance may or may not occur below this pressure. Kinney and Sewell {11} have pointed out, however, that this analysis may be suitable below this minimum pressure due to experimental uncertainty at low overpressures and to the relatively small overpressures existing below this minimum.

The procedure for determining the pressure-time history of a single compartment with sonic flow as presented by Kinney and Sewell {11} was generally followed to develop a computer code (P00F1). P00F1 will compute the pressure time history of a multi-compartment system with sonic or subsonic flow.

Consider the following system (Fig. 10) with given initial conditions, where volume V_1 is inside the suppressive structure, and the remaining volumes represent the space between the walls.

Assume that an explosion occurs in V_1 and heats the air in this volume, causing quasi-static pressure rise. Also assume that the initial shock wave has blown through and that sonic flow exists through area A_1. The mass flow rate out of the initial compartment can be calculated from Eq. (14). Assuming that q is negligible, the temperature rate and pressure rate can be determined from Eqs. (15) and (12), respectively.

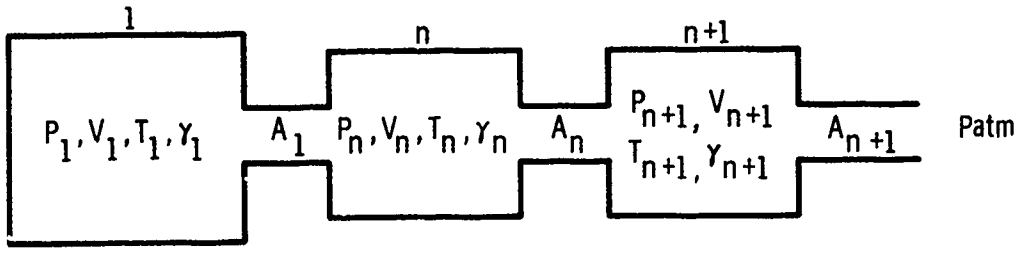


Fig. 10 - Schematic for venting calculations

The pressure P_n in the downstream compartments is dependent upon the change in the mass in the compartment due to the mass flow in $\dot{m}_{n-1}$ and the mass flow out $\dot{m}_n$. This can be calculated using the equation of state coupled with a mass balance of the system,

$$P_n = RT_n (\Delta m_n + \dot{m}_n)/V \qquad (16)$$

$$\Delta m_n = (\dot{m}_{n-1} - \dot{m}_n)\Delta t \qquad (17)$$

where $\dot{m}_{n-1}$ is known from the initial calculation. $\dot{m}_n$ is dependent upon P_n, making it necessary to solve Eqs. (16) and (17) simultaneously for P_n after substitution of Eq. (14) into Eq. (17). The temperature change and resulting temperature for the selected time increment in the n-th compartment can be calculated from the initial temperature and Eq. (15), using $\dot{m}_{n-1}$. With P_n and T_n, $\dot{m}_n$ can be calculated. This procedure is used for all compartments downstream of the initial compartment. After a complete pass is made through the system of compartments, the pressure in the initial compartment at the next time increment is determined from the pressure rate. The procedure is then repeated until the quasi-static pressure goes to zero.

The input parameters required for P00F1 are the initial values of vent area, discharge coefficient, mass, volume, pressure, temperature, atmospheric pressure, specific heat ratio, gas constant, and time increment for each compartment. The output of P00F1 lists the pressure as a function of time and also plots these results.

Predictions of pressure versus time using P00F1 have been compared to experimental data and to results using Proctor's code [19] and to the equation developed by Kinney and Sewell [11]. Generally, the total time for the overpressure to equal zero is 10-20% larger for the P00F1 predictions than for the other predictions. The difference is less when P00F1 is programmed to assume sonic flow exists throughout the venting process.

DISCUSSION

Development programs are being supported by the U. S. Army's plant modernization program for the design and application of uniformly vented suppressive structures. These structures should provide better protection of personnel and facilities while reducing the safety distances from potential hazards. In this paper we have presented scaling laws which apply to the blast waves that emanate from suppressive structures as well as to quasi-static pressure rise and decay from a detonation in a confined volume. Using external blast pressure data recently acquired, we have updated earlier curve fits for predicting peak side-on pressures from suppressive structures and free-field detonations. In the process we have empirically defined a method for computing relative vent areas for multi-layered, uniformly vented structures so that predictions of external pressures and the degree of reduction of these pressures can be made for a variety of wall configurations. Using experimental data from one-opening cubicles and suppressive structures, a similar method for estimating effective vent areas is given which correlates with quasi-static pressure decay times.

Along with external side-on pressure predictive equations for specific structures and all types of suppressive structures for which data are available, predictive equations for side-on impulse have also been generated. Reflected pressure loading of the suppressive structures is discussed briefly, and a summary graph is given for estimating the normally reflected peak pressures and impulses as a function of

the scaled distance. For the quasi-static pressure load (which follows the reflected impulsive load when a detonation occurs in a relatively closed volume), graphs are also presented for estimating the maximum quasi-static pressure and venting times. Finally, the development of a computer code to estimate the intrapanel pressures caused by the internal quasi-static pressure is presented.

From the work reported in this paper, it is apparent that suppressive structures can be designed to significantly attenuate overpressures and impulses in blast waves which emanate from them, compared to explosions occurring in the open or in frangible structures. Specific applications for these structures can have quite different requirements for blast attenuation, depending on factors such as the magnitude of the potential explosive hazard, proximity to adjacent structures or operations,or whether personnel are normally allowed near the building or operation. For each application, allowable blast overpressures or impulses, or both, can undoubtedly be established versus distance or at specific distances from the suppressive structure. As an example, the Category 1 structure discussed in some detail in References {4} and {24} was designed to attenuate the blast overpressure from 2500 lb of Composition B exploding in a melt kettle, to 50% or less of the free-field overpressure at the intraline distance for this quantity of explosive. This requirement then dictated the blast attenuation by the suppressive structure, and hence dictated much of the detail of the vent panel designs. The equations presented in this paper would easily allow a choice of a different blast attenuation for a number of vent panel configurations. For applications where the blast hazard is less severe, the required attenuation can perhaps be less, and more "open" panel designs will result. This, in turn, will affect blowdown pressures and the structural design of the suppressive structure. The designer should, of course, realize that blast attenuation is only one aspect of suppressive structure design, with containment of fragments, or attenuation of fireballs or firebrands often being equally important, or overriding, factors which must be considered.

This paper is in some respects a progress report on blast pressure studies in the suppressive structures program. Considerable related work is presently under way, with Edgewood Arsenal sponsorship. More test data are being obtained or evaluated for internal reflected pressures, blowdown pressures, and blast waves emanating from model or full-scale structures of several different configurations and panel designs. The experiments are being supported by or compared to predictions using gas dynamic or blast physics analyses or computer codes. Because of this ongoing work, some of the prediction curves or equations presented here may be somewhat modified, and will undoubtedly be supplemented by additional predictions for intrapanel pressures and other parameters which are at present ill defined.

REFERENCES

1. H. J. Goodman, "Compiled Free-Air Data on Bare Spherical Pentolite," Rept. 1092, Feb. 1960.

2. W. H. Jack, Jr., "Measurements of Normally Reflected Shock Waves from Explosives Charges," BRL Memo Rept. 1499, 1963.

3. W. E. Baker, Explosions in Air, University of Texas Press, Austin, Texas, 1973.

4. W. E. Baker, P. S. Westine, P. A. Cox, and E. D. Esparza, "Analysis and Preliminary Design of a Suppressive Structure for a Melt Loading Operation," EA Tech. Rept. 1, Contract DAAD05-74-C-0751, March 1974.

5. R. N. Schumacher and W. O. Ewing, "Blast Attenuation Outside of Cubical Enclosures Made Up of Selected Suppressive Structure Panel Configurations," BRL MR 2537, Sept. 1975.

6. D. M. Koger and G. L. McKown, "Category 5 Suppressive Shield," EA-TM-76001, June 1975.

7. J. F. Proctor and W. S. Filler, "A Computerized Technique for Blast Loads from Confined Explosions," 14th Annual Explosives Safety Seminar, New Orleans, La., 8-10 Nov. 1972, pp. 99-124.

8. W. A. Keenan and J. E. Tancreto, "Blast Environment from Fully and Partially Vented Explosions in Cubicles," Civil Engineering Lab. Tech. Rept. 51-027, Feb. 1974.

9. S. Zilliacus, W. E. Phyillaier, and P. K. Shorrow, "The Response of Clamped Circular Plates to Confined Explosive Loadings," NSRDC Rept. 3987, Feb. 1974.

10. J. F. Proctor, "Internal Blast Damage Mechanisms Computer Program," 62 JTCG/ME-73-3, Joint Technical Coordinating Group for Munitions Effectiveness, 10 April 1973.

11. G. F. Kinney and R. G. S. Sewell, "Venting of Explosions," NWC Tech. Memo. 2448, July 1974.

12. W. E. Baker and G. A. Oldham, "Estimates of Blowdown of Quasi-static Pressures in Vented Chambers," EA Contract Rept. EM-CR-76029 (in publication).

13. J. A. Owczarek, Fundamentals of Gas Dynamics, Int. Textbook Co., Scranton, Pa., 1964.

14. "Proof Testing of the 81 mm Shield," Rept. EA-4E33B, Feb. 1974.

15. A. H. Lasseigne, "200 PSI Proof Test of the 81 mm Suppressive Shield,"Rept. EA-4E33K, Oct. 1974.

16. A. H. Lasseigne, "Static and Blast Pressure Investigation for the Chemical Agent Munition Demilitarization System: Sub-Scale," Rept. EA-FR-4C04, Nov. 30, 1973.

17. "Final Report Application of Suppressive Structure Concepts to Chemical Agent Munition Demilitarization System (CAMDS)," Rept. EA-FR-2B02, July 27, 1973.

18. "81 mm Suppressive Shielding Technical Data Package," Rept. EA-4E33, Jan. 1974.

19. C. Kingery, R. Schumacher, and W. Ewing, "Internal Pressure from Explosions in Suppressive Structures," BRL IMR 403, June 1975.

20. W. D. Kennedy, "Explosions and Explosives in Air," in Effects of Impact and Explosion, Summary Tech. Rept. of Div. 2, NDRC, Vol. 1, 1946.

21. O. T. Johnson, J. D. Patterson II, and W. C. Olson, "A Simple Mechanical Method for Measuring the Reflected Impulse of Air Blast Waves," BRL Memo Rept. 1088, 1957.

22. A. B. Wenzel and E. D. Esparza, "Measurements of Pressures and Impulses at Close Distances from Explosive Charges Buried and In Air," SwRI Final Rept., Contract DAAK02-71-C-0393, Aug. 1972.

23. H. R. W. Weibull, "Pressures Recorded in Partially Closed Chambers at Explosion of TNT Charges," Annals of the New York Academy of Sciences, 152, Art. 1, pp. 357-361.

24. W. E. Baker, P. A. Cox, E. D. Esparza, and P. S. Westine, "Design Study of a Suppressive Structure for a Melt Loading Operation," EA Contract Rept. EM-CR-76043 (in publication).

Discussion

Mr. Ferritto (Naval Civil Engineering Lab): How do you calculate the pressures and also what are the period and the resistance of the shell?

Mr. Baker: The pressures were calculated based on compiled data from Henry Goodman's work primarily which means Pentolite spheres, so we did not take into account the fact that the charge might be of some other shape. If you got very close to the wall that might affect things but I don't really think it does for the standoffs that we are talking about. The initial shock durations were very near the natural periods of these shells in almost all cases so we were in the regime for the initial shocks. The duration of the fundamental periods were also a few miliseconds so therefore there was resonance between repeated shocks and the chamber response and that was accounted for in our calculations. The gas venting pressure is very long because you are not allowing any venting.

Mr. Ferritto: What was the resistance level of the shell, the long duration resistance capacity of the shell?

Mr. Baker: Way beyond what was possible with any of these charges.

Mr. Mathews (Sandia Laboratories): Did you consider the auxiliary problem of fragment damage from the experiment?

Mr. Baker: No. The tests that are to be run in this chamber would all be for bare charges, or if they have fragmenting charges, they were willing to put in internal frag stops so it was not considered in this design.

Mr. Brockton (Naval Surface Weapons Center): Being crowded by neighbors I was curious about the sort of criteria were you working to for quietness?

Mr. Baker: Nothing specific; if we could have zero venting they would love it and it turns out that in this case that is what happened. I think that these really would be quiet, you would only have whatever sound would be generated on the outside by the shell driving the air and that would be very low because the velocities are low. There shouldn't be any venting needed for this chamber.

DEVELOPMENT OF STRUCTURES FOR INTENSE GROUND MOTION ENVIRONMENTS*

T. O. Hunter and G. W. Barr
Sandia Laboratories
Albuquerque, New Mexico

The development of the technology to insure the survivability of deep buried structures subjected to short-duration, high-intensity ground motion environments requires the integration and utilization of numerous analytical techniques, design concepts, and material characterizations. Sandia Laboratories recently completed a program to develop a large structure designed to survive the ground motion environment resulting from a nuclear detonation in volcanic tuff. The paper details (1) the analyses which established the characteristics of the ground motion environment and supported the structural design, (2) the design of an experiment chamber and commensurate protective structure, and (3) the results of the utilization of the design on an underground nuclear test. The results are compared with the analytical prediction, thereby reflecting on the validity of the models.

INTRODUCTION

Sandia Laboratories, in conjunction with its role in the development of nuclear weapons, has recently completed a program in which analysis, design, and testing were performed for large structures subjected to the intense ground motions resulting from nuclear detonations in volcanic tuff [1, 2].

The ground motion environment at the location of the structure is typically characterized by short-duration, high-intensity stress and acceleration pulses. This "free field" environment can consist of acceleration amplitudes which exceed 1000 g's and peak stress levels which are in excess of several kilobars (1 kilobar = approximately 15, 000 psi).

The objective of the program was the development of an experiment chamber and commensurate structures which would protect internal components from high stress and acceleration levels and thereby allow posttest recovery. In addition, the chamber had to meet other functional requirements such as accommodations for the local recording of data and the provision for a large high-speed closure system which would seal off the chamber opening.

BACKGROUND

At the initiation of the development program, limited specific information was available about the ground motion environment at the location considered. Even less definitive data had been gained about the response of structures to such environments. Consequently, an experiment [3] was conducted to establish a reference for further investigations. This experiment consisted of the emplacement, at a comparable location on an underground test, of a prototype experiment chamber which had been developed to investigate the functioning of the closure system and the resulting general structural behavior. The emplacement configuration for this ground motion experiment is depicted in Figure 1. The chamber was surrounded by cellular concrete in a cavity with an elliptical cross-section. The function

*Work performed in this paper was jointly supported by the Energy Research and Development Administration and the Defense Nuclear Agency.

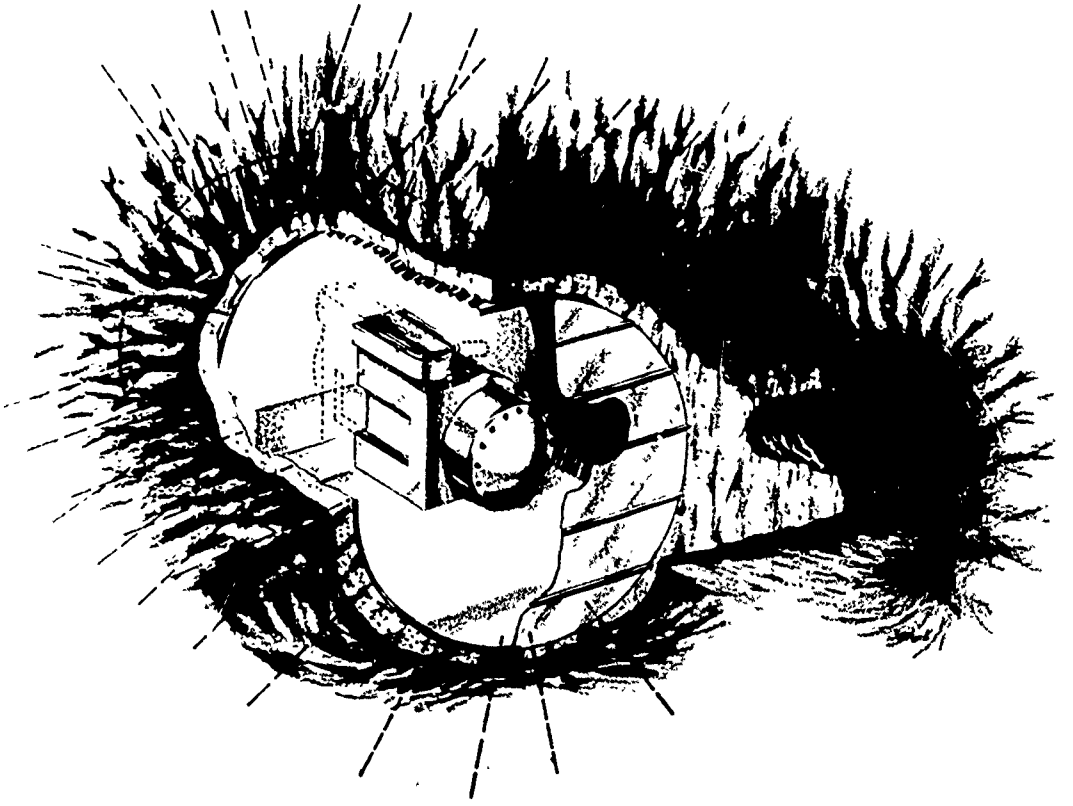


Figure 1. Ground Motion Experiment Emplacement

of the cellular concrete was to accommodate the deflection of the cavity wall and thereby limit the stress applied to the chamber. The free-field environment and the chamber were instrumented to determine the resultant responses.

The results of the ground motion experiment were extremely informative. Accelerometer data, which could only be obtained for about 8 milliseconds after ground shock arrival, indicated that the prototype chamber experienced a maximum acceleration of less than 100 g's, while the free-field acceleration exceeded 2000 g's. The free-field stress, however, exceeded expectations by about 50%, resulting in removal of the voids in the cellular concrete and the transmission of stress to the structure. This transmitted stress exceeded the capacity of the chamber, resulting in significant damage as indicated by Figure 2.

The ground motion experiment provided, in spite of some unexpected results, basic reference information for the free-field environment, the performance of stress mitigation systems, and structural response of the experiment chamber. This reference could then be used to establish the design of the new mitigation system and experiment chamber which would be developed.

SYSTEM DESIGN

The design of the entire protective system which was ultimately utilized is shown in Figure 3. The heart of the system was the experimental chamber which provided the ultimate protection for its contents. This chamber was a steel weldment consisting of large, thick-walled, cylindrical chambers with extensive reinforcing ribs. An integral part of the chamber is the closure system which placed a 1600-kg (3500 lb) titanium door across a 1-metre opening. This door was pneumatically operated and closed the opening very rapidly. The experiment chamber was designed to withstand a hydrostatic pressure of approximately 10^8 pascals (1.0 kilobar).

The protective structures, whose function was to attenuate the free-field stress and

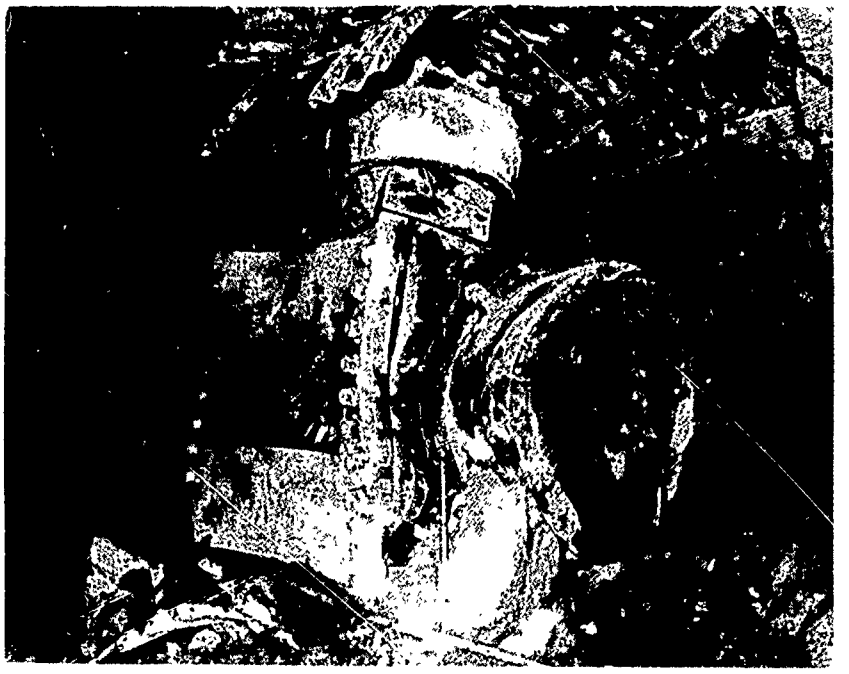


Figure 2. Ground Motion Experiment Results

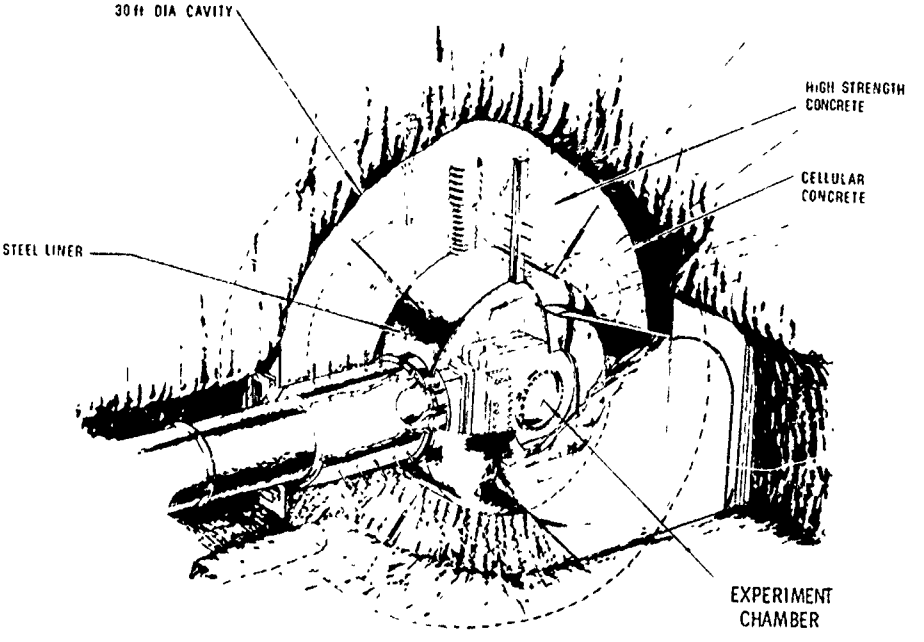


Figure 3. Protective Structure Configuration

acceleration to levels below the design capacity of the chamber and its contents, consisted of two principal components: (1) a high-strength spherical concrete shell and (2) an envelope of cellular concrete which surrounded the experiment chamber. A thin 0.0254-metre (1.0 in.) steel liner separated the cellular concrete and the structural concrete. The concrete sphere was approximately 9.1 metres (~30 ft) in diameter, while the area filled with cellular concrete was approximately 4.25 metres (14 ft) in diameter and 6.1 metres (20 ft) long.

The structural concrete was utilized to limit the deformations of the cavity containing the cellular concrete. If it could "withstand" the free-field stress in a manner similar to a thick-walled pressure vessel, the deformations of the inner cavity would be small; hence, the stress transmitted to the chamber would be limited to the "crush" strength of the cellular concrete.

The experiment chamber also contained an on-board data recording system which would allow long-duration recording of environmental and response data. Since data at these locations had typically been of short duration due to the limited survivability of connecting instrumentation cables, a tough, highly deformable cable system was also employed to provide as much real time data as possible.

The free-field environment was also monitored with "in situ" gages which were recorded via transmission through cables to recording trailers. In addition, devices were develcped which would measure and locally record the free-field stress and acceleration.

This protective system design was developed utilizing an array of analytical techniques to investigate alternate mitigation configurations. These analyses, which were developed and conducted in concert with the design effort, played a fundamental role in determining the dimensions and specifications for the configuration described.

ANALYSIS

The analytical program which was conducted in support of this development was a combination of simulation testing, material testing, and several analytical techniques. A statement of the basic problem which was addressed is depicted in Figure 4. It was necessary to resolve not only the response of the structure but also the appropriate system geometry, the free-field stress, and the motion characteristics of the experiment chamber.

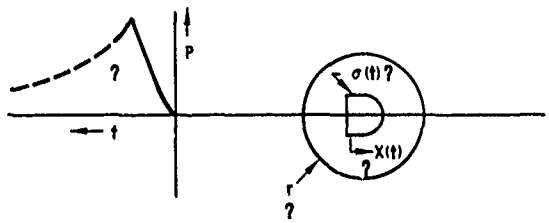


Figure 4. Basic Problem Statement

Free-Field Description

An essential part of the analysis effort was the quantification of the characteristics of the ground shock pulse. Resolution of the rise times, peak amplitudes, and duration of the stress wave in the rock material was required. In addition, particle motion histories were required to provide a complete description.

A one-dimensional Lagragian hydrocode and data from previous nuclear detonations were utilized to provide a description of the stress pulse.

Calculations [4] were performed on a wide range of probable material parameters for volcanic tuff with specific attention given to those data determined from coring programs. Parameter studies included the effects of varying water content, porosity, density, sonic velocity, elastic yield strength, and the pressure at which complete compaction was anticipated. The CHART D hydrocode [5] was utilized for these calculations in conjunction with continual correlation with precedent information. The prediction for the free-field stress pulse which was established by these analyses is shown in Figure 5.

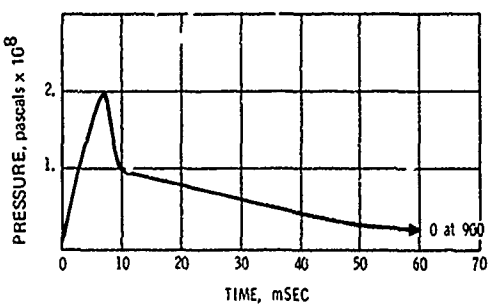


Figure 5. Free-Field Pressure Pulse

Rock-Structure Interaction

Upon determination of the free-field characteristics at the proposed location, the problem of the rock structure interaction could then be addressed. This problem posed a significant challenge for the analytical techniques which were available. Specific concerns were the adequacy of models in accounting for nonlinear material behavior, arbitrary dynamic loading, large deflections, and two-dimensional geometries.

Due to the complexity of treating the determination of stress and motion histories for the complete system, the problem was subdivided into two dynamic analyses: (1) the concrete shell with the cellular concrete and the experiment chamber modeled as a hydrodynamic material with a rigid inclusion, and (2) the concrete shell with an inner void instead of the cellular concrete and the experiment chamber. This latter model is consistent with the assumption that the concrete shell was to be designed for minimum deflection and hence a small compaction of the cellular concrete. If small deflections of the structural concrete could be achieved, the motion of the structure could then be analyzed independently by treating the system as a rigid body in a foam-filled void.

Two methods were utilized to determine the stress transmitted to the experiment chamber: a finite element technique which was developed for this application, HONDO [6], and a two-dimensional finite-difference stress wave code, TOODY [7]. The analytical model which was the basic field description in both methods is shown in Figure 6.

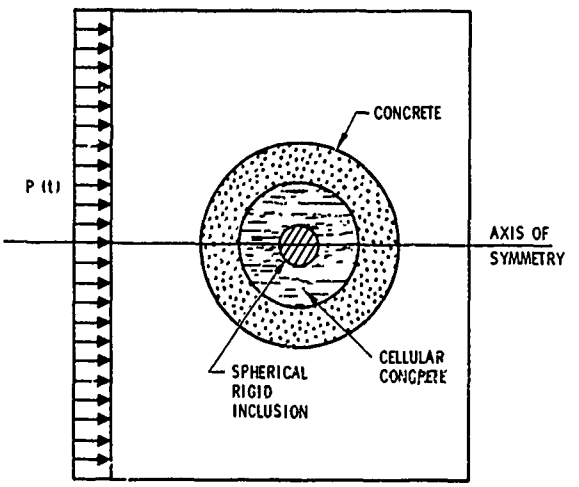


Figure 6. Analytical Model

Parameter Studies

Prior to detailed calculations on the specific system configuration, numerous parameter studies were performed on simple geometries to determine the sensitivity of deformations and stresses on variations in tuff, concrete, and cellular concrete properties. Linear elastic finite element studies performed on the model shown in Figure 6 with a central void (no structure or cellular concrete) indicated that deformations of any cavity were extremely sensitive to the shear strength of the host material, while relatively insensitive to the bulk behavior.

Information and intuition gained from the parameter studies were then used to develop a material testing program for all materials anticipated.

Material Testing

A testing program was initiated at Waterways Experiment Station, Sandia Laboratories, and other material testing laboratories to determine the bulk and shear behavior of concrete, tuff, and cellular concrete at the stress levels which were expected [8, 9]. Rate effects were incorporated by testing at three distinct loading regimes: (1) pseudo static, (2) millisecond pulse rise times, and (3) microsecond rise times. Uniaxial, triaxial, and hydrostatic tests were performed on selected samples.

The general bulk behavior observed in these three materials is shown in Figure 7. Numerous test results indicated that the pressure volume relation for concrete and tuff

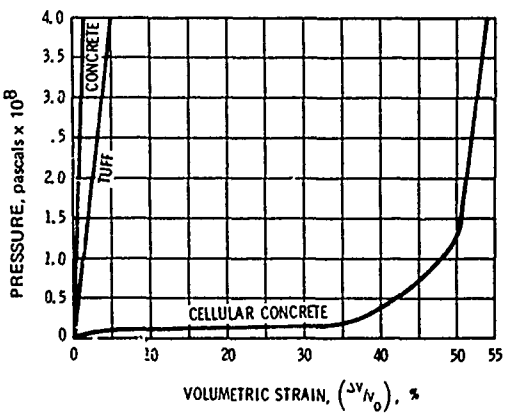


Figure 7. Pressure Volume Relations

could be modeled with sufficient accuracy with a linear elastic assumption, while cellular concrete was clearly nonlinear with volumetric deformations approaching 35% allowable at the nominal crush strength.

The respective shear behavior as characterized from triaxial test data is shown in Figure 8. These data indicated that, at the high confining pressures which could be anticipated, cellular concrete could support little shear stress and hence approach fluidic behavior; tuff could support only modest shear stress, while structural concrete, given sufficient attention to achieve high strength, could be expected to support significant shear loads.

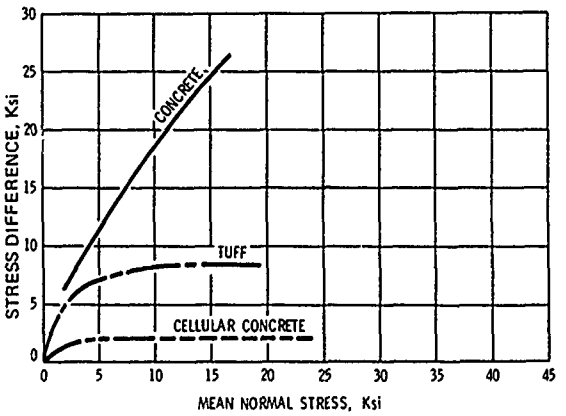


Figure 8. Static Triaxial Failure Data

TOODY Analyses

With sufficient background developed on parameter sensitivity and material behavior, specific analyses [10] were then performed on some selected configurations utilizing the TOODY code. Various constitutive models including linear elastic, hydrodynamic, and distended material were incorporated. Indicative of the results of these analyses are stress time histories for elements within the structural concrete as the stress wave engulfs the system. Figures 9 and 10 indicate the radial and tangential components of stress in the concrete shell at a point 0.76 metre (2.5 ft) from the outer surface in the horizontal plane. Similarity between these results and the classical solution of compressively loaded thick-walled spheres lent credibility to the calculations performed.

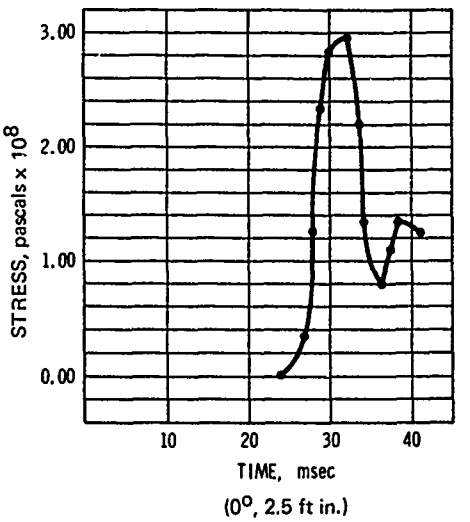


Figure 9. Radial Stress

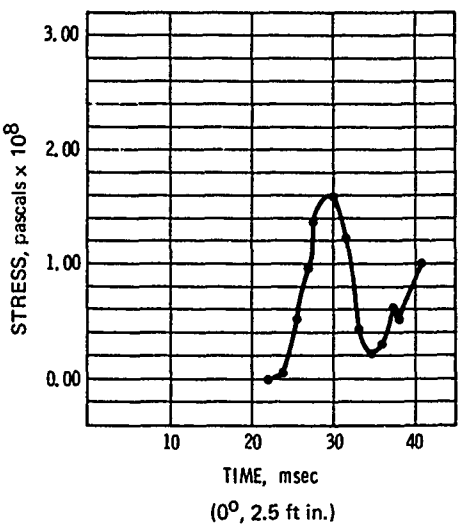


Figure 10. Tangential Stress

Finite Element Analyses

The finite element analyses [11, 12] which were performed on the final configuration were directed at correlating the shear stresses in the concrete shell with properties of concrete observed in the testing program. This accounting for a limit on shear stress of any element required the development of a new constitutive relationship which included a shear

failure criterion [13] and ultimately resulted in the final version of the HONDO code.

Figure 11 presents, by comparing J_2 (the second invariant of the stress deviator) and the mean confining pressure, the data which were measured during the triaxial tests on the concrete which was developed to exhibit high shear strength. Compared with these data are failure envelopes which are accounted for in the constitutive relation utilized in the HONDO code. Figure 12 presents the deflections corresponding to each failure envelope in the inner radius (4.24 metres) of the concrete sphere. The testing data indicated that the concrete mixed in the field (6×10^7 pascals unconfined compressive strength) could be bounded by the envelopes presented in these two figures. Hence, the deflections could be limited, which was the design basis for the entire system.

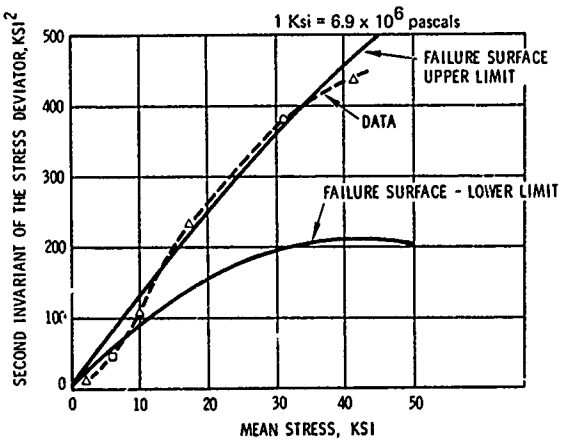


Figure 11. Failure Model Data Comparison

Motion Analysis

The assumption of low deformation of the concrete/cellular concrete interface as predicted by the finite element analysis allowed the application of a lumped parameter model for the determination of the motion history of the experimental chamber. Acceleration, velocity, and displacement histories were determined from a one-dimensional, nonlinear model. A simple two-degree-of-freedom calculation was performed in which the link of cellular concrete between the chamber and the protective structure was modeled as a piecewise linear function of the relative displacement. This "stiffness" was developed from the pressure-volume behavior of the cellular concrete which

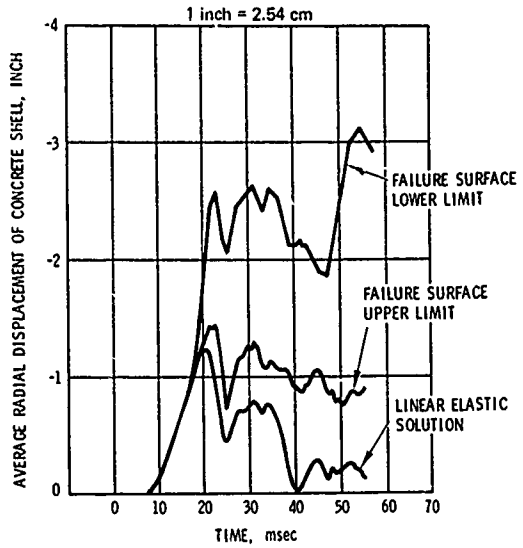


Figure 12. Influence of Failure Models on Cavity Deformation

was determined from material properties tests and scale model tests.

EXPERIMENTAL RESULTS

Active data were taken during the utilization of this design on an underground nuclear detonation which indicated that, to a large measure, many of the analytical predictions were confirmed. Figure 13 indicates the comparison of the free-field pressure pulse obtained from the active data with the prediction previously shown in Figure 5. Although the rise characteristics differ, the agreement of peak amplitude and decay characteristics was considered excellent.

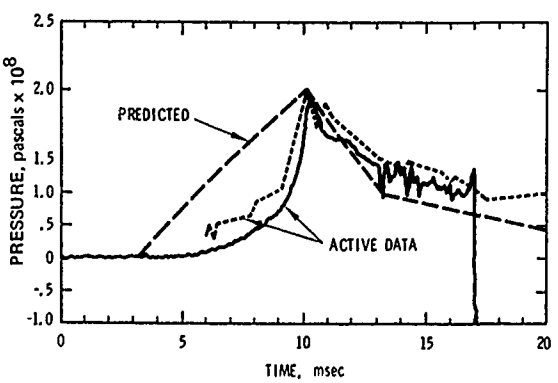


Figure 13. Free-Field Pressure

A comparison of the acceleration of the experiment chamber and the calculations obtained from the lumped parameter model is shown in Figure 14. The free-field acceleration assumed as input to the motion analysis discussed above is included in Figure 15 as a reference. Not only was the basic agreement satisfactory, but these data were also an early indicator that the modeling was adequate and that the deformations of the structural shell were indeed small.

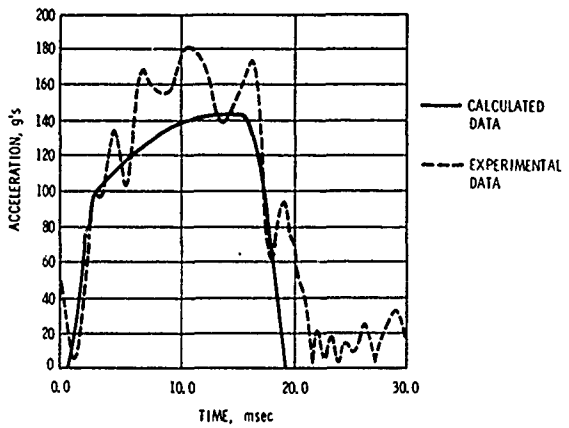


Figure 14. Acceleration Data vs Prediction

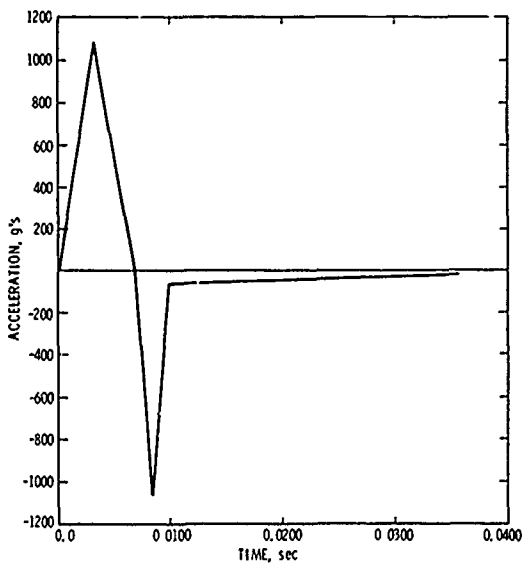


Figure 15. Free-Field Acceleration Motion Analysis

A mining reentry was initiated to obtain visual observation of the entire protective system performance. Examination of the structure revealed that little structural damage was evident. The experiment chamber was virtually undamaged structurally as shown in Figure 16. Closer examination indicated that deformations of the steel liner separating the structural concrete and the cellular concrete were small and agreed closely with the predictions which had been made. Figure 17 depicts a buckle in the roof of the liner which indicates, when considered with a similar buckle on the floor, radial deformation of approximately 0.076 to 0.01 metre (3 to 4 in.). Components inside the experiment chamber were protected and found to be functioning.

CONCLUSIONS

The technology for designing structures to survive in intense ground motion environments was demonstrated by this development program. Active data and visual examination confirmed that the analyses and assumptions made were accurate and sufficiently refined to establish the structural design.

Large structures capable of maintaining openings as large as 4.3 metres in diameter and of successfully encountering ground pressures approaching 2×10^8 pascals can be designed and analyzed. Accelerations of large structures can be reduced a factor of 10 from free-field accelerations if attenuating material such as cellular concrete is used in combination with competent structural design. Finite-element, finite-difference, and lumped-parameter calculational techniques can be successfully employed to predict the severity of ground motion environments and to determine the associated responses of large structures to these environments. These techniques can account for nonlinear material behavior, asymmetrical loading conditions, and large deformations. Sufficient accuracy can be obtained from these methods to provide a basis for varying structural dimensions and materials so that optimum design conditions can be approached. These methods cannot be effective, however, unless adequate material models are incorporated and testing programs which certify their validity are performed.

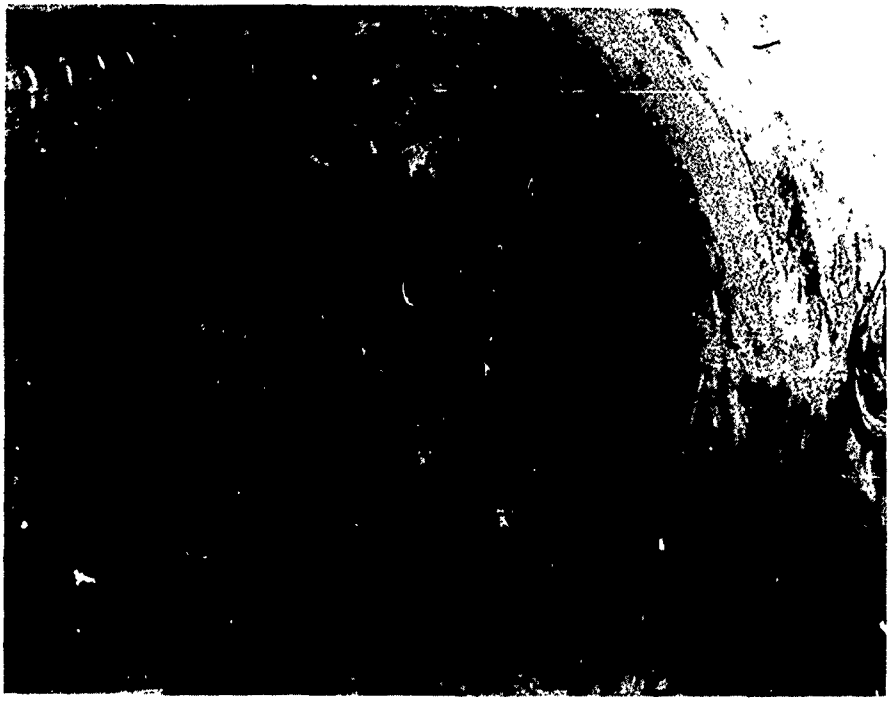


Figure 16. Posttest Experiment Chamber



Figure 17. Liner Deformation

ACKNOWLEDGMENTS

The authors wish to acknowledge those individuals who were principally responsible for various analyses and analytical developments mentioned here. For the finite element analyses, our appreciation is expressed to R. D. Krieg and S. W. Key for constitutive model and code development and to S. N. Burchett, J. A. Milloy, and W. A. Von Riesemann for performance of various calculations and material property studies. For the calculations to determine the free-field environment, we must credit R. A. Bass. The TOODY calculations were performed by F. F. Dean. Coordination of the material testing program was performed by C. W. Gulick, and R. E. Stinebaugh was responsible for the mechanical design.

REFERENCES

1. T. O. Hunter, "Analysis of High Fluence Experimentation," Sandia Laboratories, Albuquerque, New Mexico, unpublished report.

2. T. O. Hunter and G. W. Barr, "High Fluence Recovery Development Progress Report," Sandia Laboratories, Albuquerque, New Mexico.

3. C. W. Gulick, "First Ground Motion Experiment Reentry (Cellular Concrete Evaluation)," Sandia Laboratories, Albuquerque, New Mexico.

4. R. C. Bass, Sandia Laboratories, Albuquerque, New Mexico, unpublished work.

5. S. L. Thompson, "CHART D - A Computer Program for Calculating Problems of Coupled Hydro Dynamic Motion and Radiation Flow in One Dimension," Sandia Laboratories, Albuquerque, New Mexico, SC-RR-69-613, November 1969.

6. S. W. Key, "HONDO - A Finite Element Computer Program for the Large Deformation Dynamic Response of Axisymmetric Solids," Sandia Laboratories, Albuquerque, New Mexico, SLA-74-0039, April 1974.

7. S. E. Benzley, L. D. Bertholf, and G. E. Clark, "TOODY II-A, A Computer Program for Two Dimensional Wave Propagation," Sandia Laboratories, Albuquerque, New Mexico, SC-DR-69-516, October 1969.

8. S. J. Green, et al., "Mechanical Properties of Tuff from Nevada Test Site," Terra-Tek Report, TR-72-34, November 1972.

9. J. Q. Ehrgott, "Investigation of the Static Uniaxial Strain and Triaxial Shear Response of Cellular Congress," U. S. Army Engineer Waterways Experiment Station, Vicksburg, Mississippi, Febraury 1972.

10. F. F. Dean, "Two Dimensional Lagrangian Code Calculations of Structures Subjected to Extreme Earth Motion Environments," Sandia Laboratories, Albuquerque, New Mexico, SLA-74-0202, to be published.

11. S. N. Burchett, J. A. Milloy, and W. A. Von Riesemann, "Finite Element Analysis of an Underground Protective Test Station Subjected to Severe Ground Motion," Sandia Laboratories, pager given at "Computer Use by Engineers Symposium," Lawrence Livermore Laboratory, October 1974.

12. W. A. Von Riesemann and S. N. Burchett, "Analysis of an Underground Protective Test Station Subjected to Severe Ground Motion," Joint Winter Meeting, New Mexico Section and El Paso Branch, ASCE, Las Cruces, New Mexico, February 16, 1973.

13. R. D. Krieg, "A Simple Constitutive Description for Cellular Concrete," Sandia Laboratories, Albuquerque, New Mexico, SC-DR-72-0833.

Discussion

Mr. Zara (McDonnell Douglas Astronautics): How refined a grid work did you use for the representation or the idealization of these large volumes of concrete?

Mr. Hunter: The grid work varied with the location within the system. Near the edges of the boundary it was probably many feet. Near the center where the details of the structural interaction were important, around the concrete interface, or the concrete tuff interface, it was on the order of a few feet or less; for example we did not model such things as the 1 in. (.025 m) steel liner because that is very difficult to do when you have mesh sizes on the order of several feet. That was not modeled but the concrete which was 6 ft or 8 ft (1.8 m or 2.5 m) in radial dimension would have multiple meshs within it in both calculations.

Mr. Zara: Over what period of time did you conduct this study?

Mr. Hunter: The study took a year and that included all of the aspects including construction, fabrication, instrumentation, and testing.

Dr. Sevin (DNA): There is a substantial history of testing structural configurations, cylinders, spheres, and so on dating back to the early 60's. There is no question that the environment for your particular experiment was extremely severe. It seems to me that it is well to point out the influence of the host rock in deciding upon the structural configuration and the approach you are going to take. Tuff being a fairly pourous weak material gives you little choice but to approach the structure as a pressure vessel. In more competent materials you could have had the choice of looking into some accommodation between fully restraining the host material with the structure and looking to the structural configuration which itself could accommodate some deformations. I don't know precisely the point you wanted to convey regarding the analytical capabilities but it is my own feeling that these are somewhat extreme environments when we are looking at failure of materials such as concrete and steel under reverse loading conditions and the state of the art is not adequate in a general sense. I don't think we know how concrete behaves in a consistant plasticity sense. I think also as I understand this experiment it had to be a conservative design and so that I don't believe you are offering it as a consequence of a design procedure which is cost effective in any sense. You really wanted that package inside to be there when you got back. So I think the state of the art of structural design for such kinds of environments is developing and I would appreciate your comment on what you think you have really demonstrated regarding the ability to treat these high performance structures in an effective manner. Also were the comparisons of predictions and measurements in fact pretest predictions or after the fact?

Mr. Hunter: Let me respond to the latter. All of the comparisons were pretest predictions versus observations in the experiment. I think I basically agree with all of your comments. There is a tremendous difference between a material which is stronger than structural materials such as concrete, like granite which presents a much more difficult problem. We specifically solved the problems of large deformations, high stresses, and as you said conservative design. I feel that it sets upper bound as far as knowing what parameters need to be included in such an analysis. It treats thick walled spherical shells and not thin walled concrete spherical shells where the failure behavior and specifically the effect of inner boundary conditions would be much more fundamental. I think I would try to apply these conclusions primarily to the problem that was done but realizing that there are meaningful data there for more detailed refined calculations for systems that have parameters that may not be so enormous in the loads that are encountered but where there is more concern about the details of the stress behavior. I would not try to apply these results to a similar problem with a thinner concrete whell in a material like granite. I would try to apply it in a case of tuff out to pressure levels of maybe a half or a third of these magnitudes if the structures were in fact fairly large and thick; but if they are not, you failure criteria would have to be different.

Mr. Chen (TRW Systems): Does your two dimensional model account for the structure media interaction or do you just apply a uniform pressure?

Mr. Hunter: No basically the two dimensional model was used for the structure interaction problem. In this particular case the two dimensional model, using the finite difference approach, did not account for any failure mechanism, that is it did not account for any gross non-linearity of the system. But it applies to the structure because it solves the equations of motion and the constitutive media interaction relations which you put in, in a two dimensional sense.

DESIGN STUDY OF AN EXPERIMENTAL BLAST CHAMBER

W. E. Baker and P. A. Cox
Southwest Research Institute
San Antonio, Texas

This paper covers the preliminary design considerations for an experimental blast chamber intended for repetitive firings of explosive charges up to 13.61 kg in weight, with minimal disturbance to personnel in the vicinity. It includes a survey of past work in blast chamber design, the evaluation of several alternate design concepts and the results of analyses performed to establish chamber material, spherical or cylindrical shape, size and thickness. Responses to initial and reflected blast waves are included, as well as stresses from internal static pressures. Effects of chamber evacuation on modification of loading and chamber stresses are shown. Other factors addressed in the paper are chamber venting for unevacuated chambers, responses to charges detonated off-center, lining with shock-absorbing materials, and spalling effects.

INTRODUCTION

Experiments with explosives can be conducted at outdoor ranges or within suitably designed blast chambers. Although large-scale experiments are limited to the former type of facility, many smaller scale experiments can and have been expediously performed within blast chambers of various sizes and designs. The advantages of such chambers for small-scale testing are many, with the primary one being the ability to conduct tests in a controlled environment independent of weather conditions. Also, instrumentation, which would in itself be destroyed by the explosions, can be employed with suitably designed chambers containing view ports, and the ambient atmospheric conditions for tests can be controlled in some type of chambers. These advantages prompted the Detonation and Deflagration Dynamics Laboratory of the BRL to fund a preliminary design study of such a chamber, tailored to their own requirements. This paper is based upon that study.

In this study, we conducted a critical survey of the literature pertaining to blast chamber design and also evaluated several alternative design concepts for blast chambers. The survey was broad in scope and included methods for transient and static load prediction, methods for blast load attenuation at the chamber walls, methods for predicting chamber response to blast loading and a review of pertinent experimental results. Spherical, cylindrical and rectangular chambers were all covered by the survey. However, evaluations performed in this study were limited to spherical and cylindrical geometries.

For the evaluations, quite complete analyses were made of the dynamic and static stresses induced in spherical chambers, first by centrally located explosive charges and then by eccentrically located charges. For cylindrical chambers, less complete analyses were possible, but responses to centrally located charges were computed. Calculations were performed for steel chambers only. Concrete construction was eliminated from consideration for several reasons. First, although concrete construction is ideally suited for rectangular blast chambers, it is less suitable than steel for chambers with curved walls, particularly for walls with double curvature, such as for spherical chambers or the endcaps of cylindrical chambers. One reason is that special forms for the curved walls are required, whereas for flat walls, standard forms are available. A second reason is that the response of spherical and cylindrical chambers is largely a membrane

PRECEDING PAGE BLANK-NOT FILMED

type response with tensile stresses predominating. This is particularly true for centrally located charges. Concrete with its low tensile strength is obviously not ideally suited for such application. A third reason is that the design requirements for the chamber included the detonation of off-center charges near viewing ports. Overpressures for off-center detonations can be quite high, easily exceeding the tensile and also the compressive stress of high-grade concrete. To overcome spallation problems, if indeed they can be overcome for these conditions, would require the use of fiber-reinforced concrete and special transverse reinforcing which can significantly increase cost. It was for these reasons that concrete construction was eliminated from consideration early in the study.

The analyses performed considered a range of chamber sizes, and a minimum practical size for a working chamber was arbitrarily assumed to be 3.66 m in diameter for either a sphere or cylinder. When comparing spheres and cylinders, however, it was assumed that a sphere would require a diameter which was larger than that of a cylinder to achieve the same efficiency in working space. The final considerations in chamber design were spallation, shock attenuating materials, chamber openings, and general construction costs. Relative costs were estimated on a weight basis. Detailed design considerations of viewing ports and doors were not included in the study.

SURVEY OF RELATED WORK

Although blast chambers are in relatively wide use at a number of government and commercial facilities, all too often no rational methods have been employed in their design. In this part of the paper, we report the results of our survey of methods of measuring and predicting the transient and long term pressures for explosives detonated within blast chambers, methods of prediction and measurement of response of blast chambers to the pressures, and the design of existing chambers.

When an explosive charge is detonated within a chamber, an intense air blast wave is formed which moves outward from the charge at supersonic velocity and reflects from the walls of the chamber. Depending upon the geometry of the charge and the chamber, a relatively simple blast wave system or an exceedingly complex one will be reflected from the walls of the chamber, implode toward the center, and re-reflect several times. The reflecting shock wave pattern will eventually be dissipated through irreversible thermodynamic processes, and the pressure and temperature within the air or other gas contained in the chamber will rise and produce an essentially static pressure increase. If the chamber is vented, this "static" pressure rise will decrease by exhaust of the higher pressure gas within the chamber through the vent. Even if the chamber is completely sealed, the pressure will fall on a longer time scale because the high temperature explosion products will transfer heat to and through the walls of the chamber, and the gas on cooling will reduce the chamber pressure. For a blast chamber of reasonable size, the time scale for the duration of the first shocks reflecting from the walls will be of the order of milliseconds, reverberation times will be several milliseconds, time for pressure to return to ambient in a vented chamber may be an appreciable fraction of a second, while times for pressure to return to ambient by heat transfer may be many seconds.

The initial shock pressure on the walls of a chamber may be relatively easy to predict based on existing blast data or may be exceedingly difficult to predict, dependent upon the geometry of the chamber. The primary sources of data for reflected blast wave properties are an excellent compilation by Goodman[1], measurements of normally-reflected blast wave properties under sea level and simulated high altitude conditions, made by Jack[2], and Jack and Armendt[3]. These three references include measurements of peak pressures, time histories, and impulses from blast waves which are normally reflected from a rigid surface. Reference 3 includes measurements conducted under simulated high altitude conditions. An additional source of data is Wenzel and Esparza[4], wherein both normally and obliquely reflected pressures and impulses were measured for explosive charges located very close to rigid, flat reflecting surfaces. Another source of compiled data, more recent than Goodman's and allowing predictions closer to the explosive source, is Chapter 6 of Reference 5 by Baker.

Although many of the experiments reported in References 2-4 were conducted with very small explosive charges, the data can be scaled to any desired weight of charge using well known blast scaling laws. If the ambient gas in the chamber is air at normal sea level

atmospheric pressure and temperature, then Hopkinson's or cube root scaling can be applied to predict blast pressures and durations of blast pressures on the chamber walls. If the gas in the chamber is air at reduced pressure, as would be true in a partially evacuated chamber, then Sach's scaling law can be applied for prediction of blast wave properties. Both of these laws are derived, and experimental data given to confirm them in Chapter 3 of Reference 5. Under certain conditions for strong blast waves, i.e., blast waves close to the explosive source, Sachs' scaling no longer applies. This is discussed in Chapter 3 of Reference 5 and is also evident in the data reported in Reference 3. One may therefore have difficulty in accurately predicting normally reflected blast wave properties in a partially evacuated chamber if the explosive charge is located near the wall of the chamber.

The reverberation times, i.e., times for blast waves to reflect from the chamber wall, traverse the chamber and reach the wall a second time, have seldom been measured but can be reasonably well estimated from compiled data on times of arrival of shock waves which are transmitted freely through the air. References 1 and 5 both contain compilations that can be used to estimate these reverberation times. Proctor and Filler[6] do show some pressure records with the repeated reflections characteristics of reverberations in a chamber.

The long time pressure rise in a closed chamber in which an explosive has been detonated is caused primarily by the addition of the heat energy available in the explosive to the air or other gas within a chamber. A small additional pressure rise is caused by conversion of the solid explosive to mols of gas which are added to the gas already present in the chamber. The study of these relatively long term pressure rises has received considerable attention in recent years, as is evident from three pertinent papers presented at the 14th Annual Explosive Safety Seminar. One of these papers, by Proctor and Filler, has already been mentioned. The other two are a paper on internal explosions in vented and unvented chambers by Sewell and Kinney,[7] and a paper by Keenan and Tancreto on effects of venting and frangibility on blast environment from explosions in cubicles[8]. All three of these papers include data and/or methods of estimating the long term pressure rises caused by internal explosions in chambers which are either vented or unvented. Reference 6 also discusses a computer program developed for the rapid estimation of blast loads from confined explosions. Weibull[9] also has reported some detailed measurements of pressure-time histories on the walls of partially-closed chambers from the detonations of TNT charges.

In all of the preceding studies, the aim has been to measure or predict either the short term or long term pressures which would be applied to the walls of a blast chamber or vessel containing an explosion. In designing a vessel or chamber to contain explosions, this is only the first step in the process. Let us now review past work in prediction or measurement of the responses of pressure vessels, blast chambers, explosive storage cubicles, and other similar structures to the effects of internal explosions.

The simplest type of structure to analyze as a blast chamber is a spherical pressure vessel subjected to the blast from a centrally located explosive charge. Baker and Allen[10] report a dynamic analysis of the response of thick spherical shells to the reflected blast wave loading from a centrally detonated explosive charge. They also report the results of a limited series of experimental tests and show that the test results agree with the analysis. Baker[11] presented an analysis method for the elastic-plastic response of thin spherical shells to spherically symmetric internal blast loading. Again, data are presented in this reference for comparison with the prediction method both for elastic response of the shells and for response which includes plastic deformation and permanent strain. Loving[12] reports the results of a series of proof tests of a spherical blast chamber subjected to internal detonation of TNT explosive charges. Strain gauges were mounted on the chamber, and maximum strains recorded. This reference will be discussed later in our review of past work on design of blast chambers.

There have been several studies of response of cylindrical shells to internal blast loading. de Malherbe, et al[13] report a relatively simple method of analysis for the response of a cylindrical shell to transient internal pressure. They also report experimental data on both the pressures within and strain response of a long cylinder produced by the internal detonation

of a gas mixture. Another study applicable to cylindrical vessels is an entirely empirical one by Mackenzie, et al[14]. They were concerned with containing the effects of explosives which were to be irradiated in a nuclear reactor. They presented data for diameters and thicknesses of cylinders of various materials which can contain detonation of explosives without rupture. The cylinders were, however, bulged considerably by the effects of the internal detonations. Finally, Hanna, et al[15], described the results of a series of experiments on response of cylindrical pressure vessels with spherical end caps to blast waves from internal detonations. Strain measurements were reported at a number of locations on a series of shells which were scale models of each other. This paper contained no analysis because it was designed primarily to test the scaling of response of structures of this type to internal blast loading. However, the data indicate the quantities of explosive which can be safely detonated within a pressure vessel which is of other than spherical shape.

We found only one study of the response of a containment structure, resembling a pressure vessel, to explosions which occur anywhere other than at the center of the vessel. This study, for the elastic response of spherical vessels to eccentrically loaded explosive charges, is reported by Baker, et al[16]. The response prediction method given in this reference is much more complex than those in References 10, 11 or 13 because many modes of vibration of the spherical shell are excited by the asymmetric loading. Reference 16 also contains limited comparisons of predicted response with measurements of strains generated by eccentrically located explosive charges. The comparisons appear to be good enough for most engineering purposes.

Compared to past work in the prediction and measurement of response of spherical or cylindrical pressure vessels to internal explosions, there has been very little effort devoted to prediction or measurement of the response of rectangular chambers to such loads. Furthermore, most past studies were limited to steel vessels of a single thickness of material. There has been, however, an extensive program, supported by the Department of Defense Explosive Safety Board (DDESB), for design and analysis of protective structures. These efforts have been devoted to designing structures of reinforced concrete which, although heavily damaged, will prevent propagation of an explosion from one explosive storage cubicle to the next, or will prevent projection of damaging fragments in the event of an accidental explosion within a cubicle. This work is well summarized by Cohen and Dobbs in Reference 17. Unfortunately, because of the emphasis on gross structural damage (limit design) of the structure, the work is of little use to this study of chambers designed for repeated detonations.

One of the problems of concern in the use of reinforced concrete structures as blast chambers is the possibility of spalling of the outside wall of the structure as an intense compression shock wave is transmitted through the wall and reflected as a tensile wave. The basic phenomenology of spalling or scabbing, as it is sometimes called, is well known[18]. Spalling can be prevented either by limiting the magnitude of the shock overpressure on the inner surface of a wall or by attenuating the shock before reaching the wall by use of granular or other energy absorbing materials. In a study of lining materials for reduction of reponse of a reactor containment vessel to internal explosions, Hanna and Ewing [19] reported that several materials which are good acoustic absorbers also markedly reduce the strains generated in a spherical shell by the detonation of internal explosives. Several of the materials tested also withstood a number of experiments with no apparent deterioration. Some limited studies of use of such materials as cellular concrete and sulphur foam to attenuate strong shocks sufficiently to prevent spalling in concrete are reported by Sullivan and Bombich [20]. Unfortunately, materials of this kind work best when they are crushed by the initial blast loading. They would therefore not be efficient for use in a blast chamber intended for repetitive testing.

Although it is apparent from the preceding discussions that there exists a considerable body of empirical data and methods for estimating pressure loading and response of blast chambers to this loading, there have been few instances of rational design of blast chambers based on such knowledge. The most apparent case is the design discussed by Loving in Reference 12. It is clear that the author has an excellent practical knowledge of the requirements of a blast chamber and that he also was aware of the effects of the transient pressures from first shock arrival, even through

his design was based on the long term hydrostatic pressure rise. Loving rated the shapes of chambers for containing internal blast on the basis of their ability to contain a given pressure for a given cost with spherical being the most desirable, cylindrical with hemispherical ends the next most desirable, cylindrical with flat ends next and cubical or rectangular least desirable. Reference 12 includes the results of tests of a spherical chamber of 3.66 m diameter with a 19.05 mm wall thickness subjected to internal explosions of charges ranging up to 6.80 kg of TNT. This report, and a patent by Loving on such a blast chamber listed as Reference 21, gives more details of the design of his chamber. Because the chamber is spherical, an open grating is required as a working floor. The door is inward opening, and the chamber also has observation ports, venting through a small vent area containing a muffler, and a blower system for clearing explosive gases from the chamber after firing. Loving reports that the blast attenuation outside the chamber, with the very small vent area and muffling of the gases which escape subsequent to the explosion, reduces the annoyance to persons outside the chamber to an insignificant level.

The basic spherical chamber design devised and patented by Loving has been copied and modified for use at several different agencies. One such modification is reported by Bartkowiak and Kuchta[22]. The vessel was basically the same size as that built and tested by Loving, but incorporated a double door arrangement with one opening inward and one opening outward, so that it could be used for tests while partially evacuated, as well as for tests with high initial internal pressure. Although not reported in the literature, similar vessels have been built and are in use at the U.S. Army MERDC, Boeing Aircraft Company and at the U.S. Naval Ordnance Laboratory using a vessel originally built for the General Motors Defense Research Laboratory. The largest spherical blast chamber in use is probably the 9.14-m diameter, 76.20-mm thick steel blast sphere at BRL.

Blast chambers of various sizes made of reinforced concrete exist at a number of U.S. government and foreign ballistics research and test agencies, but very few of these were designed in a rational manner. They have varying amounts of venting, and most of them were apparently designed by the expedient of simply making them extremely massive and extremely strong. We have found only two papers which described the design of such facilities. In one paper Bergman[23] shows the design of a laboratory with two test chambers capable of withstanding the detonation of 4.54 kg of TNT without damage. As in the chambers designed by Loving, these have very small venting. The design is of massive reinforced concrete with heavy footings and with floors, walls, and ceiling heavily laced together reinforcing. No details are given regarding the design of the structure. The design apparently evolved by a trial and error process. In the other paper Fling and Linse[24] describe the design and operation of a cylindrical chamber with domed roof and foundation. The chamber is 12.19 m in diameter, and made of 0.61 m thick reinforced concrete. It has a number of viewports and a large, 3.05 m by 3.05 m access door. Work is performed on a false floor at ground level. The chamber has very small vent area, and large exhaust fans to clear explosion products after test. Design was accomplished by estimation of the natural vibration period of structural components (in a manner which is not clearly defined), estimation of equivalent dynamic load factors using these vibration periods, and calculation of static stresses based on normally reflected blast pressures and the dynamic load factors. Internal static pressure increases were estimated from old work preceding that of References 6-8, and standoffs to prevent spalling of the concrete were estimated from work summarized in Reference 17. The chamber has been tested and used repeatedly with explosive charges equivalent to 22.68 kg of TNT, with no damage. The authors report that no air shocks escape the chamber, and that noise levels out side are low.

Cowan and Willis[25] report the design of an inexpensive rectangular chamber with considerable venting. These authors used some simple analysis methods, but relied primarily on scale model tests to estimate the response of and strength needed for a full-scale chamber. The construction methods used in the full scale chambers differed markedly from the typical heavily reinforced concrete structures used for the other box-shaped blast chambers. The basic construction method used by Cowan and Willis consisted of a structural steel framework supporting double walls filled with a 0.61 m thickness of sand. This method has the decided advantage of much lower cost than a reinforced concrete structure of equivalent

size and thickness, and the sand also apparently possesses considerable energy absorbing capability which limits damage to the structure. Thumpston [26] also reports a design of a rectangular cubicle based on model tests. He tested first an overstrength model instrumented with pressure gages to measure wall loading, and then built structural models of the reinforced concrete cubicle to determine safe explosive limits. This model was tested with model charges of increasing weight until it failed. The cubicle had a large vent area, and blast measurements were also made outside the cubicle.

The capability of spherical and cylindrical steel vessels for complete containment of explosive effects has been well demonstrated by the design and test of vessels for containing the blast and fragments from clandestine explosive devices, reported by Rogers and Taylor [27]. Steel vessels, 0.91 m in diameter, with 25.40 mm thick walls were used to contain explosions of up to 3.63 kg of Comp B, and 1.83 m diameter vessels of the same material and thickness contained explosions of up to 11.34 kg of Comp B. These authors report that their vessels were designed using Los Alamos hydrodynamic codes for vessel loading and response calculations, but give no details. They also note that the vessel steel must be ductile at operating temperatures, and that expanded vermiculite used to fill the vessels greatly reduced shock loading of the vessels. Evacuation of the vessels prior to detonation of the devices reduced the resulting blast loading.

DESIGN REQUIREMENTS

Prior to considering specific designs of blast chambers, we list the requirements for the BRL chamber:

1. The chamber must withstand without damage repeated internal detonation of up to 13.61 kg of explosive (type not specified).

2. Most of the charges detonated within the chamber (90%) will not exceed 4.54 kg in weight. Special provisions such as chamber evacuation are allowable to accept charges with weights between 4.54 kg and 13.61 kg.

3. The chamber is to be fabricated of steel or reinforced concrete.

4. Rectangular box shape for a chamber has no particular advantage operationally, but perhaps should be considered, in addition to spherical and cylindrical designs, because it lends itself to reinforced concrete construction, and might therefore cost substantially less than a steel spherical or cylindrical chamber.

5. The effects of venting are to be considered even though complete containment of blast is preferred. Complete containment will allow the chamber to be used near existing laboratories with minimal disturbance of personnel during firing. Substantial venting would require location of a chamber in a remote area, which would be acceptable only if a vented chamber can be built at substantially less cost than an unvented chamber.

6. Effects of "granular" material in reducing blast pressure or impulse are to be considered.

7. Reverberation time is to be computed and its effect on chamber response considered.

8. Relationships between chamber size and cost are to be considered.

9. Spalling of chamber walls is to be considered.

10. Two viewports of good optical quality, located 90° from each other, are desired.

11. Some planned tests require detonation of explosives near one viewport. We should determine how close to a viewport or wall one can safely test.

In the following sections of this paper, we analyze various chamber designs and sizes based on these requirements.

GENERAL CONSIDERATIONS IN BLAST CHAMBER DESIGN

It is quite clear from our survey of previous work in blast chamber design and test that it is entirely feasible to build a chamber which will withstand without damage repeated internal detonations of 13.61 kg of the most energetic conventional explosive, with or without venting. Our efforts were therefore, devoted to optimizing the

design for minimum cost and maximum utility.

One's ability to analyze loading and response of a blast chamber increases in difficulty as geometry changes from spherical to cylindrical. The initial loading from a centrally-located charge in a spherical chamber is simply the normally reflected pressure-time history, which can be obtained by scaling data of Reference 2 or 5 for sea level ambient conditions, or by scaling data of Reference 3 or 5 for partially evacuated ambient conditions. Reverberation times can also be easily calculated for this situation, using scaled times of arrival and the assumption that the reflected wave "implodes" to the center of the sphere and then reflects again with no losses. If the blast source is located off center in a sphere, one can also calculate the shock loading, even though it is now a fairly complex function of azimuth angle and time, by scaling compiled blast data in References 1 or 5. This was done in estimating transient loading on a spherical shell in Reference 16. Reverberation times can also be reasonably accurately estimated for this case.

Estimation of the transient blast loading on a cylindrical chamber with dome end caps is much more difficult than for a sphere, even for a blast source located at the center of the chamber. Only the loading on the cylindrical part of the shell can be predicted with any accuracy. As soon as the initial blast front passes the junction of the cylindrical part with the end caps, the reflection process becomes too complex to estimate, and no measurements of these loads exists. However, reverberation times can probably be estimated with reasonable accuracy.

For any chamber geometry, the "static" pressure rise, with or without venting, is entirely independent of the chamber geometry References 6, 7 and 8 provide experimentally-verified methods for predicting this pressure rise for vented and unvented chambers, given type and quantity of explosive, chamber volume, and chamber vent area.

In analysis of chamber response to internal blast pressures, it is clear that plastic response, cracking, or other permanent deformation cannot be tolerated. Therefore, analyses or test results of containment structures which can suffer damage, such as the plastic response analysis in References 11, and designs of explosive storage cubicles in Reference 17, do not apply. Concentrating on elastic response predictions or measurements, we utilized the analytical methods of References 10, 11 and 16 for prediction or response of spherical vessels, and experimental data from References 13 and 15 for guiding us in design of cylindrical vessels. As for the loading, the degree of complexity in estimating chamber response also increases markedly with change from spherical to cylindrical geometry.

ANALYSIS OF SPHERICAL CHAMBERS

Central Charges

Theory

Our first stage in the analysis of spherical blast chambers was to use the very simple elastic response theory from Reference 11 as a basis for determining chamber wall thickness versus chamber diameter for centrally located explosive sources. The method is applicable to evacuated or non-evacuated chambers because the ambient pressure only changes the loading parameters.

In Reference 11, the radial displacement u of a thin elastic spherical shell of radius a and thickness h, made of material of density ρ, elastic modulus E, and Poisson's ratio ν, is determined as a function of time for an internal pressure pulse given by

$$p(t) = P_r(1 - t/T), \quad 0 < t \leq T,$$
$$p(t) = 0 \qquad , \quad t \geq T \tag{1}$$

The displacement is

$$u = K(1 - t/T - \cos \omega t + \sin \omega t/\omega T), \quad 0 < t \leq T \tag{2}$$

$$u = A \cos \omega(t - T) + B \sin \omega(t - T), \quad t \geq T \tag{3}$$

where

$$K = P_r/\omega^2 \rho h$$

$$A = K\left(\frac{\sin \omega T}{\omega T} - \cos \omega T\right)$$

$$B = K\left(\sin \omega T + \frac{\cos \omega T}{\omega T} - 1/\omega T\right) \tag{4}$$

and the circular vibration frequency ω is given by

$$\omega^2 = 2E/\left[\rho a^2(1-\nu)\right] \qquad (5)$$

Time history of membrane stress in the shell (equal in any direction because of spherical symmetry) is

$$\sigma_\phi = \sigma_\theta = \sigma = \frac{E}{(1-\nu)}\frac{u}{a} \qquad (6)$$

For static pressure, membrane stress is simply

$$\sigma = \frac{Pa}{2h} \qquad (7)$$

When blast wave duration T is short compared to the natural vibration period of shell ($\omega T < 0.4$), the maximum dynamic displacements and stresses will occur after the loading is over, and are given very nearly by

$$u_{max} = (A^2 + B^2)^{1/2} = \frac{P_r T}{2}\frac{1}{\omega\rho h} \qquad (8)$$

$$\sigma_{max} = \frac{P_r T}{2}\frac{1}{h}[E/2\rho(1-\nu)]^{1/2} \qquad (9)$$

But, $P_r T/2$ equals the integral under the pressure-time history for the blast wave reflected from the chamber wall, i.e., the reflected impulse

$$\frac{P_r T}{2} = I_r \qquad (10)$$

so that

$$u_{max} = I_r \frac{1}{\omega\rho h} \qquad (8a)$$

$$\sigma_{max} = \frac{I_r}{h}[E/2\rho(1-\nu)]^{1/2} \qquad (9a)$$

Eq. (9a) is used when $\omega T \leq 0.4$, to calculate maximum dynamic stress in the chamber. If $\omega T > 0.4$, Eq. (2) or (3) and (6) are used. Eq. (7) is only for computing stress under static internal pressure.

Chamber Response - Ambient Initial Conditions

Let us now consider the dynamic and static pressures for Pentolite charges weighing 4.54 kg and 13.61 kg, contained in unvented spheres of various radii, a, at sea level ambient conditions. We assumed a range of specific values for "a" and determined reflected pressure, P_r, reflected impulse, I_r, and arrival times, t_a, from compiled blast data in Reference [5]. These values are included in Table I except that the pulse duration, T_r, has been given in place of I_r for an equivalent triangular pulse. Chamber radii range from 1.83 to 3.66 m.

Before making the response calculations for the chamber, it is worthwhile to examine the relationships between reverberation time, chamber fundamental resonance and the load duration (pulse length). Reverberation times for charges detonated at the center of the spherical shells can be estimated from the time of arrival, t_a, given in Table I. On reflection from the vessel wall, the blast wave will implode toward the center, and re-reflect at the center to again transmit outward and reload the wall. A lower limit for reverberation time can be obtained by assuming that the times for implosion and re-reflection equal the initial time of arrival of the blast wave measured from the charge detonation. Reverberation time t_r is therefore at least twice the time of arrival t_a. The ratio of the reverberation time, t_r, to the pulse duration, T_r, is given in Table II. One can see that the reverberation times are about six times as long as blast wave durations. We can also compare reverberation times to shell vibration periods given by

$$\tau = 2\pi/\omega \qquad (11)$$

From Eq. (5) we see that the circular vibration frequency, ω is independent of shell thickness. Using the material values for steel, ω is computed for each shell radius of Table I. Values of ω, τ and the ratio of the reverberation time, t_r, to shell fundamental period, τ, are all given in Table II. These values were computed using the following values for steel:

$$E = 207 \times 10^6 \text{ kPa}$$

$\nu = 1/3$

$\rho = 7.85\ Mg/m^3$

One can see that none of the shells completes more than a very few cycles of vibration before arrival of the second shock. In so few cycles, shell vibration would not damp appreciably, so response to the second and perhaps later pulses should be considered with new shell velocity and displacement at time t_r as "initial conditions" for later response. Later stresses could be greater or less than maximum from the first pulse, depending upon the phase relationships. Thus, multiple loadings must be considered in the analysis. This can be done readily for centrally located charges but will not be practical for eccentric charges because of the long computational time involved, and the difficulty in predicting reverberation times and magnitudes for subsequent shock waves after the first. Even for central charges some estimate must be made of the dissipation rate of the blast waves.

TABLE I
Reflected Blast Loading for Spherical Chambers
(Single Pulse)

W(kg)	a(m)	P_r(kPa)	T_r(msec)	t_a(msec)
4.54	1.83	3854	0.453	.888
	2.43	1593	0.833	1.59
	3.05	953	1.115	2.74
	3.66	621	1.425	3.78
13.61	1.83	13652	0.273	.453
	2.43	5688	0.482	.785
	3.05	2310	0.945	1.18
	3.66	1448	1.262	1.72

Response calculations were first performed considering only the initial pulse. From Table II it is apparent that the product ωT_r is greater than 0.4 and therefore the approximate forms for impulse response, equation (8a) and (9a) do not apply. The maximum response can occur either during loading (in which case Eq. (2) applies) or after the loading (in which case Eq. (3) applies). The criterion for determining when the maximum occurs is whether the shell velocity, $\dot{u}$, is positive or negative at end of loading, $t = T$. Taking the derivative of Eq. (2), we see that at $t = T$,

$$\dot{u} = \frac{K}{T}(-1 + \omega T \sin \omega T + \cos \omega T) \ldots \quad (12)$$

Because K, given by Eq. (4), and T are positive quantities, the parenthetical expression in Eq. (12) determines the sign of $\dot{u}$. If it is negative, the maximum occurs for $t < T$; if it is positive, the maximum occurs for $t > T$. In the former case, the time t for maximum must be evaluated from Eq. (12) by setting $\dot{u} = 0$, and then Eq. (2) is used to calculate u_{max}. In the latter case, the maximum can be computed by using the maximum amplitude

$$\frac{(A^2 + B^2)^{1/2}}{K} = \left[1 + \frac{2}{(\omega T)^2}(1 - \omega T \sin \omega T - \cos \omega T)\right]^{1/2} \quad (13)$$

These computations have been made, and are given in Table III for the specific shell diameters and loading durations of Table I. If we call the dimensionless amplitude given by Eq. (13) or the maximum value of the parenthetical expression in Eq. (2) A, then we find that

TABLE II
Comparison of Reverberation Time, Pulse Duration and Chamber Resonance

W (kg of Pentolite)	a (m)	T_r^* (msec)	$t_r = 2t_a$ (msec)	$\frac{t_r}{T_r}$	ω (1/msec)	τ (msec)	t_r/τ
4.54	1.83	0.453	1.776	3.92	4.859	1.293	1.38
	2.43	0.833	3.18	3.82	3.644	1.723	1.85
	3.05	1.115	5.48	4.92	2.914	2.155	2.54
	3.66	1.425	7.56	5.31	2.429	2.585	2.92
13.61	1.83	0.273	.906	3.32	4.859	1.292	.70
	2.43	0.482	1.570	3.26	3.644	1.723	.91
	3.05	0.945	2.36	2.46	2.914	2.155	1.09
	3.66	1.262	3.44	2.72	2.429	2.585	1.33

*repeated from Table I

$$\sigma_{max} = \frac{P_r a}{2h} \bar{A} \qquad (14)$$

and $\bar{A}$ is essentially a dynamic load factor (compare to Eq. (7) for stress under static pressure). If we assume that steel can easily be obtained for the chamber with a yield stress of $\sigma_y = 414$ MPa, and use a safety factor of 1.5, then we limit σ_{max} to 276 MPa. Eq. (14), values of $\bar{A}$ in Table III and values of P from Table I allow immediate calculation of shell thickness. This is also given in Table III. Shell thickness versus radius from Table III is shown graphically in Fig. 1 for both charge weights.

The results of Fig. 1 are for the response of the shell to the first pressure pulse only. As indicated earlier the ratio of t_r/τ in Table II indicates that subsequent pressure pulses may enhance the response. This is particularly true if t_r is near a whole multiple of τ. This obviously occurs for a 2.74 m radius chamber for both the 4.54 kg and 13.61 kg charges. We thus investigated a chamber of this size for the effect of multiple loadings. It is apparent that a similar condition could exist at other chamber radii also, but it would occur for other charge weights.

Loading conditions, reverberation times, and shell response parameter $\bar{A}$ for 2.74 m radius chambers were calculated according to the methods described previously, and are listed in Table IV. The maximum stress for the first pulse, calculated from Eq. (14), is also shown. Two combinations of shell thickness and charge weight were analyzed, a thickness of 35.56 mm for 13.61 kg charges and a thickness of 17.78 mm inch for 4.54 kg charges. Because the shell thickness were chosen from Fig. 1 to be considerably greater than the thicknesses needed to attain the design stress of 276 MPa, these stresses are considerably less. But, one can see that the reverberation times are very nearly even multiples of the vibration period for <u>both</u> shells, and the shell response to repeated pulses will be very nearly directly additive. The pulses do attenuate, as is evident from the limited data in Reference 6, 9, and 26. Some are attenuated to negligible values on the first reflection. Others exhibit more or less exponential decay, and attenuation of succeeding pulses by about 50% seems to represent the worst reverbera-

TABLE III
Computed Maximum Response of Spherical Vessel
for Central Charge (single pulse)

W, kg of Pentolite	a, m	ω, sec^{-1}	ωT_r	$\dot{u}$ @ $t = T_r$	Dimensionless Amplitude, $\bar{A}$	Shell Thickness h, mm for σ_{max} = 276 MPa
4.54	1.83	4,859	2.201	+	0.9602	12.268
	2.43	3,644	3.035	-	1.160	8.179
	3.05	2,914	3.249	-	1.194	6.274
	3.66	2,429	3.460	-	1.225	5.029
13.61	1.83	4,859	1.327	+	0.6317	28.600
	2.43	3,644	1.755	+	0.805	20.244
	3.05	2,914	2.755	-	1.106	14.122
	3.66	2,429	3.064	-	1.165	11.176

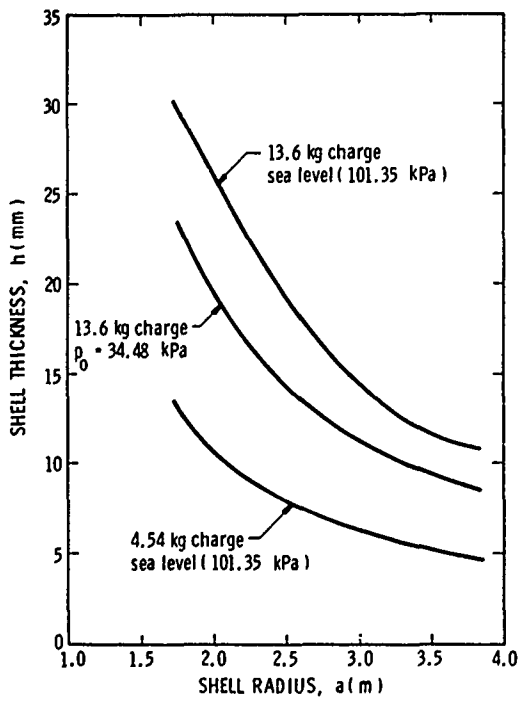


Fig. 1. Required Thickness of Spherical Shells for Central Charges

tions. Our estimate of shell response will therefore be made by assuming exact resonance of pulses with the shell period, and assuming two more pulses after the first, each attenuated in amplitude by 50%. Eq. (14) then yields the estimated maximum stress for three pulses merely by replacing P_r by $\sum_{i=1}^{3} (P_r)_i$, where $(P_r)_2 = (P_r)_1/2$, and $(P_r)_3 = (P_r)_2/2$. Neglecting reverberations after the third one, this yields a multiplier of 1.75. The estimated maximum stresses are then given in the last column of Table IV. These can be seen to be less than the design stress of 275 MPa.

Chamber Response - Reduced Initial Pressure

If a spherical shell is partially evacuated before detonation of an explosive charge within it, the initial reflected blast pressure can be reduced, and the reverberation time is affected. Static pressure rise is also somewhat reduced, as will be seen later when the quasi-static loading is considered. Furthermore, the pressure differential across the shell prior to firing will induce a compressive stress which must be unloaded by the tensile stresses generated by internal dynamic or static pressure before the shell can fail. So, partial evacuation before firing appears to be an attractive means of minimizing shell size, thickness or cost for occasional firing of large explosive charges. One must, however, assure that the shell is thick enough that it will not buckle under the differential pressure after evacuation. This can easily be checked using equations for the critical

TABLE IV
Response of 2.74 m Radius Spheres to Central Charges

chg. wt. / shell thickness	ω $msec^{-1}$	P_r kPa	T_r msec	t_r msec	t_r/τ	$\bar{A}$	σ_{max}, MPa one pulse	σ_{max}, MPa three pulses
W = 4.54 kg h = 17.78 mm	3.238	1207	0.985	4.25	2.19	1.1852	110	193
W = 13.61 kg h = 35.56 mm	3.238	3723	0.650	1.98	1.028	0.9291	133	233

buckling pressure. Eq. (15), from Reference [28], p. 496, is the classical equation for buckling of spherical shells under external pressures.

$$p_{cr} = \frac{2Eh^2}{a^2[3(1-\nu^2)]^{1/2}} \qquad (15)$$

Experimental work and later analyses [29] have shown that this equation is unconservative, and that buckling can occur at critical pressures as low as 1/5 of the "classical" value. We will therefore use Eq. (15) divided by five to evaluate buckling of evacuated chambers, once these chamber dimensions have been established.

First, let us assume the same shell diameters as before, and calculate blast loads for shells partially evacuated to several different ambient pressures. Only a 13.61 kg blast source will be considered and, as before, the specific energy of Pentolite was used to compute the total charge energy of the explosion. Blast parameters of reflected pressure, P_r, duration, T_r, time of arrival t_a, and reverberation time, t_r for initial ambient pressures of 34.48, 6.90 and 0.69 kPa were again determined from Reference 5. Note in Table V that reflected overpressures decrease as initial ambient pressure decreases, but that durations first decrease compared to data for sea level conditions in Table I, but then increase with further decrease in initial ambient pressure. The change in reverberation times with decreasing pressure is somewhat surprising. They get progressively shorter until, in one instance, this time is even less than the blast wave duration. It seems apparent that response of the chamber to repeated pulses must be considered when calculating response of evacuated spheres, if the spheres are well evacuated.

Let us consider response of spherical chambers evacuated only to 34.48 kPa absolute pressure. Here, the reverberation time is 5 to 6 times the blast wave duration, and no enhancement of the initial shock will occur. Also, this partial vacuum is easy to achieve with a simple mechanical pump and a "dirty" chamber. Multiple loading will still be significant because reverberation occurs within the first few cycles of shell response. In fact, by comparing t_r in Table IV to τ in Table II, it is apparent that t_r is approximately 2τ for the 2.74 m radius chamber. This is the same condition that occurred for the 4.54 kg charge in the unevacuated 2.74 m radius chamber.

Dynamic maximum stress for the initial pulse can be computed in exactly the same manner as before, but we must account for the reduction of peak stress by precompression of the shell by the vacuum. Combining Eq. (7) and (14), we have:

$$\sigma_{max} = \frac{a}{2h}[P_r \bar{A} - (p_o' - p_o)] \qquad (16)$$

where p_o' is ambient pressure outside the shell.

This equation can be inverted to calculate thickness h for any allowable value of σ_{max}. The results of the response calculations to the 13.61 kg charge detonated under an ambient pressure p_o = 34.48 kPa, for our design allowable σ_{max} = 275 MPa are given in Table VI. (For all of these calculations, $\dot{u}\big|_{t=T}$ is positive, so Eq. (13) determines A). The results are also plotted in Fig. 1, for comparison with needed shell

TABLE V
Blast Loading for Evacuated Spherical Shells, 13.61 kg Pentolite

p_o, kPa	a, m	t_a, msec	P_r, kPa	T_r, msec	$t_r = 2t_a$, msec
34.475	1.83	0.500	10239	0.287	1.00
	2.43	0.820	5447	0.360	1.64
	3.05	1.210	3103	0.486	2.42
	3.66	1.700	1551	0.804	3.40
6.895	1.83	0.390	5378	0.435	0.780
	2.43	0.640	3241	0.455	1.28
	3.05	0.950	2172	0.478	1.90
	3.66	1.280	1496	0.535	2.56
.690	1.8	0.185	2399	0.875	0.370
	2.4	0.318	1310	0.908	0.636
	3.0	0.472	862	0.906	0.944
	3.7	0.645	614	0.923	1.29

TABLE VI
Response of Spherical Chambers to 13.61 kg Pentolite at Initial Pressure of 34.48 kPa (one pulse only)

a (m)	α_T	$\bar{A}$	$\left[P_r\bar{A} - (p_o' - p_o)\right]$ (kPa)	h (mm)	P_{cr} (kPa)
1.83	1.395	0.661	6701.3	22.22	7481
2.43	1.312	0.625	3337.9	14.76	1855
3.05	1.416	0.669	2009.2	11.10	669
3.66	2.078	0.920	1360.4	9.02	310

thicknesses for non-evacuated spheres. One can see that reducing the ambient pressure to 34.48 kPa before firing 13.61 kg charges reduces the required shell thickness, but it is still greater than that which is required for 4.54 kg charges at sea level. Also shown in Table VI are values of buckling pressure, p_{cr}, divided by 5. These can be seen to lie well above the applied pressure $p_o' - p_o$ = 66.88 kPa, even for the largest and thinnest shell. So, static buckling during evacuation is not problem.

The effect of multiple pulses on the response of a 2.74 m radius shell will also be checked for the evacuated chamber. For a shell thickness of 17.78 mm, which was found to be adequate for a 4.54 kg charge in the unevacuated chamber (refer to Table IV), the maximum stress in the evacuated shell produced by the first pulse from a 13.61 kg charge is σ_{max} = 194,232 kPa. Using the same multiplicative factor as before for unevacuated shells (because this loading is also very nearly in resonance with the shell), the maximum stress is σ_{max} = 339,923 kPa. This exceeds our design allowable by about 23%, so for this loading condition shell thickness should probably be increased, say to h = 22.86 mm. Then, σ_{max} = 264,354 kPa which is below design allowable. However, eccentric charge locations are desirable, which will increase the shell stresses even more. Therefore, eccentric charges must be considered before suggesting a shell design thickness for a spherical chamber.

Eccentric Charges

From the foregoing calculations of spherical chamber response to centrally located explosive charges, it is evident that a steel spherical chamber of reasonable thickness will easily withstand the effects of internal detonations of up to 13.61 kg of explosive, if the explosive is located at the center of the chamber. But, we also wish to know how close to the chamber wall one can safely detonate charges. To make this estimate, we employed the methods of Reference 16 for elastic response of spherical shells to eccentric blast sources.

Based upon our calculation for the response of an 5.49 m diameter sphere to multiple pulses, we determined that the following shell thicknesses are required for centrally located charges:

4.54 kg at P_o = 101.36 kPa : h = 12.70 mm

13.61 kg at P_o = 34.48 kPa : h = 22.86 mm

13.61 kg at P_o = 101.36 kPa : h = 30.48 mm

The required shell thicknesses for P_o = 101.36 kPa were obtained by direct ratio of the results in Table IV to give a shell stress of about 275,800 kPa. For eccentric charges the shell stresses will obviously increase locally. Thus, a shell thickness of 31.75 mm will be checked for 4.54 kg charge at P_o = 101.36 kPa and 13.61 kg charge at 34.48 kPa. For 13.61 kg charge in unevacuated chambers, the allowable eccentricity will be established for a shell thickness of 44.45 mm. In all cases, the shell diameter will be 5.49 m and the allowable stress will be 275,800 kPa as before.

In Reference 16, it was shown that the blast pressure loading on the inner surface of a spherical chamber for an eccentrically located blast source could be described by the function of polar angle φ and time t as

$$p(x,t) = 0, \quad t < t_a(x) \text{ or } t > t_a(x) + T(x)$$

$$p(x,t) = P_r(x)\left[1 - \frac{t - t_a(x)}{T(x)}\right] \qquad (17)$$

$$t_a(x) < t < t_a(x) + T(x)$$

where $x = \cos\phi$; and the arrival time $t_a(x)$, reflected overpressure $P_r(x)$, and duration $T(x)$ are given by blast data such as those in Reference 1, 4 and 5. In solving for the shell response to this loading, the data can be used directly to define the loading, but can be more conveniently approximated by suitable, explicit functions. Numerical studies [16] have shown that, in general, the following approximation is adequate.

$$P_r(x) = C_1/(1 - C_2x)$$

$$t_a(x) = C_3(1 - x) \qquad (18)$$

$$T(x) = C_4 - C_5x$$

where C_1 through C_5 are dimensional and nondimensional constants which characterize the eccentric blast loading. The nonseparable function for the eccentric blast loading (17) can be written:

$$p(x,t) = \frac{C_1}{1 - C_2 x}\left[1 - \frac{t - C_3(1-x)}{C_4 - C_5 x}\right], \qquad (19)$$

$$C_3(1-x) < t < C_3(1-x) + C_4 - C_5 x$$

Note that the function $p(x,t)$ has a sudden jump along the line $t = C_3(1-x)$, representing the moving pressure front. The constants C_1 through C_5 are determined empirically for any specific loading condition.

Using either direct numerical values for loading $p(x,t)$, or the functional form of Eq. (19), the equations of motion can be solved by computer using the finite-difference equations corresponding to the differential equations for elastic motions of a thin, spherical shell. The basic equations are

$$\nabla^2 v + (1-\nu)\left(\frac{1}{1-x^2}\right)v + (1+\nu)(1-x^2)^{1/2} w_{,x} = A\ddot{v} \qquad (20a)$$

$$-(1-x^2)^{1/2}\left[v_{,x} - \frac{x}{1-x^2}v\right]$$

$$-2w = \frac{A}{1+\nu}\ddot{w} + Bp(x,t) \qquad (20b)$$

In these equations, v and w are tangential and radial displacements respectively, dots denote derivatives with respect to time, and commas denote partial derivatives with respect to spatial variables. The constants A and B depend on shell materials and dimensions, and are given by

$$A = (1-\nu^2)\rho a^2/E$$

$$B = (1-\rho)a^2/Eh \qquad (21)$$

Our finite-difference code based on these equations is described in detail in Reference 30, and is shown in Reference 16 to give essentially the same results as a classical, infinite-series solution. We used the code to predict locations and magnitudes of dynamic stresses for several eccentric locations of 13.61 kg and 4.54 kg explosive charges within the chambers.

Loading on the chamber for eccentric charges was again determined using the data of Reference 5. Procedures for calculating these loads are given in the Appendix along with examples in graphical form of the reflected pressure, pulse duration and time of arrival. Values are presented as a function of the polar angle φ. Reverberation times were not estimated for the eccentric charges and the response to multiple loading was not determined. We believe that reverberation times for the pressure waves will be approximately the same as for center charges and that the decay rates for subsequent waves will also be comparable; thus we will simply apply a factor based on the results for central charges to estimate enhancement in the response due to multiple loading.

Results of these calculations are presented graphically in Fig. 2. Peak stress in the shell wall versus charge eccentricity are given for the 4.54 kg charge in the unevacuated 31.75 mm thick chamber, for the 13.61 kg charge in the evacuated 31.75 mm thick chamber, and for the 13.61 kg charge in the unevacuated 44.45 mm thick chamber. As before the stresses determined for a single pulse were increased by a factor of 1.75 to estimate peak stresses for multiple reflections. If we choose for the design stress 275 MPa, allowable eccentricities are established for the various charge weight-thickness-initial pressure combinations. Although we did not analyze other combinations of charge weights and thicknesses, it is apparent that a 44.45 mm thick chamber is suitable for detonating 13.61 kg charges at eccentricities of up to 1.34 m (standoff from wall of 1.39 m) without evacuating the chamber. Smaller charges could obviously be detonated at greater eccentricities and also greater eccentricities could be achieved for 13.61 kg charges by evacuating the chamber. The optimum thickness, therefore, is probably between 31.75 mm and 44.45 mm depending upon the permissible combination of eccentricity, charge weight and initial chamber pressure desired.

Quasi-Static Loading

Static pressure rise after many reverberations is shown in References 6, 7, 8 to be a function of W/V, where W is charge weight of a given type of explosive and V is chamber volume, and of initial ambient conditions in the chamber. The ratio of W/V is the major determinant of the pressure rise. The primary physical process involved in the static pressure rise is the addition of the heat of combustion or detonation to the air present in the chamber. If the W/V ratio is small, there will be sufficient oxygen present in the

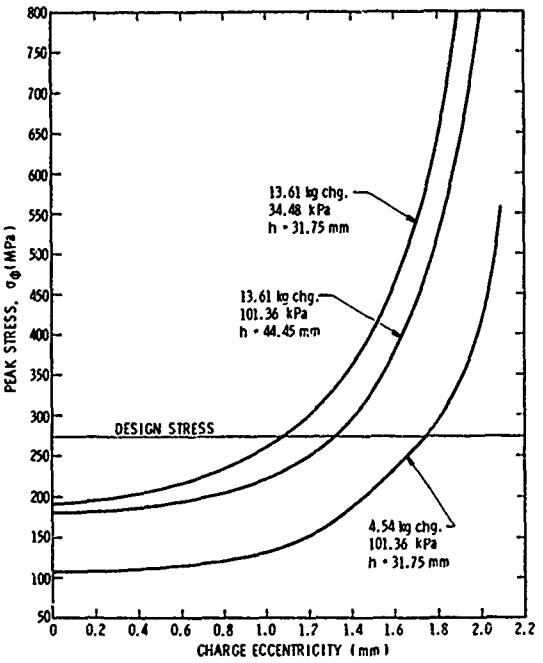


Fig. 2. Results for Eccentric Charges in 2.74 m Radius Spherical Chambers--Effect of Reverberation Included

chamber. If the W/V ratio is small, there will be sufficient oxygen present in the chamber for complete afterburning, and the heat of combustion of the explosive is therefore added to the air. Conversely, if this ratio is large, insignificant afterburning will occur and only the heat of detonation will be added to the air. When static pressure rise is plotted as a function of W/V, there is therefore a transition region indicated by an inflection in the curve as shown in Fig. 3 (taken from Reference 6). This inflection region occurs for smaller values of W/V as initial ambient pressure is reduced. Plots for reduced initial pressures can be found in Reference 6. From graphs such as Fig. 3 the static pressure rise for any specific explosive and initial pressure in the chamber can be found. These static pressures are only weakly dependent on explosive type, provided conventional secondary explosives are used, because heats of combustion and explosion for all explosives of this class are very nearly the same. Data are available for different explosives, however [6,9], and one can estimate static pressure rises for an untested explosive by the methods suggested in Reference 6 or by using curves such as Fig. 3 for an explosive with essentially identical heat values. We will simply use Fig. 3 without modification to

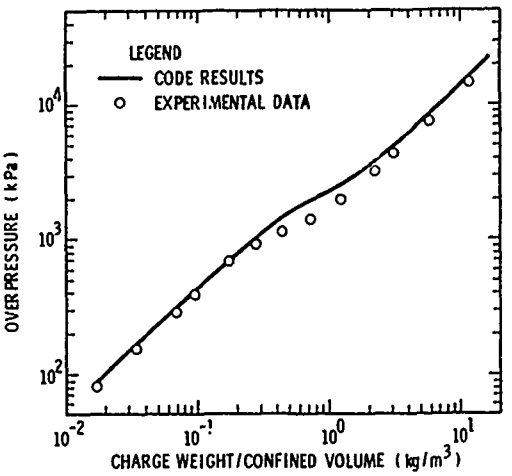


Fig. 3. Confined-Explosion Gas Pressure for RDX/WAX 89.5/10.5 in Air at Sea Level (Ref. 6)

to estimate the peak static pressure since the static pressure is lower with lower initial pressure. Once static pressures have been determined, membrane stress in the shell is obtained from Eq. (7), or this equation is inverted to obtain shell thickness h for an allowable stress σ. For the shells we are considering, we have calculated the static pressures using Fig. 3 and the shell thicknesses to withstand these pressures for σ = 275,800 kPa. These values are given in Table VII. By comparing with results of Table III, one can see that the shell thickness is determined by the initial blast loading, rather than the static pressure rise. This also implies that venting will have a negligible effect upon the required shell thickness.

If a spherical chamber design is chosen our calculations for central charges show that it is preferable to evacuate the shell to about a third of an atmosphere for 13.61 kg charges. A shell designed for a certain allowable stress to the above conditions will also be stressed to about the same level if 4.54 kg charge is detonated without chamber evacuation. If we assume a chamber of diameter midway between the extremes of diameter considered, i.e., 5.49 m diameter, then a shell thickness between 31.75 mm and 44.45 mm is suggested, depending on the permissible combination of charge weight, eccentricity and initial pressures which are desired for the chamber. Additional calculations will be required to finalize a chamber thickness based on more definitive design criteria.

TABLE VII
Static Pressures and Shell Thicknesses, Spherical Chambers Designed to σ = 275 MPa

W, kg	a, m	V m^3	W/V kg/m^3	P, kPa	h, mm
4.54	1.83	4.31	0.354	1103	3.658
	2.43	60.72	.0753	310	1.372
	3.05	118.59	.0283	186	1.029
	3.66	350.76	.1298	69	.4572
13.61	1.83	4.31	1.062	1586	5.258
	2.43	60.74	.2243	896	3.962
	3.05	118.62	.1147	483	2.667
	3.66	350.85	.0388	186	1.234

ANALYSIS OF CYLINDRICAL CHAMBERS

Equations governing the response of cylindrical chambers to uniform transient internal blast loads are given by DeMalherbe, et al [13]. They are identical to those for spherical charges except that the expression for the circular frequency, ω, is given by

$$\omega = \sqrt{\frac{E}{\rho a^2}} \qquad (22)$$

in place of Eq. (5) for spherical chambers. Based upon the computed response, the stress in the cylindrical shell is then calculated by

$$\sigma_{max} = \frac{P_r a}{h} \bar{A} \qquad (23)$$

where $\bar{A}$ is the same as defined for the spherical chamber and is equivalent to ϕ in Reference 13. Furthermore, if we conservatively assume that the response of the cylindrical shell is adequately described by a thin ring cut from the shell on either side of a diametral plane passing through the charge, then the pressure loads calculated for the spherical chamber apply. This assumption neglects the longitudinal decay of the pressure in the chamber and in effect assumes uniform pressure over the length of the chamber for computing the peak wall stresses.

Table I gives the pressure loads for central charges in unevacuated chambers. Shell thicknesses of cylindrical chambers calculated for the first pressure pulse produced by these loads are given in Table VIII. Ratios of reverberation time to pulse duration remain the same as given in Table II; however, the ratio of reverberation time to shell period is changed and so is included additionally in Table VIII. Note that reverberation occurs within the first two cycles of shell response and will certainly enhance the shell response.

Before proceeding with additional calculations for the multiple shock reflections and eccentric charges, however, some comparisons were made between spherical and cylindrical chamber on the basis of results obtained for the first pressure pulse for central charges in unevacuated chambers. Comparisons were based on shell weight which would be one indication of chamber construction cost. To compare shell weights some assessment of working space efficiency was required. It was decided that, to have equal efficiency, a spherical chamber should have a working height (or clearance) equal to the height of the cylindrical portion of the cylindrical chamber at the same radius. It was further decided hat a practical design for a cylindrical chamber would be a 2.13 m high cylindrical section above

TABLE VIII
Shell Thickness of Unevacuated Cylindrical Chambers for Central Charges (single pulse)

E kg, Pentolite	a (m)	ω (1/msec)	τ (msec)	$\frac{t_r^*}{\tau}$	$\frac{\dot{u}\|t = T_r}{\|\dot{u}\|t = T_r\|}$	$\bar{A}$	h (mm)
4.54	1.83	2.806	2.24	.793	+	.608	15.54
	2.43	2.105	2.98	1.07	+	.804	11.33
	3.05	1.684	3.73	1.47	+	.851	8.94
	3.66	1.403	4.47	1.69	+	.893	7.34
13.61	1.83	2.806	2.24	.405	+	.377	34.14
	2.43	2.105	2.98	.526	+	.493	24.79
	3.05	1.684	3.73	.633	+	.741	18.92
	3.66	1.403	4.47	.769	+	.811	15.57

*From Table II

the base (to allow for 1.98 m doors in the cylindrical section) with a hemispherical cap. An additional 0.61 m of the cylindrical section is buried in concrete. We judged that the support for the spherical shell would then be equal in cost to the concrete base of the cylindrical chamber. These relationships are shown schematically in Fig. 4.

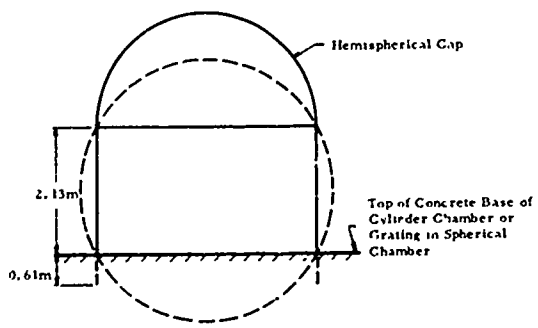


Fig. 4. Diagram Showing Assumed Relationship for Equal Working Efficiency and Assumed Cylindrical Chamber Geometry

Based on these assumptions, the shell weights are computed in Table IX and compared in Fig. 5. Comparisons in Fig. 5 are based on the following radii for equivalent spherical and cylindrical chambers:

Radii (m)	
Spherical Chamber	Cylindrical Chamber
1.83	1.48
2.43	2.19
3.05	2.86
3.66	3.50

Notice that the size difference becomes less as the chambers increase in size and that the difference doesn't significantly affect the breakeven point between spherical and cylindrical chamber weight. Setting the height of the cylindrical section of the chamber at 2.13 m regardless of its diameter is what makes the weight of the cylindrical chamber more competitive with that of the spherical chamber as size increases. A different assumption, such as setting the height as a percentage of the diameter, would give a different result, less favorable to the cylindrical chamber. For our assumptions the breakeven point occurs for chambers larger than 7.32 m in diameter. The weight difference when starting with 3.05m radius spherical chamber is illustrated in Fig. 5.

As a result of these weight comparisons (based on results for only one loading condition as described previously), and because the BRL chamber will probably be less than 6.10 m in diameter, a spherical chamber appears to be preferable to a cylindrical one. Thus, no further evaluations were made for cylindrical chambers.

OTHER CONSIDERATIONS

Venting

As indicated by the analysis of spherical chambers, the maximum stresses in the shell are produced by the initial transient overpressure wave and the first few reverberations. Stresses generated in the shell by the quasi-static pressure rise were significantly lower. The first few reverberations of the pressure

TABLE IX
Weights of Spherical and Cylindrical Chambers

W (kg Pentolite)	a (m)	Spherical Chamber h(mm)	Spherical Chamber wt(kg)	Cylindrical Chamber h(mm)	Cylindrical Chamber wt. of cyl. sect. (kg)	Cylindrical Chamber wt. of cap* (kg)	Cylindrical Chamber wt. total (kg)
4.54	1.83	12.27	4076	15.44	3839	2265	6104
	2.43	8.18	4815	11.33	3748	2408	6155
	3.05	6.27	5764	8.94	3694	2882	6576
	3.66	5.03	6649	7.34	3638	3324	6962
13.61	1.83	28.60	9588	34.14	8529	4794	13,323
	2.43	20.24	11,977	24.79	8224	5989	14,213
	3.05	14.12	13,008	18.92	7831	6504	14,336
	3.66	11.18	14,800	15.57	7725	7400	15,125

*1/2 Spherical Shell Wt.

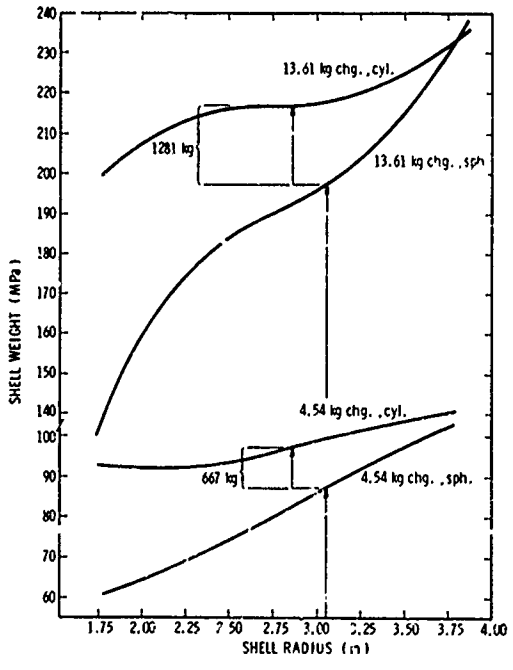


Fig. 5. Comparison of Shell Weights--Central Charges, Non-evacuated Chambers, Results for 1st Pressure Pulse Only.

wave occur in about 15 msec or less which is insufficient time for significant decay to occur for reasonable size vent areas. Thus, only a small muffled vent area is required to vent the tank slowly while limiting outside disturbances.

Spallation

Spalling in steel chambers is not a problem in the range of overpressures for which these chambers will be designed. This is apparent from our own experience in observing the response of steel to much higher overpressures. For example, no spallation was observed in the measurements reported in Reference 4 in which overpressures on steel plates and the ends of steel bars exceeded 2068.5 MPa. Our general observation that spallation is not a problem for the BRL blast chamber is also supported by Rinehart [18]. He states that the stress, σ, required to produce spall in metals is exceedingly high, 1034.25 MPa, corresponding to particle velocities v, of 30.48 to 60.96 m/sec. The relationship between particle velocity and the instantaneous normal stress at a point is given by Rinehart as

$$\sigma = \rho C_L v \qquad (24)$$

where ρ is the material density and C_L is the dilatational wave speed given by

$$C_L = \left[3K\ (1 - \nu)/\rho(1 + \nu) \right]^{1/2} \qquad (25)$$

For steel with $K = 199.54 \times 10^6$ kPa, $\rho = 7.854$ kg/m^3 and $\nu = .33$

$$C_L = 6270 \text{ m/sec}$$

An upper limit of 68.9 MPa overpressure on the walls of the BRL chamber is probably reasonable based upon our calculations (see Fig. 5 and the Appendix). The corresponding particle velocity corresponding to this normal stress is now found from Eq. (24)

$$v = 1.40 \text{ m/sec}$$

The values of stress and velocity are well below the critical values given by Rinehart.

Chamber Lining

Lining of the chamber with foam material, either resilient or crushable, can significantly reduce either blast pressure or impulse imparted to the chamber walls and thus reduce the total amount of steel in the chamber. But, the installation of this material will be expensive, and effective crushable materials must be replaced quite often. General maintenance would be difficult, and utilization of the chamber would be seriously impaired. For these practical reasons, the use of such energy absorbers or pulse shapers should not be seriously considered.

Doors, Viewports and Other Openings

The chamber will have at least one access door, two viewports 90° apart, and probably several small openings for muffled venting and exhausting or pumping a vacuum. The shell near these openings must be sufficiently thickened and reinforced that its full tensile strength is not compromised.

If an unevacuated shell design is chosen, the main door and other closures for openings must open inward and seat on seals to provide positive sealing for internal blast loading. The closures must themselves be designed to remain elastic under blast loading, which can be done with the aid of existing elastic response computer codes.

If an evacuated shell is chosen, double closures both inside and outside must be installed, with the outer closure opening outward and providing a vacuum seal and the inner ones being blast-resistant.

Glass viewports can undoubtedly be designed on the basis of past experience with similar ports at BRL and at Sandia Corporation [31]. Good optical clarity is required, and thick, shock-resistant glass or transparent plastic can be employed. Detailed design was beyond the scope of this study.

Cost Factors

We did not try to estimate actual costs for the chamber designs but only attempted to establish relative values. As reinforced concrete construction was eliminated early in the study (mainly because rectangular chambers were eliminated), weight comparisons between two steel chambers were used as an indication of relative cost. Other factors would of course, enter into the construction costs but we felt shell weight would predominate. On this basis, spherical and cylindrical chambers were compared (see Section entitled Analysis of Cylindrical Chambers) and the spherical chamber chosen as being the preferred geometry for the BRL design.

CONCLUSIONS AND RECOMMENDATIONS

This predesign study included a critical survey of the published literature pertaining to the analysis, design, fabrication and testing of spherical, cylindrical and rectangular blast chambers. Rectangular chambers were not evaluated sufficiently as an alternative design, and so, our conclusions and recommendations are based primarily upon analysis of spherical and cylindrical chambers.

Conclusions

1. It is entirely feasible to design a blast chamber to contain repeated detonations of up to 13.61 kg of energetic explosive in evacuated chambers.

2. Eccentric charge locations are also feasible but required shell thickness increases sharply for large eccentricities (small standoff distances from wall).

3. It will reduce the structural weight and thus the cost to evacuate the chamber prior to detonating the larger charges. Other considerations such as the effect

on working efficiency and the initial cost of a vacuum system must be carefully considered, however.

4. For very low vacuums, the reverberation times are greatly reduced, causing enhancement of the initial shock. Moderate vacuum (34.48 kPa) is easier to achieve, avoids the initial pressure wave enhancement and yet still reduces the overpressures on the chamber significantly.

5. Pressure wave reverberation occurs within the first few cycles of chamber resonance and increases the response above that produced by the initial shock. Shell thickness must be increased to accommodate the pressure wave reverberation or restrictions must be set on certain combinations of charge weight and initial chamber pressure to avoid a resonance condition.

6. Venting the chamber will not significantly reduce peak shell wall stresses because maximum response is produced by initial pressure loading, or the first few reverberations.

7. Quasi-static pressure rise is not a factor in design of this particular chamber.

8. A spherical chamber is lighter and thus cheaper than a cylindrical chamber for chamber diameters of 7.32 m or less.

Recommendations

The final recommendations of this study are of two types, specific recomendations for chamber design, and more general recommendations which refer to related or additional studies which merit consideration.

Specifically, we recommend:

1. Steel in preference to reinforced concrete for spherical or cylindrical chambers.

2. No inclusion of energy-absorbing liners.

3. No, or minimal, venting.

4. Spherical chamber as more economical than cylindrical chamber, for chamber diameter of 7.32 m or less.

5. Evacuated chamber for larger charge weights if the effect on efficiency is small, and if there is a favorable tradeoff between initial costs of vacuum systems versus reduced chamber construction costs.

6. Tentative chamber dimensions (diameter and thickness) for an unevacuated steel spherical chamber of 5.48 m and 44.45 mm, and for an evacuated spherical steel chamber of 5.48 m and 31.75 mm.

Generally, we recommend:

1. An additional study of the effect of multiple loading due to pressure wave reverberation of shell response from eccentric charges.

2. Evaluation of rectangular reinforced concrete or steel frame chambers as an alternative to steel spherical chambers.

REFERENCES

1. H. J. Goodman, "Compiled Free-Air Blast Data on Bare Spherical Pentolite," BRL Rept. 1092 Aberdeen Proving Ground, Maryland 1960.

2. W. H. Jack, Jr., "Measurements of Normally Reflected Shock Waves from Explosive Charges," BRL Memo Rept. 1499, Aberdeen Proving Ground, Maryland, 1963

3. W. H. Jack, Jr., and B. F. Armendt, "Measurements of Normally Reflected Shock Parameters from Explosive Charges Under Simulated High Altitude Conditions," BRL Rept. 1280, Aberdeen Proving Ground, Maryland, 1965.

4. A. B. Wenzel and E. D. Esparza, "Measurements of Pressures and Impulses at Close Distances from Explosive Charges Buried and in Air," Final Rpt., Contract No. DAAK02-71-C-0393, Southwest Research Institute, San Antonio, Texas, Aug. 21, 1972.

5. W. E. Baker, Explosions in Air. University of Texas Press, Austin, Texas, 1973.

6. J. F. Proctor and W. S. Filler, "A Computerized Technique for Blast Loads from Confined Explosions," Minutes of the 14th Annual Explosive Safety Seminar, pp. 99-124, New Orleans, Louisiana, Nov. 8-10, 1972.

7. R. G. S. Sewell and G. F. Kinney, "Internal Explosions in Vented and Unvented Chambers," Minutes of the 14th Annual Explosive Safety Seminar, pp. 87-98, New Orleans, Louisiana, Nov. 8-10, 1972.

8. W. A. Keenan and J. E. Tancreto, "Effects of Venting and Frangibility on Blast Environment from Explosions in Cubicles," Minutes of the 14th Annual Explosive Safety Seminar, pp. 125-161, New Orleans, Louisiana, Nov. 8-10, 1972.

9. H. R. W. Weibull, "Pressures Recorded in Partially Closed Chambers at Explosion of TNT Charges," Annals of the New York Academy of Sciences, 152, Article 1, pp. 357-361 Oct. 1968.

10. W. E. Baker and F. J. Allen, "The Response of Elastic Spherical Shells to Spherically Symmetric Internal Blast Loading," Proc. of the Third U.S. National Congress of Applied Mechanics, ASME, New York, pp. 79-88, 1958.

11. W. E. Baker, "The Elastic-Plastic Response of Thin Spherical Shells to Internal Blast Loading," J. of Appl. Mech., 27, Series E, 1, pp. 139-144 March 1960.

12. F. A. Loving, "A Spherical, Sound-Muffling Barricade," Rpt. RE-59-29, E. I. duPont de Nemours & Co., Eastern Laboratory, Gibbstown, New Jersey, 1959.

13. M. C. deMalherbe, R. D. Wing, A. J. Laderman and A. K. Oppenheim, "Response of a Cylindrical Shell to Internal Blast Loading," J. of Mech. Engr. Sci., 8, 1, pp. 91-98, 1966.

14. A. MacKenzie, E. W. Dalrymple and F. Schwartz, "Design of Pressure Vessels for Confining Explosives," Picatinny Arsenal Tech. Memo. 1643, Dover, New Jersey, July 1965 (AD 467 730).

15. J. W. Hanna, W. O. Ewing, Jr. and W. E. Baker, "The Elastic Response to Internal Blast Loading of Models of Outer Containment Structures for Nuclear Reactors," Nuclear Science and Engineering, 6, pp. 214-221, 1959.

16. W. E. Baker, W. C. L. Hu, and T. R. Jackson, "Elastic Response of Thin Spherical Shells to Axisymmetric Blast Loading," J. of Appl. Mech., 33, Series E. 4, pp. 800-806, 1966.

17. E. Cohen and N. Dobbs, "Design Procedures and Details for Reinforced Concrete Structures Utilized in Explosive Storage and Manufacturing Facilities," Annals of the New York Academy of Sciences, 152, Article 1, pp. 452-490, Oct. 1968.

18. N. Davids, (editor), International Symposium on Stress Wave Propagation in Materials, Interscience Publishers, Inc., New York, New York, 1960.

19. J. W. Hanna and W. O. Ewing, Jr., "Effectiveness of Lining Materials in Increasing the Blast Resistance of a Simulated Outer Containment Vessel for a Nuclear Reactor," BRL Memo. Rpt. No. 1341, Aberdeen Proving Ground, Maryland, April 1966.

20. B. R. Sullivan and A. A. Bombich, "Evaluation of Methods of Attenuating Blast Pressures on Walls," Annals of the New York Academy of Sciences, Article 1, pp. 519-531, Oct. 1968.

21. F. A. Loving, Jr., "Sound Reducing Explosives Testing Facility," U.S. Patent No. 2, 940, 300, June 14, 1960.

22. A. Bartkowiak and J. M. Kuchta, "A Large Spherical Vessel for Combustion Research," I&EC Process Design and Development, 5, pp. 436-439, Oct. 1966.

23. S. G. A. Bergman, "Swedish Protective Structures for Manufacturing Units Constituting Explosion Hazard in the Range 1-2,000 Pounds of TNT," Annals of the New York Academy of Sciences," Article I, pp. 500-510, Oct. 1968.

24. R. S. Fling & V. Linse, "Design and Operation of a Blast Containment Structure," Behavior and Utilization of Explosives in Engineering Design, N. Mex. Sec. of the ASME, pp. 167-173, (date unknown).

25. G. R. Cowan and F. M. Willis, "Barricading Against Vented Explosions," Minutes of the 10th Explosive Safety Seminar, 1968.

26. N. S. Thumpston, "A Model Study of the Effect of an Explosion in an Oxidation Cubicle," Annals of the New York Academy of Sciences, Article 1, pp. 871-900, Oct. 1968.

27. B. T. Rogers and R. W. Taylor, "Total Confinement of Clandestine Explosives," FBI Law Enforcement Bulletin, 42, 8, pp. 2-7, 31, Aug. 1973.

28. S. Timoshenko, Theory of Elastic Stability, 1st Edition, McGraw-Hill Book Company, Inc., New York, 1936.

29. J. G. Pulos and M. A. Krenzke, "Recent Developments in Pressure Hull Structures and Materials for Hydrospace Vehicles," Rpt. 2137, David Taylor Model Basin, Dept. of the Navy, Dec. 1965.

30. W. E. Baker, W. C. L. Hu and T. R. Jackson, "Elastic Response of Thin Spherical Shells to Axisymmetric Transient Loading," Tech. Rpt. 1, Project No. 02-1635, Southwest Research Institute, San Antonio, Texas Aug. 1965.

31. J. O. Davis and P. E. Jockle, Jr., "Design and Development of a Four-Foot by Six-Foot Explosion-Proof Window," Minutes of the 14th Annual Explosives Safety Seminar, pp. 1223-1236, 1972.

APPENDIX

Blast Loading for Eccentric Charges

The method used for calculating blast loading for eccentric charges is the same as that employed by Baker, et al, in Reference 16, except that a newer source of compiled blast data is used (Reference 5). An example case will be given here to illustrate the method.

The first step in the method is calculation of distances to the shell for various eccentric charge locations. The law of cosines gives (see Figure A1)

$$d^2 = e^2 + a^2 - 2\,ea\cos\phi \qquad (A1)$$

where d is distance from charge to shell, ϕ is polar angles, e is charge eccentricity and a is shell radius. Note that a minus e is the shortest distance from charge to shell at $\phi = 0°$. For all calculations in this report we assumed a = 2.74 m and 15° increments in ϕ. Eq. (A1) was then used to calculate d for each value of ϕ.

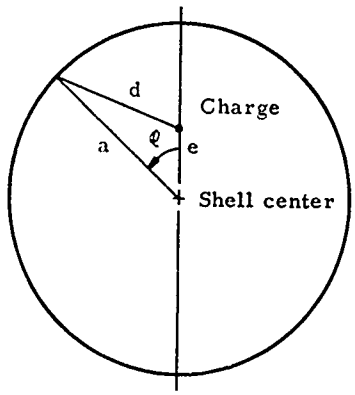


Fig. A1. Geometry for Eccentric Charges

The desired blast loading parameters are reflected peak overpressure P_r, duration of linearly-decaying pressure at any shell location T_r, and time of arrival of the blast wave t_a at a given shell location*. These parameters are obtained graphically from scaled charges of blast parameters for bare, spherical Pentolite in Chapter 6 of Reference 5. The dimensionless scaled parameters which are read from that reference are:

---

*Normally reflected blast parameters apply for obliquely reflected strong shocks up to angles of obliquity up to about 39° (see Reference 5, Chapter 1). For all cases we calculated, this angle was below the critical angle.

$$\left.\begin{aligned} \bar{t}_a &= (t_a a_o p_o^{1/3}/E^{1/3}) \\ \bar{P}_r &= (P_r/p_o) \\ \bar{I}_r &= (I_r a_o/p_o^{2/3}E^{1/3}) \end{aligned}\right\} \qquad (A2)$$

These parameters are unique functions of dimensionless scaled distance:

$$\bar{R} = (dp_o^{1/3}/E^{1/3}) \qquad (A3)$$

In these expressions, sound velocity a_o = 340 m/sec for all of our cases. Ambient pressure p_o took on several values, dependent on assumed shell evacuation. Total charge energy E was 2.316×10^7 N-m for 4.5 kg Pentolite charges, and 6.95×10^7 N-m for 13.61 kg charges.

The procedure used to calculate the blast parameters was to first calculate $\bar{R}$ from d, and assumed ambient pressure p_o and charge energy E. Then, $\bar{t}_a$, $\bar{P}_r$ and $\bar{I}_r$ were read from graphs in Chapter 6 of Reference 5. Next, the scaled duration $\bar{T}_r$ for a linearly decaying pressure pulse was calculated from

$$\bar{T}_r = \frac{2\bar{I}_r}{\bar{P}_r} \qquad (A4)$$

The resulting scaled parameters were then "unscaled" using inverted forms of Eq. (A2)*.

An example of the results of calculation of one set of blast parameters, using the method just described, is given graphically in Fig. A2.

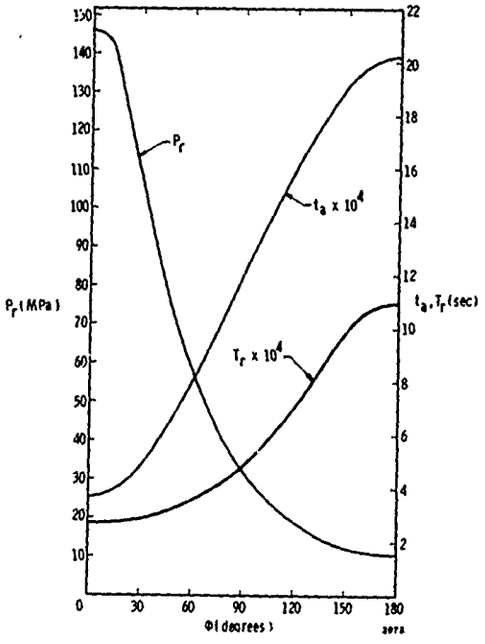


Fig. A2. Blast Parameters for 13.61 kg Charge, e = 1.22 m, p_o = 34.48 kPa.

*All times scale in the same manner, so T_r was obtained from $\bar{T}_r$ using the same multipliers as for $\bar{t}_a$.

FRAGMENT VELOCITIES FROM BURSTING CYLINDRICAL AND SPHERICAL PRESSURE VESSELS

R. L. Bessey and J. J. Kulesz
Southwest Research Institute
San Antonio, Texas

An analytical method is used to describe bursting gas reservoirs and to predict the maximum fragment velocity attained by pieces from the fragmenting containment vessels. The method assumes that the fragments are accelerated while gas escapes through the rupture cracks between the fragments. As internal pressure is reduced by the escaping gas, nearly constant fragment velocities are finally attained. The resultant fragment velocities may be used as initial velocities in trajectory equations for fragment hazard analysis. Results show that the maximum fragment velocities obtained for both cylindrical and spherical containment vessel geometries are nearly independent of the number of fragments chosen, n, for $n > 10$. The results are compared to existing data on maximum fragment velocities for bursting pressurized glass vessels. The predicted values for the spherical vessels pressurized with air are within 6% of the experimental values.

INTRODUCTION

An investigation of the hazard of a rupturing gas confinement vessel includes assessment of both the effects of blast damage and of primary fragment damage. Primary fragments may be defined as the fragments emanating from the material of a containment vessel which ruptures as a result of gas under high pressure. The high pressure may be generated in a dynamic process from the conversion of a high explosive such as in the case of a bomb or by some quasi-static process such as the case of the relatively slow overpressurization of a boiler, or a rocket pressurant tank. An estimate of great relevance to fragment hazard assessments is what is the initial velocity of the primary fragments. Trajectory analysis may then be used to determine what the range and terminal energy of the fragment may be, and what hazards it may thus constitute. Under work sponsored by the Aerospace Safety Research and Data Institute (ASRDI), NASA-Lewis Research Center {1,2}, a method has been devised for estimating primary fragment initial velocities for vessels of various geometries and for various breakup configurations.

Earlier analytical efforts to determine the initial velocity of primary fragments have generally modeled the bursting process in one of three ways. First it has been assumed that the potential energy of the high pressure gas (or of a fixed mass of high explosive) is partitioned, upon rupture of the confinement vessel, between the kinetic energy of primary fragments and that of the expanding internal gas. In this model, all fragments are assumed to have the same initial velocity. The model has especially been used to describe cases where high explosives are confined by cored or uncored cylindrical or spherical shells or plate-high explosive sandwich configurations {3, 4}. Fragment velocity is given deterministically as a function of a charge to mass ratio. In a second type of model, available energy is partitioned between the kinetic energy of the fragments, adiabatic expansion of the confined gas, and the plastic deformation

of the confinement vessel prior to rupture {5}. A curve for the elastic-plastic response of the vessel material must be assumed, and analysis is carried out with time dependent, two dimensional finite difference codes. This model has been especially applied to problems involving metal-encased high explosives where the dynamics of the explosion process are such that the casing may double its radius before rupture occurs. Thus, the energy used up in the plastic deformation of the casing may be a significant portion of the total available energy.

A third type of model partitions available energy between kinetic energy of the fragments, energy used in the adiabatic or isothermal expansion of the confined gas, and loss of energy with the escape of the confined gas through the cracks formed between fragments at rupture {6-8}. These models assume the efflux of the high pressure internal gas through the cracks formed between the fragments according to mass rate of flow equations for an ideal gas passing through an ideal nozzle. Some breakup pattern for the confinement vessel must be assumed in order to estimate crack areas. The models involve the solution of nonlinear simultaneous differential equations by numerical means; maximum fragment velocity is attained as the pressure of the confined gas drops to ambient levels. In general, no loss of energy is assumed as a result of plastic vessel deformation. Thus, these models seem particularly applicable to processes where plastic deformation of the confinement vessel before rupture is minimal or where the velocity of the vessel walls immediately prior to rupture is low compared to the fragment velocities after rupture. This is the case for vessels brought to the bursting pressure relatively slowly by "mechanical" overpressurization or heating in contrast to the more dynamic process of the detonation of high explosive in intimate contact with a ductile metal bomb casing, for instance.

Figure 1 illustrates the conceptualization of several breakup patterns for fragmenting spherical and cylindrical vessels. Models for a spherical vessel fragmenting into halves are discussed in Refs. {6} and {7}. A sphere fragmenting into n fragments of circular projection (Fig. 1a) is discussed in Ref. {8}. Two additional models, that for a cylinder fragmenting into halves and that for a cylinder fragmenting into axial strip fragments (Fig. 1b and c), are discussed below. Limited data from experiments on spherical vessels show that the n-fragment

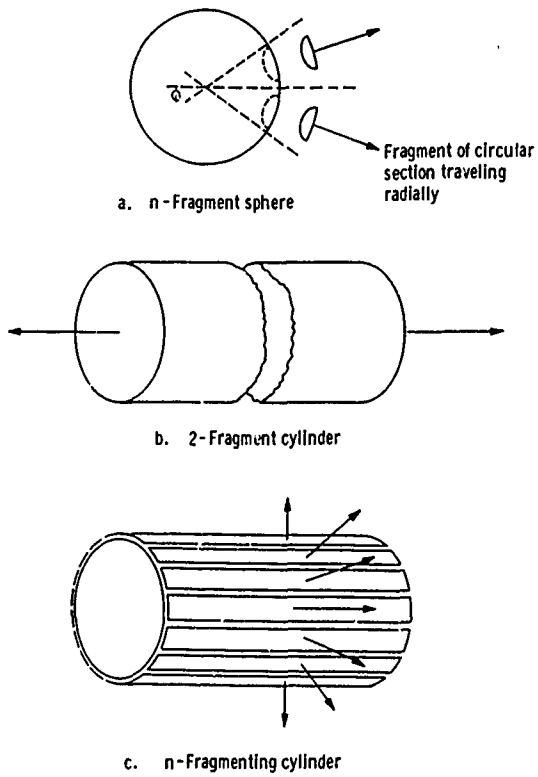


Fig. 1 - Conceptual models of bursting confinement vessels

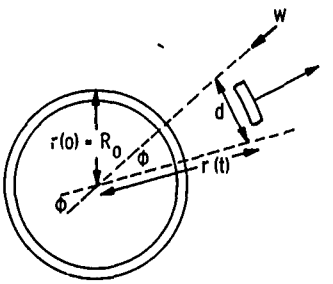
model can predict fragment velocities fairly well. Results for the n-fragment cylinder compare reasonably well with those for the n-fragment sphere for equivalent volumes and initial conditions. Nomographs generated by computer code solutions of the models may be used to obtain quick, reasonably accurate estimates of initial fragment velocities for bursting confinement vessels under various conditions.

ANALYTICAL MODELS FOR CYLINDERS

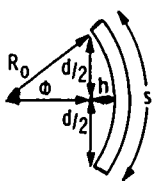
A cylinder fragmenting into two equal pieces at the axis center (Fig. 1b) may be analyzed exactly like the similar case for the sphere {7}, with the appropriate enclosed volume and vessel mass values substituted in the equations for dimensionless groups [Eqs. (11) and (12) of Ref. {7}]. Results are dependent on cylinder length because the mass of the cylinder end pieces must be taken into account.

Figure 1c shows the conceptualization of a cylinder fragmenting into n fragments. For this case, the

fragments are axial strips which move radially from the center of the cylinder; cylinder ends are fixed. Figure 2 shows the geometric parameters of the cylinder used in the analysis. A cylinder of length L and radius R is assumed to burst into n strip fragments of width d and thickness t_h. A cross-section of each strip is a segment of the cross-section of the cylinder having a segment height of h and segment diameter d. In the following analysis the projected area of each fragment is obtained from the surface area and the initial subtended angle of the fragment at the center of the cylinder, with the result Eq. (6). Next, the area of a crack about any fragment at any time is obtained by assuming the cracks only form lengthwise along the cylinder, and by obtaining an equation for the width of these cracks in terms of the initial radius of the cylinder and the radial distance r the fragment has traveled at any time, t. The equation for crack area is given in Eq. (9). One of the differential equations of motion derived on the basis of an adiabatic gas expansion and radial motion of the fragments is the same for this analysis as it was for the n-fragment sphere, as are the equations for nondimensionalization of time and displacement; see Eq. (10). A second differential equation, Eq. (28), is obtained from the perfect gas law assumption, an equation for the mass flow of gas through the cracks formed between the fragments [Eq. (14)] and cylinder geometry considerations. Values for the nondimensionalized constants are also obtained through these considerations and are given in Eqs. (29) and (30).



a. Cylinder cross section



b. Strip fragment cross section

Fig. 2 - Geometric parameters for a fragmenting cylinder

ANALYSIS FOR A CYLINDRICAL SHELL FRAGMENTING INTO N STRIP FRAGMENTS

Variable List:

A - term in Eq. (11)

A_f - fragment area

a_{oo} - sound speed in confined gas, $\tau = 0$

a_* - critical sound speed in mass flow equation

B - term in Eq. (11)

C - term in Eq. (11)

D - term in Eq. (11)

d - width of fragment segment

F - fragment projected area

g - nondimensionalized displacement of a fragment

h - segment height (see Fig. 2)

k - mass flow rate coefficient

L - cylinder length

M - mass of contained gas at any instant, τ

M_f - fragment mass

M_t - cylindrical shell mass

n - number of fragments

P - crack perimeter about a fragment

P_* - nondimensionalized pressure

P_o - pressure of confined gas at any instant, τ

P_{oo} - initial pressure of confined gas

R - initial cylinder radius

r - fragment displacement at any instant, τ

s - segment length

T_o - temperature of confined gas at any instant, τ

t_h - shell thickness

V_o - volume of confined gas at any instant, τ

V_s - volume of shell material

w - crack width

x - nondimensionalizing constant for displacement

α - nondimensional constant

β - nondimensional constant

Θ - nondimensionalizing constant for time

θ - angle subtended at the center of the cylinder by a fragment $\tau = 0$

κ - ratio of specific heats for confined gas

ρ_o - confined gas density at any instant, τ

ρ_* - critical density of gas in mass flow equation

ρ_s - density of shell material

τ - time

ξ - nondimensionalized time

Prime denotes derivatives with respect to ξ.

From considerations of the cylinder geometry (see Fig. 2),

$$M_t = \rho_s V_s = \pi\rho_s L \cdot \left[(R + t_h)^2 - R^2\right] \quad (1)$$

$$A_f = \frac{2\pi RL}{n} \quad (2)$$

$$F = L \cdot d = L \cdot 2 \cdot \left[R^2 - (R - h)^2\right]^{1/2} \quad (3)$$

From Fig. 2,

$$A_f = L \cdot S \ , \quad S = \theta R \ ,$$

$$\theta = \cos^{-1}\left(\frac{R - h}{R}\right)$$

Therefore,

$$A_f = L \cdot R \cdot \cos^{-1}\left(\frac{R - h}{R}\right) \quad (4)$$

From Eqs. (2) and (4),

$$h = R\left(1 - \cos\frac{2\pi}{n}\right) \quad (5)$$

From Eqs. (5) and (3),

$$F = 2L \cdot R\left[1 - \left(\cos\frac{2\pi}{n}\right)^2\right]^{1/2} \quad (6)$$

The crack area at any time τ for fragment i is

$$(Pw)_i = 2\,L \cdot w \quad (7)$$

From Fig. 2 it may be seen that

$$w = \theta\left[r(\tau) - R\right] = \frac{2\pi}{n} \cdot \left[r(\tau) - R\right] \quad (8)$$

From Eqs. (7) and (8),

$$(Pw)_i = \frac{4\pi L}{n} \cdot \left[r(\tau) - R\right] = \frac{4\pi L \cdot R}{n}\left(\frac{r(\tau)}{R} - 1\right) \quad (9)$$

From Ref. [8], Eqs. (14), (15) and (16),

$$g'' = nP_* \left[1 - \frac{(g')^2}{(P_*)^{(\kappa-1)/\kappa}}\right]^{\kappa/(\kappa-1)}$$

$$X = \frac{M_t a_{oo}^2}{FP_{oo}}\left(\frac{2}{\kappa - 1}\right) \quad (10)$$

$$\Theta = \frac{M_t a_{oo}}{FP_{oo}}\left(\frac{2}{\kappa - 1}\right)^{1/2}$$

From differentiation of the ideal gas equation,

$$\frac{dP_o(\tau)/d\tau}{P_o(\tau)} = \frac{1}{\rho_o(\tau)V_o(\tau)}\frac{dM(\tau)}{d\tau} + \frac{1}{T_o(\tau)} \cdot \frac{dT_o(\tau)}{d\tau} - \frac{1}{V_o(\tau)}\frac{dV_o(\tau)}{d\tau} \quad (11)$$

$$A = B + C - D$$

Using the variable changes $P_o(\tau) = P_{oo} \cdot P_*(\xi)$ and $\tau = \theta\xi$, term A becomes

$$A = \frac{1}{\theta} \frac{P'_*(\xi)}{P_*(\xi)} \tag{12}$$

and using these variable changes with the ideal gas law, term C becomes

$$C = \frac{1}{\theta} \frac{\kappa - 1}{\kappa} \frac{P'_*}{P_*} \tag{13}$$

The confined gas mass flow rate through the cracks is [from Eq. (7), Ref. {8}]

$$\frac{dM(\tau)}{d\tau} = -k\rho_* a_* Pw \tag{14}$$

The total crack area around n fragments

$$Pw = \Sigma(Pw)_i = n(Pw)_i$$

And from Eqs. (9) and (14),

$$\frac{dM(\tau)}{d\tau} = -k\rho_* a_* 4\pi L \cdot R \cdot \left(\frac{r(\tau)}{R} - 1 \right) \tag{15}$$

But from the cylindrical geometry,

$$V_o(\tau) = \pi r^2(\tau) \cdot L \tag{16}$$

Thus, from Eqs. (11), (15) and (16), term B becomes

$$B = \frac{1}{\rho_o(\tau) V_o(\tau)} \frac{dM(\tau)}{d\tau} = -\frac{4k\rho_* a_* R}{\rho_o(\tau)} \cdot \left[\frac{1}{Rr(\tau)} - \frac{1}{r^2(\tau)} \right] \tag{17}$$

From standard one-dimensional flow relationships [Eq. (8), Ref. {7}],

$$\rho_* = \rho_o(\tau) \left(\frac{2}{\kappa + 1} \right)^{1/(\kappa-1)} \tag{18}$$

$$a_* = a_o(\tau) \left(\frac{2}{\kappa + 1} \right)^{1/2}$$

Assuming an adiabatic gas expansion,

$$a_o(\tau) = a_{oo} P_*^{(\kappa-1)/2\kappa} \tag{19}$$

and nondimensionalizing displacement and time,

$$r(\tau) = Xg(\xi) \ , \ \tau = \theta\xi \tag{20}$$

we obtain from Eqs. (17), (18) and (19),

$$B = \frac{-4ka_{oo} P_*^{(\kappa-1)/2\kappa} R \left(\frac{2}{\kappa+1} \right)^{(\kappa+1)/2(\kappa-1)}}{X^2 g^2(\xi)} \cdot \left[\frac{Xg(\tau)}{R} - 1 \right] \tag{21}$$

From Eq. (11),

$$D = \frac{1}{V_o(\tau)} \frac{dV_o(\tau)}{d\tau} \tag{22}$$

Differentiating Eq. (16) gives

$$\frac{dV_o(\tau)}{d\tau} = \frac{d\pi r^2(\tau) \cdot L}{d\tau} = \pi L \cdot 2r(\tau) \cdot \frac{dr(\tau)}{d\tau} \tag{23}$$

Thus,

$$D = \frac{1}{V_o(\tau)} \frac{dV_o(\tau)}{d\tau} = \frac{2}{r(\tau)} \cdot \frac{dr(\tau)}{d\tau} \tag{24}$$

Changing the variable with Eq. (20), term D becomes

$$D = \frac{2}{Xg(\xi)} \frac{X}{\theta} g'(\xi) = \frac{2}{\theta} \frac{g'(\xi)}{g(\xi)} \tag{25}$$

From Eqs. (11), (12), (13), (21) and (25),

$$\frac{P'_*}{P_*} g^2 = -\frac{4k\kappa\theta a_{oo} g \left(\frac{2}{\kappa+1} \right)^{(\kappa+1)/2(\kappa-1)}}{X} \cdot P_*^{(\kappa-1)/2\kappa} + \frac{\theta 4k\kappa a_{oo} R \left(\frac{2}{\kappa+1} \right)^{(\kappa+1)/2(\kappa-1)}}{X^2} \cdot P_*^{(\kappa-1)/2\kappa} - 2\kappa g g' \tag{26}$$

From Eq. (10),

$$\frac{\Theta}{X} = \frac{1}{a_{oo}} \left(\frac{2}{\kappa - 1}\right)^{-1/2}$$

$$\frac{\Theta}{X^2} = \frac{FP_{oo}}{M_t a_{oo}^3} \left(\frac{2}{\kappa - 1}\right)^{-3/2} \qquad (27)$$

Assume constants α and β such that Eq. (26) becomes

$$\frac{P'_*}{P_*} g^2 = \left[- \alpha g + \alpha\beta\right] P_*^{(\kappa-1)/2\kappa} - 2\kappa g g' \qquad (28)$$

Then, from Eqs. (26), (27) and (28),

$$\alpha = 4k\kappa \left(\frac{2}{\kappa + 1}\right)^{(\kappa+1)/2(\kappa-1)} \cdot \left(\frac{2}{\kappa - 1}\right)^{-1/2} \qquad (29)$$

$$\beta = R \left(\frac{2}{\kappa - 1}\right)^{-1} \frac{FP_{oo}}{M_t a_{oo}^2} \qquad (30)$$

Differential Eqs. (10) and (28) are solved simultaneously by an iterative computer code using the Runge-Kutta integration techniques. The initial conditions are

$$g(0) = \frac{R}{X}, \quad P_*(0) = 1.0, \text{ and}$$

$$g'(0) = 0$$

A sample output for this type of code for the n-fragment sphere may be seen in Ref. {8}. Since M_t and F are both proportional to L, for the n-fragment cylinder,

$\frac{M_t}{F}$ is independent of the cylinder length,

and L drops out of the equations for β, X, and Θ; i.e., the cylinder length does not enter into the solution for Eqs. (10) and (28).

Some results for equivalent volume n-fragment cylinder and sphere models are shown in Figs. 3 and 4. As may be seen in the figures, if more than ten fragments are assumed for either case, the maximum initial fragment velocity, v_f, is independent of n. In general, the cylinder models predict higher fragment velocities than the sphere for an equivalent initial volume and state condition of the confined gas. This is probably due to the fixed end assumption for the cylinder model and the fact that the assumed cylindrical divergence of the fragments would cause the cracks to open up slower between the cylinder fragments than between the spherically diverging fragments of the sphere. Figure 3 shows that v_f increases with the volume of contained gas for either model. Figure 4 gives an example of the variation of v_f with mass ratio where M_{os}, the mass of a volume of gas at STP for the volume $V_o(0)$ is a nondimensionalizing factor. From the figure it may be seen that v_f is not highly sensitive to the specific heat ratio of the confined gas, but decreases rapidly with the confinement vessel mass for a fixed $V_o(0)$ and P_{oo}.

Figures 5 and 6 are example plots for the quick estimation of maximum fragment velocities expected from bursting cylindrical spherical vessels of various mass ratios. In the figures, v_f and P_{oo} are normalized to ambient sound speed and pressure to obtain $\bar{v}$ and $\bar{p}$, respectively. Plots similar to this may be generated for cylindrical and spherical vessels of other dimensions to provide tables from which initial fragment velocity estimates can be quickly obtained for hazard analysis assessments.

Some experimental data for initial fragment velocities from bursting containment vessels are available to check the predictions of fragment velocities from the models and tables generated from the models. For example, D. W. Boyer, et al., {9} have measured fragment velocities from bursting glass spheres of various dimensions where the spheres were pressurized with air or helium (He). Table 1 lists the data from the Boyer report and compares them with values obtained from the code solutions of the model for the n-fragment spheres. Values for v_f are also given which have been obtained by linear interpolation from tables of nomographs such as that of Fig. 5. The code data compare rather well with the experimental data. Some accuracy is lost in interpolation from the tables, but it appears that this would be a reasonable method of obtaining approximate initial fragment velocities. Results from the n-fragment sphere model have already compared well to those for titanium alloy spheres bursting under air pressure {8}. Available experimental data for fragmenting cylinders are available entirely from high explosive bomb arena tests. It is not expected that the model is applicable to this situation

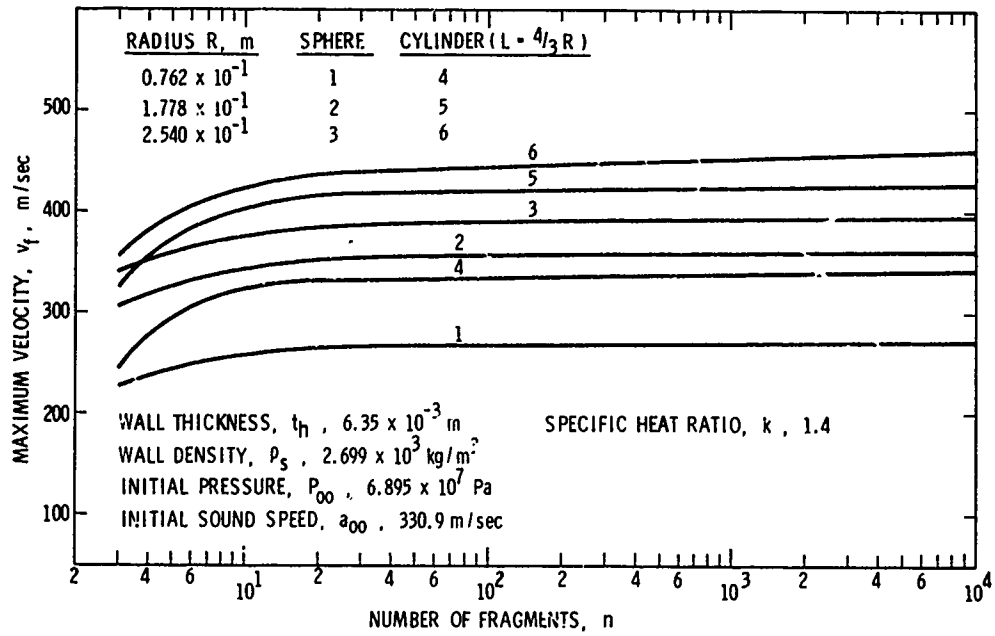


Fig. 3 - Maximum fragment velocity as a function of number of fragments for equivalent volume cylinders and spheres

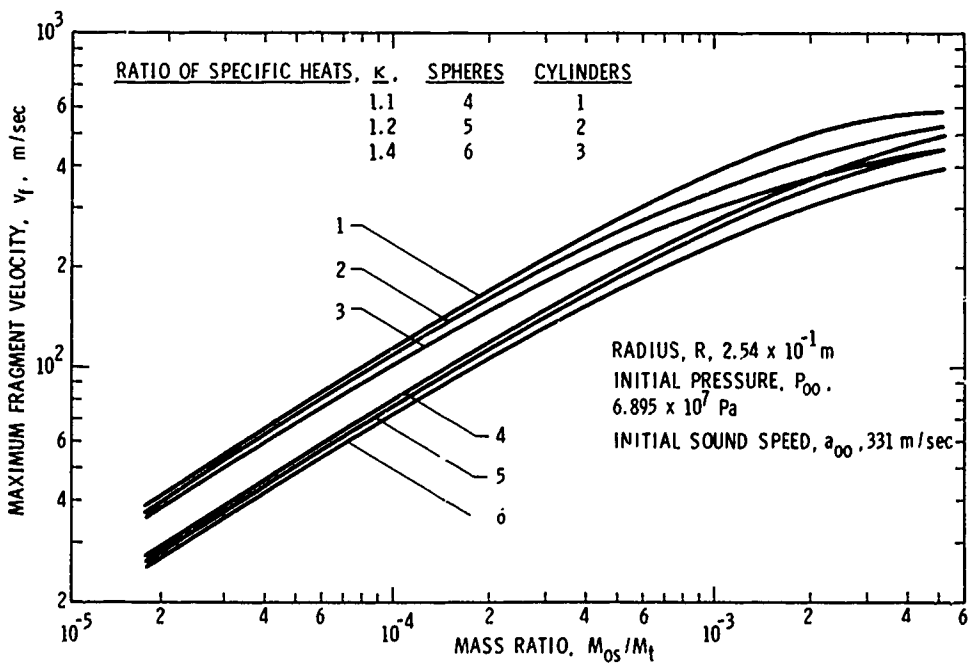


Fig. 4 - Maximum fragment velocity as a function of mass ratio for spheres and cylinders of equivalent volume

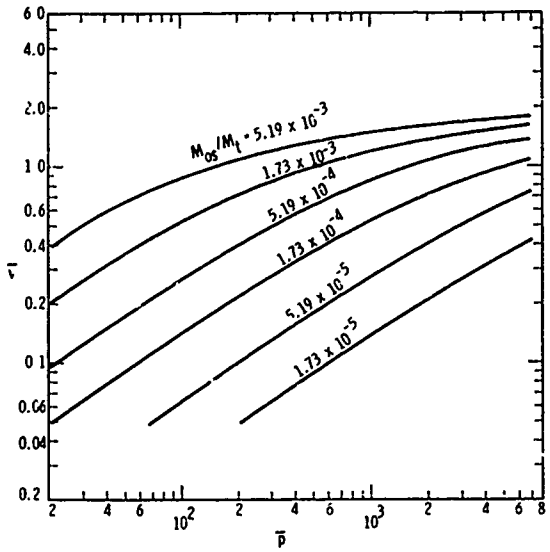


Fig. 5 - Fragment velocities for contained air in a cylinder of radius 0.254 m

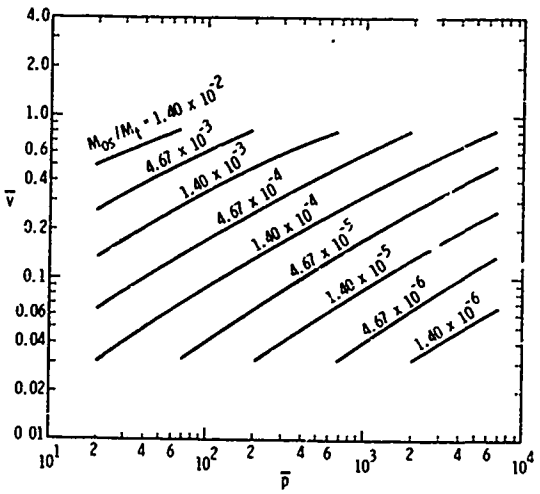


Fig. 6 - Fragment velocities for contained air in a sphere of radius 0.0762 m

TABLE 1
Initial Fragment Velocities, v_f, from Bursting Glass Spheres
(ρ = 2.6 gm/cm^3)

Sphere Characteristics		Pressurizing Gas		Initial Fragment Velocities		
Radius cm	Wall Thickness cm	Type	Pressure Pa	v_f(Boyer)* m/s	v_f(Code) m/s	v_f(Tables) m/s
1.27	0.100	Air	2.25×10^6	51.8	51.5	57.6
2.54	0.100	Air	2.25×10^6	75.6	80.2	84.4
6.35	0.190	Air	1.38×10^6	69.8	78.0	75.6
1.27	0.100	He	2.25×10^6	44.2	38.4	43.6
2.54	0.100	He	2.25×10^6	79.4	61.6	64.0

where the strain in the casing expansion may be a significant part of the available energy.

Some results for a cylindrical confinement vessel with hemispherical end plates fragmenting into halves at the axial center point are shown in Fig. 7. These more massive fragments attain considerably lower initial velocities than n-fragmenting cylinders of equivalent geometry and initial conditions.

CONCLUSIONS

Analytical models have been developed to predict the initial velocities

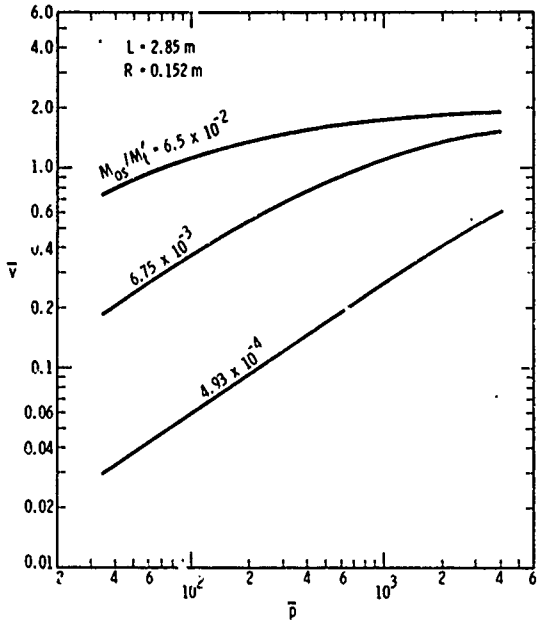


Fig. 7 - Velocities for half cylinder fragments with hemispherical end caps for a vessel containing air

of fragments from spherical and cylindrical confinement vessels rupturing from high pressure gas. The model for a spherical vessel fragmenting into n fragments has been validated by some available experimental data, indicating that the techniques may be applied to situations where the confinement vessel does not expand greatly before rupture. The model for a cylindrical vessel fragmenting into n fragments predicts somewhat higher initial fragment velocities than the spherical model for equivalent volumes. Nomographs generated from the models may be used to obtain reasonable estimates of fragment velocities through interpolation without requiring computer code runs for each specific case. Fragment velocities predicted are not too sensitive to gas parameters such as the specific heat ratio, but vary with the initial volume and pressure of the confined gas and the mass of the confinement vessel.

Fragment velocities for a breakup pattern where very few relatively large fragments are produced, such as the case of a cylinder rupturing in halves at the axial midpoint or into less than ten radially diverging strip fragments, are much lower than those of a breakup pattern where relatively more fragments of less mass are produced. This type of analysis in general may be expected to provide a means for simple estimates of initial fragment velocities which may be used to assess the hazard of gas confinement vessels bursting under pressure.

REFERENCES

1. W. E. Baker, V. B. Parr, R. L. Bessey, and P. A. Cox, "Assembly and Analysis of Fragmentation Data for Liquid Propellant Vessels," NASA CR-134538, 1973.

2. W. E. Baker, et al., "Assessment of Risks from Fragments and Pressure Waves from Exploding Liquid Propellant Tanks and Gas Storage Vessels," NASA CR Report (to be published), 1975.

3. R. W. Gurney, "The Initial Velocity of Fragments from Bombs, Shells and Grenades," BRL Report No. 405, Sept. 1943.

4. T. B. Sterne, "A Note on the Initial Velocities of Fragments from Warheads," BRL Report No. 648, Sept. 1947.

5. R. R. Karpp and W. W. Predebon, "Calculation of Fragment Velocities from Fragmentation Munitions," Proc. of First International Symposium on Ballistics, Ed. by E. J. Bryant, BRL, Aberdeen Proving Ground, Md., Nov. 1974.

6. G. L. Grodzovskii and T. A. Kukanov, "Motion of Fragments of a Vessel Bursting in a Vacuum," Inzhenemyi Zhumal - Soviet Engineering Journal, Vol. 5, No. 2, pp. 352-355, Mar./Apr. 1965.

7. D. E. Taylor and C. T. Price, "Velocities of Fragments from Bursting Gas Reservoirs," Journal of Engineering for Industry, Vol. 93, pp. 981-985, Nov. 1971.

8. R. L. Bessey, "Fragment Velocities from Exploding Liquid Propellant Tanks," The Shock and Vibration Bulletin, No. 44, Part 3, pp. 133-139, Aug. 1974.

9. D. W. Boyer, H. L. Brode, I. I. Glass, and J. G. Hall, "Blast from a Pressurized Sphere," UTIA Report No. 48, Jan. 1958.

DESIGN OF A BLAST LOAD GENERATOR FOR OVERPRESSURE TESTING

P. Lieberman, J. O'Neill, D. Freeman, A. Gibbs
TRW Defense and Space Systems Group
Redondo Beach, California 90278

This paper discusses the requirements and design features of a blast load generator which can essentially simulate the overpressure history of an atomic weapon burst in a 7-ft diameter and 9-ft high test volume. The overpressure history parameters, rise time to peak pressure, peak pressure and pressure pulse decay time, are considered in the design of the blast load generator parameters, inert driver gas and pressurization, driver section cross-sectional area and volume, driver section vent hole and time delay, driven section cross-sectional area and volume, and filling materials and their layered depths. A computer code prediction of environment performance prior to construction of the blast load generator, as well as the measurements of the performance, are both presented.

INTRODUCTION

It is required to establish a blast load environment in a soil and/or water test bed containing a target structure. This environment is specified by (1) peak pressure, (2) rise time to peak pressure, (3) total impulse within a short time period associated with shock loading of the target structure and (4) total impulse within the positive phase duration.

Ideally, the best performance would be for:

- peak pressure (1000 psi)
- rise time to peak pressure
  - surface targets (5 milliseconds)
  - 20 feet deep buried targets (10 milliseconds)
- loading time to deliver total impulse of significance to structural response (50 milliseconds)
- duration of the positive phase (1 second)

The use of a large chemical explosive source in a field test can establish the peak pressure and rapid rise time loads of interest over large test bed volumes. At regions just outside of the crater, the peak airblast loads may range from 500 to 1500 psi. But the positive phase duration may typically range from 10 to 50 milliseconds, with a high degree of spikedness that produces an initial slope intercept of about 2 milliseconds. Thus, for test structures of about 3 cubic feet in volume, the peak pressure sensitivity and acceleration sensitivity could be properly evaluated. The total impulse however, would be too small to excite the longer period structural modes for their contribution to a potential failure. Except for this technical limitation, this approach is economical for evaluating a large number of test structures.

The use of a buried trench containing the target structure, an explosive filled cavity above the structure, and an overhead berm above the cavity will permit the establishment of the high peak pressure and fast rise times over a small volume. But the rapid upward propulsion of the overhead berm by the explosive gases results in uncovering the closed volume of the cavity in a few milliseconds, and therefore, the applied loads are too short. This approach is economical for evaluating a small number of test structures.

The use of a blast load generator in a closed volume permits the duration of the load to be extended, and the load to more closely conform to the overall shape of the blast wave history. There are a number of such blast load generators available. For testing a small number of test structures, these facilities are excellent choices; but if the number of test structures are more than two or three dozen, it may become more economical to consider the construction of a new facility specifically tailored for the requirements of the test structure evaluation.

PRECEDING PAGE BLANK-NOT FILMED

The purpose of this paper is to describe the design of a blast load generator which uses a closed volume. For the attainment of rapid rise times, the driver section can utilize explosives. But for safe, economical, reproducible, and more maintenance-free operation, the driver section uses pressurized inert gas in a small diameter pipe. This sacrifices the rapid rise time. The pressure decay history is controlled by a special vent system.

DESIGN CONSIDERATIONS

The design considerations include:

- size of test volume
- peak pressure
- rise time to peak pressure
- decay history for early time

Aside from these special considerations, there are the general considerations of the construction of a large vessel containing a high pressure with limited permissible leakage and easy access to test structures.

A. Special Considerations

1. Test Volume

The dimensions of the target structure that were of interest in the first test series were 14 by 14 by 28 inches. This would indicate that a 6.75-ft diameter by 9-ft high test volume would be sufficient to reduce wall reflection interference effects. However, for soil test media the wall friction effects must be considered.

2. Peak Pressure

The peak pressure that could structurally be contained in a closed container with a removable cover and a 6.75-ft diameter, is of the order of 1000-psi. In order to achieve this pressure in the test volume, it is necessary to use even higher pressures in the driver section.

For the sudden release of driver gas into the driven test volume, where the driver and driven sections are of comparable diameters, the test volume is pressurized by a series of shock waves and rarefaction waves that eventually approach the thermodynamic equilibrium pressure. Thus a 1200-psi driver section pressure would require that the free gas volume in the driven section be no more than 20% of the driver section volume, in order to achieve a 1000-psi thermodynamic equilibrium pressure. The early time oscillations will cause spikes with amplitudes higher than the final thermodynamic equilibrium pressure. However, the rise time is extremely rapid, and can be on the order of several milliseconds.

As the driver section shrinks in diameter compared to the driven section, the peak pressure of the oscillations are reduced and the rise time to equilibrium pressure in the test volume is increased. But the smaller diameter can accommodate a higher pressure, so that the degradation in rise time is not so severe.

Thus to sustain the highest possible peak pressure in the test volume it will be necessary to reduce the free volume in the test chamber. The free volume consists of both the initial space above the test bed as well as the space created by the compaction of the water or soil test bed.

3. Rise Time to Peak Pressure

The rise to peak pressure would be instantaneous in the test volume if the chamber and driven chamber were of the same diameter, if there were no restricting orifice between the driver and driven chambers, and if the drive were by explosives which completely filled the space above the test bed.

When a test volume is filled through an orifice from a much larger reservoir, there is introduced a rise time. Table 1 was derived by use of the FACTS and CAPER computer program[1]. The rise time is found to be directly proportional to the test volume and inversely proportional to the orifice area. For a 0.393-ft^3 free space to be filled through a 0.5-ft diameter orifice; the rise time to half-pressure is 1.05 milliseconds. This represents a rise time much smaller than will be encountered by other effects.

The rise time is also altered by the introduction of a vent in the driven chamber (Table 2). In the first case of Table 2, if there were no vent the rise time to half-pressure is 3.35 milliseconds, or about 7.00 milliseconds to full pressure. But with the addition of a 3.0-inch diameter side vent the rise time increases from 7.0 milliseconds for no vent to 12 milliseconds with a vent. Thus if the chamber volumes and orifices are kept within the realm of the first case of Table 2, the rise times associated with gas filling will be much less than the rise times associated with the compression of the liquid or soil in the test volume. This latter effect will therefore control the rise time of the test volume pressure, and will be discussed next.

The most important effect on the rise time is that due to the pressurization of a compressible medium by a smaller diameter driver chamber. The strong pressure wave launched at the driver chamber attenuates as it enters larger cross sections. Multiple reflections of the launched wave between the driver chamber and a distant wall results in a gradual rise in pressure of the larger diameter driven chamber. Numerical examples are as follows:

The propagation of a step wave at the water surface of the test volume (Figure 1) undergoes multiple reflections at each change in cross section area. Based upon work in Reference 2, a computer program was written at TRW

to evaluate the pressure histories at stations M1, M2, M3 and M4 of Figure 1. When a 1000-psi step wave is applied at the surface the response station attains 950-psi at different times, depending upon the test volume materials and dimensions (Table 3). For 1.0- and 1.5-foot diameter standpipes, and 7-foot diameter tanks having a concrete base, the table shows the rise times to 950-psi for different filler materials. When the system is filled with water, the rise times range from 10 to 17.5 milliseconds. But if soil is introduced into the test volume the rise time increases from 120 to 180 milliseconds. Increasing the standpipe diameter from 1 to 1.5 feet in diameter more than halves the rise time. Raising the spring constant and reducing the mass of the concrete base decreases the rise time. The friction coefficient between the test volume material and facility wall strongly influences the rise time.

By considering the gas filling rise time of the order of 12 milliseconds, and the water pressurization of 20 milliseconds, it should be expected that the rise time in the water test volume will be at least 32 milliseconds.

4. Decay History

The pressure decay in the test volume would not occur at all if there were no way to vent the applied pressurized gas. The placement of a vent in the applied pressure volume will induce a pressure loss with time. The smaller the pressurized volume and the larger the vent hole, the faster the pressure history decay.

Figure 2 was calculated on the basis of the FACTS/CAPER code. For a 1150 psig pressurization of the driver chamber with volume 6.65 cubic feet, connected through a 4-in orifice to a driven chamber wi a volume of 0.80 cubic feet, Figure 2 shows th peak pressure and the impulse at 200 ms achieved in the driver test chamber as a function of the diameter of the side-vent orifice. Figure 2 shows that a 2-inch diameter side-vent orifice would yield a 983 psig peak pressure, and an impulse of 153 psig-sec at 200 ms.

B. General Considerations

The general considerations deal with the cover hold-down bolts, the cover seal, the wall structural configurations, the floor/wall interface, the vent hole system, the test media, and the wall friction.

The cover and bolting to the chamber was the most difficult structural design problem. To support a 1000-1500 psi chamber pressure over the 6.75-ft diameter (about 8,000,000 pounds of load) a large number of bolts were required. The design of the cover includes considerations for the rapid removal of the bolts and lifting of the cover to remove test specimens (Figure 3).

The maintenance of pressure by the cover seal was achieved by the use of water in the large diameter structure and use of a large neoprene water stop to prevent water loss through the annulus around the removable cover.

The cylindrical walls of the test chamber were built of steel shell sections varying from 7 to 15 feet in diameter, with concrete filler between the steel shell segments. The chamber wall was extended to allow attachment of the rim of the closure with three rows of bolts.

The floor/wall interface required a steel internal liner to eliminate leakage between the concrete walls and concrete floor.

The vent system has a hydraulic time delay (Figure 4) so arranged that the high pressure driver gases can pressurize the test volume without venting, but after an adjustable delay the vent is opened so that the vent size then tailors the pressure decay. With minimum or no delay it is possible to deliberately overpressurize the driven chamber initially in order to achieve a faster rise time, but to then use a larger vent hole to attain the required peak pressure.

The use of water as a test medium in the driven chamber is the easiest to handle and yields the fastest rise times. The use of dry soil results in the most difficult loading problem, the most difficult water/soil seal problem to assure dry soil, and the most difficult soil (usually wetted after post shot puncture of the seal) removal problem.

The wall friction is especially important for soil test media. The applied load at the top of the soil media may not transmit completely to the test structure because of the soil arching and soil partial attachment to the walls. But for the water test medium, these problems are eliminated.

PRESSURE HISTORY RESULTS

The calculated pressure history at each of four locations in the blast load generators, for Case A-3 of Table 3, are shown in Figures 5, 6, 7 and 8. In Figure 5, the pressure history in the middle of the upper portion of the standpipe is shown. The step-rise to 1000 psi is attained immediately, but reflections from the area enlargement at the end of the standpipe causes the pressure to fall from 1000 psi as the small column of water at the top accelerates. However, after 4.5 milliseconds when the reflections start returning from the almost rigid bottom of the blast load generator, the average pressure starts rising again.

In Figure 6, the pressure history in the lower portion of the standpipe shows pressure spikes to 600 psi during the first 2 milliseconds, then a decay to 150 psi at 4.5 milliseconds, a gradual rise in pressure after 4.5 milliseconds because of reflections from the rigid bottom of

the blast load generator, and the onset of oscillations about the 1000 psi level because of the hydroelastic effect.

In Figure 7, the reflections in the 7-foot diameter portion of the blast load generator appears as marked steps in the pressure history. After about 20 milliseconds, the pressure history starts to show the hydroelastic oscillations of the water column pressures interacting with the facility wall longitudinal stretch and the bowing of the facility floor. A lid pressure gage located in the upper portion of the tank showed these effects.

In Figure 8, the pressure history shows a less oscillatory environment.

The measured peak pressures are shown in Figure 9. The calculated pressure at M3 reached 1000 psi at 20 milliseconds (Figure 7) compared to the measured pressure P_2 which shows 25 milliseconds (Figure 9). The calculated peak pressure was 1100 psi (Figure 7) while the measured peak pressure was between 1100 and 1300 psi (Figure 9). Since it was not possible to locate the 1.0-foot diameter standpipes at the Hill AFB source as required by the calculations of Figures 5-8, 0.5-foot diameter pipes were used which induced greater measured time delays than calculated. Also, the Figures 5-8 calculations do not include the gas-filling rise time of a few milliseconds.

For a water-filled blast load generator the peak pressures of 1000 psi and rise time of about 20 milliseconds permits simulation of blast loads transmitted to targets through soil depths of at least 40 feet. But to achieve the required pressure decay it will be necessary to use helium gas drivers or to increase the vent hole area (Appendix A).

For a soil-filled blast load generator, the peak pressures are achieved with higher starting pressures because of the greater compressibility of soil which causes the given quantity of driver gas to expand into a larger final volume. The rise time extends to the order of 100 millisecond. Thus this parameter is too distorted to be useful for blast load testing, but is acceptable with regard to impulse testing to a given "static" overpressure.

CONCLUSIONS

The blast load generator (Figure 10) can be used to test up to 1000 psi peak pressure sensitivity and early-time (200 ms) impulse sensitivity of target structures. The impulse can be varied by using spiked waves to square wave applied pressure histories.

With the current driver section, the rise time is about 50 to 60 milliseconds for a water test volume. This can be improved by the use of higher driver pressures, or by going to 1.0 to 2.0-foot diameter driver chambers. This would also assist in sustaining higher peak pressures for highly compressible test media. This is especially true when compressibility is deliberately introduced to simulate not only acceleration and velocity environments, but also to simulate large displacements.

When no change in driver chamber diameter is permitted, for soil tests and for soil tests with a back-up layer of low impedance crushable solid, it will be required to increase the driver chamber volume in order to sustain the 1000 psi peak pressure in the test volume.

ACKNOWLEDGEMENT

This work was performed through the support of the United States Air Force, SAMSO, Contract No. F04701-73-C-0336. The authors are indebted to John Karagozian for his design suggestions and construction supervision services. Also, appreciation is extended to the personnel at Hill AFB, Utah, who assisted in the construction and test work. Dr. H. F. Korman assisted with the development of material presented in the Appendix.

REFERENCES

1. Seidman, M., "Analysis of Flow Between Large Cavities", TRW IOC 69-6114.2-43, (CAPER - Computer Program).
2. Lieberman, P., A. H. Wiedermann, and G. Nagumo, "Design Methods for Hardened Pipe Systems", U.S. Army Engineer, Contract DACA87-69-C-0005, IITRI Project Number J6161.

APPENDIX - PRESSURE HISTORY

The pressure decay history in the driver chamber is derived in this Appendix in order to develop the decay history relationship on the following parameters:

- Volume of the driver chamber, (V_o)
- Cross-sectional area of vent, (A^*)
- Stagnation temperature of stored gas at the start of the venting, (T_{o_i})
- Stagnation pressure of the stored gas at the start of venting, (P_{o_i})
- Gas properties
  - Specific heat ratio, (γ)
  - Molecular weight, (MW)
  - Speed of sound at the start of the venting, (C_{o_i})

The pressure decay history in the chamber, (P_o), is given by

$$\frac{P_{o_i}}{P_o} = \left\{ 1 + \frac{\gamma-1}{2}\sqrt{\frac{g_c}{MW}\,\gamma\left(\frac{2}{\gamma+1}\right)^{\frac{\gamma+1}{\gamma-1}}}\; R_o\, T_{o_i}\cdot\frac{A^*}{V_o}\, t \right\}^{\frac{2\gamma}{\gamma-1}}$$

or

$$\frac{P_{o_i}}{P_o} = \left[1 + \frac{\gamma-1}{2}\left(\frac{2}{\gamma+1}\right)^{\frac{\gamma+1}{2(\gamma-1)}} \frac{C_{o_i} A^*}{V_o} t\right]^{\frac{2\gamma}{\gamma-1}}$$

where

t Time
R_o Universal gas constant

The pressure history relation is derived from the following three relationships:

- Equation-of-state

$$P_o = \frac{m}{V_o} R T_o$$

or

$$\frac{dP_o}{P_o \cdot dt} = \frac{1}{m}\frac{dm}{dt} + \frac{1}{T_o}\frac{dT_o}{dt}$$

where

m Instantaneous mass in Volume V_o

- Critical mass flow through an orifice (Flegner's formula)

$$\frac{dm}{dt} = \left[\frac{\gamma g_c \cdot MW}{R_o}\left(\frac{2}{\gamma+1}\right)^{\frac{\gamma+1}{\gamma-1}} T_c^{-1}\right]^{\frac{1}{2}} A^* P_o$$

- Adiabatic process

$$\frac{dT_o}{T_o} = \frac{\gamma - 1}{\gamma}\frac{dP_o}{P_o}$$

Figure A-1 shows the pressure history attainable by venting through an orifice, using a gas whose molecular weight is 28.98 lb_m/mole. Three different values of γ are shown to indicate the sensitivity to the expansion thermodynamic process. The results are presented in non-dimensional form for convenient use in other applications.

A more rapid pressure history decay (Figure A-1) can be accomplished by:

- Increasing the initial temperature
- Increasing the vent area
- Decreasing the initial volume
- Changing the gas to a
  - Lower molecular weight gas
  - Higher specific heat ratio gas

The latter effects can be more readily seen in the formulas for the air, hydrogen, argon and helium gases (Table A-1). The table shows that it is wiser to use room temperature helium than heated air to achieve the same decay time.

TABLES

TABLE 1
FILLING TIME BETWEEN CHAMBERS

V_1/V_2	DRIVER VOLUME V_1 (ft^3)	DRIVEN VOLUME V_2 (ft^3)	ORIFICE DIAMETER d (ft)	COMPUTED RISE TIME TO HALF-PRESSURE
10	70	7	0.83	0.00725
20	7.85	0.393	0.25	0.00425
10	7.85	0.785	0.50	0.00216
20	15.71	0.785	0.50	0.00215
10	15.71	1.57	0.83	0.00160
20	7.85	0.393	0.50	0.00105

CORRELATION FOR TABLE 1 CALCULATIONS

$$t_{50\%} = 0.00067 \frac{V_2\ (ft^3)}{d^2\ (ft)^2}$$

for $V_1 >> V_2$

TABLE 2

FILLING TIME BETWEEN CHAMBERS WITH A VENTED CHAMBER

GIVEN						DERIVED		
DRIVER CHAMBER PRESSURE P_1 (psia)	DRIVER CHAMBER VOLUME V_1 (ft^3)	ORIFICE DIAMETER BETWEEN DRIVER/ DRIVEN CHAMBERS D_1 (in)	INITIAL DRIVEN CHAMBER PRESSURE P_2 (psia)	DRIVEN CHAMBER VOLUME V_2 (ft^3)	ORIFICE DIAMETER IN DRIVEN CHAMBER D_2 (in)	TIME TO PEAK PRESSURE t_p (ms)	PEAK PRESSURE P_p (psia)	TOTAL IMPULSE TO 200_{ms} I_{200} (psig-sec)
1464.7	13.25	4.8	14.7	0.8	3.0	12	1281	195
1464.7	13.25	4.8	14.7	1.8	3.0	25	1168	181
1464.7	13.25	4.8	14.7	2.8	3.0	36	1078	170
1464.7	13.25	4.8	14.7	4.0	3.0	47	990	158
1464.7	13.25	4.8	14.7	7.2	3.0	72	828	132
1464.7	13.25	4.8	14.7	7.2	3.0	72	1016	164
1464.7	13.25	4.8	14.7	10.4	3.0	92	701	112
1464.7	13.25	4.8	14.7	13.6	3.0	109	615	96

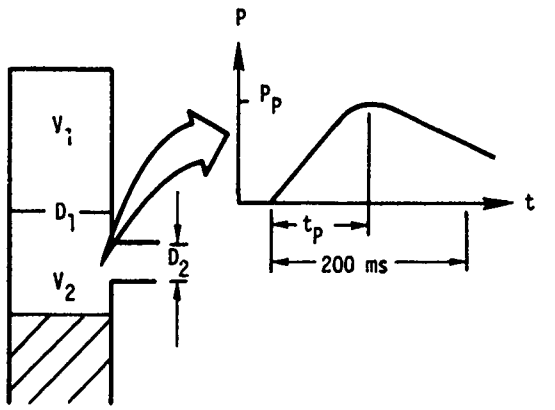
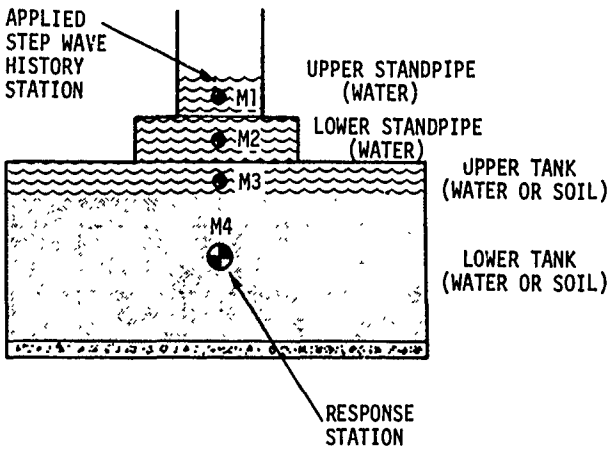


TABLE 3

RISE TIME RESPONSE TO A 1000-PSI STEPWAVE AT MIDWAY DOWN LOWEST TANK

	WATER IN UPPER STANDPIPE		WATER IN LOWER STANDPIPE		UPPER PART OF LOWER TANK			MIDDLE PART OF LOWER TANK		
	LENGTH (FT)	DIAMETER (FT)	LENGTH (FT)	DIAMETER (FT)	MATERIAL	LENGTH (FT)	DIAMETER (FT)	MATERIAL	LENGTH (FT)	DIAMETER (FT)
A-1	0.8	1.5	0.8	1.5	Water	0.8	7.0			
A-2	0.8	1.0	0.8	1.5	Water	0.8	7.0			
A-3	0.8	1.0	0.8	1.5	Water	0.8	7.0			
A-4	0.5	1.0	0.5	1.0	Water	0.5	7.0			
B-1	0.6	1.5	0.8	1.5	Water	0.8	7.0			
B-2	0.8	1.0	0.8	1.0	Water	0.8	7.0			
B-3	1.6	1.0	1.6	1.0	Water	0.8	7.0			
B-4	1.6	1.0	1.6	1.0	Water	0.8	7.0			
B-5	1.6	1.0	1.6	1.0	Soil	0.5	7.0			
C-1			1.6	1.0	Water	0.8	7.0	Soil	3.0	7.0
C-2			1.6	1.0	Water	0.8	7.0	Soil	3.0	7.0

	LOWER PART OF LOWER TANK			CONCRETE TANK FLOOR		FRICTION COEFFICIENT	RISE TIME TO 950 PSI	REMARKS
	MATERIAL	LENGTH (FT)	DIAMETER (FT)	SPRING CONSTANT (LB/IN)	WEIGHT (LB)	$\frac{PSI}{(FPS)^2}$	(MILLISEC)	
A-1	Water	8.5	7.0	10^6	10^9	.05	10	Baseline case for water
A-2	Water	8.5	7.0	10^6	10^9	.05	17.5	Decrease in diameter of upper standpipe
A-3	Water	8.5	7.0	10^9	10^6	.05	13.5	Increase in natural frequency of floor
A-4	Water	8.5	7.0	10^6	10^9	.05	19	Decrease in both diameters and lengths of standpipes
B-1	Soil	8.5	7.0	10^6	10^9	.05	120	Baseline case for water/soil
B-2	Soil	8.5	7.0	10^6	10^9	.05	280	Decrease in standpipe diameters
B-3	Soil	8.5	7.0	10^6	10^9	.05	280	Increase in standpipe lengths
B-4	Soil	8.5	7.0	10^9	10^5	.05	260	Increase in natural frequency of floor
B-5	Soil	8.5	7.0	10^9	10^6	.05	255	Soil replaces water at top
C-1	Water	5.5	7.0	10^9	10^6	.05	80	Baseline case for water/soil/water
C-2	Water	5.5	7.0	10^9	10^6	0.00	20	Decrease of wall friction



PROPERTY \ MATERIAL	SOIL	WATER
ACOUSTIC VELOCITY (FPS)	1000	4660
DENSITY (PCF)	100	62.4

FIGURE 1 MODEL OF BLAST LOAD GENERATOR

- DRIVER CHAMBER VOLUME = 6.65 ft^3 AND INITIALLY AT 1150 psig
- ORIFICE BETWEEN DRIVE AND TEST CHAMBER, D_1 = 4 in. (SEE TABLE 2)
- TEST CHAMBER VOLUME = 0.8 ft^3

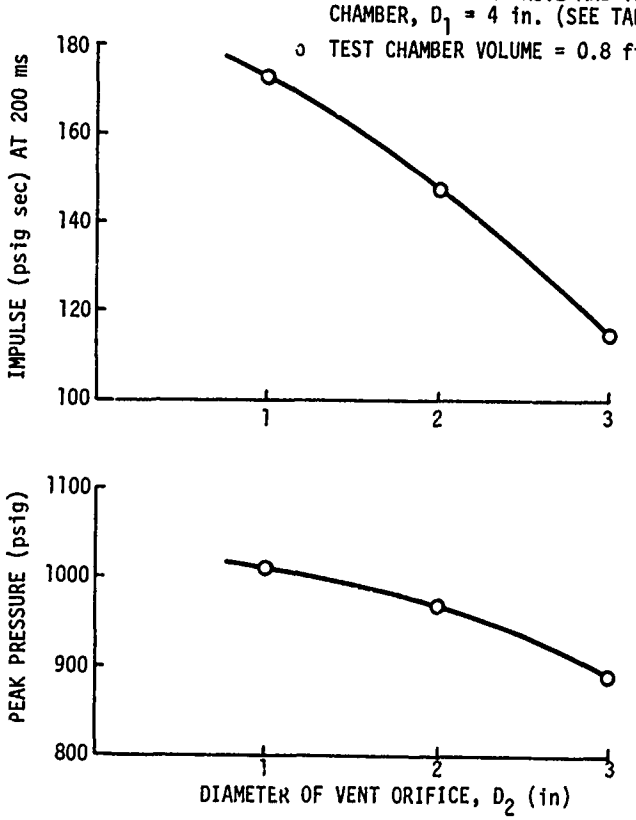


FIGURE 2 PEAK PRESSURES AND EARLY-TIME (200 ms) IMPULSE IN TEST CHAMBER

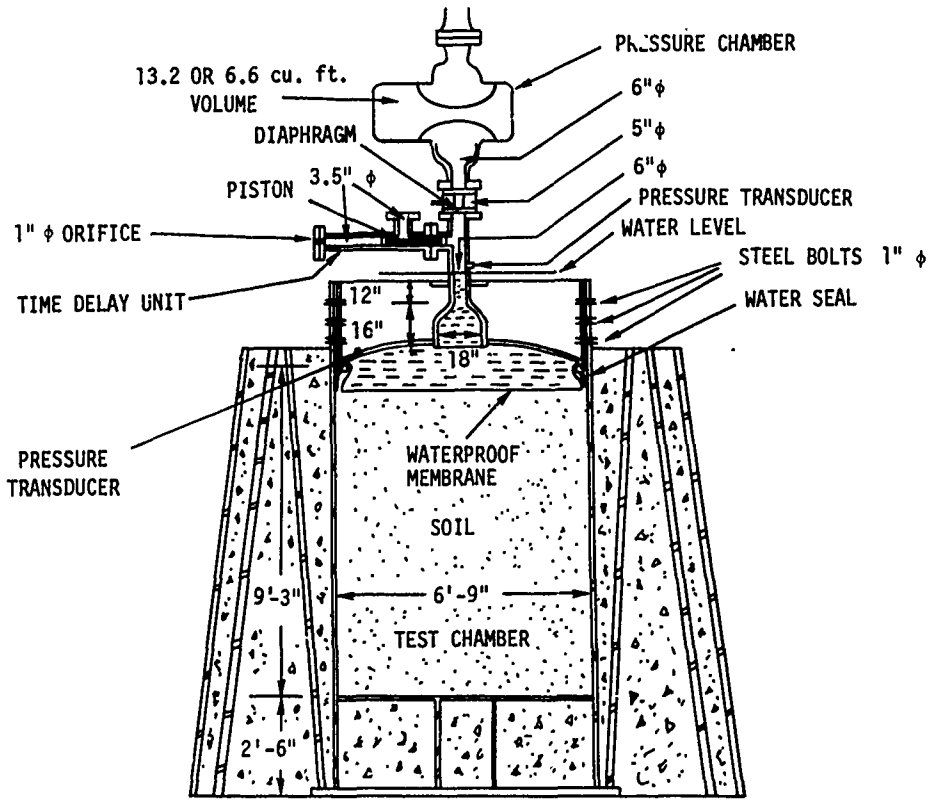


FIGURE 3 BLAST LOAD GENERATOR

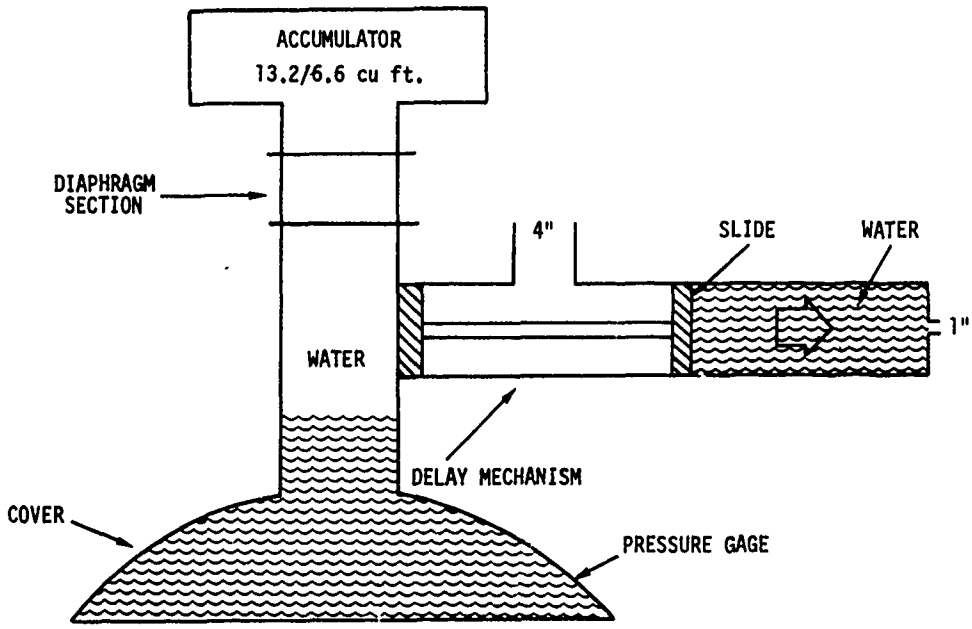


FIGURE 4 DELAY MECHANISM

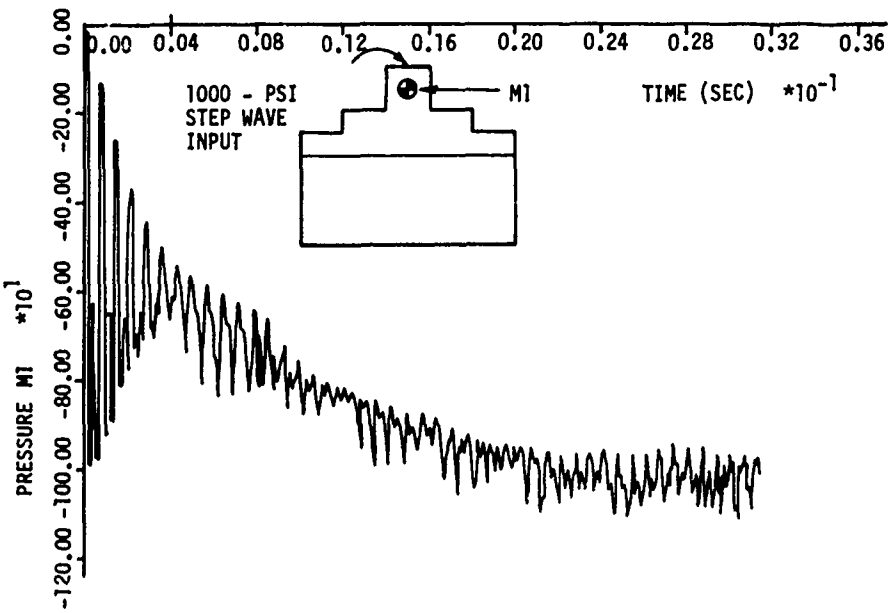


FIGURE 5 PRESSURE HISTORY IN MIDDLE OF UPPER STANDPIPE

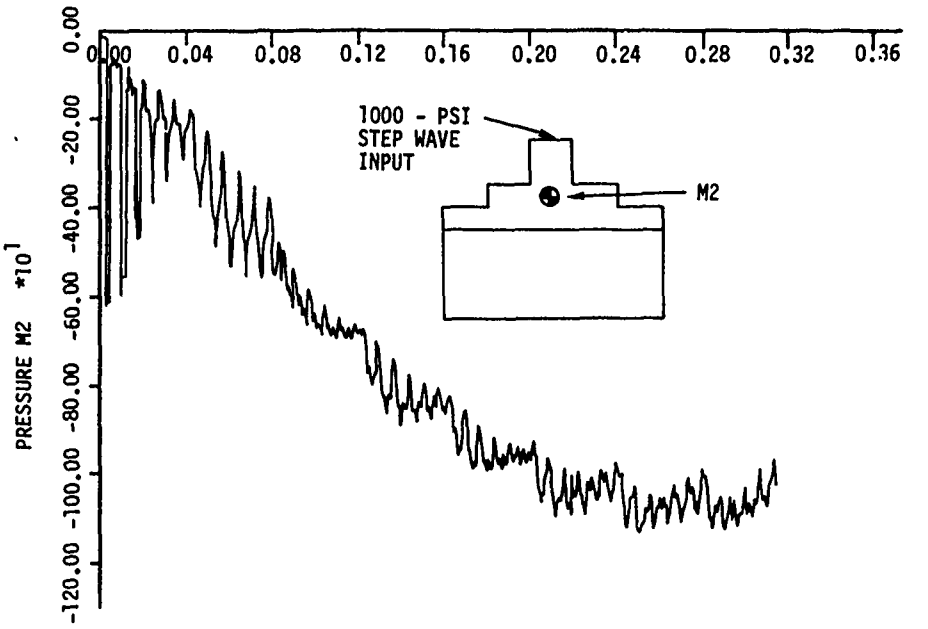


FIGURE 6 PRESSURE HISTORY IN MIDDLE OF LOWER STANDPIPE

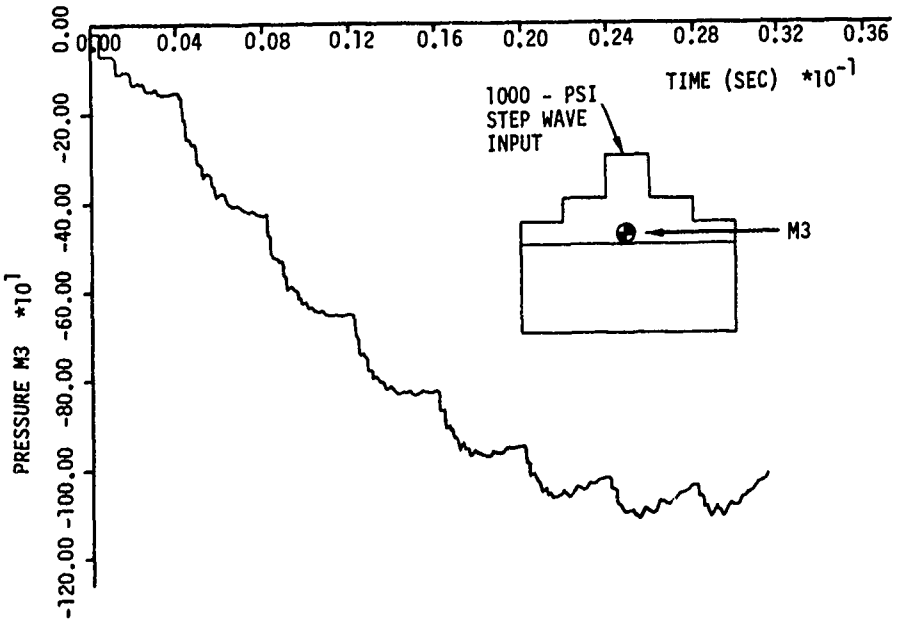


FIGURE 7 HISTORY IN MIDDLE OF UPPER TEST CHAMBER

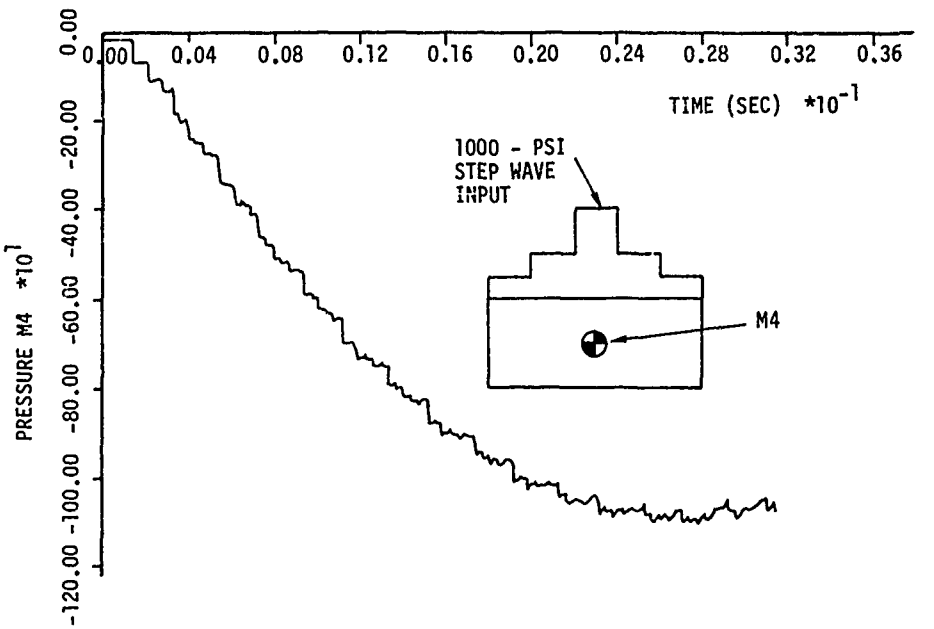
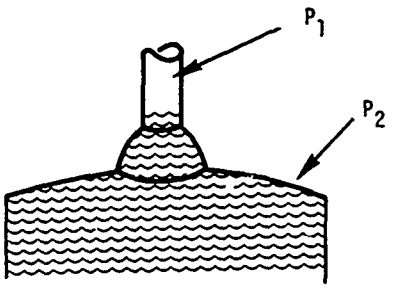


FIGURE 8 PRESSURE HISTORY IN MIDDLE OF LOWER TEST CHAMBER



ACCUMULATOR
VOLUME = 6.6 cu. ft.
PRESSURE = 1600 psi
VENT DIAMETER = 4.0 in.
DELAY ORIFICE DIAMETER FOR WATER = 1.0 in.
DELAY PISTON INITIAL DISPLACEMENT = 0.0 in.

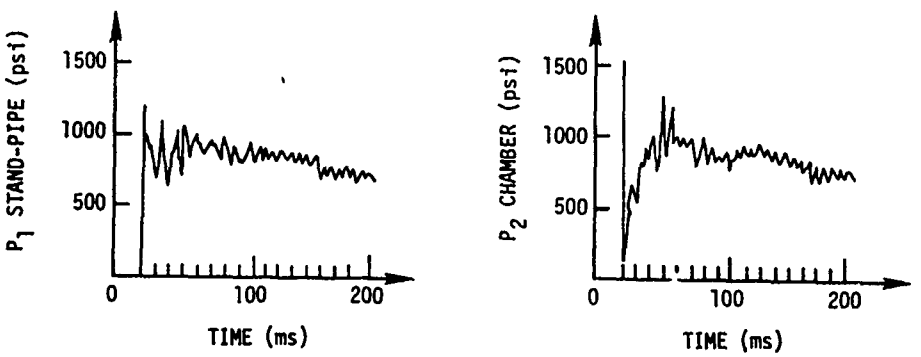
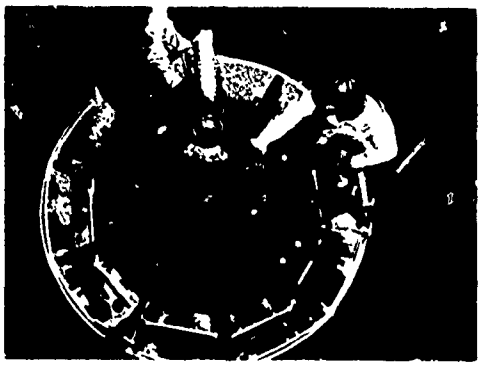


FIGURE 9 MEASURED PRESSURE HISTORIES



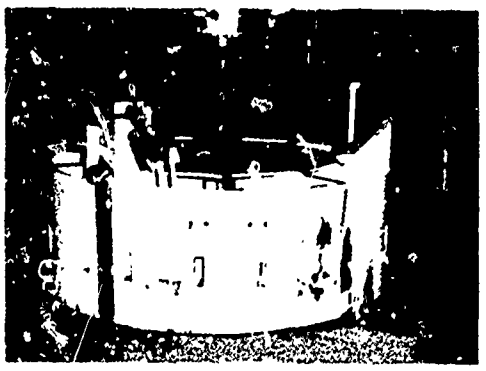
FIGURE 10 PHOTOGRAPH OF BLAST LOAD GENERATOR



1) TOP VIEW OF TEST CHAMBER LID, DIAPHRAGM SECTION, AND DELAY MECHANISM

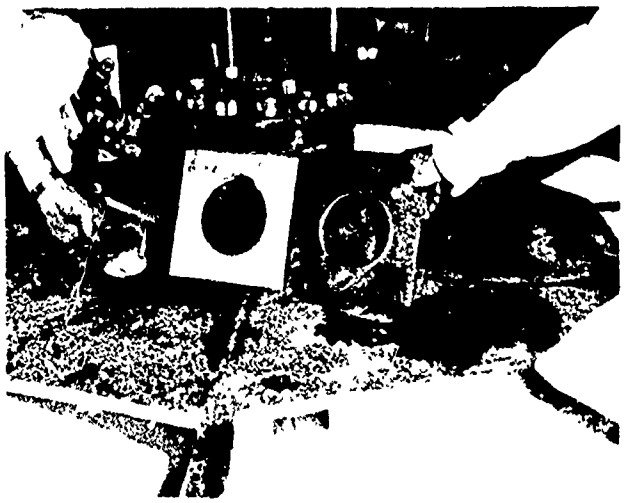


2) TOP VIEW OF TEST CHAMBER

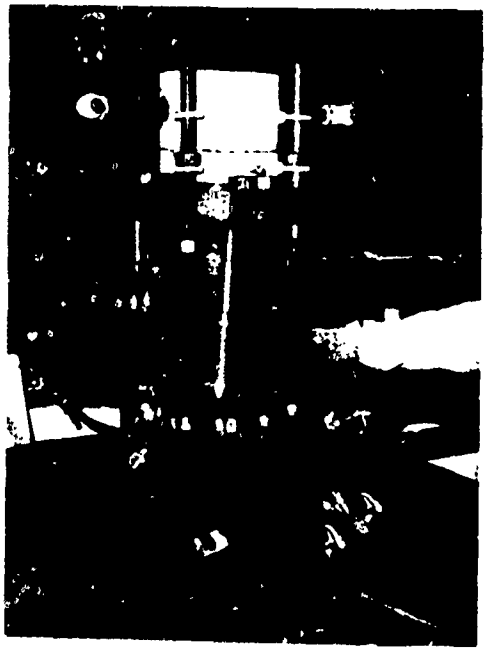


3) LID AND DELAY MECHANISM

FIGURE 10b TOP PORTION OF TEST CHAMBER



1) BURST DIAPHRAGMS



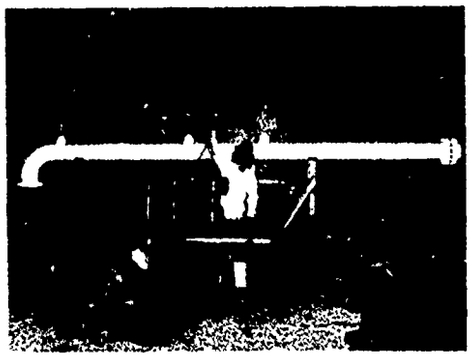
2) DOUBLE DIAPHRAGM SECTION, WATER LEVEL PORT, AND GAGE PORT

FIGURE 10c BURST DIAPHRAGM SECTION

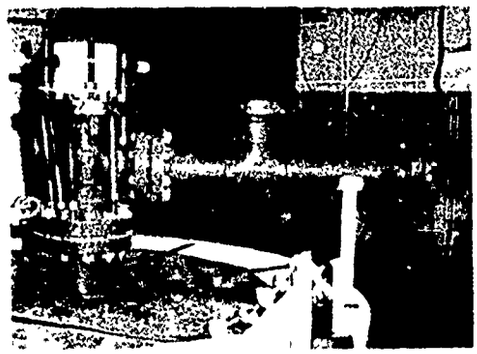
TABLE A-1 DECAY HISTORY DEPENDENCE ON GAS PROPERTIES

	Specific Heat Ratio γ	Acoustic Velocity C_{o_i} (fps)	Pressure Decay History Formula $\frac{P_{o_i}}{P_o}$	Pressure Decay $t = 0.050$ sec $\frac{A^*}{V_o} = 0.0083\ ft^{-1}$ $\frac{P_{o_i}}{P_o}$
Air	1.4	1128	$(1 + 130.55 \frac{A^*}{V_o} t)^7$	1.447
Hydrogen	1.4	4275	$(1 + 494.78 \frac{A^*}{V_o} t)^7$	3.696
Argon	1.66	1049	$(1 + 197.48 \frac{A^*}{V_o} t)^5$	1.483
Helium	1.66	3305	$(1 + 622.18 \frac{A^*}{V_o} t)^5$	3.153

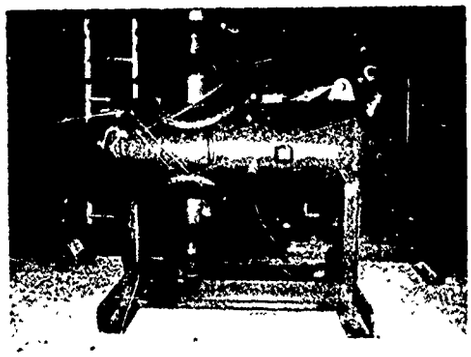
$$\frac{A^*}{V_o} = \frac{.05\ ft^2}{6\ ft^3} = 0.0083\ ft^{-1}$$



1) TWO 6.6 CUBIC FEET DRIVER SECTIONS



2) DELAY MECHANISM



3) 6.6 CUBIC FEET DRIVER SECTION

FIGURE 10d DRIVER SECTIONS

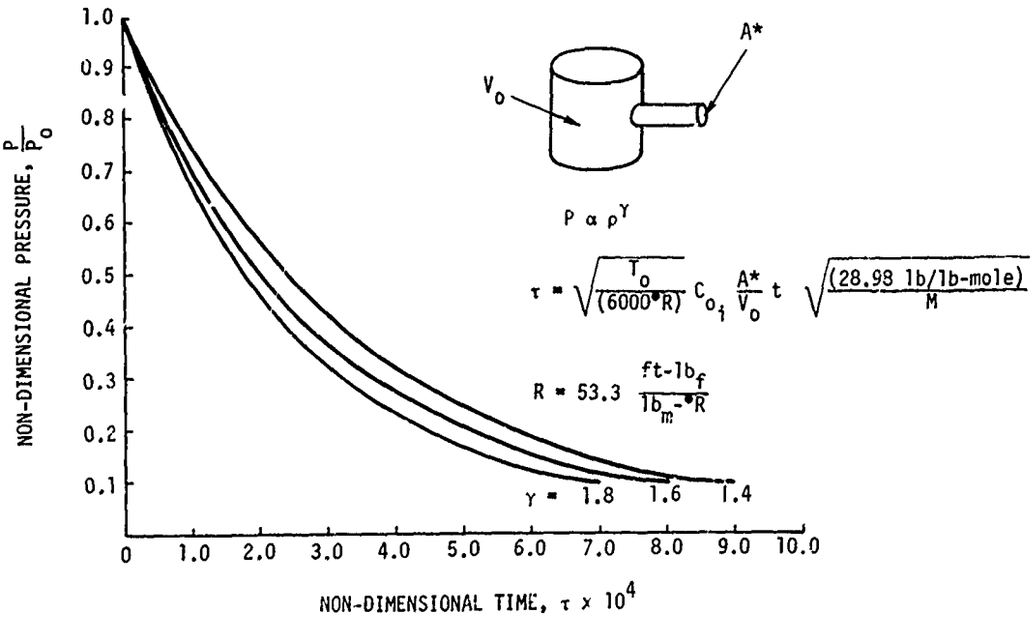


FIGURE A-1 PRESSURE DECAY HISTORY

DEVELOPMENT OF A SHRAPNEL CONTAINMENT SYSTEM FOR EXPLOSIVE-TO-ELECTRIC TRANSDUCERS

P. H. Prasthofer*
Exxon Production Research Company
Houston, Texas

A shrapnel containment system has been developed to ensure safety of personnel and elimination of collateral damage to surrounding componentry from the operation of explosive-to-electric transducers. This has been achieved within the size and weight constraints necessary to make these devices competitive with their electronic counterparts.

INTRODUCTION

Expolsive-to-electric transducers are used to generate current or voltage in a number of applications. These components, while often more reliable than their electronic counterparts, do create a hazard because of their explosive content. For some time there has been an interest in developing containment systems that would eliminate the hazard in two major areas: (1) safety of personnel handling the device and (2) prevention of collateral damage to surrounding componetry during both intentional and unintentional operation. To satisfy these goals, the vessel must contain all hazardous shrapnel, but may vent gaseous detonation products. In addition, the vessel weight and volume must be small enough to make the total component-containment system physically competitive with electronic devices. Such a vessel was developed in the study described below.

Following a brief review of the literature on containment systems, the containment process is discussed, and the analytical and experimental studies are described.

HISTORICAL REVIEW

Most of the published work dealing with the confinement of explosions addresses the design of structures resistant to the blast and shrapnel effects from the detonation of large explosive devices such as military ordnance or large pyrotechnic devices such as fuel tanks. "Large" and "small" in this context refer to explosive TNT equivalents on the order of kilograms and grams, respectively. The literature concerning containment of small quantities of explosives is somewhat sparse. One of the earliest papers on the subject is by Zimmer and Asaoka [1] and deals with the confinement of small quantities of nitroglycerin in polyethylene containers. Duffey and Mitchell [2] give an analytical description of the impulse delivered to the wall of a long cylinder by a centrally located spherical explosive charge and verify some of the results experimentally. The application of distended materials to explosive containment, particularly distended metals (metal "foams"), as shock mitigators and energy absorbers was pioneered experimentally by Benedick [3]. The use of vermiculite as well as plastics has been studied at the Los Alamos

*Senior Research Engineer, Exxon Production Research Company, Houston, Texas, formerly Member of the Technical Staff, Sandia Laboratories, Livermore, California. This work was supported by the United States Atomic Energy Commission Contract Numbers AT-(29-1)-789.

Scientific Laboratory. An effort to develop analytical design parameters for containment vessels using distended materials was first published by Anderson [4]. Anderson considers a spherical vessel and, for constant volume, optimizes the foam density and vessel thickness to yield minimum total weight. He does not, however, take into account shrapnel or temperature increases due to foam compaction. On the basis of Benedick's experimental work, Barr and Dahlgren [5] extended this approach using several concentric shells separated by layers of distended metal. They use numerical hydrocode calculations to examine, as a function of time after detonation, the redistribution of internal and kinetic energies in the vessel. The shock-mitigating properties of distended materials, not necessarily within the context of explosive confinement, have been investigated by a number of experimenters [6-12]. Analytically, a constitutive equation-of-state model was developed by Herrmann [13], whose work also contains a good bibliography of earlier work on distended material models.

A number of related papers are of use in the study of explosive confinement. Kennedy [14] extends the Gurney equations to estimate shrapnel velocities, and thus momentum and energy, for a wide range of charge and shrapnel geometries. Duffey [15] derives dynamic scaling laws for structures, taking into account rate effects. The results of the interaction of explosive detonations with their surroundings is discussed for various cases (e.g., metal forming with explosives, etc.) in a collection of papers published by the New Mexico Section of the ASME [16].

PHENOMENOLOGY

General Considerations

A convenient way to analyze the containment process is to consider energy distribution, momentum distribution, and stress distribution.

Energy distribution is perhaps the most intuitive aspect of containment. The chemical energy released by the explosive is transformed into internal energy in the absorber material, interral (strain) energy in the containing vessel, and kinetic energy of the absorber and vessel. If gases are not vented, the residual energy of the gaseous detonation productions must also be accounted for. The internal energy absorbed in a material during shock compaction is schematically depicted in Figure 1.

A. Initial state
B. Shocked-up state
C. Final relieved state

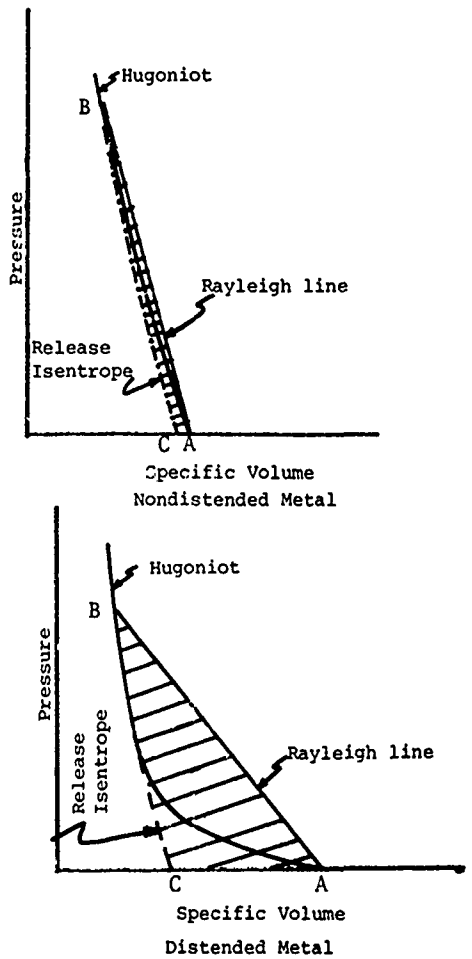
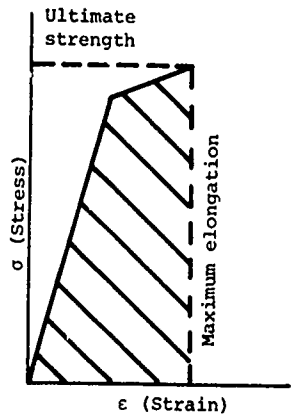


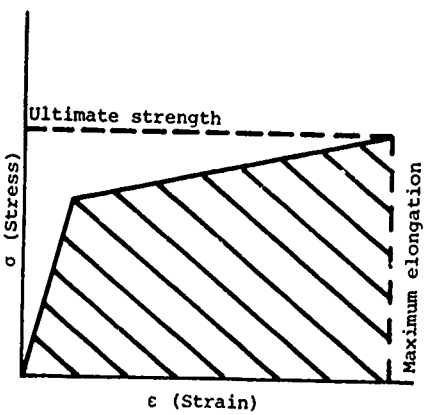
Figure 1. Internal Energy During Shock Compaction. The shaded area represents the irreversible internal energy absorbed by the material during shock compaction.

The Hugoniot represents the locus of all points that can be reached during shock compaction. The internal energy of a material when shocked from Point A to point B on the Hugoniot is the area under the Rayleigh line. The energy recovered when the final state C is reached is the area under the release isentrope. Thus the shaded area between the Rayleigh line and the release isentrope is the irreversible internal energy of compaction generally given off in the form of heat. (For a more detailed treatment, see,

for example, Reference 17.) Note that the irreversible internal energy, because of the large permanent volume change, is very high for distended materials, making them particular well suited for energy absorption. Since the remaining energy must be transformed into strain energy in the containing vessel, its material properties must be chosen to maximize strain energy. The allowable strain energy per unit volume in a material is equal to $\int \sigma d\varepsilon$ and is schematically illustrated for an example. As illustrated in Figure 2, materials with high ductility should be selected over higher-strength low-ductility materials for maximum strain energy. Note that in metals, ductility tends to decrease with increasing tensile strength.



High Strength—Low Ductility



Moderate Strength—High Ductility

Figure 2. Strain Energy as a Function of Ductility. (Strain energy is given by $\int \sigma \, d \, \varepsilon$, represented by the shaded area under the stress-strain curve.)

A momentum balance must be performed in addition to the energy balance, because conservation of momentum must be satisfied. (It is assumed that enough time has elapsed so that rigid body rather than wave mechanics dominates.) The impulse generated by the explosive imparts momentum to the absorber material and the outer vessel. This total momentum must be reduced to zero by the reaction of the stresses in the outer vessel. (The momentum of the gaseous detonation products must be included if no venting occurs.)

$$\Delta(mv) = \int \sigma A dt \qquad (1)$$

i.e., the total change in momentum must equal the integral of the time history of the stresses in the outer vessel.

An alternative procedure is to insert a material like honeycomb between the distended material and the outer vessel. This configuration, suggested by Davidson [18], results in the following momentum balance:

$$\Delta(mv) = \underbrace{\int F dt}_{\text{honeycomb}} + \underbrace{\int \sigma A dt}_{\text{shell}} \qquad (2)$$

The honeycomb exerts a constant force over a long period of time and thus reduces both the peak stress and the strain energy of the outer vessel. The increase in total mass due to the honeycomb is, of course, small.

In trying to optimize the absorber distention ratio, one is tempted to reason as follows: for constant explosive impulse, conservation of momentum dictates the use of high-density absorber materials in order to increase the total mass and thus decrease velocity. This leads, however, to a paradox first pointed out by Anderson [4]. Increasing the density of the absorber introduces additional tamping around the explosive and thereby raises the impulse delivered by the explosive, since the efficiency of high explosive is increased by tamping. This in turn increases the momentum imparted to the containment vessel. One can then infer the existence of an optimum distention ratio for which the decrease in velocity dominates the increase in momentum.

In addition to the energy and momentum conservation laws, one must consider the peak stresses imparted to the outer vessel. If the peak stresses are sufficiently high, the vessel may fracture or spall before the containment process has equilibrated. Thus the absorber material must also be selected for its stress wave attenuation characteristics. Distended metals are again well suited to this purpose. Stress is attenuated by the inverse of the square of the thickness of the absorber [19].

The physical containment problem is, of course, greatly complicated by the presence of shrapnel and three-dimensional effects, which may in specific cases render simple models invalid. Some general conclusions can still be drawn, however. The energy-absorbing material must be able to undergo a substantial volume change to result in significant PdV (pressure times volume change) work while simultaneously causing a sufficient attenuation in the stress imparted to the outer vessel. The outer containing vessel must be of high ductility, rather than high strength and low ductility, to maximize the allowable strain energy. These conclusions will be quantized somewhat in the following sections.

Consideration of a Specific Geometry

Ideally, one would like to gain some insight into the physical significance of various parameters involved in containment before one resorts to experimental methods. One approach is to investigate the optimization of a simple containment geometry. Anderson [4] attempted to solve a problem of this type in which he fixed the total volume (i.e., r = constant) and minimized the total weight by changing the distention ratio and container thickness. Because of simplifying assumptions made to allow a partly closed-form solution, the range of distention ratio considered was outside the range of practical interest for containment applications. However, two qualitatively important discoveries came out of this study: (1) the existence of an optimum absorber distention ratio to vessel thickness relation and (2) the significance of tamping the explosive in performing a momentum balance.

A numerical study was performed with the one-dimensional Lagrangian wave propagation code WONDY [20] and the two-dimensional code TOODY [21]. Two primary areas were investigated: (1) the effect of different absorber constitutive materials when the distention ratio is kept constant and (2) the effect of different densities and density gradients when the constitutive material is held constant. The applicability of the absorber material model used in the code to the range of densities investigated was studied experimentally and was found to be quite adequate. Spherical as well as rectangular geometries were considered.* The criteria selected were internal and kinetic energies of the containment vessel, as well as peak stress in the containment vessel. Densities investigated were in the range of 25 percent ($\alpha = 4$) to 50 percent ($\alpha = 2$) of solid theoretical density.† Typical results for rectangular geometry are shown in

*A sample configuration is given in the Appendix.

†The selection of the density range was based to a large extent on the experimental work by Benedick [3]. An interesting aside can also be shown: For the "snowplow" distended material model (the distended material is compacted to full density at negligible pressure), the attenuation by the absorber of the pressure due to an initial impulse I_o, as a function of specific volume V_o of the theoretical solid, distention ratio α, and absorber thickness x is given by

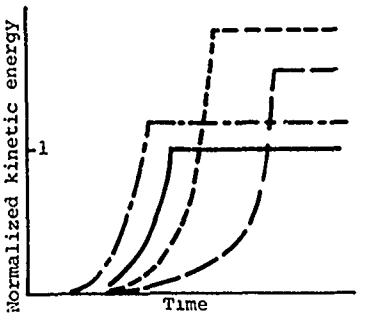
$$P = \frac{I_o^2 V_o \alpha^2}{(\alpha - 1) x^2}$$

For a given material (V_o = constant), constant thickness, and constant impulse I_o, setting

$$\frac{\partial P}{\partial \alpha}_{I_o,\, V_o,\, x} = 0$$

yields a minimum value of $\alpha = 2$, thus showing not only the existence of an optimum distention ratio, but also yielding a value (50 percent dense) similar to that determined experimentally by Benedick.

Figure 3. Kinetic energy versus time and stress versus time in the outer vessel are given for absorber densitites of 25 and 50 percent and layered configurations of 25 percent (inner layer) and 50 percent (outer layer), as well as 50 percent (inner layer) and 25 percent (outer layer).



50 percent dense absorber

25 percent dense absorber

inner layer 50 percent
outer layer 25 percent

inner layer 25 percent
outer layer 50 percent

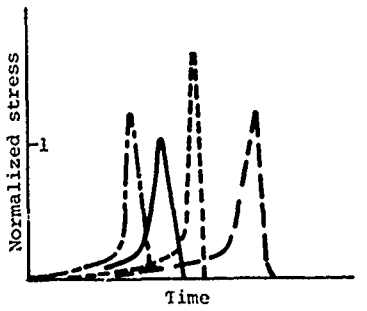


Figure 3. Kinetic Energy and Stress in the Outer Containing Vessel Normalized to the Case of a 50-Percent Dense Energy Absorber.

The conclusions, applying both to rectangular and spherical geometries, are as follows:

1. Distention ratio rather than constitutive material is the significant property when the solid densities are similar.
2. The higher-density absorbers are more efficient, but if a density gradient is desired for weight savings, the absorber should increase in density as the distance from the explosive increases.

The first conclusion has been suggested by previous investigators. The second conclusion is contrary to earlier results and may be due to the fact that the lower-density absorber around the explosive tends to decrease the effective impulse. Note, however, that this study assumed gases to be vented and thus did not consider temperature increases due to compaction of the distended material as significant parameters. In nonvented vessels, temperature increases must be taken into account, as they result in increased gas pressure and consequently in increased residual stress in the vessel.

EXPERIMENTAL STUDY

The purpose of the experimental study was twofold: to gain a better understanding of containment phenomenology, and to develop prototype containment systems compatible with present explosive component requirements.

A review of the literature and preliminary analytical results suggested that the containment method using distended materials as energy absorbers as proposed by Benedick [3] was most promising in terms of immediate payoff, as well as for future improvements. Thus sintered metals, primarily iron and steel, were selected as the energy absorbers. In cases where layering of the sintered metals with low-density absorbers was studied, refractory brick and carbon foam were used. After an initial experiment with moderately ductile (15 - 20 percent elongation) aluminum (chosen because of its low weight), a highly ductile (45 - 55 percent elongation) stainless steel of moderate strength (7 kilobar) was used exclusively for the containing vessel. A threaded joint, rather than a bolted connection, was chosen to join the two vessel halves. This method provides a more integrated connection and reduces the number of parameters involved in the study, i.e., vessel strength rather than bolt configuration will tend to dominate. With these basic constitutive system elements chosen, the parameters selected for optimization were vessel size and wall

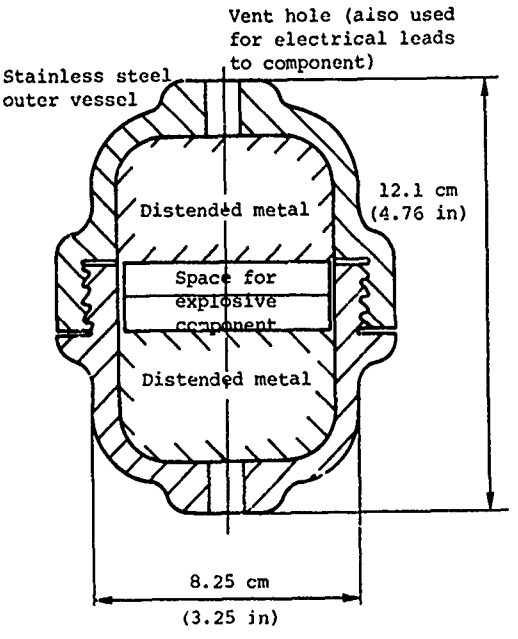


Figure 4. Typical Containment System.

thickness and absorber material thickness and distention. A representative vessel is shown in Figure 4.

Initial sizing was determined by scaling from earlier applicable experiments and dimensional guidelines developed from the computer calculations. A representative component was then detonated inside the containment system. Visual inspection was made of plastic flow in the vessel, and average strain was estimated. Typical pre- and postshot photographs demonstrating vessel deformation are shown in Figure 5. Pre- and postshot radiographs were taken to indicate approximate degree of densification of the absorber material by measuring the relative compaction. Typical radiographs are shown in Figure 6.

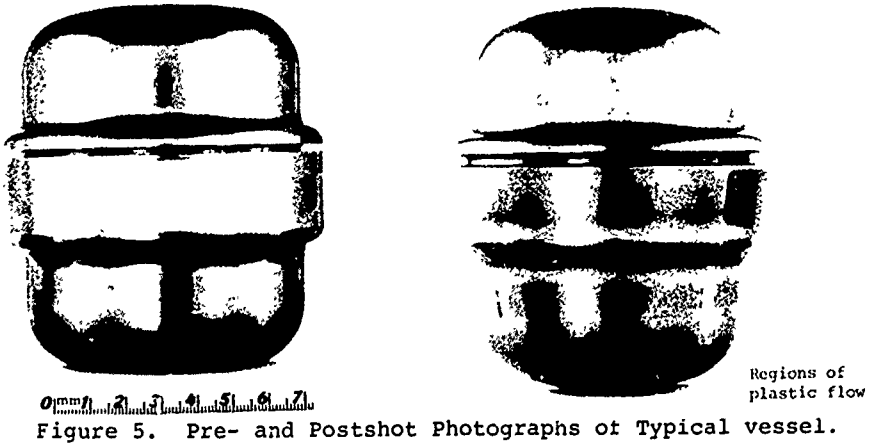


Figure 5. Pre- and Postshot Photographs of Typical vessel.

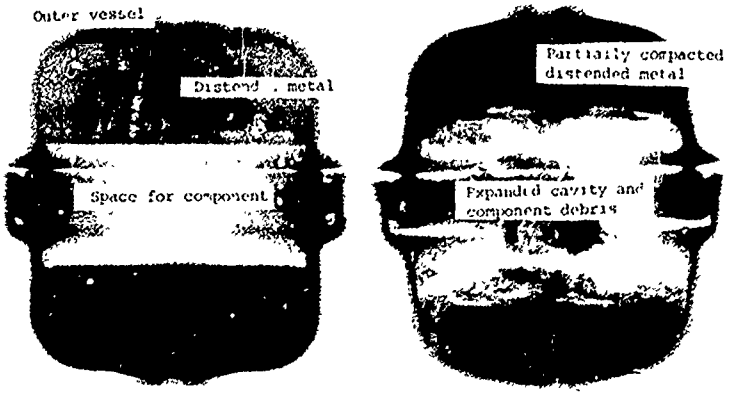


Figure 6. Pre- and Postshot Radiographs of Typical Containment Vessel.

Whenever a vessel succesfully contained an explosion, the data gained were used to design the next configuration. Overdesign for a particular amount of explosive was determined by lack of plastic flow in the outer vessel and an insufficient amount of compaction of the absorber material. Four primary means of iteration were used, either singly or in combination. First, the absorber weight was reduced by means of a layer of low-density foam in place of some of the original sintered iron. The amount of replacement was determined largely from the radiographs. Second, the wall thickness of the outer vessel was reduced. This was done primarily when inspection showed a lack of plasticity. Third, the size of the vessel was reduced when there was evidence of lack of compaction of the absorber, coupled with little apparent deformation of the vessel. Fourth, the same configuration was used again with a larger explosive charge, thus providing a starting point for a new array of design iterations.

RESULTS

The results of the experimental series were highly encouraging. A wide variety of explosive components ranging from 8 to 38 grams of high explosive were sucessfully contained. The range of containment system dimensions is illustrated in Figure 7.

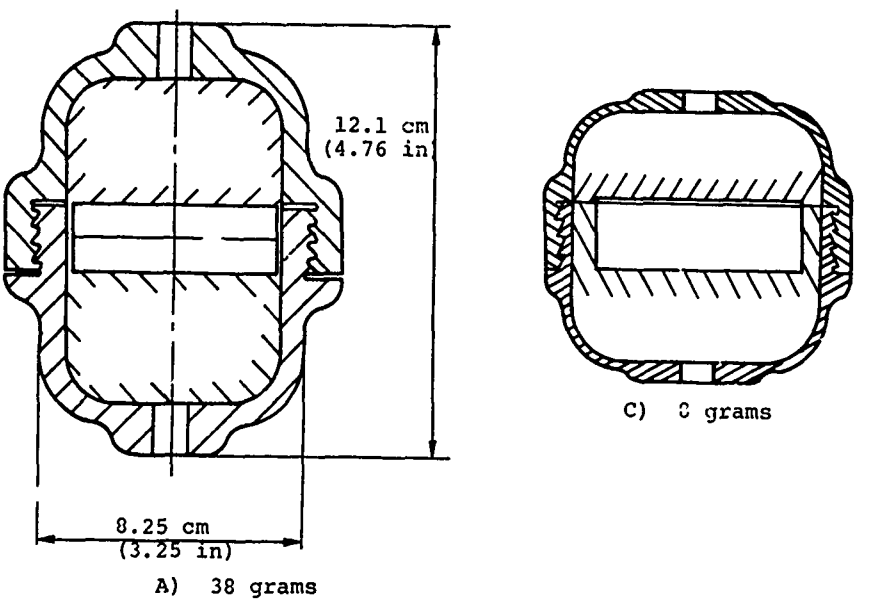


Figure 7. Typical Range of Containment Vessel Dimensions and Approximate Quantity of High Explosive Contained. (Vessels are shown to the same scale.)

A design goal of a containment system weight to explosive charge weight ratio* of approximately 150 (corresponding to a contained weight of 1/3 pound per gram of explosive) was set at the inception of the program. Initial designs yielded ratios of approximately 300, and final configurations ranged down to a ratio of less than 110.

MOUNTING OF THE CONTAINMENT VESSEL

A preliminary investigation was made of possible vessel mounting configurations. One possible mounting scheme is illustrated in Figure 8. Significant reductions in mounting hardware weight can be achieved with minimal effort.

*Containment weight to explosive charge weight ratio is a convenient way of quantizing containment efficiency. Since the explosive content of a specific explosive component, e.g., an explosive-to-electric transducer, is known, the total contained weight of the system can then be assessed and compared with nonexplosive devices.

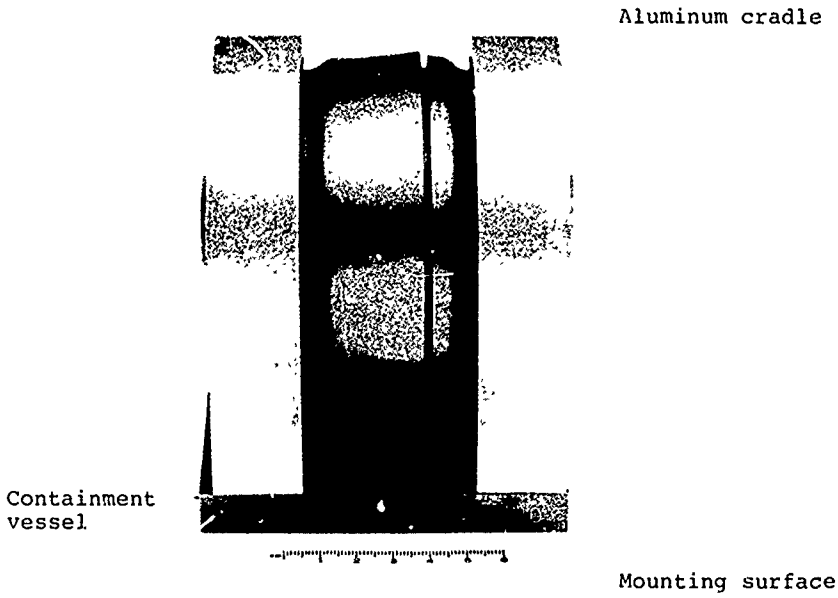


Figure 8. Postshot View of a Containment System in an Aluminum Cradle Lined with Adiprene Pads.

Further investigations of the short- and long-term mechanical properties of the sintered metals should be undertaken. The effect of grain size and grain structure on these properties should also be determined.

CONCLUSIONS

The containment of explosive-to-electric transducers has been shown to be achievable within the size and weight constraints necessary to make them competitive with electronic devices.

Containment weight to explosive charge weight ratios of less than 110 were realized. Given a specific application, a total containment system with a weight-to-charge ratio on the order of 150 can be easily designed using the techniques outlined in this study.

APPENDIX - SAMPLE GEOMETRY OF CONTAINMENT VESSEL

The geometry of the rectangular (infinite plate) computer model is illustrated in Figure A-1.

The standard WONDY [20] equation of state for high explosive and elastic-plastic materials was used. For the distended steel, the P-α model for distended materials was used. Further, the distended steel was not allowed to resist tensile stresses. Typical running times were on the order of 40 seconds. Normalized plots of the redistribution with time of the energy in the system for distended steel are given in Figure A-2. Note that in the 25 percent dense case a significantly greater amount of energy is distributed into the outer plate (containing vessel) than in the 50 percent dense case. In other words, the containment process was less efficient.

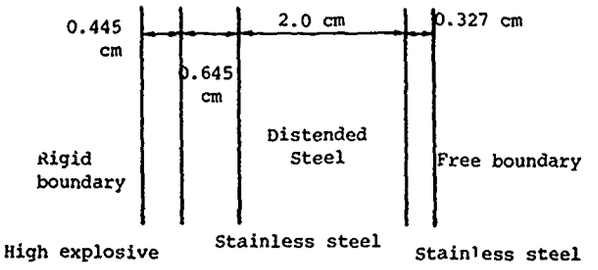
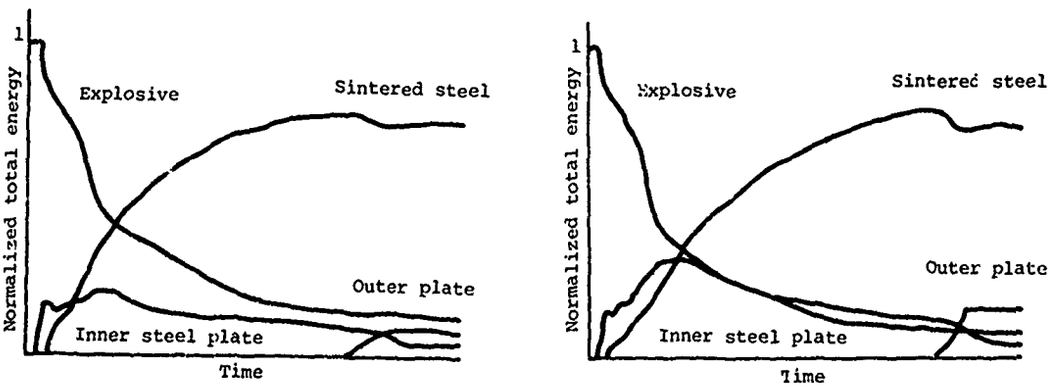


Figure A-1. Schematic of the One-Dimensional Computer Model. The explosive and inner plate represent the component, the distended steel is the absorber, and the outer plate is the containing vessel.



a) 50 percent dense absorber

b) 25 percent dense absorber

Figure A-2. Redistribution of Energy in the Containment System.

REFERENCES

1. M. F. Zimmer and L. K. Asaoka, "Explosive Safety Container," Explosivstoffe, Nr. 11, 1963.

2. T. A. Duffey and D. E. Mitchell, Containment of Explosives in Cylindrical Shells, Sandia Laboratories, SC-DR-720197, May 1972.

3. W. B. Benedick, Sandia Laboratories, Albuquerque, unpublished work.

4. P. D. Anderson, Containment of HE Explosions in Foam-Filled Spherical Shells, Sandia Laboratories, SC-DR-72-0591, August 1972.

5. G. E. Barr and D. A. Dahlgren, Confinement of a Detonation, Sandia Laboratories, SC-RR-72-0748, May 1973.

6. R. R. Boade, "Experimental Shock-Loading Properties of Porous Materials and Analytical Methods to Describe these Properties," Shock Waves and the Mechanical Properties of Solids, Syracuse University Press, Syracuse, N. Y., 1971.

7. B. M. Butcher and C. H. Karnes, Dynamic Compaction of Porous Iron, Sandia Laboratories, SC-RR-67-3040, April 1968.

8. R. R. Boade, Fitting Porous Material Hugoniot Data to the P-α Model and Some Hugoniot Data for a Pressed Copper Powder, Sandia Laboratories, SC-RR-69-364, July 1969.

9. R. R. Boade, "Principal Hugoniot, Second-Shock Hugoniot and Release Behavior of Pressed Copper Powder," J. of Applied Physics, Vol. 41, No. 11, October 1970.

10. R. R. Boade, "Compression of Porous Copper by Shock Waves," J. of Applied Physics, Vol. 39, No. 12, 1968.

11. R. M. German and V. Ham, Distended Iron for Energy Absorption Applications, Sandia Laboratories, SLL-73-0309, February 1974.

12. P. H. Prasthofer, "Static Compaction Properties of Distended Iron," unpublished research.

13. W. Herrman, "Constitutive Equation for the Dynamic Compaction of Ductile Porous Materials," J. of Applied Physics, Vol. 40, No. 6, May 1969.

14. J. E. Kennedy, Gurney Energy of Explosives: Estimation of the Velocity and Impulse Imparted to Driven Metal, Sandia Laboratories, SC-RR-70-790, December 1970.

15. T. A. Duffey, "Scaling Laws for Fuel Capsules Subjected to Blast, Impact, and Thermal Loading," 1971 Intersociety Energy Conversion Engineering Conference Proceedings, SAE, p. 38, August 1971.

16. "Behavior and Utilization of Explosives in Engineering Design," Proceedings of the 12th Annual Symposium, New Mexico Section ASME, Universtiy of New Mexico College of Engineering, March 1972.

17. G. E. Duvall and G. R. Fowles, "Shock Waves," High Pressure Physics and Chemistry, Vol. 2, Academic Press, 1962.

18. L. Davison, Sandia Laboratories, Albuquerque, unpublished work.

19. D. B. Hayes, Introduction to Stress Wave Phenomena, Class Notes, Sandia Laboratories, SLA-73-0801, August 1973.

20. R. J. Lawrence and D. S. Mason, WONDY IV - A Computer Program for One-Dimensional Wave Propagation With Rezoning, Sandia Laboratories, SC-RR-710284, August 1971.

21. S. E. Benzley and L. D. Borthoff, TOODY II-A, A Computer Program for Two-Dimensional Wave Propagation, Sandia Laboratories, SC-DR-69-516, 1969.

ANALYSIS OF CONCRETE ARCH MAGAZINE USING FINITE ELEMENT TECHNIQUES

J. M. Ferritto
Civil Engineering Laboratory
Naval Construction Battalion Center
Port Hueneme, California

The existing standard earth-covered concrete arch igloo magazine has been analyzed using finite element techniques and found capable of withstanding a total long-duration dynamic pressure of 25 psi (172 kPa) from the detonation of a nuclear weapon. The arch load capacity was increased to a limit of 100 psi (690 kPa) by the addition of soil fill above the structure and on its sides to produce a much flatter slope, reducing drag and reflected pressures.

INTRODUCTION

The Department of Defense has for many years stored explosive components of various weapon systems in earth-mounded arch magazines or igloos. Several varieties of reinforced concrete arch igloos have been used; one of the most prevalent used has been the circular barrel arch such as the Department of the Army, Office of the Chief Engineer's standard igloo, OCE Drawing Number 33-15-06.

The arch spans about 27 feet (8.22 m) and has a height at the crown of about 13 feet (3.96 m). The thickness of the reinforced concrete varies from 16 inches (0.4 m) at the base to 6 inches (0.15 m) at the crown. Reinforcing steel in the direction of the arch consists of No. 5 bars at 12-inch (0.30 m) centers on each face with a uniform concrete cover of 1-5/8 inches (0.041 m).

The arch igloos are covered with 2 feet (0.6 m) of soil, forming an earth berm sloping outward with a horizontal-to-vertical ratio of 2:1.

The objective of this project was to examine and upgrade the blast resistance of this arch to long-duration loading effects produced by a detonation of a nuclear weapon. The relatively steep slope of the earth berm results in an increase in loading from the reflection of the side-on overpressure blast wave and from the dynamic drag forces caused by the blast wind pressure. Further, the loading is principally on the side of the structure, producing a significantly asymmetrical loading condition on the arch. An approximate analysis indicated that the structure in its existing configuration would fail at a very low overpressure (less than 10 psi (69 kPa) side-on overpressure, equal to 25 psi (172 kPa) total dynamic pressure). To upgrade the hardness of the structure, it would be necessary to decrease the reflected pressure wave, the dynamic drag pressure, and/or the asymmetrical characteristics of the load applications. To achieve these results, it was proposed to flatten the slope to as near horizontal as possible (less than 4:1) and to increase the height of soil cover over the arch. The hardness level of the modified structure was evaluated using the finite element technique. This report presents the results of the finite element analysis and the recommended modifications to the existing structure to upgrade its hardness to a side-on overpressure level of 100 psi (690 kPa).

ANALYSIS OF ARCH STRUCTURE

Finite Element Technique

The finite element method idealizes a continuum as an assemblage of a finite number of discrete structural elements interconnected at a number of joints or nodal points. This discussion considers planar sections idealized by being segmented into quadrilaterals. The program used in this study was NONSAP [1,2], a structural analysis program for static and dynamic analysis of nonlinear structural systems. The University of California at Berkeley (under sponsorship of the Bureau of Mines) and Engineering/Analysis Corporation (under contract from CEL) developed the program.

Two element types were used in this study -- the truss and the two-dimen-

sional continuum. The truss element has two nodes and is capable of transmitting axial force only. The lumped mass matrix technique was used which lumps half of the element's mass at each of the two nodes. The two-dimensional continuum element is an arbitrary quadrilateral shape used in this case to represent the plane strain idealization. The element may have any number of nodes between four and eight. Nodes above four are considered as midside nodes. Displacement interpolation functions are written to include midside nodes and are omitted when not used. The mass of the element is lumped equally at all of its node points. The program can perform a dynamic analysis by either numerical time integration or an eigenvalue method of mode superposition.

Material Models

Linear material properties were defined using a Young's modulus for truss elements and by a Young's modulus and Poisson's ratio for two-dimensional continuum elements. Nonlinear properties for the truss elements were defined by a series of stress and strain points. Nonlinear two-dimensional continuum elements were defined by a series of points at which the loading bulk modulus, unloading bulk modulus, and shear modulus were defined as functions of the volumetric strain. Tensile stresses were limited to set values in nonlinear concrete and soil elements. The following relationships hold for plane strain problems.

$$\varepsilon_v = \frac{\sigma_a}{K} = \frac{\sigma_x + \sigma_y + \sigma_z}{E}(1 - 2\mu)$$

$$K = \frac{E}{3(1 - 2\mu)}$$

$$G = \frac{E}{2(1 + \mu)}$$

where ε_v = volumetric strain

σ_a = average stress

E = Young's modulus

μ = Poisson's ratio

K = Bulk modulus

G = Shear modulus

The nonlinear two-dimensional continuum material model used incorporates crack propagation capability. Initially, the element material is treated as isotropic. When a principal tensile stress exceeds the allowed limit, the material becomes orthotropic; and the modulus in the "cracked" direction is divided by 100 to simulate the presence of a crack.

Arch Without Soil Cover

As a preliminary step in developing an understanding of the behavior of the structure, it was decided to study the arch by itself without any soil cover. A model was developed having 72 two-dimensional continuum elements to represent the concrete and 72 truss elements to represent the reinforcing steel (Figure 1). The base of the arch was restrained (or fixed) against translation and rotation.

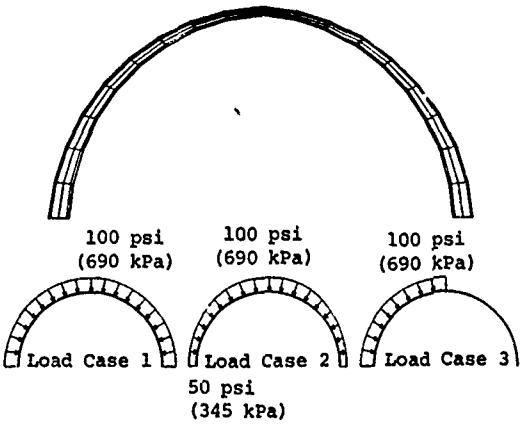


Figure 1. Finite Element mesh of arch without soil cover.

The material properties of the arch were considered to be linear. The Young's modulus of steel reinforcing was assumed to be 29,000,000 psi (2.0×10^8 kPa), and the area of the truss elements representing the steel was determined by dividing the actual bar area by the bar spacing. In this manner, the steel reinforcement was represented as a continuum through the length of the arch, allowing, the use of a planar model. The dynamic concrete material in the two-dimensional continuum elements was modeled by an average Young's modulus of 3,000,000 psi (2.06×10^7 kPa) and a Poisson's ratio of 0.17.

Load Case 1. A uniform static pressure of 100 psi was applied around the arch. The thrust at the crown was computed by integrating the element stress contributions over the cross section. This value was found to be approximately equal to the thrust computed by simple pipe formula.

conc ele 3,464 psi x 1.625 sq in. = 5,630 lb
conc ele 2,786 psi x 1.375 sq in. = 3,830 lb
conc ele 2,156 psi x 1.375 sq in. = 2,970 lb
conc ele 1,511 psi x 1.625 sq in. = 2,460 lb
steel truss ele force = 769 lb
steel truss ele force = 414 lb

Total thrust = 16,073 lb (71,500 N)

$$\sigma = Prt$$

$$P = \frac{\sigma}{rt}$$

where σ = Pipe compression stress

r = Pipe radius (160 inches in this case)

t = Pipe wall thickness

σ/t = Pipe thrust

P = 16,073/160 = 100 psi (690 kPa)

The deflection of the crown of the arch was 0.0506 inch (1.42 mm). This demonstrates the inherent stiffness of the arch section in symmetrical ring compression. The region with highest stress was the crown section. The arch structures were constructed a number of years ago with a design concrete strength of 2,500 psi (17,240 kPa). Applying a dynamic increase factor of 1.25 plus an age factor, ultimate concrete strengths of 4,000 psi (27,580 kPa) would not be considered excessive. By assuming a 4,000-psi (27,580-kPa) dynamic concrete strength, one would expect that the formation of the first hinge point at the crown would occur at a uniform pressure of 140 psi (965 kPa). This is based on the stress in element 27 (2,840 psi, 19,581 kPa) and assumes crushing of the concrete cover. The steel stress would be above dynamic yield in compression (assumed to be 48,000 psi, 330,960 kPa). The ductility of this section is severely limited by the buckling of the reinforcement and by the minimum depth of the section at the crown. Because the arch has a varying thickness, the formation of a second hinge would not occur; rather a spreading of the existing area of crushing, followed by collapse, would be expected.

Load Case 2. In case 2, the arch was loaded with a symmetrical static pressure of 50 psi (345 kPa) at the base increasing to 100 psi (690 kPa) at the crown. This loading was thought to more accurately represent the effect of the soil cover in transmitting load to the arch. The deflection of the crown was 0.138 inch (3.5 mm). The first hinge would form at the crown at a load of about 160 psi (1103 kPa) at the crown, decreasing to 80 psi (551 kPa) at the base. The reinforcing steel would be at the yield point in compression; as in case 1 failure would occur as progressive yielding and buckling at the crown.

Load Case 3. Half the arch was loaded with a uniform pressure of 100 psi (690 kPa). Deflections were several inches. Hinging would occur at the base and at the crown region. The pressure causing the first hinge to form at the base would be about 30 psi (206 kPa). The data from the elastic analysis of the arch half loaded was very difficult to interpret. To obtain a better understanding of the failure mechanism under gross asymmetric loading, a static nonlinear analysis was performed. A bilinear concrete model with compression yielding at 4,000 psi (27,580 kPa) and tensile cracking at 400 psi (2,758 kPa) was used. The steel reinforcement was also a bilinear model both in tension and compression. Figure 2 gives the deflection of the structure. Figure 3 summarizes the arch behavior for various increments of load. The maximum capacity of the arch is about 25 psi (172 kPa). This loading condition closely represents the arch in its existing condition with minimum soil cover.

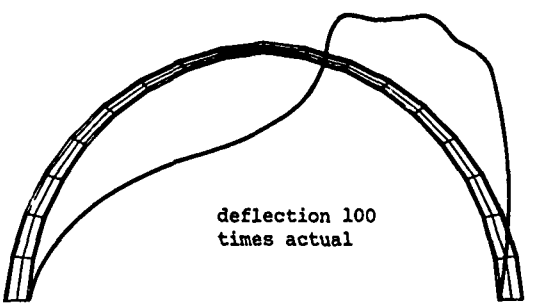


Figure 2. Deflection of arch under load case 3.

Eigenvalue Analysis. An eigenvalue analysis was performed to obtain the natural periods and mode shapes of the arch.

Arch With Soil Cover

To model the proposed method for upgrading the hardness of the structure, a second finite element mesh was prepared. In this mesh the structure was covered by soil 4 feet (1.2 m) deep above the crown and horizontal (see Figure 4). Since the mesh had a much larger number of elements, the arch was represented by a single element in thickness rather than the four elements used in the arch without soil cover. The linear material properties and arch thickness were calculated as in the equations below to produce the same elastic axial and flexural stiffness as the actual section.

$$E_s I_s + E_c I_c = E_t I_t$$

$$E_s A_s + E_c A_c = E_t A_t$$

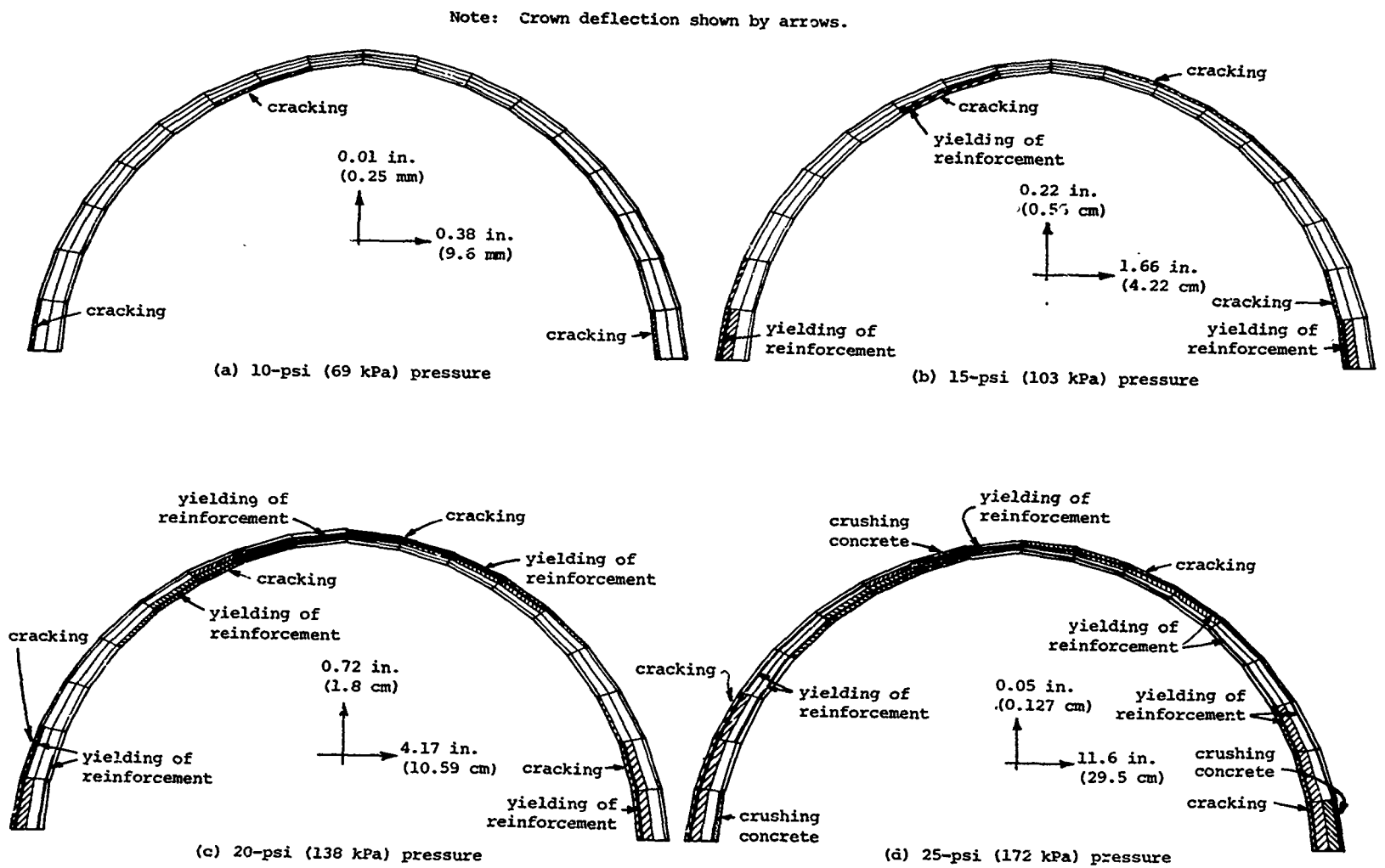


Figure 3. Behavior of arch under asymmetric load for various load increments.

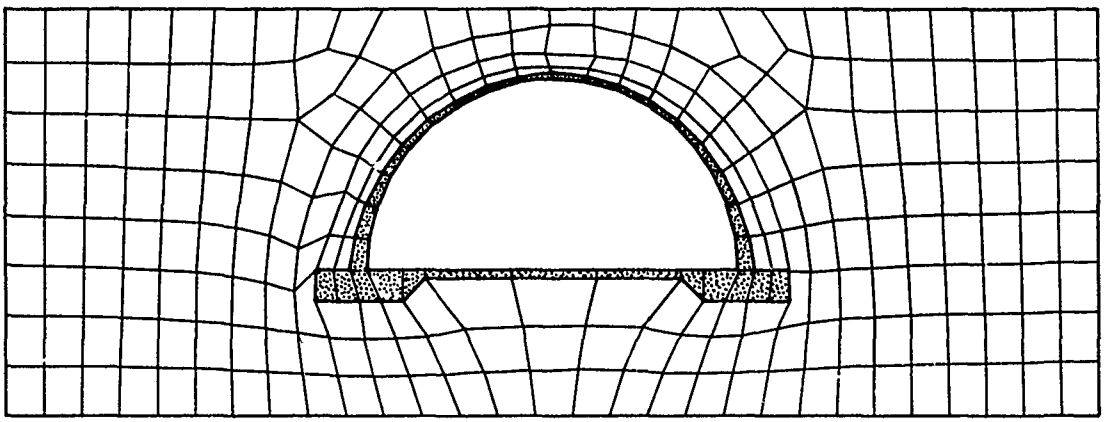


Figure 4. Finite element mesh of arch covered with soil.

where E_s = Young's modulus of steel

E_c = Young's modulus of concrete

E_t = Equivalent Young's modulus

I_s = Moment of inertia of steel

I_c = Average moment of inertia of concrete

I_t = Equivalent moment of inertia

A_s = Area of steel

A_c = Area of concrete

A_t = Equivalent area of concrete

As shown in Figure 4, a total of 266 elements and 307 node points were used in the mesh.

The portion of the mesh representing the ground surface was loaded with a 100-psi (690 kPa) static load. The thrust and moment along the arch are shown in Figure 5. Figure 6 gives the thrust-moment capacities of various sections of the arch.

The critical section is the crown section governed by thrust. By comparison of the calculated thrust-moment loading (196 kips (0.87 N) at 100 psi (690 kPa)) with the allowable thrust-moment capacity (270 kips (1.2 N)) at which yielding occurs, the pressure on the ground surface at which yield occurs is 138 psi. Since the pressure loading is nearly hydrostatic in this case, the load capacity of the arch should agree with that computed above when the arch was modeled by four elements in thickness without soil. The agreement is excellent -- 138 psi (951 kPa) to 140 psi (965 kPa) -- indicating the modeling of the arch by one-element-thick sections was accurate enough.

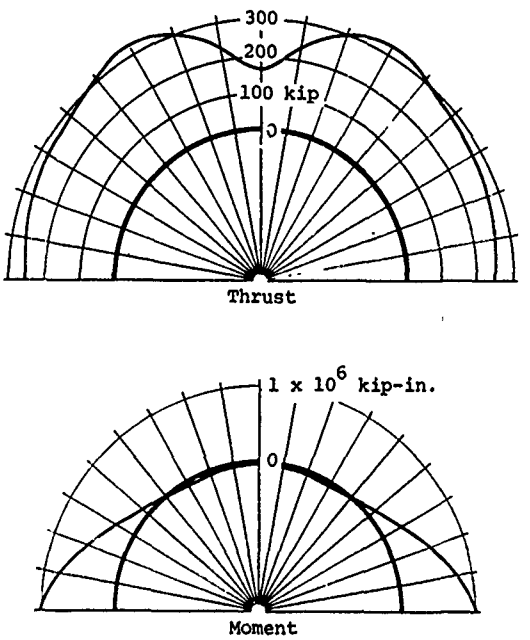


Figure 5. Thrust and moment of arch covered with soil, 100-psi static load.

An eigenvalue analysis was performed to determine mode shapes and natural periods of the arch covered with soil. The soil mass increases the natural period from 72 msec to 118 msec. The first mode shape of the arch without soil is similar to that of the arch with soil. However, higher mode shapes differ somewhat; the soil mass seems to restrain the arch.

A linear dynamic analysis was performed using the direct-integration

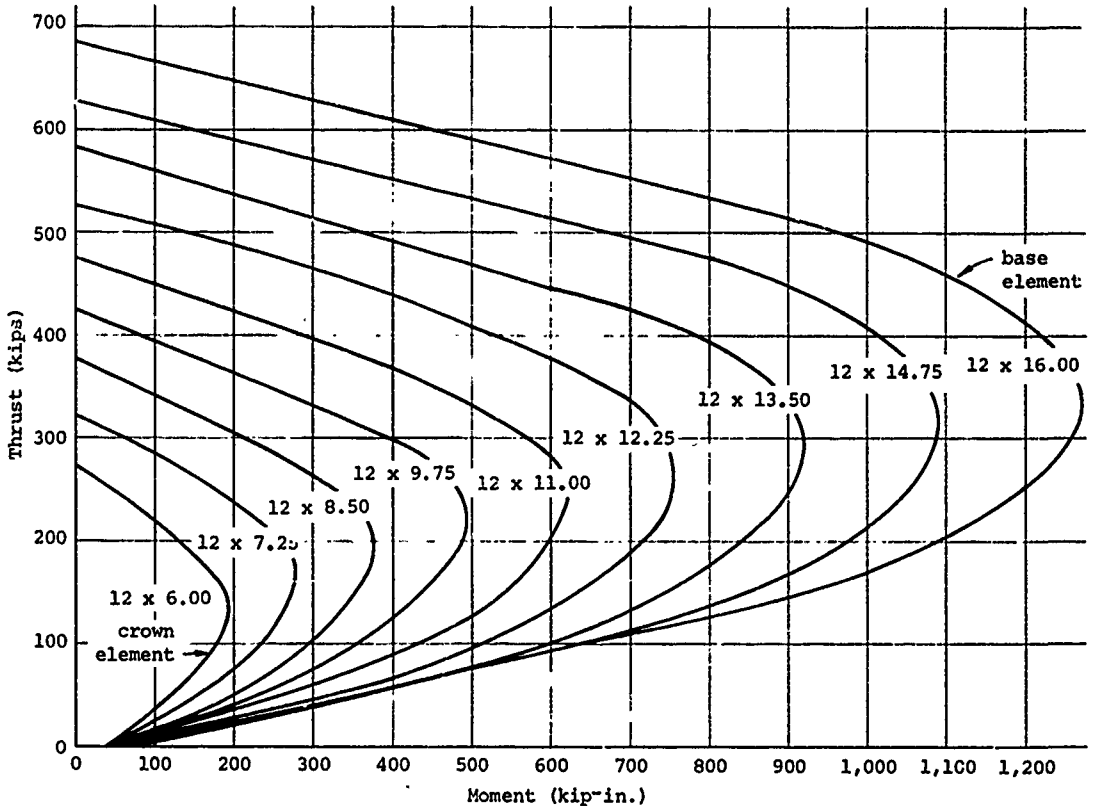


Figure 6. Thrust-moment capacity of arch sections.

method with a time increment of 0.5 msec. A 100-psi (690-kPa) traveling wave (moving from left to right) was used to load the ground surface; the pressure wave had a triangular shape with an effective positive wave duration as determined from Reference 3. The wave moved across the ground at the rate of 3 ft/msec (0.91 m/msec). Thrust-moment diagrams and pressure loads were computed for various time increments (Figure 7). The peak loading determined from the thrust-moment diagrams occurred at 34 msec. The moving wave produced a loading more asymmetric than the static loads. By using the thrust-moment loadings it was determined that the load at which the structures became inelastic (formed a first hinge) was 80 psi (551 kPa). Points of high stress (hinge formation) are shown in Figure 8. If the structure were considered as a single-degree-of-freedom system with a natural period of 118 msec, the required structural resistance for a structure to remain elastic would be 1.8 times the load or 144 psi (993 kPa) (1.8 x 80 psi (551 kPa)). Since the stresses approach the ultimate capacity of the concrete (thrust rather than moment), the probability of failure over large areas of the arch is high.

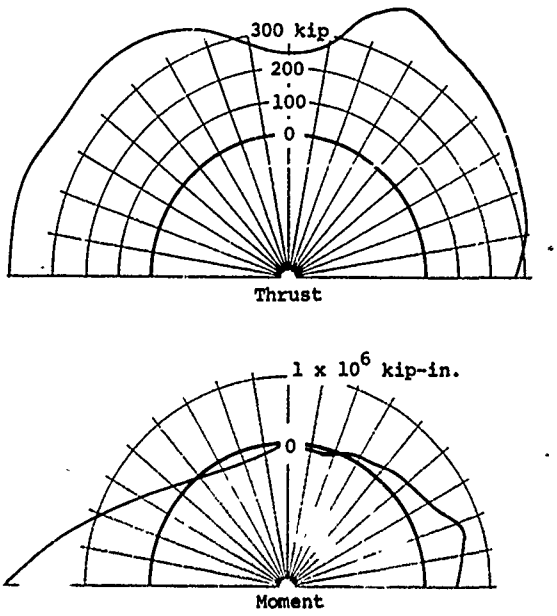


Figure 7. Thrust and moment of arch for time T = 34 msec, 100-psi (690-kPa) dynamic wave on surface.

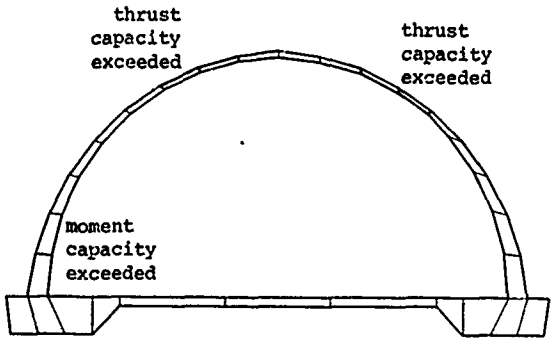


Figure 8. Points of high stress in arch at T = 34 msec.

Therefore, it is necessary that the ductility factor allowed must be low -- 1.3 to 1.5 [3]. Using the response of a single-degree-of-freedom system with a structural resistance of 144 psi (993 kPa) and a ductility factor of 1.4, the maximum total load capacity of the arch is 105 psi (724 kPa). Eliminating the dead load, the arch would be able to carry about 100 psi (690 kPa) side-on overpressure on the ground surface. This represents the maximum pressure that can be carried without structural modification of the arch. The deflection history of the crown of the arch is given in Figure 9.

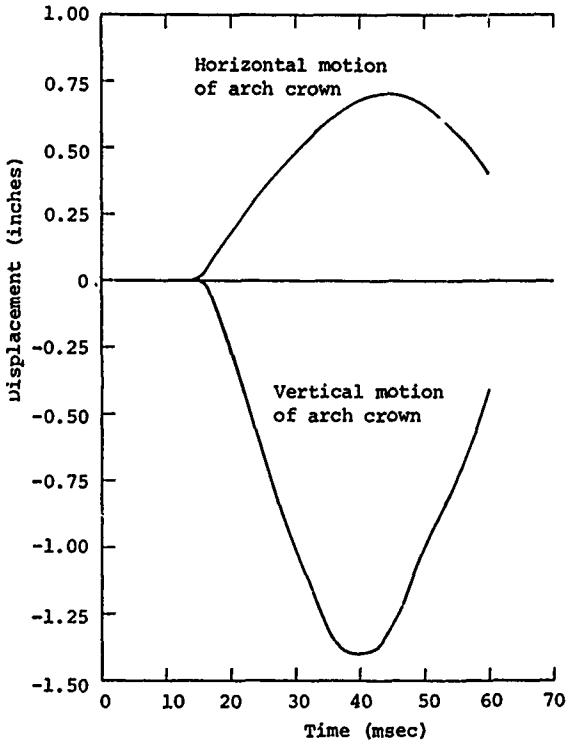


Figure 9. Deflection of crown of arch.

SUMMARY

The standard earth-covered arch was analyzed in its existing configuration and found capable of resisting a total dynamic long duration pressure of only 25 psi (172 kPa) (10 psi (69 kPa) overpressure). The loading produces an asymmetric condition mainly caused by the reflected pressure wave and the drag pressure. The soil cover above the arch was widened to flatten the slope to as near horizontal as possible. The structure was found to be capable of resisting a side-on overpressure of 100 psi.

REFERENCES

1. Engineering Analysis Corporation. E/AC Report 74-2: User's manual for N NONSAP, by K. J. Bathe and F. E. Peterson. Berkeley, CA (CEL Contract No. N62399-73-C0019) (under preparation).

2. Engineering Analysis Corporation. E/AC Report 73-3: July 1974. Theoretical basis for NONSAP, by K. J. Bathe and F. E. Peterson. Berkeley, CA (CEL Contract N62399-72-C0010) (under preparation).

3. Air Force Special Weapons Center. AFSWC TDR 62-138: Air Force Design Manual: Principles and practices for design of hardened structures. Kirtland Air Force Base, NM.